



The
University
Of
Sheffield.

**Utilising Intermolecular Interactions to
Propagate and Sustain a Series of Porous
Materials**

Thomas Michael Roseveare

**A thesis submitted to The University of Sheffield in partial fulfilment of the
requirements for the degree of Doctor of Philosophy**

Department of Chemistry

University of Sheffield

Sheffield, S3 7HF

February 2018

"Excellere Contende"

Dedicated to my family

Table of Contents

Abstract	vi
Author's Declaration	viii
Acknowledgements	ix
Abbreviations and Acronyms	x
Chapter 1: Crystal Engineering and Dynamic Porous Crystals: An Introduction	
1.1 Crystal Engineering	1
1.2 Intermolecular Interactions	1
1.2.1 Hydrogen Bonding	1
1.2.2 Halogen Bonding	2
1.2.3 Ionic Interactions	3
1.2.4 π - π Interactions	3
1.2.5 Dispersion Interactions	4
1.3 Coordination Polymers	4
1.4 1st, 2nd and 3rd Generation of Porous Coordination Polymers	5
1.5 Gas adsorption: Classification of Isotherms	8
1.6 An Example of Dynamics in 3D	9
1.7 An Example of Dynamics in 2D	11
1.8 An Example of Dynamics in 1D	13
1.8.1 The 1D Coordination Polymer $[M_2(bz)_4(pyZ)]_n$	13
1.8.2 Functionalised 1D Paddlewheel Systems	16
1.9 Porosity of Molecular Crystals	20
1.10 Conclusion	23
1.11 References	24
Chapter 2: Probing the Porosity of a Family of 1D Halogen-Functionalised Coordination Polymers	
2.1 Introduction	33
2.2 Aims	35
2.3 Experimental	36
2.3.1 Synthetic Procedures	36
2.3.1.1 Synthesis of $[Cu_2(4Ibz)_4(pyZ)]_n$ (2.1(I))	37
2.3.1.2 Synthesis of $[Cu_2(4Brbz)_4(pyZ)]_n$ (2.2(Br))	37
2.3.1.3 Synthesis of $[Cu_2(4Clbz)_4(pyZ)]_n$ (2.3(Cl))	37
2.3.1.4 Synthesis of $[Cu_2(4Fbz)_4(pyZ)]_n$ (2.4(F))	38
2.3.2 Single-Crystal X-Ray Diffraction	38
2.3.3 Powder X-Ray Diffraction (PXRD)	38
2.3.4 Volumetric Nitrogen and Carbon Dioxide Adsorption Studies	39
2.3.5 <i>In situ</i> Powder X-Ray Diffraction Studies during CO ₂ Adsorption and Desorption	39
2.3.6 <i>In situ</i> Single-Crystal X-Ray Diffraction Studies during CO ₂ Adsorption and Desorption	40

2.4 Results and Discussion	41
2.4.1 Synthesis of 2.1(I) , 2.2(Br) , 2.3(Cl) and 2.4(F)	41
2.4.2 Crystal Packing	42
2.4.3 Volumetric N ₂ and CO ₂ Gas Adsorption	49
2.4.4 <i>In situ</i> Powder Diffraction Studies During CO ₂ Adsorption/Desorption	53
2.4.5 <i>In Situ</i> Single-Crystal Diffraction Studies During CO ₂ Adsorption/Desorption	59
2.4.6 Crystallographic Determination of CO ₂ molecule location(s)	67
2.5 Conclusion	72
2.6 Future Work	73
2.7 References	75
2.8 Appendix	79
Appendix 2.8.1: Single-Crystal Data	79
Appendix 2.8.2: <i>In situ</i> PXRD Data	79
Appendix 2.8.3: <i>In situ</i> Single-crystal Data	83
Chapter 3: Further Functionalisation of a Family of 1D Halogen-Functionalised Coordination Polymers	
3.1 Introduction	91
3.2 Aims	93
3.3 Experiment	94
3.3.1 Synthetic Procedures	94
3.3.1.1 Synthesis of [Cu ₂ (4Ibz) ₄ (NH ₂ pyz)] _n (3.1(I))	95
3.3.1.2 Synthesis of [Cu ₂ (4Brbz) ₄ (NH ₂ pyz)] _n (3.2(Br))	95
3.3.1.2 Synthesis of [Cu ₂ (4Clbz) ₄ (NH ₂ pyz)] _n (3.3(Cl))	96
3.3.1.2 Synthesis of [Cu ₂ (4Fbz) ₄ (NH ₂ pyz)] _n (3.4(F)).....	96
3.3.2 Single-Crystal X-Ray Diffraction	97
3.3.3 Powder X-ray Diffraction (PXRD)	97
3.3.4 Thermogravimetric Analysis (TGA)	98
3.3.5 Single-Crystal Desolvation Studies.....	98
3.3.6 Volumetric Nitrogen and Carbon Dioxide Adsorption Studies	99
3.3.7 <i>In situ</i> Powder X-ray Diffraction during CO ₂ and N ₂ Adsorption and Desorption	100
3.3.8 <i>In situ</i> Single-Crystal X-Ray Diffraction Studies during CO ₂ and N ₂ Adsorption and Desorption	100
3.4 Results and Discussion	101
3.4.1 Synthesis of 3.1(I) , 3.2(Br) , 3.3(Cl) and 3.4(F)	101
3.4.2 Crystal Packing	102
3.4.3 Thermogravimetric Analysis	109
3.4.4 Desolvation studies.....	110
3.4.5 Volumetric N ₂ and CO ₂ Gas Adsorption	113
3.4.6 <i>In situ</i> Powder Diffraction and Single-Crystal Studies during CO ₂ Adsorption/Desorption	120

3.4.6.1 Overview.....	120
3.4.6.2 Study of 3.2(Br)	121
3.4.6.3 Studies of 3.3(Cl)	122
3.4.6.4 Studies of 3.4(F)	125
3.4.6.5 Summary.....	128
3.4.7 <i>In situ</i> Powder and Single-Crystal Diffraction Studies during N ₂ Adsorption/Desorption.....	129
3.4.7.1 Overview.....	129
3.4.7.2 Studies of 3.3(Cl)	130
3.4.7.3 Studies 3.4(F)	131
3.4.7.4 Summary.....	133
3.4.8 Crystallographic Determination of CO ₂ and N ₂ molecule location(s)	133
3.4.8.1 Single-crystal diffraction studies	133
3.4.8.2 Powder diffraction studies	136
3.4.8.3 Summary.....	142
3.5 Conclusions	142
3.6 Future Work	143
3.7 References	144
3.8 Appendices.....	148
Appendix 3.8.1: Single-Crystal Data.....	148
Appendix 3.8.2: <i>In situ</i> PXRD Data	150
Appendix 3.8.3: <i>In situ</i> Single-Crystal Data	155
Appendix 3.8.4: TGA	161
Chapter 4: Gaseous Guest Inclusion within a Family of Halogen-Functionalised Stellated Molecular Clusters	
4.1 Introduction	165
4.2 Aims	170
4.3 Experimental.....	171
4.3.1 Synthetic Procedure.....	171
4.3.1.1 Synthesis of [Cr ₃ O(4-Ibz) ₆ (MeOH) ₃][NO ₃] (4.1(I))	171
4.3.1.2 Synthesis of [Cr ₃ O(4-Brbz) ₆ (MeOH) ₃][NO ₃] (4.2(Br))	172
4.3.1.3 Synthesis of [Cr ₃ O(4-Clbz) ₆ (MeOH) ₃][NO ₃] (4.3(Cl))	172
4.3.2 Single-Crystal X-Ray Diffraction	172
4.3.3 Thermogravimetric Analysis (TGA)	173
4.3.4 Single-Crystal Desolvation Studies.....	173
4.3.5 Powder X-Ray Diffraction Analysis and Aging Studies	174
4.3.6 Volumetric Nitrogen and Carbon Dioxide Adsorption Studies	174
4.3.7 Gravimetric Carbon Dioxide Adsorption Studies	175
4.3.7.1 CO ₂ Uptake of 4.1(I) at 298 K	175

4.3.7.2 CO ₂ Uptake of 4.2(Br) at 298 K	175
4.3.7.3 CO ₂ Uptake of 4.3(Cl) at 298 K.....	176
4.3.8 <i>In situ</i> Powder X-Ray Diffraction during CO ₂ Adsorption and Desorption	176
4.3.9 <i>In situ</i> Single-crystal X-Ray Diffraction Studies during CO ₂ Adsorption	176
4.4 Results and Discussion	177
4.4.1 Synthesis of 4.1(I) , 4.2(Br) and 4.3(Cl)	177
4.4.2 Crystal Packing	177
4.4.3 Thermogravimetric analysis (TGA).....	181
4.4.4 Single-Crystal Desolvation Studies.....	185
4.4.5 Powder X-Ray Diffraction (PXRD) Aging Studies	191
4.4.6 Volumetric and Gravimetric N ₂ and CO ₂ Adsorption Studies for 4.1(I) , 4.2(Br) and 4.3(Cl)	193
4.4.7 <i>In situ</i> Powder X-Ray Diffraction and Single-Crystal Diffraction Studies During CO ₂ Adsorption/Desorption.....	197
4.4.7.1 Overview.....	197
4.4.7.2 Studies of 4.1(I)	197
4.4.7-3 Studies of 4.2(Br)	199
4.4.7-4 Study of 4.3(Cl)	200
4.4.7-5 Structural Characterisation	201
4.4.7-6 Conclusion	202
4.5 Conclusion.....	203
4.6 Future Work	204
4.7 References	205
4.8 Appendices.....	211
Appendix 4.8.1 Single-Crystal X-Ray Diffraction Data	211
Appendix 4.8.2 Powder X-Ray Diffraction Data	212
Appendix 4.8.3 <i>In situ</i> Powder X-Ray Diffraction Data	214
Appendix 4.8.4 <i>In situ</i> Single-Crystal X-Ray Diffraction Data	215
Chapter 5: Solvent-Induced Structural Transformations with a Porous Molecular Solid	
5.1 Introduction	219
5.2 Aims	222
5.3 Experimental	222
5.3.1 Synthetic Procedure.....	222
5.3.2 Mechanochemical Liquid-Assisted Grinding (LAG)	223
5.3.3 Powder X-Ray Diffraction of LAG samples	223
5.3.4 Crystallisation of 5(Br) Solvates.....	223
5.3.5 Thermogravimetric Analysis	224
5.3.6 <i>In situ</i> Powder X-Ray Diffraction Studies during Variable Temperature.....	224
5.3.7 <i>In situ</i> Single-Crystal Diffraction Studies during Variable Temperature	224

5.4 Results and Discussion	225
5.4.1 Synthesis	225
5.4.2 Mechanochemical Solvent Screening	225
5.4.3 Structural Characterisation and Thermal Stability Tests of 5(Br)·CHCl₃	228
5.4.4 Thermal Stability Tests of 5(Br)·toluene and 5(Br)·p-xylene	231
5.4.5 Thermal Stability Tests of 5(Br)·o-xylene and 5(Br)·DCM	233
5.4.6 Thermal Stability tests of 5(Br)·m-xylene	234
5.5 Conclusions	235
5.6 Future Work	236
5.7 References	238
5.8 Appendices	241
Appendix 5.8.1 Mechanochemistry and Aging PXRD Data	241
Appendix 5.8.2 Variable Temperature PXRD Data.....	242
Appendix 5.8.3 Variable Temperature Single-Crystal Data.....	251
Chapter 6: Overall Conclusions	
6.1 Overall Conclusions	253
6.2 References	254

Abstract

Overview

The work presented in this thesis focuses on guest inclusion in a series of 1D coordination polymer and molecular crystals all featuring halogen functionality. This work seeks to understand the porous properties of the materials as function of the halogen present.

Chapter 1 acts as an overview of crystal engineering, intermolecular interactions and dynamic porous materials. This brief overview of porous materials focuses on 3D, 2D, 1D and molecular porous crystals with a common paddlewheel secondary building unit (SBU).

Chapter 2 reports a family of halogen functionalised 1D coordination polymers, $[\text{Cu}_2(4\text{Xbz})_4(\text{pyz})]_n$ (4Xbz = 4-halobenzoate, pyz = pyrazine and X = I, Br, Cl and F). Prior to this work three of the four polymers (X = I, Br and Cl) had been reported to have halogen-dependent gated CO_2 inclusion properties. This chapter focuses on understanding the halogen-dependent CO_2 inclusion via a series of *in situ* powder and single-crystal diffraction studies under increasing (and decreasing) pressures of CO_2 . This work concluded that guest inclusion was directly related to the shifting apart of 1D coordination polymers and, as a consequence, a disruption of the halogen-bonding interactions. It was also noted that the location of the gaseous guest was consistent with locations observed in some analogous coordination polymers.

Chapter 3 extends the work presented in Chapter 2 with functionalization of the pyrazine linker to produce a series of analogous 1D coordination polymers ($[\text{Cu}_2(4\text{Xbz})_4(\text{NH}_2\text{pyz})]_n$). The presence of the amine group on the pyrazine linker resulted in the formation of solvates using the same synthetic methods employed in Chapter 2 as well as an absence of interpenetration and large solvent-filled voids in the case of the iodo-functionalised polymer (**3.1(I)**). The production of solvates led to investigation of different solvent systems and desolvation methods to obtain solvent-free forms of the coordination polymers. The solvent-free polymers were then tested for gaseous guest inclusion (N_2 and CO_2), firstly using volumetric analysis and then using *in situ* single-crystal and powder diffraction studies while exposing crystalline materials to increasing (and decreasing) pressures of gas. This work demonstrated that the introduction of the amino-functionality results in a shift in the gate pressure for CO_2 adsorption, relative to polymers in Chapter 2, but had minimal effect on location of gaseous guests within the pores.

Chapter 4 describes a study designed to exploit packing inefficiencies of a series of inorganic stellated clusters, $[\text{Cr}_3\text{O}(4\text{Xbz})_6(\text{MeOH})_3][\text{NO}_3]$ (X = I, Br and Cl), which are based on a common SBU featured in MOF research. Synthesis of this family of stellated clusters resulted in a consistent packing motif for the three clusters and solvent-filled cavities. The clusters were tested for thermal stability and it was concluded that solvent loss could be achieved at room temperature. Crystalline samples were then tested for stability when stored in air and for gaseous guest inclusion (N_2 and CO_2). Gaseous guest inclusion was demonstrated by volumetric and gravimetric adsorption and by *in situ* crystallographic studies, but the samples underwent a phase transformation when stored in air which made the samples' guest inclusion potential less clear.

The final chapter of this thesis probes the stability of a potential organic molecular porous material, 2,4,6-tris(4-bromophenoxy)-1,3,5-triazine (**5(Br)**), which had been previously reported in three distinct phases. Mechanochemical liquid-assisted grinding (LAG) was used to screen a series of solvents and identify solvents that produce the desired inclusion phases. These LAG experiments were successful in identifying solvents of interest as well as a 4th, previously unreported, guest-included phase. The stability of the guest-included phases were in turn tested at room temperature and high temperature using powder diffraction. This revealed the phase with large open channels was level stable than the phase with discrete cavities. The as yet unreported phase also was shown to undergo a single-crystal-to-single-crystal phase transformation upon removal of solvent.

Author's Declaration

The work presented in this PhD thesis, with the exception of the gravimetric adsorption data presented in Chapter 4, is the original work of the author. The gravimetric adsorption studies were performed and analysed in collaboration with Dr. Craig McAnally and Dr. Ashleigh Fletcher at the University of Strathclyde. The rest of the work within these pages was conducted at and with the support of the University of Sheffield and Diamond Light Source. The conclusions and views expressed are those of the author and not the previously mentioned institutions.

Thomas Roseveare

February 2018

Acknowledgements

First and foremost I would like to thank and acknowledge my supervisor, Prof Lee Brammer, for guiding me through this project and ensuring that I stayed focused and considered the final goals of each piece of work. Thanks also for giving me the freedom and support to pursue other research interest and extra-curricular activities.

Secondly I would like to thank the Brammer group for culturing a fun and constructive environment to work in. I will always remember the fish mugs, the top trumps, the bespoke t-shirts, the late nights (early mornings) at Diamond with random videos made more hilarious by sleep deprivation. During my time in the group I have got to know some great friends and I would like to thank them all. The first generation of group members I would like to thank, let's call them the supervisors, Inigo, Jason, Adrian and Ramida for welcoming me into the group and initially supporting me through my first year when I was bright-eyed MChem student. The second generation I would like to thank, the collaborators, Elliot, Craig, Rebecca and Jamie for being open to research/non-research discussion and valuing my opinions despite being out of my depth on many occasions. The final generation of the group I would like to thank, the new members, Stephen, Feifan and Danny for continuing the friendly culture of the group and being patient during these last few months. I would also like to thank the numerous MChem and summer students for their involvement in forwarding my own personal research interests, the interests of the group and helping me in becoming a better supervisor/teacher.

I would also like to thank the fantastic support staff and the department in general for ensuring the department and analytical services run smoothly without them I wouldn't be able to complete the majority of this work. Thanks also go to the support staff at Diamond Light Source (especially Mark) for development of the facilities that allowed me to carry out the *in situ* diffraction studies. Special mention goes to Harry for training me to use diffraction software in the third year of my undergraduate and during my PhD trusting me to assist him in troubleshooting diffractometer issues; you have truly taught me more than I can remember. A special mention also goes to Craig in his new role as service crystallographer for being open to our suggestions and keeping me on my toes with crystallography questions.

Throughout my PhD I have also been heavily involved in teaching, through the Graduate Teaching Assistant scheme, and would like to thank the teaching staff and postgraduate demonstrator that have made the undergraduate labs an enjoyable environment to teach in. I would especially like to thank Colin for being open to suggestions and changes and Julie for giving me the opportunity to teach in China.

I would also like to thank the postgraduate community within the department, especially the Ward, Weinstein, Dawson and Foster groups, for making the department an enjoyable place to work as well as providing lively discussions, which often got livelier at the pub, on a wide spectrum of topics. I would especially like to thank Theo and the enablers for their support and being open to attending numerous random events in obscure venues in Sheffield and, often, further afield. I wish to, also, acknowledge the fine pubs and coffee shops in this exceptional city for providing me with great food, drink and memories. Finally I would like to thank my entire family, to whom this thesis is dedicated to, for their support and acceptance of my absent mindedness within these last few months. I couldn't have done this without you.

Abbreviations and Acronyms

NH₂pyz = Aminopyrazine

1,4-BDCH₂ = 1,4-benzenedicarboxylic acid

1,4-BDC = 1,4-benzenedicarboxylate

2-X-1,4-BDC = functionalised 1,4-benzenedicarboxylate

bz = Benzoate

n-Xbz = n-functionalised benzoate (n = 2, 3 or 4)

4-Xbz = 4-Xbenzoate (X = F, Cl, Br, I, OMe)

3-Xbz = 3-Xbenzoate (X = F, Cl or Me)

BnOH = benzyl Alcohol

CSD = Cambridge Structure Database

cent = centroid

4-Cl-2-OMebz = 4-Chloro-2-methoxybenzoate

DABCO = 1,4-diazabicyclo[2.2.2]octane

DCM = Dichloromethane

2,3-diFbz = 2,3-difluorobenzoate

diMepyz = 2,3-dimethylpyrazine

EtOH = Ethanol

Etpyz = Ethylpyrazine

EtMepyz = 2-Ethyl-3-Methylpyrazine

HOF = Hydrogen-Bonded Organic Framework

IUPAC = International Union of Pure and Applied Chemistry

LAG = Liquid- Assisted Grinding

MAC = Multiple Analysing Crystal

MOF = Metal-Organic Framework

MeCN = Acetonitrile

MeOH = Methanol

Mepyz = Methylpyrazine

H₂muco = *trans,trans*-muconic acid

P = pressure

p/p⁰ = relative pressure

PeOH = Pentanol

PrOH = Propanol

4-Phbz = 4-phenylbenzoate

phen = phenazine

ppeb = 4-[(perfluorophenyl)ethynyl]benzoate

PSD = Position-Sensitive Detector

Pyz = Pyrazine

Ypyz = functionalised pyrazine

PXRD = Powder X-Ray Diffraction

SBU = Secondary bridging unit

Sol = solvent

TGA = Thermogravimetric Analysis

THF = tetrahydrofuran

Chapter 1:

Crystal Engineering and Dynamic Porous Crystals: An Introduction

1.1 Crystal Engineering

The field of X-ray crystallography recently celebrated its centenary.¹ During this time this analytical technique has gone from data acquisition times of days to minutes. This has allowed for this static technique, routinely used for determining the structure of simple small molecules to complex macromolecules, to be used to record the dynamic phase transformations observed when crystalline materials are perturbed. These processes allow for better understanding of crystalline materials when exposed to external stimuli (light, heat or pressure).

The development of X-ray crystallography and its ability to observe the packing of molecules in the solid state led to the development of a new field of chemical research namely crystal engineering. The field of crystal engineering uses commonly observed packing traits, intermolecular interactions and coordination bonding to produce crystalline materials with specific properties. This field has, in part, progressed due to the continued development of the CSD (Cambridge Structure Database)²⁻⁶ a repository of small molecule crystal structures. The CSD has allowed for data mining of the 900,000+ structures within the database and has resulted in the identification of common intermolecular interaction motifs,⁷ as well as making informed decisions relating to structure prediction,² pharmaceutical therapeutics⁸ and the identification of new porous materials.^{6,9,10} The CSD has also transformed the ability to educate students and the public on both crystallography and the broader context of chemistry with the ability to easily visualise^{11,12} or even 3D-print¹³ chemical structures and visualise the interactions between molecules⁷ in the solid state.

The informed approach made possible through repositories like the CSD, coupled with the constant development of diffraction capabilities at synchrotron and other radiation sources, such as Diamond Light Source^{14,15} in the UK, makes the field of crystal engineering an exciting and dynamic area of research.

1.2 Intermolecular Interactions

A key component of crystal engineering is applying the knowledge of common interaction motifs observed between functional groups. These intermolecular interactions are weaker than covalent and coordination bonding, but nevertheless it is often these weaker forces that dictate how systems pack in the solid state. These forces can also be harnessed when designing porous materials to have a preference for an intended guest, by tailoring the functionality decorating the pore walls¹⁶ to possess favourable host-guest interactions. Generally, intermolecular interactions are highly variable, ranging from the potential of being highly directional and almost predictable to being highly diffuse and unpredictable. This section is intended to introduce the concepts of intermolecular interactions and the types that are observed within the solid state.

1.2.1 Hydrogen Bonding

The first of these intermolecular interactions, the hydrogen bond, is the most studied of intermolecular interactions. These forces, referred to as the key to molecular recognition,¹⁷ are responsible for many physical and chemical phenomena. From the anomalous boiling point of water to the secondary structures of biological systems, hydrogen bonding is responsible for

them all. These interactions, as the name suggests, occur between a hydrogen atom (a hydrogen bond donor) and an acceptor. The hydrogen bond donor (referred to as D–H) possess a positive electrostatic potential on the hydrogen. This positive potential in turn interacts with a negative electrostatic potential present on a hydrogen bond acceptor (referred to as A) forming a favourable interaction. These interactions are stronger and more directional (favouring a 180° D–H⋯A angle¹⁷) (**Figure 1.2.1-1**) than non-directional dispersion interactions. The strength of these interactions means they are commonly observed within the solid state. The predictability also results in these interactions being greatly utilised in the field of crystal engineering with certain functional groups having very predictable hydrogen bonding capabilities. For example a carboxylic acid group possesses both a hydrogen donor (the hydroxyl group) and acceptor (the carbonyl). This functionality can form a range of different hydrogen bond motifs (**Figure 1.2.1-2**) including hydrogen bonding dimers and polymeric chains. The hydrogen bonding motif formed is often dictated by the rest of the molecule the carboxyl is attached to.

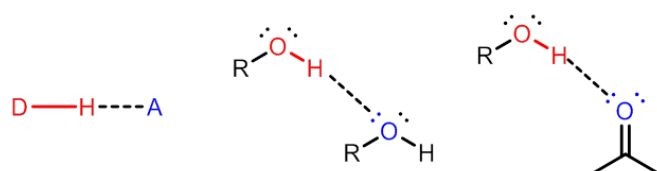


Figure 1.2.1-1. Hydrogen bonding interactions

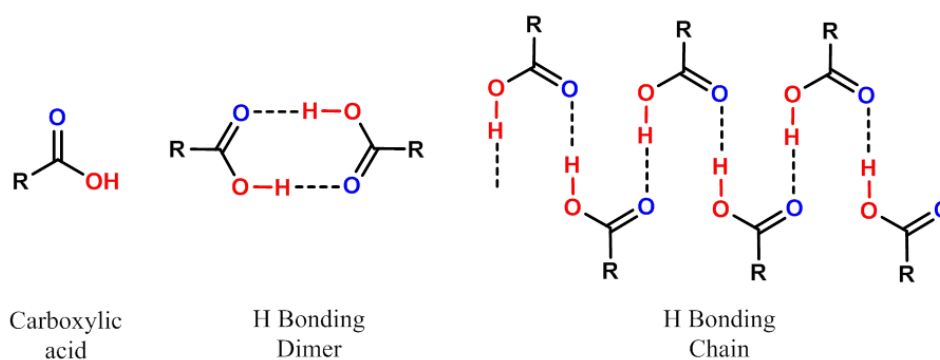


Figure 1.2.1-2. Hydrogen bonding motifs formed with carboxylic acids

1.2.2 Halogen Bonding

The halogen bonds are similar in strength to hydrogen bonds and have more predictable directionality. These interactions, as the name suggests, are comparable to hydrogen bonds^{17,18} consisting of an interaction between a halogen (or halogen bond donor, instead of a hydrogen bond donor) and an acceptor (similarly to the hydrogen bond donor being an area of negative electrostatic potential). These interactions occur, in the case of a carbon-halogen bond as the halogen bond donor, due to the electrostatic potential around the halogen being negative perpendicular to the bond with the region of halogen *trans* to its σ -bond possessing an area of positive electrostatic potential. This positive potential is often referred to as a “ σ -hole”¹⁹ and the size and strength of this σ -hole is dependent on both the halogen and the environment of the halogen (**Figure 1.2.2-1**). Looking at halogens in the same environment (analogous molecules) the trend is such that the largest σ -hole is observed for iodine and the σ -hole decreases as you move up the group (**Figure 1.2.2-1**). The presence of the σ -hole allows for the halogen to

interact with a series of different electronegative functional groups (**Figure 1.2.2-1**). Due to the halogen possessing both areas of positive and negative potential halogen bonding can occur between two halogens (**Figure 1.2.2-1**). This halogen-halogen interaction is observed in two distinct motifs referred to as type I and type II (**Figure 1.2.2-1**).²⁰⁻²² Type I interactions are largely dispersion driven and arguably not halogen bonds, where the two R-X...X angles are equivalent. Type II interactions are classified as halogen bonds and are when one of the R-X...X angles is ca. 90° with the other angle is ca. 180°.

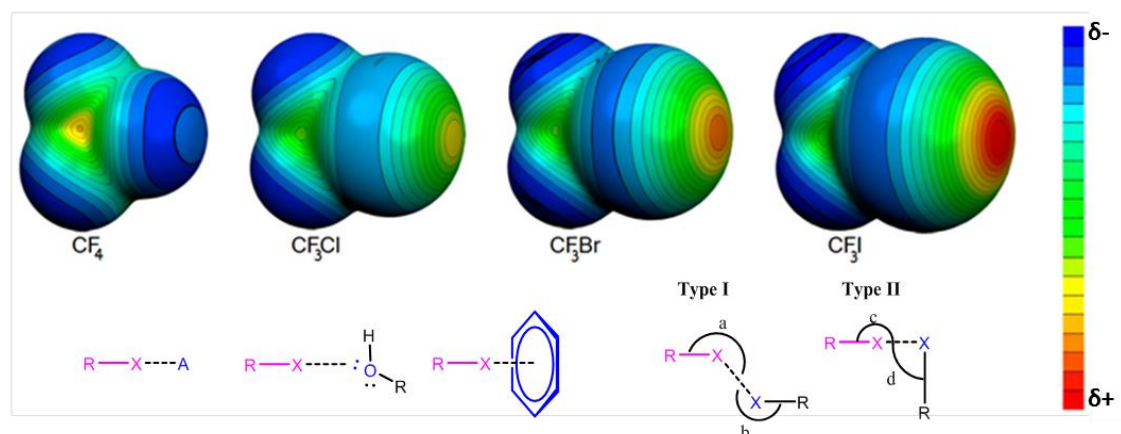


Figure 1.2.2-1. Halogen Bonding. Image, in part, adapted from reference 19 with permission

Halogen bonding interactions have proven to be an interesting and useful field of study within crystal engineering with work focusing on fundamental understanding and competition with hydrogen bonding,^{23,24} providing insight within the pharmaceutical industry.^{22,25-27} Halogen bonding has also proved to be a useful tool within supramolecular chemistry²⁸ and catalysis.^{29,30} They have also been employed to produce molecular systems which could exhibit intrinsic or extrinsic porosity.^{31,32} More recently research has also focused on characterising intermolecular interactions of other p-block elements (chalcogen, pnictogen and tetrel bonding).³³

1.2.3 Ionic Interactions

Not to be confused with coordination bonding, ionic interactions occur between charged atoms or molecules. As well as being strong intermolecular interactions between oppositely charged atoms or molecules they also lead to an overall neutral species. These ion-ion interactions are comparable in strength to a covalent bond.³⁴ These interactions are not directional, but negatively charged counter-ions of metal complexes often feature in secondary intermolecular interactions³⁴ such as hydrogen or halogen bonding.

1.2.4 π - π Interactions

The delocalisation of π -systems leads to a series of interactions which can occur between aromatic systems (**Figure 1.2.4-1**).^{34,35} These possibilities are face-to-face, where the two rings (one electron-rich and one electron-poor) directly overlay one another, offset where the rings only partially overlay one another and edge-to-face interaction, where two rings are perpendicular to one another. As well as forming a series of $\pi \cdots \pi$ or C-H $\cdots\pi$ interactions, the delocalised system possesses a large area of negative electrostatic potential, which can act as a halogen bond acceptor, analogous to an edge-to-face interaction (**Figure 1.2.2-1**).³⁶

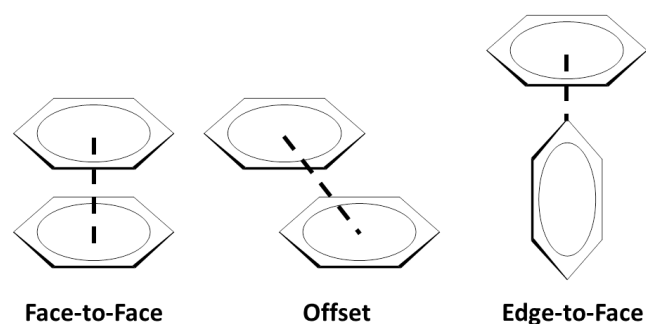


Figure 1.2.4-1. Type of $\pi\cdots\pi$ stacking interactions

1.2.5 Dispersion Interactions

Finally the weakest and least directional of the intermolecular interactions are dispersion interactions, or van der Waals interactions, which occur through the interaction of instantaneous dipoles between functional groups. These interactions are weaker than the more directional interactions previously discussed. However large non-polar regions of a molecule (e.g. long alkyl chains) can lead to a significant interaction within the solid state and can also dictate the secondary structure of a variety of supramolecular systems dependent of solvent environment.

1.3 Coordination Polymers

Coordination polymers consist of inorganic coordination nodes (or secondary building units, SBUs) connected by multi-topic organic linkers (**Figure 1.3.1**). Despite being proposed as early as 1959³⁷ it was not until the late 80s that this field of research started to grow.^{38–40} Following the initial synthesis of these inorganic polymeric systems it was shown that they could possess a large potential for porosity.^{41–43} The regular polymeric structure with large pore spaces has meant that coordination polymers have been tested for a range of applications including gas storage and separation,^{44,45} drug delivery,^{46,47} catalysis^{48–50} and sensing.^{51,52}

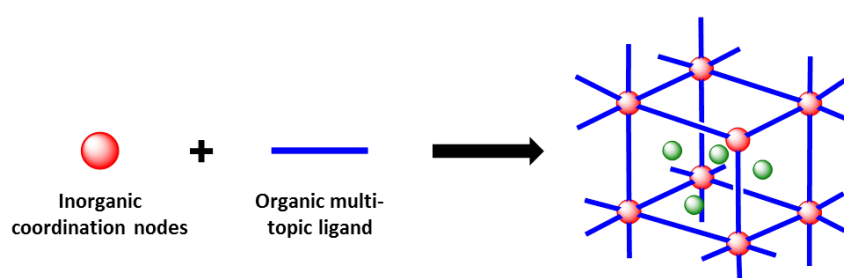


Figure 1.3-1. Schematic of a coordination polymer

Part of the reason this class of materials has garnered a lot of attention is the versatility of these systems. Firstly a range of metal coordination nodes (**Figure 1.3-2**) can be produced based on the metal selected and secondly this node can be combined with a plethora of different organic linkers to obtain multiple different topologies with a range of different pore spaces. For example, the paddlewheel inorganic coordination node (**Figure 1.3-3**) consists of two M(II) metal centres connected with four bridging carboxylates (site 1) and the two axial sites available for a second linker (site 2). This SBU is very versatile with the ability to produce 3D networks, 2D grids,

1D chains or molecular clusters dependent on the linkers selected. This versatility coupled with the fact that the organic linkers can be functionalised, allows for the production of multiple coordination polymers with multiple topologies and multiple interior functionality of the pore spaces within them.

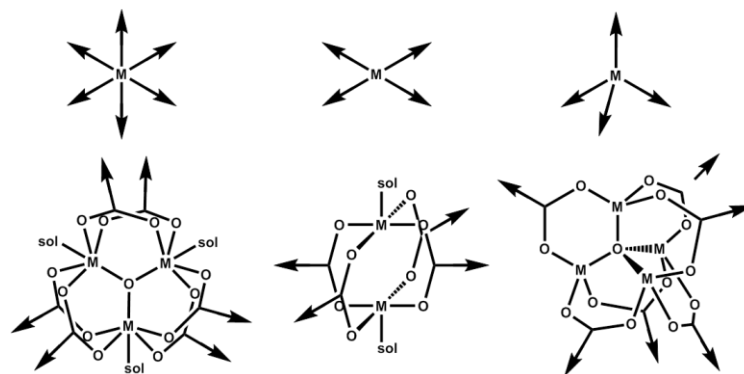


Figure 1.3-2. Examples of secondary building units (SBUs).

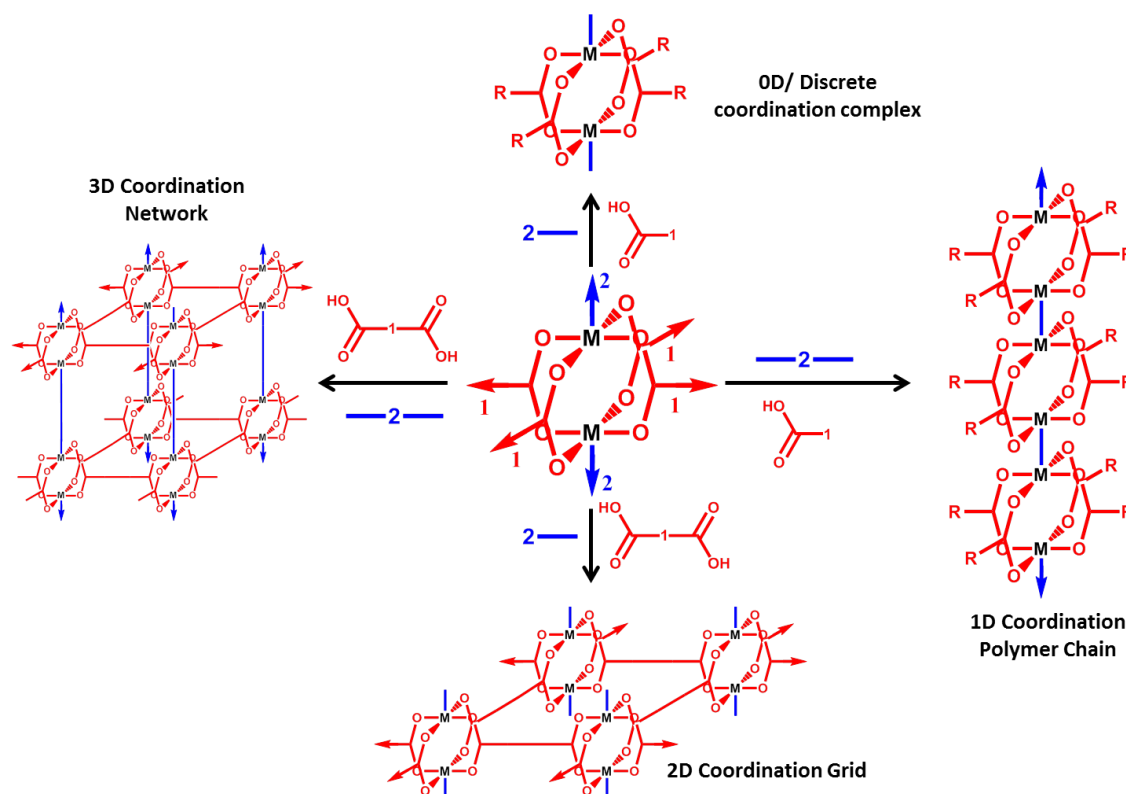


Figure 1.3-3. The paddlewheel SBU, which can be used to produce a range of different coordination polymers.

1.4 1st, 2nd and 3rd Generation of Porous Coordination Polymers

As the field of coordination polymers progressed, with more examples being tested for gas adsorption, it was noted by Kitagawa^{53,54} that although the majority of these materials maintained rigidly defined pores in the presence and absence of guest molecules, there were an increasing number of examples that did not behave like this. Kitagawa has charted the evolution of porous behaviour in these materials by defining three different generations of porous coordination polymers (Figure 1.4.1). First generation porous coordination polymers contained

pore spaces in the as-synthesised form with the synthesis solvent present within the pores. Upon desolvation of a 1st generation material an irreversible collapse of the pore would occur, with addition of the original solvent or a secondary guest being unable to reverse the collapse. Second generation materials, where the majority of materials are now grouped, contain rigidly defined pores which showed minimal change in the presence or absence of guest. Finally, 3rd generation materials would undergo structural changes, often involving pore closing, upon desolvation, but would reopen upon reintroduction of the original guest or a secondary guest. The discovery of 3rd generation materials was promising, providing the potential of designing materials with pore spaces that will selectively include guest molecules or change shape to form more favourable host-guest interactions.

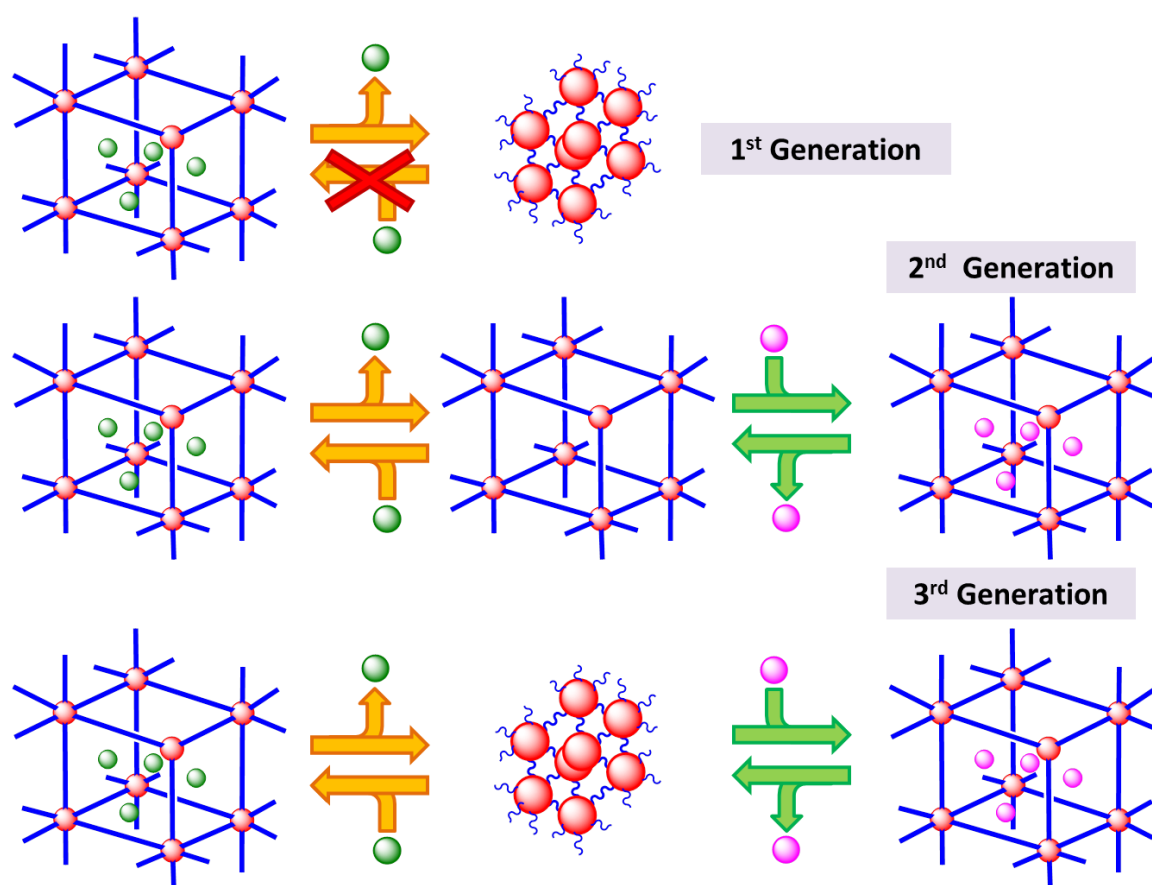


Figure 1.4-1. 1st, 2nd and 3rd Generation porous coordination polymers

Kitagawa⁵⁴ also observed four main modes of dynamic guest response (**Figure 1.4-2**). The first being an induced fit, where the pore contracts to allow the pore to adopt a size and shape complementary to the guest included. The second is by breathing where the pore initially is smaller than the guest but can expand to accommodate the guest. The third transition is a guest-exchange transformation (or deformation), where the introduction of a new guest invokes a phase transition and the new guest displaces the original guest. The final transition is what Kitagawa refers to as a healing type pore, where removal of the guest results in a collapse of the pore completely, much like a 1st generation porous materials, however on reapplication of the guest and the pores expand to re-accommodate the guest. These processes can improve guest retention, due to the pore shape changing to improve host-guest interactions. These dynamic

responses, especially the ones exhibiting pore expansion, can also lead to higher uptake in comparison to the initial void space. These dynamic motions occur in different ways depending on the connectivity of the coordination polymer (3D frameworks, 2D grids or 1D chains), which will be discussed in subsequent sections.

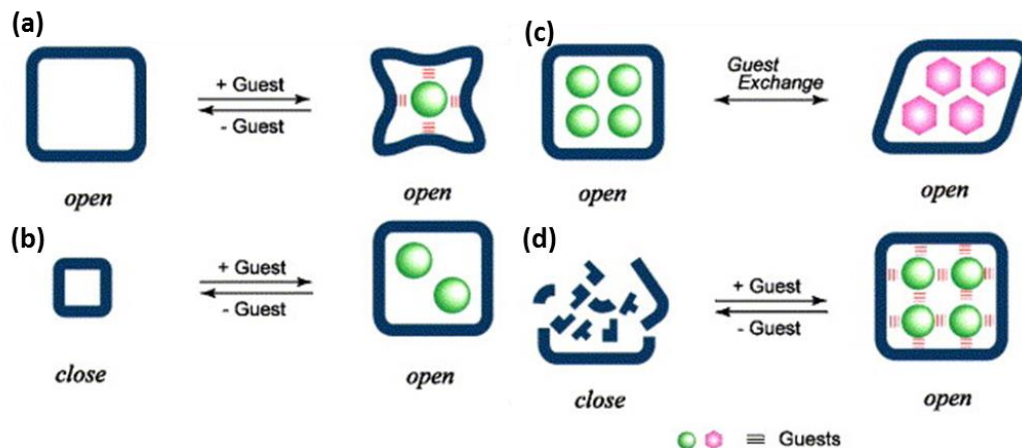


Figure 1.4-2. Four types of dynamic response observed by Kitagawa. Reproduced from reference 54 with permission.

The dynamics of 3rd generation porous materials have been observed through three main methods of analysis. The first is comparison of crystalline samples following synthesis, activation and solvent exchange (**Figure 1.4-3**). Comparison of the packing can lead to identification of discrepancies in packing. A packing discrepancy, however, is inconclusive in isolation, being the properties of a 1st generation materials, therefore re-introduction of the guest (or a second guest) is required. The second method of analysis (inclusion experiments) typically involves volumetric or gravimetric gas adsorption (**Figure 1.4-3**). The adsorption experiments often display multi-step gated expansion and hysteresis, which could be interpreted as a dynamic pore opening. The third method of analysis is to record diffraction data while perturbing the crystalline material with temperature or pressure. These experiments are useful for identifying guest sites⁵⁵ but also helps to determine whether the material undergoes a structural change (**Figure 1.4-3**).⁵⁶ Ideally these *in situ* diffraction studies would be recorded while adsorption isotherms are also being carried out allowing for uptake and structural changes to be quantified on the same sample.⁵⁷⁻⁶⁰

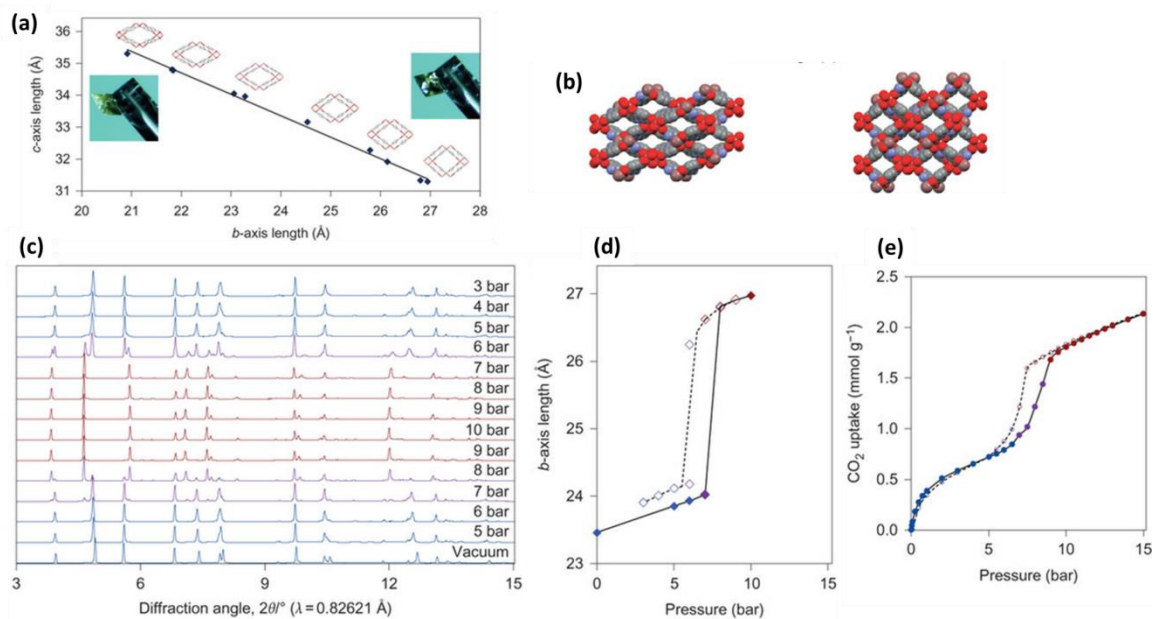


Figure 1.4-3. A 3rd generation porous material reported by the Brammer Group⁶¹ where (a) single-crystal heating study demonstrated a change in the *c*- and *b*-axes. (b) The large structural change as a result of solvent loss. (c) In situ PXRD study with increasing CO₂ pressure (298 K). (d) *b*-axis vs. pressure of the in situ PXRD study. (e) Gravimetric CO₂ adsorption (298 K) performed. Images adapted from reference⁶¹ with permission.

1.5 Gas adsorption: Classification of Isotherms

A technique that has been heavily used within the field of coordination polymer research in the context of gas storage and separation is gas adsorption analysis (either gravimetric or volumetric). These techniques have allowed determination of the quantity of adsorbate (guest) included, as well as the shape of the isotherm being attributed to different types of adsorption. In 1985 an IUPAC (International Union of Pure and Applied Chemistry) commission sought to classify the types of adsorption isotherms and concluded that there were six main isotherm curves.⁶² These six isotherms were widely accepted within the scientific community, but the field was reviewed again 30 years later in a second IUPAC technical report which identified some slight caveats to the previously defined six isothermal curves (**Figure 1.5-1**).⁶³

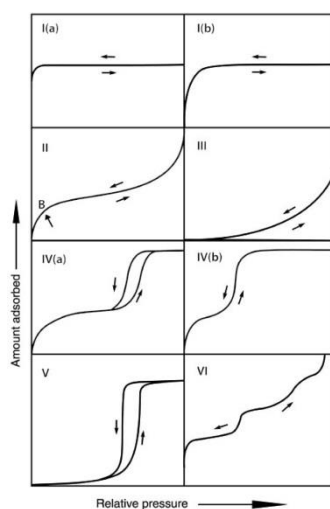


Figure 1.5-1. The IUPAC adsorption isotherm classifications © as reported in 2015 and published by De Gruyter.⁶³

Type I isotherms consist of reversible adsorption and desorption curves with high uptake at low relative pressure (p/p^0). This type of isotherm is typically observed in microporous systems (pore size < 2 nm, e.g. activated carbon or zeolites).⁶³ The high uptake at low p/p^0 is due to enhanced adsorbent-adsorptive interactions in narrow pores. This isotherm also features two subsets (Type I(a) and Type I(b)), Type I(a) for materials with mainly micropores and Type I(b) in materials that have a larger pore size distribution featuring both micropores and mesopores (2.5 nm). Type II isotherms also feature reversible adsorption and desorption curves with an initial adsorption curve present (up to point B) followed by a secondary uptake (after point B). This type of isotherm is observed for nonporous or macroporous materials (pore size > 50 nm) with adsorption before point B being monolayer coverage and after point B as a result of multilayer coverage. Type III isotherms feature reversible adsorption and desorption curves with minimal uptake at low p/p^0 with uptake at higher p/p^0 . The lack of uptake at low p/p^0 is indicative of an absence of monolayer coverage as a result of weak adsorbent-adsorbate interactions. The uptake at higher p/p^0 occurs as a result of molecular clustering leading to multilayer coverage around favourable sites in the materials.⁶³ Type III isotherms are typically observed for nonporous or macroporous materials with weak host-guest interactions. Type IV isotherms consists of initial uptake at low pressure followed by a gated uptake at higher p/p^0 , the desorption either results in hysteretic properties (Type IV(a)) or a reversible desorption (Type IV(b)). This type of isotherm occurs in mesoporous materials (pore size 2-50 nm) with the isotherm initially demonstrating monolayer coverage, followed by molecular clustering and condensation of the adsorbate within a the pores. Hysteresis (Type IV(a)) is observed in cases where pore spaces are wider than 4 nm, the hysteretic behaviour being due to pore blocking or narrow pore openings. The lack of hysteresis (Type IV(b)) occurs for materials with pore spaces smaller than 4 nm, typically these pores are cylindrical or conical in shape with tapered pore openings.⁶³ Type V isotherms display minimal uptake of low p/p^0 with a large inclusion of guest occurring at a gate pressure. This isotherm is typically observed in micro- or mesoporous materials with weak adsorbent-adsorbate interactions, with the large uptake at higher p/p^0 being as a result molecular clustering followed by pore filling. Finally type VI features reversible adsorption and desorption curves with initial uptake at low p/p^0 followed by a series of clearly defined steps as p/p^0 is increased. This isotherm occurs as a result of layer-by-layer coverage of a uniform nonporous surface.⁶³

1.6 An Example of Dynamics in 3D

A 3D coordination network consists of organic linkers and coordination nodes that propagate the network in three dimensions. The network is constrained by coordination bonding in 3D leading to two possible modes of pore space flexibility (**Figure 1.6-1**). The first occurs when a 3D network is interpenetrated, this allows for the two independent networks to universally shift relative to one another resulting in a dynamic pore space.⁶⁴⁻⁶⁷ Alternatively dynamic 3D frameworks can be achieved through the use of flexible linkers or coordination geometries.⁶⁸ This dynamic behaviour often occurring through hinge bending of bridging carboxylates (**Figure 1.6-2**)⁶⁹⁻⁷⁴ or through distortion of the coordination geometry at the metal centre.^{61,75,76}

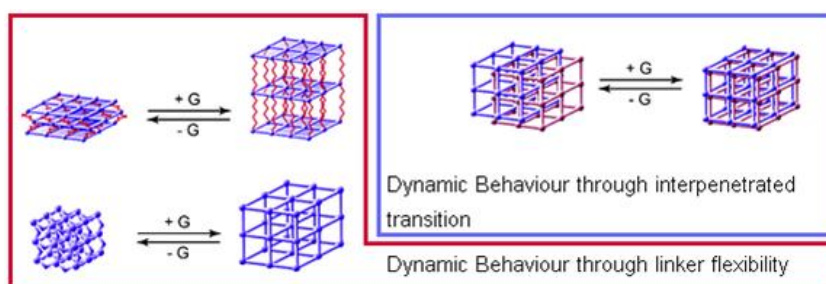


Figure 1.6-1. Modes of guest inclusion in 3D coordination polymer. Image adapted from reference 53 with permission.

One particular example of a dynamic 3D coordination polymer is $[\text{Zn}_2(1,4\text{-BDC})_4(\text{DABCO})]$ (1,4-BDC = 1,4-benzenedicarboxylate, DABCO = 1,4-diazabicyclo[2.2.2]octane) which forms a pillared framework (**Figure 1.3-3**). It was observed that this pillared framework would undergo guest-dependent phase transformations which involve a change in the $\text{Zn}_{2(\text{cent})}\cdots\text{O}_{2(\text{cent})}\cdots\text{ring}_{(\text{cent})}$ angle (cent = centroid) (**Figure 1.6-2**). This angle is guest dependent, with pore spaces narrowing when solvents were included and expanding upon solvent removal (activation) (**Figure 1.6-2**).⁷⁴ It was also demonstrated that this flexibility often led to stepped adsorption isotherms with promising guest selectivity.^{77,78}

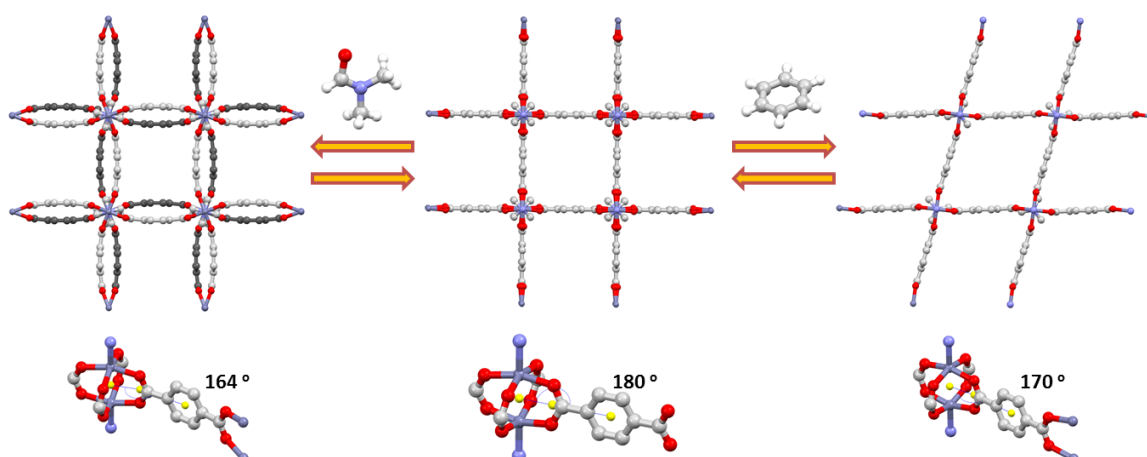


Figure 1.6-2. The guest-dependent structures of $[\text{Zn}_2(1,4\text{-BDC})_4(\text{DABCO})]$ ⁷⁴ and the variation in $\text{Zn}_{(\text{cent})}\cdots\text{O}_{2(\text{cent})}\cdots\text{ring}_{(\text{cent})}$ angle. Colour scheme Zn, metallic blue; C, grey (dark and light to highlight variation between layers); O, red; N, blue, centroid, yellow. Solvent, hydrogens and disorder omitted for clarity.

Later studies of this system nicely highlight the versatility of coordination polymers, with initial studies demonstrating that guest uptake could be tailored with the use of mixed metal systems (Zn and Cu).⁷⁹ Work also focused on synthesising functionalised versions (2-X-1,4-BDC, X = NH_2 , NO_2 , Br, Cl or OH)^{80–83} as a method of tailoring the flexibility of the material. Further work led to using these functional groups (X = NH_2 or OH) as reactive components which could be further functionalised allowing for modulation of the flexibility as well as tailoring the selectivity of the material.^{16,84–90} It was also observed that flexibility was not exclusive to the Zn system, with examples of Co systems having similar properties.^{91–93} Further work also explored whether this flexibility could be achieved with different dicarboxylate linkers, which either showed analogous flexibility^{94–97} or that the substituent present had a significant effect on the pore spaces.^{98,99}

1.7 An Example of Dynamics in 2D

A 2D grid exhibit three main mechanism of dynamic behaviour, which are, in part, dictated by the packing of the grids. The first involves similar ligand or SBU flexibility to that observed in the 3D framework described in Section 1.5. This allows for adaptation of pore space within the 2D grids.^{100–103} The other two depend on how the layers stack on top of one another (**Figure 1.7-1**). The grids stack either with inorganic coordination nodes eclipsed or offset (**Figure 1.7-1**). These two stacking motifs lead either to 1D channels running through the material (eclipsed nodes) or to discrete cavities (offset nodes). Therefore a dynamic response can be observed by shifting of layers, resulting in cavities converting into channels and allowing for guest inclusion.^{104–108} Alternatively, if the 2D grids feature pendant groups protruding above and below the layers, causing interdigitation (**Figure 1.7-1**), the interdigitation limits the ability for layers to slide and generate channels running through the 2D layers. Therefore guest channels are formed by 2D layers moving apart (**Figure 1.7-1**).^{109–113}

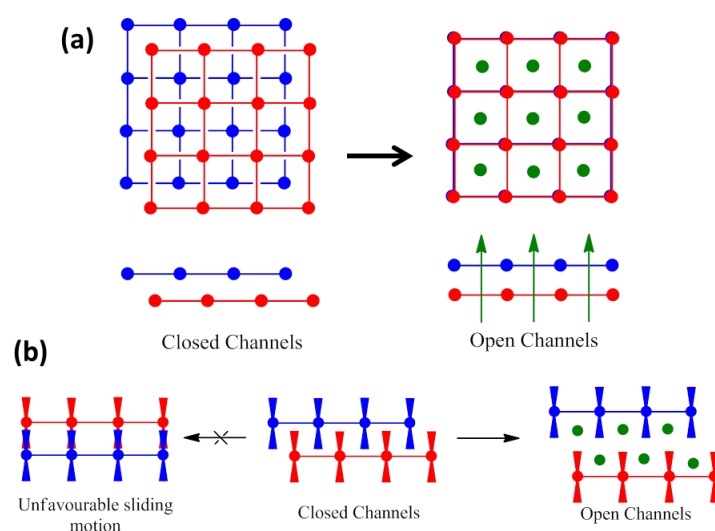


Figure 1.7-1. The two possible motions of 2D coordination polymer layers (a) shifting of layers parallel to layer propagation and (b) moving apart of layers perpendicular to layer propagation.

Continuing the theme of coordination polymers constructed with the paddlewheel SBU leads to a slight change in application focus for 2D grids. The layers typically pack in an offset motif with reports demonstrating improved gas uptake through pillaring of 2D grids to form 3D frameworks.^{114,115} One of these studies, by Chen and co-workers,¹¹⁵ demonstrated that a reversible 2D to 3D transformation could be achieved from $[\text{Zn}_2(1,4\text{-BDC})_4(\text{H}_2\text{O})_2]$ to the pillared MOF discussed in Section 1.5, $([\text{Zn}_2(1,4\text{-BDC})_4(\text{DABCO})])$ (**Figure 1.7-2**). This work also showed promising selectivity of C_2H_2 over CO_2 and CH_4 in the case of the 2D grid, with the adsorption isotherm showing a gated adsorption of C_2H_2 (**Figure 1.7-2**). This gate could correspond to some dynamic motion, but further *in situ* diffraction or spectroscopic work was not undertaken.

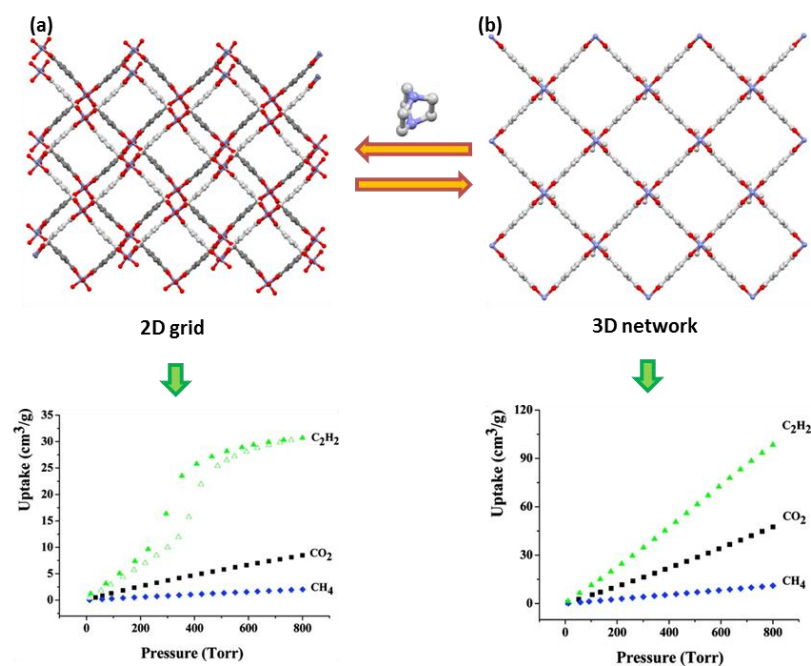


Figure 1.7-2. The reversible pillaring from (a) $[\text{Zn}_2(1,4\text{-BDC})_4(\text{H}_2\text{O})]$ to (b) $[\text{Zn}_2(1,4\text{-BDC})_4(\text{DABCO})]$ and the effect this has on volumetric adsorption (296 K). Colour scheme consistent with **Figure 1.6-2**. Volumetric isotherms replicated from reference ¹¹⁵ with permission.

The primary focus for these 2D grids has been removal of the axial sites,¹¹⁶ leading to vacant metal sites for use in catalysis, later work leading to delamination of a bulk material to produce metal-organic nanosheets^{117–121} with potential applications in catalysis and as membranes for gas separation.^{122,123} This has meant that less focus has been placed on these materials for their potential dynamic behaviour. Work has, however, demonstrated that uptake and selectivity can be achieved dependent on the ligand present of the axial sites.^{124–126} One nice example presented Mir and co-workers¹²⁶ reports four 2D grids constructed with either 1,4-benzenedicarboxylic acid (1,4-BDC_{H2}) or *trans,trans*-muconic acid (H₂muco) and 4-halopyridine (Cl or Br) coordinated in the axial positions (**Figure 1.7-3**). The two different dicarboxylates lead to two distinct halogen-bonding interactions, a X $\cdots\pi$ interaction for the 1,4-BDC systems and a type I²² X \cdots X interaction for the muco systems (**Figure 1.7-3**). These two halogen-bonding interactions lead a variation in the offset nature of the 2D grids resulting in one network which adsorbs CO₂ (the muco systems) and the 1,4-BDC network not adsorbing CO₂.*

* The absence of CO₂ gas adsorption is stated for the BDC systems, but the adsorption isotherms are not reported within this paper.

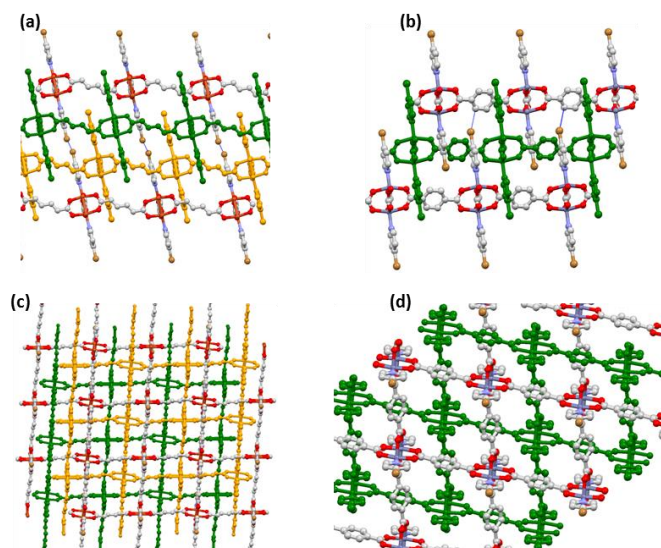


Figure 1.7-3. The two different halogen-bonding interactions for (a) $[\text{Zn}_2(\mu\text{co})_4(4\text{-Brpy})_2]$ and (b) $[\text{Zn}_2(1,4\text{-BDC})_4(4\text{-Brpy})_2]$ (4-Brpy = 4-bromopyridine)¹²⁶ and (c and d) the effect these interactions have on the stacking of 2D layers. Colour scheme consistent with **Figure 1.6-2**, off-set layers in yellow and green.

1.8 An Example of Dynamics in 1D

Dynamic behaviour can occur by two means in 1D coordination polymer. The first simply involves the coordination polymers shifting a part from one another (**Figure 1.8-1**),^{127,128} which leads to an expansion in the channels presents in the crystal or a conversion of pore space from discrete cavities to channels. The second occurs as a result of straightening of a zig-zag chain (**Figure 1.8-1**),^{128,129} which occurs through changes in the angle between the SBU and the propagating linker.

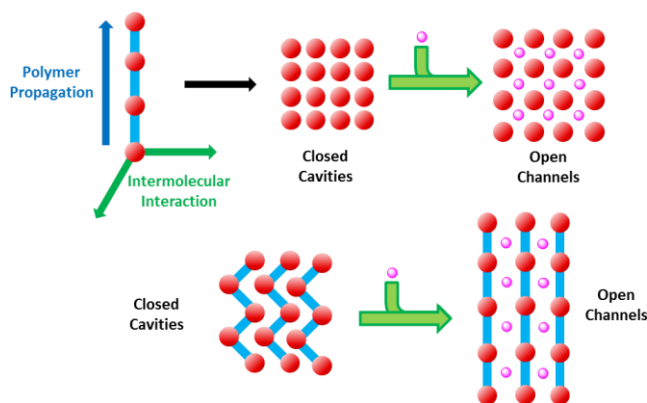


Figure 1.8-1. Modes of dynamic response possible for 1D coordination polymers

1.8.1 The 1D Coordination Polymer $[\text{M}_2(\text{bz})_4(\text{pyz})]_n$

One particular, well-studied, 1D coordination polymer, which has shown to include a variety of different guests (**Table 1.8.1-1**), is $[\text{M}_2(\text{bz})_4(\text{pyz})]_n$ (M = Cu or Rh, bz = benzoate and pyz = pyrazine). This polymer consists of the same paddlewheel SBU previously discussed connected with pyrazine linkers (**Figure 1.8.1-1**). The polymer chains in turn pack in a parallel arrangement, with neighbouring chains being offset, leading to offset $\pi \cdots \pi$ stacking ($\text{bz}_{(\text{cent})} \cdots \text{pyz}_{(\text{cent})} = 3.987(2)$ Å) and edge-to-face ($\text{bz}_{(\text{cent})} \cdots \text{C}_{\text{pyz}} = 4.237(4)$ Å) interactions between the benzoates and pyrazines

of neighbouring chains (**Figure 1.8.1-1**). The polymer features small channels running perpendicular to the direction of polymer propagation (**Figure 1.8.1-1**). It was demonstrated by Takamizawa and co-workers that these materials could adsorb quantities of N_2 ,^{130,131} characterised by a type I adsorption isotherm.⁶³ This preliminary result led to a series of guest inclusion studies being performed (**Table 1.8.1-1**).

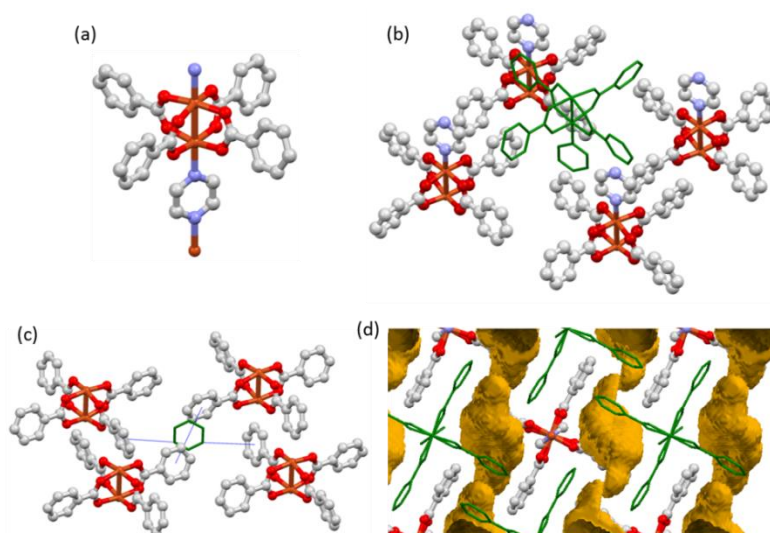


Figure 1.8.1-1. (a) $[Cu_2(bz)_4(py_2z)]_n$ formula unit. (b) Offset packing of polymer chains. (c) The π - π stacking interactions present. (d) The solvent-accessible void. Colour scheme consistent with **Figure 1.6-2**, Cu, orange; offset chain, green capped sticks; voids, yellow surfaces.

The guest inclusion experiments involved subjecting crystals to either high pressure or ambient conditions in a vapour environment of the intended guest.¹³² The high-pressure method employed a single crystal in a thick-walled capillary placed in a liquid nitrogen bath. The chosen gaseous guest was allowed to condense inside the capillary, which was then sealed and warmed to room temperature subjecting the crystal to a high pressure of gas. Complementary techniques such as DSC (differential scanning calorimetry), and volumetric and gravimetric adsorption were performed to confirm guest inclusion. Subsequent single-crystal diffraction studies had some common outcomes when guest uptake occurred. The first was that a phase transformation from a guest-free $C2/c$ phase to a guest-included $P-1$ phase was observed. This phase transformation is accompanied by a moving apart of polymer chains (**Figure 1.8.1-2**), a volume expansion and the channels running perpendicular to the polymer chains increasing in size (**Figure 1.8.1-2**). In a lot of these guest inclusion studies it was also possible to model the guest in the cleft of the paddlewheel consistently for a variety of guests (**Figure 1.8.1-2**). Due to this wide variety of studies demonstrating inclusion of a wide variety of gaseous and vapour phase guest by variable unit cell volume expansions the materials was then tested for applications as a separation membrane with the diffusion of solvent vapour through a medium of $[M_2(bz)_4(py_2z)]_n$ proving successful at separating a variety of organic solvents.^{133,134}

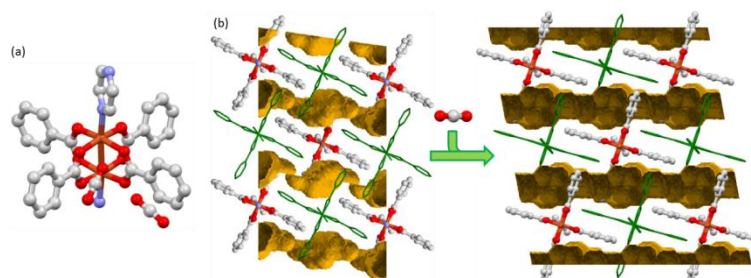


Figure 1.8.1-2. (a) Modelled CO₂ positions in $[\text{Cu}_2(\text{bz})_4(\text{pyz})]_n$ ¹³⁵ and (b) the effect CO₂ inclusion has on the solvent accessible channels.

Table 1.8.1-1. Single-crystal guest-inclusion studies of $[\text{M}_2(\text{bz})_4(\text{pyz})]_n$.

Formula	Guest Included	Space Group	Volume (Å ³)	Z	T(K)	Vol/Z (Å ³)	% Volume Increase	Reference
Pyrazine								
[Cu ₂ (bz) ₄ pyz] _n	Guest Free	C 2/c	3309.76	4	293	827.44		136
		C 2/c	3308.01	4	298	827.00		137
		C 2/c	3219.27	4	90	804.82		138
	CO ₂	P -1	880.20	1	293	880.20	6.38	139
		P -1	863.50	1	90	863.50	7.29	135
	CH ₄	C 2/c	3418.75	4	298	854.69	3.35-4.34	140
		P -1	831.98	1	90	831.98	3.38	140
	O ₂	P -1	838.94	1	90	838.94	4.24	141
	Ar	C 2/c	3391.30	4	298	847.83	2.52	142
	Kr	C 2/c	3442.05	4	298	860.51	4.05	142
	Xe	P -1	888.67	1	298	888.67	7.46	142
	MeOH	P -1	827.98	1	90	827.98	2.42-2.88	133,143
	EtOH	P -1	898.10	1	293	898.10	8.54	136
		P -1	866.08	1	90	866.08	7.61	144
	n-PrOH	C 2/c	3290.31	4	90	822.58	2.21	133
	n-BuOH	P -1	847.65	1	90	847.65	5.32	133
	n-PeOH	P -1	849.36	1	90	849.36	5.53	133
MeOH/MeCN	P -1	835.99	1	90	835.99	3.87	143	
MeCN	P -1	862.24	1	90	862.24	7.13	143	
[Rh ₂ (bz) ₄ pyz] _n	Acetone	C 2/m	1838.06	2	90	919.03	14.19	138a
	DCM	P -1	922.71	1	293	922.71	11.67	145a
	Guest Free	C 2/m	1672.13	2	298	836.07		135
		C 2/c	3302.08	4	90	825.52		135
	CO ₂	C 2/c	3213.40	4	10	803.35		146
		P -1	880.32	1	298	880.32	5.29	147
	CH ₄	P -1	867.94	1	90	867.94	5.14	135
		P -1	859.68	1	298	859.68	2.82	148
	N ₂	P -1	840.96	1	90	840.96	1.87	148
		P -1	854.10	1	298	854.10	2.16	132
	O ₂	P -1	826.60	1	90	826.60	0.13	132
		P -1	827.20	1	298	827.19	-1.06	146
	H ₂	P -1	846.89	1	90	846.89	2.59-3.54	146
		C 2/c	3246.77	4	10	811.69	1.04	149
	Ar	C 2/c	3258.04	4	90	814.51	-1.33	150
	Kr	P -1	855.96	1	298	855.96	2.38	142
	Xe	P -1	863.43	1	298	863.43	3.27	142
	MeOH	P -1	865.70	1	298	865.70	3.54	142
	EtOH	P -1	833.74	1	90	833.74	1.00	133
	n-PrOH	P -1	863.88	1	90	863.88	4.65	133
n-BuOH	C 2/c	3304.57	4	90	826.14	0.08	133	
n-PeOH	P -1	870.77	1	90	870.77	5.48	133	
MeCN	P -1	887.69	1	90	887.69	7.53	133	
	P -1	849.36	1	90	849.36	2.89	151	

^a Crystallised as a solvate and not obtained by an *in situ* inclusion study, therefore potentially not representative of the inclusion phase.

	NO	<i>P</i> -1	825.15	1	90	825.15	-0.04	132
	N ₂ O	<i>P</i> -1	880.03	1	93	880.03	8.48	152
	N ₂ O ₄	<i>C</i> 2/ <i>c</i>	3360.75	4	90	840.19	1.78	132
	CS ₂	<i>P</i> 1	845.24	1	90	845.24	2.39	153
	SO ₂	<i>P</i> -1	866.24	1	90	866.24	4.93	132

1.8.2 Functionalised 1D Paddlewheel Systems

The extensive demonstration of guest inclusion within the one-dimensional coordination polymers described above resulted in further research on analogous coordination polymers. There are two potential areas of adaptation from the original $[M_2(bz)_4(pyz)]_n$ material, these being to add functionality to the pyrazine unit or to the benzoate units (**Figure 1.8.2-1**).

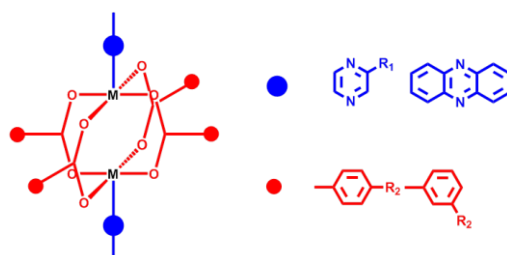


Figure 1.8.2-1. The paddlewheel SBU and potential functionality that can be applied to site 1 and site 2.

Takamizawa and co-workers reported a series of coordination polymers, in tandem with the original polymer, with substituted pyrazine linkers (**Table 1.8.2-1**). The purpose of adding a substituent to the pyrazine linkers was partly to see whether this affected the quantity of guest included¹³¹ as well as to determine whether the gate pressure of the materials could be controlled.^{135,154,155} An alkyl substituent present on the pyrazine resulted in a bending of the polymer chain. These materials exhibited similar behaviour to the original system with volume expansion being observed upon guest inclusion, but with small differences from the parent material. Firstly the materials crystallise in a guest-free triclinic *P*-1 phase instead of the monoclinic phase observed for the parent material. Guest inclusion then occurred either by a phase transformation resulting in halving the unit cell volume in the case of the mono-substituted pyrazines (and halving *Z* from 2 to 1) or by a volume expansion of the guest-free phase in the di-substituted materials. The di-substituted systems also exhibiting a smaller expansion than the mono-substituted systems (**Table 1.8.2-1**). These phase transformations also caused a straightening of the 1D chain for the mono-substituted systems, but the zig zag chains were maintained in the di-substituted systems (**Figure 1.8.2-2**)

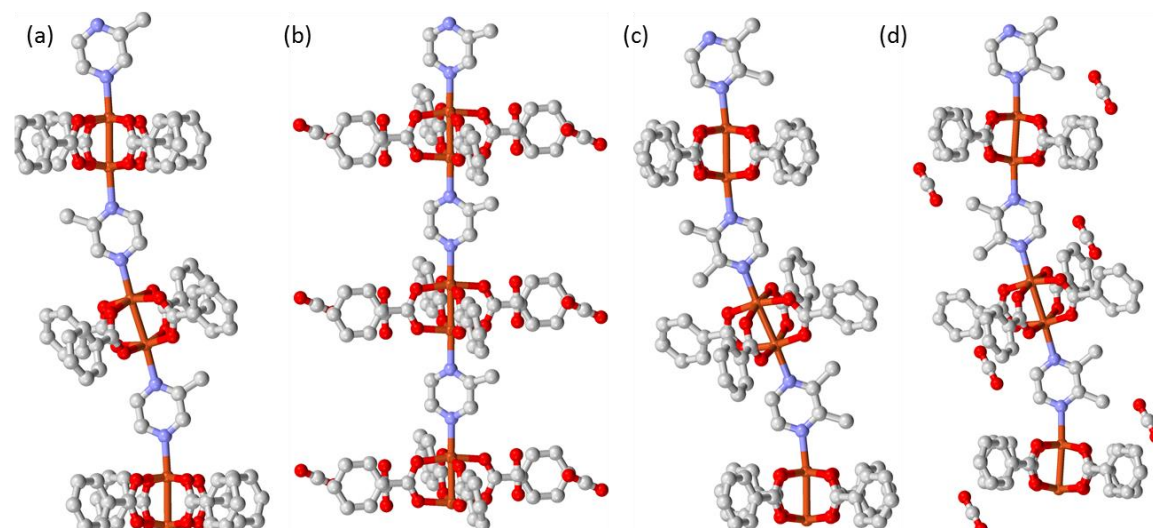


Figure 1.8.2-2. The observed bending of coordination polymers $[Cu_2(bz)_4(Mepyz)]_n$ (a and b) and $[Cu_2(bz)_4(2,3-DiMepyz)]_n$ (c and d) (where Mepyz = methylpyrazine and 2,3-DiMepyz = 2,3-dimethylpyrazine) in the as-synthesised phase (a and c) and the CO_2 including phase (b and d).¹³⁵ Minor components of disorder removed for clarity. Colour scheme consistent with **Figure 1.7.1-1**.

Table 1.8.2-1. Single-crystal guest-inclusion studies of $[M_2(bz)_4(R-pyz)]_n$ and $[M_2(bz)_4(R',R'-pyz)]_n$ with alkyl-substituted[®] pyrazine linker derivatives.

Formula	Guest Included	Space Group	Volume	Z (\AA^3)	T (K)	Vol/Z (\AA^3)	% Volume Increase	Reference
Methylpyrazine (Mepyz)								
$[Cu_2(bz)_4(Mepyz)]_n$	Guest Free	<i>P</i> -1	1625.75	2	90	812.88		135
	CO_2	<i>P</i> -1	900.08	1	90	900.06	10.73	135
$[Rh_2(bz)_4(Mepyz)]_n$	Guest Free	<i>P</i> -1	1626.17	2	90	813.09		135
	CO_2	<i>P</i> -1	893.31	1	90	893.31	9.87	135
	O_2	<i>P</i> -1	868.62	1	90	868.62	6.83	156
Ethylpyrazine (Etpyz)								
$[Rh_2(bz)_4(Etpyz)]_n$	Guest Free	<i>P</i> -1	1626.43	2	90	813.22		154
	CO_2	<i>P</i> -1	901.69	1	90	901.69	10.88	154
2,3-Dimethylpyrazine (diMepyz)								
$[Cu_2(bz)_4(2,3-diMepyz)]_n$	Guest Free	<i>P</i> -1	1636.16	2	90	818.08		135
	CO_2	<i>P</i> -1	1660.37	2	90	830.19	1.48	135
$[Rh_2(bz)_4(2,3-diMepyz)]_n$	Guest Free	<i>P</i> -1	1640.51	2	90	820.26		135
	CO_2	<i>P</i> -1	1738.47	2	90	869.24	5.97	135
2-Ethyl-3-Methylpyrazine (EtMepyz)								
$[Rh_2(bz)_4(EtMepyz)]_n$	Guest Free	<i>P</i> -1	1647.37	2	90	823.69		155
	CO_2	<i>P</i> -1	1649.17	2	90	824.59	0.11	155

Further work by Akutagawa et al.^{157,158} produced analogous 1D coordination polymers connected via pyrazine linkers, but with functionality present on the benzoate ligands. The first of their reports focused on $[Cu_2(4-Xbz)_4(pyz)]_n$ ($X = Cl, Br, I$ and OMe).¹⁵⁷ All four polymers display interpenetrated packing analogous to the parent benzoate system. This work demonstrated that, despite these systems being isostructural, the inclusion of CO_2 (volumetric adsorption at 195 K) was dependent on the functionality present, with the increasing size of halogen resulting in an increase in gate pressure for CO_2 adsorption and the iodo system not adsorbing CO_2 (**Figure 1.8.2-3**). The 4-halobenzoate polymers that included CO_2 ($X = Cl$ and Br) showed similar maximum uptake (2.8 CO_2 molecules per formula unit) suggesting similar solvent-accessible void space, but *in situ* diffraction studies were not carried out to confirm this. The second paper focused on *meta*-substituted benzoates (3-Fbz, 2,3-diFbz, 3-Mebz and 3-Clbz), which crystallised

with similar offset polymer chains but the presence of the *meta*-substituents led to formation of acetonitrile solvates. These materials crystallising as solvates meant that they were activated by heating to 373 K prior to volumetric gas adsorption analysis, which resulted in a slight loss of crystallinity, but maintained the same phase. All four polymers were tested for CO₂ inclusion by volumetric adsorption (at 195 K), with gated uptake being observed in all four materials (**Figure 1.8.2-3**). Volumetric analysis of the two 3-halobenzoate-containing materials showed analogous uptake of CO₂ (ca. 2.8 CO₂ molecules per formula unit) (**Figure 1.8.2-3**), suggesting similar solvent accessible voids but *in situ* diffraction studies were again not carried out.

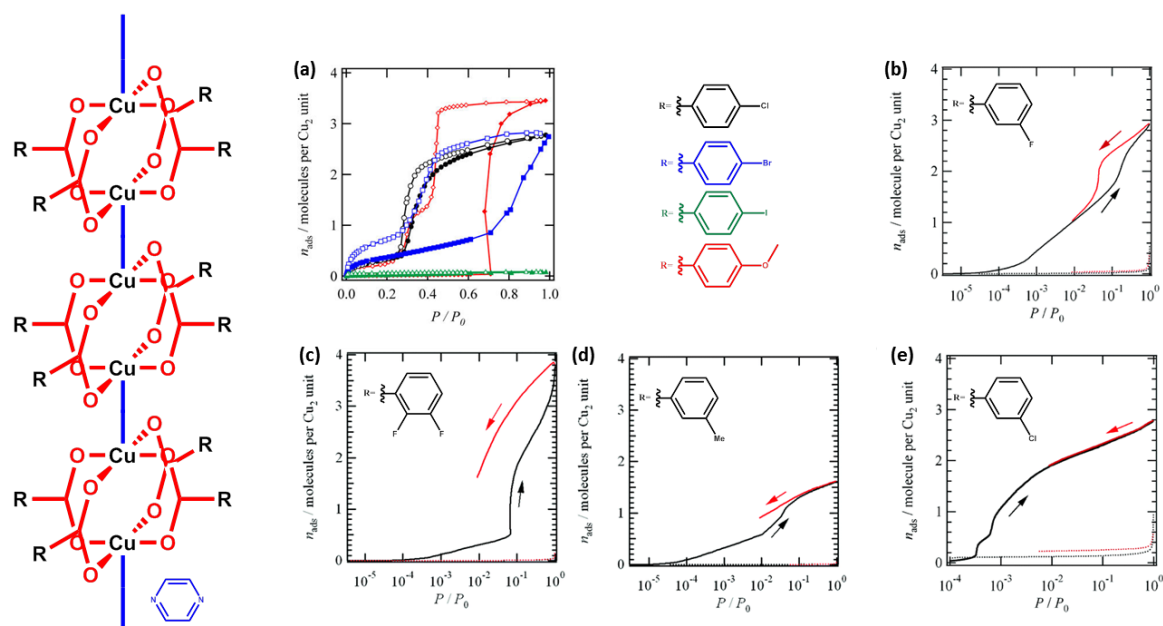


Figure 1.8.2-3. Volumetric CO₂ adsorption isotherms for a series of coordination polymers $[\text{Cu}_2(n\text{-Xbz})_4(\text{pyz})]_n$ containing (a) *para*-¹⁵⁷ and (b-e) *meta*-substituted¹⁵⁸ benzoates. Graphs reproduced from references ¹⁵⁷ and ¹⁵⁸ with permission

Takamizawa et al. produced $[\text{Cu}_2(4\text{-Fbz})_4(\text{Mepyz})]_n$ ¹⁵⁹ functionalising both the benzoate ligands and the pyrazine linker. The presence of the fluorine on the benzoate units had little effect, producing analogous packing to the original parent system ($[\text{M}_2(\text{bz})_4(\text{pyz})]_n$) with interpenetrated linear polymer chains (**Figure 1.8.2-4**). Whereas previous studies on guest inclusion within these systems often involved guest inclusion using high pressure leading to an overall phase transition and subsequent channel expansion to incorporate guests. This research intended to demonstrate that the small channels and slight dynamic behaviour could be employed as a means of H₂ permeation with potential application as a H₂ purification system. This involved the construction of a $[\text{Cu}_2(4\text{-Fbz})_4(\text{Mepyz})]_n$ membrane which showed higher selectivity for H₂ over both CO and CH₄.

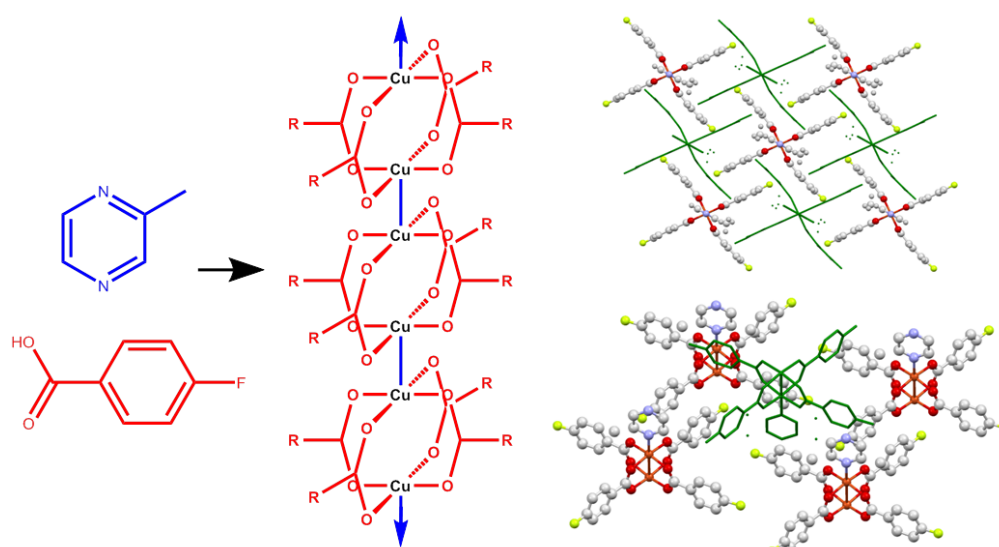


Figure 1.8.2-4. $[Cu_2(4-Fbz)_4(Mepyz)]_n$ reported by Takamizawa et al.¹⁵⁹ shows isostructural packing and interpenetration to $[M_2(bz)_4(py)]_n$. Colour consistent with **Figure 1.8.1-1**; F, yellow.

The adaptation of both benzoate ligand and pyrazine linker led to several examples of 1D coordination polymers where the polymers no longer pack as interpenetrated chains (**Figure 1.8.2-5**).^{160–162} The lack of interpenetration leads to much larger potential void spaces than the parent system ($[M_2(bz)_4(py)]_n$). The absence of interpenetration was achieved by Kitagawa and co-workers in $[M_2(4-Cl-2-OMebz)_4(phen)]_n$ ($M = Rh$ and Ru , 4-Cl-2-OMebz = 4-Chloro-2-methoxybenzoate and phen = phenazine).¹⁶¹ The combination of *para-ortho*-substituted benzoates and the bulky phenazine linkers led to the polymer chains being unable to pack as closely as the original systems resulting in large solvent filled channels (**Figure 1.8.2-5**). The solvent could be removed by heating under vacuum, leading to *ca.* 23 % reduction in the unit cell volume. Despite this large decrease in the void volume, volumetric adsorption analysis showed uptake of CO_2 (at 195 K), O_2 (at 90 K) and NO (at 121 K) (for Rh and Ru), as well as N_2 uptake (at 77 K), being observed for the Rh system. The NO isotherms show a two-step gated uptake with a maximum inclusion of 8 and 6 molecules of NO per formula unit (for Ru and Rh , respectively). This also led to a hysteretic character for NO uptake. This gated process is rationalised as the first gate opening being due to physisorption, with the second gate opening being associated with host-guest interactions (**Figure 1.8.2-6**). Samples of each material were exposed to pressures of CO_2 and NO (5.2 kPa at 195 K and 20 kPa at 121 K, respectively) during *in situ* PXRD measurements, which established unit cell expansion. Unfortunately the pressure of NO could not be increased further to observe the second expansion.

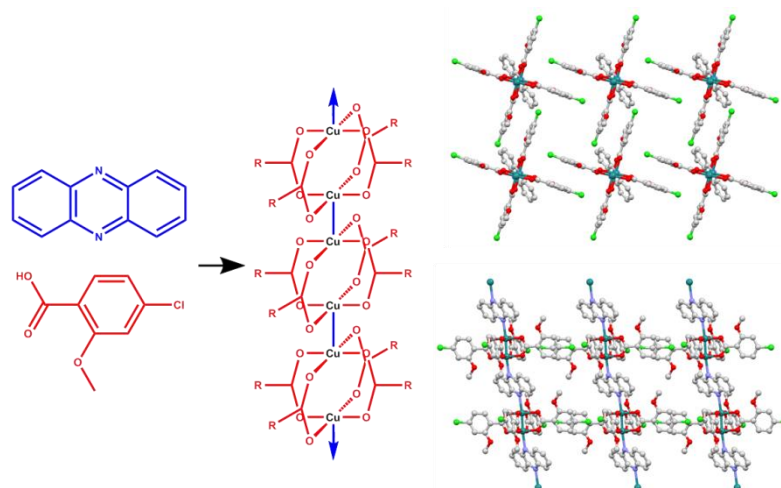


Figure 1.8.2-5. The absence of interpenetration present in $[M_2(4\text{-Cl-2-OMebz})_4(\text{phen})]_n$ leading large solvent-filled void spaces. Colour scheme consistent with **Figure 1.8.1-1**, Ru, turquoise; Cl, green. Solvent molecules and hydrogen atoms omitted for clarity.

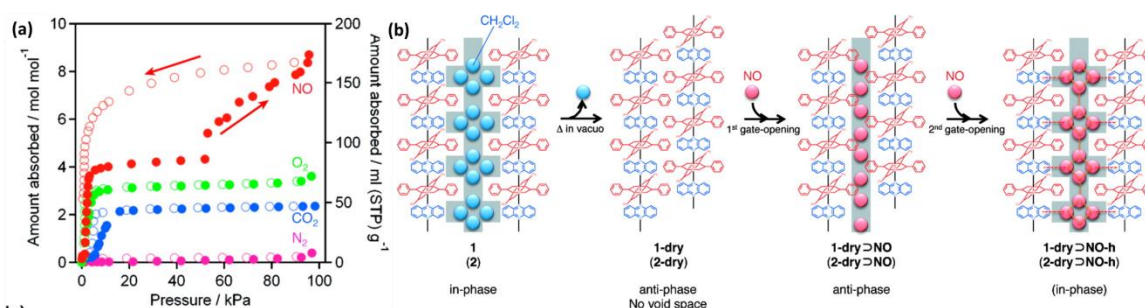


Figure 1.8.2-6. (a) Volumetric adsorption isotherms of $[Ru_2(4\text{-Cl-2-OMebz})_4(\text{phen})]_n$ for several gases, N_2 at 77 K (pink), CO_2 at 195 K (blue), O_2 at 90 K (green) and NO at 121 K (red) (adsorption – filled circles; desorption – empty circles). (b) Proposed gating mechanism of NO inclusion. Images reproduced from reference ¹⁶¹ with permission

1.9 Porosity of Molecular Crystals

Conventionally for a material to be porous it has to possess rigidly defined pore channels or networks.¹⁶³ This has meant that, typically, materials for which a pore space is sustained by coordination or covalent bonding were tested for guest inclusion. However, in recent years it has been demonstrated that porosity can be achieved where channels are formed through inefficient packing¹⁶⁴ or through intermolecular interactions^{165,166} within molecular crystals. It has also been demonstrated that porosity can also be achieved in crystals with discrete cavities.^{167,168} Normally molecules in the crystalline state are perceived to be densely packed with analogies to a wall of bricks often being drawn (**Figure 1.9-1**), however there are two cases in which a molecular crystalline material can possess porosity. The first involves intrinsic porosity,^{169–171} which is when the pore space is within the molecule itself, typical examples being supramolecular macrocycles. To extend the “wall of bricks” analogy these systems would be comparable to building a wall solely of ventilation bricks (**Figure 1.9-1**). The second involves extrinsic porosity;^{164,172} which is where a molecule packs inefficiently, resulting in void spaces between molecules. To continue the “wall of bricks” analogy this would be equivalent building a wall with brick that cannot pack without leaving gaps either due to the shape of the brick or certain faces only interacting with other faces (**Figure 1.9-1**). In the as-synthesised crystals the

spaces between molecules are filled with smaller solvent molecules. Desolvation tests and guest-inclusion studies are then needed to ascertain whether the material is truly porous.¹⁷³

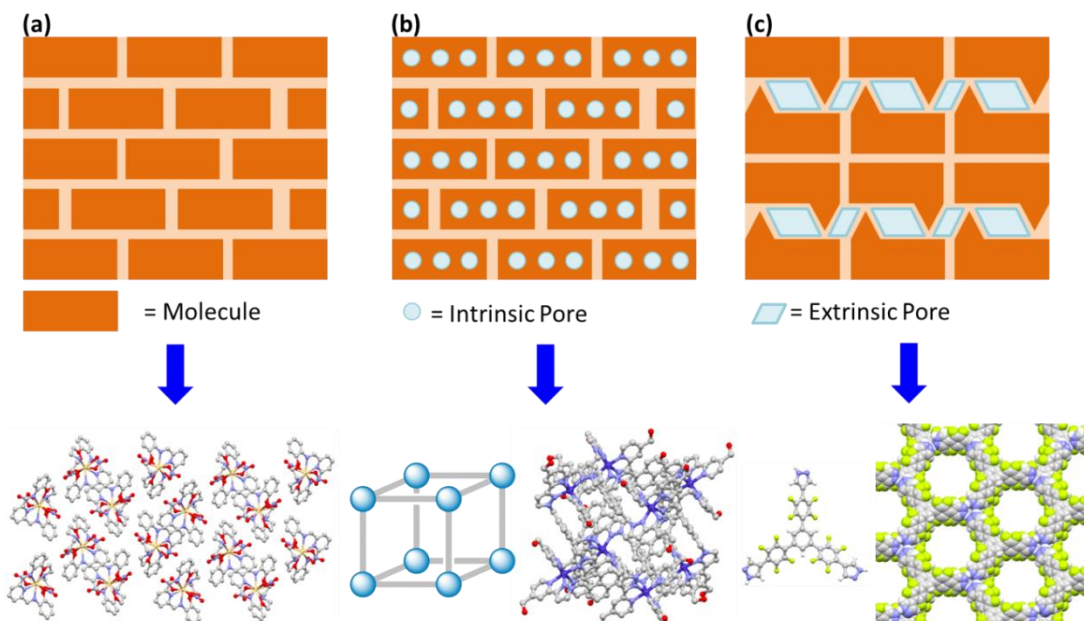


Figure 1.9-1. The wall of bricks analogy for (a) a close-packed molecule,¹⁷⁴ (b) an intrinsically porous cage¹⁷⁰ and (c) an extrinsically porous molecule.¹⁶⁵

In order to produce an extrinsically porous molecular crystals there are two characteristics that can be tailored. The first is the promotion of inefficient packing; this can be achieved by designing a molecule with the awkward shape. Typically, inefficient packing is achieved by using a molecule with multiple rigid components protruding from a central point in multiple directions (**Figure 1.9-2**). The second characteristic to consider is to functionalise the awkwardly shaped molecule in order to promote the formation of intermolecular interactions that will propagate and sustain a pore space (**Figure 1.9-2**).

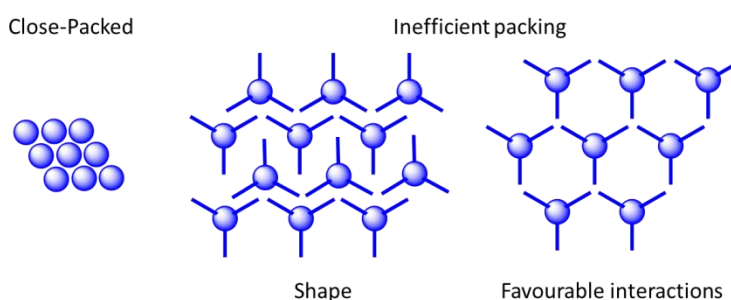


Figure 1.9-2. Simply inefficient packing diagrams

An example that features the same paddlewheel SBU discussed in the coordination polymer sections (Section 1.6-1.8) is the recent work reported by Masaoka et al.^{175,176} This work focuses on a Rh paddlewheel with bridging 4-[(perfluorophenyl)ethynyl]benzoate (ppeb) ligands. The presence of the electron-rich and electron-poor aromatic rings results in a regular co-operative $\pi \cdots \pi$ interaction. A preliminary report demonstrated that regular 1D chains or 2D grids of $\pi \cdots \pi$ interactions could be achieved, dictated by the number of ppeb ligands coordinated to the Rh

paddlewheel.¹⁷⁵ A second study focused of the 2D $\pi\cdots\pi$ stacking grids, first demonstrating that the stacking of these 2D grids is dependent on the ligand present in the axial site (THF, 3-pentone or adamantylamine) (**Figure 1.9-3**) similar to the effects on uptake observed for 2D coordination polymer networks (Section 1.6).

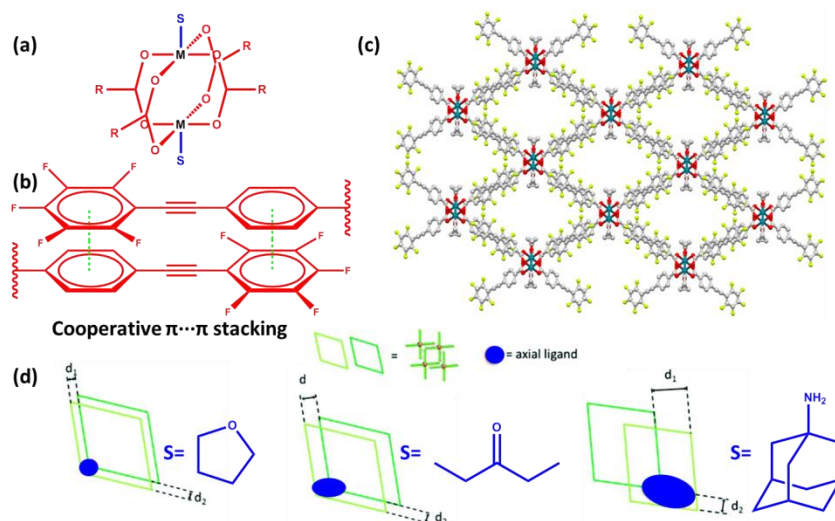


Figure 1.9-3. (a) The Rh paddlewheel in $[Rh_2(ppeb)_4(L)_2]$ and (b) the co-operative $\pi\cdots\pi$ stack between ppeb ligands, this leading to (c) 2D networks. (d) The packing of 2D networks is in turn affected by the molecule (L) coordinated in the axial site. Image, in part, replicated from reference¹⁷⁶ with permission.

Thermogravimetric analysis demonstrated that the volatile crystallisation solvent (diethyl ether) was lost prior to analysis and the axial ligand being could be removed in the case of the THF- and 3-pentone-containing materials. PXRD patterns recorded for the desolvated materials show a phase change, but it is unclear what this phase corresponds to without powder fitting of the pattern, which was not reported. Exposure to solvent vapour (THF and 3-pentone) also revealed that the solvents could be easily displaced. It was then demonstrated, by volumetric adsorption (CO_2 at 195 K), that the quantity of CO_2 included depended on the orientation of the 2D layers (**Figure 1.9-4**). Similarly, the PXRD patterns measured after volumetric adsorption studies did not match that of the as-synthesised form.

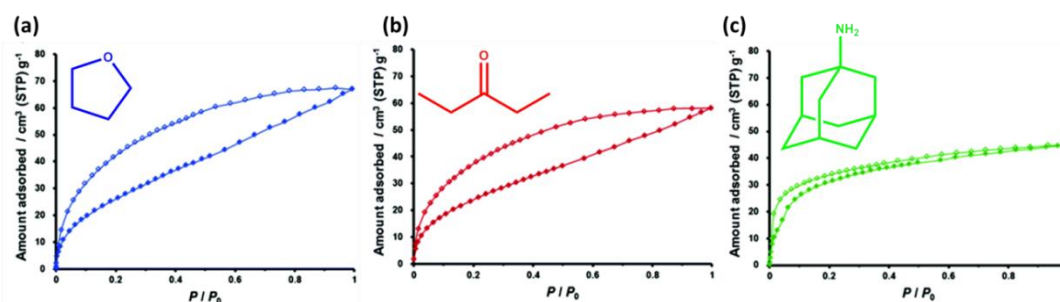


Figure 1.9-4. Volumetric adsorption of CO_2 (at 195 K) for $[Rh_2(ppeb)_4(L)_2]$ with (a) THF, (b) 3-pentone and (c) 1-adamantylamine axial ligands (L). Samples were evacuated at $40^\circ C$ prior to analysis to ensure solvent was removed, but axial ligands were retained. Image, in part. Replicated from reference¹⁷⁶ with permission.

Masaoka and co-workers were also able to exploit the packing inefficiencies of a second Rh paddlewheel molecule, combined with a light-harvesting ligand (3-(1,8-

naphthalimido)propanoate) to produce a photocatalyst (**Figure 1.9-5**).¹⁷⁷ The four naphthalimide linkers form a series of $\pi\cdots\pi$ interactions to produce 3D framework with 1D solvent-filled channels running through (**Figure 1.9-5**). The crystalline form of this material was insoluble in water and a variety of organic solvents. It was demonstrated that H_2 was evolved upon irradiation ($\lambda > 320$ nm) of a suspension a sample of the framework in a buffer solution.

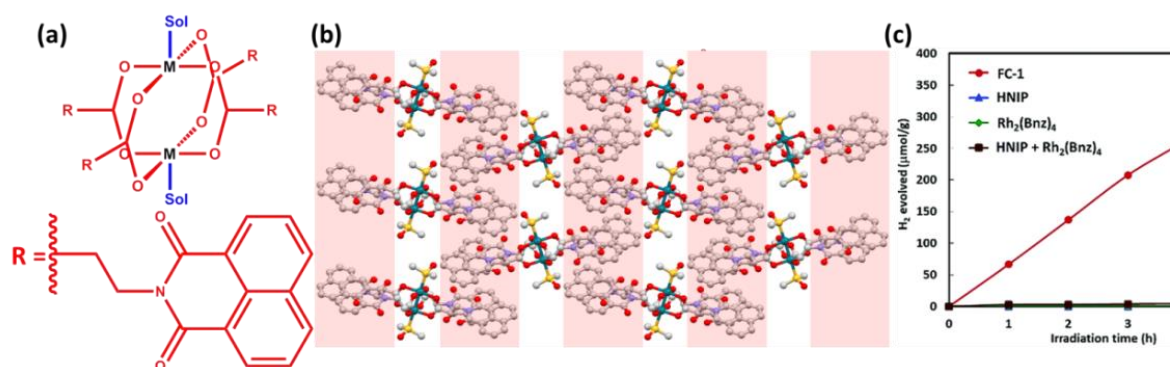


Figure 1.9-5. (a) The photocatalyst produced by Masaoka.¹⁷⁷ (b) The π stacking (shaded red) within the crystal structure. (c) H_2 evolution of the photocatalyst (FC-1, red) compared to the ligand (HNIP, blue), the Rh benzoate paddlewheel ($[Rh_2(bz)_4]$, green) and a mixture of the ligand and $[Rh_2(bz)_4]$ (brown). Graph replicated from reference¹⁷⁷ with permission.

1.10 Conclusion

In conclusion, a review of the literature has shown that 3rd generation porosity can be achieved in a series of 3D, 2D and 1D coordination polymers with a common SBU (the paddlewheel). Firstly, a series of 3D pillared networks have been reported with the basic formula $[Zn_2(bdc)_2(DABCO)]$. Flexibility was observed through the flexing of the $Zn_{(cent)}\cdots O_{2(cent)}\cdots 1,4$ - $bdc_{(cent)}$ angle. These preliminary results led to this flexibility being exploited with the design of functionalised 1,4-bdc linkers to tailor the flexibility and subsequent selectivity of these systems. Secondly a series of 2D grids with the basic formula $[M_2(1,4-bdc)_2]$ were reported with gas uptake being dependent of the co-ordinated axial ligands and functionality present on the 1,4-bdc linkers. Unfortunately, despite gated adsorption isotherms being reported, *in situ* diffraction studies are yet to be reported for these systems so it is unclear whether these gates can be attributed to a dynamic motion of 2D grids. It was then noted that a wide variety of 1D polymers with the basic formula $[M_2(bz)_4(pyz)]_n$ have been reported, the parent coordination polymer $([M_2(bz)_4(pyz)]_n)$ showing the inclusion of a wide variety of guests. The uptake occurs by the polymer chains moving apart and an expansion in the solvent-accessible channels. This work was then followed with studies of functionalisation of the pyrazine linker as well as the benzoate ligand. This resulted in changes in crystal packing as well as gas uptake potential. A combination of functionalisation of the pyrazine and benzoate ligands resulted in a lack of interpenetration and large solvent-accessible channels being formed. Finally this paddlewheel SBU has been successfully employed to produce a series of porous molecular crystals. This was achieved through a combination of exploiting the inefficient packing of the paddlewheel SBU with the intermolecular interactions, achieved by selection of an appropriate coordinating carboxylate. Later work also demonstrated that an analogous molecular paddlewheel could be used a heterogeneous photocatalyst.

1.11 References

- 1 S. W. Wilkins, *Acta Crystallogr. Sect. A: Found. Crystallogr.*, 2013, **69**, 1–4.
- 2 F. H. Allen and W. D. S. Motherwell, *Acta Crystallogr. Sect. B: Struct. Sci.*, 2002, **58**, 407–422.
- 3 C. F. Macrae, I. J. Bruno, J. A. Chisholm, P. R. Edgington, P. McCabe, E. Pidcock, L. Rodriguez-Monge, R. Taylor, J. Van De Streek and P. A. Wood, *J. Appl. Crystallogr.*, 2008, **41**, 466–470.
- 4 C. R. Groom and F. H. Allen, *Angew. Chem. Int. Ed.*, 2014, **53**, 662–671.
- 5 C. R. Groom, I. J. Bruno, M. P. Lightfoot and S. C. Ward, *Acta Crystallogr. Sect. B: Struct. Sci. Cryst. Eng. Mater.*, 2016, **72**, 171–179.
- 6 P. Z. Moghadam, A. Li, S. B. Wiggin, A. Tao, A. G. P. Maloney, P. A. Wood, S. C. Ward and D. Fairen-Jimenez, *Chem. Mater.*, 2017, **29**, 2618–2625.
- 7 G. M. Battle and F. H. Allen, *J. Chem. Educ.*, 2012, **89**, 38–44.
- 8 P. A. Wood, N. Feeder, M. Furlow, P. T. A. Galek, C. R. Groom and E. Pidcock, *CrystEngComm*, 2014, **16**, 5839–5848.
- 9 J. D. Evans, D. M. Huang, M. Haranczyk, A. W. Thornton, C. J. Sumbly and C. J. Doonan, *CrystEngComm*, 2016, **18**, 4133–4141.
- 10 N. B. McKeown, *J. Mater. Chem.*, 2010, **20**, 10588–10597.
- 11 G. M. Battle, G. M. Ferrence and F. H. Allen, *J. Appl. Crystallogr.*, 2010, **43**, 1208–1223.
- 12 G. M. Battle, F. H. Allen and G. M. Ferrence, *J. Chem. Educ.*, 2011, **88**, 891–897.
- 13 P. A. Wood, A. A. Sarjeant, I. Bruno, C. F. Macrae, H. E. Maynard-Casely and M. Towler, *CrystEngComm*, 2017, **19**, 690–698.
- 14 D. R. Allan, S. P. Collins, G. Evans, D. Hall, K. McAuley, R. L. Owen, T. Sorensen, C. C. Tang, F. von Delft, A. Wagner and H. Wilhelm, *Eur. Phys. J. Plus*, 2015, **130**, 1–20.
- 15 H. Nowell, S. A. Barnett, K. E. Christensen, S. J. Teat and D. R. Allan, *J. Synchrotron Radiat.*, 2012, **19**, 435–441.
- 16 S. Henke, R. Schmid, J. D. Grunwaldt and R. A. Fischer, *Chem. Eur. J.*, 2010, **16**, 14296–14306.
- 17 G. R. Desiraju, J. J. Vittal and A. Ramanam, *Crystal Engineering A Textbook*, World Scientific Publishing, 1st (ed.), 2011.
- 18 J. Sirirak, W. Phonsri, D. J. Harding, P. Harding, P. Phommon, W. Chaoprasa, R. M. Hendry, T. M. Roseveare and H. Adams, *J. Mol. Struct.*, 2013, **1036**, 439–446.
- 19 T. Clark, M. Hennemann, J. S. Murray and P. Politzer, *J. Mol. Model.*, 2007, **13**, 291–296.
- 20 V. R. Pedireddi, D. Shekhar Reddy, B. Stish Goud, D. C. Craig, A. D. Rae and G. R. Desiraju, *J. Chem. Soc. Perkin Trans. 2*, 1994, 2353–2360.
- 21 P. Metrangolo and G. Resnati, *IUCrJ*, 2013, **1**, 5–7.

- 22 G. Cavallo, P. Metrangolo, R. Milani, T. Pilati, A. Priimagi, G. Resnati and G. Terraneo, *Chem. Rev.*, 2016, **116**, 2478–2601.
- 23 C. B. Aakeröy, C. L. Spartz, S. Dembowski, S. Dwyre and J. Desper, *IUCrJ*, 2015, **2**, 498–510.
- 24 C. C. Robertson, J. S. Wright, E. J. Carrington, R. N. Perutz, C. A. Hunter and L. Brammer, *Chem. Sci.*, 2017, **8**, 5392–5398.
- 25 M. Baldrighi, G. Cavallo, M. R. Chierotti, R. Gobetto, P. Metrangolo, T. Pilati, G. Resnati and G. Terraneo, *Mol. Pharm.*, 2013, **10**, 1760–1772.
- 26 C. B. Aakeröy, D. Welideniya, J. Desper and C. Moore, *CrystEngComm*, 2014, **16**, 10203–10209.
- 27 D. Choquesillo-Lazarte, V. Nemeč and D. Cincic, *Crystengcomm*, 2017, **19**, 5293–5299.
- 28 L. C. Gilday, S. W. Robinson, T. A. Barendt, M. J. Langton, B. R. Mullaney and P. D. Beer, *Chem. Rev.*, 2015, **115**, 7118–7195.
- 29 J.-P. Gliese, S. H. Jungbauer and S. M. Huber, *Chem. Commun.*, 2017, **53**, 12052–12055.
- 30 P. Wonner, L. Vogel, M. Düser, L. Gomes, F. Kniep, B. Mallick, D. B. Werz and S. M. Huber, *Angew. Chem. Int. Ed.*, 2017, **56**, 12009–12012.
- 31 K. Raatikainen and K. Rissanen, *Chem. Sci.*, 2012, **3**, 1235–1239.
- 32 L. Turunen, F. Pan, N. K. Beyeh, J. F. Trant, R. H. A. Ras and K. Rissanen, *Cryst. Growth Des.*, 2018, **18**, 513–520.
- 33 L. Brammer, *Faraday Discuss.*, 2017, **203**, 485–507.
- 34 J. W. Steed and J. L. Atwood, *Supramolecular Chemistry*, John Wiley and Sons, Chichester, 2000.
- 35 C. A. Hunter, *Chem. Soc. Rev.*, 1994, **23**, 101–109.
- 36 H. Wang, W. Wang and W. J. Jin, *Chem. Rev.*, 2016, **116**, 5072–5104.
- 37 O. Asai, M. Kishita and M. Kubo, *J. Phys. Chem.*, 1959, **63**, 96–99.
- 38 B. F. Hoskins and R. Robson, *J. Am. Chem. Soc.*, 1989, **111**, 5962–5964.
- 39 B. F. Hoskins and R. Robson, *J. Am. Chem. Soc.*, 1990, **112**, 1546–1554.
- 40 B. F. Abrahams, B. F. Hoskins and R. Robson, *J. Am. Chem. Soc.*, 1991, **113**, 3606–3607.
- 41 O. M. Yaghi, H. Li, C. Davis, D. Richardson and T. L. Groy, *Acc. Chem. Res.*, 1998, **31**, 474–484.
- 42 H. Li, M. Eddaoudi, M. O’Keeffe and O. M. Yaghi, *Nature*, 1999, **402**, 276–279.
- 43 G. Férey, C. Mellot-Draznieks, C. Serre, F. Millange, J. Dutour, S. Surblé and I. Margiolaki, *Science*, 2005, **309**, 2040–2042.
- 44 J. R. Li, Y. Ma, M. C. McCarthy, J. Sculley, J. Yu, H. K. Jeong, P. B. Balbuena and H. C. Zhou, *Coord. Chem. Rev.*, 2011, **255**, 1791–1823.

- 45 H. Furukawa, K. E. Cordova, M. O’Keeffe and O. M. Yaghi, *Science*, 2013, **341**, 1–12 (1230444).
- 46 P. Horcajada, C. Serre, M. Vallet-Regí, M. Sebban, F. Taulelle and G. Férey, *Angew. Chem. Int. Ed.*, 2006, **45**, 5974–5978.
- 47 P. Horcajada, R. Gref, T. Baati, P. K. Allan, G. Maurin, P. Couvreur, G. Férey, R. E. Morris and C. Serre, *Chem. Rev.*, 2012, **112**, 1232–1268.
- 48 L. Ma, C. W. Abney and W. Lin, *Chem. Soc. Rev.*, 2009, **38**, 1248–1256.
- 49 Y. Chen, D. Wang, X. Deng and Z. Li, *Catal. Sci. Technol.*, 2017, **7**, 4893–4904.
- 50 J. Lee, O. K. Farha, J. Roberts, K. a Scheidt, S. T. Nguyen and J. T. Hupp, *Chem. Soc. Rev.*, 2009, **38**, 1450–1459.
- 51 L. E. Kreno, K. Leong, O. K. Farha, M. Allendorf, R. P. Van Duyne and J. T. Hupp, *Chem. Rev.*, 2012, **112**, 1105–1125.
- 52 Y. Cui, Y. Yue, G. Qian and B. Chen, *Chem. Rev.*, 2012, **112**, 1126–1162.
- 53 S. Kitagawa and K. Uemura, *Chem. Soc. Rev.*, 2005, **34**, 109–119.
- 54 K. Uemura, R. Matsuda and S. Kitagawa, *J. Solid State Chem.*, 2005, **178**, 2420–2429.
- 55 E. J. Carrington, I. J. Vitórica-Yrezábal and L. Brammer, *Acta Crystallogr. Sect. B: Struct. Sci. Cryst. Eng. Mater.*, 2014, **70**, 404–422.
- 56 J.-P. Zhang, P.-Q. Liao, H.-L. Zhou, R.-B. Lin and X.-M. Chen, *Chem. Soc. Rev.*, 2014, **43**, 5789–5814.
- 57 V. Bon, I. Senkovska, D. Wallacher, A. Heerwig, N. Klein, I. Zizak, R. Feyerherm, E. Dudzik and S. Kaskel, *Microporous Mesoporous Mater.*, 2014, **188**, 190–195.
- 58 S. Krause, V. Bon, I. Senkovska, U. Stoeck, D. Wallacher, D. M. Töbrens, S. Zander, R. S. Pillai, G. Maurin, F. X. Coudert and S. Kaskel, *Nature*, 2016, **532**, 348–352.
- 59 N. Kavooosi, V. Bon, I. Senkovska, S. Krause, C. Atzori, F. Bonino, J. Pallmann, S. Paasch, E. Brunner and S. Kaskel, *Dalton Trans.*, 2017, **46**, 4685–4695.
- 60 J. Schaber, S. Krause, S. Paasch, I. Senkovska, V. Bon, D. M. Töbrens, D. Wallacher, S. Kaskel and E. Brunner, *J. Phys. Chem. C*, 2017, **121**, 5195–5200.
- 61 E. J. Carrington, C. A. McAnally, A. J. Fletcher, S. P. Thompson, M. R. Warren and L. Brammer, *Nat. Chem.*, 2017, **9**, 882–889.
- 62 K. S. W. Sing, D. H. Everett, R. A. W. Haul, L. Moscou, R. a. Pierotti, J. Rouquérol and T. Siemieniewska, *Pure Appl. Chem.*, 1985, **57**, 603–619.
- 63 M. Thommes, K. Kaneko, A. V. Neimark, J. P. Olivier, F. Rodriguez-Reinoso, J. Rouquerol and K. S. W. Sing, *Pure Appl. Chem.*, 2015, **87**, 1051–1069.
- 64 K. Seki, *Phys. Chem. Chem. Phys.*, 2002, **4**, 1968–1971.
- 65 K. Biradha and M. Fujita, *Angew. Chem. Int. Ed.*, 2002, **41**, 3392–3395.
- 66 R. Kitaura, K. Seki, G. Akiyama and S. Kitagawa, *Angew. Chem. Int. Ed.*, 2003, **42**, 428–431.

- 67 S. Bureekaew, H. Sato, R. Matsuda, Y. Kubota, R. Hirose, J. Kim, K. Kato, M. Takata and S. Kitagawa, *Angew. Chem. Int. Ed.*, 2010, **49**, 7660–7664.
- 68 G. Férey and C. Serre, *Chem. Soc. Rev.*, 2009, **38**, 1380–1399.
- 69 C. Serre, F. Millange, C. Thouvenot, M. Noguès, G. Marsolier, D. Louër and G. Férey, *J. Am. Chem. Soc.*, 2002, **124**, 13519–13526.
- 70 T. Loiseau, C. Serre, C. Huguenard, G. Fink, F. Taulelle, M. Henry, T. Bataille and G. Férey, *Chem. Eur. J.*, 2004, **10**, 1373–1382.
- 71 R. K. Motkuri, P. K. Thallapally, S. K. Nune, C. a Fernandez, B. P. McGrail and J. L. Atwood, *Chem. Commun.*, 2011, **47**, 7077–7079.
- 72 P. K. Thallapally, J. Tian, M. R. Kishan, C. A. Fernandez, S. J. Dalgarno, P. B. McGrail, J. E. Warren and J. L. Atwood, *J. Am. Chem. Soc.*, 2008, **130**, 16842–16843.
- 73 P. G. Yot, Q. Ma, J. Haines, Q. Yang, A. Ghoufi, T. Devic, C. Serre, V. Dmitriev, G. Férey, C. Zhong and G. Maurin, *Chem. Sci.*, 2012, **3**, 1100–1104.
- 74 D. N. Dybtsev, H. Chun and K. Kim, *Angew. Chem. Int. Ed.*, 2004, **43**, 5033–5036.
- 75 L. D. Devries, P. M. Barron, E. P. Hurley, C. Hu and W. Choe, *J. Am. Chem. Soc.*, 2011, **133**, 14848–14851.
- 76 J. P. Zhang, Y. Y. Lin, W. X. Zhang and X. M. Chen, *J. Am. Chem. Soc.*, 2005, **127**, 14162–14163.
- 77 K. Uemura, Y. Yamasaki, Y. Komagawa, K. Tanaka and H. Kita, *Angew. Chem. Int. Ed.*, 2007, **46**, 6662–6665.
- 78 J. Y. Lee, D. H. Olson, L. Pan, T. J. Emge and J. Li, *Adv. Funct. Mater.*, 2007, **17**, 1255–1262.
- 79 O. Kozachuk, K. Khaletskaya, M. Halbherr, A. Bétard, M. Meilikhov, R. W. Seidel, B. Jee, A. Pöpl and R. A. Fischer, *Eur. J. Inorg. Chem.*, 2012, 1688–1695.
- 80 K. Uemura, F. Onishi, Y. Yamasaki and H. Kita, *J. Solid State Chem.*, 2009, **182**, 2852–2857.
- 81 K. Uemura, Y. Yamasaki, F. Onishi, H. Kita and M. Ebihara, *Inorg. Chem.*, 2010, **49**, 10133–10143.
- 82 Z. Chen, S. Xiang, H. D. Arman, P. Li, D. Zhao and B. Chen, *Eur. J. Inorg. Chem.*, 2011, 2227–2231.
- 83 Y. Zhao, H. Wu, T. J. Emge, Q. Gong, N. Nijem, Y. J. Chabal, L. Kong, D. C. Langreth, H. Liu, H. Zeng and J. Li, *Chem. Eur. J.*, 2011, **17**, 5101–5109.
- 84 Z. Wang and S. M. Cohen, *J. Am. Chem. Soc.*, 2009, **131**, 16675–16677.
- 85 S. Henke, D. C. Florian Wieland, M. Meilikhov, M. Paulus, C. Sternemann, K. Yussenko and R. A. Fischer, *CrystEngComm*, 2011, **13**, 6399–6404.
- 86 S. Henke, A. Schneemann, A. Wütscher and R. A. Fischer, *J. Am. Chem. Soc.*, 2012, **134**, 9464–9474.
- 87 N. C. Burtch, H. Jasuja, D. Dubbeldam and K. S. Walton, *J. Am. Chem. Soc.*, 2013, **135**,

- 7172–7180.
- 88 S. Henke, W. Li and A. K. Cheetham, *Chem. Sci.*, 2014, **5**, 2392–2397.
- 89 V. Bon, J. Pallmann, E. Eisbein, H. C. Hoffmann, I. Senkovska, I. Schwedler, A. Schneemann, S. Henke, D. Wallacher, R. A. Fischer, G. Seifert, E. Brunner and S. Kaskel, *Microporous Mesoporous Mater.*, 2015, **216**, 64–74.
- 90 I. Schwedler, S. Henke, M. T. Wharmby, S. R. Bajpe, A. K. Cheetham and R. A. Fischer, *Dalton Trans.*, 2016, **45**, 4230–4241.
- 91 J. Seo, R. Matsuda, H. Sakamoto, C. Bonneau and S. Kitagawa, *J. Am. Chem. Soc.*, 2009, **131**, 12792–12800.
- 92 K. K. Tanabe, Z. Wang and S. M. Cohen, *J. Am. Chem. Soc.*, 2008, **130**, 8508–8517.
- 93 L. G. Zhu and H. P. Xiao, *Zeitschrift für Anorg. und Allg. Chemie*, 2008, **634**, 845–847.
- 94 N. Klein, C. Herzog, M. Sabo, I. Senkovska, J. Getzschmann, S. Paasch, M. R. Lohe, E. Brunner and S. Kaskel, *Phys. Chem. Chem. Phys.*, 2010, **12**, 11778–11784.
- 95 H. C. Hoffmann, B. Assfour, F. Epperlein, N. Klein, S. Paasch, I. Senkovska, S. Kaskel, G. Seifert and E. Brunner, *J. Am. Chem. Soc.*, 2011, **133**, 8681–8690.
- 96 N. Klein, H. C. Hoffmann, A. Cadiou, J. Getzschmann, M. R. Lohe, S. Paasch, T. Heydenreich, K. Adil, I. Senkovska, E. Brunner and S. Kaskel, *J. Mater. Chem.*, 2012, **22**, 10303–10312.
- 97 V. Bon, N. Klein, I. Senkovska, A. Heerwig, J. Getzschmann, D. Wallacher, I. Zizak, M. Brzhezinskaya, U. Mueller and S. Kaskel, *Phys. Chem. Chem. Phys.*, 2015, **17**, 17471–17479.
- 98 D. Tanaka, S. Horike, S. Kitagawa, M. Ohba, M. Hasegawa, Y. Ozawa and K. Toriumi, *Chem. Commun.*, 2007, **0**, 3142–3144.
- 99 R. Matsuda, W. Kosaka, R. Kitaura, Y. Kubota, M. Takata and S. Kitagawa, *Microporous Mesoporous Mater.*, 2014, **189**, 83–90.
- 100 Q. Wei, M. Nieuwenhuyzen, F. Meunier, C. Hardacre and S. L. James, *Dalton Trans.*, 2004, 1807–1811.
- 101 K. Takaoka, M. Kawano, M. Tominaga and M. Fujita, *Angew. Chem. Int. Ed.*, 2005, **44**, 2151–2154.
- 102 P. Kanoo, R. Sambhu and T. K. Maji, *Inorg. Chem.*, 2011, **50**, 400–402.
- 103 J. Seo, C. Bonneau, R. Matsuda, M. Takata and S. Kitagawa, *J. Am. Chem. Soc.*, 2011, **133**, 9005–9013.
- 104 K. Biradha, Y. Hongo and M. Fujita, *Angew. Chem. Int. Ed.*, 2002, **41**, 3395–3398.
- 105 K. Uemura, S. Kitagawa, M. Kondo, K. Fukui, R. Kitaura, H. C. Chang and T. Mizutani, *Chem. Eur. J.*, 2002, **8**, 3586–3600.
- 106 H. F. Clausen, R. D. Poulsen, A. D. Bond, M. A. S. Chevallier and B. B. Iversen, *J. Solid State Chem.*, 2005, **178**, 3342–3351.

- 107 M.-H. Zeng, X.-L. Feng and X.-M. Chen, *Dalton Trans.*, 2004, 2217–2223.
- 108 K. L. Gurunatha and T. K. Maji, *Inorg. Chem.*, 2009, **48**, 10886–10888.
- 109 H. J. Choi and M. P. Suh, *J. Am. Chem. Soc.*, 2004, **126**, 15844–15851.
- 110 G. J. Halder and C. J. Kepert, *J. Am. Chem. Soc.*, 2005, **127**, 7891–7900.
- 111 A. Kondo, H. Noguchi, S. Ohnishi, H. Kajiro, A. Tohdoh, Y. Hattori, W.-C. Xu, H. Tanaka, H. Kanoh and K. Kaneko, *Nano Lett.*, 2006, **6**, 2581–2584.
- 112 R. A. Agarwal and S. Mukherjee, *Polyhedron*, 2016, **105**, 228–237.
- 113 S. Hiraide, H. Tanaka and M. T. Miyahara, *Dalton Trans.*, 2016, **45**, 4193–4202.
- 114 R. Kitaura, F. Iwahori, R. Matsuda, S. Kitagawa, Y. Kubota, M. Takata and T. C. K. O, *Inorg. Chem.*, 2004, **43**, 6522–6524.
- 115 Z. Chen, S. Xiang, D. Zhao and B. Chen, *Cryst. Growth Des.*, 2009, **9**, 5293–5296.
- 116 C. G. Carson, K. Hardcastle, J. Schwartz, X. Liu, C. Hoffmann, R. A. Gerhardt and R. Tannenbaum, *Eur. J. Inorg. Chem.*, 2009, 2338–2343.
- 117 Z. Q. Li, L. G. Qiu, W. Wang, T. Xu, Y. Wu and X. Jiang, *Inorg. Chem. Commun.*, 2008, **11**, 1375–1377.
- 118 P.-Z. Li, Y. Maeda and Q. Xu, *Chem. Commun.*, 2011, **47**, 8436–8438.
- 119 J. A. Foster, S. Henke, A. Schneemann, R. A. Fischer and A. K. Cheetham, *Chem. Commun.*, 2016, **52**, 10474–10477.
- 120 Y. N. Li, S. Wang, Y. Zhou, X. J. Bai, G. S. Song, X. Y. Zhao, T. Q. Wang, X. Qi, X. M. Zhang and Y. Fu, *Langmuir*, 2017, **33**, 1060–1065.
- 121 C. Kutzscher, A. Gelbert, S. Ehrling, C. Schenk, I. Senkovska and S. Kaskel, *Dalton Trans.*, 2017, **46**, 16480–16484.
- 122 Y. Peng, Y. Li, Y. Ban, H. Jin, W. Jiao, X. Liu and W. Yang, *Science*, 2014, **346**, 1356–1359.
- 123 T. Rodenas, I. Luz, G. Prieto, B. Seoane, H. Miro, A. Corma, F. Kapteijn, F. X. Llabrés I Xamena and J. Gascon, *Nat. Mater.*, 2015, **14**, 48–55.
- 124 Z. Chen, S. Xiang, H. D. Arman, P. Li, S. Tidrow, D. Zhao and B. Chen, *Eur. J. Inorg. Chem.*, 2010, 3745–3749.
- 125 A. Pariyar, J. Stansbery, R. L. Patel, X. Liang and A. Choudhury, *J. Coord. Chem.*, 2016, **69**, 1957–1969.
- 126 F. Ahmed, S. Roy, K. Naskar, C. Sinha, S. M. Alam, S. Kundu, J. J. Vittal and M. H. Mir, *Cryst. Growth Des.*, 2016, **16**, 5514–5519.
- 127 T. Y. Ho, S. M. Huang, J. Y. Wu, K. C. Hsu and K. L. Lu, *Cryst. Growth Des.*, 2015, **15**, 4266–4271.
- 128 S. Takamizawa, E. I. Nataka, T. Akatsuka, R. Miyake, Y. Kakizaki, H. Takeuchi, G. Maruta and S. Takeda, *J. Am. Chem. Soc.*, 2010, **132**, 3783–3792.

- 129 C. Dou, W. Kosaka and H. Miyasaka, *Chem. Lett.*, 2017, **46**, 1288–1291.
- 130 R. Nukada, W. Mori, S. Takamizawa, M. Mikuriya, M. Handa and H. Naono, *Chem. Lett.*, 1999, **28**, 367–368.
- 131 W. Mori, H. Hoshino, Y. Nishimoto and S. Takamizawa, *Chem. Lett.*, 1999, **28**, 331–332.
- 132 C. Kachi-Terajima, T. Akatsuka, M. Kohbara and S. Takamizawa, *Chem. Asian J.*, 2007, **2**, 40–50.
- 133 S. Takamizawa, C. Kachi-Terajima, M.-A. Kohbara, T. Akatsuka and T. Jin, *Chem. Asian J.*, 2007, **2**, 837–848.
- 134 S. Takamizawa, M. Kohbara and R. Miyake, *Chem. Asian J.*, 2009, **4**, 530–539.
- 135 S. Takamizawa, E. I. Nataka, T. Akatsuka, R. Miyake, Y. Kakizaki, H. Takeuchi, G. Maruta and S. Takeda, *J. Am. Chem. Soc.*, 2010, **132**, 3783–3792.
- 136 S. Takamizawa, *Angew. Chem. Int. Ed.*, 2015, **54**, 7033–7036.
- 137 Y. Takasaki and S. Takamizawa, *Nat. Commun.*, 2015, **6**, (8934) 1–5.
- 138 S. Takamizawa, T. Akatsuka and R. Miyake, *CrystEngComm*, 2010, **12**, 82–84.
- 139 S. Takamizawa, Y. Takasaki and R. Miyake, *Chem. Commun.*, 2009, **2**, 6625–6627.
- 140 S. Takamizawa, E.-I. Nakata and R. Miyake, *Dalton Trans.*, 2009, **2**, 1752–1760.
- 141 S. Takamizawa, E. Nakata, T. Saito, T. Akatsuka and K. Kojima, *CrystEngComm*, 2004, **6**, 197–199.
- 142 T. Ueda, K. Kurokawa, T. Eguchi, C. Kachi-terajima and S. Takamizawa, *J. Phys. Chem.*, 2007, **2**, 1524–1534.
- 143 S. Takamizawa and R. Miyake, *Chem. Commun.*, 2009, **0**, 4076–4078.
- 144 S. Takamizawa, T. Saito, T. Akatsuka and E. Nakata, *Inorg. Chem.*, 2005, **44**, 1421–1424.
- 145 I. H. Hwang, Y. D. Jo, H. Kim, K. B. Kim, K.-D. D. Jung, C. Kim, Y. Kim and S.-J. J. Kim, *Inorganica Chim. Acta*, 2013, **402**, 39–45.
- 146 S. Takamizawa, E. Nakata and T. Saito, *Angew. Chem.*, 2004, **43**, 1368–1371.
- 147 S. Takamizawa, E. Nakata, T. Saito and K. Kojima, *CrystEngComm*, 2003, **5**, 411–413.
- 148 S. Takamizawa, E. Nakata, T. Saito and T. Akatsuka, *Inorg. Chem.*, 2005, **44**, 1362–1366.
- 149 S. Takamizawa, E. Nakata and T. Saito, *CrystEngComm*, 2004, **6**, 39–41.
- 150 S. Takamizawa and E. Nakata, *CrystEngComm*, 2005, **7**, 476–479.
- 151 S. Takamizawa and R. Miyake, *CrystEngComm*, 2010, **12**, 2728–2733.
- 152 S. Takamizawa, E. Nakata and T. Saito, *Inorg. Chem. Commun.*, 2003, **6**, 1415–1418.
- 153 S. Takamizawa, E. Nakata and T. Saito, *Chem. Lett.*, 2004, **33**, 538–539.
- 154 S. Takamizawa, K. Kojima and T. Akatsuka, *Inorg. Chem.*, 2006, **45**, 4580–4582.

- 155 S. Takamizawa and M. Kohbara, *Dalton Trans.*, 2007, 3640–3645.
- 156 S. Takamizawa, E. Nakata and T. Akatsuka, *J. Am. Chem. Soc.*, 2008, **130**, 17882–17892.
- 157 K. Takahashi, N. Hoshino, T. Takeda, S. Noro, T. Nakamura, S. Takeda and T. Akutagawa, *Inorg. Chem.*, 2015, **54**, 9423–9431.
- 158 K. Takahashi, N. Hoshino, T. Takeda, S.-I. Noro, T. Nakamura, S. Takeda and T. Akutagawa, *Dalton Trans.*, 2014, **43**, 9081–9.
- 159 Y. Takasaki and S. Takamizawa, *J. Am. Chem. Soc.*, 2014, **136**, 6806–6809.
- 160 A. D. Burrows, M. F. Mahon, P. R. Raithby, A. J. Warren, S. J. Teat and J. E. Warren, *CrystEngComm*, 2012, **14**, 3658–3666.
- 161 W. Kosaka, K. Yamagishi, A. Hori, H. Sato, R. Matsuda, S. Kitagawa, M. Takata and H. Miyasaka, *J. Am. Chem. Soc.*, 2013, **135**, 18469–18480.
- 162 J. Zhang, W. Kosaka, H. Fukunaga, S. Kitagawa, M. Takata and H. Miyasaka, *Inorg. Chem.*, 2016, **55**, 12085–12092.
- 163 J. Tian, P. K. Thallapally and B. P. McGrail, *CrystEngComm*, 2012, **14**, 1909–1919.
- 164 S. Takamizawa, M. Kohbara, T. Akatsuka and R. Miyake, *New J. Chem.*, 2008, **32**, 1782–1787.
- 165 T.-H. Chen, I. Popov, W. Kaveevivitchai, Y.-C. Chuang, Y.-S. Chen, O. Daugulis, A. J. Jacobson and O. Š. Miljanic, *Nat. Commun.*, 2014, **5**, (5131) 1–7.
- 166 M. I. Hashim, C. W. Hsu, H. T. M. Le and O. Š. Miljanic, *Synlett*, 2016, **27**, 1907–1918.
- 167 J. L. Atwood, L. J. Barbour, A. Jerga and B. L. Schottel, *Science*, 2002, **298**, 1000–1002.
- 168 J. L. Atwood, L. J. Barbour and A. Jerga, *Science*, 2002, **296**, 2367–2369.
- 169 I. J. Vitórica-Yrezábal, D. F. Sava, G. A. Timco, M. S. Brown, M. Savage, H. G. W. Godfrey, F. Moreau, M. Schröder, F. Siperstein, L. Brammer, S. Yang, M. P. Atfield, J. J. W. McDouall and R. E. P. Winpenny, *Angew. Chem. Int. Ed.*, 2017, **56**, 5527–5530.
- 170 J. S. Wright, A. J. Metherell, W. M. Cullen, J. R. Piper, R. Dawson and M. D. Ward, *Chem. Commun.*, 2017, **53**, 4398–4401.
- 171 T. Tozawa, J. T. a Jones, S. I. Swamy, S. Jiang, D. J. Adams, S. Shakespeare, R. Clowes, D. Bradshaw, T. Hasell, S. Y. Chong, C. C. Tang, S. P. Thompson, J. Parker, A. Trewin, J. Bacsa, A. M. Z. Slawin, A. Steiner and A. I. Cooper, *Nat. Mater.*, 2009, **8**, 973–978.
- 172 S. Takamizawa, T. Akatsuka and T. Ueda, *Angew. Chem. Int. Ed.*, 2008, **47**, 1689–1692.
- 173 L. J. Barbour, *Chem. Commun.*, 2006, 1163–1168.
- 174 H. Adams, D. E. Fenton, A. Macías, E. Spey and L. Valencia, 1999, **1**, 4131–4137.
- 175 T. Itoh, M. Kondo, M. Kanaïke and S. Masaoka, *CrystEngComm*, 2013, **15**, 6122–6126.
- 176 T. Itoh, M. Kondo, H. Sakamoto, K. Wakabayashi, M. Kanaïke, K. Itami and S. Masaoka, *Dalton Trans.*, 2015, **44**, 15334–15342.

177 P. Chinapang, M. Okamura, T. Itoh, M. Kondo and S. Masaoka, *Chem. Commun.*, 2018, **54**, 1174–1177.

Chapter 2:

Probing the Porosity of a Family of 1D Halogen- Functionalised Coordination Polymers





2.1 Introduction

The construction of metal-organic frameworks, coordination polymers and the initial demonstration of hysteretic porosity have led to attempts to generate materials with both selectivity and retention of desired guests.¹ The pursuit of guest retention has resulted in a multitude of materials which display guest retention. For the most part this has been achieved utilising three core concepts, the first employing interior functionalisation of the pore space to aid with favourable host-guest interactions,^{2,3} the second being the use of systems with pores comparable in size to the intended guest resulting in the guest interacting with multiple surfaces of the host to aid guest retention³⁻⁶ and finally the use of a flexible framework systems which can alter pore shape and size to aid interactions between host and guest.⁷⁻¹⁰ One potential method of designing porous systems with flexible “shape-fit” pore spaces is rather than to focus on a 3D framework system instead to look at lower dimensional systems with small micropores which can be forced open by the addition of a guest. This method has been successfully employed by Takamizawa and co-workers, demonstrating that the one-dimensional coordination polymers $[M_2(bz)_4(pyz)]_n$ (where M = Cu or Rh, bz = benzoate, pyz = pyrazine, **Figure 2.1.1**), can be employed as a host for a range of small molecule guests.¹¹⁻¹⁹ These materials consist of a copper or rhodium paddlewheel unit with benzoate ligands. This inorganic coordination node (or secondary building unit, SBU) is then propagated in one dimension with pyrazine linkers, (**Figure 2.1.1**). These materials show dramatic expansion for a range of gas- and vapour-phase guests, but in many cases this expansion requires a large initial gate pressure. Further work on this class of materials saw the development of new materials by functionalisation of both the benzoate ligands as well as the connecting linker.

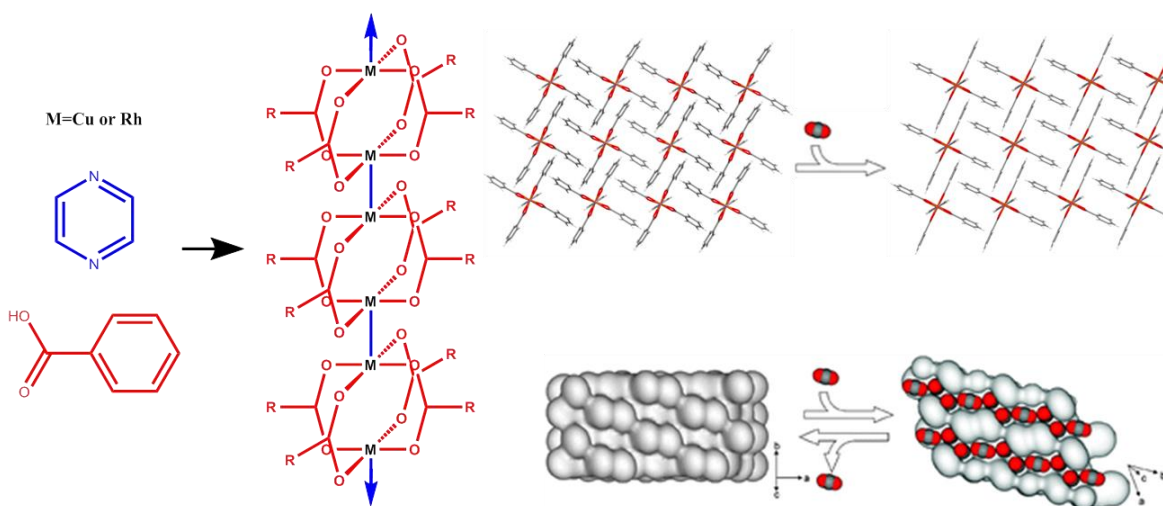


Figure 2.1.1. (a) Simplified skeletal structure of $[M_2(bz)_4(pyz)]_n$, (b) demonstrated CO_2 guest inclusion by Takamizawa and coworkers. Adapted in part with permissions from reference 16

Previous work carried out within the Brammer group has looked at the interplay between halogen bonding, hydrogen bonding and coordination bonding in a series of copper paddlewheel systems with iodo-functionalised benzoate ligands.²⁰⁻²² This work focused on an analogous paddlewheel SBU containing either 3- or 4-iodobenzoate ligands. These studies explored the crystal engineering of these systems when varying the propagating linker length

(from 1,4-diazabicyclo[2.2.2]octane to bis-pyridylethane, **Figure 2.1.2**). It was demonstrated that the formation of the paddlewheel SBU was dependent on the linker length, and the position of the iodine substituent in some instances disrupted the ability to form coordination polymer networks.

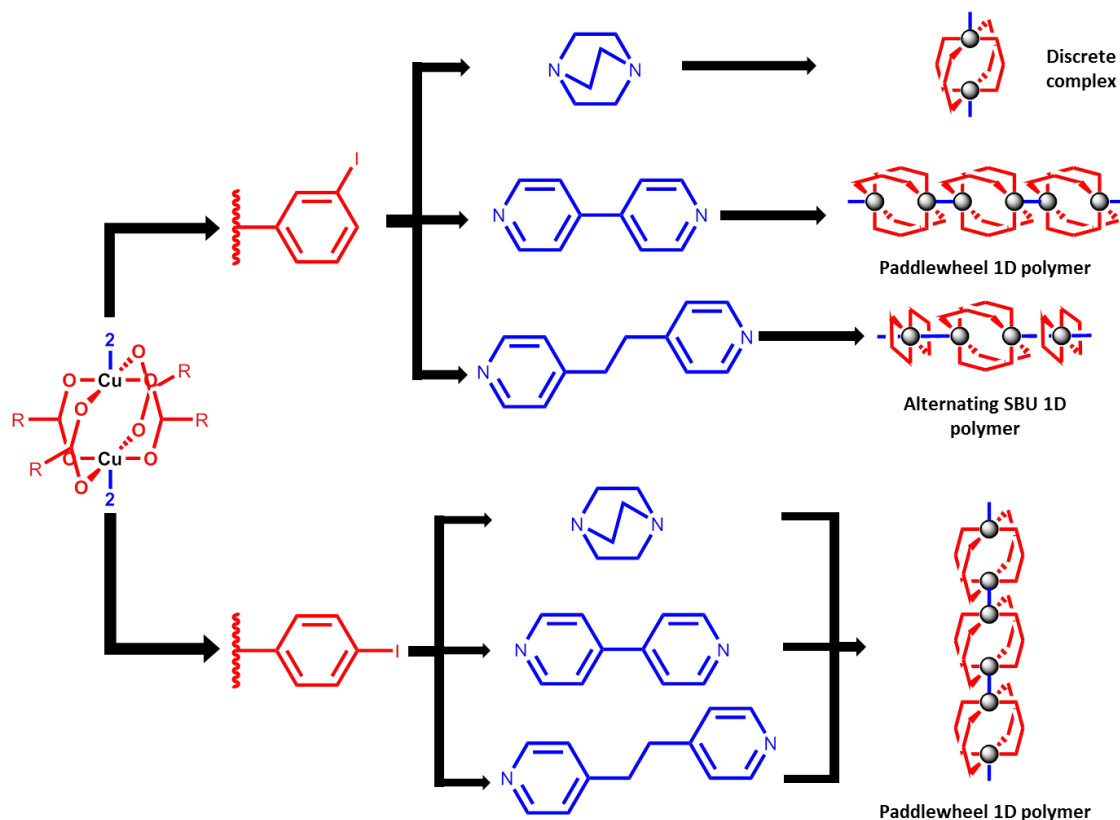


Figure 2.1.2. Summary of previous work carried out in the Brammer group focusing on a family of copper iodobenzoate complexes and coordination polymers.^{20–22}

In more recent work, Akutagawa and co-workers demonstrated with a family of 1D coordination polymers, $[\text{Cu}_2(4\text{-Xbz})_4\text{pyz}]_n$ ($4\text{-Xbz} = 4\text{-halobenzoate}$, where $X = \text{I}, \text{Br}$ or Cl), that gated adsorption of CO_2 was dependent on the halogen functionality present.⁵ This was shown by performing volumetric gas adsorption on the three materials. The volumetric adsorption studies (CO_2 at 195K) demonstrated no uptake in the case of the iodo-containing system and gated adsorption in the case of the bromo and chloro systems. The gates with respect to the bromo and chloro derivatives occurred at p/p^0 values of 0.8 and 0.3, respectively (**Figure 2.1.3**). Both the bromo- and chloro-containing materials demonstrated comparable quantities of CO_2 uptake, suggesting these two materials possess similar void spaces. The original work, however, reports void spaces (determined using PLATON²³ at atmospheric pressure and 110 K) of 44.1 and 22.5 \AA^3 per formula unit for the chloro and bromo systems, respectively.⁵ This suggests that at least the bromo functionalised material may undergo a structural transformation to generate a comparable void space to the chloro derivative. However, no investigation of structural changes in these materials was reported.

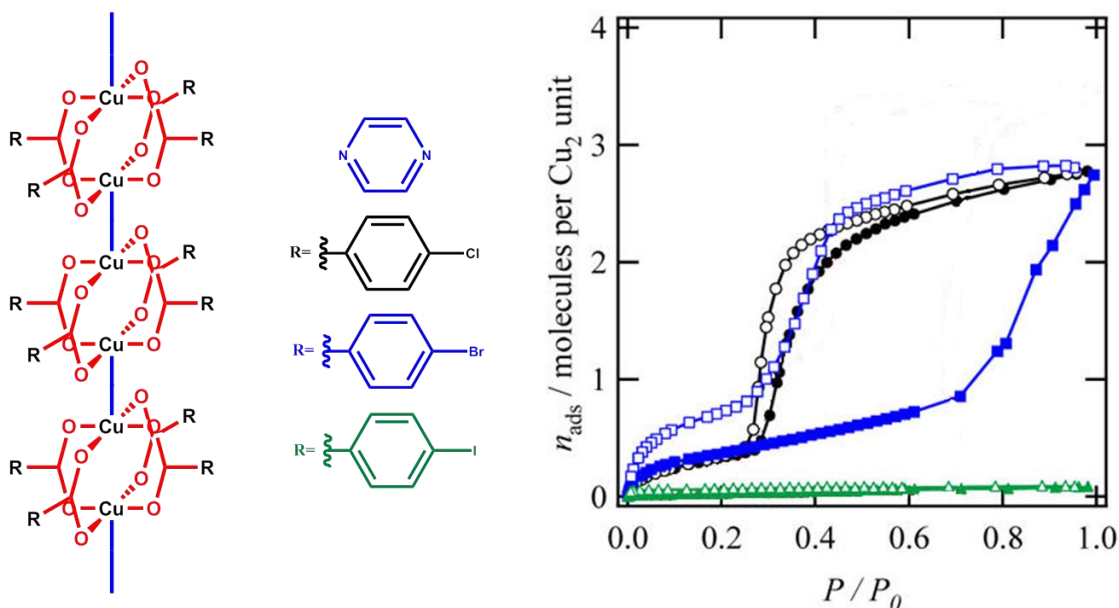


Figure 2.1.3. Volumetric CO₂ adsorption isotherms (195 K) (right) for a family of 1D coordination polymers, [Cu₂(4-Xbz)₄(pyz)]_n (X = I, Br, Cl) (left). Adapted with permission from reference 5.

The studies in this chapter follow on from these preliminary volumetric gas adsorption studies by Akutagawa et al.⁵ As well as looking at the three published materials the family of coordination polymers is extended further with the synthesis of the corresponding coordination polymer with fluorine- functionalised benzoates. This work focuses on quantifying the uptake of CO₂ in this family of coordination polymers and determining the structural response through a series of *in situ* crystallographic studies during gas uptake, which were carried out at Diamond Light Source.^{24–26}

2.2 Aims

The purpose of this work was to synthesise a family of 1D coordination polymers with the formula [Cu₂(4-Xbz)₄(pyz)]_n (X = I, Br, Cl and F; pyz= pyrazine). Previously published work has demonstrated a difference in CO₂ uptake of three of these systems,⁵ but in the absence of *in situ* structural studies during gas uptake it is not known how gas uptake within these materials is achieved. This chapter reports the synthesis of these three known systems and one previously unpublished material ([Cu₂(4-Fbz)₄pyz]_n, **2.4(F)**) and attempts to understand the nature of CO₂ inclusion through the use of *in situ* crystallographic studies during gas uptake on both single crystal and bulk powder samples (**Figure 2.2.1**).

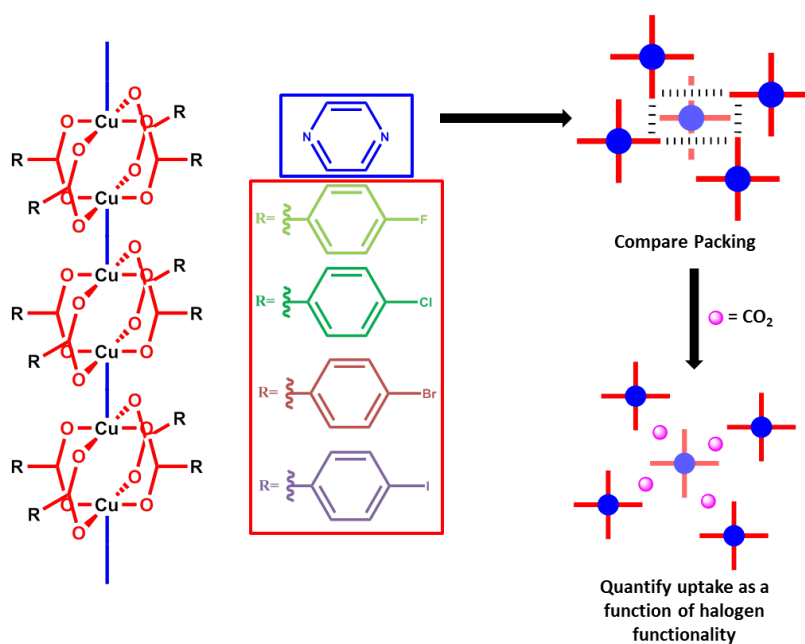


Figure 2.2.1- Summary of the proposed aims of this chapter

2.3 Experimental

2.3.1 Synthetic Procedures

All solvents (HPLC grade) and reagents were purchased from Sigma Aldrich, VWR or Alfa Aesar. Reagents and solvents were used as received without further purification.

The synthesis of the series of 1D coordination polymers was carried out by two methods. Method 1 involves a solvent layering approach adapted for this work from a previous report.²² This method produced single crystals suitable for structure characterisation in the case of the iodobenzoate and bromobenzoate systems, but in the case of the chlorobenzoate and fluorobenzoate systems this resulted in the formation of crystalline powders. Powder X-ray diffraction analysis confirmed that these samples were the desired coordination polymers. Larger crystals could be obtained by employing a vapour diffusion method (Method 2) adapted from a previously published synthesis of an analogous system, $[\text{Cu}_2(4\text{-Fbz})_4(2\text{-Mepyz})]_n$ (Mepyz = methylpyrazine).⁶

Method 1

Copper(II) acetate monohydrate (2 mmol) was dissolved in 6 mL methanol in a 14 mL vial. In a second 37 mL vial 4-halobenzoic acid (4 mmol) and pyrazine (2 mmol) were dissolved in benzyl alcohol. Sonication was employed to aid dissolution of these two mixtures. To the second vial 1 mL of benzyl alcohol was layered on top, followed by 1 mL of methanol. Finally the copper acetate solution was layered on top of the two buffer layers. Samples were then left undisturbed to allow for diffusion of the reaction mixture and crystallisation of desired product. Crystal formation was observed after *ca.* 1 week. Samples were in turn filtered and washed with methanol for standard characterisation or single crystals suitable for structure characterisation were selected directly from the mother liquor.

Method 2

Copper(II) acetate monohydrate (2 mmol) and 4-halobenzoic acid (4 mmol) were dissolved in 5 mL methanol in a 14 mL vial. In a second 37 mL vial pyrazine (6 mmol) was dissolved in 5 mL methanol. Sonication was employed to aid dissolution of these two solutions. The 14 mL vial containing the copper acetate and 4-halobenzoic acid solution was then placed in the larger 37 mL vial containing the pyrazine solution. The cap of the inner vessel was loosened and pierced to allow for slow vapour diffusion of pyrazine into the inner vessel. Crystal formation was observed after *ca.* 1 month. Following crystallisation, samples were filtered and washed with methanol for standard characterisation or single crystals suitable for structure analysis were extracted directly from the mother liquor.

2.3.1.1 Synthesis of $[\text{Cu}_2(\text{4Ibz})_4(\text{pyz})]_n$ (2.1(I))

Method 1

Coordination polymer **2.1(I)** was synthesised using method 1. Copper(II) acetate monohydrate (40.9 mg, 0.20 mmol), 4-iodobenzoic acid (111.4 mg, 0.45 mmol) and pyrazine (18.5 mg, 0.23 mmol). Yield (75.0 mg, 61.23 %). Elemental Calcd.: C 32.16, H 1.67, N 2.34, I 42.47 %. Found: C 32.38, H 2.05, N 2.30, I 42.54 %.

2.3.1.2 Synthesis of $[\text{Cu}_2(\text{4Brbz})_4(\text{pyz})]_n$ (2.2(Br))

Method 1

Coordination polymer **2.2(Br)** was synthesised using method 1. Copper(II) acetate monohydrate (38.8 mg, 0.19 mmol), 4-bromobenzoic acid (96.1 mg, 0.48 mmol) and pyrazine (17.0 mg, 0.21 mmol). Yield (58.4 mg, 59.67 %). Elemental Calcd.: C 38.17, H 2.00, N 2.78, Br 31.73%. Found: C 38.40, H 2.24, N 2.91, Br 30.33 %.

Method 2

Coordination polymer **2.2(Br)** was synthesised using method 2. Copper(II) acetate monohydrate (40.3 mg, 0.20 mmol), 4-bromobenzoic acid (96.3 mg, 0.48 mmol) and pyrazine (59.5 mg, 0.74 mmol). Yield (46.8 mg, 46.04 %). Elemental Calcd.: C 38.16, H 2.00, N 2.78, Br 31.73 %. Found: C 38.06, H 2.23, N 2.79, Br 31.49 %.

2.3.1.3 Synthesis of $[\text{Cu}_2(\text{4Clbz})_4(\text{pyz})]_n$ (2.3(Cl))

Method 1

Coordination polymer **2.3(Cl)** was synthesised using method 1. Copper(II) acetate monohydrate (40.9 mg, 0.20 mmol), 4-chlorobenzoic acid (79.0 mg, 0.51 mmol) and pyrazine (15.9 mg, 0.20 mmol). Yield (35.5 mg, 41.77 %). Elemental Calcd.: C 46.34, H 2.43, N 3.38, Cl 17.10 %. Found: C 45.93, H 2.69, N 3.33, Cl 16.37 %.

Method 2

Coordination polymer **2.3(Cl)** was synthesised using method 2. Copper(II) acetate monohydrate (44.6 mg, 0.22 mmol), 4-chlorobenzoic acid (68.5 mg, 0.44 mmol) and pyrazine

(50 mg, 0.62 mmol). Yield (61.7mg, 68.01 %). Elemental Calcd.: C 46.34, H 2.43, N 3.38, Cl 17.10 %. Found: C 45.90, H 2.59, N 3.34, Cl 17.06 %.

2.3.1.4 Synthesis of $[\text{Cu}_2(\text{4Fbz})_4(\text{pyz})]_n$ (**2.4(F)**)

Method 1

Coordination polymer **2.4(F)** was synthesised using method 1. Copper(II) acetate monohydrate (40.9 mg, 0.20 mmol), 4-fluorobenzoic acid (56.6 mg, 0.40 mmol) and pyrazine (15.3 mg, 0.19 mmol). Yield (23.9 mg, 30.99 %). Elemental Calcd.: C 50.33, H 2.64, N 3.67 %. Found: C 49.70, H 2.76, N 3.64 %.

Method 2

Coordination polymer **2.4(F)** was synthesised using method 2. Copper(II) acetate monohydrate (44.5 mg, 0.22 mmol), 4-fluorobenzoic acid (57.4 mg, 0.41 mmol) and pyrazine (52.8 mg, 0.66 mmol). Yield (44.7 mg, 57.16 %). Elemental Calcd.: C 50.33, H 2.64, N 3.67 %. Found: C 49.73, H 2.64, N 3.73 %.

2.3.2 Single-Crystal X-Ray Diffraction

Single crystals of **2.2(Br)**, **2.3(Cl)** and **2.4(F)** suitable for structure determination were selected from samples extracted from the mother liquor suspended in perfluoropolyether oil (FOMBLIN Y), mounted onto a mylar tip. Data were collected on either on a Smart APEX-2 CCD diffractometer equipped with a graphite monochromator Mo-K α sealed-tube source or a Bruker D8 Venture Single Crystal Diffractometer equipped with a μS Microfocus Cu-K α sealed-tube source and a Photon 100 CMOS (Complementary Metal Oxide Sensor) Detector with shutterless capability. Sample temperature was maintained using an Oxford Cryosystems Cryostream Device. Data were corrected for absorption using empirical methods (SADABS) based on symmetry-equivalent reflections and measurements at different azimuthal angles.²⁷⁻²⁹ Structure solution was achieved by direct methods and the crystal structure was refined using full-matrix least-squares against weighted F^2 values using SHELXL³⁰ within Olex2.³¹ Non-hydrogen and non-disordered atoms were refined anisotropically. Hydrogen atoms were placed in calculated positions, refined to idealized geometries (riding model) and assigned a fixed isotropic displacement parameter.

Disorder of one of the aromatic rings was observed in the case of **2.2(Br)**. The two ring orientations were refined with occupancies 61.6(9):38.4(9). The ring geometry was constrained either to be flat or to be a regular hexagon. Details of the data collection are outlined in **Table 2.3.2-1** (Appendix 2.8.1).

2.3.3 Powder X-Ray Diffraction (PXRD)

Samples were filtered under vacuum from the mother liquor and washed with methanol. Once dry, samples were ground into a fine powder using a pestle and mortar. The crystalline samples were then analysed using a Bruker D8 Advance X-ray powder diffractometer equipped with a LynxEye XE Detector, a Cu-K α sealed-tube source and a variable motorised slit. Samples were placed onto a low-background sample holder and data were collected while rotating the

sample at 15 rpm. Data were collected at room temperature between $4^\circ \leq 2\theta \leq 60^\circ$ ($3^\circ \leq 2\theta \leq 60^\circ$ for **2.4(F)**) in steps of 0.02° . The data were then analysed and Pawley refinement³² carried out using the TOPAS program with input files being prepared using jEdit editor.^{33,34} Details of these fits are outlined in **Table 2.3.3-1**.

Table 2.3.3-1. Summary of Pawley refinements of **2.1 (I)**, **2.2(Br)**, **2.3(Cl)** and **2.4(F)**

	Space Group	Volume (Å ³)	a (Å)	b (Å)	c (Å)	α (°)	β (°)	γ (°)	R _{wp}	R _{wp'}	Parameters
2.1(I)	I4 ₁ /a	7121.1(3)	18.9499(3)	18.9499(3)	19.8304(5)	90	90	90	0.0554	0.1300	539
2.2(Br)	I4 ₁ /a	6806.8(3)	18.5838(3)	18.5838(3)	19.7095(4)	90	90	90	0.0488	0.1119	519
2.3(Cl)	I2/m	1687.0(1)	12.3166(5)	9.8157(4)	14.3301(9)	90	103.159(4)	90	0.0741	0.1667	293
2.4(F)	I2/m	1673.5(1)	12.0217(4)	9.74812(4)	14.6570(8)	90	103.022(3)	90	0.0527	0.1013	289

2.3.4 Volumetric Nitrogen and Carbon Dioxide Adsorption Studies

Samples **2.3(Cl)** and **2.4(F)** were analysed for adsorption of N₂ and CO₂ gases using a Micromeritics 2020 Plus Volumetric Gas Analyser. N₂ isotherms were recorded at 77 K and CO₂ isotherms at 195 K. Prior to isotherms being recorded samples were initially stored in a vacuum oven at 80 °C for 12 hours. Following this treatment samples were then subjected to a degas condition on the Micromeritics instrument, which consisted of an evacuation in which the sample was heated to 60 °C (10 °C/min) and pressure was reduced to 4 μmHg (5 mmHg/s). Following this evacuation phase a heating phase was applied in which the sample was held under vacuum at 120 °C for 1000 mins.

Following volumetric analysis samples were recovered and analysed via powder X-ray diffraction following the procedure outlined in Section 2.3.3. Pawley refinements³² were carried out using TOPAS.^{33,34} The results of these fits are outlined (**Table 2.3.4-1**).

Table 2.3.4-1. Summary of Pawley refinements of **2.3(Cl)** and **2.4(F)** post volumetric adsorption analysis

	Space Group	Volume (Å ³)	a (Å)	b (Å)	c (Å)	α (°)	β (°)	γ (°)	R _{wp}	R _{wp'}	Parameters
2.3(Cl)^a	I2/m	1683.5(1)	12.3131(4)	9.8108(5)	14.3058(9)	90	103.057(4)	90	0.0786	0.1563	297
2.3(Cl)^b	I2/m	1683.5(2)	12.3134(4)	9.8110(6)	14.3029(9)	90	103.016(4)	90	0.0759	0.158	299
2.4(F)^a	I2/m	1663.6(1)	12.0070(5)	9.7472(5)	14.5756(8)	90	102.780(3)	90	0.0616	0.117	293
2.4(F)^b	I2/m	1669.0(3)	12.0082(9)	9.7386(9)	14.6494(17)	90	103.040(8)	90	0.077	0.165	294

^a following volumetric adsorption and desorption of N₂. ^b following volumetric adsorption and desorption of CO₂.

2.3.5 *In situ* Powder X-Ray Diffraction Studies during CO₂ Adsorption and Desorption

Samples of **2.1(I)**, **2.2(Br)**, **2.3(Cl)** and **2.4(F)** were studied by PXRD during CO₂ adsorption and desorption by utilising an *in situ* gas cell on beamline I11 at Diamond Light Source.^{26,35,36} Samples were loaded into a 0.7 mm quartz capillary, sealed in a gas cell and evacuated ($\approx 10^{-5}$ mbar) on the beamline before an initial powder pattern was recorded. Samples were then dosed to sequential increasing (and decreasing) pressures of CO₂ allowing a 30-minute

equilibration period prior to data collection. In the case of **2.1(I)** *in situ* experiments were carried out at room temperature, whereas samples of **2.2(Br)**, **2.3(Cl)** and **2.4(F)** were recorded at both room temperature and at 195 K with the temperature being maintained with the use of an Oxford Cryosystems Cryostream plus 700 series low-temperature device. The 30-minute equilibration time was sufficient in the case of **2.3(Cl)** and **2.4(F)**, but **2.2(Br)** at 195 K required an extended equilibration time of 2 hours to observe a guest-included phase. All room temperature measurements and the 195 K measurements of **2.3(Cl)** and **2.4(F)** were recorded using a PSD (position-sensitive detector)²⁶ and the 195 K data recorded for **2.2(Br)** were recorded utilising the MAC (Multiple Analysing Crystal)^{35,36} detector to avoid high background fluorescence.

Data were fitted using Pawley refinement³² using the TOPAS program.^{33,34} The data collected at 195 K were then fitted using Rietveld refinement³⁷ using TOPAS.^{33,34} Starting structural models were adapted from single-crystal structures. Location of CO₂ sites was attempted with the use of a rigid-body model, allowing for refinement of position and occupancy of the CO₂, with the initial position and occupancy being randomised and allowed to converge to a minimum. Refinement details are outlined in **Tables 2.3.5-1 to 2.3.5-10** (Appendix 2.8.2).

2.3.6 *In situ* Single-Crystal X-Ray Diffraction Studies during CO₂ Adsorption and Desorption

Single crystals of **2.1(I)**, **2.2(Br)**, **2.3(Cl)** and **2.4(F)** were structurally characterised during CO₂ adsorption and desorption on beamline I19 at Diamond Light Source^{24,25,38} utilising the *in situ* gas cell instrumentation developed at the beamline. Single crystals were selected directly from the mother liquor and glued, either with epoxy or superglue, on to a long mylar microloop. Once the glue had dried these loops were then inserted into a capillary gas cell with glue being applied to the edge of the pin to ensure samples did not move during data collection. The gas cell was then sealed and evacuated ($\approx 10^{-5}$ mbar) on the beamline. Following alignment an initial data collection was recorded with the sample under vacuum. This was then followed by dosing the cell with successive increasing (and decreasing) pressures of CO₂, allowing for 30-minute equilibration times between dosing and data collection. In the case of **2.1(I)** a single crystal was tested at 1 bar CO₂ pressure at low temperature (195K and 100K) but demonstrated minimal unit cell change so further pressure steps were not investigated, whereas for **2.2(Br)**, **2.3(Cl)** and **2.4(F)** data were only recorded at 195K, but in a series of pressure steps across the full pressure range between 0-1 bar CO₂. Due to radiation damage for **2.4(F)** two studies were carried out, one focusing on the adsorption of the material (**Table 2.3.6-4**, Appendix 2.8.3) and a second focusing on the desorption of the material (**Table 2.3.6-5**, Appendix 2.8.3).

The data were processed using CryAlisPro³⁹ using a predetermined instrument model determined from a strongly diffracting reference crystal to enable more accurate determination of the orientation matrix used for integration of diffraction intensities. Data were corrected for absorption using empirical methods (SADABS) based on symmetry-equivalent reflections and measurements at different azimuthal angles.²⁷⁻²⁹ Structure solution was achieved by direct methods and the crystal structure was refined using full-matrix least-squares against weighted F^2 values using SHELXL³⁰ within Olex2.³¹ Non-hydrogen and non-

disordered atoms were refined anisotropically. Hydrogen atoms were placed in calculated positions, refined to idealized geometries (riding model) and assigned a fixed isotropic displacement parameter. A summary of the data processing is outlined (**Table 2.3.6-1-5**, Appendix 2.8.3).

In the case of **2.1(I)** and **2.2 (Br)** disorder analogous to that previously described was observed (see Section 2.3.2 and previously published work^{5,40}). This was resolved as a two-part orientational disorder of the aromatic ring, with the minor component being constrained to be a regular hexagon. The displacement ellipsoids of the disordered ring were modelled anisotropically applying restraints to the size and direction of the displacements. In the case of **2.4(F)** restraints were applied to the fluorobenzoates in an attempt to idealise the shape of the aromatic rings. Guest modelling of CO₂ was carried out in the studies of **2.3(Cl)** and **2.4(F)**. In **2.3(Cl)** this was achieved by modelling a CO₂ molecule with a partial occupancy. In **2.4(F)** a similar partial occupancy was applied but additional bond distance constraints were also applied.

2.4 Results and Discussion

2.4.1 Synthesis of 2.1(I), 2.2(Br), 2.3(Cl) and 2.4(F)

Coordination polymers **2.1(I)**, **2.2(Br)**, **2.3(Cl)** and **2.4(F)** were synthesised in moderate yields by room-temperature solvent diffusion methods, the phase purity being confirmed by powder X-ray diffraction and elemental analysis. For **2.3(Cl)** and **2.4(F)** method 1 (solvent diffusion), which had been used to obtain single crystals of **2.1(I)** and **2.2(Br)**, did not result in suitable single crystals, leading to the application of method 2 (vapour diffusion). On carrying out the synthesis multiple times an impurity identified by powder X-ray diffraction to be the molecular compound [Cu₂(4-Xbz)₄(MeOH)₂], was noted on some occasions.ⁱ Formation of this impurity could be prevented by ensuring suitable stoichiometric ratios of reagent or alternatively could be removed by washing the product mixture with hot methanol (**Figure 2.4.1-1**)

ⁱ Although analogous molecular compounds, [Cu₂(4Ibz)₄(ROH)₂], feature in the literature^{22,60-62} molecular compound with coordinated methanol (with 4-Ibz, 4-Brbz and 4-Clbz) were synthesised during failed coordination polymer synthesis (using method 1) with 2,4,6-Tri(4-pyridyl)-1,3,5-triazine as a desired linker.

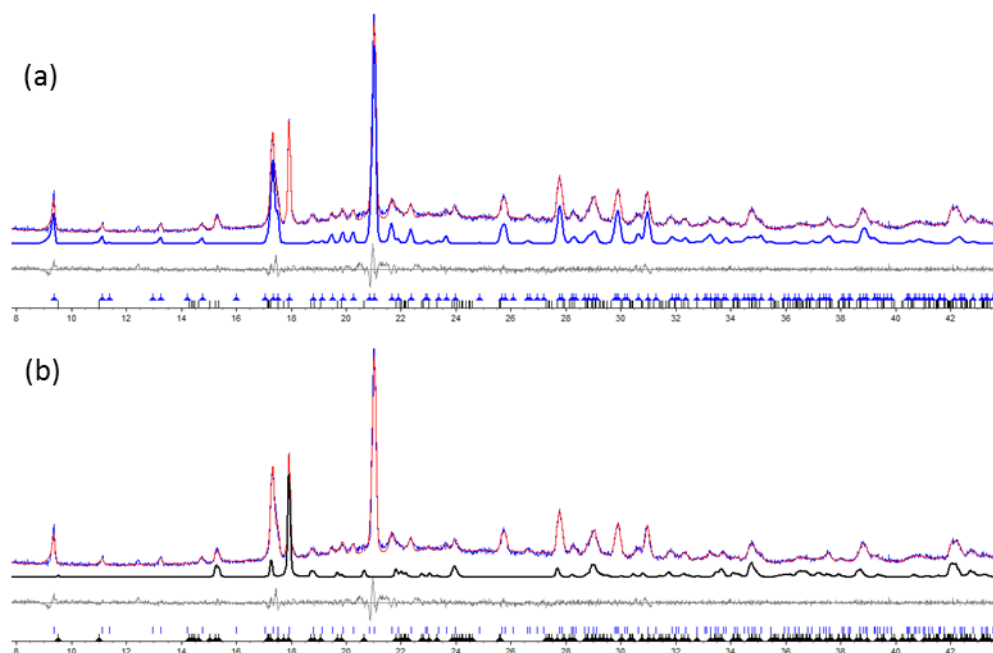


Figure 2.4.1-1. Example Pawley fit of a mixed phase resulting from the synthesis of **2.1(I)**, highlighting (a) the **2.1(I)** phase (in bold blue) and (b) the impurity ($[\text{Cu}_2(4\text{Ibz})_4(\text{MeOH})_2]$) phase (in bold black).

2.4.2 Crystal Packing

All four coordination polymers crystallise without entrapped solvent. Thus desolvation is not required prior to gas adsorption studies. The four structures can be grouped into two packing arrangements with distinct space groups. Samples **2.1(I)** and **2.2(Br)** crystallise in tetragonal space group $I4_1/a$ and samples **2.3(Cl)** and **2.4(F)** in monoclinic $C2/m$ (non-standard setting $I2/m$ is used throughout to allow use of a β angle closer to 90°). On comparing the packing of these systems it is noted there are a series of similar packing traits. Firstly all four systems exhibit network interpenetration (**Figure 2.4.2-1**) with neighbouring polymer chains being offset by a formula unit. This interpenetration results in the closest contacts between polymer chains being the halogen to pyrazine distance (**Figure 2.4.2-1**). This offset packing is analogous to the packing observed in $[\text{M}_2(\text{bz})_4(\text{pyz})]_n$ as well as in a number of analogous 1D coordination polymers with functionality present on the benzoate ligands and/or the linker (**Figure 2.4.2-2**).^{5,6,19,41}

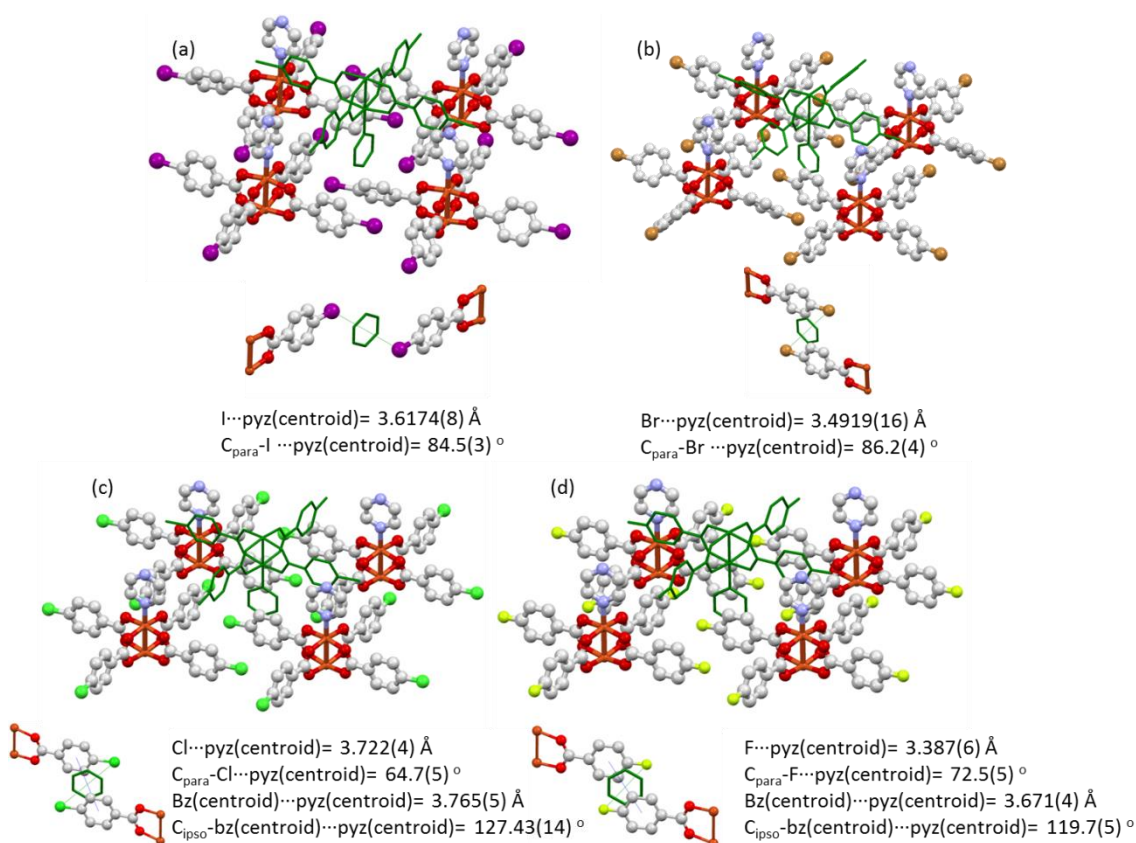


Figure 2.4.2-1. Crystal structures of (a) **2.1(I)**, (a) **2.2(Br)**, (c) **2.3(Cl)** and (d) **2.4(F)** showing network interpenetration; secondary images show the inter-network close contact with distances and angles. Primary network shown in ball and stick representation with Cu, Orange; C, grey; N, blue; O, red; I, purple; Br, brown; Cl, green; interpenetrated polymer shown in dark green capped sticks representation.

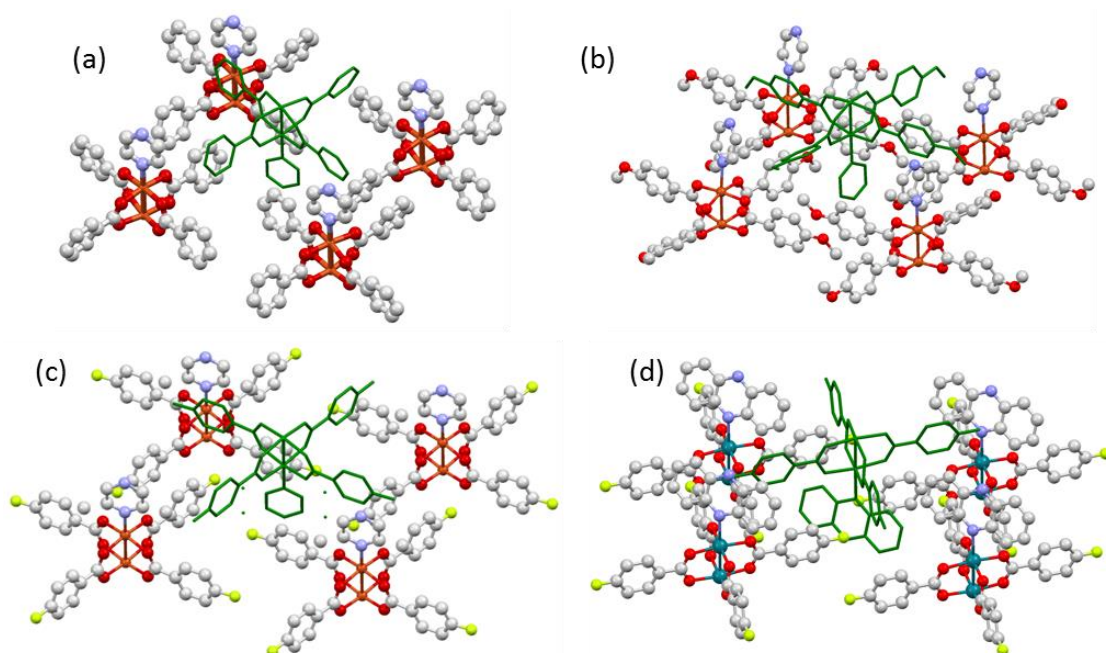


Figure 2.4.2-2. Images of the interpenetration observed other 1D coordination polymers. (a) $[\text{Cu}_2(\text{bz})_4(\text{pyz})]_n$ ¹⁹ (b) $[\text{Cu}_2(4\text{-OMebz})_4(\text{pyz})]_n$ (4-OMebz = 4-methoxybenzoate),⁵ (c) $[\text{Cu}_2(4\text{-Fbz})_4(\text{MePyz})]_n$ (MePyz = methylpyrazine)⁶ and (d) $[\text{Rh}_2(4\text{-Fbz})_4(\text{phen})]_n$ (phen = phenazine).⁴¹ Colour scheme as in **Figure 2.4.2-1**; Rh, turquoise.

Coordination polymers **2.1(I)** and **2.2(Br)** consist of two crystallographically distinct neighbouring paddlewheel units connected by a pyrazine linker, one ordered and one with benzoate groups rotationally disordered over two orientations (**Figure 2.4.2-3**). The two distinct paddlewheel units appear in the asymmetric unit as one quarter of the paddlewheel. The 4-halobenzoate ligands (iodo or bromo) project linearly from the centre of the paddlewheel SBU with $\text{Cu}_2(\text{cent})\cdots\text{O}_2(\text{cent})\cdots\text{ring}(\text{cent})$ angles of $176.9(1)^\circ$ and $176.2(2)^\circ$ for **2.1(I)** and $178.3(2)^\circ$ and $176.9(3)^\circ$ for **2.2(Br)** (cent = centroid) (**Figure 2.4.2-3**).

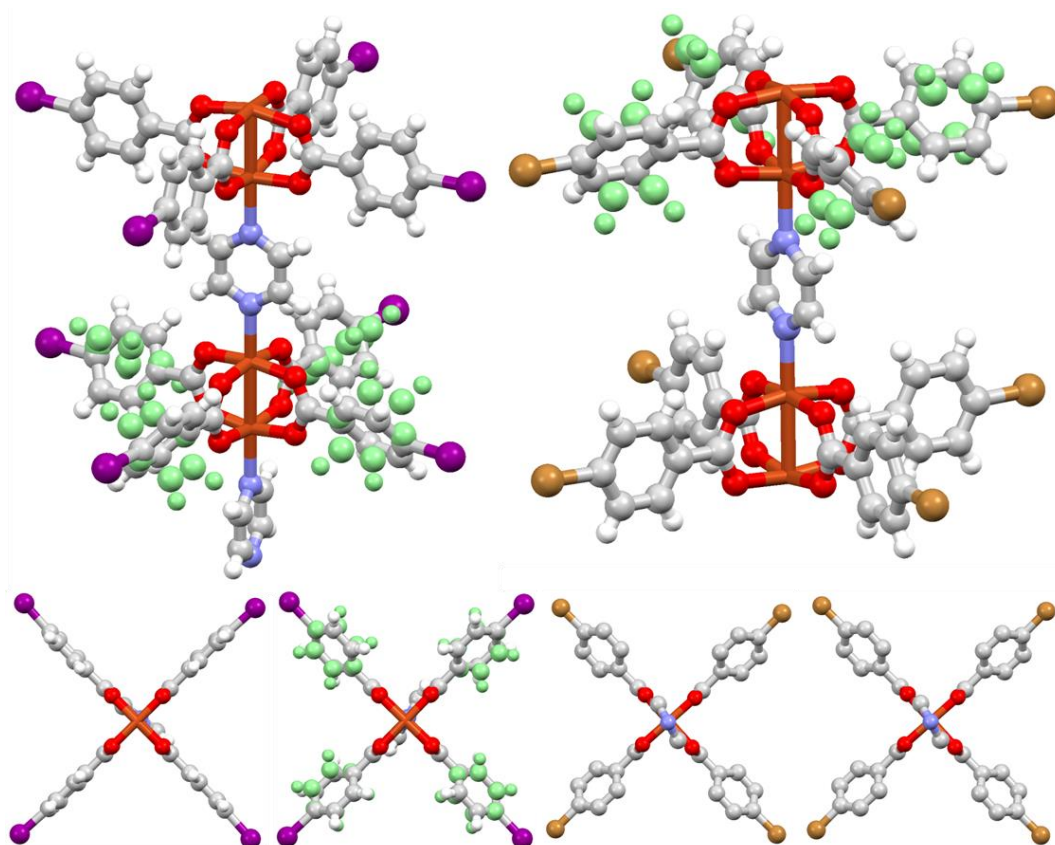


Figure 2.4.2-3. The two crystallographically distinct paddlewheels observed in **2.1(I)** and **2.2(Br)** (top) and highlighting the linear nature of the benzoate groups relative to the central paddlewheel SBU (bottom). Colour scheme as in **Figure 2.4.2-1**; H, white; 2nd orientation of disordered aryl ring shown in green.

The coordination polymers **2.1(I)** and **2.2(Br)** extend along the *c*-axis. The halogen functionality is involved in a series of $\text{C}-\text{X}\cdots\pi$ halogen bonding interactions with neighbouring coordination polymers. The $\text{C}-\text{I}$ vector points towards the carbon (C_{ipso}) of the aromatic ring with the carboxylate functional group. This suggests an interaction with the delocalised ring π -system including the COO^- functionality. This interaction is observed at $\text{X}\cdots\text{C}_{\text{ipso}}$ distances of $3.473(7) \text{ \AA}$ and $4.059(7) \text{ \AA}$ for **2.1(I)** and $3.398(9) \text{ \AA}$ and $4.120(9) \text{ \AA}$ for **2.2(Br)** (**Figure 2.4.2-4**). These two $\text{C}-\text{X}\cdots\pi$ interactions occur antiparallel to each other with a centroid-centroid distance between the antiparallel aromatic rings of $4.671(5) \text{ \AA}$ and $4.584(4) \text{ \AA}$ for **2.1(I)** and **2.2(Br)**, respectively (**Figure 2.4.2-4**). These interactions then propagate to form a two-dimensional halogen-bonding network. This network is then interpenetrated with a second network of coordination polymers as previously discussed (**Figure 2.4.2-1**).

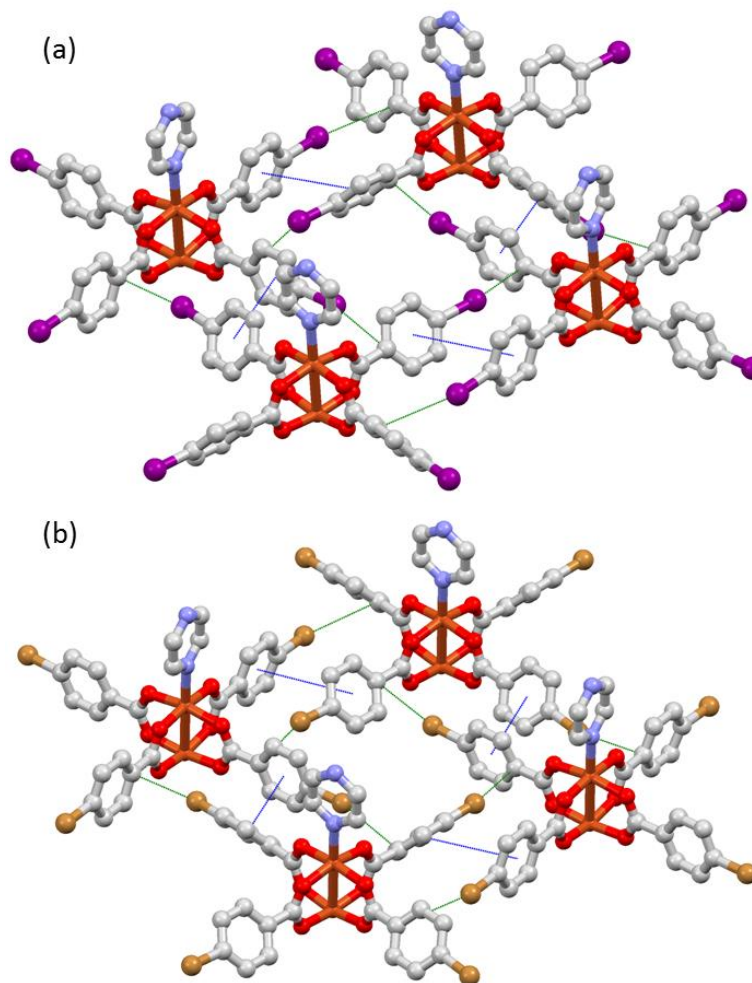


Figure 2.4.2-4. The observed halogen-bonding network of **2.1(I)** (a) and **2.2(Br)** (b). Colour scheme as in **Figure 2.4.2-1**, C-X...C_{ipso} halogen bonds represented with green lines and π...π interactions shown with blue lines.

The crystal structures of **2.3(Cl)** and **2.4(F)** are isostructural and comprised of one unique paddlewheel unit containing two crystallographically independent benzoates groups (**Figure 2.4.2-5**). Coordination of these ligands involves slight rotation about the O...O vector of the carboxylate group with $\text{Cu}_{2(\text{cent})}\cdots\text{O}_{2(\text{cent})}\cdots\text{ring}_{(\text{cent})}$ angles of $166.0(2)^\circ$ and $174.53(18)^\circ$ for **2.3(Cl)** and $165.28(17)^\circ$ and $177.56(14)^\circ$ for **2.4(F)** (**Figure 2.4.2-5**) analogous to the deformation seen in “breathing” carboxylate MOFs.^{10,42–44}

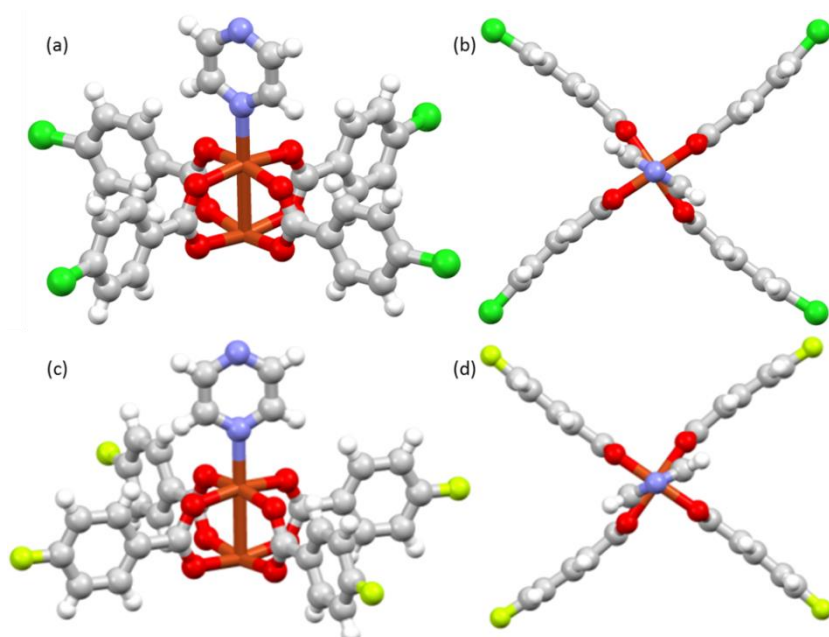


Figure 2.4.2-5. Formula units of (a) **2.3(Cl)** and (c) **2.4(F)** and the bending of the benzoates (b) and (d). Colour scheme as in **Figure 2.4.2-1**.

Coordination polymers **2.3(Cl)** and **2.4(F)** propagate along the *b*-axis. The 1D coordination polymers exhibit similar packing, forming two cooperative antiparallel C–Cl \cdots π interactions with Cl \cdots C_{ipso} distances of 3.455(14) Å and 4.049(13) Å in the case of **2.3(Cl)**. The fluoro functionalised polymer, **2.4(F)**, despite the absence of a halogen σ -hole, exhibits comparable F \cdots C_{ipso} distances of 3.376(14) Å and 4.561(13) Å (**Figure 2.4.2-6**). The longer X \cdots C_{ipso} (for **2.3(Cl)**) and both (for **2.4(F)**) distances are greater than the sum of van der Waals radii for each structure.^{45,46} The halobenzoate ligand that forms the shorter of these two halogen-bonding interactions also forms a $\pi\cdots\pi$ interaction with centroid-centroid distances of 4.021(10) Å and 4.142(10) Å for **2.3(Cl)** and **2.4(F)**, respectively. The longer halogen-bonding interactions result in the aromatic rings being offset with extended centroid-centroid distances of 6.390(12) Å and 6.350(9) Å for **2.3(Cl)** and **2.4(F)** respectively (**Figure 2.4.2-6**).

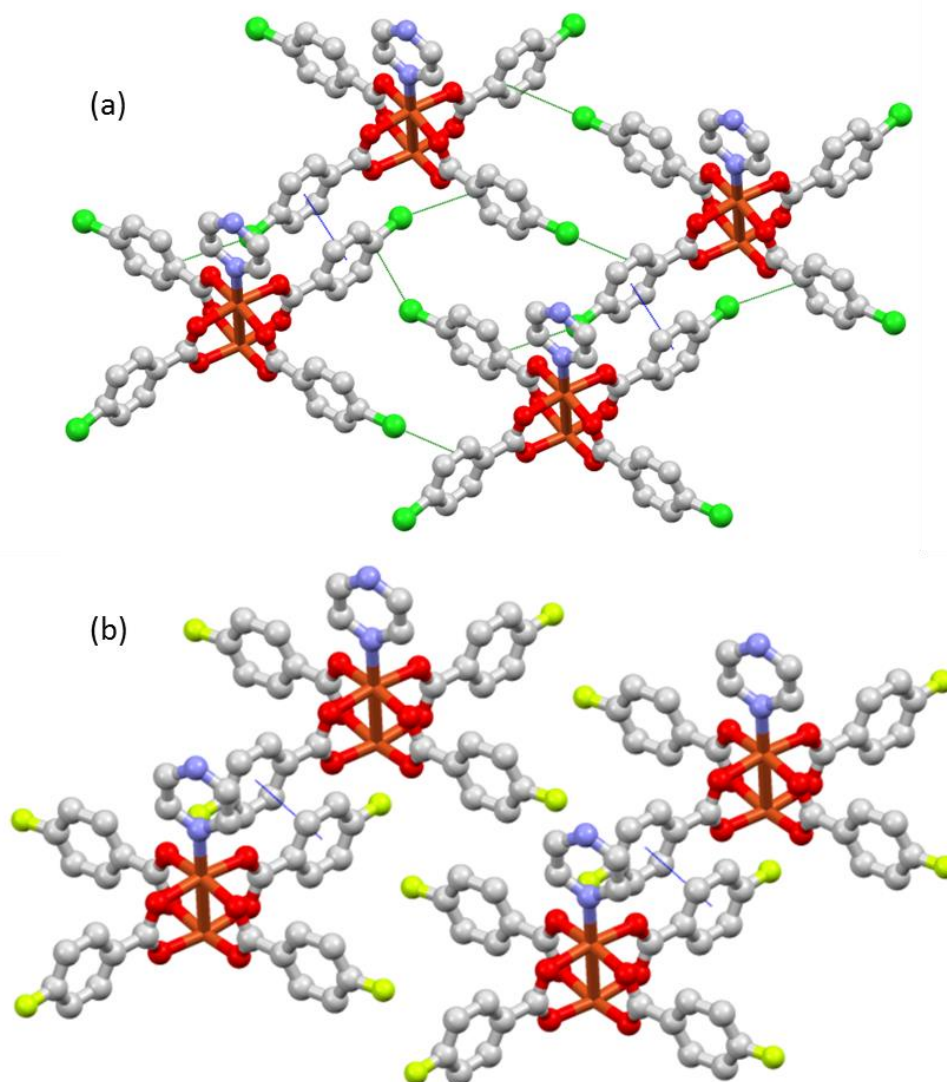


Figure 2.4.2-6. The observed halogen bonding network of **2.3(Cl)** (a) and **2.4(F)** (b). Colour scheme as in **Figure 2.4.2-1**, C-X...C_{ipso} interactions represented with green lines and π...π interaction shown with blue lines.

When considering materials for potential applications as porous hosts it is important to consider the solvent-accessible void of the material. In this case solvent-accessible void spaces were calculated using PLATON CALC VOID.²³ Calculations used a probe radius of 1.2 Å, with the major component of the disordered rings observed in **2.1(I)** and **2.2(Br)** being retained to give a more appropriate approximation of the void space present. In all four of the systems the accessible pore space consists of discrete cavities (**Figure 2.4.2-7**). The relative size of the pore spaces can be correlated directly with the size of the halogen functionality present (**Table 2.4.2-1**) with the largest (percentage) void space occurring in **2.4(F)** and the smallest in **2.1(I)**. The void space in the case of the isostructural **2.1(I)** and **2.2(Br)** materials are situated around the pyrazine (**Figure 2.4.2-7**). In the case of the isostructural **2.3(Cl)** and **2.4(F)** systems the void is situated in the cleft of the paddlewheel SBU (**Figure 2.4.2-7**). The absence of a channel void space alludes to the reason for the previously published volumetric CO₂ adsorption isotherms of **2.2(Br)** and **2.3(Cl)** exhibiting gated uptake.⁵ These gates could be due to the material having to undergo a significant structural change to allow for the inclusion of guest. The

previously published volumetric CO₂ adsorption study demonstrates no uptake in the case of **2.1(I)**, this could be due to the materials being insufficiently flexible to undergo the required phase transformation.

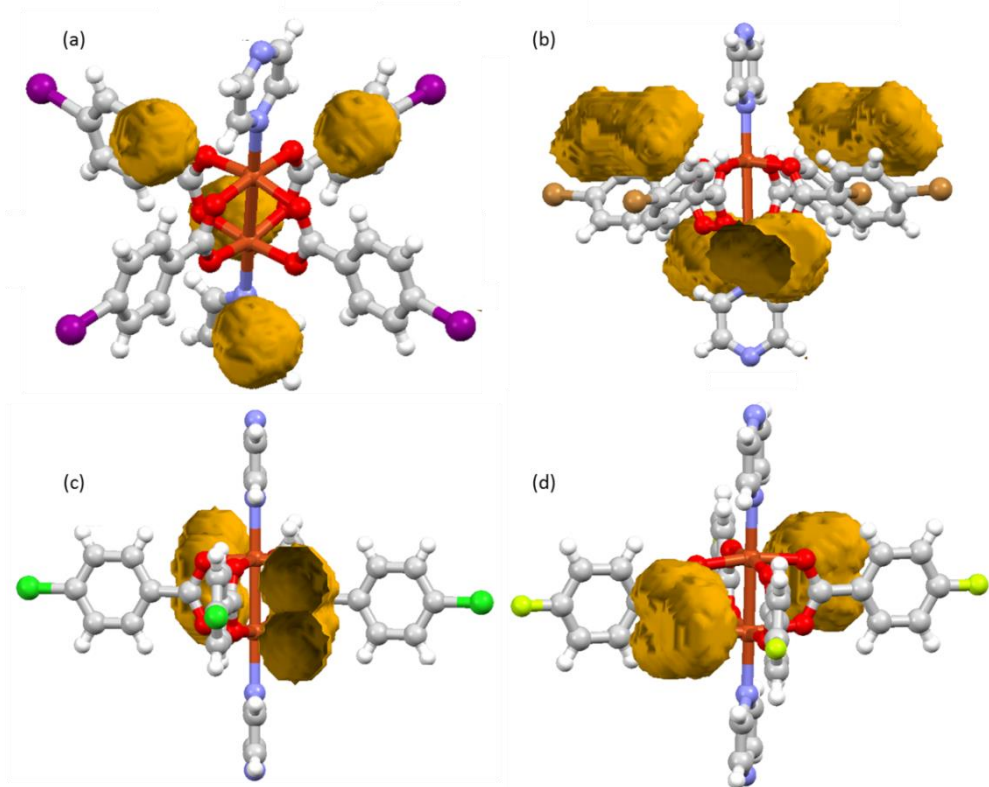


Figure 2.4.2-7. Calculated void spaces for **2.1(I)** (a), **2.2(Br)** (b), **2.3(Cl)** (c) and **2.4(F)** visualised using Mercury.⁴⁷ Colour scheme as in **Figure 2.4.2-1**, void spaces displayed as surfaces in yellow.

Table 2.4.2-1. Solvent-accessible void for **2.1(I)**, **2.2(Br)**, **2.3(Cl)** and **2.4(F)** calculated using PLATON CALC VOID²³

	Space Group	Volume (Å ³)	Z	Probe Radius (Å)	Void Space (Å ³)	Percentage Void Space	Void vol./Z (Å ³)
2.1(I)	<i>I</i> ₄ / <i>a</i>	6934.4(12)	8	1.2	161.5	2.30%	20.19
2.2(Br)	<i>I</i> ₄ / <i>a</i>	6726.5(7)	8	1.2	335.1	5.00%	41.89
2.3(Cl)	<i>I</i> ₂ / <i>m</i>	1650.6(3)	2	1.2	96.5	5.80%	48.25
2.4(F)	<i>I</i> ₂ / <i>m</i>	1595.1(2)	2	1.2	134.2	8.40%	67.10

In conclusion despite the four systems crystallising in two different space groups all four of the systems exhibit analogous interpenetration to each other and a number of previously reported 1D coordination polymers.^{5,6,19,41} This interpenetration leads to analogous antiparallel X··π and π··π interaction motifs to those previously reported by Brammer and co-workers.²² Comparison of the four systems' solvent-accessible voids reveals a clear trend, with the largest halogen possessing the smallest void space and the smallest halogen possessing the largest

void space. All of these void spaces consist of discrete cavities suggesting that guest inclusion may require a phase transformation to allow guests to be adsorbed into the material.

2.4.3 Volumetric N₂ and CO₂ Gas Adsorption

Volumetric analysis of N₂ and CO₂ adsorption was carried out on **2.3(CI)** and **2.4(F)**. These data were used to confirm the volumetric adsorption and desorption isotherms previously reported by Akutagawa et al. for **2.3(CI)**⁵ and to ascertain whether **2.4(F)** demonstrated similar uptake properties.

Both the N₂ and CO₂ isotherms for **2.3(CI)** were consistent with the previous reported.⁵ Thus, the N₂ study, shows a type V isotherm⁴⁸ suggesting initial weak adsorbent-adsorbate interactions, followed by a gradual uptake of N₂, following molecular clustering, with a maximum uptake of ca. 1.7 N₂ molecules per formula unit of coordination polymer (**Figure 2.4.3-1**). The desorption isotherm showed a large hysteresis suggesting a high level of gas retention. The CO₂ adsorption study (**Figure 2.4.3-2**) shows the same stepped isotherm (type IV(b)),⁴⁸ as previously observed, with gated uptake occurring at p/p^0 of ca. 0.3. Prior to this gate pressure an initial uptake of 0.5 CO₂ per formula unit is observed, leading to a maximum uptake of ca. 2.8 CO₂ per formula unit at a $p/p^0 = 1.0$. The desorption isotherm indicates minimal guest retention, but does follow the same gating as observed in the absorption (i.e. no hysteresis). This type of isotherm suggests cylindrical pore spaces with closed tapered ends.⁴⁸ To ensure samples remained unchanged following adsorption/desorption study samples were subsequently analysed via powder X-ray diffraction. Pawley fitting of the diffraction patterns established that minimal change had occurred to the samples. This suggests that if any structural changes occur during the inclusion of guest, these are then reversed upon desorption.

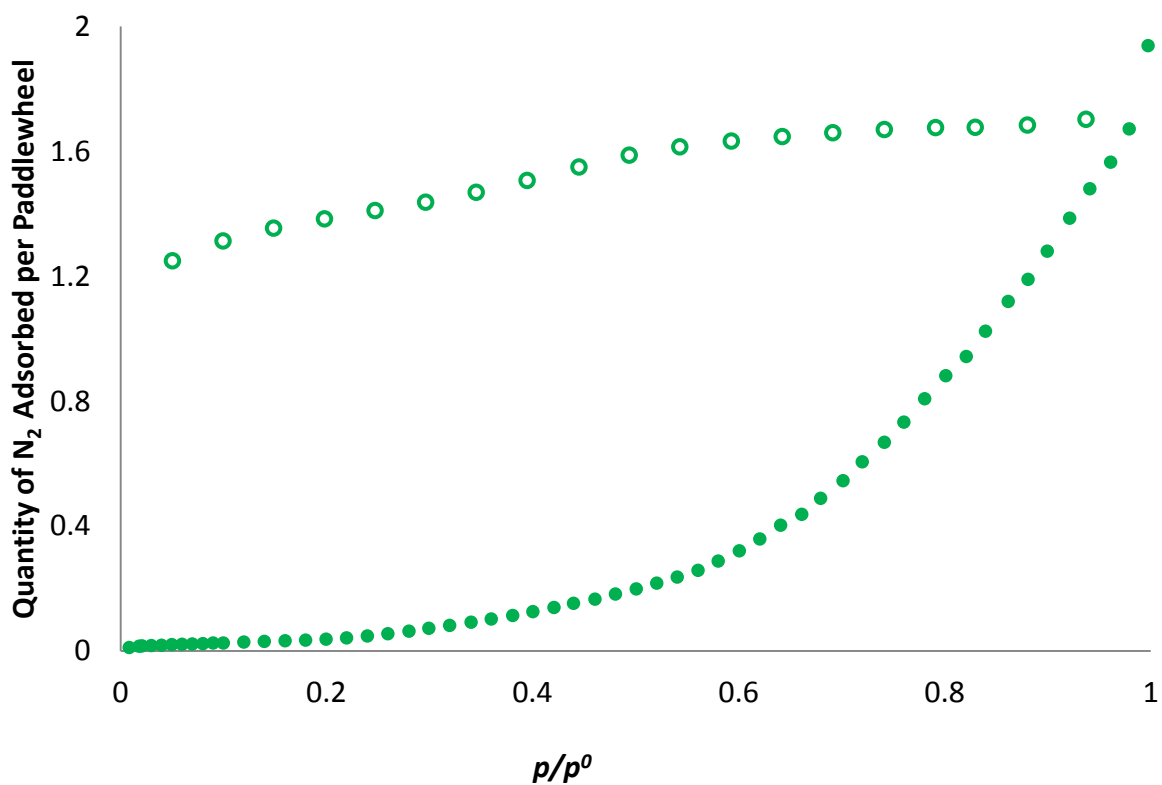


Figure 2.4.3-1. Volumetric N₂ isotherms for 2.3(Cl) at 77 K (adsorption- solid circles, desorption- open circles).

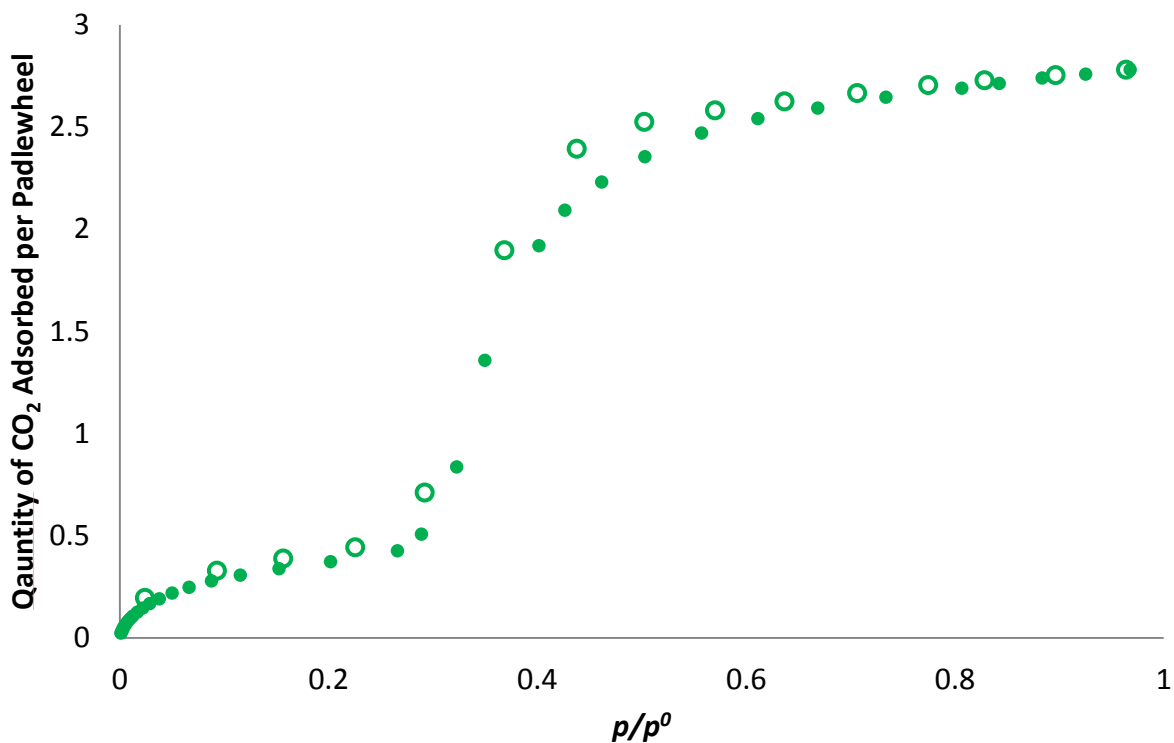
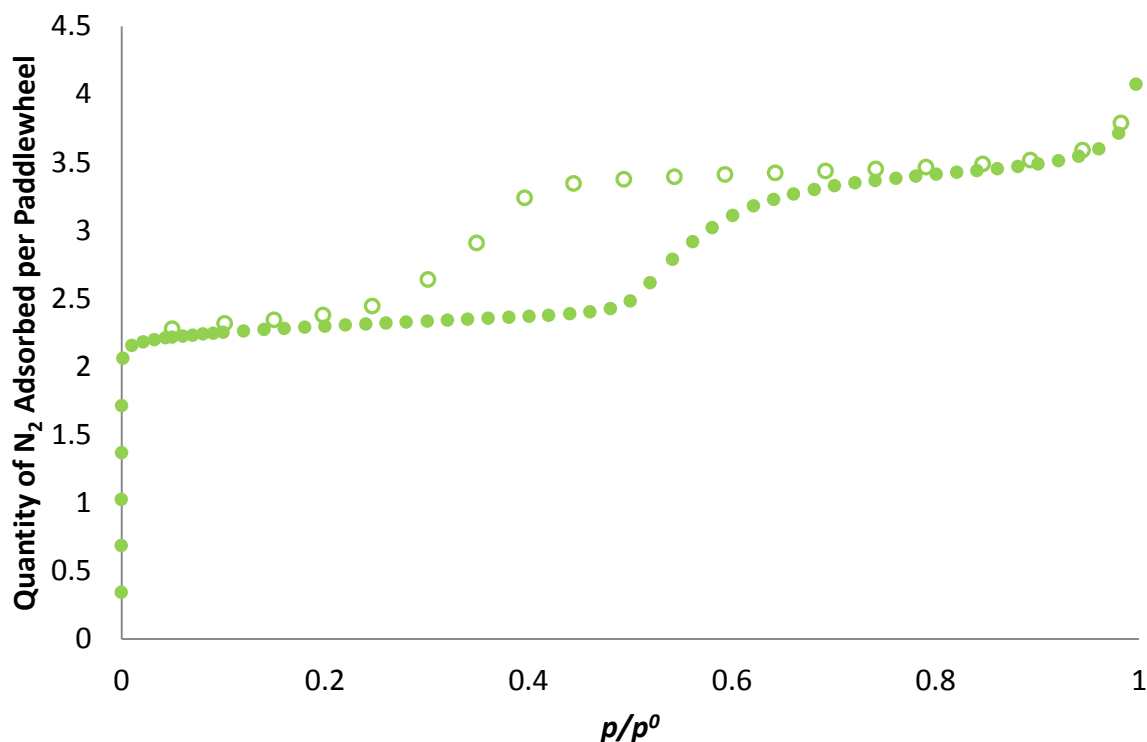


Figure 2.4.3-2. Volumetric CO₂ isotherm for 2.3(Cl) at 195 K (adsorption- solid circles, desorption- open circles).

For **2.4(F)** N₂ adsorption follows a type IV(a)⁴⁸ stepped isotherm (**Figure 2.4.3-3**). This isotherm shows a large uptake at $p/p^0 < 0.01$ (**Figure 2.4.3-3**), resulting in the inclusion of *ca.* 2.3 N₂ molecules per formula unit. This is followed by a secondary gated uptake at a p/p^0 0.5-0.6 leading to a maximum uptake of *ca.* 3.5 N₂ molecules per formula unit. The desorption isotherm is also stepped, but shows a substantial hysteresis. Desorption occurs at p/p^0 of *ca.* 0.45-0.25. This suggests the material has narrow uniform cylindrical pores.⁴⁸ The CO₂ adsorption also exhibits a type IV(b) isotherm⁴⁸ with an initial uptake of 0.5 CO₂ at p/p^0 of 0.1 followed by a gradient change and a maximum uptake of *ca.* 2.8 CO₂ per formula unit (**Figure 2.4.3-4**). The desorption isotherm shows no hysteresis.

The CO₂ isotherm for **2.4(F)** follows the trend of the previously published isotherms of **2.3(Cl)**, **2.2(Br)** and **2.1(I)**.⁵ In the case of **2.4(F)**, **2.3(Cl)** and **2.2(Br)** there is an initial adsorption at low pressure, followed by a plateau region and further adsorption above a gate pressure, with **2.1(I)** displaying no uptake of CO₂. **2.2(Br)**, **2.3(Cl)** and **2.4(F)** all showing similar overall quantities of CO₂ adsorbed. The gate pressure in each case directly correlates to the halogen present, with **2.2(Br)** having the largest gate pressure ($p/p^0 \approx 0.85$) and **2.4(F)** possessing the smallest gate pressure at $p/p^0 \approx 0.1$.



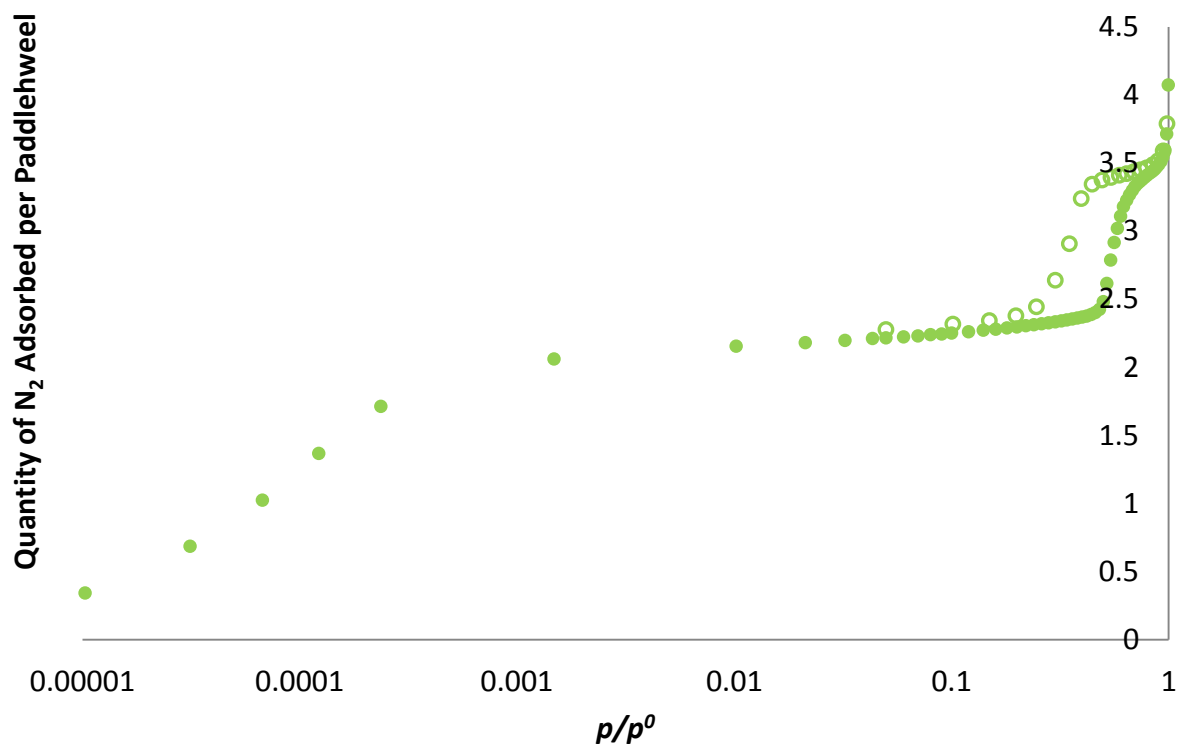


Figure 2.4.3-3- Volumetric N_2 isotherm for **2.4(F)** at 77 K (adsorption- solid circles, desorption- open circles). Relative pressure shown with a linear scale (top) and a logarithmic scale (bottom).

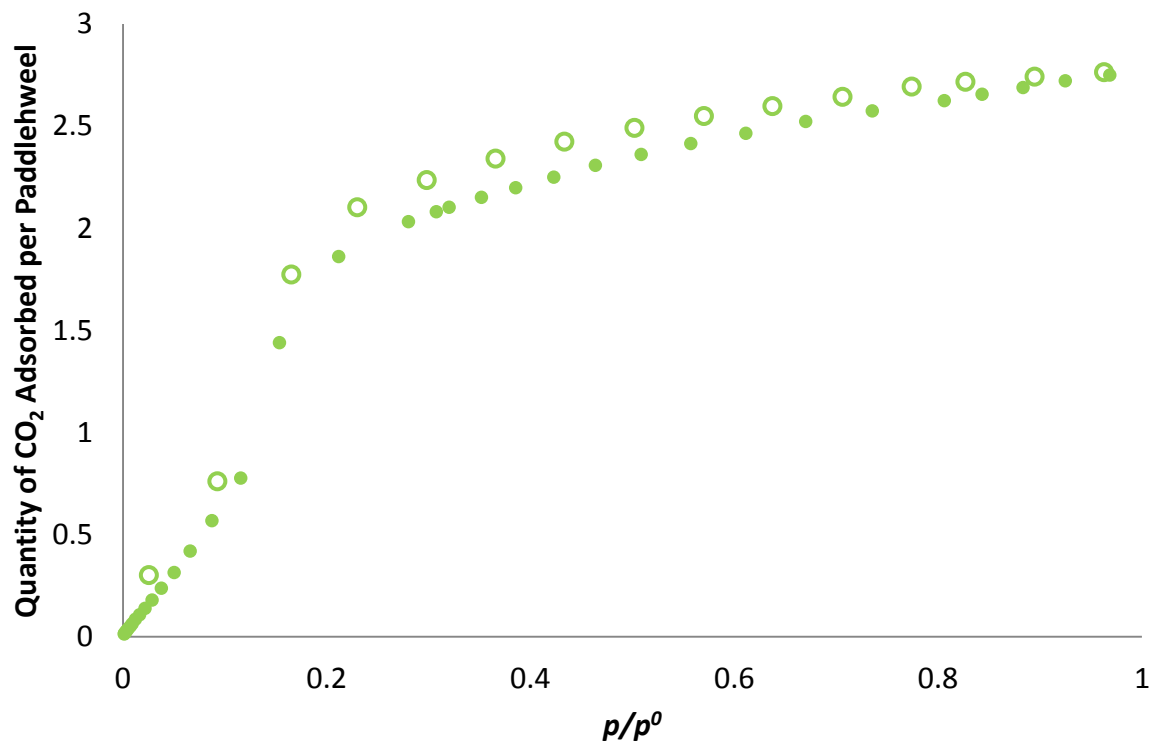


Figure 2.4.3-4. Volumetric CO_2 isotherm of **2.4(F)** at 195 K (adsorption- solid circles, desorption- open circles).

2.4.4 *In situ* Powder Diffraction Studies During CO₂ Adsorption/Desorption

As outlined in Section 2.3.5 samples of the four materials were analysed by powder X-ray diffraction while being exposed to increasing/decreasing pressures of CO₂ at the I11 beamline at Diamond Light Source.^{26,35,36} These experiments involved dosing powder samples with pressures of CO₂, allowing 30 minutes equilibration time and collecting data. This strategy was applied to all four materials with the equilibration time of **2.2(Br)** at 1 bar being extend to 2 hours and then 2 hours 50 minutes following no observed structural changes at shorter equilibration times. Data were fitted by both Pawley³² and Rietveld³⁷ methods in the TOPAS program.^{33,34} Details of these fits are outlined in the tables in Appendix 2.8.2.

The change in unit cell volume for the structure of each compound is presented as a function of relative pressure (p/p^0) of CO₂ in **Figure 2.4.4-1**. No significant change in volume ($\Delta V = 4.9(2)$ Å³, 0.07%) is observed for **2.1(I)** at room temperature, suggesting no adsorption of CO₂. Further studies at 195 K were not conducted, as the results from the study of **2.2(Br)** infer that no change would be observed for **2.1(I)** at 195 K. Compounds **2.2(Br)** ($\Delta V = 465.27(77)$ Å³, 13.9%), **2.3(Cl)** ($\Delta V = 182.41(31)$ Å³, 11.0%) show gated expansion, whereas **2.4(F)** ($\Delta V = 40.5(1)$ Å³, 2.5%) shows a gradual expansion on increasing pressure.

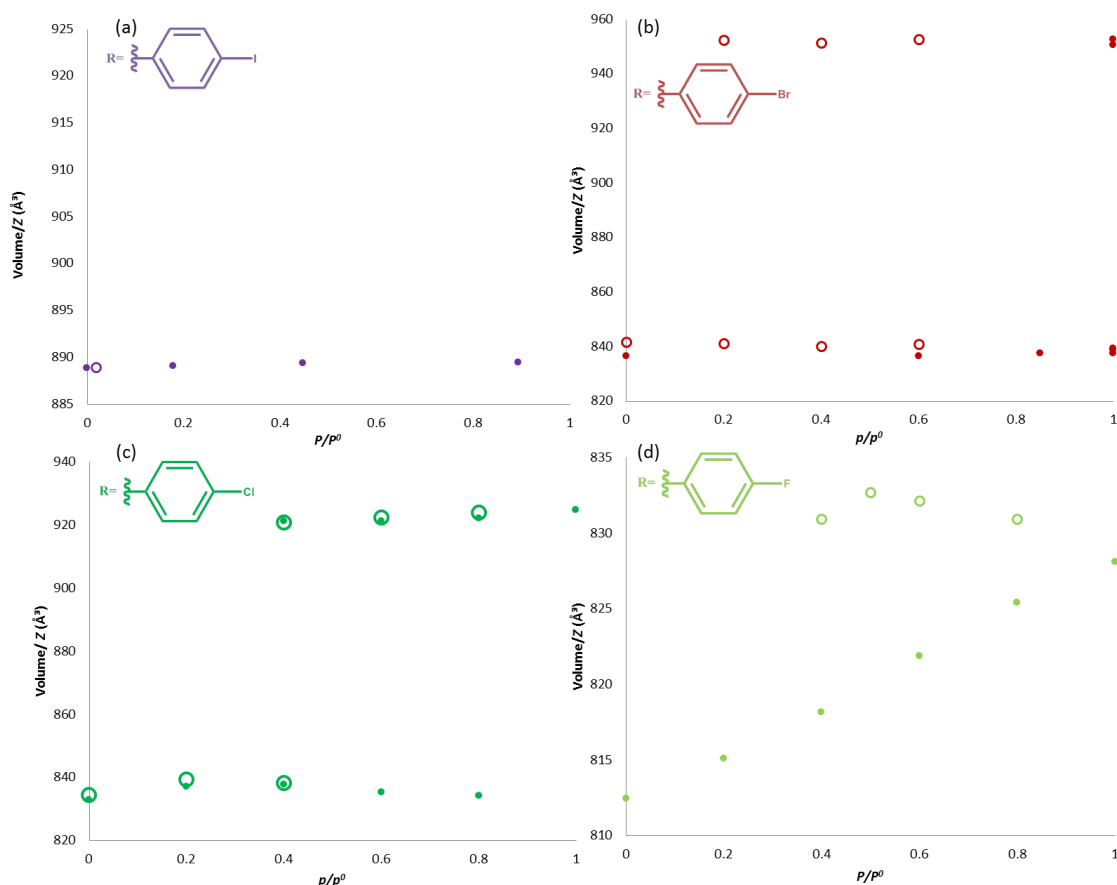


Figure 2.4.4-1. Plots of volume per formula unit, V/Z , vs p/p^0 from *in situ* powder diffraction studies during CO₂ adsorption (solid circles) and desorption (open circles) for (a) **2.1(I)**, (b) **2.2(Br)**, (c) **2.3(Cl)** and (d) **2.4(F)**. Data recorded at 195 K for **2.2(Br)** and **2.3(Cl)** and **2.4(F)** and 298 K for **2.1(I)**. Where two symbols (two volumes) are represented at a given pressure is due to a two-phase fit of the powder pattern.

The gated expansion observed for **2.2(Br)** does not occur at the gate pressure ($p/p^0 \approx 0.85$) previously observed in the volumetric adsorption study.⁵ This discrepancy in the gate pressure could be due to longer equilibration times between pressure steps being needed for the PXRD study. Thus, no change in volume was observed when using equilibration time of 30 mins for each pressure increase step up to and including $p/p^0 = 1.0$. An extended equilibration period of 2 h at $p/p^0 = 1$, however, led to an expansion of the unit cell, consistent with gating. A two-phase powder pattern was recorded. Rietveld³⁷ fitting of showed a maximum conversion to the expanded phase of 47(1) %, which was unchanged after further 50 mins at $p/p^0 = 1.0$ (**Figure 2.4.4-2**). This expanded phase requires a reduction in the symmetry with a phase change from the original tetragonal $I4_1/a$ to a monoclinic $C2/c$ cell. This monoclinic cell is comparable to those observed in the previously reported $[\text{Cu}_2(\text{bz})_4(\text{pyz})]_n$ both in guest-free form¹⁹ and with the inclusion of a series of guests (CH_4 ,¹⁵ Ar,¹³ Kr,¹³ PrOH¹² or acetone¹⁸) and is analogous to the CO_2 -including phase observed in **2.3(CI)**. The desorption steps demonstrate a large structural hysteresis. Two-phase Rietveld fitting indicates that a large fraction of the sample is converted back to the closed phase in the range $0.6 < p/p^0 < 0.4$, but the expanded phase is retained in some of the sample until $p/p^0 = 0.2$ (**Figure 2.4.4-2**). The final vacuum measurement shows full conversion to the original closed phase.

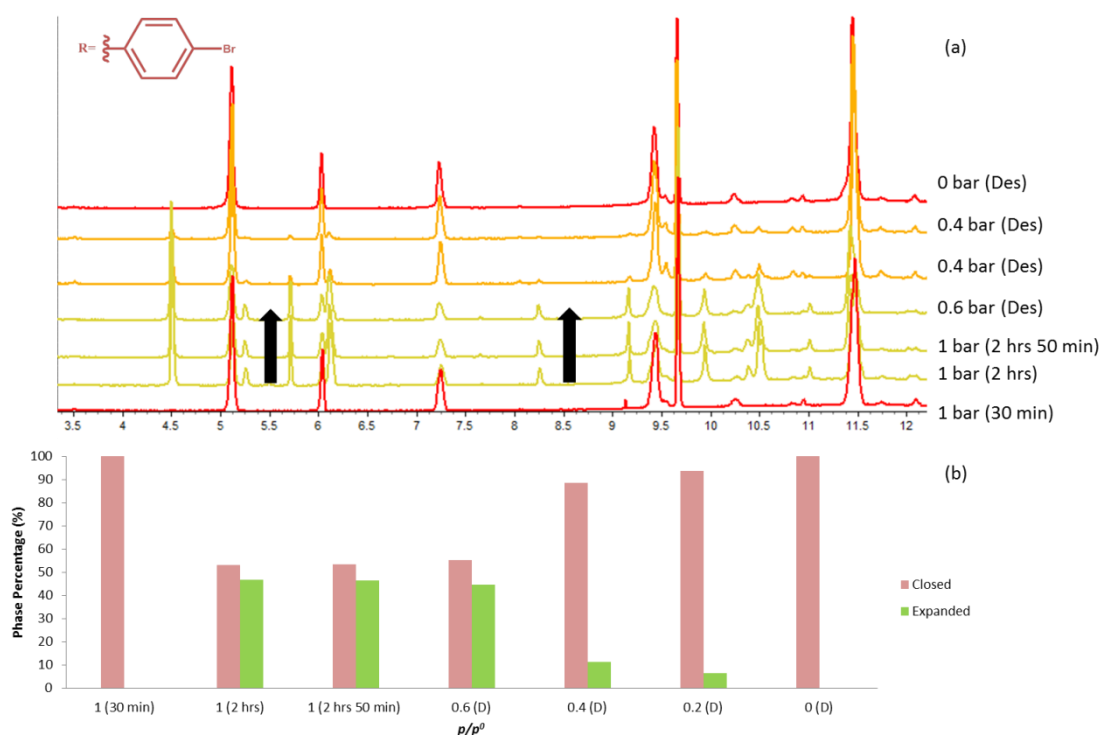


Figure 2.4.4-2. (a) Stacked PXRD patterns from in situ study of **2.2(Br)** while increasing (and decreasing) pressures of CO_2 are applied at 195 K. (b) Bar chart of the phase percentage of the expanded ($C2/c$) and closed ($I4_1/a$) phases as determined by Rietveld fitting.³⁷

This expansion and change in symmetry sees a transformation of the unit cell shown schematically in **Figure 2.4.4-3**. This results in the coordination polymers propagating along the b -axis, in the expanded structure, (propagating along the c -axis in the closed phase). This axis shows minimal change ($-0.0021(11) \text{ \AA}$, -0.01%). The material shows a major expansion in the c -axis, of the expanded phase, (b -axis of the closed phase) of 16.69 % ($3.0827(22) \text{ \AA}$) and a minor

expansion in the in the a -axis of 0.12 % (0.0227(12) Å). This expansion is accompanied by a 12.841(7) ° increase in the β angle (from 90 ° to 102.841(7) °). This demonstrates that the uptake of CO₂ is accompanied by minimal change in the direction of propagation of the coordination polymer, but with major changes in the directions of the halogen-bonded networks. Thus, the coordination polymers move apart with the uptake of CO₂ (**Figure 2.4.4-3**).

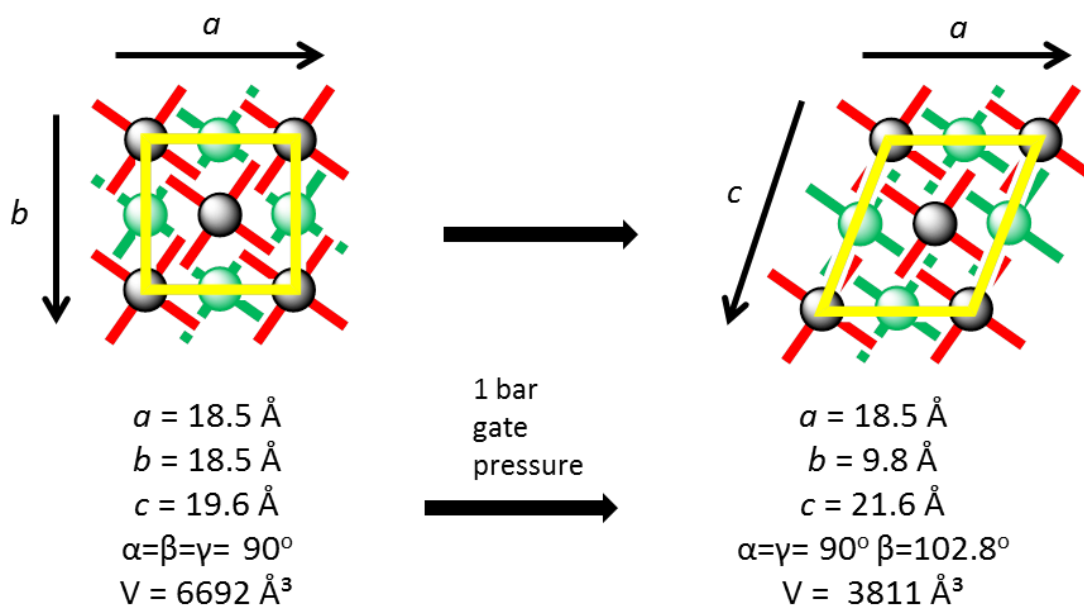


Figure 2.4.4-3. Representation of the transformation observed when **2.2(Br)** is exposed to 1 bar pressure of CO₂ over long duration, at 195 K, viewed from the direction of polymer propagation (the c -axis (left) and b -axis (right) in the case of the closed and expanded phases, respectively). Polymers represented at red crosses with black spheres, green crossed signifying the interpenetrated network and yellow lines highlighting the unit cell axes.

The gated expansion observed for **2.3(Cl)** results in an 11.0 % volume expansion. This gate opening is initially observed at $p/p^0 = 0.4$, with the expanded form as a minor phase, and full conversion being observed at $p/p^0 = 1$. Upon CO₂ pressure reduction the material then exhibits a slight hysteresis with full conversion to the closed phase occurring at $p/p^0 = 0.2$ (**Figure 2.4.4-4**). The expansion occurs by a phase transformation from space group $I2/m$ to $C2/c$, resulting in a doubling of the number of formula units per unit cell ($Z = 2$ becomes $Z = 4$). This $C2/c$ phase is consistent with the expanded phase observed in **2.2(Br)** and some previously reported guest including phases of $[\text{Cu}_2(\text{bz})_4(\text{pyz})]_n$ (guests: CH₄,¹⁵ Ar,¹³ Kr,¹³ PrOH¹² or acetone¹⁸).

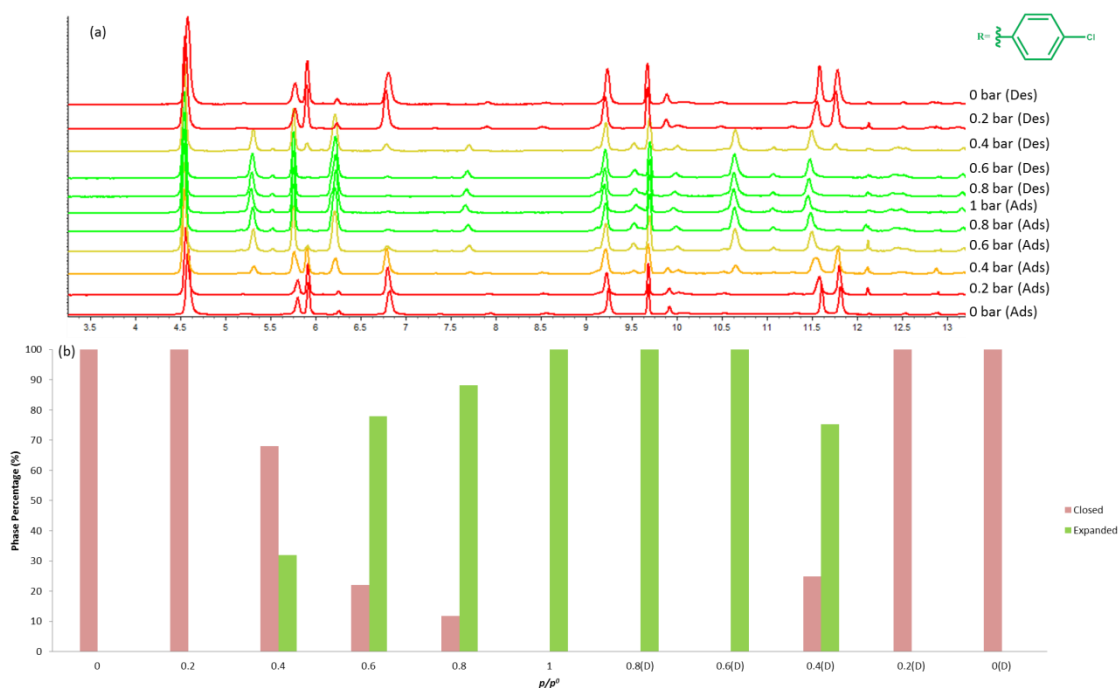


Figure 2.4.4-4. (a) Stacked PXRD patterns from in situ study of **2.3(Cl)** while increasing (and decreasing) pressures of CO_2 are applied at 195 K. (b) Bar chart of the phase percentage of the expanded (C2/c) and closed (I2/m) phases as determined by Rietveld fitting.³⁷

As previously observed with **2.2(Br)**, **2.3(Cl)** shows minimal change along the axis parallel to coordination polymer propagation (the b -axis, $\Delta b = -0.0300(4)$ Å, -0.3 %). The change in symmetry results in the a - and c -axes of the closed and expanded phases being no longer comparable, therefore the observed expansion was quantified by measuring the distances between neighbouring copper atoms in the expanded phase. This shows a major expansion in the c -axis of 7.29 % (1.041(11) Å) and a minor expansion in the a -axis of 1.91 % (0.2345(9) Å). This expansion in the a - and c -axes is accompanied by a $-4.446(4)^\circ$ reduction in the β angle. This study demonstrates that both **2.2(Br)** and **2.3(Cl)** show consistent behaviour in response to increasing CO_2 pressure with polymer chain moving apart but with minimal compression or elongation of the coordination polymer (**Figure 2.4.4-5**). Both samples exhibit gated inclusion of CO_2 consistent with the previously reported⁵ and presented (in Section 2.4.3) volumetric adsorption data.

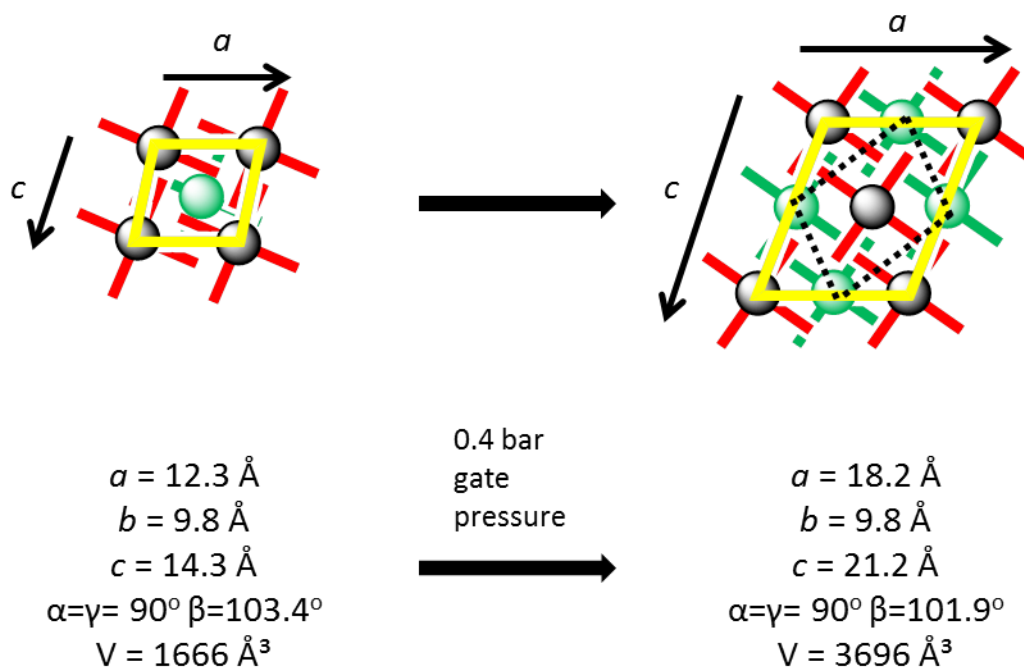


Figure 2.4.4-5. Representation of the transformation observed for **2.3(Cl)** exposed to increasing pressures of CO_2 , at 195 K, viewed from the direction of polymer propagation (b -axis). Colour scheme as described in **Figure 2.4.4-3**, black dashed lines representing the original unit cell axes.

Finally the study of **2.4(F)** also displays behaviour consistent with the volumetric adsorption experiment (**Figure 2.4.3-4**), demonstrating a 2.49 % volume expansion. This expansion occurs by a gradual expansion of a single phase, as indicated by a shifting of 2θ values of diffraction peaks, (**Figure 2.4.4-6**) rather than growth of peaks for a second phase as observed for **2.2(Br)** and **2.3(Cl)**. The largest shifts in 2θ values correspond to $h0l$ Miller indices (e.g. a 0.14° shift is observed in the peak corresponding to the $20-1$ reflection). This suggests that the largest changes are observed in the a - and c -axes, perpendicular to the direction of propagation of the coordination polymer. This observation is consistent with that for **2.2(Br)** and **2.3(Cl)**, with polymer chains moving apart and showing minimal polymer chain compression or elongation.

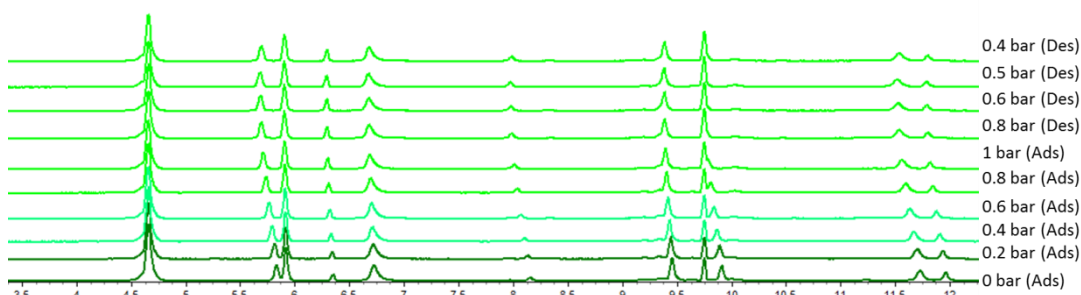


Figure 2.4.4-6. Stacked PXRD patterns from in situ study for **2.4(F)** during exposure to increasing (and decreasing) pressures of CO_2 (at 195K) showing the shifting of peak positions.

This modest volume expansion, in comparison to **2.2(Br)** and **2.3(Cl)**, is as a result of an expansion in the *a*- (1.7 %, 0.2050(6) Å) and *c*-axes (0.14 %, 0.0206(10) Å) with minimal change in the *b* axis (0.03 %, 0.0309(5) Å) and a reduction in the β angle ($-1.547(4)^\circ$). The largest volume increase, relative to the original volume, is observed during the desorption. Despite this modest expansion a large hysteresis is observed during the desorption process. This material, as with **2.2(Br)** and **2.3(Cl)**, demonstrates expansion in unit cell axes perpendicular to the direction of propagation of the coordination polymer, **Figure 2.4.4-7**.

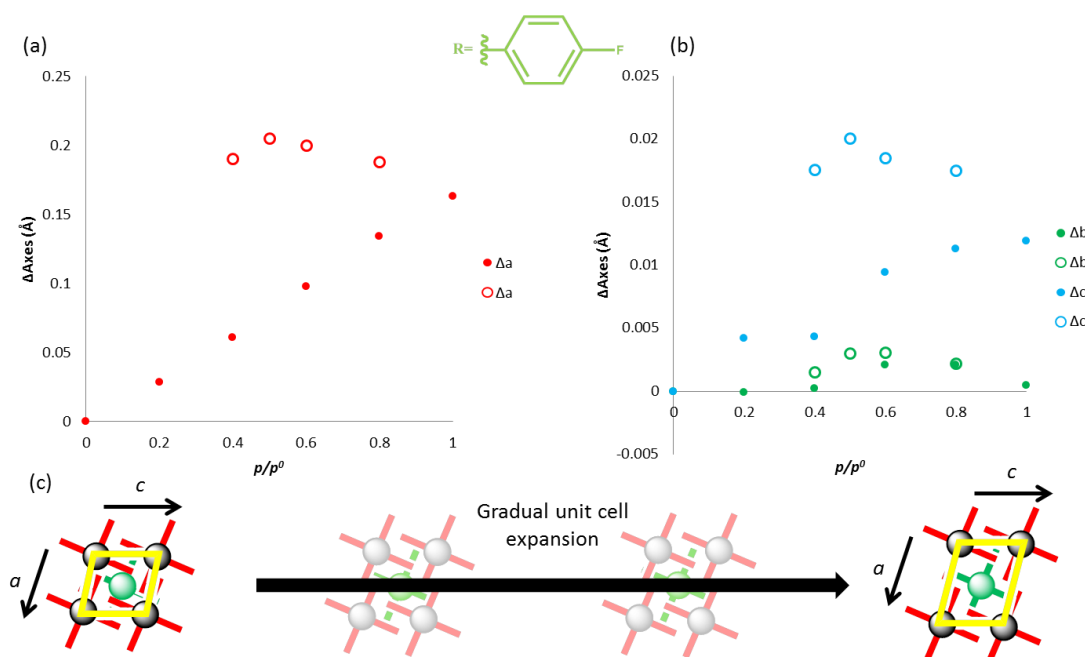


Figure 2.4.4-7. (a) and (b) Plots of the change in unit cell axes *a* (red), *b* (green) and *c* (blue) vs p/p^0 for **2.4(F)** when subjected to increasing (filled circles) and decreasing (open circles) pressure of CO_2 at 195 K. (c) Scheme representing the motion of polymers during expansion of the structure upon increasing pressure of CO_2 . Colour scheme consistent with **Figure 2.4.4-3**.

The family of halobenzoate coordination polymers show consistent response to CO_2 environments as the previously reported⁵ and presented (Section 2.4.3) volumetric analysis, an interesting observation is made comparing the 195 K and 298 K studies. In the case of **2.4(F)** the 298 K study shows a larger volume expansion (8 %, 132.36(10) Å³) at $p/p^0 = 0.9$, with major expansions in the *a*- and *c*-axes and no observable hysteresis (**Figure 2.4.4-8**). The chloro system, **2.3(Cl)**, however shows minimal expansion (0.5 %, 8.36(8) Å³) with no gated expansion despite a maximum $p/p^0 = 0.7$. Similarly **2.2(Br)** shows minimal expansion (0.16 %, 11.0(3) Å³) (**Table 2.3.5-4**, Appendix 2.8.2) despite a maximum $p/p^0 = 0.9$ (**Figure 2.4.4-8**). This suggests that propensity for the inclusion of CO_2 in **2.2(Br)** and **2.3(Cl)** is temperature dependent. This change in behaviour could require increased equilibration times, than 30 min, or a shifting of the materials gate pressure.

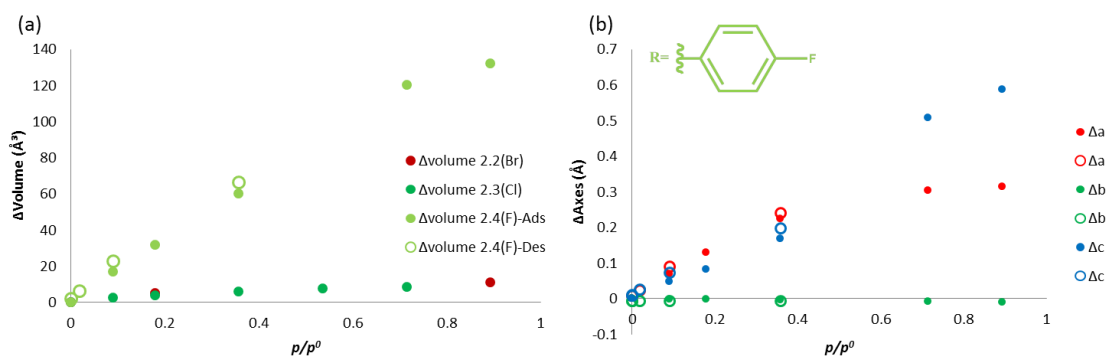


Figure 2.4.4-8. (a) Volume expansion of **2.4(F)-RT-CO₂**, **2.3(Cl)-RT-CO₂** and **2.2(Br)-RT-CO₂**. (b) The axis changes of **2.4(F)-RT-CO₂**.

To conclude, the *in situ* powder diffraction studies during CO₂ adsorption/desorption for the family of 1D coordination polymers $[\text{Cu}_2(4\text{-Xbz})_4(\text{pyz})]_n$ show consistent behaviour to the previously published⁵ and our reported (section 2.4.3) volumetric adsorption studies. The materials show volume expansion due to increase in unit cell dimensions perpendicular to the direction of polymer propagation. There is a clear trend in the uptake in relation to the 2D halogen-bonded network. The strongest halogen-bond interaction, in **2.1(I)**, corresponds to minimal unit cell expansion. Samples of **2.2(Br)** and **2.3(Cl)** show gated expansion leading to a guest-included phase (C2/c) consistent with previously reported guest-included phases of $[\text{Cu}_2(\text{bz})_4(\text{pyz})]_n$ (guests: CH₄,¹⁵ Ar,¹³ Kr,¹³ PrOH¹² or acetone¹⁸). Finally, **2.4(F)** exhibits gradual volume expansion indicated by diffraction peak position shifts rather than formation of a new expanded phase observed for **2.2(Br)** and **2.3(Cl)**. The samples also appear to show temperature-dependent inclusion of CO₂ with samples of **2.2(Br)** and **2.3(Cl)** showing minimal unit cell change while being exposed to high pressures of CO₂ at 298 K.

2.4.5 In Situ Single-Crystal Diffraction Studies During CO₂ Adsorption/Desorption

In situ single-crystal diffraction studies were carried out at a series of increasing and decreasing pressures of CO₂ for compounds **2.1(I)**, **2.2(Br)**, **2.3(Cl)** and **2.4(F)**. Samples were exposed to successive increasing and decreasing pressures of CO₂ allowing 30 min equilibration times between dosing and data acquisition. Details of the data processing and structure solutions are outlined in Section 2.3.6 and Appendix 2.8.3. In this section, unit cell parameters are plotted against p/p^0 .

Limited studies of **2.1(I)** demonstrated that minimal changes in cell volume occur between vacuum and 1 bar CO₂ measurement at 195 K or 100 K (Table 2.3.6-1, Appendix 2.8.3), consistent with the previously reported volumetric adsorption study (195 K)⁵ and *in situ* PXRD studies (298 K, Section 2.4.4), which indicate negligible CO₂ uptake. The study of **2.2(Br)** also demonstrated minimal unit cell volume change ($\Delta V = 13.6(6) \text{ \AA}^3$, 0.2 %, Figure 2.4.5-1) consistent with the *in situ* PXRD studies that used 30-mins equilibration times after each pressure step. An extended equilibration time was not explored. The absence of the phase transformation from tetragonal to (expanded) monoclinic phase could be as a result of slow

adsorption kinetics (as during the PXRD study). This effect may be compounded by increased crystal size, which has been shown to affect gas adsorption capacity^{49,50} and flexible behaviour related to gas adsorption,⁵¹ in MOFs.

Single crystals of both **2.3(CI)** and **2.4(F)** show a structural response to CO₂ pressure consistent with the previously discussed *in situ* PXRD studies (Section 2.4.4). Compound **2.3(CI)** undergoes a gated expansion ($\Delta V = 179.6(7) \text{ \AA}^3$, 10.67 %) at a gate pressure $p/p^0 = 0.4$ during CO₂ adsorption and a corresponding contraction at $p/p^0 = 0.2$ during desorption (**Figure 2.4.5-1**). The volume expansion is consistent with that observed in the PXRD studies ($\Delta V = 182.4(3) \text{ \AA}^3$, 11.0 %). The expansion does not result in the same phase transformation from *I2/m* to *C2/c*, however, as the original *I2/m* symmetry is maintained.

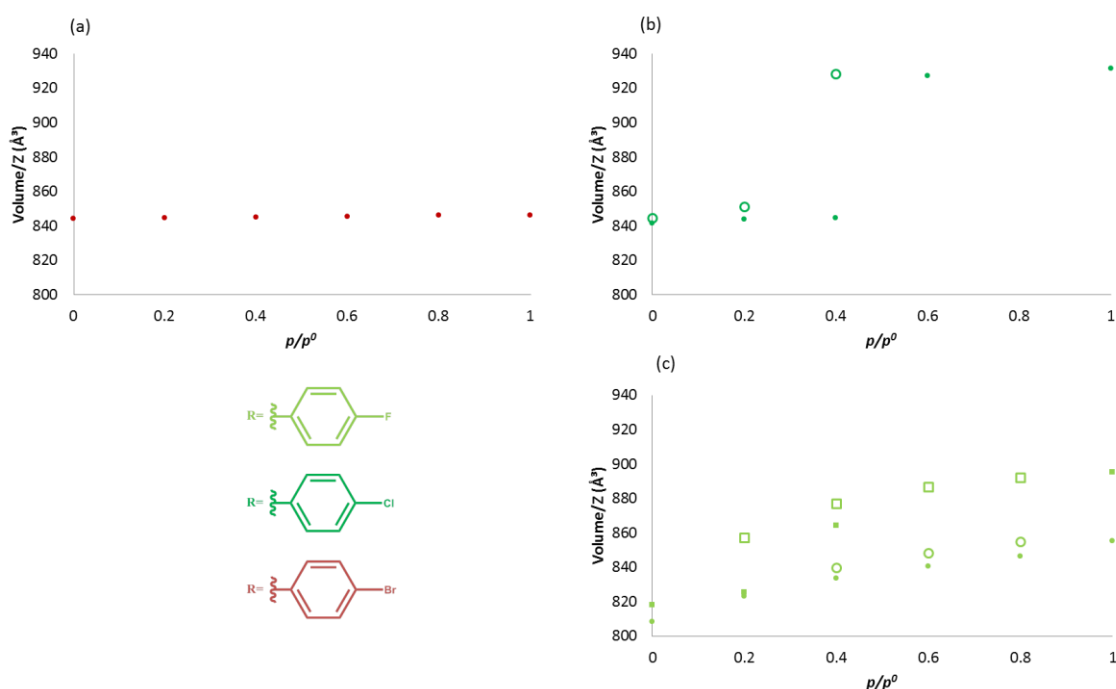


Figure 2.4.5-1. Plots of volume per formula unit, V/Z , vs p/p^0 for (a) **2.2(Br)**, (b) **2.3(CI)** and (c) **2.4(F)** on exposure to increasing (solid circles) and decreasing (open circles) pressure of CO₂ at 195 K. Square symbols for (c) **2.4(F)** represent a second study.

This transformation from *I2/m* to *C2/c* can be confirmed by attempting to fit the powder data with the observed single-crystal unit cell (**Figure 2.4.5-2**). In this fit two peaks at 5.5 and 6.8° 2 θ are not fitted. Both of these peaks grow and deplete during the adsorption and desorption of CO₂ pressure, confirming that they are associated with the CO₂ included phase.

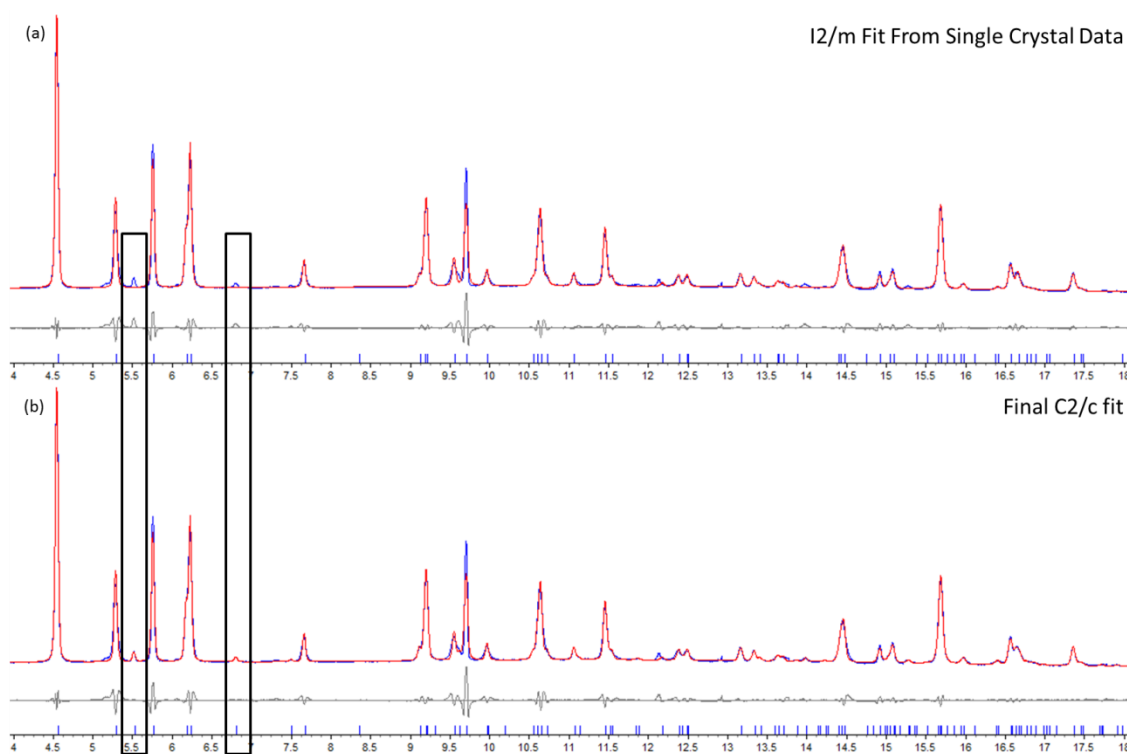


Figure 2.4.5-2. Pawley fits of the *in situ* PXRD pattern at 1 bar CO₂ of **2.3(Cl)** (a) using the unit cell from the single-crystal data and (b) the fit to using the C2/c unit cell. The black boxes highlight the peaks not included in the I2/m fit.

Compound **2.4(F)** underwent some degradation during the *in situ* single-crystal diffraction study, believed to be a consequence of radiation damage. This resulted in two separate studies being carried out one focusing primarily on CO₂ adsorption steps (**Table 2.3.6-4**) and the second prioritising desorption steps (**Table 2.3.6-5**). Each study showed analogous gradual volume expansions consistent with the *in situ* PXRD study and volumetric adsorption study previously discussed. The observed unit cell volume expansions, however, differ in magnitude in the three diffraction studies. The PXRD study shows $\Delta V_{\max} = 2.5\%$ ($40.5(1) \text{ \AA}^3$), whereas the two single-crystal diffraction studies show maximum expansion of 5.8% ($93.8(5) \text{ \AA}^3$) and 9.4% ($153.9(3) \text{ \AA}^3$), the latter focussing primarily on desorption. The maximum expansion is observed at $p/p^0 = 1.0$ ($P_{\text{CO}_2} = 1 \text{ bar}$) for the two single-crystal studies, but (unusually) occurs during the desorption of the PXRD study.

The volume expansions for **2.3(Cl)** and **2.4(F)** are as a result of consistent unit cell axis changes to those observed in the *in situ* PXRD studies. Significant increases occur in the *a*- and *c*-axes whereas the *b*-axis remains unchanged (**Figure 2.4.5-3**). This is consistent with the coordination polymer chains moving apart, breaking the intermolecular interactions between polymer chains, but with no compression or elongation of the polymer chains being observed.

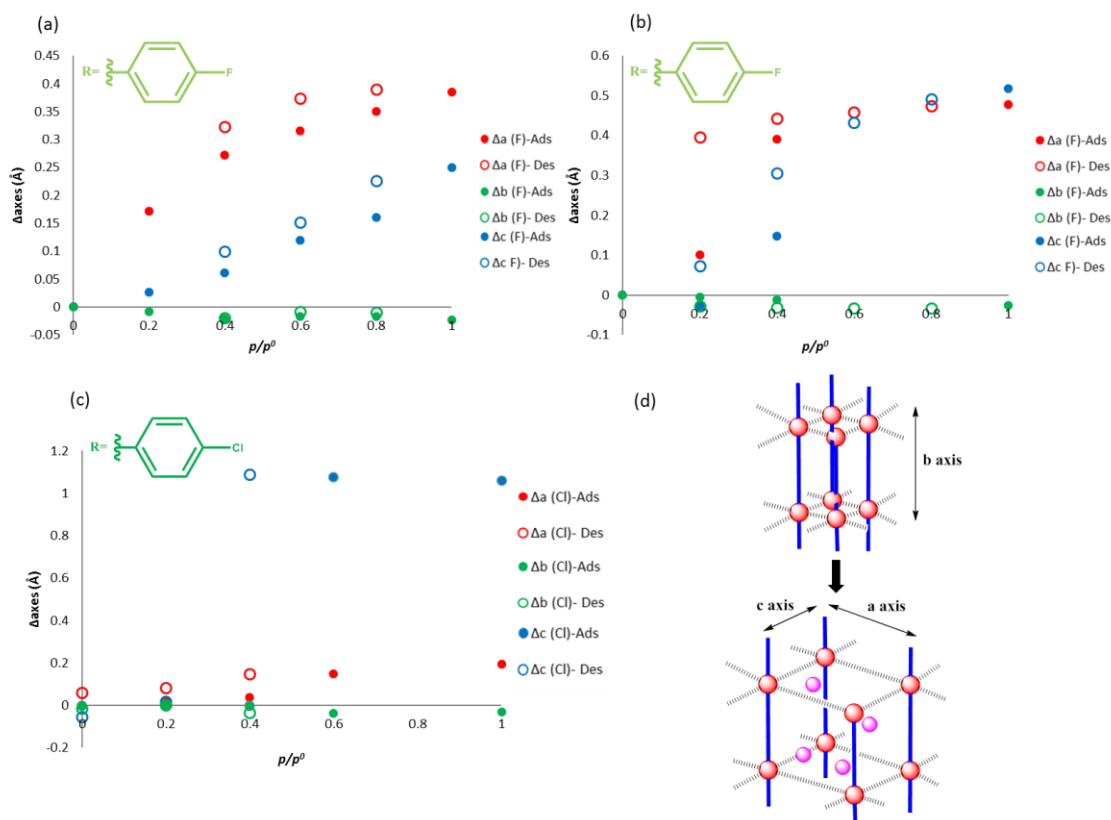


Figure 2.4.5-3. Plot of Δ axis vs p/p^0 for single-crystal studies of **2.4(F)** (a and b) and **2.3(Cl)** (c) while being subjected to increasing (solid circles) and decreasing (open circles) of CO_2 at 195 K. (d) Scheme demonstrating the moving apart of polymer chains with minor compression/elongation of polymers (interpenetration not displayed for clarity).

The structural response to CO_2 uptake is also observed through conformational changes of the coordination polymers as well as the packing between polymer chains. The paddlewheel SBU shows a straightening of the bridging benzoate units (**Figure 2.4.5-4**). In **2.3(Cl)** the $\text{Cu}_{2(\text{cent})}\cdots\text{O}_{2(\text{cent})}\cdots\text{ring}_{(\text{cent})}$ deformation angles at the initial vacuum measurement are $175.45(9)^\circ$ and $165.3(1)^\circ$ but straighten to $178.7(3)^\circ$ and $177.1(3)^\circ$ at $p/p^0 = 1$ and return to $175.6(4)^\circ$ and $166.5(4)^\circ$ upon desorption to vacuum. This is also observed for one of the benzoate ligands in **2.4(F)** with the other benzoate being linear in the as-synthesised form (**Figure 2.4.5-4**). This straightening has a direct impact on the available void space.

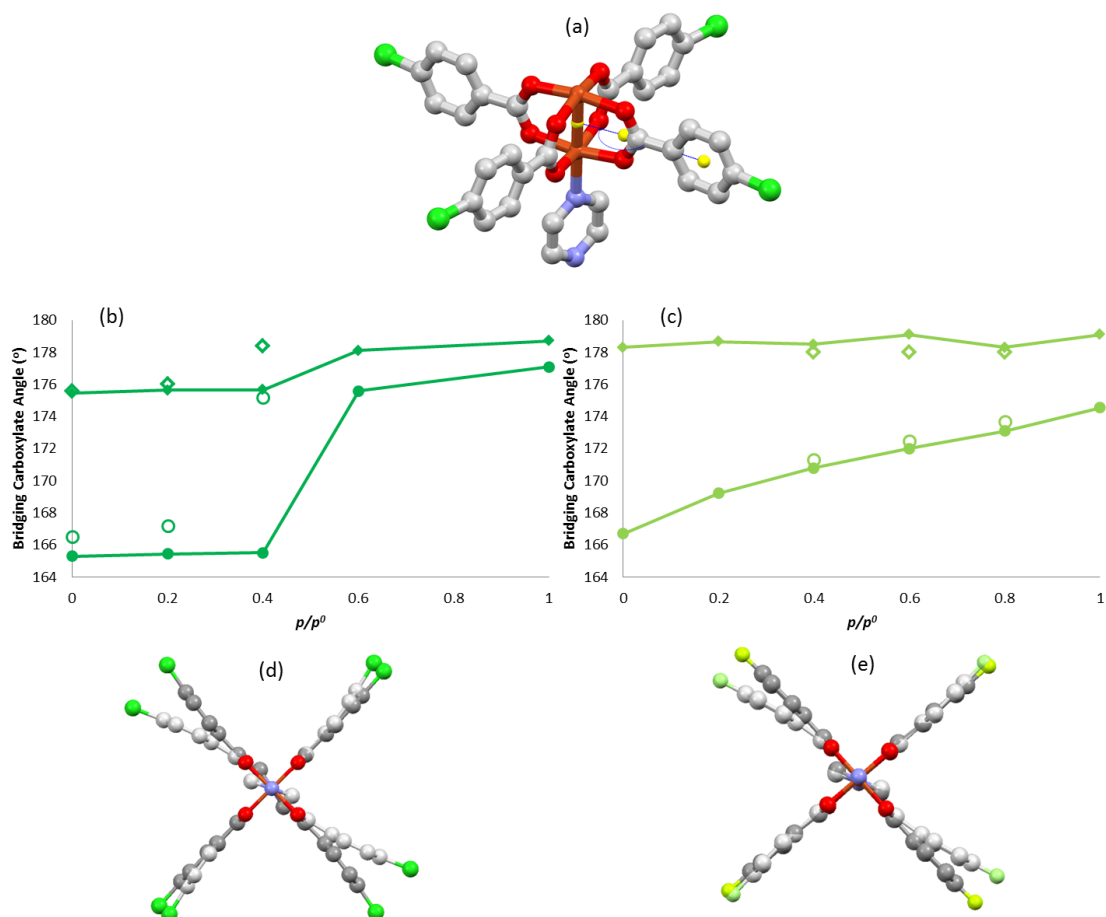


Figure 2.4.5-4. (a) Definition of $\text{Cu}_{2(\text{cent})}\cdots\text{O}_{2(\text{cent})}\cdots\text{ring}_{(\text{cent})}$ deformation angle (centroids displayed in yellow). Plot of deformation angle vs p/p^0 for (b) **2.3(Cl)** and (c) **2.4(F)** (c) during adsorption (filled shapes) and desorption (empty shapes) of CO_2 at 195K. Overlays of structures of (d) **2.3(Cl)** and (e) **2.4(F)** at initial vacuum and 1 bar (vacuum structure in lighter colours). Colour scheme consistent with **Figure 2.4.2-1**.

In Section 2.4.2 the packing of the coordination polymers was described. For **2.1(I)** and **2.2(Br)** 2D halogen-bonded networks connect neighbouring coordination polymers via $\text{C-X}\cdots\pi$ halogen bonds. For **2.3(Cl)**, although the packing is similar to **2.1(I)** and **2.2(Br)**, this is reduced to a 1D halogen-bonded chain due to an elongation of $\text{Cl}\cdots\pi$ separations in one direction. Packing in **2.4(F)** is isostructural to **2.3(Cl)**, except that all $\text{F}\cdots\pi$ contacts are elongated. The *in situ* single-crystal diffraction studies show that upon exposure to CO_2 gas pressures results in expansion of both independent $\text{F}\cdots\pi$ distances ($\text{F}\cdots\text{C}_{\text{ipso}}$ measurement consistent with Section 2.4.2)(**Figure 2.4.5-5**). For **2.3(Cl)**, however, the shorter of the $\text{Cl}\cdots\pi$ distances ($\text{Cl}\cdots\text{C}_{\text{ipso}}$) shows a minor compression (ca. 1% reduction) but the longer of the two $\text{Cl}\cdots\pi$ distances undergoes a large expansion (ca. 38% expansion) (**Figure 2.4.5-5**). This suggests that the 1D halogen-bonded chains are retained in **2.3(Cl)** upon the uptake of CO_2 .

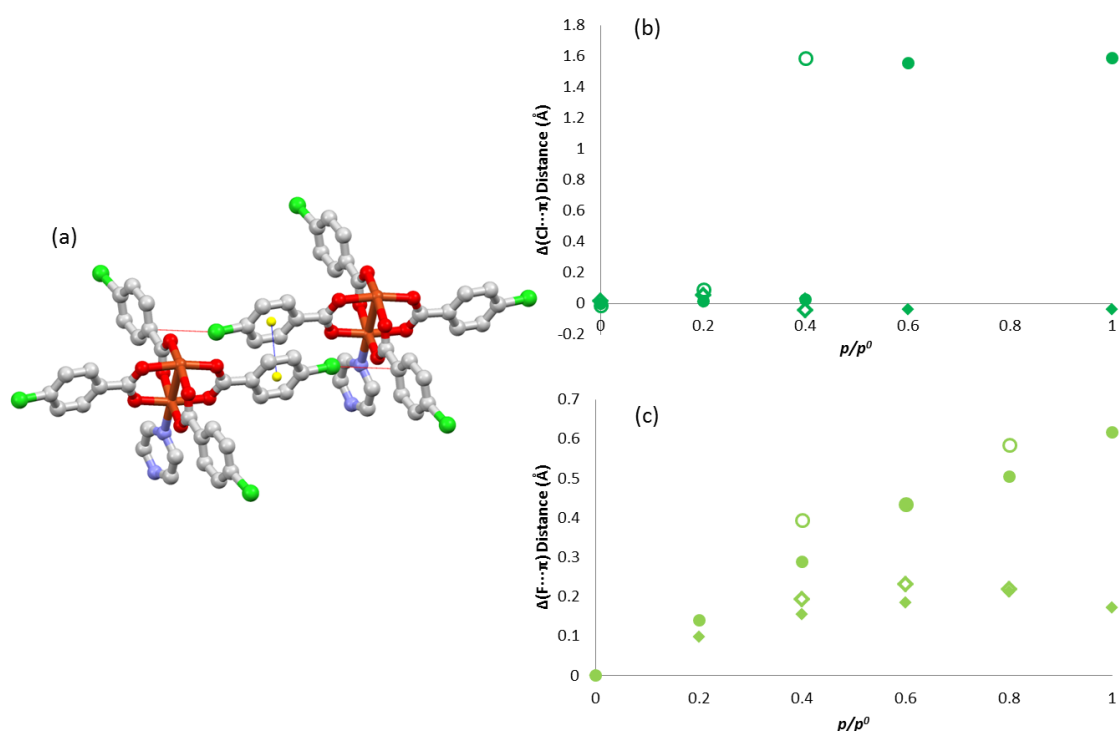


Figure 2.4.5-5. (a) X... π distance (measuring to C_{ipso} , represented with a red dashed line) and the π ... π distance (measured between ring centroids, blue dashed line). Changes in Cl... π (**2.3(Cl)**, (b)) and F... π (**2.4(F)**, (c)) intermolecular distance as a function of p/p^0 during CO_2 adsorption (filled shapes) and desorption (open shapes) at 195 K. Colour scheme consistent with **Figure 2.4.5-4**.

The X... π interactions occur in anti-parallel pairs centring on a potential π ... π stack. In the case of the retained X... π interaction the short π ... π distance is also retained (**Figure 2.4.5-6**). The elongated X... π distance results in an elongation of the corresponding π ... π distance (**Figure 2.4.5-6**). This means that polymer chains which are aligned in the crystal move apart through either the retention of a 1D halogen-bonded chain (**2.3(Cl)**) (**Figure 2.4.5-7**) or through a universal moving apart of polymer chains (**2.4(F)**).

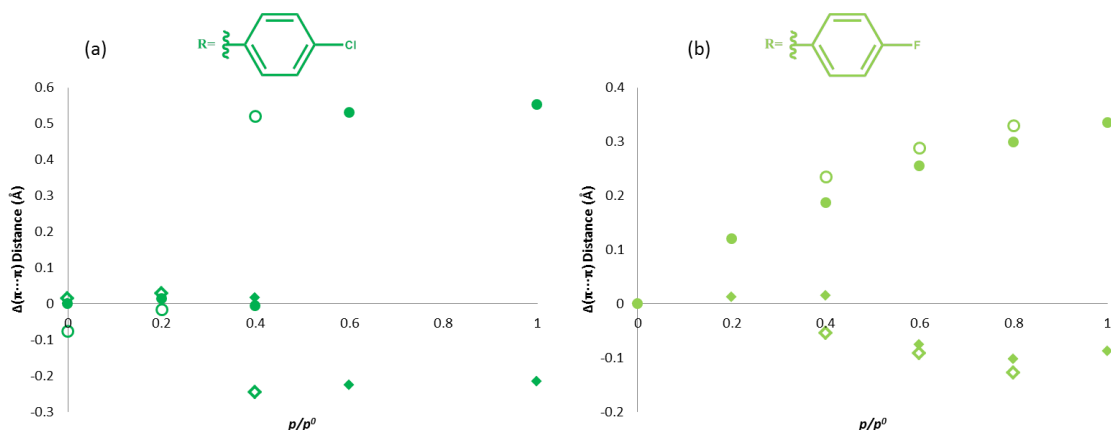


Figure 2.4.5-6. Change in π ... π intermolecular distances as a function of p/p^0 for (a) **2.3(Cl)** and (b) **2.4(F)** during CO_2 adsorption (filled shapes) and desorption (empty shapes) at 195 K.

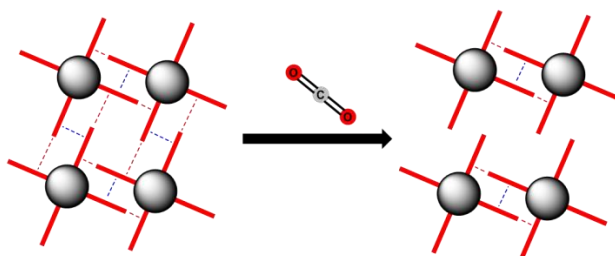


Figure 2.4.5-7. Schematic showing the motion of neighbouring polymer chains of **2.3(Cl)**. Colour scheme consistent with **Figure 2.4.4-3**, $X \cdots \pi$ contact displayed with red dashed lines, $\pi \cdots \pi$ displayed with blue dashed lines and interpenetrated polymers omitted for clarity.

As discussed in Section 2.4.2 the polymer chains are interpenetrated analogous to the packing of a number of previously reported systems. This interpenetration leads to the closest contacts between offset polymer chains being between the pyrazine (pyz) linker and the benzoate (bz) or halogen (**Figure 2.4.5-8**). Exposure to increasing pressures of CO_2 results in an elongation of the $\pi_{\text{bz}} \cdots \pi_{\text{pyz}}$ distance and a decrease in the $X \cdots \pi_{\text{pyz}}$ distance, being accompanied with an increase in the $C_{\text{ipso}} \cdots \pi_{\text{bz}} \cdots \pi_{\text{pyz}}$ and $C_{\text{para}} - X \cdots \pi_{\text{pyz}}$ angles (**Figure 2.4.5-8**). This motion of offset chains is consistent with chains sliding apart (**Figure 2.4.5-8**).

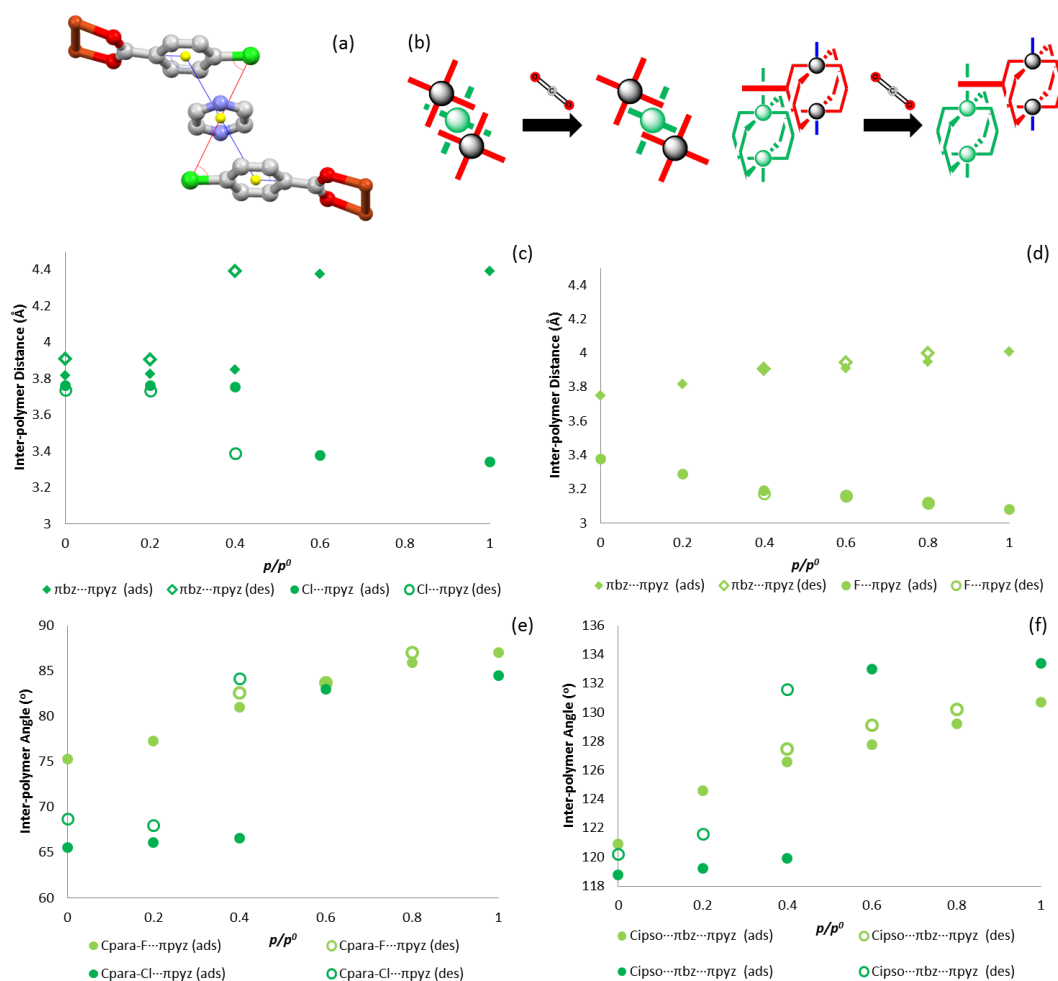


Figure 2.4.5-8. (a) Definition of the distances and angles measured between offset polymer chains. Ring centroids are shown as yellow spheres (b) Schematic of the observed motion of offset polymer chains upon exposure to CO_2 . Plots of the $\pi_{\text{bz}} \cdots \pi_{\text{pyz}}$ and $\pi_{\text{bz}} \cdots \pi_{\text{pyz}}$ distances vs. p/p^0 for (c) **2.3(Cl)** and (d) **2.4(F)** on increasing (filled shapes) and decreasing (open shapes) pressures of CO_2 at 195 K. (e) Plots of $C_{\text{para}} - X \cdots \pi_{\text{pyz}}$ and (f) $C_{\text{ipso}} \cdots \pi_{\text{bz}} \cdots \pi_{\text{pyz}}$ angles vs p/p^0 for **2.3(Cl)** and **2.4(F)** on increasing (filled shapes) and decreasing (open shapes) of pressures CO_2 at 195 K.

The structure solutions obtained during the *in situ* CO₂ adsorption studies of **2.2(Br)**, **2.3(Cl)** and **2.4(F)** were analysed using PLATON CALC VOID²³ to quantify variations in solvent-accessible void. The changes in solvent-accessible void were consistent with the observations of unit cell volume changes for **2.2(Br)**, showing minimal change, and for **2.3(Cl)** and **2.4(F)**, showing void space expansion consistent with the unit cell volume expansion (Figure 2.4.5-9). The maximum void spaces for **2.3(Cl)** and **2.4(F)** are similar in magnitude at 381.5 Å³ and 385.0 Å³, respectively. These comparable void spaces corroborate the equivalent maximum uptake of CO₂ observed volumetrically (reported in Section 2.4.3). The void spaces initially observed as discrete cavities (Figure 2.4.2-7) connect together in the expanded phases for **2.3(Cl)** and **2.4(F)** to form channels (Figure 2.4.5-9). This formation of channels will be a contributing factor in gas permeating into the material. These pore spaces also corroborate the expected cylindrical pore spaces which are expected for Type IV(b) isotherms.

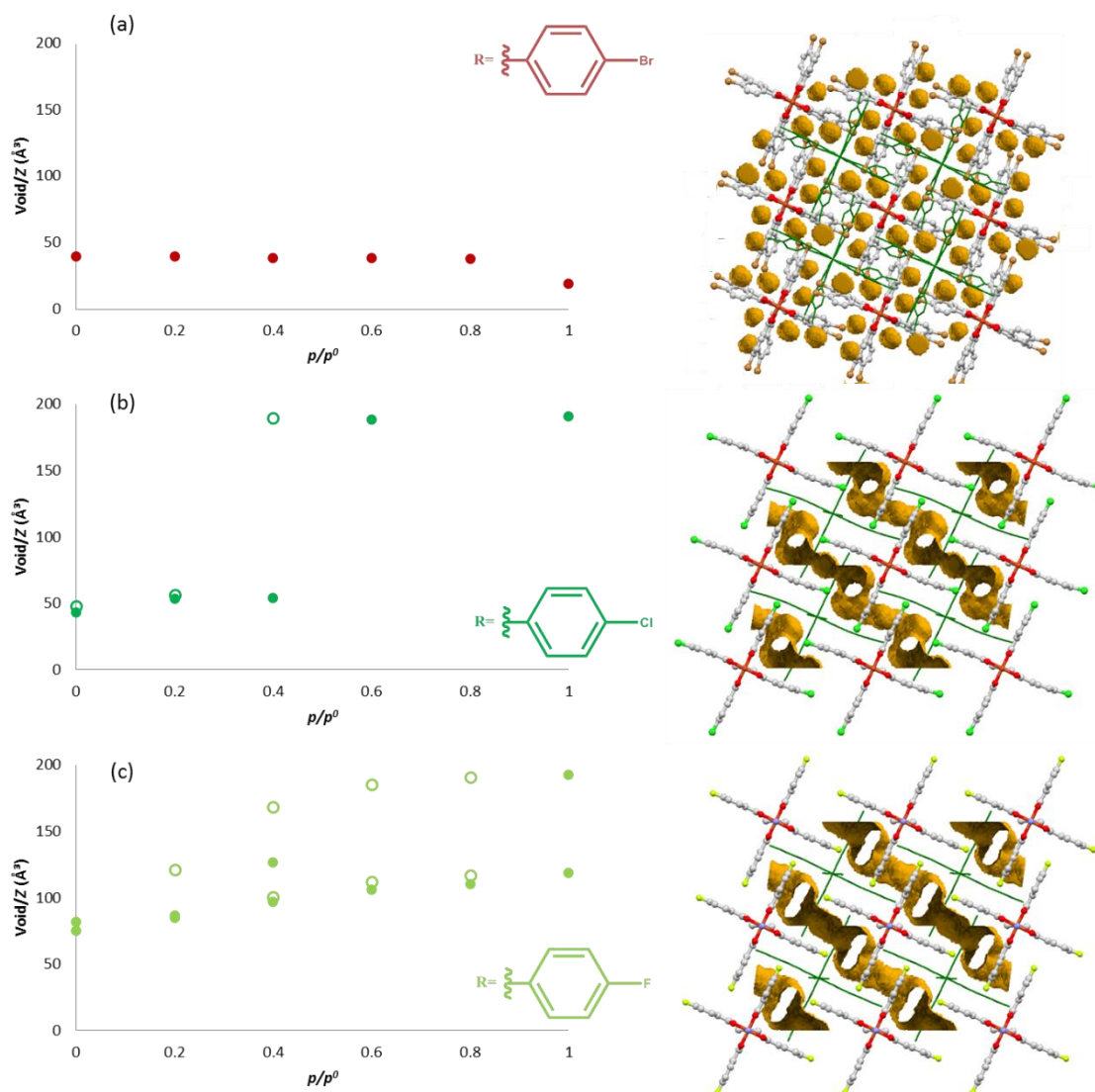


Figure 2.4.5-9. Void space/Z as a function of p/p^0 for adsorption (filled circles) and desorption (empty circles) of CO₂ at 195 K for (a) **2.2(Br)**, (b) **2.3(Cl)** and (c) **2.4(F)** with the void spaces visualised using the program Mercury.⁴⁷ Colour scheme consistent with Figure 2.4.2-7.

In conclusion the *in situ* single-crystal diffraction studies have demonstrated behaviour for three of the systems consistent with the previously discussed powder studies. Single-crystals of **2.1(I)** and **2.2(Br)** show no change in structure upon exposure to pressures of CO₂. Unfortunately, due to time constraints, samples of **2.1(I)** and **2.2(Br)** could not be tested for longer equilibration times. Single-crystals of **2.3(Cl)** and **2.4(F)** did show volume expansion with increasing CO₂ pressure, resulting from expansion in the *a*- and *c*-axes due to a moving apart of polymer chains. Comparison of the interactions discussed in Section 2.4.2 concluded this expansion sees the retention of a 1D halogen-bonded chain in the study of **2.3(Cl)** and a universal moving apart of polymers in **2.4(F)**. Finally, comparison of the void spaces corroborated the volumetric studies in Section 2.4.3 with equivalent void spaces observed for the expanded forms of **2.3(Cl)** and **2.4(F)**.

2.4.6 Crystallographic Determination of CO₂ molecule location(s)

As previously discussed in **Chapter 1** the extensive studies of [M₂(bz)₄(pyz)]_n (M = Cu, Rh) by Takamizawa and co-workers showed a consistent guest site for a wide range of guests.^{11-15,19,52-58} The work highlights a distinct guest site, irrespective of included guest, located in the cleft of the paddlewheel. This is the largest available pore space with the only host-guest interactions being observed between the aromatic rings and the guest. The successful modelling of a number of guest molecules within these materials makes it unsurprising that the *in situ* single-crystal diffraction studies of **2.3(Cl)** and **2.4(F)** reveal that the largest residual electron density peaks are situated in an identical cleft to that of [M₂(bz)₄(pyz)]_n (**Figure 2.4.6-1**). Such residual electron peaks are not observed in the studies of **2.3(Cl)** and **2.4(F)** under vacuum and at low CO₂ pressures, but become prominent at higher pressures and subsequently diminish upon desorption of CO₂ after pressure reduction.

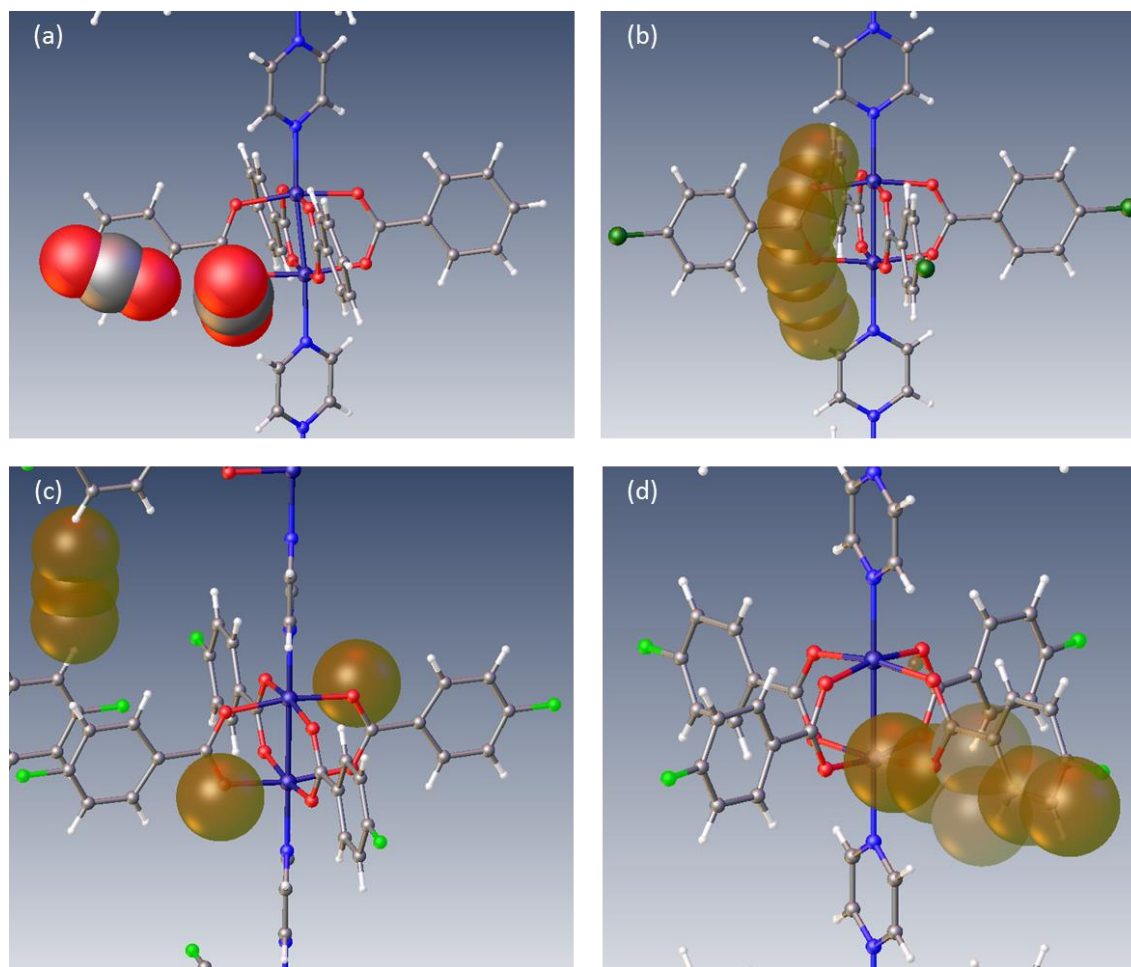


Figure 2.4.6-1. (a) Crystal structure of $[\text{Cu}_2(\text{bz})_4\text{pyz}]_n$ with CO_2 molecules modelled.⁵⁹ Residual electron density in (b) **2.3(Cl)-1barCO₂** and (c and d) **2.4(F)-1barCO₂**. Colour scheme Cu, dark blue; O, red; C, grey; N, blue; H, white; F, light green; Cl, green; residual electron density peaks, brown (space filled).

Monitoring the residual electron density with the use of PLATON SQUEEZE²³ (**Figure 2.4.6-2**), it can be seen that there is an increase in the electron density within the void space which directly correlates to the volume expansion. It is then possible to model the residual electron density (**Figure 2.4.6-1**) as partial-occupancy CO_2 molecules (**Figure 2.4.6-3**).

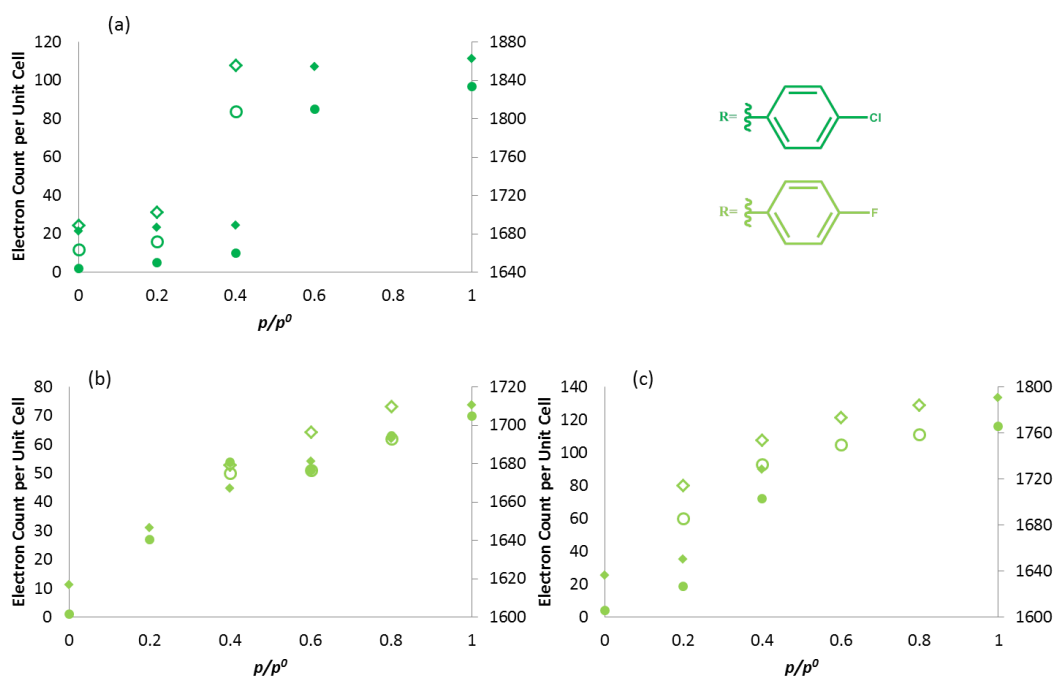


Figure 2.4.6-2-Combined graphs of unit cell volume (diamonds) and residual electron count (circles) as determined by PLATON SQUEEZE²³ from in situ single-crystal diffraction studies during CO₂ adsorption (filled symbols) and desorption (open symbols) at 195 K for (a) **2.3(Cl)** and (b and c) **2.4(F)**.

	CO ₂ Per Formula Unit	
2.3(Cl)-Vac	0	
2.3(Cl)-0.2bar CO ₂	0	
2.3(Cl)-0.4bar CO ₂	0	
2.3(Cl)-0.6bar CO ₂	1	
2.3(Cl)-1bar CO ₂	1	
2.3(Cl)-0.4bar CO ₂ (D)	0.5	
2.3(Cl)-0.2bar CO ₂ (D)	0	
2.3(Cl)-Vac (D)	0	
2.4(F)-Vac	0	
2.4(F)-0.18bar CO ₂	0	
2.4(F)-0.40bar CO ₂	0	
2.4(F)-0.63bar CO ₂	0	
2.4(F)-0.80bar CO ₂	0	
2.4(F)-1bar CO ₂	0.5	
2.4(F)-0.80bar CO ₂ (D)	0	
2.4(F)-0.59bar CO ₂ (D)	0	
2.3(Cl)-0.4bar CO ₂ (D)	0	
2.4(F)-Vac	0	
2.4(F)-0.19bar CO ₂	0	
2.4(F)-0.40bar CO ₂	0	
2.4(F)-1bar CO ₂	1	
2.4(F)-0.80bar CO ₂ (D)	0	
2.4(F)-0.59bar CO ₂ (D)	0	
2.4(F)-0.41bar CO ₂ (D)	0	
2.4(F)-0.19bar CO ₂ (D)	0	

Figure 2.4.6-3. Table of the occupancy of modelled CO₂ molecules from in situ single-crystal diffraction studies of adsorption and desorption of CO₂ at 195 K for **2.3(Cl)** (top) and **2.4(F)** (bottom and middle) and an accompanying image of the modelling of CO₂ molecules at maximum occupancy. Colour scheme consistent with **Figure 2.4.6-1**.

Despite the lower-resolution data recorded in the *in situ* PXRD studies residual electron density consistent with the positions in the single-crystal studies is observed (**Figure 2.4.6-4**). Rietveld refinement³⁷ of rigid-body CO₂ molecules resulted in these molecules being located in analogous sites to those of the single-crystal diffraction studies (**Figure 2.4.6-5**). The PXRD study of **2.3(Cl)** also identified a secondary site situated closer to the chlorine functionality (**Figure 2.4.6-6**) and resembling the two observed sites from the previous work by Takamizawa et al.⁵⁹ (**Figure 2.4.6-1**).

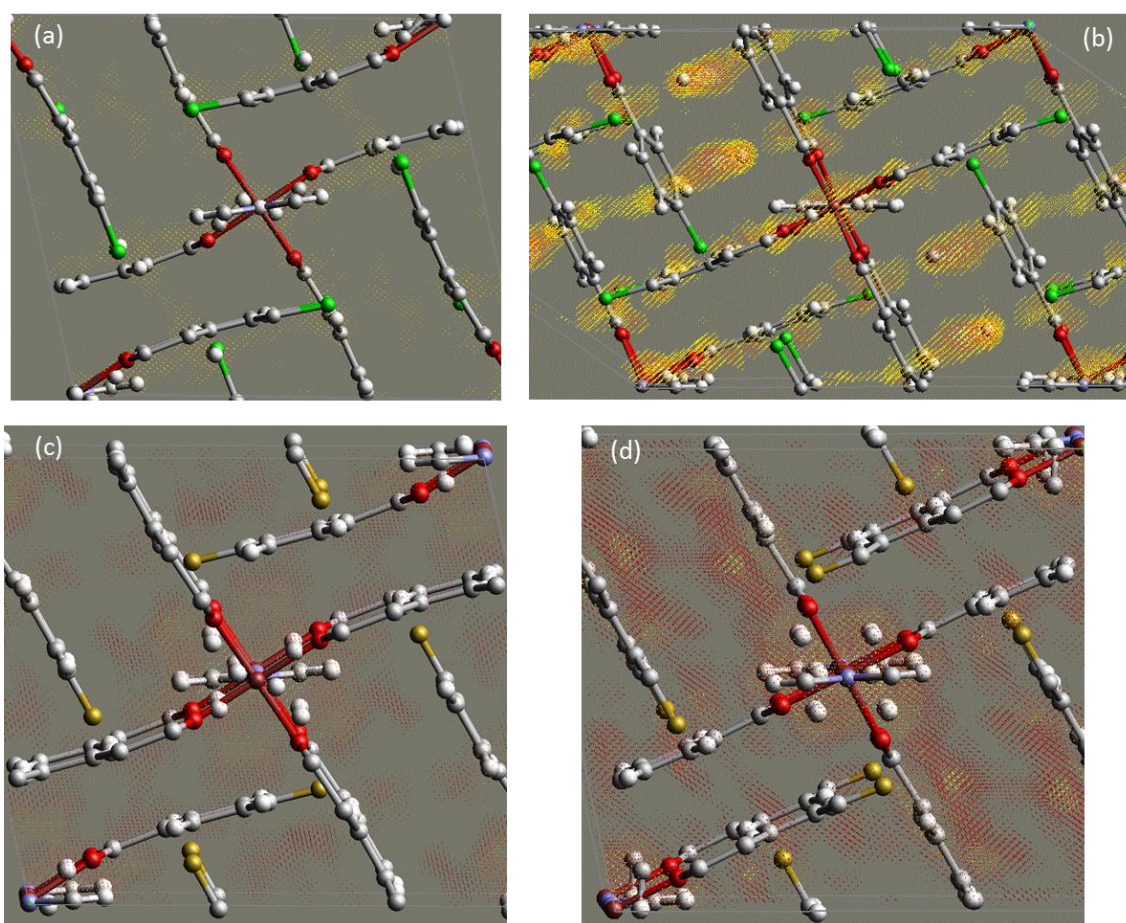


Figure 2.4.6-4. Comparison of residual electron densities, following Rietveld refinement³⁷ in TOPAS,^{33,34} for **2.3(Cl)** (a and b) and **2.4(F)** (c and d). Diffraction data measurement under vacuum (a and c) and at 1 bar CO₂ (b and d). Electron density contours are plotted using the standard cloud visualizer settings in TOPAS. Colour scheme Cu, brown; O, red; N, blue; C, grey; H, white; Cl, green; F, yellow.

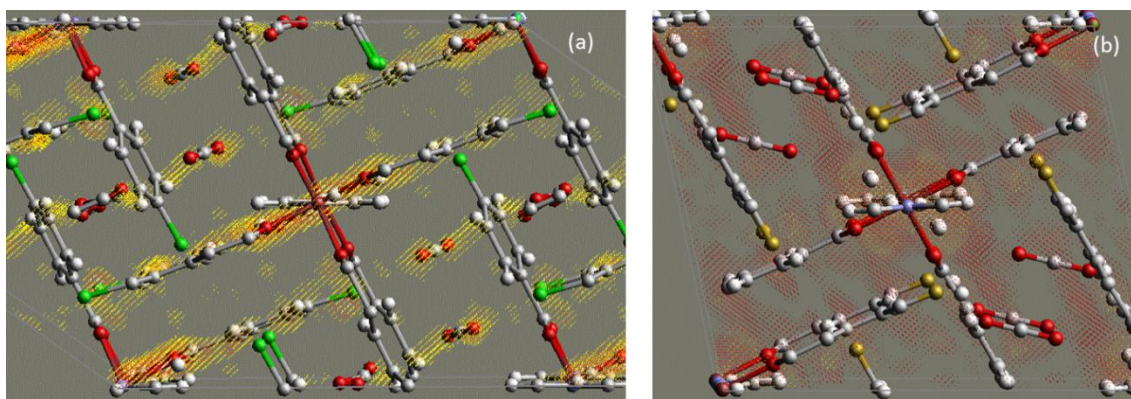


Figure 2.4.6-5. Images of the CO₂ molecules modelled as rigid-bodies Rietveld refinement³⁷ for (a) **2.3(Cl)** and (b) **2.4(F)** dosed to 1 bar CO₂ at 195 K. Colour scheme and images created as outlined in **Figure 2.4.6-4**.

The occupancies of the CO₂ sites were also refined to determine whether the occupancy increases with increasing CO₂ pressure. The change in total CO₂ occupancy as a function of pressure is similar for **2.3(Cl)** and **2.4(F)**, but the maximum uptake is much lower for **2.4(F)**. In the case of **2.4(F)** no phase change occurs on expansion of the structure and CO₂ site occupancy increases with increasing pressure (**Figure 2.4.6-7**). Upon reduction of CO₂ at pressure hysteresis was observed, with retention of CO₂ at low pressure (**Figure 2.4.6-8**). For **2.3(Cl)** a phase change from a contracted to an expanded form occurs. Approximately constant CO₂ site occupancy for the (expanded) guest-including phase is observed (**Figure 2.4.6-6**) but overall uptake increases as the percentage of the material in the (expanded) guest-included phase increases with CO₂ pressure; a similar hysteresis to that of **2.4(F)** is observed (**Figure 2.4.6-8**).

	T (K)	P (bar)	Phase	CO ₂ Occupancy		Total
				Per Formula Unit Site 1	Site 2	
2.3(Cl)-Vac	195	0	100.0(0)	n/a	n/a	n/a
2.3(Cl)-0.2 bar CO ₂	195	0.2	100.0(0)	n/a	n/a	n/a
2.3(Cl)-0.4 bar CO ₂	195	0.4	68.0(3)	n/a	n/a	n/a
			32.0(3)	2.000(16)	n/a	2.000(23)
2.3(Cl)-0.6 bar CO ₂	195	0.6	22.0(5)	n/a	n/a	n/a
			78.0(5)	1.026(16)	1.574(16)	2.600(23)
2.3(Cl)-0.8 bar CO ₂	195	0.8	11.8(7)	n/a	n/a	n/a
			88.2(7)	1.122(18)	1.476(19)	2.598(26)
2.3(Cl)-1.0bar CO ₂	195	1	100.0(0)	1.422(14)	1.210(15)	2.632(21)
2.3(Cl)-0.8 bar CO ₂ (D)	195	0.8	100.0(0)	1.384(14)	1.182(15)	2.566(21)
2.3(Cl)-0.6 bar CO ₂ (D)	195	0.6	100.0(0)	1.360(14)	1.162(15)	2.522(21)
2.3(Cl)-0.4 bar CO ₂ (D)	195	0.4	24.8(4)	n/a	n/a	n/a
			75.2(4)	1.04(16)	1.586(16)	2.626(23)
2.3(Cl)-0.2 bar CO ₂ (D)	195	0.2	100.0(0)	n/a	n/a	n/a
2.3(Cl)-Vac (D)	195	0	100.0(0)	n/a	n/a	n/a

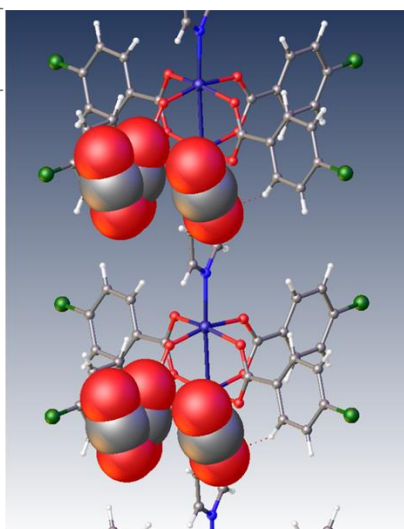


Figure 2.4.6-6. Table of the refined occupancies of CO₂ molecules determined by Rietveld fits³⁷ of PXRD recorded for **2.3(Cl)** during increasing (and decreasing) pressure of CO₂ at 195 K. Occupancies are expressed as the total per formula unit accounting for the percentage of each phase present. Accompanying image shows the two refined CO₂ sites. Colour scheme consistent with **Figure 2.4.6-1**.

	T (K)	P (bar)	CO ₂ Occupancy Per Formula Unit
2.4(F)-Vac	195	0	n/a
2.4(F)-0.2 bar CO ₂	195	0.2	n/a
2.4(F)-0.4 bar CO ₂	195	0.4	0.278(4)
2.4(F)-0.6 bar CO ₂	195	0.6	0.440(5)
2.4(F)-0.8 bar CO ₂	195	0.8	0.522(5)
2.4(F)-1 bar CO ₂	195	1	0.598(5)
2.4(F)-0.8 bar CO ₂ (D)	195	0.8	0.612(4)
2.4(F)-0.6 bar CO ₂ (D)	195	0.6	0.622(4)
2.4(F)-0.5 bar CO ₂ (D)	195	0.5	0.618(4)
2.4(F)-0.4 bar CO ₂ (D)	195	0.4	0.562(4)

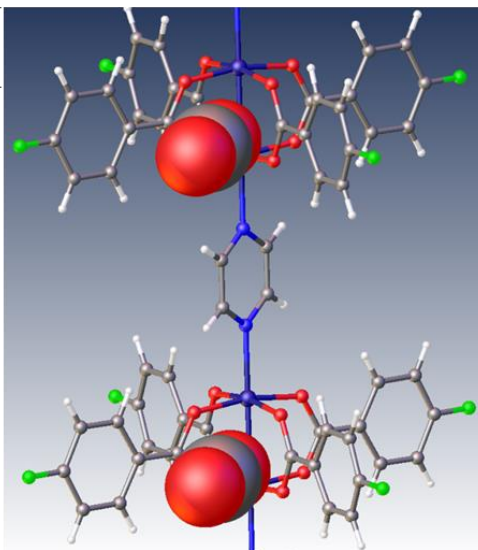


Figure 2.4.6-7. Table of the refined occupancies of CO₂ molecules determined by Rietveld fits³⁷ of PXRD recorded for **2.4(F)** during increasing (and decreasing) pressure of CO₂ at 195 K. Occupancies are expressed as the total per formula unit. Accompanying image shows the refined CO₂ site. Colour scheme consistent with **Figure 2.4.6-1**.

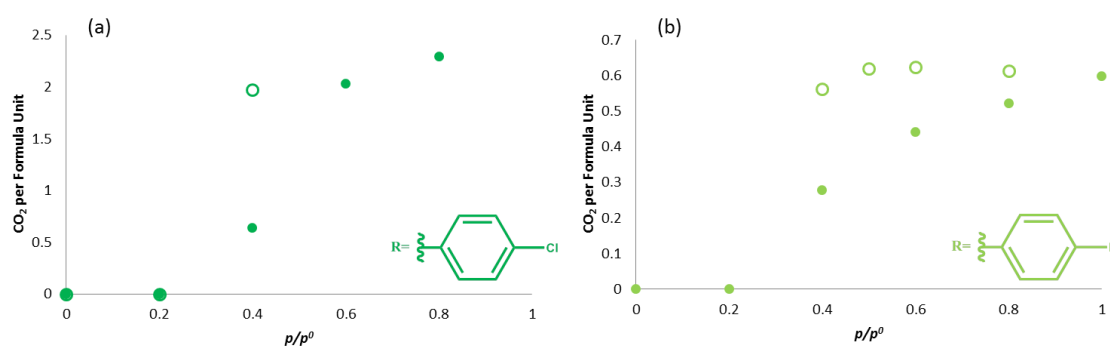


Figure 2.4.6-8. Number of CO₂ molecules per formula unit vs p/p^0 determined by Rietveld fits³⁷ from PXRD studies of (a) **2.3(Cl)** and (b) **2.4(F)** during increasing (filled circles) and decreasing (empty circles) of CO₂ pressures at 195 K.

In conclusion further analysis of both single-crystal diffraction and PXRD *in situ* CO₂ uptake studies of **2.3(Cl)** and **2.4(F)** identified residual electron density situated predominantly in the cleft of the paddlewheel unit. The location of this electron density is consistent with the guest locations identified in previous studies of $[M_2(bz)_4(pyZ)]_n$. It was possible to model the electron density as CO₂ molecules of partial occupancy, but total occupancies are lower than the expected *ca.* 2.8 molecules per formula unit determined from the volumetric adsorption measurements. This difference could be related to data quality, which may also limit the possibility to identify alternative sites of low occupancy.

2.5 Conclusion

This chapter has focused on a family of halogen-functionalised 1D coordination polymers, $[Cu_2(4-Xbz)_4(pyZ)]_n$ ($X = I$ (**2.1(I)**), Br (**2.2(Br)**), Cl (**2.3(Cl)**) and F (**2.4(F)**)), which demonstrate variable uptake of CO₂ as a function of the halogen functionality present. Three of the four systems demonstrated gated adsorption of CO₂ gas with similar maximum uptakes of CO₂ (approx. *ca.* 2.8 molecules per formula unit). The uptake properties are related to halogen

bonding of the functional groups. All systems exhibit analogous packing of polymer chains with interpenetration being observed and the presence of either 2D or 1D halogen-bonded networks between adjacent polymer chains. This halogen-bonded network is involved in determining the materials' gate pressure for CO₂. This gate pressure increases with increasing halogen bonding strength. Thus, the fluoro derivative (**2.4(F)**), which lacks halogen bonding capability exhibits a gradual uptake of CO₂ accompanied by a gradual unit cell expansion. The chloro derivative (**2.3(Cl)**), which exhibits a 1D halogen-bonding chain, requires a gate pressure of $p/p^0 = 0.2$ to overcome the intermolecular interactions present, leading to unit cell expansion. The bromo derivative (**2.2(Br)**) showed a gate pressure of $p/p^0 = 0.75$ during volumetric gas adsorption measurements. Extended equilibration times were required during the *in situ* PXRD study to observe the gating; these extended equilibrations were implemented only at $p/p^0 = 1.0$. The gated CO₂ uptake by **2.2(Br)** occurs through a phase transformation from the original tetragonal phase ($I4_1/a$) containing the 2D halogen-bonded network to a monoclinic phase ($C2/c$) more similar to the guest-included phase of the chloro and fluoro systems. Finally the iodo derivative (**2.1(I)**) exhibits no uptake and undergoes minimal structural changes or volume change on exposure to CO₂ gas pressure. However, considering the long equilibration time required for **2.2(Br)** it cannot be ruled out that uptake may be observed following much longer equilibration times.

The uptake of CO₂ in **2.2(Br)**, **2.3(Cl)** and **2.4(F)** occurred in conjunction with an expansion in the volume of the unit cell. This expansion corresponds mainly to changes in the *a*- and *c*-axes, which lie perpendicular to the direction of coordination polymer propagation. This demonstrates that uptake involves the moving apart of polymer chains with negligible compression or elongation of these chains. Further structural characterisation identifies, in the case of **2.3(Cl)** and **2.4(F)**, that the volume expansion is also accompanied with a straightening of the bridging benzoates due to rotation of the ligand coordination about the O...O vector of the carboxylate groups.

Finally it was possible to model partial-occupancy CO₂ molecule guests in both PXRD and single-crystal *in situ* studies of **2.3(Cl)** and **2.4(F)**. These guest molecules were observed in the cleft of the paddlewheel consistent with guest sites observed in previously reported [M₂(bz)₄(pyz)]_n systems.^{11–15,19,52–58}

2.6 Future Work

This chapter focused primarily on the uptake of CO₂ within this family of coordination polymers, which demonstrate tailored uptake related to halogen functionality present. Considering the breadth of work carried out on analogous systems, it should be feasible to study inclusion of other guests. A suitable prospect would be to look more closely at the N₂ inclusion. This has been touched upon within this chapter and in previously published work with the use of volumetric adsorption analyses (**Figure 2.6-1**), which show key differences to the CO₂ adsorption studies. Notably, **2.2(Br)** shows no N₂ uptake which suggests that N₂ has an insufficient interaction to instigate a phase transformation. The type V isotherm⁴⁸ observed for N₂ adsorption by **2.3(Cl)** suggests initial weak adsorbent-adsorbate interactions before molecular clustering of N₂ allowing for inclusion, followed by a large hysteresis likely due to

small pore openings. Finally, **2.4(F)** shows a large uptake of N₂ at relatively low pressures, with further gated expansion at $p/p^0 = 0.5$. This suggests the same initial gradual expansion, observed in the *in situ* PXRD and single-crystal CO₂ studies of **2.4(F)**, followed by accessing a further expanded phase. The quantity of N₂ adsorbed also varies with halogen functionality, an outcome which was not observed in the CO₂ adsorption studies. Alternative further studies could emulate the work of Takamizawa in looking at either inclusion of solvents,^{12,17,18,58} noble gases¹³ or use of these systems in separation of gases.⁶

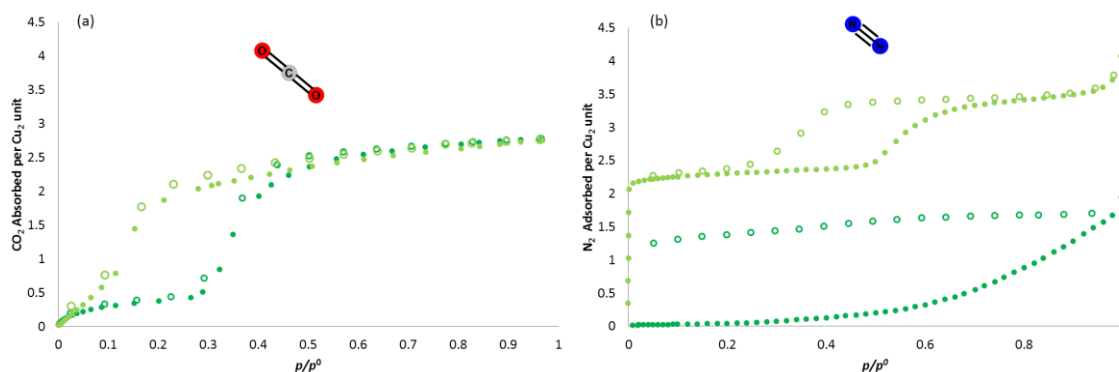


Figure 2.6-1. Volumetric adsorption isotherms studies for **2.3(Cl)** (green) and **2.4(F)** (light green) reported in this chapter. (a) CO₂ at 195 K and (b) N₂ at 77 K (adsorption- solid circles, desorption- open circles).

Further work could look at synthesizing systems with further functionality on the pyrazine ligand to accompany the halogen functionality of the benzoates. Two similar systems have been reported [Cu₂(4-Fbz)₄(Mepyz)]_n (**Figure 2.6-2**), by Takamizawa et al.,⁶ is isostructural to **2.4(F)** and shows uptake of gaseous guests.

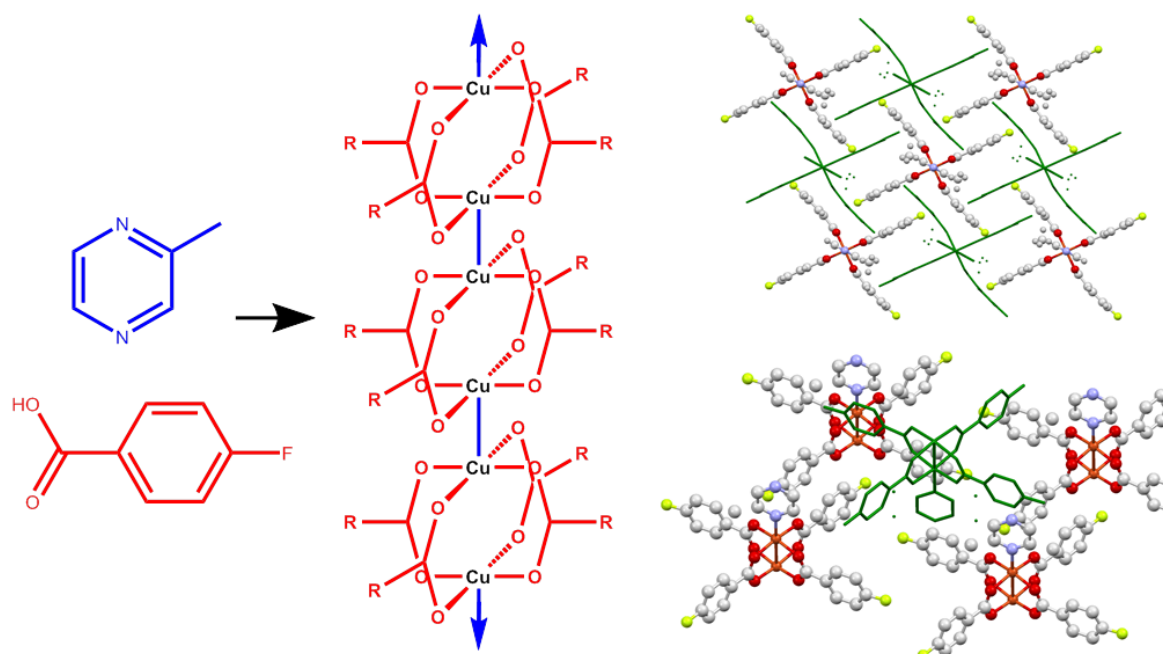


Figure 2.6-2. [Cu₂(4-Fbz)₄(2-Mepyz)]_n synthesised by Takamizawa et al.⁶ shows packing and interpenetration isostructural to that observed in **2.4(F)**. Colour scheme consistent with **Figure 2.4.2-1**.

$[\text{Cu}_2(4\text{-Ibz})_4(\text{NH}_2\text{pyz})]_n$ (NH_2pyz = aminopyrazine) is arguably more interesting in the context of searching for a gas storage material.⁴⁰ This coordination polymer exhibits the same 2D halogen-bonding network observed in **2.1(I)** (**Figure 2.6-3**) but the presence of the amino functionality results in the absence of an interpenetrated structure and a potential solvent-accessible void of 50% of the total volume of the crystals. The prospect of producing a 1D coordination polymer with a 50% void space sustained by halogen bonding is too tempting to leave in the last lines of a thesis chapter and will therefore be discussed in the following chapter in greater detail, alongside its bromo, chloro and fluoro analogues.

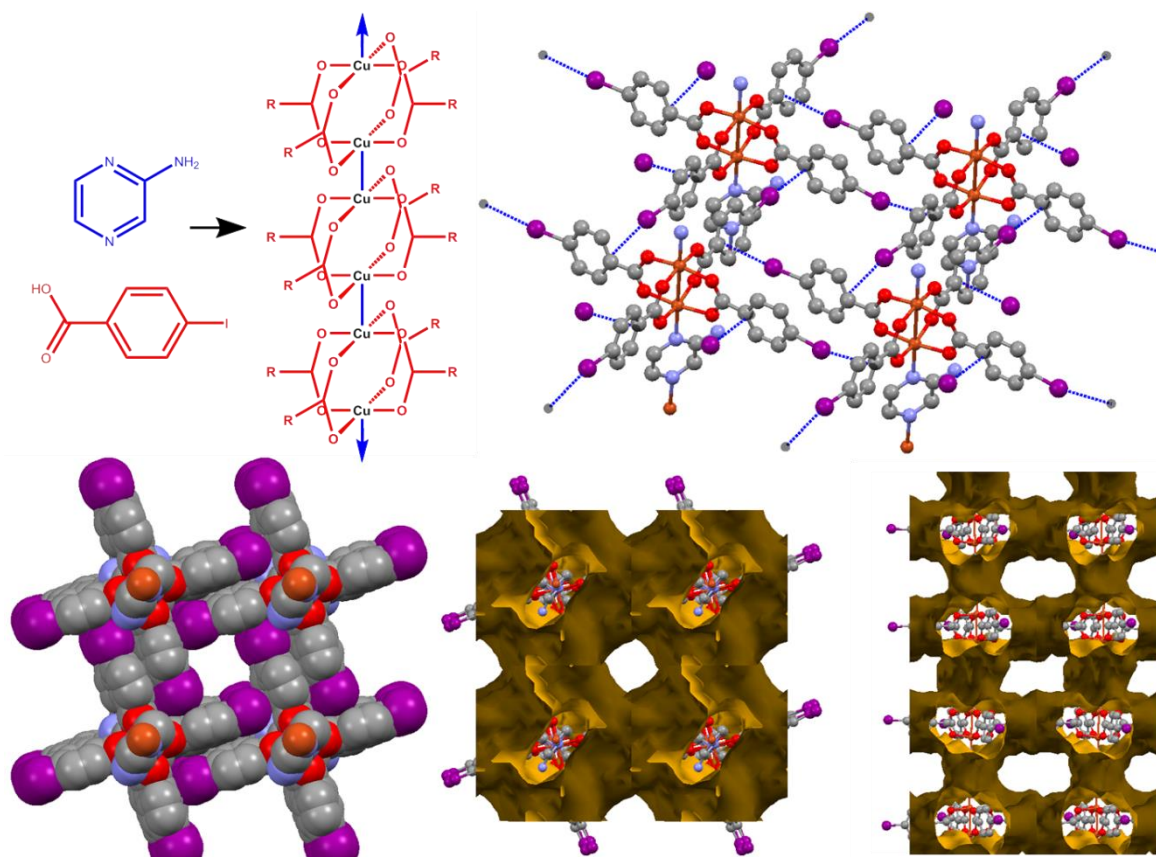


Figure 2.6-3. Packing of $[\text{Cu}_2(4\text{-Ibz})_4(2\text{-NH}_2\text{pyz})]_n$ previously published by Burrows et al.⁴⁰ and the void space visualised using Mercury⁴⁷. Colour scheme consistent with **Figure 2.4.2-7**.

2.7 References

- 1 J.-R. Li, R. J. Kuppler and H.-C. Zhou, *Chem. Soc. Rev.*, 2009, **38**, 1477–1504.
- 2 S. Biswas and P. Van Der Voort, *Eur. J. Inorg. Chem.*, 2013, 2154–2160.
- 3 X. Lu, D. Jin, S. Wei, Z. Wang, C. An and W. Guo, *J. Mater. Chem. A*, 2015, **3**, 12118–12132.
- 4 S. Kitagawa, R. Kitaura and S. Noro, *Angew. Chem. Int. Ed.*, 2004, **43**, 2334–2375.
- 5 K. Takahashi, N. Hoshino, T. Takeda, S. Noro, T. Nakamura, S. Takeda and T. Akutagawa, *Inorg. Chem.*, 2015, **54**, 9423–9431.

- 6 Y. Takasaki and S. Takamizawa, *J. Am. Chem. Soc.*, 2014, **136**, 6806–6809.
- 7 S. Kitagawa and K. Uemura, *Chem. Soc. Rev.*, 2005, **34**, 109–119.
- 8 K. Uemura, R. Matsuda and S. Kitagawa, *J. Solid State Chem.*, 2005, **178**, 2420–2429.
- 9 Z.-J. Lin, J. Lü, M. Hong and R. Cao, *Chem. Soc. Rev.*, 2014, **43**, 5867–5895.
- 10 A. Schneemann, V. Bon, I. Schwedler, I. Senkovska, S. Kaskel and R. A. Fischer, *Chem. Soc. Rev.*, 2014, **43**, 6062–6096.
- 11 S. Takamizawa, E. Nakata and T. Saito, *Chem. Lett.*, 2004, **33**, 538–539.
- 12 S. Takamizawa, C. Kachi-Terajima, M.-A. Kohbara, T. Akatsuka and T. Jin, *Chem. Asian J.*, 2007, **2**, 837–848.
- 13 T. Ueda, K. Kurokawa, T. Eguchi, C. Kachi-terajima and S. Takamizawa, *J. Phys. Chem.*, 2007, **2**, 1524–1534.
- 14 S. Takamizawa, E. Nakata and T. Akatsuka, *J. Am. Chem. Soc.*, 2008, **130**, 17882–17892.
- 15 S. Takamizawa, E.-I. Nakata and R. Miyake, *Dalton Trans.*, 2009, **2**, 1752–1760.
- 16 S. Takamizawa, Y. Takasaki and R. Miyake, *Chem. Commun.*, 2009, **2**, 6625–6627.
- 17 S. Takamizawa and R. Miyake, *CrystEngComm*, 2010, **12**, 2728–2733.
- 18 S. Takamizawa, T. Akatsuka and R. Miyake, *CrystEngComm*, 2010, **12**, 82–84.
- 19 S. Takamizawa, E. I. Nataka, T. Akatsuka, R. Miyake, Y. Kakizaki, H. Takeuchi, G. Maruta and S. Takeda, *J. Am. Chem. Soc.*, 2010, **132**, 3783–3792.
- 20 P. Smart, G. Mínguez Espallargas and L. Brammer, *CrystEngComm*, 2008, **10**, 1335–1344.
- 21 P. Smart, Á. Bejarano-Villafuerte and L. Brammer, *CrystEngComm*, 2013, **15**, 3151–3159.
- 22 P. Smart, Á. Bejarano-Villafuerte, R. M. Hendry and L. Brammer, *CrystEngComm*, 2013, **15**, 3160–3167.
- 23 A. L. Spek, *Acta Crystallogr. Sect. C: Struct. Chem.*, 2015, **71**, 9–18.
- 24 D. R. Allan, S. P. Collins, G. Evans, D. Hall, K. McAuley, R. L. Owen, T. Sorensen, C. C. Tang, F. von Delft, A. Wagner and H. Wilhelm, *Eur. Phys. J. Plus*, 2015, **130**, 1–20.
- 25 H. Nowell, S. A. Barnett, K. E. Christensen, S. J. Teat and D. R. Allan, *J. Synchrotron Radiat.*, 2012, **19**, 435–441.
- 26 S. P. Thompson, J. E. Parker, J. Marchal, J. Potter, A. Birt, F. Yuan, R. D. Fearn, A. R. Lennie, S. R. Street and C. C. Tang, *J. Synchrotron Radiat.*, 2011, **18**, 637–648.
- 27 G. M. Sheldrick, *SADABS, Empirical Absorption Correction program*, Univ. Göttingen, 1995, based on the methods of Blessing.
- 28 L. Krause, R. Herbst-Irmer, G. M. Sheldrick and D. Stalke, *J. Appl. Crystallogr.*, 2015, **48**, 3–10.

- 29 R. H. Blessing, *Acta Crystallogr. Sect. A: Found. Adv.*, 1995, **A51**, 33–38.
- 30 G. M. Sheldrick, *Acta Crystallogr. Sect. C: Struct. Chem.*, 2015, **71**, 3–8.
- 31 O. V. Dolomanov, L. J. Bourhis, R. J. Gildea, J. A. K. Howard and H. Puschmann, *J. Appl. Crystallogr.*, 2009, **42**, 339–341.
- 32 G. S. Pawley, *J. Appl. Crystallogr.*, 1981, **14**, 357–361.
- 33 A. A. Coelho, *Topas Academic, Version 4.1*, see <http://www.topas-academic.net>.
- 34 A. A. Coelho, J. Evans, I. Evans, A. Kern and S. Parsons, *Powder Diffr.*, 2011, **26**, S22–S25.
- 35 N. Tartoni, S. P. Thompson, C. C. Tang, B. L. Willis, G. E. Derbyshire, A. G. Wright, S. C. Jaye, J. M. Homer, J. D. Pizzey and A. M. T. Bell, *J. Synchrotron Radiat.*, 2007, **15**, 43–49.
- 36 S. P. Thompson, J. E. Parker, J. Potter, T. P. Hill, A. Birt, T. M. Cobb, F. Yuan and C. C. Tang, *Rev. Sci. Instrum.*, 2009, **80**, (075107) 1–9.
- 37 H. M. Rietveld, *J. Appl. Crystallogr.*, 1969, **2**, 65–71.
- 38 S. A. Barnett, H. Nowell, M. R. Warren, A. Wilcox and D. R. Allan, *Protein Pept. Lett.*, 2015, **23**, 211–216.
- 39 CrysAlisPRO, *Oxford Diffraction /Agilent Technologies UK Ltd*, Yarnton, England.
- 40 A. D. Burrows, M. F. Mahon, P. R. Raithby, A. J. Warren, S. J. Teat and J. E. Warren, *CrystEngComm*, 2012, **14**, 3658–3666.
- 41 W. Kosaka, K. Yamagishi, H. Yoshida, R. Matsuda, S. Kitagawa, M. Takata and H. Miyasaka, *Chem. Commun.*, 2013, **49**, 1594–1596.
- 42 G. Férey and C. Serre, *Chem. Soc. Rev.*, 2009, **38**, 1380–1399.
- 43 E. J. Carrington, C. A. McAnally, A. J. Fletcher, S. P. Thompson, M. R. Warren and L. Brammer, *Nat. Chem.*, 2017, **9**, 882–889.
- 44 D. N. Dybtsev, H. Chun and K. Kim, *Angew. Chem. Int. Ed.*, 2004, **43**, 5033–5036.
- 45 A. Bondi, *J. Phys. Chem.*, 1964, **68**, 441–451.
- 46 S. Alvarez, *Dalton Trans.*, 2013, **42**, 8617–8636.
- 47 C. F. Macrae, I. J. Bruno, J. A. Chisholm, P. R. Edgington, P. McCabe, E. Pidcock, L. Rodriguez-Monge, R. Taylor, J. Van De Streek and P. A. Wood, *J. Appl. Crystallogr.*, 2008, **41**, 466–470.
- 48 M. Thommes, K. Kaneko, A. V. Neimark, J. P. Olivier, F. Rodriguez-Reinoso, J. Rouquerol and K. S. W. Sing, *Pure Appl. Chem.*, 2015, **87**, 1051–1069.
- 49 G. Kumari, K. Jayaramulu, T. K. Maji and C. Narayana, *J. Phys. Chem. A*, 2013, **117**, 11006–11012.
- 50 C. Zhang, J. A. Gee, D. S. Sholl and R. P. Lively, *J. Phys. Chem. C*, 2014, **118**, 20727–20733.
- 51 Y. Hijikata, S. Horike, D. Tanaka, J. Groll, M. Mizuno, J. Kim, M. Takata and S. Kitagawa,

- Chem. Commun.*, 2011, **47**, 7632–7634.
- 52 S. Takamizawa, E. Nakata and T. Saito, *Inorg. Chem. Commun.*, 2003, **6**, 1415–1418.
- 53 S. Takamizawa, E. Nakata, T. Saito, T. Akatsuka and K. Kojima, *CrystEngComm*, 2004, **6**, 197–199.
- 54 S. Takamizawa, T. Saito, T. Akatsuka and E. Nakata, *Inorg. Chem.*, 2005, **44**, 1421–1424.
- 55 S. Takamizawa, E. Nakata, T. Saito and T. Akatsuka, *Inorg. Chem.*, 2005, **44**, 1362–1366.
- 56 S. Takamizawa and E. Nakata, *CrystEngComm*, 2005, **7**, 476–479.
- 57 C. Kachi-Terajima, T. Akatsuka, M. Kohbara and S. Takamizawa, *Chem. Asian J.*, 2007, **2**, 40–50.
- 58 S. Takamizawa and R. Miyake, *Chem. Commun.*, 2009, **0**, 4076–4078.
- 59 S. Takamizawa, E. Nakata and T. Saito, *Inorg. Chem. Commun.*, 2004, **7**, 1–3.
- 60 R.-Z. Hu, Z.-D. Liu, M.-Y. Tan and H.-L. Zhu, *Acta Crystallogr. Sect. E: Struct. Reports Online*, 2004, **60**, m946–m947.
- 61 S. J. Jenniefer and P. T. Muthiah, *Chem. Cent. J.*, 2013, **7**, (35) 1-15.
- 62 V. Mollica Nardo, F. Nicoló, A. Saccà, G. Bruno and I. Ielo, *Acta Crystallogr. Sect. E: Struct. Reports Online*, 2013, **69**, m221–m221.

2.8 Appendix

Appendix 2.8.1: Single-Crystal Data

Table 2.3.2-1. Data collection, structure solution and refinement parameters for **2.2(Br)**, **2.3(Cl)** and **2.4(F)**

	2.2 (Br)	2.3 (Cl)	2.4 (F)
	$[\text{Cu}_2(4\text{-Brbz})_2(\text{pyz})]_n$	$[\text{Cu}_2(4\text{-Clbz})_2(\text{pyz})]_n$	$[\text{Cu}_2(4\text{-Fbz})_2(\text{pyz})]_n$
	$\text{C}_{32}\text{H}_{20}\text{Br}_4\text{Cu}_2\text{N}_2\text{O}_8$	$\text{C}_{32}\text{H}_{20}\text{Cl}_4\text{Cu}_2\text{N}_2\text{O}_8$	$\text{C}_{32}\text{H}_{20}\text{F}_4\text{Cu}_2\text{N}_2\text{O}_8$
Crystal habit	Needle	Block	Needle
Crystal colour	Clear Bluish Green	Clear Bluish Green	Clear Bluish Green
Crystal size (mm)	0.3x0.05x0.05	0.6x0.4x0.3	0.24x0.018x0.016
Crystal system	Tetragonal	Monoclinic	Monoclinic
Space group	$I4_1/a$	$I2/m$	$I2/m$
a (Å)	18.5109(8)	12.2365(18)	11.8094(6)
b (Å)	18.5109(8)	9.7580(7)	9.6791(5)
c (Å)	19.6307(15)	14.2231(12)	14.3331(12)
α (°)	90	90	90
β (°)	90	103.610(5)	103.192(3)
γ (°)	90	90	90
V (Å ³)	6726.6(8)	1650.6(3)	1595.10(18)
Density (g cm ⁻³)	1.989	1.669	1.59
Temperature (K)	150	100	100
μ (mm ⁻¹)	6.07	1.666	2.332
Wavelength (Å)	0.71073	0.71073	1.54178
2θ range (°)	6.604 to 50.052	3.958 to 52.886	8.778 to 121.996
Reflns. collected	5352	10439	10706
Independent reflns. [R_{int}]	2949 [0.0672]	1772 [0.1902]	1157 [0.0987]
Reflns. used in refinement, n	2949	1772	1157
LS parameters, p	204	122	122
Restraints, r	6	0	0
$R1$ (F) ^a $I > 2.0\sigma(I)$	0.0793	0.1001	0.0622
$wR2$ (F^2) ^a , all data	0.2507	0.2116	0.1455
S (F^2) ^a , all data	1.074	1.051	1.072

$$^a R1(F) = \sum(|F_o| - |F_c|) / \sum|F_o| ; wR2(F^2) = [\sum w(F_o^2 - F_c^2)^2 / \sum w F_o^4]^{1/2} ; S(F^2) = [\sum w(F_o^2 - F_c^2)^2 / (n + r - p)]^{1/2}$$

Appendix 2.8.2: *In situ* PXRD Data

Table 2.3.5-1. Pawley fits of *in situ* PXRD data during CO₂ adsorption for **2.1(I)** at room temperature, $\lambda = 0.82562(1)$ Å

	T (K)	P (bar)	Space Group	Volume (Å ³)	a (Å)	b (Å)	c (Å)	α (°)	β (°)	γ (°)	R_{wp}	R_{wp}'	Parameters
2.1(I)-RT-CO₂	298	0	$I4_1/a$	7110.8(2)	18.9415(2)	18.9415(2)	19.8193(3)	90	90	90	0.0511	0.1892	2078
	298	10	$I4_1/a$	7112.3(2)	18.9428(2)	18.9428(2)	19.8209(2)	90	90	90	0.0470	0.1817	2081
	298	25	$I4_1/a$	7114.6(2)	18.9445(2)	18.9445(2)	19.8236(2)	90	90	90	0.0450	0.1751	2081
	298	50	$I4_1/a$	7115.7(2)	18.9451(2)	18.9451(2)	19.8257(2)	90	90	90	0.0435	0.1713	2081
	298	1	$I4_1/a$	7111.0(2)	18.9432(2)	18.9432(2)	19.8164(2)	90	90	90	0.0481	0.1916	2079
	200	1	$I4_1/a$	7023.6(2)	18.8629(2)	18.8629(2)	19.7398(2)	90	90	90	0.0499	0.1899	2081

Table 2.3.5-2. Pawley fits of *in situ* PXRD data during CO₂ adsorption/desorption for **2.2(Br)** at 195K. $\lambda = 0.82602(1)$ Å

	T (K)	P (bar)	Space Group	Volume (Å ³)	a (Å)	b (Å)	c (Å)	α (°)	β (°)	γ (°)	R_{wp}	R_{wp}'	Parameters
2.2(Br)-195K-CO₂	195	Vac	<i>I4₁/a</i>	6691.58(33)	18.4694(4)	18.4694(4)	19.6165(5)	90	90	90	0.1363	0.2240	1946
	195	0.6	<i>I4₁/a</i>	6692.13(36)	18.4732(4)	18.4732(4)	19.6102(5)	90	90	90	0.1288	0.1952	1946
	195	0.85	<i>I4₁/a</i>	6701.18(43)	18.4866(5)	18.4866(5)	19.6083(5)	90	90	90	0.1231	0.1949	1946
	195	1 ^A	<i>I4₁/a</i>	6713.04(54)	18.5030(7)	18.5030(7)	19.6081(7)	90	90	90	0.1214	0.2086	1946
	195	1 ^B	<i>I4₁/a</i>	6708.66(35)	18.4896(4)	18.4896(4)	19.6238(4)	90	90	90	0.0928	0.1600	4140
			<i>C2/c</i>	3803.59(20)	18.4766(6)	9.8065(3)	21.5345(7)	90	102.885(3)	90			
	195	1 ^C	<i>I4₁/a</i>	6713.92(52)	18.5009(5)	18.5009(5)	19.6152(10)	90	90	90	0.0714	0.1047	4140
			<i>C2/c</i>	3814.02(14)	18.5035(4)	9.8075(1)	21.5562(5)	90	102.843(2)	90			
	195	0.6	<i>I4₁/a</i>	6719.20(56)	18.5160(6)	18.5160(6)	19.5985(10)	90	90	90	0.0688	0.1026	4140
			<i>C2/c</i>	3812.97(15)	18.4909(4)	9.8041(2)	21.5784(5)	90	102.910(2)	90			
	195	0.4	<i>I4₁/a</i>	6726.76(27)	18.5058(4)	18.5058(4)	19.6422(3)	90	90	90	0.0800	0.1098	4140
			<i>C2/c</i>	3816.64(32)	9.8033(5)	9.8033(5)	21.5429(10)	90	102.773(4)	90			
	195	0.2	<i>I4₁/a</i>	6738.34(31)	18.5235(4)	18.5235(4)	19.6385(4)	90	90	90	0.0738	0.0982	4140
			<i>C2/c</i>	3810.32(28)	18.4824(8)	9.8259(5)	21.5437(9)	90	103.121(3)	90			
195	Vac	<i>I4₁/a</i>	6735.82(39)	18.5251(4)	18.5251(4)	19.6277(6)	90	90	90	0.0988	0.2151	1946	

^A standard 30 minute equilibration; ^B 2 hour equilibration; ^C 2 hours 50 minute equilibration time.

Table 2.3.5-3. Rietveld fits of *in situ* PXRD data during CO₂ adsorption/desorption for **2.2(Br)** at 195K. $\lambda = 0.82602(1)$ Å

	T (K)	P (bar)	Space Group	Volume (Å ³)	a (Å)	b (Å)	c (Å)	α (°)	β (°)	γ (°)	% of each phase present	R_{wp}	R_{wp}'	Parameters
2.2(Br)-195K-CO₂	195	Vac	<i>I4₁/a</i>	6691.54(42)	18.4694(5)	18.4694(5)	19.6165(6)	90	90	90	100.0	0.1867	0.4413	19
	195	0.6	<i>I4₁/a</i>	6691.67(49)	18.4728(6)	18.4728(6)	19.6095(7)	90	90	90	100.0	0.1814	0.4501	19
	195	0.85	<i>I4₁/a</i>	6700.38(61)	18.4862(7)	18.4862(7)	19.6067(9)	90	90	90	100.0	0.1791	0.4642	19
	195	1 ^A	<i>I4₁/a</i>	6710.95(83)	18.5013(10)	18.5013(10)	19.6056(11)	90	90	90	100.0	0.1791	0.4835	19
	195	1 ^B	<i>I4₁/a</i>	6701.1(10)	18.4813(11)	18.4813(11)	19.6193(18)	90	90	90	53.2(8)	0.1833	0.4674	29
			<i>C2/c</i>	3802.40(53)	18.4721(11)	9.8093(8)	21.5243(20)	90	102.856(7)	90	46.8(8)			
	195	1 ^C	<i>I4₁/a</i>	6714.9(11)	18.5026(12)	18.5026(12)	19.6144(20)	90	90	90	53.5(8)	0.1737	0.4660	29
			<i>C2/c</i>	3810.83(58)	18.4921(11)	9.8072(9)	21.5521(22)	90	102.841(7)	90	46.5(8)			
	195	0.6	<i>I4₁/a</i>	6726.2(12)	18.5208(13)	18.5208(13)	19.6088(21)	90	90	90	55.3(8)	0.1679	0.4732	29
			<i>C2/c</i>	3811.04(64)	18.4834(12)	9.8035(10)	21.5767(24)	90	102.901(8)	90	44.7(8)			
	195	0.4	<i>I4₁/a</i>	6720.26(54)	18.4993(6)	18.4993(6)	19.6370(8)	90	90	90	88.5(6)	0.1583	0.4166	29
			<i>C2/c</i>	3805.4(13)	18.4615(25)	9.8192(25)	21.5443(41)	90	103.000(19)	90	11.5(6)			
	195	0.2	<i>I4₁/a</i>	6729.26(63)	18.5148(8)	18.5148(8)	19.6305(9)	90	90	90	93.6(6)	0.1576	0.4374	29
			<i>C2/c</i>	3809.3(22)	18.4692(41)	9.8170(42)	21.5660(66)	90	103.042(31)	90	6.4(6)			
195	Vac	<i>I4₁/a</i>	6732.31(70)	18.5220(8)	18.5220(8)	19.6240(10)	90	90	90	100.0	0.165	0.4681	19	

^A standard 30 minute equilibration; ^B 2 hour equilibration; ^C 2 hours 50 minute equilibration time.

Table 2.3.5-4. Pawley fits of *in situ* PXRD data during CO₂ adsorption for **2.2(Br)** at room temperature. $\lambda = 0.82562(1)$ Å

	T (K)	P (bar)	Space Group	Volume (Å ³)	a (Å)	b (Å)	c (Å)	α (°)	β (°)	γ (°)	R_{wp}	R_{wp}'	Parameters
2.2(Br)-RT-CO₂	298	0	<i>I4₁/a</i>	6799.8(3)	18.5886(4)	18.5886(4)	19.6782(4)	90	90	90	0.0196	0.2663	1058
	298	10	<i>I4₁/a</i>	6804.9(3)	18.5938(3)	18.5938(3)	19.6828(3)	90	90	90	0.0151	0.2181	1067
	298	50	<i>I4₁/a</i>	6810.8(3)	18.5983(3)	18.5983(3)	19.6903(4)	90	90	90	0.0174	0.2311	1070

Table 2.3.5-5. Pawley fits of *in situ* PXRD data during CO₂ adsorption/desorption for **2.3(Cl)** at 195K. Expanded phase highlighted in **bold**. $\lambda = 0.82586(1) \text{ \AA}$.

T (K)	P (bar)	Space Group	Volume (\AA^3)	a (\AA)	b (\AA)	c (\AA)	α ($^\circ$)	β ($^\circ$)	γ ($^\circ$)	R_{wp}	R_{wp}'	Parameters	
195	0	<i>I</i> 2/ <i>m</i>	1665.773(6)	12.2679(2)	9.7817(2)	14.2721(4)	90	103.439(2)	90	0.0727	0.2178	577	
195	0.2	<i>I</i> 2/ <i>m</i>	1673.80(8)	12.2975(3)	12.2975(3)	14.3280(4)	90	103.728(2)	90	0.0762	0.2285	578	
195	0.4	<i>I</i> 2/ <i>m</i>	1676.10(5)	12.2833(2)	9.7785(1)	14.3721(3)	90	103.845(2)	90				
		<i>C</i>2/<i>c</i>	3687.32(13)	18.2064(4)	9.7499(2)	21.2623(4)	90	102.322(2)	90	0.03689	0.07943	1729	
195	0.6	<i>I</i> 2/ <i>m</i>	1680.98(5)	12.3935(2)	9.7563(1)	14.2952(3)	90	103.466(1)	90				
		<i>C</i>2/<i>c</i>	3686.38(9)	18.2042(2)	9.7498(1)	21.2566(3)	90	102.285(1)	90	0.0377	0.07775	1733	
2.3(Cl)-195K-CO ₂	195	0.8	<i>I</i> 2/ <i>m</i>	1648.48(14)	12.2639(6)	9.8336(4)	14.1080(7)	90	104.327(4)	90	0.04999	0.11046	1721
		<i>C</i>2/<i>c</i>	3690.93(9)	18.2170(3)	9.7547(1)	21.2484(4)	90	102.177(1)	90				
	195	1	<i>C</i> 2/ <i>c</i>	3696.30(11)	18.2545(3)	9.7529(1)	21.2164(4)	90	101.884(1)	90	0.06119	0.1297	1165
	195	0.8	<i>C</i> 2/ <i>c</i>	3693.03(10)	18.2342(3)	9.7528(1)	21.2308(4)	90	102.003(1)	90	0.05899	0.14342	1160
	195	0.6	<i>C</i> 2/ <i>c</i>	3689.26(10)	18.2181(3)	9.7524(1)	21.2352(4)	90	102.083(1)	90	0.05707	0.13986	1160
	195	0.4	<i>I</i> 2/ <i>m</i>	1679.03(6)	12.3154(2)	9.7894(2)	14.3149(3)	90	103.373(2)	90			
		<i>C</i>2/<i>c</i>	3688.21(10)	18.1976(3)	9.7566(1)	21.2561(4)	90	102.235(1)	90	0.04739	0.11276	1726	
	195	0.2	<i>I</i> 2/ <i>m</i>	1678.99(8)	12.3198(3)	9.7787(2)	14.3353(5)	90	103.543(2)	90	0.0766	0.2031	577
	195	0	<i>I</i> 2/ <i>m</i>	1668.83(8)	12.2844(3)	9.7822(2)	14.2638(5)	90	103.191(2)	90	0.0800	0.2127	577

Table 2.3.5-6. Rietveld fits of *in situ* PXRD data during CO₂ adsorption/desorption for **2.3(Cl)** at 195K. Expanded phase highlighted in **bold**. $\lambda = 0.82586(1) \text{ \AA}$.

P (bar)	Space Group	Volume (\AA^3)	a (\AA)	b (\AA)	c (\AA)	α ($^\circ$)	β ($^\circ$)	γ ($^\circ$)	% of each phase present	CO ₂ Site 1	CO ₂ Site 2	R_{wp}	R_{wp}'	Parameters	
0	<i>I</i> 2/ <i>m</i>	1665.72(7)	12.2675(3)	9.7816(2)	14.2726(4)	90	103.446(2)	90	100.0	n/a	n/a	0.0875	0.2874	21	
0.2	<i>I</i> 2/ <i>m</i>	1673.99(9)	12.2972(3)	9.7793(3)	14.3298(5)	90	103.736(2)	90	100.0	n/a	n/a	0.0862	0.2863	21	
0.4	<i>I</i> 2/ <i>m</i>	1676.01(12)	12.3088(4)	9.7768(4)	14.3367(7)	90	103.728(4)	90	68.0(3)	n/a	n/a				
	<i>C</i>2/<i>c</i>	3685.52(42)	18.1923(10)	9.7604(6)	21.2463(16)	90	102.332(5)	90	32.0(3)	1.000(16)	n/a	0.07946	0.21805	38	
0.6	<i>I</i> 2/ <i>m</i>	1675.11(54)	12.3398(26)	9.7607(17)	14.3067(21)	90	103.565(17)	90	22.0(5)	n/a	n/a				
	<i>C</i>2/<i>c</i>	3685.84(27)	18.1973(7)	9.7533(4)	21.2542(10)	90	102.289(3)	90	78.0(5)	0.513(16)	0.787(16)	0.10817	0.28819	45	
2.3(Cl)-195K-CO ₂	0.8	<i>I</i> 2/ <i>m</i>	1700.5(18)	12.3716(93)	9.8980(51)	14.2812(62)	90	103.501(52)	90	11.8(7)	n/a	n/a	0.11911	0.3133	45
	<i>C</i>2/<i>c</i>	3690.30(29)	18.2161(8)	9.7534(4)	21.2498(11)	90	102.191(3)	90	88.2(7)	0.561(18)	0.738(19)				
	1	<i>C</i> 2/ <i>c</i>	3696.26(30)	18.2543(8)	9.7516(4)	21.2204(11)	90	101.899(3)	90	100.0	0.711(14)	0.605(15)	0.12613	0.3352	35
	0.8	<i>C</i> 2/ <i>c</i>	3693.41(30)	18.2375(8)	9.7513(4)	21.2342(11)	90	102.025(3)	90	100.0	0.692(14)	0.591(15)	0.1243	0.33269	35
	0.6	<i>C</i> 2/ <i>c</i>	3689.40(29)	18.2205(8)	9.7507(4)	21.2393(11)	90	102.112(3)	90	100.0	0.680(14)	0.581(15)	0.12292	0.33008	35
	0.4	<i>I</i> 2/ <i>m</i>	1677.14(36)	12.3339(16)	9.7623(12)	14.3246(16)	90	103.498(12)	90	24.8(4)	n/a	n/a			
	<i>C</i>2/<i>c</i>	3683.22(26)	18.1912(7)	9.7507(4)	21.2496(10)	90	102.260(3)	90	75.2(4)	0.520(16)	0.793(16)	0.10177	0.27533	45	
	0.2	<i>I</i> 2/ <i>m</i>	1678.80(9)	12.3158(3)	9.7791(2)	14.3387(5)	90	103.557(2)	90	100.0	n/a	n/a	0.0870	0.2605	21
	0	<i>I</i> 2/ <i>m</i>	1668.92(9)	12.2843(3)	9.7823(3)	14.2650(5)	90	103.199(2)	90	100.0	n/a	n/a	0.0937	0.2776	21

Table 2.3.5-7. Pawley fits of *in situ* PXRD data during CO₂ adsorption for **2.3(Cl)** at room temperature. $\lambda = 0.82586(1) \text{ \AA}$.

T (K)	P (bar)	Space Group	Volume (\AA^3)	a (\AA)	b (\AA)	c (\AA)	α ($^\circ$)	β ($^\circ$)	γ ($^\circ$)	R_{wp}	R_{wp}'	Parameters	
298	0	<i>I</i> 2/ <i>m</i>	1683.48(6)	12.3079(2)	9.8036(2)	14.3295(4)	90	103.181(2)	90	0.0650	0.2141	1723	
298	5	<i>I</i> 2/ <i>m</i>	1685.96(5)	12.3145(2)	9.8026(1)	14.3503(3)	90	103.281(1)	90	0.0603	0.1968	1726	
298	10	<i>I</i> 2/ <i>m</i>	1687.43(5)	12.3208(2)	9.8015(1)	14.3596(3)	90	103.322(1)	90	0.0637	0.2018	1721	
2.3(Cl)-RT-CO ₂	298	20	<i>I</i> 2/ <i>m</i>	1689.61(5)	12.3298(2)	9.8004(1)	14.3721(3)	90	103.370(1)	90	0.0553	0.1834	1726
	298	30	<i>I</i> 2/ <i>m</i>	1691.16(5)	12.3345(2)	9.8002(1)	14.3836(3)	90	103.428(1)	90	0.0557	0.1858	1726
	298	40	<i>I</i> 2/ <i>m</i>	1691.84(5)	12.3376(2)	9.7979(2)	14.3917(3)	90	103.471(1)	90	0.0386	0.1884	1726
	298	0	<i>I</i> 2/ <i>m</i>	1683.54(6)	12.3109(2)	9.8007(2)	14.3304(3)	90	103.173(1)	90	0.0438	0.2246	1726

Table 2.3.5-8. Pawley fits of *in situ* PXRD data during CO₂ adsorption/desorption for **2.4(F)** at 195K. $\lambda = 0.82586(1)$ Å.

T (K)	P (bar)	Space Group	Volume (Å ³)	a (Å)	b (Å)	c (Å)	α (°)	β (°)	γ (°)	R_{wp}	R_{wp}'	Parameters
195	0	<i>I2/m</i>	1624.50(8)	11.9037(3)	9.7107(2)	14.4210(5)	90	102.959(2)	90	0.0859	0.2585	779
195	0.2	<i>I2/m</i>	1629.79(7)	11.9315(3)	9.7106(2)	14.4253(5)	90	102.801(2)	90	0.0842	0.2575	779
195	0.4	<i>I2/m</i>	1636.48(7)	11.9647(3)	9.7118(2)	14.4293(5)	90	102.570(2)	90	0.0840	0.2615	786
195	0.6	<i>I2/m</i>	1643.60(7)	12.0007(3)	9.7130(2)	14.4322(5)	90	102.307(2)	90	0.0840	0.2624	791
195	0.8	<i>I2/m</i>	1650.89(7)	12.0383(3)	9.7135(1)	14.4343(5)	90	102.014(2)	90	0.0812	0.2549	794
195	1	<i>I2/m</i>	1657.23(7)	12.0689(3)	9.7133(2)	14.4396(5)	90	101.757(2)	90	0.0804	0.2524	794
195	0.8	<i>I2/m</i>	1662.57(7)	12.0941(3)	9.7140(2)	14.4444(4)	90	101.553(2)	90	0.0766	0.2438	796
195	0.6	<i>I2/m</i>	1664.27(7)	12.1040(3)	9.7140(2)	14.4422(4)	90	101.454(2)	90	0.0755	0.2430	796
195	0.5	<i>I2/m</i>	1665.63(7)	12.1098(3)	9.7138(2)	14.4458(5)	90	101.421(2)	90	0.0768	0.2456	797
195	0.4	<i>I2/m</i>	1662.67(7)	12.0958(3)	9.7132(2)	14.4450(4)	90	101.563(2)	90	0.0762	0.2439	795
220	0.2	<i>I2/m</i>	1641.88(11)	11.9773(5)	9.7154(3)	14.4574(7)	90	102.588(3)	90	0.0881	0.2757	787
280	0	<i>I2/m</i>	1647.26(8)	11.9935(3)	9.7199(2)	14.4755(5)	90	102.535(2)	90	0.0848	0.2609	791

^a Cryostream cooling failed during the desorption resulting in elevated temperatures for measurements at 0.2 bar and vacuum.**Table 2.3.5-9.** Rietveld fits of *in situ* PXRD data during CO₂ adsorption/desorption for **2.4(F)** at 195K. $\lambda = 0.82586(1)$ Å.

T (K)	P (bar)	Space Group	Volume (Å ³)	a (Å)	b (Å)	c (Å)	α (°)	β (°)	γ (°)	CO ₂ Occu	R_{wp}	R_{wp}'	Parameters
195	0	<i>I2/m</i>	1624.9(1)	11.9029(4)	9.7105(3)	14.4261(7)	90	102.970(3)	90	0.000	0.1046	0.3433	24
195	0.2	<i>I2/m</i>	1630.2(1)	11.9312(4)	9.7104(3)	14.4303(6)	90	102.810(3)	90	0.000	0.1038	0.3465	24
195	0.4	<i>I2/m</i>	1636.3(1)	11.9636(4)	9.7107(3)	14.4304(7)	90	102.571(3)	90	0.139(4)	0.1053	0.3577	31
195	0.6	<i>I2/m</i>	1643.8(1)	12.0006(4)	9.7126(4)	14.4355(7)	90	102.319(3)	90	0.220(5)	0.1118	0.3816	31
195	0.8	<i>I2/m</i>	1650.8(1)	12.0369(5)	9.7126(4)	14.4374(7)	90	102.026(3)	90	0.261(5)	0.1097	0.3752	31
195	1	<i>I2/m</i>	1656.2(1)	12.0657(5)	9.7110(5)	14.4380(8)	90	101.761(3)	90	0.299(5)	0.1093	0.3732	31
195	0.8	<i>I2/m</i>	1661.9(1)	12.0911(5)	9.7127(4)	14.4436(8)	90	101.551(3)	90	0.306(4)	0.1068	0.3697	32
195	0.6	<i>I2/m</i>	1664.3(1)	12.1029(5)	9.7136(4)	14.4446(7)	90	101.457(3)	90	0.311(4)	0.1053	0.3673	31
195	0.5	<i>I2/m</i>	1665.4(1)	12.1079(5)	9.7135(4)	14.4467(7)	90	101.423(3)	90	0.309(4)	0.1064	0.3698	32
195	0.4	<i>I2/m</i>	1661.9(1)	12.0930(5)	9.7120(4)	14.4437(7)	90	101.563(3)	90	0.281(4)	0.1045	0.3621	31
220	0.2	<i>I2/m</i>	1642.0(2)	11.9756(6)	9.7155(5)	14.4607(10)	90	102.587(4)	90	0.000	0.1066	0.3630	23
280	0	<i>I2/m</i>	1647.4(1)	11.9930(5)	9.7195(4)	14.4782(7)	90	102.540(3)	90	0.000	0.1042	0.3505	24

^a Cryostream cooling failed during the desorption resulting in elevated temperatures for measurements at 0.2 bar and vacuum.**Table 2.3.5-10.** Pawley fits of *in situ* PXRD data during CO₂ adsorption for **2.3(CI)** at room temperature. $\lambda = 0.82586(1)$ Å.

T (K)	P (bar)	Space Group	Volume (Å ³)	a (Å)	b (Å)	c (Å)	α (°)	β (°)	γ (°)	R_{wp}	R_{wp}'	Parameters
298	0	<i>I2/m</i>	1644.13(8)	11.9818(3)	9.7159(2)	14.4721(5)	90	102.609(2)	90	0.0918	0.2995	1712
298	5	<i>I2/m</i>	1661.00(8)	12.0506(3)	9.7146(2)	14.5202(5)	90	102.269(2)	90	0.0862	0.2868	1689
298	10	<i>I2/m</i>	1675.95(7)	12.1107(3)	9.7144(2)	14.5541(5)	90	101.820(2)	90	0.0828	0.2753	1700
298	20	<i>I2/m</i>	1704.50(8)	12.2057(3)	9.7129(2)	14.6399(5)	90	100.862(2)	90	0.0805	0.2829	1719
298	40	<i>I2/m</i>	1764.31(8)	12.2853(3)	9.7087(2)	14.9799(5)	90	99.084(2)	90	0.0804	0.2903	1732
298	50	<i>I2/m</i>	1776.49(6)	12.2956(3)	9.7067(2)	15.0601(3)	90	98.752(1)	90	0.0753	0.2636	1801
298	20	<i>I2/m</i>	1710.68(7)	12.2228(3)	9.7095(2)	14.6708(4)	90	100.724(2)	90	0.0823	0.2744	1732
298	5	<i>I2/m</i>	1667.15(6)	12.0737(3)	9.7104(2)	14.5459(4)	90	102.152(2)	90	0.0779	0.2458	1697
298	1	<i>I2/m</i>	1650.58(6)	12.0071(3)	9.7105(2)	14.4995(4)	90	102.486(2)	90	0.0820	0.2634	1697
298	0	<i>I2/m</i>	1646.33(6)	11.9909(4)	9.7109(2)	14.4840(4)	90	102.537(2)	90	0.0829	0.2619	1686
298	0	<i>I2/m</i>	1646.08(7)	11.9917(4)	9.7104(2)	14.4808(4)	90	102.522(2)	90	0.0826	0.2658	1684

Appendix 2.8.3: *In situ* Single-crystal Data**Table 2.3.6-1.** Summary of *in situ* single-crystal data during CO₂ adsorption study for **2.1(I)**, at variable temperature

	2.1(I)-Vac [Cu₂(4-<i>l</i>bz)₄(<i>pyz</i>)_n] C ₃₂ H ₂₀ I ₄ Cu ₂ N ₂ O ₈	2.1(I)-1bar CO₂ [Cu₂(4-<i>l</i>bz)₄(<i>pyz</i>)_n] C ₃₂ H ₂₀ I ₄ Cu ₂ N ₂ O ₈	2.1(I)-1bar CO₂ [Cu₂(4-<i>l</i>bz)₄(<i>pyz</i>)_n] C ₃₂ H ₂₀ I ₄ Cu ₂ N ₂ O ₈
Crystal habit	Needle	Needle	Needle
Crystal colour	Clear Bluish Green	Clear Bluish Green	Clear Bluish Green
Crystal size (mm)	0.15x0.06x0.02	0.15x0.06x0.02	0.15x0.06x0.02
Crystal system	Tetragonal	Tetragonal	Tetragonal
Space group	<i>I</i> 4 ₁ / <i>a</i>	<i>I</i> 4 ₁ / <i>a</i>	<i>I</i> 4 ₁ / <i>a</i>
a (Å)	19.0067(5)	18.9505(2)	18.9022(3)
b (Å)	19.0067(5)	18.9505(2)	18.9022(3)
c (Å)	19.8926(8)	19.8359(3)	19.7974(4)
α (°)	90	90	90
β (°)	90	90	90
γ (°)	90	90	90
V (Å ³)	7186.3(5)	7123.5(2)	7073.5(2)
Density (g cm ⁻³)	2.254	2.229	2.245
Temperature (K)	298	195	100
μ (mm ⁻¹)	4.323	4.359	4.39
Wavelength (Å)	0.6889	0.6889	0.6889
2θ range (°)	4.154 to 53.142	4.166 to 53.126	2.888 to 53.132
Reflns. collected	28826	28186	28554
Independent reflns. [<i>R</i> _{int}]	4118 [0.0937]	4077 [0.0889]	4060 [0.0640]
Reflns. used in refinement, <i>n</i>	4118	4077	4060
LS parameters, <i>p</i>	232	244	244
Restraints, <i>r</i>	120	123	123
<i>R</i> 1 (<i>F</i>) ^a <i>I</i> >2.0σ(<i>I</i>)	0.0723	0.0808	0.0787
<i>wR</i> 2 (<i>F</i> ²) ^a , all data	0.2079	0.2355	0.2250
<i>S</i> (<i>F</i> ²) ^a , all data	1.011	1.045	1.048

^a = $R1(F) = \Sigma(|F_o| - |F_c|) / \Sigma|F_o|$; $wR2(F^2) = [\Sigma w(F_o^2 - F_c^2)^2 / \Sigma w F_o^4]^{1/2}$; $S(F^2) = [\Sigma w(F_o^2 - F_c^2)^2 / (n + r - p)]^{1/2}$

Table 2.3.6-2. Summary of *in situ* single-crystal data during CO₂ adsorption study for **2.2(Br)** at 195K.

	2.2(Br)-Vac [Cu ₂ (4-Brbz) ₄ (pyz)] _n C ₃₂ H ₂₀ Br ₄ Cu ₂ N ₂ O ₈	2.2(Br)-0.2bar CO₂ [Cu ₂ (4-Brbz) ₄ (pyz)] _n C ₃₂ H ₂₀ Br ₄ Cu ₂ N ₂ O ₈	2.2(Br)-0.4bar CO₂ [Cu ₂ (4-Brbz) ₄ (pyz)] _n C ₃₂ H ₂₀ Br ₄ Cu ₂ N ₂ O ₈
Crystal habit	Plate	Plate	Plate
Crystal colour	Clear Bluish Green	Clear Bluish Green	Clear Bluish Green
Crystal size (mm)	0.156×0.039×0.026	0.156×0.039×0.026	0.156×0.039×0.026
Crystal system	Tetragonal	Tetragonal	Tetragonal
Space group	<i>I</i> 4 ₁ / <i>a</i>	<i>I</i> 4 ₁ / <i>a</i>	<i>I</i> 4 ₁ / <i>a</i>
a (Å)	18.5455(3)	18.5477(4)	18.5527(5)
b (Å)	18.5455(3)	18.5477(4)	18.5527(5)
c (Å)	19.6374(4)	19.6348(6)	19.6372(7)
α (°)	90	90	90
β (°)	90	90	90
γ (°)	90	90	90
V (Å ³)	6754.0(3)	6754.7(4)	6759.2(4)
Density (g cm ⁻³)	1.981	1.981	1.98
Temperature (K)	195	195	195
μ (mm ⁻¹)	5.55	5.549	5.545
Wavelength (Å)	0.6889	0.6889	0.6889
2θ range (°)	2.928 to 50.988	2.928 to 58.946	2.928 to 58.928
Reflns. collected	43093	58606	57247
Independent reflns. [<i>R</i> _{int}]	3463 [0.0824]	5165 [0.1206]	5165 [0.1519]
Reflns. used in refinement, <i>n</i>	3463	5165	5165
LS parameters, <i>p</i>	244	244	229
Restraints, <i>r</i>	52	52	55
<i>R</i> 1 (<i>F</i> ^o) > 2.0σ(<i>I</i>)	0.1604	0.2183	0.2517
<i>wR</i> 2 (<i>F</i> ^o) ^a , all data	0.3749	0.4759	0.5267
<i>S</i> (<i>F</i> ^o) ^a , all data	1.448	1.449	1.518
	2.2(Br)-0.6bar CO₂ [Cu ₂ (4-Brbz) ₄ (pyz)] _n C ₃₂ H ₂₀ Br ₄ Cu ₂ N ₂ O ₈	2.2(Br)-0.8bar CO₂ [Cu ₂ (4-Brbz) ₄ (pyz)] _n C ₃₂ H ₂₀ Br ₄ Cu ₂ N ₂ O ₈	2.2(Br)-1bar CO₂ [Cu ₂ (4-Brbz) ₄ (pyz)] _n C ₃₂ H ₂₀ Br ₄ Cu ₂ N ₂ O ₈
Crystal habit	Plate	Plate	Plate
Crystal colour	Clear Bluish Green	Clear Bluish Green	Clear Bluish Green
Crystal size (mm)	0.156×0.039×0.026	0.156×0.039×0.026	0.156×0.039×0.026
Crystal system	Tetragonal	Tetragonal	Tetragonal
Space group	<i>I</i> 4 ₁ / <i>a</i>	<i>I</i> 4 ₁ / <i>a</i>	<i>I</i> 4 ₁ / <i>a</i>
a (Å)	18.5546(7)	18.5593(5)	18.5598(5)
b (Å)	18.5546(7)	18.5593(5)	18.5598(5)
c (Å)	19.6392(11)	19.6444(9)	19.6466(9)
α (°)	90	90	90
β (°)	90	90	90
γ (°)	90	90	90
V (Å ³)	6761.3(6)	6766.5(5)	6767.6(5)
Density (g cm ⁻³)	1.979	1.977	1.977
Temperature (K)	195	195	195
μ (mm ⁻¹)	5.543	5.539	5.538
Wavelength (Å)	0.6889	0.6889	0.6889
2θ range (°)	2.926 to 58.92	2.926 to 58.954	2.926 to 50.992
Reflns. collected	57958	58040	41818
Independent reflns. [<i>R</i> _{int}]	5165 [0.3504]	5174 [0.1915]	3467 [0.1445]
Reflns. used in refinement, <i>n</i>	5165	5174	3467
LS parameters, <i>p</i>	204	192	192
Restraints, <i>r</i>	12	3	3
<i>R</i> 1 (<i>F</i> ^o) > 2.0σ(<i>I</i>)	0.2683	0.2806	0.3055
<i>wR</i> 2 (<i>F</i> ^o) ^a , all data	0.3952	0.5773	0.5981
<i>S</i> (<i>F</i> ^o) ^a , all data	1.332	1.500	1.875

$$^a = R1(F) = \Sigma(|F_o| - |F_c|) / \Sigma|F_o| ; wR2(F^2) = [\Sigma w(F_o^2 - F_c^2)^2 / \Sigma w F_o^4]^{1/2} ; S(F^2) = [\Sigma w(F_o^2 - F_c^2)^2 / (n + r - p)]^{1/2}$$

Table 2.3.6-3. Summary of *in situ* single-crystal data during CO₂ adsorption and desorption study for **2.3(Cl)** at 195K.

	2.3(Cl)-Vac [Cu ₂ (4-Clbz) ₄ (pyz)] _n C ₃₂ H ₂₀ Cl ₄ Cu ₂ N ₂ O ₈	2.3(Cl)-0.2bar CO₂ [Cu ₂ (4-Clbz) ₄ (pyz)] _n C ₃₂ H ₂₀ Cl ₄ Cu ₂ N ₂ O ₈	2.3(Cl)-0.4bar CO₂ [Cu ₂ (4-Clbz) ₄ (pyz)] _n C ₃₂ H ₂₀ Cl ₄ Cu ₂ N ₂ O ₈
Crystal habit	Plate	Plate	Plate
Crystal colour	Clear Bluish Green	Clear Bluish Green	Clear Bluish Green
Crystal size (mm)	0.20×0.10×0.02	0.20×0.10×0.02	0.20×0.10×0.02
Crystal system	Monoclinic	Monoclinic	Monoclinic
Space group	<i>I</i> 2/ <i>m</i>	<i>I</i> 2/ <i>m</i>	<i>I</i> 2/ <i>m</i>
a (Å)	12.3023(7)	12.3263(9)	12.3412(15)
b (Å)	9.8004(4)	9.7985(5)	9.7955(6)
c (Å)	14.3712(9)	14.3758(9)	14.3700(12)
α (°)	90	90	90
β (°)	103.790(6)	103.691(7)	103.506(11)
γ (°)	90	90	90
V (Å ³)	1682.74(16)	1686.96(19)	1689.1(3)
Density (g cm ⁻³)	1.637	1.633	1.78
Temperature (K)	195	195	195
μ (mm ⁻¹)	1.506	1.503	1.519
Wavelength (Å)	0.6889	0.6889	0.6889
2θ range (°)	3.804 to 54.654	3.8 to 54.676	3.804 to 54.67
Reflns. collected	10554	10549	10536
Independent reflns. [<i>R</i> _{int}]	2170 [0.0653]	2178 [0.0721]	2184 [0.1248]
Reflns. used in refinement, <i>n</i>	2170	2178	2184
LS parameters, <i>p</i>	122	122	122
Restraints, <i>r</i>	0	0	0
<i>R</i> 1 (<i>F</i>) ^a <i>I</i> > 2.0σ(<i>I</i>)	0.0518	0.0553	0.0746
<i>wR</i> 2 (<i>F</i> ²) ^a , all data	0.1519	0.1638	0.2298
<i>S</i> (<i>F</i> ²) ^a , all data	1.055	1.038	1.005
	2.3(Cl)-0.6bar CO₂ [Cu ₂ (4-Clbz) ₄ (pyz)] _n ·2CO ₂ C ₃₄ H ₂₀ Cl ₄ Cu ₂ N ₂ O ₁₂	2.3(Cl)-1bar CO₂ [Cu ₂ (4-Clbz) ₄ (pyz)] _n ·2CO ₂ C ₃₄ H ₂₀ Cl ₄ Cu ₂ N ₂ O ₁₂	2.3(Cl)-0.4bar CO₂ (D) [Cu ₂ (4-Clbz) ₄ (pyz)] _n ·1CO ₂ C ₃₃ H ₂₀ Cl ₄ Cu ₂ N ₂ O ₁₀
Crystal habit	Plate	Plate	Plate
Crystal colour	Clear Bluish Green	Clear Bluish Green	Clear Bluish Green
Crystal size (mm)	0.20×0.10×0.02	0.20×0.10×0.02	0.20×0.10×0.02
Crystal system	Monoclinic	Monoclinic	Monoclinic
Space group	<i>I</i> 2/ <i>m</i>	<i>I</i> 2/ <i>m</i>	<i>I</i> 2/ <i>m</i>
a (Å)	12.451(3)	12.498(3)	12.452(3)
b (Å)	9.7633(14)	9.7702(16)	9.7646(19)
c (Å)	15.446(2)	15.432(3)	15.460(3)
α (°)	90	90	90
β (°)	99.049(18)	98.785(19)	99.09(2)
γ (°)	90	90	90
V (Å ³)	1854.3(6)	1862.3(6)	1856.1(7)
Density (g cm ⁻³)	1.643	1.636	1.563
Temperature (K)	195	195	195
μ (mm ⁻¹)	1.382	1.376	1.373
Wavelength (Å)	0.6889	0.6889	0.6889
2θ range (°)	3.794 to 54.678	3.794 to 54.67	3.792 to 54.678
Reflns. collected	11591	11659	11678
Independent reflns. [<i>R</i> _{int}]	2406 [0.2191]	2417 [0.2716]	2408 [0.2491]
Reflns. used in refinement, <i>n</i>	2406	2417	2408
LS parameters, <i>p</i>	134	134	134
Restraints, <i>r</i>	0	0	0
<i>R</i> 1 (<i>F</i>) ^a <i>I</i> > 2.0σ(<i>I</i>)	0.1143	0.1096	0.1252
<i>wR</i> 2 (<i>F</i> ²) ^a , all data	0.3556	0.3582	0.3980
<i>S</i> (<i>F</i> ²) ^a , all data	0.951	0.932	1.001

^a $R1(F) = \sum(|F_o| - |F_c|)/\sum|F_o|$; $wR2(F^2) = [\sum w(F_o^2 - F_c^2)^2 / \sum w F_o^4]^{1/2}$; $S(F^2) = [\sum w(F_o^2 - F_c^2)^2 / (n + r - p)]^{1/2}$

Table 2.3.6-3[cont.]. Summary of *in situ* single-crystal data during CO₂ adsorption and desorption study for **2.3(Cl)** at 195K.

	2.3(Cl)-0.2bar CO₂ (D) [Cu₂(4-Clbz)₄(pyz)]_n C ₃₂ H ₂₀ Cl ₄ Cu ₂ N ₂ O ₈	2.3(Cl)-Vac (D) [Cu₂(4-Clbz)₄(pyz)]_n C ₃₂ H ₂₀ Cl ₄ Cu ₂ N ₂ O ₈
Crystal habit	Plate	Plate
Crystal colour	Clear Bluish Green	Clear Bluish Green
Crystal size (mm)	0.20×0.10×0.02	0.20×0.10×0.02
Crystal system	Monoclinic	Monoclinic
Space group	<i>I</i> 2/ <i>m</i>	<i>I</i> 2/ <i>m</i>
a (Å)	12.384(3)	12.364(3)
b (Å)	9.8023(15)	9.7870(16)
c (Å)	14.390(4)	14.316(5)
α (°)	90	90
β (°)	102.98(3)	102.86(3)
γ (°)	90	90
V (Å ³)	1702.3(7)	1688.8(8)
Density (g cm ⁻³)	1.618	1.631
Temperature (K)	195	195
μ (mm ⁻¹)	1.489	1.501
Wavelength (Å)	0.6889	0.6889
2θ range (°)	3.806 to 54.672	3.822 to 54.658
Reflns. collected	10458	10369
Independent reflns. [<i>R</i> _{int}]	2197 [0.2217]	2175 [0.2142]
Reflns. used in refinement, <i>n</i>	2197	2175
LS parameters, <i>p</i>	122	122
Restraints, <i>r</i>	0	0
<i>R</i> 1 (<i>F</i>) ^a <i>I</i> >2.0σ(<i>I</i>)	0.1145	0.1277
<i>wR</i> 2 (<i>F</i> ²) ^a , all data	0.3774	0.4157
<i>S</i> (<i>F</i> ²) ^a , all data	1.004	1.039

$$^a = R1(F) = \frac{\sum(|F_o| - |F_c|)}{\sum|F_o|}; wR2(F^2) = \frac{[\sum w(F_o^2 - F_c^2)^2 / \sum w F_o^4]^{1/2}}{S(F^2) = [\sum w(F_o^2 - F_c^2)^2 / (n + r - p)]^{1/2}}$$

Table 2.3.6-4. Summary of *in situ* single-crystal data during CO₂ adsorption and desorption study of **2.4(F)** at 195K.

	2.4(F)-Vac [Cu₂(4-Fbz)₄(pyz)]_n C ₃₂ H ₂₀ F ₄ Cu ₂ N ₂ O ₈	2.4(F)-0.18bar CO₂ [Cu₂(4-Fbz)₄(pyz)]_n C ₃₂ H ₂₀ F ₄ Cu ₂ N ₂ O ₈	2.4(F)-0.40bar CO₂ [Cu₂(4-Fbz)₄(pyz)]_n C ₃₂ H ₂₀ F ₄ Cu ₂ N ₂ O ₈
Crystal habit	Needle	Needle	Needle
Crystal colour	Clear Bluish Green	Clear Bluish Green	Clear Bluish Green
Crystal size (mm)	0.167×0.051×0.017	0.167×0.051×0.017	0.167×0.051×0.017
Crystal system	Monoclinic	Monoclinic	Monoclinic
Space group	<i>I2/m</i>	<i>I2/m</i>	<i>I2/m</i>
a (Å)	11.9185(9)	12.0896(14)	12.190(2)
b (Å)	9.6936(3)	9.6850(4)	9.6733(6)
c (Å)	14.3383(10)	14.3650(15)	14.399(2)
α (°)	90	90	90
β (°)	102.558(7)	101.792(11)	100.932(18)
γ (°)	90	90	90
V (Å ³)	1616.91(18)	1646.5(3)	1667.0(5)
Density (g cm ⁻³)	1.568	1.54	1.521
Temperature (K)	195	195	195
μ (mm ⁻¹)	1.283	1.259	1.244
Wavelength (Å)	0.6889	0.6889	0.6889
2θ range (°)	3.912 to 51.002	3.896 to 51.006	3.896 to 50.986
Reflns. collected	5833	5812	5857
Independent reflns. [<i>R_{int}</i>]	1658 [0.0671]	1707 [0.0788]	1719 [0.0885]
Reflns. used in refinement, <i>n</i>	1658	1707	1719
LS parameters, <i>p</i>	122	122	122
Restraints, <i>r</i>	5	0	10
<i>R</i> 1 (<i>F</i>) ^a / >2.0σ(<i>I</i>)	0.0779	0.0941	0.0893
<i>wR</i> 2 (<i>F</i> ²) ^a , all data	0.1850	0.2606	0.2733
<i>S</i> (<i>F</i> ²) ^a , all data	1.006	1.030	0.9950
	2.4(F)-0.63bar CO₂ [Cu₂(4-Fbz)₄(pyz)]_n C ₃₂ H ₂₀ F ₄ Cu ₂ N ₂ O ₈	2.4(F)-0.80bar CO₂ [Cu₂(4-Fbz)₄(pyz)]_n C ₃₂ H ₂₀ F ₄ Cu ₂ N ₂ O ₈	2.4(F)-1bar CO₂ [Cu₂(4-Fbz)₄(pyz)]_n·1CO₂ C ₃₃ H ₂₀ F ₄ Cu ₂ N ₂ O ₁₀
Crystal habit	Needle	Needle	Needle
Crystal colour	Clear Bluish Green	Clear Bluish Green	Clear Bluish Green
Crystal size (mm)	0.167×0.051×0.017	0.167×0.051×0.017	0.167×0.051×0.017
Crystal system	Monoclinic	Monoclinic	Monoclinic
Space group	<i>I2/m</i>	<i>I2/m</i>	<i>I2/m</i>
a (Å)	12.2341(19)	12.269(3)	12.303(3)
b (Å)	9.6763(6)	9.6768(8)	9.6699(8)
c (Å)	14.458(2)	14.499(3)	14.588(3)
α (°)	90	90	90
β (°)	100.758(17)	100.45(2)	99.69(2)
γ (°)	90	90	90
V (Å ³)	1681.4(4)	1692.9(5)	1710.7(5)
Density (g cm ⁻³)	1.508	1.498	1.568
Temperature (K)	195	195	195
μ (mm ⁻¹)	1.233	1.225	1.221
Wavelength (Å)	0.6889	0.6889	0.6889
2θ range (°)	3.886 to 51.006	3.884 to 50.98	3.89 to 51.004
Reflns. collected	6071	6049	6159
Independent reflns. [<i>R_{int}</i>]	1733 [0.0856]	1739 [0.0935]	1758 [0.0886]
Reflns. used in refinement, <i>n</i>	1733	1739	1758
LS parameters, <i>p</i>	122	122	143
Restraints, <i>r</i>	10	8	28
<i>R</i> 1 (<i>F</i>) ^a / >2.0σ(<i>I</i>)	0.0995	0.1120	0.0925
<i>wR</i> 2 (<i>F</i> ²) ^a , all data	0.2681	0.3032	0.2469
<i>S</i> (<i>F</i> ²) ^a , all data	0.972	1.031	0.952

$$^a R1(F) = \sum(|F_o| - |F_c|) / \sum|F_o| ; wR2(F^2) = [\sum w(F_o^2 - F_c^2)^2 / \sum w F_o^4]^{1/2} ; S(F^2) = [\sum w(F_o^2 - F_c^2)^2 / (n + r - p)]^{1/2}$$

Table 2.3.6-4[cont.]. Summary of *in situ* single-crystal data during CO₂ adsorption and desorption study for **2.4(F)** at 195K.

	2.4(F)-0.80bar CO₂ (D) [Cu ₂ (4-Fbz) ₄ (pyz)] _n C ₃₂ H ₂₀ F ₄ Cu ₂ N ₂ O ₈	2.4(F)-0.59bar CO₂ (D) [Cu ₂ (4-Fbz) ₄ (pyz)] _n C ₃₂ H ₂₀ F ₄ Cu ₂ N ₂ O ₈	2.3(Cl)-0.4bar CO₂ (D) [Cu ₂ (4-Fbz) ₄ (pyz)] _n C ₃₂ H ₂₀ F ₄ Cu ₂ N ₂ O ₈
Crystal habit	Needle	Needle	Needle
Crystal colour	Clear Bluish Green	Clear Bluish Green	Clear Bluish Green
Crystal size (mm)	0.167×0.051×0.017	0.167×0.051×0.017	0.167×0.051×0.017
Crystal system	Monoclinic	Monoclinic	Monoclinic
Space group	<i>I2/m</i>	<i>I2/m</i>	<i>I2/m</i>
a (Å)	12.309(3)	12.292(3)	12.241(3)
b (Å)	9.6845(8)	9.6856(7)	9.6741(8)
c (Å)	14.565(3)	14.490(3)	14.438(3)
α (°)	90	90	90
β (°)	100.02(2)	100.493(19)	100.82(2)
γ (°)	90	90	90
V (Å ³)	1709.8(6)	1696.3(5)	1679.4(6)
Density (g cm ⁻³)	1.483	1.495	1.471
Temperature (K)	195	195	195
μ (mm ⁻¹)	1.213	1.222	1.233
Wavelength (Å)	0.6889	0.6889	0.6889
2θ range (°)	3.882 to 51.006	3.88 to 51.004	3.886 to 51.002
Reflns. collected	6290	6276	5685
Independent reflns. [<i>R_{int}</i>]	1778 [0.1155]	1761 [0.1025]	1737 [0.0951]
Reflns. used in refinement, <i>n</i>	1778	1761	1737
LS parameters, <i>p</i>	122	122	122
Restraints, <i>r</i>	10	8	8
<i>R</i> 1 (<i>F</i>) ^a <i>I</i> >2.0σ(<i>I</i>)	0.1179	0.1177	0.1073
<i>wR</i> 2 (<i>F</i>) ^a , all data	0.3212	0.3138	0.3026
<i>S</i> (<i>F</i>) ^a , all data	1.072	1.066	0.986

$$^a R1(F) = \sum(|F_o| - |F_c|) / \sum |F_o| ; wR2(F^2) = [\sum w(F_o^2 - F_c^2)^2 / \sum w F_o^4]^{1/2} ; S(F^2) = [\sum w(F_o^2 - F_c^2)^2 / (n + r - p)]^{1/2}$$

Table 2.3.6-5. Summary of in situ single crystal CO₂ sorption study for **2.4(F)**

	2.4(F)-Vac [Cu₂(4-Fbz)₄(pyz)]_n C ₃₂ H ₂₀ F ₄ Cu ₂ N ₂ O ₈	2.4(F)-0.19bar CO₂ [Cu₂(4-Fbz)₄(pyz)]_n C ₃₂ H ₂₀ F ₄ Cu ₂ N ₂ O ₈	2.4(F)-0.40bar CO₂ [Cu₂(4-Fbz)₄(pyz)]_n C ₃₂ H ₂₀ F ₄ Cu ₂ N ₂ O ₈
Crystal habit	Needle	Needle	Needle
Crystal colour	Clear Bluish Green	Clear Bluish Green	Clear Bluish Green
Crystal size (mm)	0.15×0.05×0.05	0.15×0.05×0.05	0.15×0.05×0.05
Crystal system	Monoclinic	Monoclinic	Monoclinic
Space group	<i>I2/m</i>	<i>I2/m</i>	<i>I2/m</i>
a (Å)	11.9248(6)	12.0251(9)	12.316(3)
b (Å)	9.7180(4)	9.7121(4)	9.7061(9)
c (Å)	14.5044(8)	14.4767(11)	14.652(4)
α (°)	90	90	90
β (°)	103.200(5)	102.505(8)	99.37(2)
γ (°)	90	90	90
V (Å ³)	1636.43(14)	1650.6(2)	1728.2(6)
Density (g cm ⁻³)	1.55	1.536	1.467
Temperature (K)	195	195	195
μ (mm ⁻¹)	1.267	1.256	1.2
Wavelength (Å)	0.6889	0.6889	0.6889
2θ range (°)	3.878 to 54.678	3.878 to 54.658	3.888 to 54.66
Reflns. collected	10023	10258	10582
Independent reflns. [<i>R</i> _{int}]	2133 [0.0564]	2151 [0.0697]	2251 [0.1178]
Reflns. used in refinement, <i>n</i>	2133	2151	2251
LS parameters, <i>p</i>	122	122	122
Restraints, <i>r</i>	0	0	5
<i>R</i> 1 (<i>F</i>) ^a > 2.0 <i>s</i> (<i>I</i>)	0.0552	0.0610	0.1187
<i>wR</i> 2 (<i>F</i> ²) ^a , all data	0.1571	0.179	0.3588
<i>S</i> (<i>F</i> ²) ^a , all data	1.008	1.0540	1.074
	2.4(F)-1bar CO₂ [Cu₂(4-Fbz)₄(pyz)]_n C ₃₄ H ₂₀ F ₄ Cu ₂ N ₂ O ₁₂	2.4(F)-0.80bar CO₂ (D) [Cu₂(4-Fbz)₄(pyz)]_n C ₃₂ H ₂₀ F ₄ Cu ₂ N ₂ O ₈	2.4(F)-0.59bar CO₂ (D) [Cu₂(4-Fbz)₄(pyz)]_n C ₃₂ H ₂₀ F ₄ Cu ₂ N ₂ O ₈
Crystal habit	Needle	Needle	Needle
Crystal colour	Clear Bluish Green	Clear Bluish Green	Clear Bluish Green
Crystal size (mm)	0.15×0.05×0.05	0.15×0.05×0.05	0.15×0.05×0.05
Crystal system	Monoclinic	Monoclinic	Monoclinic
Space group	<i>I2/m</i>	<i>I2/m</i>	<i>I2/m</i>
a (Å)	12.4027(12)	12.3989(11)	12.3830(12)
b (Å)	9.6925(6)	9.6852(5)	9.6851(6)
c (Å)	15.0215(17)	14.9957(14)	14.9373(15)
α (°)	90	90	90
β (°)	97.516(10)	97.725(9)	98.109(9)
γ (°)	90	90	90
V (Å ³)	1790.3(3)	1784.4(2)	1773.5(3)
Density (g cm ⁻³)	1.58	1.421	1.43
Temperature (K)	195	195	195
μ (mm ⁻¹)	1.174	1.164	1.169
Wavelength (Å)	0.6889	0.6889	0.6889
2θ range (°)	3.888 to 54.674	3.884 to 54.676	3.882 to 54.678
Reflns. collected	10843	10884	10982
Independent reflns. [<i>R</i> _{int}]	2335 [0.1142]	2323 [0.1136]	2313 [0.1060]
Reflns. used in refinement, <i>n</i>	2335	2323	2313
LS parameters, <i>p</i>	150	122	122
Restraints, <i>r</i>	30	5	5
<i>R</i> 1 (<i>F</i>) ^a > 2.0 <i>s</i> (<i>I</i>)	0.1040	0.1250	0.1246
<i>wR</i> 2 (<i>F</i> ²) ^a , all data	0.3379	0.3855	0.3703
<i>S</i> (<i>F</i> ²) ^a , all data	1.064	1.284	1.198

$$^a = R1(F) = \Sigma(|F_o| - |F_c|) / \Sigma|F_o| ; wR2(F^2) = [\Sigma w(F_o^2 - F_c^2)^2 / \Sigma w F_o^4]^{1/2} ; S(F^2) = [\Sigma w(F_o^2 - F_c^2)^2 / (n + r - p)]^{1/2}$$

Table 2.3.6-5[cont.]. Summary of in situ single crystal CO₂ sorption study of **2.4(F)**

	2.4(F)-0.41bar CO₂ (D)	2.4(F)-0.19bar CO₂ (D)
	[Cu₂(4-Fbz)₄(pyz)]_n	[Cu₂(4-Fbz)₄(pyz)]_n
	C₃₂H₂₀F₄Cu₂N₂O₈	C₃₂H₂₀F₄Cu₂N₂O₈
Crystal habit	Needle	Needle
Crystal colour	Clear Bluish Green	Clear Bluish Green
Crystal size (mm)	0.15×0.05×0.05	0.15×0.05×0.05
Crystal system	Monoclinic	Monoclinic
Space group	<i>I2/m</i>	<i>I2/m</i>
a (Å)	12.3679(12)	12.3202(11)
b (Å)	9.6874(5)	9.6896(5)
c (Å)	14.8095(16)	14.5772(14)
α (°)	90	90
β (°)	98.693(10)	99.874(9)
γ (°)	90	90
V (Å ³)	1754.0(3)	1714.4(3)
Density (g cm ⁻³)	1.446	1.479
Temperature (K)	195	195
μ (mm ⁻¹)	1.182	1.21
Wavelength (Å)	0.6889	0.6889
2θ range (°)	3.882 to 54.67	3.882 to 54.674
Reflns. collected	10946	10739
Independent reflns. [<i>R_{int}</i>]	2289 [0.1024]	2240 [0.0958]
Reflns. used in refinement, <i>n</i>	2289	2240
LS parameters, <i>p</i>	122	122
Restraints, <i>r</i>	5	10
<i>R</i> 1 (<i>F</i>) ^a <i>I</i> > 2.0σ(<i>I</i>)	0.1251	0.1116
<i>wR</i> 2 (<i>F</i> ²) ^a , all data	0.3761	0.3368
<i>S</i> (<i>F</i> ²) ^a , all data	1.1690	1.044

$$^a = R1(F) = \frac{\sum(|F_o| - |F_c|)}{\sum|F_o|} ; wR2(F^2) = \frac{[\sum w(F_o^2 - F_c^2)^2 / \sum w F_o^4]^{1/2}}{} ; S(F^2) = \frac{[\sum w(F_o^2 - F_c^2)^2 / (n + r - p)]^{1/2}}{}$$

Chapter 3:

Further Functionalisation of a Family of 1D Halogen- Functionalised Coordination Polymers



3.1 Introduction

As discussed in Chapter 1, studies of benzoate-pyrazine coordination polymers, $[M_2(bz)_4(pyz)]_n$, led to testing of analogous systems with substituted pyrazine linkers.¹⁻⁵ Such studies focused on the comparison of both mono-substituted (methyl¹⁻³ and ethyl⁴) and di-substituted (2,3-dimethyl³ and 2-ethyl-3-methyl⁵) pyrazine linkers with the original pyrazine coordination polymer. The presence of substituent groups on the pyrazine resulted in a bending of the coordination polymer chain (**Figure 3.1-1**). Straightening occurred upon guest inclusion (O_2 and CO_2) in the case of the mono-substituted materials but was maintained for the di-substituted systems (**Figure 3.1-1**).

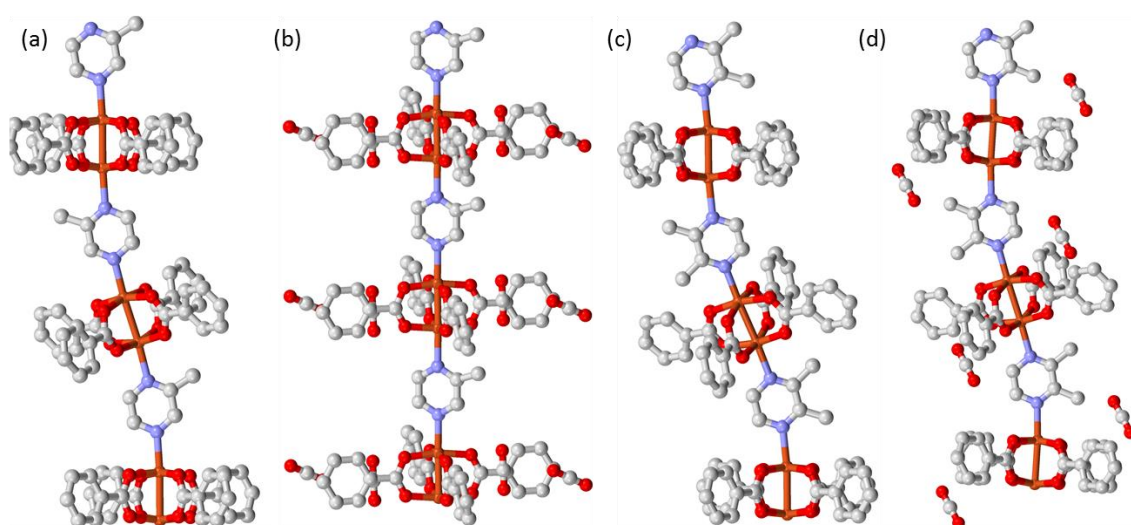


Figure 3.1-1. The observed bending of coordination polymers $[Cu_2(bz)_4(Mepyz)]_n$ (a and b) and $[Cu_2(bz)_4(2,3-DiMepyz)]_n$ (c and d) (where Mepyz = methylpyrazine and 2,3-DiMepyz = 2,3-dimethylpyrazine) in the as-synthesised phase (a and c) and the CO_2 including phase (b and d).³ Disorder removed for clarity. Colour scheme Cu, orange; O, red; N, blue; C, grey.

More recent work has focused on analogous 1D coordination polymers with substituents present on both the pyrazine linker and benzoate ligand.⁶⁻¹¹ One example directly comparable to the polymers presented in Chapter 2 (**2.1(I)**, **2.2(Br)**, **2.3(Cl)** and **2.4(F)**) is $[Cu_2(4-Fbz)_4(Mepyz)]_n$ (Mepyz = methylpyrazine).⁶ Other examples include analogous 1D polymer materials using Rh or Ru as the central metals and connected by phenazine linkers. Studies have focused on the effect of *ortho*- and/or *para*-substituted benzoates for applications in uptake of large quantities of CO_2 ⁷ or in attempts to design materials with selectivity for NO .⁸⁻¹¹

In Chapter 2 it was shown that a family of coordination polymers, $[Cu_2(4-Xbz)_4(pyz)]_n$, exhibit gated inclusion of the CO_2 that is dependent on the halogen substituent. A logical next step would be to look at systems with the basic formula $[Cu_2(4-Xbz)_4(Ypyz)]_n$ (where X is a halogen and Y is a second functional group). Two previously reported examples of 1D coordination polymers that fulfil this formula.^{6,12} The first, $[Cu_2(4-Fbz)_4(Mepyz)]_n$, was reported by Takamizawa et al.⁶ is isostructural to **2.4(F)** (**Figure 3.1-2**) and was examined for selectivity in H_2 uptake.

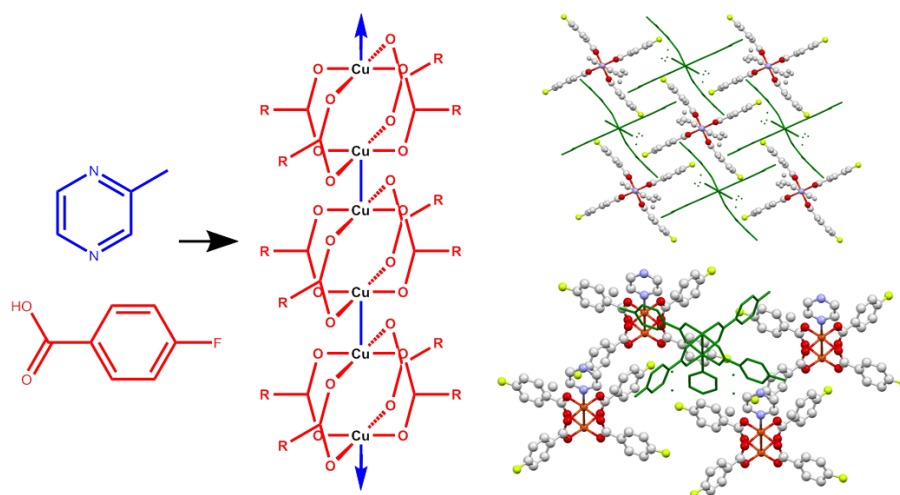


Figure 3.1-2. $[\text{Cu}_2(4\text{-Fbz})_4(\text{MepyZ})]_n$ reported by Takamizawa et al.⁶ shows isostructural packing and interpenetration to $[\text{Cu}_2(4\text{-Fbz})_4(\text{pyz})]_n$. Colour consistent with **Figure 3.1-1**; F, yellow; interpenetration, green capped sticks.

The second, $[\text{Cu}_2(4\text{-Ibz})_4(\text{NH}_2\text{pyz})]_n$ (NH_2pyz = aminopyridazine) now designated **3.1(I)**, was reported by Burrows et al.¹² The structure of **3.1(I)** resembles those of **2.1(I)** and **2.2(Br)** although without positional disorder of the benzoate groups (**Figure 3.1-3**). The three systems, **2.1(I)**, **2.2(Br)** and **3.1(I)**, feature analogous 2D halogen-bonding networks (**Figure 3.1-3**), but the presence of the amine group in **3.1(I)** results in the absence of interpenetration (**Figure 3.1-4**) observed in **2.1(I)** and **2.2(Br)**.

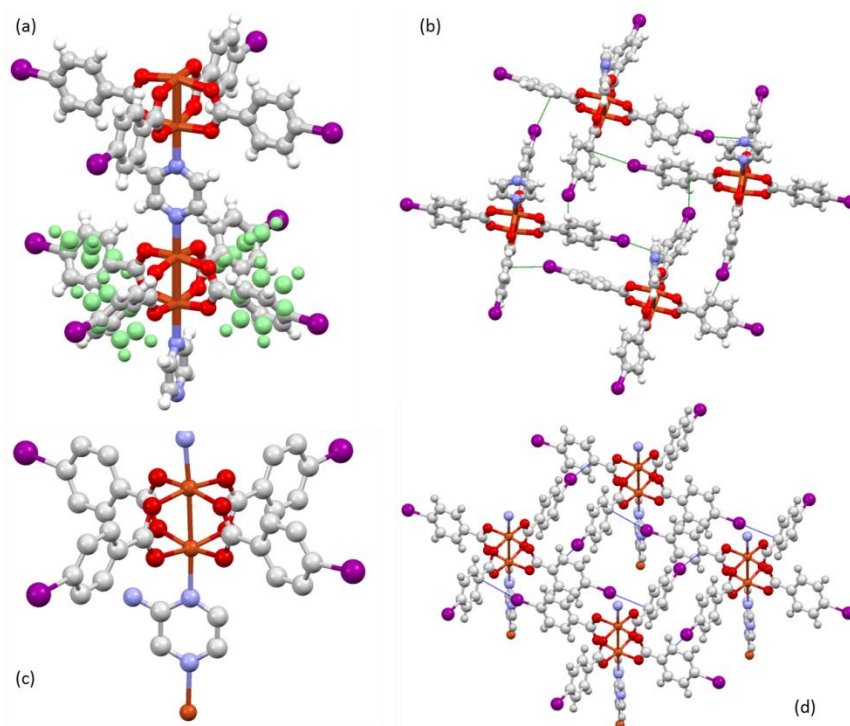


Figure 3.1-3. Analogous formula units (a and c) and 2D $\text{C-I}\cdots\pi$ halogen-bonding networks (b and d) observed in **2.1(I)** (a and b) and **3.1(I)** (c and d). Colour scheme consistent with **Figure 3.1-1**; I, purple, H, white; Disordered rings, mint green; $\text{C-I}\cdots\text{C}_{\text{ipso}}$ interactions, blue and green dashed lines.

The absence of the interpenetration in $[M_2(4-Xbz)_4(Ypyz)]_n$ coordination polymers has been observed where a large *para* substituent is present on the benzoate, e.g. $[Cu_2(4-Phbz)_4(pyiz)]_n$ (4-Phbz = 4-phenylbenzoate)¹² or when a phenazine linker is used with an *ortho* (methoxy) and *para* (chloro) substituted benzoate.^{8,11} Such absence of interpenetration also leads to a large space which is occupied by solvent (either benzyl alcohol¹² or dichloromethane^{8,11}). In the case of **3.1(I)** solvent-filled space accounts for 51% of the unit cell volume (**Figure 3.1-4**) determined by PLATON.^{13,14} This large space presents an attractive opportunity of generating a porous material upon solvent removal, where the void space is sustained through a halogen-bonded network of coordination polymers.

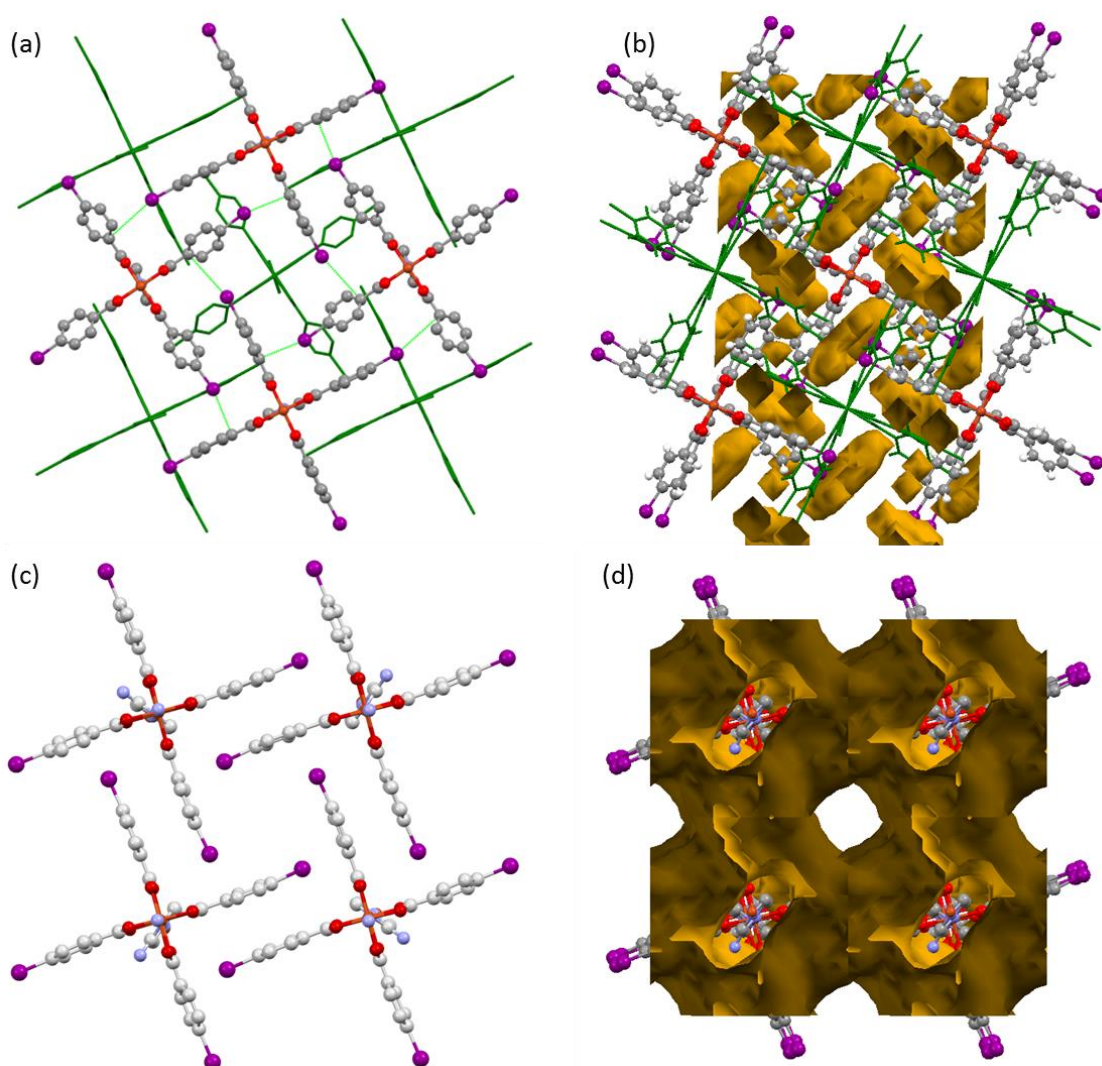


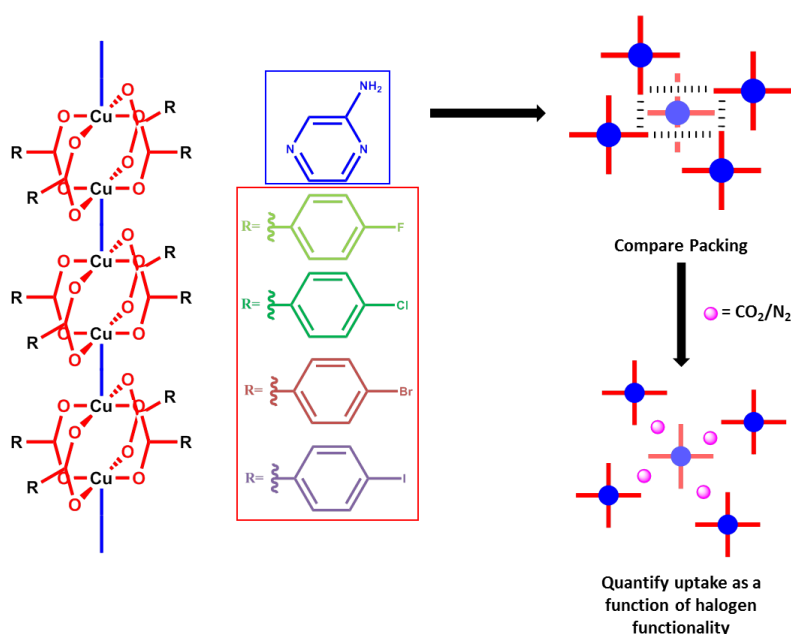
Figure 3.1-4. Comparison of the packing of (a) **2.1(I)** and (c) **3.1(I)** and the observed void spaces (b = **2.1(I)** and d = **3.1(I)**) visualised using program Mercury.¹⁵ Colour consistent with **Figure 3.1-1**; I, purple; interpenetrated network, green capped sticks; void space; yellow.

3.2 Aims

This work builds upon the work presented in Chapter 2 with the synthesis and study of an analogous family of coordination polymers with the formula $[Cu_2(4-Xbz)_4(NH_2pyz)]_n$ (where X is either I (**3.1(I)**), Br (**3.2(Br)**), Cl (**3.3(Cl)**) or F (**3.4(F)**) and NH_2pyz is aminopyrazine). This work

seeks to determine firstly whether interpenetration is observed or absent across the series and secondly to explore propensity for these systems to include gaseous guests (CO_2 and N_2). Previous research suggests that interpenetration may be observed in some cases, for example $[\text{Cu}_2(4\text{-Fbz})_4(\text{Mepy})]_n$,⁶ which might be anticipated to be similar to the proposed $[\text{Cu}_2(4\text{-Fbz})_4(\text{NH}_2\text{pyz})]_n$, is isostructural to interpenetrated $[\text{Cu}_2(4\text{-Fbz})_4(\text{pyz})]_n$ (Chapter 2). This suggests that there may be a crossover point (either **3.2(Br)** or **3.3(Cl)**) from non-interpenetration (in **3.1(I)**) to interpenetrated structure (expected for **3.4(F)**).

The porosity of **3.1(I)**, **3.2(Br)**, **3.2(Cl)** and **3.4(F)** will initially be determined using volumetric adsorption followed by *in situ* diffraction experiments at Diamond Light Source.¹⁶ In these studies it will be interesting to observe the effect that the amino functionality has both on the quantity of included guest and on guest retention, amino functionalisation ligands being a common approach used to enhance CO_2 retention within metal-organic frameworks.^{17–19}



3.3 Experiment

3.3.1 Synthetic Procedures

All solvents (HPLC grade) and reagents were purchased from Sigma Aldrich, VWR or Alfa Aesar. Reagents and solvents were used as received without further purification.

Two methods of synthesis were used. Both employ a solvent layering approach.

Method 1

Copper(II) acetate monohydrate (2 mmol) was dissolved in 6 mL methanol in a 14 mL vial. In a second 37 mL vial 4-halobenzoic acid (4 mmol) and aminopyrazine (2 mmol) were dissolved in

benzyl alcohol. Sonication was employed to aid dissolution of these two mixtures. To the second vial 1 mL of benzyl alcohol was layered on top, followed by 1 mL of methanol. Finally the copper(II) acetate solution was layered on top of the two buffer layers. Samples were left undisturbed to allow for diffusion of the reaction mixture and crystallisation of desired product. Crystal formation was observed after *ca.* 1 week. Samples were in turn filtered and washed with methanol for standard characterisation or single crystals suitable for structure characterisation were selected directly from the mother liquor.

Method 2

Copper(II) acetate monohydrate (2 mmol) was dissolved in 6 mL methanol in a 14 mL vial. In a second 37 mL vial 4-halobenzoic acid (4 mmol) and 2-aminopyrazine (2 mmol) were dissolved in 6 mL dichloromethane (DCM). Sonication was used to aid dissolution of reagents. The halobenzoic acid solubility was often a problem, but use of a suspension of the reagents was sufficient to produce the desired products. To the second vial 1 mL of dichloromethane was layered on top of the reagent solution, followed by 1 mL of methanol. The copper(II) acetate solution was then layered on top of these two buffer layers. Samples were left undisturbed at room temperature to allow for diffusion of reagents and crystallisation of products. Bluish-green crystals were observed after *ca.* 1 week. Samples were in turn filtered and washed with methanol for standard characterisation or single crystals suitable for structural characterisation were selected directly from the mother liquor.

3.3.1.1 Synthesis of $[\text{Cu}_2(4\text{Ibz})_4(\text{NH}_2\text{pyz})]_n$ (3.1(I))

Method 1 (3.1(I)·nBnOH/MeOH)

Coordination polymer **3.1(I)·nBnOH/MeOH** was synthesised using method 1. Copper(II) acetate monohydrate (39.1 mg, 0.20 mmol), 4-iodobenzoic acid (104.0 mg, 0.42 mmol), 2-aminopyrazine (18.7 mg, 0.20 mmol). Yield (67.9 mg, 57.30 %). Elemental Calcd. for $[\text{Cu}_2(4\text{-Ibz})_4(\text{NH}_2\text{pyz})]_n \cdot 2\text{BnOH} \cdot 1.5\text{MeOH}$: C 38.69, H 2.94, N 2.85, I 34.42 %. Elemental Calcd. for $[\text{Cu}_2(4\text{-Ibz})_4(\text{NH}_2\text{pyz})]_n$: C 31.75, H 1.75, N 3.47, I 41.94 %. Found: C 38.58, H 2.97, N 2.75, I 34.70 %

Method 2 (3.1(I)·nDCM/MeOH)

Coordination polymer **3.1(I)·nDCM/MeOH** was synthesised using method 2. Copper(II) acetate monohydrate (40.8 mg, 0.20 mmol), 4-iodobenzoic acid (104.0 mg, 0.42 mmol), 2-aminopyrazine (22.8 mg, 0.24 mmol). Yield (82.8 mg, 67.00 %). Elemental Calcd. for $[\text{Cu}_2(4\text{-Ibz})_4(\text{NH}_2\text{pyz})]_n \cdot 1.75\text{DCM}$: C 29.83, H 1.82, N 3.09, Cl 9.13, I 37.35 %. Elemental Calcd. for $[\text{Cu}_2(4\text{-Ibz})_4(\text{NH}_2\text{pyz})]_n$: C 31.76, H 1.75, N 3.47, Cl 0, I 41.94 %. Found: C 31.42, H 1.91, N 3.24, Cl 11.11, I 40.73 %.

3.3.1.2 Synthesis of $[\text{Cu}_2(4\text{Brbz})_4(\text{NH}_2\text{pyz})]_n$ (3.2(Br))

Method 1 (3.2(Br)·nBnOH/MeOH)

Coordination polymer **3.2(Br)·nBnOH/MeOH** was synthesised by method 1. Copper(II) acetate monohydrate (41.0 mg, 0.21 mmol), 4-bromobenzoic acid (78.6 mg, 0.39 mmol), 2-aminopyrazine (19.9 mg, 0.21 mmol). Yield (65.2 mg, 65.25 %). Elemental Calcd. for $[\text{Cu}_2(4\text{-Brbz})_4(\text{NH}_2\text{pyz})]_n \cdot \frac{2}{3}\text{BnOH} \cdot \frac{1}{2}\text{MeOH} \cdot \frac{1}{2}\text{H}_2\text{O}$: C 39.99, H 2.61, N 3.76, Br 28.63 %. Elemental Calcd. for $[\text{Cu}_2(4\text{-Brbz})_4(\text{NH}_2\text{pyz})]_n$: C 37.60, H 2.07, N 4.11, Br 31.27 %. Found: C 40.03, H 2.61, N 3.84, Br 28.63 %.

Method 2 (3.2(Br)·nDCM/MeOH)

Coordination polymer **3.2(Br)·nDCM/MeOH** was synthesised by method 2. Copper(II) acetate monohydrate (40.8 mg, 0.20 mmol), 4-bromobenzoic acid (87.5 mg, 0.44 mmol), 2-aminopyrazine (24.0 mg, 0.25 mmol). Yield (74.9 mg, 71.76 %). Elemental Calcd. for $[\text{Cu}_2(4\text{-Brbz})_4(\text{NH}_2\text{pyz})]_n \cdot \frac{2}{3}\text{H}_2\text{O}$: C 37.16, H 2.17, N 4.06, Br 30.90 % Elemental Calcd. for $[\text{Cu}_2(4\text{-Brbz})_4(\text{NH}_2\text{pyz})]_n$: C 37.60, H 2.07, N 4.11, Br 31.27 %. Found: C 36.61, H 2.48, N 4.05, Br 31.65 %.

3.3.1.2 Synthesis of $[\text{Cu}_2(4\text{Clbz})_4(\text{NH}_2\text{pyz})]_n$ (3.3(Cl))

Method 1 (3.3(Cl)·nMeOH/BnOH)

Coordination polymer **3.3(Cl)·nMeOH/BnOH** was synthesised by method 1. Copper(II) acetate monohydrate (36.5 mg, 0.18 mmol), 4-chlorobenzoic acid (62.3 mg, 0.40 mmol), 2-aminopyrazine (18.2 mg, 0.19 mmol). Yield (46.0 mg, 59.59 %). Elemental Calcd. for $[\text{Cu}_2(4\text{-Clbz})_4(\text{NH}_2\text{pyz})]_n \cdot 1\text{BnOH} \cdot \frac{1}{2}\text{MeOH}$: C 48.98, H 3.23, N 4.34, Cl 14.64 % Elemental Calcd. for $[\text{Cu}_2(4\text{-Clbz})_4(\text{NH}_2\text{pyz})]_n$: C 45.51, H 2.51, N 4.98, Cl 16.79 %. Found: 49.14, H 3.25, N 4.3, Cl 14.56 %.

Method 2 (3.3(Cl))

Coordination polymer **3.3(Cl)** was synthesised by method 2. Copper (II) acetate monohydrate (37.1 mg, 0.19 mmol), 4-chlorobenzoic acid (65.6 mg, 0.42 mmol), 2-aminopyrazine (18.1 mg, 0.19 mmol). Yield (50.8 mg, 67.3 %). Elemental Calcd. for $[\text{Cu}_2(4\text{-Clbz})_4(\text{NH}_2\text{pyz})]_n \cdot \frac{1}{2}\text{MeOH}$: C 45.37, H 2.69, N 4.88, Cl 16.48 %. Elemental Calcd. for $[\text{Cu}_2(4\text{-Clbz})_4(\text{NH}_2\text{pyz})]_n$: C 45.52, H 2.51, N 4.97, Cl 16.79 %. Found: 45.34, H 2.62, N 4.98, Cl 16.34.

3.3.1.2 Synthesis of $[\text{Cu}_2(4\text{Fbz})_4(\text{NH}_2\text{pyz})]_n$ (3.4(F))

Method 1

Attempts to produce **3.4(F)** by method 1 resulted in the formation of a greenish-blue solution with no solid product obtained.

Method 2 (3.4(F))

Coordination polymer **3.4(F)** was synthesised by method 2. Copper (II) acetate monohydrate (38.8 mg, 0.19 mmol), 4-fluorobenzoic acid (67.6 mg, 0.48 mmol), 2-aminopyrazine (19.0 mg, 0.20 mmol). Yield (28.6 mg, 37.80 %). Elemental Calcd. for $[\text{Cu}_2(4\text{-Fbz})_4(\text{NH}_2\text{pyz})]_n \cdot \frac{1}{4}\text{MeOH} \cdot \frac{1}{4}\text{H}_2\text{O}$: C 48.96, H 2.87, N 5.31, Cl 0.00 %. Elemental Calcd. for $[\text{Cu}_2(4\text{-Fbz})_4(\text{NH}_2\text{pyz})]_n$: C 49.36, H 2.72, N 5.39, Cl 0.00 %. Found: C 48.99, H 2.90, N 5.37, Cl 0.00 %.

3.3.2 Single-Crystal X-Ray Diffraction

Single crystals of the seven successful syntheses (**3.1(I)**·nBnOH/MeOH, **3.1(I)**·nDCM/MeOH, **3.2(Br)**·nBnOH/MeOH, **3.2(Br)**·nDCM/MeOH, **3.3(Cl)**·nMeOH/BnOH, **3.3(Cl)** and **3.4(F)**) suitable for structure determination were selected from samples extracted from the mother liquor suspended in perfluoropolyether oil (FOMBLIN Y), mounted onto a mylar tip. Data were collected on either on a Smart APEX-2 CCD diffractometer equipped with a graphite-monochromated Mo-K α sealed-tube source or a Bruker D8 Venture Single Crystal Diffractometer equipped with a μ S Microfocus Cu-K α sealed-tube source and a Photon 100 CMOS (Complementary Metal Oxide Sensor) Detector with shutterless capability. Sample temperature was maintained using an Oxford Cryosystems Cryostream device. Data were corrected for absorption using empirical methods (SADABS) based on symmetry-equivalent reflections and measurements at different azimuthal angles.^{20–22} Structure solution was achieved by direct methods and the crystal structure was refined using full-matrix least-squares against weighted F^2 values using SHELXL²³ within Olex2.²⁴ Non-hydrogen and non-disordered atoms were refined anisotropically. Hydrogen atoms were placed in calculated positions, refined to idealized geometries (riding model) and assigned a fixed isotropic displacement parameter.

Solvent modelling was attempted in all cases where sufficient unassigned electron density was observed. Such modelling was not successful for data obtained for **3.1(I)** obtained by both methods and crystals of **3.2(Br)** obtained by method 1. The diffuse nature of the electron density representing the disordered solvent made successful modelling challenging. The SQUEEZE¹⁴ method in the program PLATON¹³ was used to estimate the unassigned electron density and remove its contribution to the diffraction intensities. Details of the data are outlined in **Table 3.3.2-1** (Appendix 3.8.1)

3.3.3 Powder X-ray Diffraction (PXRD)

Samples were filtered under vacuum from the mother liquor and washed with methanol. Once dry, samples were ground into a fine powder using a pestle and mortar. The crystalline samples were then analysed using a Bruker D8 Advance X-ray powder diffractometer equipped with a LynxEye XE Detector, a Cu-K α sealed-tube source and a variable motorised slit. Samples were placed onto a low-background sample holder and data were collected while rotating the sample stage at 15 rpm. Data were collected at room temperature between $4^\circ \leq 2\theta \leq 60^\circ$ in steps of 0.02° . The data were then analysed and Pawley refinement²⁵ carried out using the TOPAS program with input files being prepared using jEdit editor.^{26,27} Details of these fits are outlined in **Table 3.3.3-1**.

In the case of **3.1(I)** (prepared by method 1 and 2), **3.2(Br)** (method 2) and **3.3(Cl)** (method 1), the filtering of samples led to degradation or desolvation. In order to observe the solvated phase, powder patterns were recorded in Kapton^{®i} tubing. Samples were extracted from the

ⁱ Kapton[®] (polyimide) tubing with an outer diameter of 1.05 mm, a wall thickness of 0.025 mm and an internal diameter of 1.0 mm was purchased from Goodfellow Cambridge Ltd.

mother liquor and placed into a mortar with a portion of mother liquor present. Wet samples were then ground into a slurry and loaded into a Kapton® tube. The tube was sealed at both ends with wax and then fixed to a goniometer with arc adjustment. Data were collected using Bruker D8 Advance X-ray powder diffractometer equipped with a LynxEye Detector, a Cu-K α sealed-tube source and a focusing Göbel Mirror optic operating in capillary mode. Data were collected between $4^\circ \leq 2\theta \leq 60^\circ$ at a 0.015° increment and the sample was rotated at 30 rpm during collection. The data were then analysed and Pawley refinement²⁵ carried out using the TOPAS program.^{26,27} Details of these fits are outlined in **Table 3.3.3-1**.

Table 3.3.3-1. Pawley phase fits of as-synthesised materials **3.1(I)**, **3.2(Br)**, **3.3(Cl)** and **3.4(F)**.

	Space Group	Volume (Å ³)	a (Å)	b (Å)	c (Å)	α (°)	β (°)	γ (°)	R_{wp}	R_{wp}'	Parameters
Method 1 Synthesis											
3.1(I) -sol ^a	<i>P4₁</i>	6586.1(2)	12.9456(2)	12.9456(2)	39.299(1)	90	90	90	0.0498	0.1536	1006
3.2(Br) -sol ^b	<i>I2/m</i>	2057.0(1)	12.4001(3)	9.8798(3)	17.0802(6)	90	100.568(3)	90	0.0622	0.1321	353
3.3(Cl) -sol ^{a*}	<i>I2/m</i>	1955.4(5)	12.372.(2)	9.650(2)	16.689(2)	90	101.061(9)	90	0.2865	0.4790	336
Method 2 Synthesis											
3.1(I) -sol ^a	<i>P4/ncc</i>	12990.9(12)	25.7962(9)	25.7962(9)	19.522(1)	90	90	90	0.0491	0.2320	985
3.2(Br) -sol ^a	<i>I2/m</i>	2107.47(8)	12.4268(2)	9.8528(2)	17.4558(5)	90	99.580(2)	90	0.0459	0.1152	366
3.2(Br) ^b	<i>I2/m</i>	1733.8(1)	13.1786(6)	9.9163(5)	13.2676(7)	90	90.361(5)	90	0.0470	0.1230	299
3.3(Cl) ^b	<i>I2/m</i>	1755.5(1)	12.2142(4)	9.8540(5)	15.1842(7)	90	106.144(3)	90	0.0544	0.0914	307
3.4(F) ^b	<i>I2/m</i>	1683.5(3)	11.685(1)	9.7529(7)	15.414(1)	90	106.579(8)	90	0.0934	0.1751	297

^a Sample loaded as a slurry in Kapton® tubing. ^b Sample filter under vacuum and washed with methanol. ^c **3.3(Cl)**-sol contained an unknown impurity.

3.3.4 Thermogravimetric Analysis (TGA)

Samples were prepared using the same method as outlined for the PXRD. Samples were then analysed on a Perkin Elmer Pyris1 Thermogravimetric analyser in a ceramic crucible. Samples were initially held a 25 °C for 10 mins before being heating to 600 °C at a rate of 5 °C per min.

3.3.5 Single-Crystal Desolvation Studies

Desolvation studies were carried out on a Bruker D8 Venture Single Crystal Diffractometer equipped with a μ S Microfocus Cu-K α sealed-tube source and a Photon 100 CMOS (Complementary Metal Oxide Sensor) Detector with shutterless capability. This was equipped with an Oxford Cryosystems Cryostream Plus 700 series device, which was used to provide a cooled nitrogen stream.

Due to the low mass loss observed in the TGA for **3.2(Br)-DCM/MeOH**, samples were tested initially by *ex situ* techniques. Single crystals were removed from the mother liquor and placed on a glass slide at room temperature. The crystals were then kept out of solvent at room temperature for 1 h; following this the crystals were covered in perfluoropolyether oil (FOMBLIN Y) to allow for easy selection and screening of crystals. A suitable crystal was selected and a full data collection was recorded at 100 K. Details of the data collection are outlined in **Table 3.3.5-1** (Appendix 3.8.1). Data were corrected for absorption using empirical methods (SADABS) based on symmetry-equivalent reflections and measurements at different azimuthal angles.²⁰⁻²² Structure solution was achieved by direct methods and the crystal structure was refined using full-matrix least-squares against weighted F^2 values using SHELXL²³

within Olex2.²⁴ Non-hydrogen and non-disordered atoms were refined anisotropically. Hydrogen atoms were placed in calculated positions, refined to idealized geometries (riding model) and assigned a fixed isotropic displacement parameter. The sample suffered significant loss of crystallinity resulting in only a partial structure solution being obtained. The solution required restraints to be applied to most the bond lengths and angles. The solution also featured positional disorder of the 4-bromobenzoate ligands. Two orientations were refined with occupancies 50.7(7):49.3(7).

This same protocol was applied to crystals of **3.1(I)** obtained by method 2, but this resulted in significant loss of crystallinity and unit cell parameters could not be determined for the desolvated phase.

3.3.6 Volumetric Nitrogen and Carbon Dioxide Adsorption Studies

Samples of **3.1(I)**, **3.2(Br)**, **3.3(Cl)** and **3.4(F)** obtained by method 2 were analysed for adsorption of N₂ and CO₂ gases using a Micromeritics 2020 Plus volumetric gas analyser. N₂ isotherms were recorded at 77 K and CO₂ isotherms at 195 K. Prior to isotherms being recorded samples were initially stored in a vacuum oven at 80 °C for 16 h. Following this treatment samples were subjected to a degas condition on the Micromeritics instrument, which consisted of an evacuation in which the sample was heated to 60 °C (10 °C/min) and pressure was reduced to 4 µmHg (5 mmHg/s). Following this evacuation phase a heating phase was applied in which the sample was held under vacuum at 100 °C for 1000 mins. For the CO₂ isotherm of **3.4(F)** an additional on port degas (4 µmHg at 100 °C for 120 mins) was performed without the sample tube being backfilled with N₂ to avoid N₂ inclusion prior to CO₂ isotherm.

Following volumetric adsorption studies samples were recovered and analysed via PXRD following the procedure for dry samples outlined in Section 3.3.3. For **3.2(Br)**, **3.3(Cl)** and **3.4(F)** Pawley refinements²⁵ were carried out using TOPAS.^{26,27} The results of these refinements are outlined in **Table 3.3.6-1**.

Table 3.3.6-1. Summary of Pawley refinements of **3.2(Br)**, **3.3(Cl)** and **3.4(F)** samples after volumetric adsorption studies.

	Space Group	Volume (Å ³)	<i>a</i> (Å)	<i>b</i> (Å)	<i>c</i> (Å)	α (°)	β (°)	γ (°)	<i>R</i> _{wp}	<i>R</i> _{wp'}	Parameters
3.2(Br)^a	<i>I2/m</i>	1737.0(3)	13.175(1)	9.933(1)	13.274(2)	90	90.381(9)	90	0.0723	0.2092	305
3.2(Br)^b	<i>I2/m</i>	1736.3(2)	13.1826(9)	9.9212(8)	13.276(1)	90	90.379(7)	90	0.0662	0.1877	307
3.3(Cl)^a	<i>I2/m</i>	1752.1(2)	12.2128(5)	9.8495(6)	15.1635(8)	90	106.143(3)	90	0.0548	0.0924	307
3.3(Cl)^b	<i>I2/m</i>	1754.0(2)	12.2160(5)	9.8527(6)	15.1678(8)	90	106.098(3)	90	0.0529	0.1011	307
3.4(F)^a	<i>I2/m</i>	1680.8(2)	11.6937(9)	9.7241(6)	15.4233(9)	90	106.583(6)	90	0.1064	0.1730	297
3.4(F)^b	<i>I2/m</i>	1677.4(3)	11.675(2)	9.7479(8)	15.3997(12)	90	106.845(9)	90	0.0999	0.1890	297

^a following volumetric adsorption and desorption of N₂. ^b following volumetric adsorption and desorption of CO₂.

3.3.7 *In situ* Powder X-ray Diffraction during CO₂ and N₂ Adsorption and Desorption

Samples of **3.2(Br)**, **3.3(Cl)** and **3.4(F)** were studied by PXRD during CO₂ adsorption and desorption by utilising an *in situ* gas cell on beamline I11 at Diamond Light Source.^{16,28-30} Samples were filtered under vacuum and washed with methanol and then ground. Samples were loaded into a 0.7 mm quartz capillary, sealed in a gas cell and evacuated ($\approx 10^{-5}$ mbar) on the beamline before an initial powder pattern was recorded. Samples were then dosed to sequential increasing (and decreasing) pressures of CO₂ allowing a 20-min equilibration time prior to data collection. Data were recorded at 195 K with the temperature being maintained with the use of an Oxford Cryosystem Cryostream Plus 700 series low-temperature device. In the case of **3.3(Cl)** and **3.4(F)** data were collected using a PSD (position-sensitive detector),³⁰ with data being recorded utilising the MAC (Multiple Analysing Crystal)^{28,29} detector for **3.2(Br)** to avoid high background fluorescence.

Data were fitted initially using Pawley refinement²⁵ and then fitted using Rietveld refinement,³¹ both methods using the TOPAS program.^{26,27} Starting structural models were adapted from single crystal structures. Location of CO₂ sites was attempted with the use of a rigid-body model, allowing for refinement of position and occupancy of the CO₂ molecule. The initial position and occupancy being randomised and allowed to converge to minimum. Refinement details are outlined in **Table 3.3.7-1-Table 3.3.7-6** (Appendix 3.8.2).

Samples of **2.3(Cl)** and **2.4(F)** were also studied by PXRD during N₂ adsorption and desorption utilising the same *in situ* gas cell setup. Samples were prepared as previously mentioned in the CO₂ studies. Data were collected at 90 K, the temperature being maintained with an Oxford Cryosystem Cryostream Plus 700 series low-temperature device. Following evacuation ($\approx 10^{-5}$ mbar) samples were dosed with successive pressures of N₂ leaving 25 minute (**3.3(Cl)**) or 30 minute (**3.4(F)**) equilibration time between dosing and data acquisition. Data were recorded using a PSD (position-sensitive detector).³⁰

Data were initially fitted using Pawley²⁵ refinement methods, followed by Rietveld methods,³¹ both methods using the TOPAS program.^{26,27} Starting structural models were adapted from single crystal structures. Location of N₂ sites was attempted with the use of a rigid-body allowing for refinement of position and occupancy of the N₂, with the initial position and occupancy being randomised and allowed to converge to minimum. Refinement details are outlined in **Table 3.3.7-7-Table 3.3.7-10** (Appendix 3.8.2).

3.3.8 *In situ* Single-Crystal X-Ray Diffraction Studies during CO₂ and N₂ Adsorption and Desorption

Single crystals of **3.3(Cl)** and **3.4(F)** were structurally characterised during both CO₂ and N₂ adsorption and desorption on beamline I19 at Diamond Light Source^{16,32,33} utilising the *in situ* gas cell instrumentation developed at the beamline. Single crystals were selected directly from the mother liquor and glued with super-glue, on to a long mylar microloop. Once the glue had

dried these loops were then inserted into a capillary gas cell with glue being applied to the edge of the pin to ensure samples did not move during data collection. The gas cell was then sealed and evacuated ($\approx 10^{-5}$ mbar) on the beamline. Following alignment an initial data collection was recorded with the sample under vacuum. This was then followed by dosing the cell with increasing (and decreasing) pressures of CO₂ or N₂, allowing for 20-min (CO₂) or 30-min (N₂) equilibration times. Data were recorded at 195 K and 90 K for CO₂ and N₂, respectively, the temperature being maintained with the use of an Oxford Cryosystem Cryostream Plus 700 series low-temperature device. A small quantity of vacuum grease was applied to the exterior of the capillary to minimise build-up of ice; the capillary was checked for ice formation before each data collection.

The data were processed with the CryAlisPro³⁴ programs, using a predetermined instrument model from a strongly diffracting reference crystal to enable more accurate determination of the orientation matrix used for integration of diffraction intensities. Data were corrected for absorption using empirical methods (SADABS) based on symmetry-equivalent reflections and measurements at different azimuthal angles.^{20–22} Structure solution was achieved by direct methods and the crystal structure was refined using full-matrix least-squares against weighted F^2 values using SHELXL²³ within Olex2.²⁴ Non-hydrogen and non-disordered atoms were refined anisotropically. Hydrogen atoms were placed in calculated positions, refined using idealized geometries (riding model) and assigned a fixed isotropic displacement parameter. In the case of CO₂ adsorption study for **3.3(Cl)** poor and diminishing data quality, resulted in initially restraints being applied to the displacement parameters and the bond lengths for the atoms in the aminopyrazine ligand, the displacement parameter restraints later having to be applied to all atoms for the final vacuum measurement. A summary of the crystal data is outlined in **Table 3.3.8-1-Table 3.3.8-4** (Appendix 3.8.3).

3.4 Results and Discussion

3.4.1 Synthesis of **3.1(I)**, **3.2(Br)**, **3.3(Cl)** and **3.4(F)**

Coordination polymers **3.1(I)**, **3.2(Br)**, **3.3(Cl)** and **3.4(F)** were synthesised in moderate yields either by method 1 (except **3.4(F)**) or method 2. All yielded single crystals. The purity of these samples was confirmed by PXRD and elemental analysis which indicated the presence of solvent.

Conventional sample preparation for PXRD, filtering under vacuum and washing with methanol, resulted in either degradation or desolvation of samples of **3.1(I)** and **3.3(Cl)** prepared by method 1 and **3.1(I)** and **3.2(Br)** prepared by method 2. PXRD patterns for the as-synthesised solvated forms of **3.1(I)** (prepared by method 1 and 2), **3.2(Br)** (method 2) and **3.3(Cl)** (method 1) were obtained by collecting data on slurried samples loaded in Kapton[®] tubing. A sample of **3.2(Br)** (method 2) prepared by filtering under vacuum suggests that desolvation at room temperature is achievable.

The adoption of two synthetic methods was, firstly, to replicate the previously reported synthesis of **3.1(I)** (method 1)¹² and, secondly, to prepare analogous coordination polymers

with solvents that are easier to remove at modest temperatures (method 2). Dichloromethane was used instead of benzyl alcohol in an attempt to eliminate the need of high temperatures for desolvation, since benzyl alcohol has a much higher boiling point (205 °C) than dichloromethane (38 °C). For two of the coordination polymers (**3.3(Cl)** and **3.4(F)**) method 2 produced solvent-free materials which would require minimal activation prior to gas adsorption studies. Coordination polymers **3.1(I)** and **3.2(Br)** produced by method 2 also demonstrate a room-temperature phase transformation upon filtration.

3.4.2 Crystal Packing

The two methods of synthesis produced similar 1D coordination polymers, $[\text{Cu}_2(4\text{Xbz})_4(\text{NH}_2\text{pyz})]_n$, with some slight variation in the packing of these systems which is discussed in the following paragraphs.

The structure of coordination polymer **3.1(I)-BnOH/MeOH**, synthesised by method 1 was as previously reported.¹² This structure consists of a crystallographically unique paddlewheel unit. These units are eclipsed along the polymer chain (**Figure 3.4.2-1**). Alternating aminopyrazine ligands are rotated by 90° relative to one another and the polymer chain exhibits a close to linear $\text{Cu}_{2(\text{cent})}\cdots\text{NH}_2\text{pyz}_{(\text{cent})}\cdots\text{Cu}_{2(\text{cent})}$ angle of 178.8(2)° (cent = centroid). The bridging 4-iodobenzoates also exhibit a small bending rotation about the carboxylate $\text{O}\cdots\text{O}$ vector $\text{Cu}_{2(\text{cent})}\cdots\text{O}_{2(\text{cent})}\cdots\text{ring}_{(\text{cent})}$ angles ranging from 173.4(5)° to 175.7(5)°.

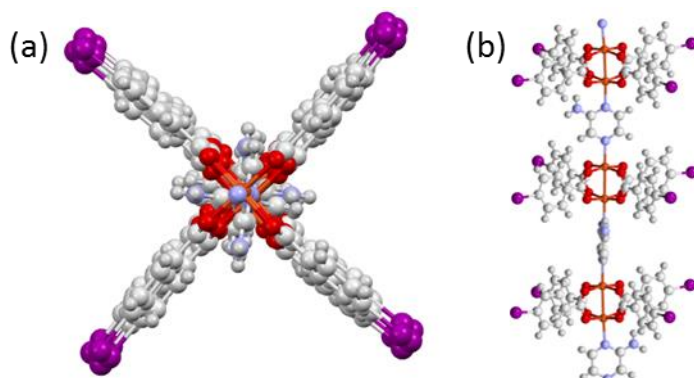


Figure 3.4.2-1. Polymer chain **3.1(I)-BnOH/MeOH** showing (a) the eclipsing of the paddlewheel units and (b) the 90° rotation of alternating NH_2pyz linkers. Colour scheme Cu, Orange; C, grey; N, blue; O, red; I, purple.

As previously stated **3.1(I)-BnOH/MeOH** exhibits a 2D halogen-bonding network analogous to that of **2.1(I)**, with all four of the iodines interacting with neighbouring aromatic rings ($\text{C}-\text{I}\cdots\text{C}_{\text{ipso}}$ 3.440(13)-3.492(15) Å) (**Figure 3.4.2-2**). As previously observed in Chapter 2 these $\text{C}-\text{I}\cdots\pi$ interactions occur in antiparallel pairs with a centroid-centroid distance between the antiparallel aromatic rings of 3.869(8) Å and 3.955(9) Å (**Figure 3.4.2-2**).

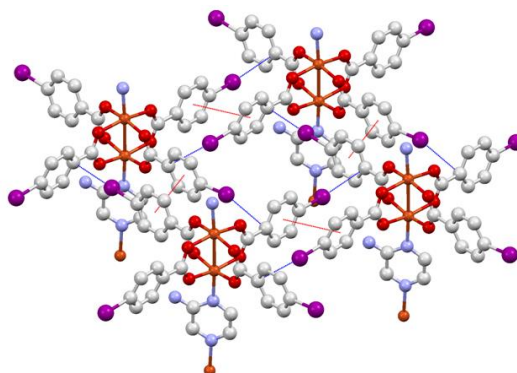


Figure 3.4.2-2. 2D network formed by C–I $\cdots\pi$ halogen-bonding interactions (blue dashed lines) accompanied by a $\pi\cdots\pi$ interactions (red dashed lines) in **3.1(I)-BnOH/MeOH**. Colour scheme consistent with **Figure 3.4.2-1**. Hydrogen atoms not shown.

As previously discussed the presence of the amino functionality, in some part, prevents the interpenetration observed in **2.1(I)**, resulting in a large space containing diffuse solvent. This diffuse solvent could not be sensibly modelled crystallographically, with attempts resulting in models for which least-squares refinement did not converge. Therefore PLATON SQUEEZE^{13,14} was employed quantify the solvent present. PLATON determined that in the 3295.6 Å³ solvent accessible void (52% of the cell volume) contained 103 electrons per formula unit this was attributed to 1.5 benzyl alcohol and one methanol molecules, which is less than observed by elemental analysis (2 benzyl alcohol and 1.5 methanol).

Coordination polymer **3.1(I)-DCM/MeOH** (method 2) resulted in an asymmetric unit containing half of the paddlewheel unit and half of the aminopyrazine ligand, which therefore exhibits positional disorder of the NH₂ group. As with **3.1(I)-DCM/MeOH** a slight rotation of the bridging benzoates was observed with Cu_{2(cent)} \cdots O_{2(cent)} \cdots ring_(cent) angles of 172.9(3) ° and 174.0(3) ° (**Figure 3.4.2-3**).

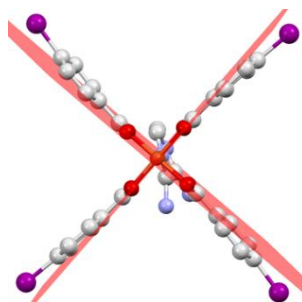


Figure 3.4.2-3. Structure of **3.1(I)-DCM/MeOH**, viewed along the *c*-axis, showing the rotation of the 4-iodobenzoate ligands. Colour scheme consistent with **Figure 3.4.2-1**. Hydrogen atoms omitted for clarity.

The iodine substituents interact in an analogous way to those in **2.1(I)** and **3.1(I)-BnOH/MeOH**, forming a 2D halogen-bonding network (C–I \cdots C_{ipso} 3.449(10) Å and 3.445(10) Å) (**Figure 3.4.2-4**). This 2D halogen-bonding network forms through antiparallel halogen-bonding pairs with a centroid-centroid distance between antiparallel benzoate rings of 3.856(7) Å analogous to distances for **2.1(I)** and **3.1(I)-BnOH/MeOH** (**Figure 3.4.2-4**).

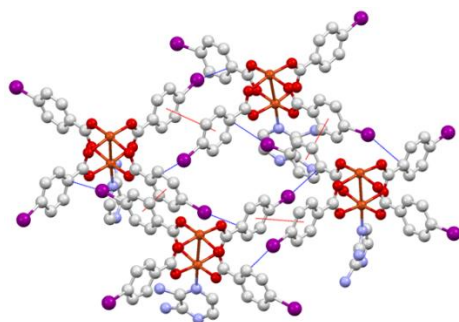


Figure 3.4.2-4. 2D network formed by C–I $\cdots\pi$ halogen-bonding interactions (blue dashed lines) accompanied by $\pi\cdots\pi$ interactions (red dashed lines) in **3.1(I)-DCM/MeOH**. Colour scheme consistent with **Figure 3.4.2-2**. Both positions for disordered amino substituent are shown. Hydrogen atoms not shown.

The polymer chains exhibit greater bending as measured by the $\text{Cu}_{2(\text{cent})}\cdots\text{NH}_2\text{pYZ}_{(\text{cent})}\cdots\text{Cu}_{2(\text{cent})}$ angle of $172.81(17)^\circ$ (cf. $178.8(2)^\circ$ for **3.1(I)-BnOH/MeOH**), but with neighbouring paddlewheels being staggered, with $\text{Ring}_{(\text{cent})}\cdots\text{Cu}_{2(\text{cent})}\cdots\text{Cu}_{2(\text{cent})}\cdots\text{Ring}_{(\text{cent})}$ torsion angles of $56.62(9)^\circ$ and $58.22(10)^\circ$ (**Figure 3.4.2-5**), rather than eclipsed in **3.1(I)-BnOH/MeOH**.

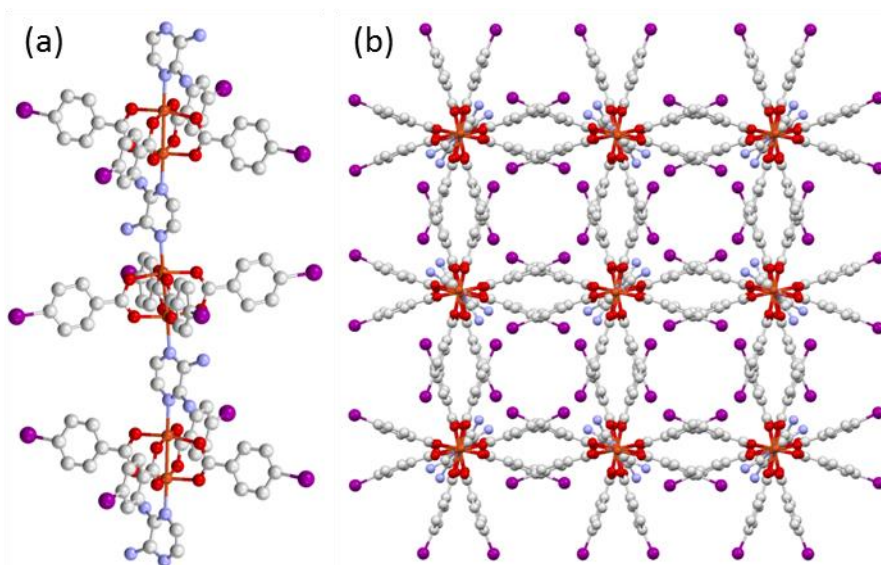
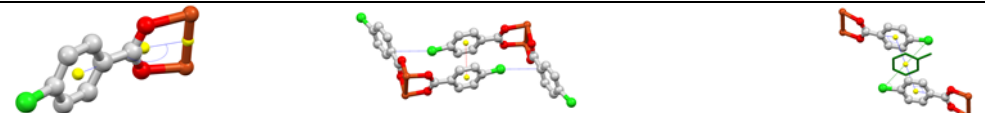


Figure 3.4.2-5: Staggering of the formula units in **3.1(I)-DCM/MeOH** showing (a) a single polymer chain and (b) the effect the staggered orientation has on the overall packing. Colour scheme consistent with **Figure 3.4.2-1**. Both positions for disordered amino substituent are shown. Hydrogen atoms not shown.

In spite of this staggered orientation the polymer exhibits the same lack of interpenetration as **3.1(I)-BnOH/MeOH** and results in a comparable solvent-accessible volume of 6137.5 \AA^3 per unit cell (50% of the cell volume). It was again necessary to use PLATON SQUEEZE^{13,14} to remove the contribution to the observed structure factors of the electron density corresponding to diffuse solvent.¹⁴ PLATON SQUEEZE found 305 electrons per formula unit which is a much larger solvent content (ca. 7.25 DCM) than observed in the elemental analysis (1.75 DCM).

The five other coordination polymers (**3.2(Br)**, **3.3(Cl)** synthesised by both methods and **3.4(F)** synthesised by method 2) are all analogous to one another. All exhibit the same interpenetration observed for the pyrazine containing analogues described in Chapter 2 and previously reported systems.^{3,6,7,35} In three cases (**3.2(Br)-BnOH/MeOH**, **3.2(Br)-DCM/MeOH** and **3.3(Cl)-BnOH/MeOH**) the samples crystallised as solvates whereas **3.3(Cl)** and **3.4(F)** crystallised without inclusion of solvent. The presence of solvent guests is reflected in the $\text{Cu}_{2(\text{cent})}\cdots\text{O}_{2(\text{cent})}\cdots\text{bz}_{(\text{cent})}$ angle (**Table 3.4.2-1**), with the solvent-free forms (**3.3(Cl)** and **3.4(F)**) having one bridging benzoate more bent (rotation about the carboxylate O_2 vector) than the solvent-included forms. This correlates with the ligand straightening observed when samples of **2.3(Cl)** and **2.4(F)** adsorb CO_2 upon increasing pressures of CO_2 (Chapter 2).

Table 3.4.2-1. Summary of the intermolecular distances (Å) and angles (°) observed in **3.2(Br)**, **3.3(Cl)** and **3.4(F)**



	$\text{Cu}_{2(\text{cent})}\cdots\text{O}_{2(\text{cent})}\cdots\text{bz}_{(\text{cent})}$		$\text{C-X}\cdots\text{C}_{\text{ipso}}$		$\text{bz}_{(\text{cent})}\cdots\text{bz}_{(\text{cent})}$		$\text{C}_{\text{ipso}}\cdots\text{bz}_{(\text{cent})}\cdots\text{NH}_2\text{pyz}_{(\text{cent})}$		$\text{C-X}\cdots\text{NH}_2\text{pyz}_{(\text{cent})}$	
	1	2	1	2	1	2	Distance	Angle	Distance	Angle
3.2(Br)-BnOH/MeOH	175.73(11)	176.07(13)	3.437(8)	6.945(7)	3.625(6)	7.785(6)	4.669(3)	136.0(3)	3.4459(9)	87.0(2)
3.2(Br)-DCM/MeOH	176.5(2)	177.19(19)	3.407(11)	7.083(3)	3.669(9)	7.832(11)	4.804(4)	139.2(5)	3.3948(14)	91.1(3)
3.3(Cl)-BnOH/MeOH	176.1(2)	174.6(2)	3.463(14)	6.758(14)	3.651(13)	7.680(12)	4.459(5)	134.4(6)	3.357(4)	86.1(4)
3.3(Cl)	177.23(7)	163.14(8)	3.570(6)	4.743(5)	3.832(4)	6.809(4)	3.7459(18)	117.0(2)	3.8084(15)	63.43(17)
3.4(F)	179.73(9)	164.36(9)	3.551(9)	5.171(7)	3.923(5)	6.711(5)	3.6788(19)	120.3(2)	3.409(4)	71.9(3)

1 and 2 denoting the first and second analogous distance (or angle).

These five coordination polymers possess the same 1D halogen-bonding network, accompanied by the same cooperative $\pi\cdots\pi$ interaction (**Table 3.4.2-1**), with $\text{C-X}\cdots\text{C}_{\text{ipso}}$ distance in the orthogonal direction being longer than the sum of the van der Waals radii^{36,37} (**Figure 3.4.2-6**). This longer $\text{C-X}\cdots\text{C}_{\text{ipso}}$ distance is also further increased in the presence of solvent guests, consistent with observation from the *in situ* adsorption studies of **2.3(Cl)** and **2.4(F)** (Chapter 2).

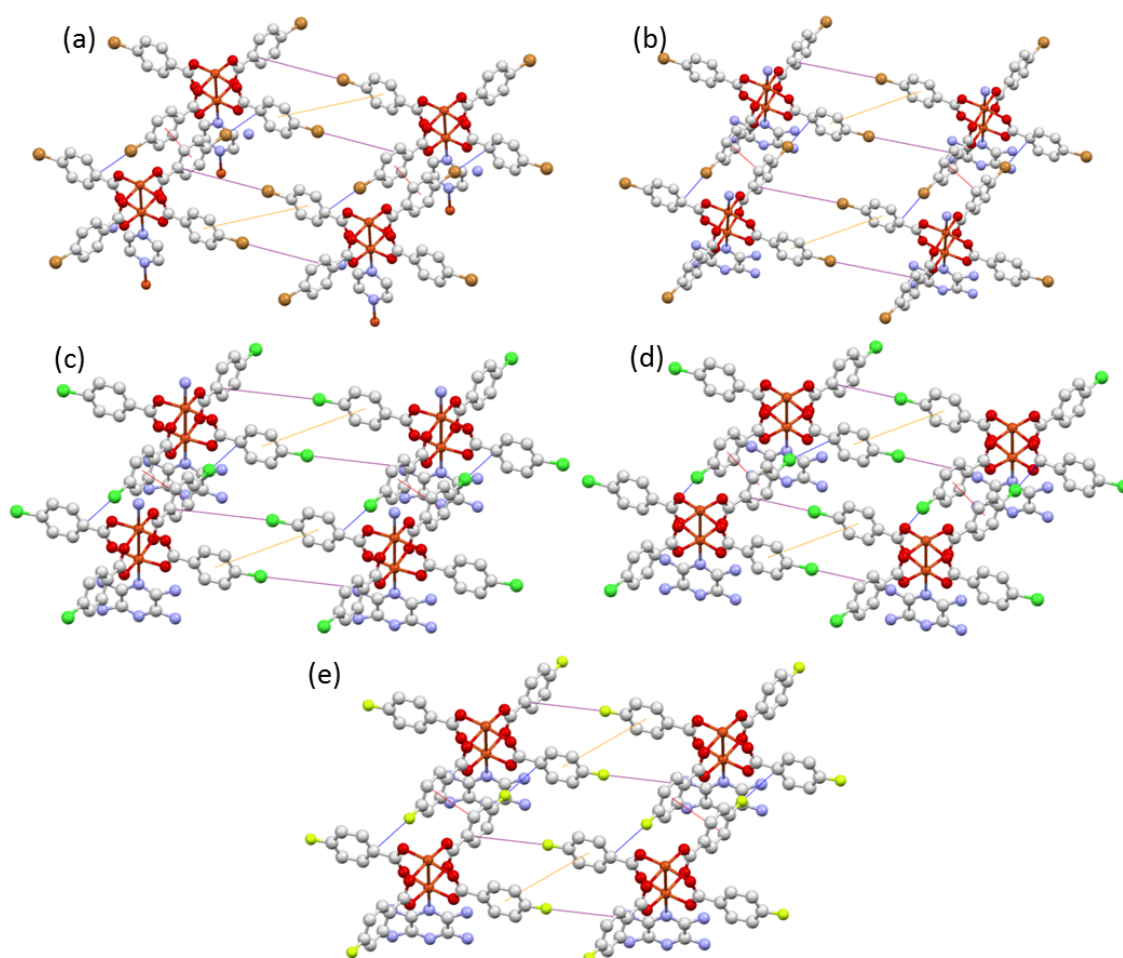


Figure 3.4.2-6. The $C-X \cdots C_{ipso}$ and $bz_{(cent)} \cdots bz_{(cent)}$ interaction for $[Cu_2(4-Xbz)_4(NH_2pyz)]_n$ polymers (a) **3.2(Br)-BnOH/MeOH**, (b) **3.2(Br)-DCM/MeOH**, (c) **3.3(Cl)-BnOH/MeOH**, (d) **3.3(Cl)** and (e) **3.4(F)**. Colour scheme consistent with **Figure 3.4.2-1**; Br, brown; Cl, green; F, yellow, $C-X \cdots C_{ipso}$ interaction, blue dashed line (purple dashed line for elongated distance); $bz_{(cent)} \cdots bz_{(cent)}$ interaction, red dashed line (orange dashed line for elongated distance).

The interpenetration (**Figure 3.4.2-7**) also results in similar closest contacts being observed between the pyrazine and either the aromatic ring of the benzoate or the halogen. In the solvent-included phase the shortest contact is observed at a $C-X \cdots NH_2pyz_{(cent)}$ angle close to 90° (**Table 3.4.2-1**), whereas this angle becomes acute with a larger $(C-X) \cdots NH_2pyz_{(cent)}$ distance in the solvent-free forms.

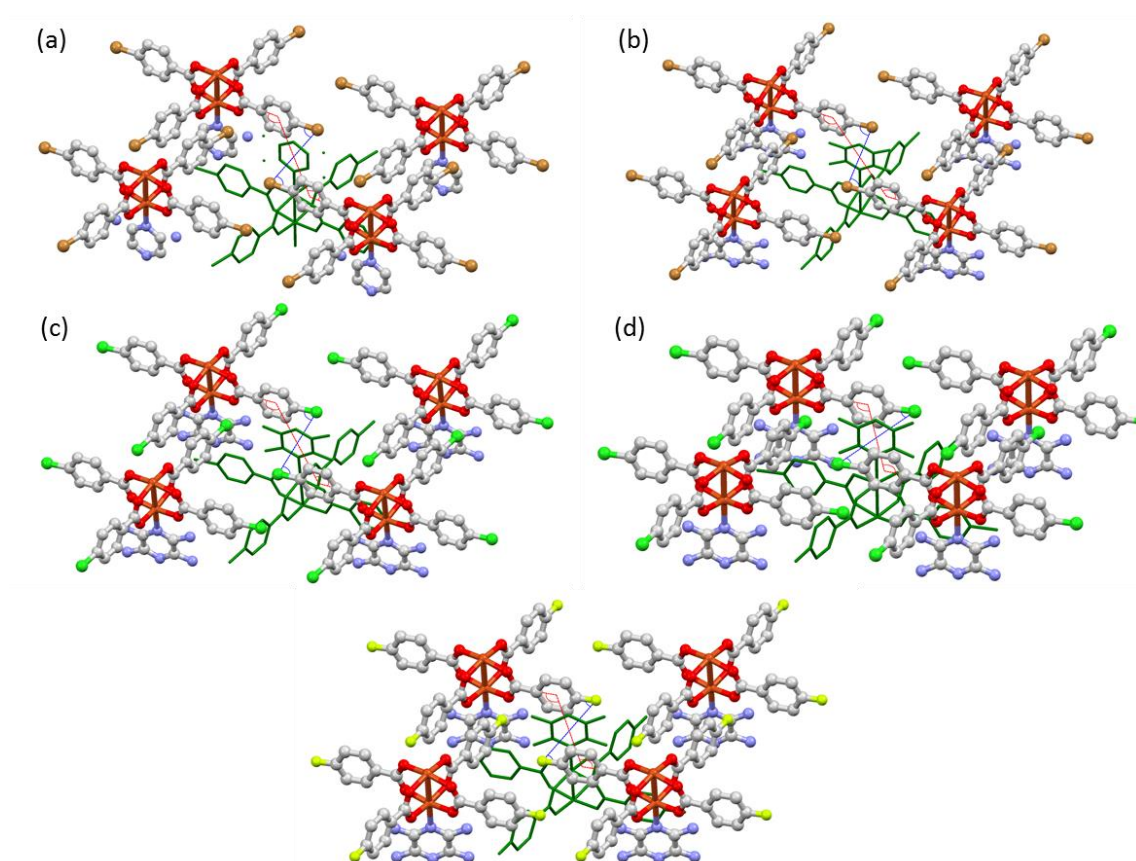


Figure 3.4.2-7. The interpenetration observed in $[\text{Cu}_2(4\text{-Xbz})_4(\text{NH}_2\text{pyz})]_n$ polymers (a) **3.2(Br)-BnOH/MeOH**, (b) **3.2(Br)-DCM/MeOH**, (c) **3.3(Cl)-BnOH/MeOH**, (d) **3.3(Cl)** and (e) **3.4(F)**. Colour scheme consistent with **Figure 3.4.2-1**; Br, brown; Cl, green; F, yellow; $\text{C-X}\cdots\text{NH}_2\text{pyz}_{(\text{cent})}$ angle, blue dashed lines; $\text{C}_{\text{ipso}}\cdots\text{bz}_{(\text{cent})}\cdots\text{NH}_2\text{pyz}_{(\text{cent})}$ angle, red dashed line; interpenetrated network shown as green capped sticks.

In the three solvated materials (**3.2(Br)-BnOH/MeOH**, **3.2(Br)-DCM/MeOH** and **3.3(Cl)-BnOH/MeOH**) residual electron density was observed in the cleft of the paddlewheel unit. This location is consistent with the guest sites reported in Chapter 2 and in previous work on $[\text{M}_2(\text{bz})_4(\text{pyz})]_n$ materials.^{3,38-47} This electron density could be modelled as disordered methanol molecules for **3.2(Br)-DCM/MeOH** and a disordered chain of benzyl alcohol molecules for **3.3(Cl)-DCM/MeOH** (**Figure 3.4.2-8**). In neither case do the solvent appear to interact with the amino functionality of the coordination polymer. The benzyl alcohol in **3.3(Cl)-BnOH/MeOH** forms an offset $\pi\cdots\pi$ interaction with the benzoate ligand with a centroid \cdots centroid distance of 3.729(5) Å (**Figure 3.4.2-8d**)

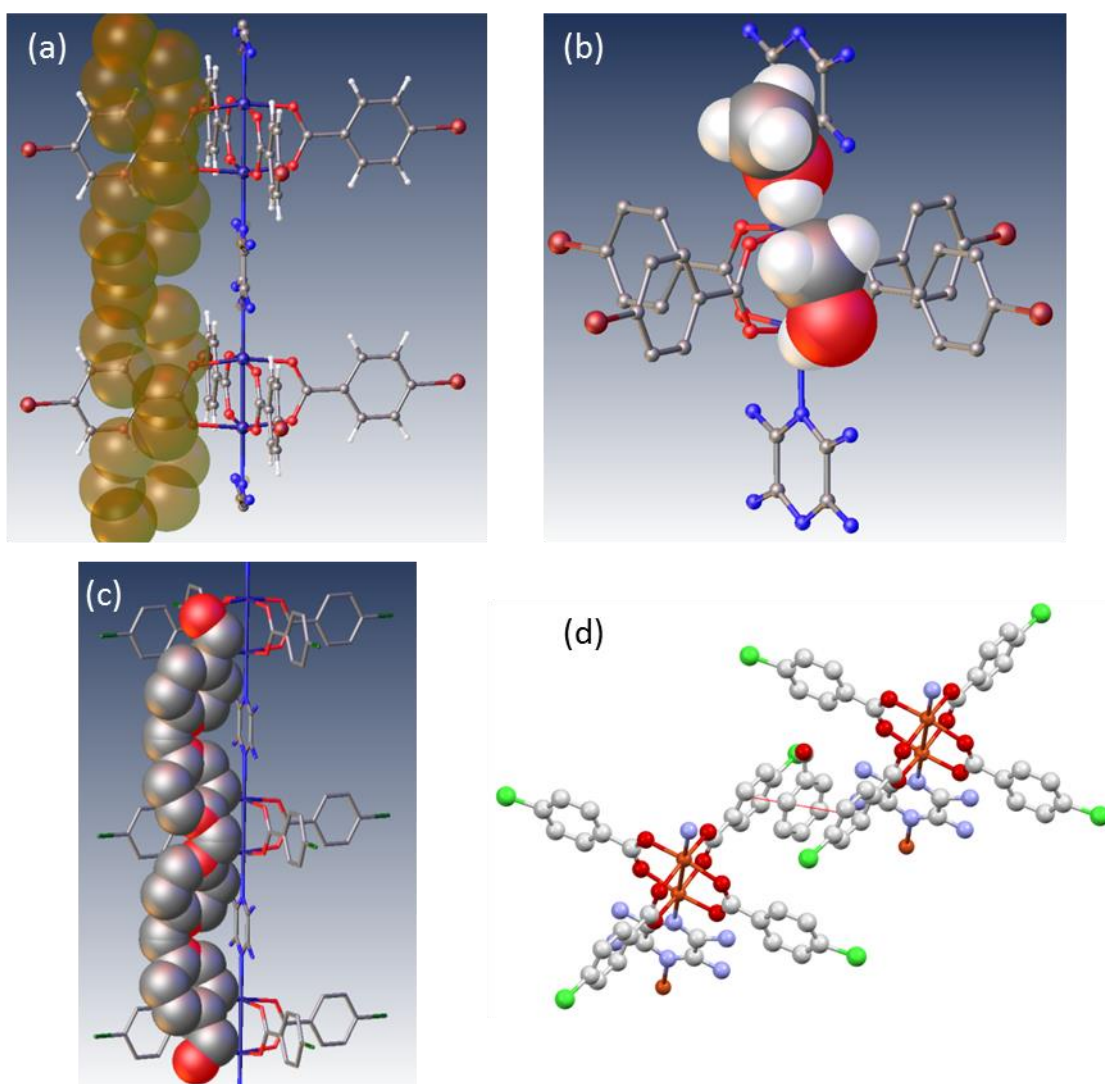


Figure 3.4.2-8. (a) Residual electron density peaks observed in **3.2(Br)-BnOH/MeOH**. Solvent modelling for (b) **3.2(Br)-DCM/MeOH** and (c) **3.3(Cl)-BnOH/MeOH**. (d) The π - π interaction between benzyl alcohol and benzoate ligands for **3.3(Cl)-BnOH/MeOH**. Colour scheme Cu, dark blue; O, red; C, grey; N, blue; Cl, green; Br, maroon; Residual electron density, brown (space filled); modelled solvent, space filled. Image (d) colour scheme consistent with **Figure 3.4.2-7**.

The residual electron density observed in **3.2(Br)-BnOH/MeOH** suggests a similar solvent disorder to that observed in **3.3(Cl)-BnOH/MeOH** (**Figure 3.4.2-8**) but could not be modelled. PLATON SQUEEZE^{13,14} was used to remove the contribution of this residual electron density. This resulted in the identification of a 423.8 Å³ solvent-accessible volume (21% of the cell volume) which contained 141 electrons per unit cell, roughly equivalent to one benzyl alcohol and one water molecule per paddlewheel unit.

Comparison of the void spaces determined by PLATON CALC VOID,^{13,14} when solvent content is not accounted for, reveals comparable void spaces in the interpenetrated solvate materials (**3.2(Br)-BnOH/MeOH**, **3.2(Br)-DCM/MeOH** and **3.3(Cl)-BnOH/MeOH**) (**Table 3.4.3-2**). This is lower than the 50 % of unit cell volume for the solvent-filled spaces in the two solvated forms of **3.1(I)**. The two solvent-free materials have smaller void spaces, with the smaller halogen (F)

have a larger void space than the larger halogen (Cl) (**3.3(Cl)** 136.0 Å³, 7.9 %; **3.4(F)** 176.7 Å³, 10.7 %). These void spaces are larger than observed for their pyrazine-containing analogues (**2.3(Cl)** 48.3 Å³; **2.4(F)** 67.1 Å³). Comparison of the solvated and solvent-free forms of **3.3(Cl)** also reveals a *ca.* 14 % increase in the extra-framework space (from 7.9 % to 21.5 %) when solvent is included, this being roughly comparable to the expansion observed for **2.3(Cl)** (Chapter 2).

Table 3.4.3-2. Determined solvent accessible void as determined by PLATON CALC VOID^{13,14}

	Space Group	Volume	Z	Probe Radius (Å)	Void Space (Å ³)	Percentage Void Space	Void Vol./Z (Å ³)
3.1(I)-BnOH/MeOH	<i>P4₁</i>	6329.0(4)	4	1.2	3291.2	52.0%	822.80
3.1(I)-DCM/MeOH	<i>P4/ncc</i>	12282.7(12)	8	1.2	6146.6	50.0%	768.33
3.1(Br)-BnOH/MeOH	<i>I2/m</i>	2001.68(13)	2	1.2	437.1	21.8%	218.55
3.1(Br)-DCM/MeOH	<i>I2/m</i>	2021.5(2)	2	1.2	441.4	21.8%	220.70
3.1(Cl)-BnOH/MeOH	<i>I2/m</i>	1934.5(5)	2	1.2	415.6	21.5%	207.80
3.1(Cl)-DCM/MeOH	<i>I2/m</i>	1712.19(11)	2	1.2	136.0	7.9%	68.00
3.4(F)-DCM/MeOH	<i>I2/m</i>	1655.92(11)	2	1.2	176.7	10.7%	88.35

In conclusion, **3.1(I)** was the only material in this family of coordination polymers, [Cu₂(4-Xbz)₄(NH₂pyz)]_n, which crystallised without interpenetration. The other three systems, **3.2(Br)**, **3.3(Cl)** and **3.7(F)**, adopt analogous packing to that observed in Chapter 2. This results in **3.2(Br)** losing the 2D halogen-bonding network observed in the pyrazine-containing analogue **2.2(Br)**. The absence of this 2D network may therefore affect the gate pressure for gas adsorption in this material. Synthesis by method 2 (DCM/MeOH) led to two coordination polymers without solvent inclusion (**3.3(Cl)** and **3.4(F)**) meaning harsh pre-treatment conditions will not be required for gas uptake studies.

3.4.3 Thermogravimetric Analysis

The seven coordination polymers were tested for desolvation by thermogravimetric analysis. There was a clear trend when comparing the materials obtained from the two synthetic methods. The materials containing benzyl alcohol (synthetic method 1) showed an initial mass loss followed by a plateau at 200 °C, the mass being attributed to loss of benzyl alcohol and methanol. Materials synthesised by method 2 (DCM/MeOH) show a small mass loss at a lower temperature due to the loss of methanol and dichloromethane which have lower boiling points than benzyl alcohol. This observation suggests that, of the two synthetic methods, method 2 (DCM/MeOH) is more suitable for producing materials which are easier to activate

for gas adsorption studies. Therefore the rest of this chapter will focus on materials produced by method 2.

The TGA analysis is discussed and presented in **Appendix 3.8.4**.

3.4.4 Desolvation studies

The potential for desolvation at ambient temperature was indicated in the preliminary PXRD phase purity checks of materials **3.1(I)** and **3.2(Br)** prepared by method 2 (DCM/MeOH). Sample preparation for PXRD by vacuum filtration and washing with methanol resulted transformation to an unknown phase, which may be a new desolvated phase. This was further supported by the small but facile mass loss observed in the TGA studies (Append 3.8.4).

Therefore preliminary desolvation studies of **3.1(I)-DCM/MeOH** and **3.2(Br)-DCM/MeOH** were conducted by removing crystals from the mother liquor and placing them on a glass slide for 1 h before being placed under oil. Single crystal diffraction measurements showed that **3.1(I)-DCM/MeOH** lost crystallinity. Data for a crystal of **3.2(Br)-DCM/MeOH** enabled unit cell dimensions to be determined and a partial structure solution.

The obtained unit cell for **3.2(Br)** has the same $I2/m$ space group as the solvated form and shows minimal change along the polymer chain ($\Delta b < 0.5\%$). There is a 5.3 % increase in the a -axis and a 22.6 % reduction in the c -axis lengths, accompanied by a $9.904(3)^\circ$ reduction in the β angle. This results in a 17.1 % reduction in the unit cell volume. The partial structure solution obtained (**Figure 3.4.2-2**) has a calculated powder pattern similar to that measured for the vacuum-filtered powder sample (noted in Section 3.3.3), which could be fitted to similar unit cell dimensions (**Figure 3.4.4-1**). This cell also is also metrically close to the tetragonal symmetry observed for the guest-free phase of **2.2(Br)** and **2.1(I)**, albeit with a unit cell four times larger in volume.

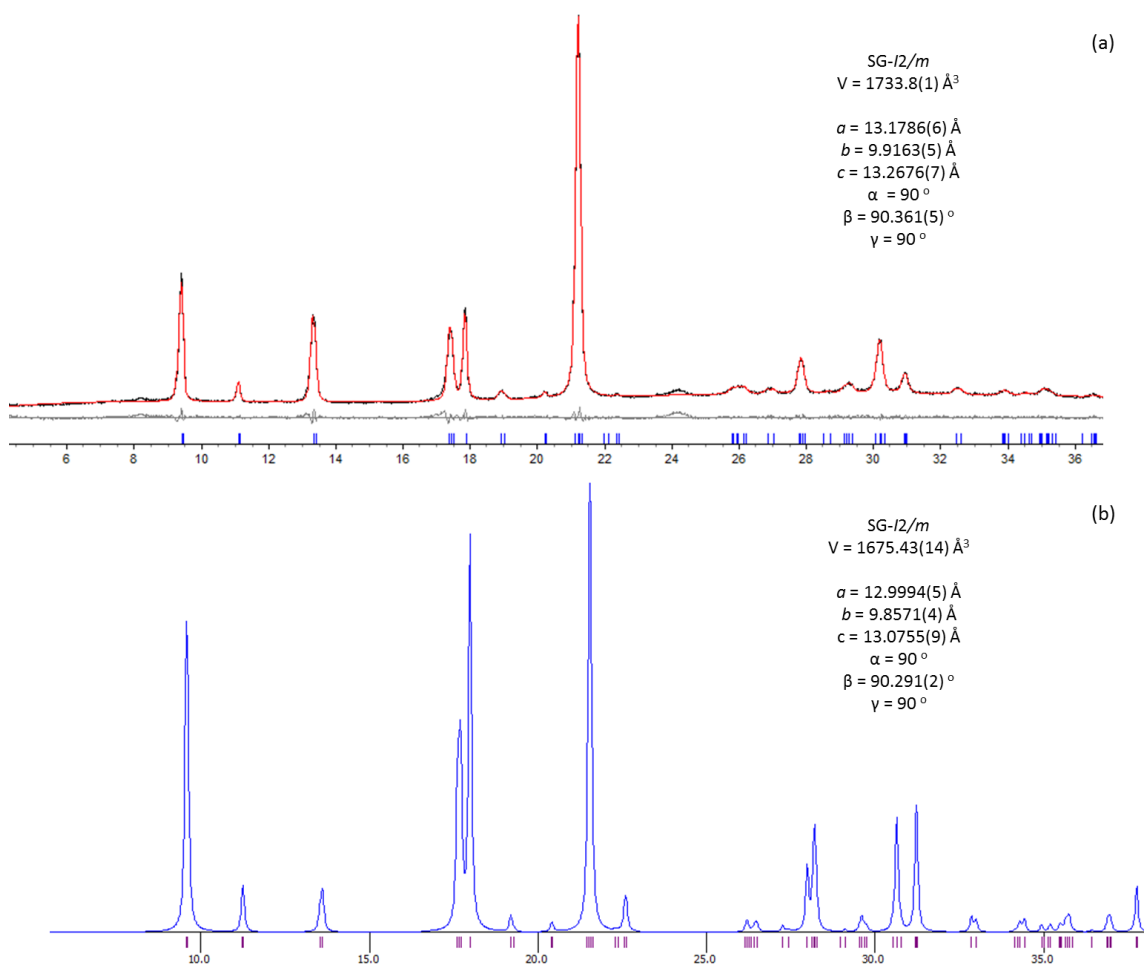


Figure 3.4.4-1. (a) Experimentally observed PXR D pattern of **3.2(Br)-DCM/MeOH** after vacuum filtration. (b) Calculated PXR D pattern from the partial single-crystal structure solution of **3.2(Br)** after desolvation in air, calculated in Mercury.¹⁵

Despite some loss of crystallinity it was possible to obtain a partial structure solution for the desolvated form of **3.2(Br)**. This showed significant positional disorder of the bromobenzoate ligands (**Figure 3.4.4-2**) resulting from two orientations of the ligands, one linear and one bent (*i.e.* rotated about the carboxylate O₂ vector). The benzoate orientations resemble the bent form observed in the solvent-free forms of **3.3(Cl)** and **3.4(F)**, which straighten in the solvent-included phase **3.3(Cl)-BnOH/MeOH**. The linear benzoate component is in close proximity to the amino group of the aminopyrazine suggesting correlated disorder of the aminopyrazine unit.

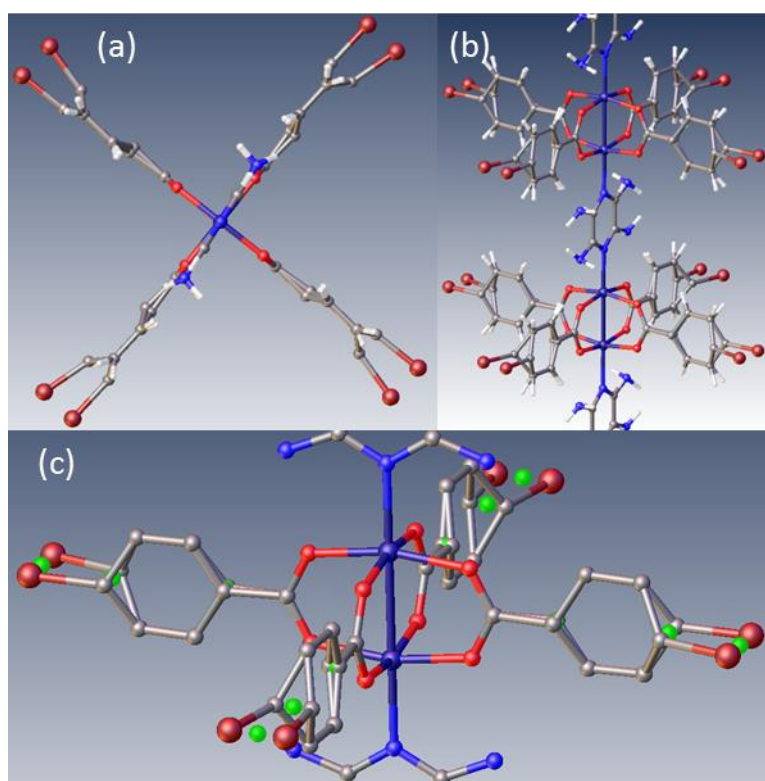


Figure 3.4.4-2. (a and b) observed disorder in **3.2(Br)** (produced by method 2 and left to dry). (c) Formula unit of **3.2(Br)** with calculated centroid in an attempt to average to disorder. Colour scheme Cu, blue; O, red; C, grey; Br, maroon; N, blue; H, white; centroid, green.

Loss of solvent leads to the reinstatement of the 2D C–Br \cdots π halogen-bonding network with C–Br \cdots C_{ipso} distances of 3.59(3) Å and 3.63(3) Å (**Figure 3.4.4-3**), accompanied by an antiparallel $\pi\cdots\pi$ interaction with bz_(cent) \cdots bz_(cent) distances of 5.02(2) Å and 4.88(2) Å. This phase also exhibits the same interpenetration as the solvated **3.2(Br)-DCM/MeOH** phase with a bz_(cent) \cdots NH₂pyz_(cent) distance of 4.735(14) Å at a C_{ipso} \cdots bz_(cent) \cdots NH₂pyz_(cent) angle of 133.8(12) ° and a C–Br \cdots NH₂pyz_(cent) distance of 4.166(10) Å at an C–Br \cdots NH₂pyz_(cent) angle of 76.3(13) ° (**Figure 3.4.4-3**). This is consistent with observations of the solvated and solvent-free phases of **3.3(Cl)** with the latter resulting in the C–X \cdots NH₂pyz_(cent) angle becoming more acute (Section 3.4.2).

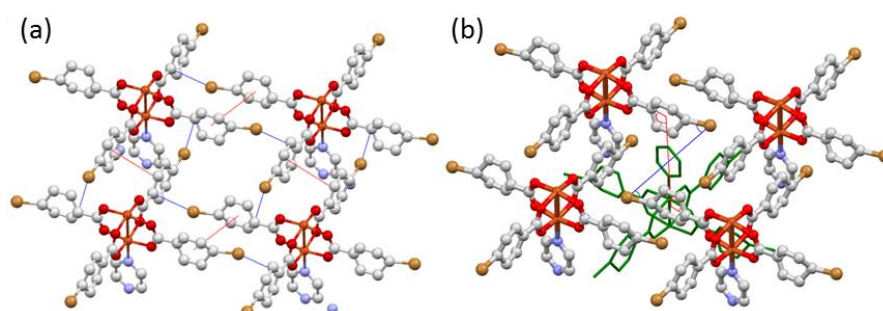


Figure 3.4.4-3. (a) 2D halogen-bonding network in the structure of desolvated **3.2(Br)** with the accompanied $\pi\cdots\pi$ interaction (network interpenetration not shown). $\pi\cdots\pi$ interaction, red dashed lines; C–Br \cdots C_{ipso}, blue dashed lines. (b) interpenetration of the desolvated **3.2(Br)** highlighting the angles C–Br \cdots NH₂pyz_(cent) (blue dashed lines) and C_{ipso} \cdots bz_(cent) \cdots NH₂pyz_(cent) (red dashed lines). Cu, orange; C, grey; O, red; N, blue; Br, brown; interpenetrated network, green (capped sticks).

3.4.5 Volumetric N₂ and CO₂ Gas Adsorption

Following the successful synthesis of the four target coordination polymers, [Cu₂(4-Xbz)₄(NH₂pyz)]_n, by method 2 (DCM/MeOH) N₂ and CO₂ volumetric adsorption analysis was carried out on each material.

It has been noted that when **3.1(I)** was filtered and washed with methanol the sample's crystallinity diminished (Section 3.3.3 and **Figure 3.4.5-1**) suggesting that the potential 50 % void space which would be generated by solvent loss is not sustained by the 2D halogen-bonding network.

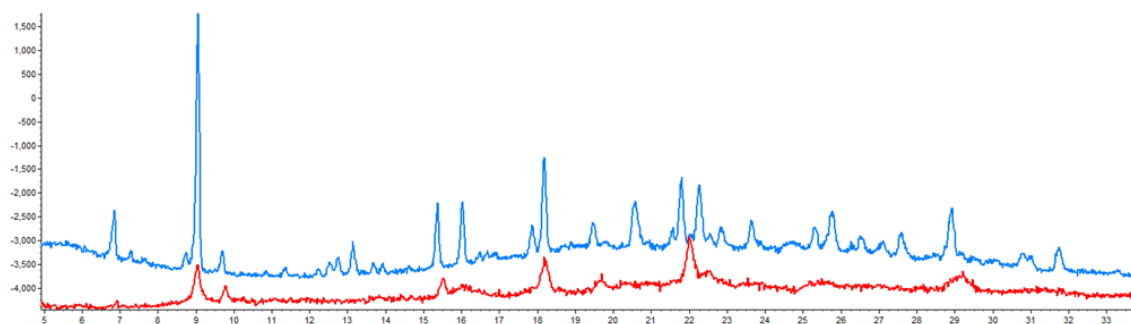


Figure 3.4.5-1. PXRD patterns of **3.1(I)** collected as a slurry (blue) and collected following filtering under vacuum (red), showing a significant loss of crystallinity.

This suggests that this material exhibits the behaviour of a 1st generation porous coordination polymer as discussed and reviewed by Kitagawa,⁴⁸ with the material undergoing an irreversible change upon removal of guest solvent. The coordination polymer **3.1(I)** was tested for volumetric adsorption of N₂ and CO₂ in order to confirm that the amorphous material was a 1st generation porous material. The volumetric N₂ study produced a type III isotherm⁴⁹ (**Figure 3.4.5-2**) suggesting a nonporous material, confirming 1st generation porous material behaviour for the inclusion of N₂.

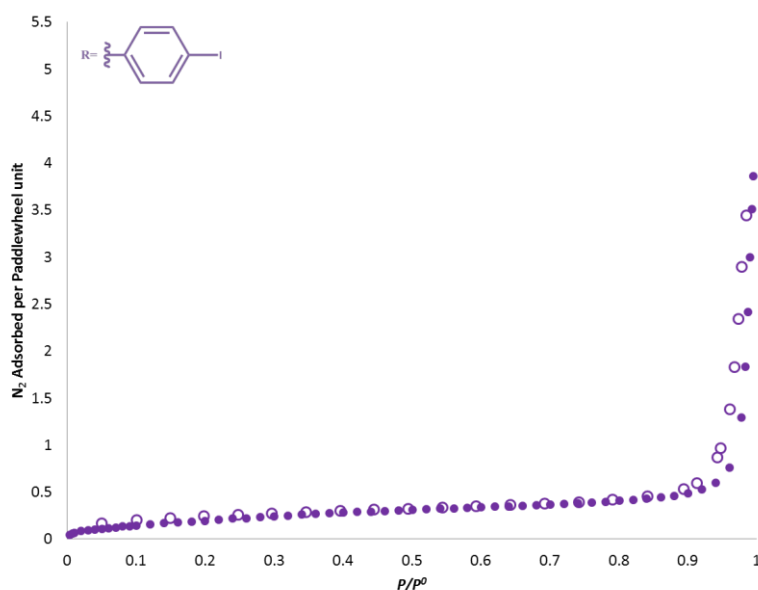


Figure 3.4.5-2. Volumetric N₂ isotherms for **3.1(I)** at 77 K (adsorption- solid circles, desorption-open circles).

The volumetric CO₂ adsorption studyⁱ resulted in a stepped (at a p/p^0 of 0.4) isotherm of type IV(a)⁴⁹ being observed (Figure 3.4.5-3) with a maximum inclusion of two CO₂ molecules per formula unit and a moderate hysteresis upon desorption. This would suggest that, with respect to CO₂, **3.1(I)** behaves as a 3rd generation porous material.⁴⁸ Comparison of the maximum uptake of CO₂ (2 CO₂ per formula unit) with that previously reported 2.75 CO₂ per formula unit for **2.2(Br)**, **2.3(Cl)**³⁵ and **2.4(F)** would suggest that the material does not possess the large 50 % potentially accessible void space, otherwise this maximum uptake would be much larger.

ⁱ Recorded on the same sample as the N₂ adsorption isotherm and performed before the N₂ study with PXRD pattern following CO₂ adsorption matching the pattern recorded following activation in the vacuum oven.

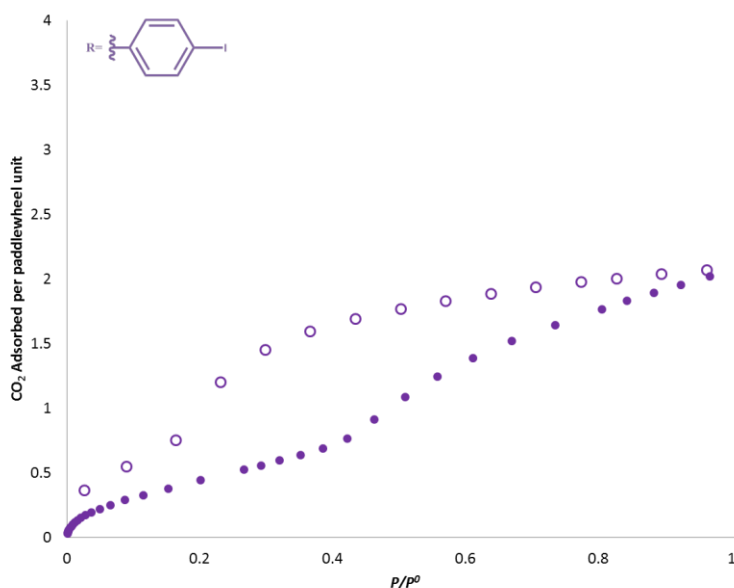


Figure 3.4.5-3. Volumetric CO₂ isotherms for **3.1(I)** at 195 K (adsorption- solid circles, desorption-open circles).

The volumetric N₂ and CO₂ⁱ adsorption analyses of **3.2(Br)** produced similar results, both producing a type V⁴⁹ isotherm. The change in uptake gradient, in both cases, occurred at relative pressure below p/p^0 of 0.1, suggesting the initially weak host-guest interactions are overcome at fairly low pressure. Both isotherms also display a hysteresis suggesting uniform pore shapes with the higher retention in the N₂ study maybe as a result of pores being blocked or tapered at the surface preventing guest desorption.⁴⁹ The maximum observed uptake for CO₂ and N₂ is 3.6 and 4.7 molecules per formula unit, suggesting larger void space than those observed in the pyrazine-containing analogues (2.75 CO₂ per formula unit observed for **2.2(Br)**, **2.3(Cl)**³⁵ and **2.4(F)**).

ⁱ Both N₂ and CO₂ adsorption analyses were carried out on the same sample with the CO₂ analysis carried out first. The sample was treated to the same degas procedure following CO₂ adsorption and before N₂ adsorption.

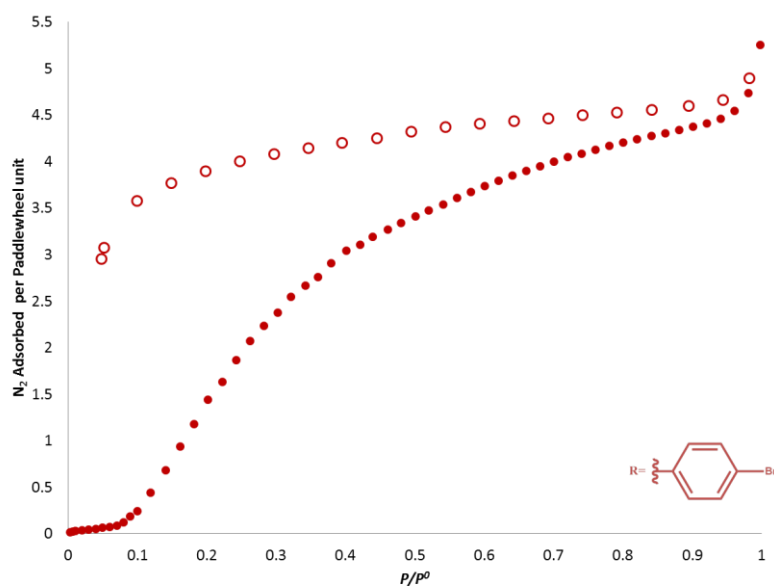


Figure 3.4.5-4. Volumetric N_2 isotherms for **3.2(Br)** at 77 K (adsorption- solid circles, desorption-open circles).

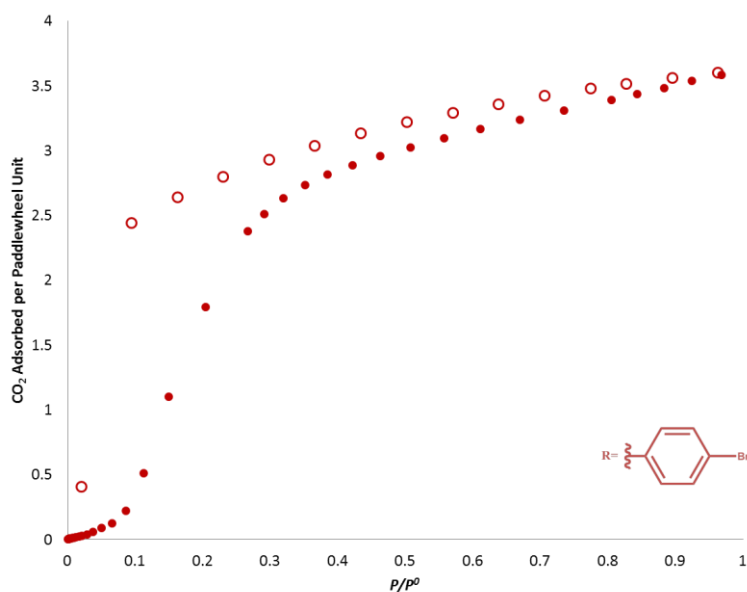


Figure 3.4.5-5. Volumetric CO_2 isotherms for **3.2(Br)** at 195 K (adsorption- solid circles, desorption-open circles).

Despite this hysteresis being observed in both volumetric studies the post-adsorption powder patterns do not contain additional peaks corresponding to a guest including phase. These patterns do however contain some unknown peaks (**Figure 3.4.5-6**). These unknown peaks were also observed, with smaller intensities, following the pre-treatment in vacuum oven prior to adsorption studies. This suggests partial degradation during pre-treatment. The small number of peaks meant that these peaks could not be indexed.

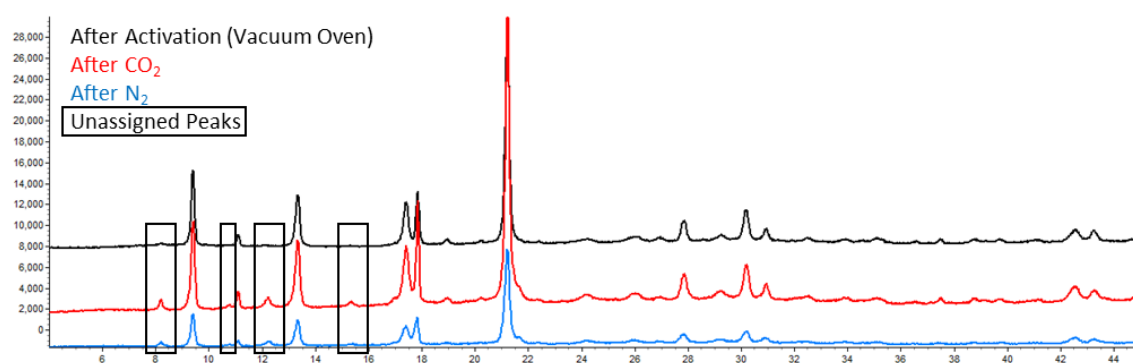


Figure 3.4.5-6. PXRD patterns of **3.2(Br)** after activation in the vacuum oven (black), following volumetric CO_2 adsorption/desorption (red) and following volumetric N_2 adsorption/desorption (blue). Black boxes highlighting the unassigned peaks.

The volumetric N_2 adsorption of **3.3(Cl)** resulted in a two-step isotherm, of type IV(a),⁴⁹ (**Figure 3.4.5-7**) with an initial small step observed at p/p^0 of 0.1 followed by a larger step at p/p^0 of 0.4. Desorption resulted in a hysteresis with only one step and retention of *ca.* two N_2 molecules per formula unit at the end of the analysis (p/p^0 0.05). This isotherm suggests cylindrical pores⁴⁹ similar to that proposed for **3.2(Br)** but the hysteresis possibly being as a result of pore blocking, preventing guest desorption.⁴⁹

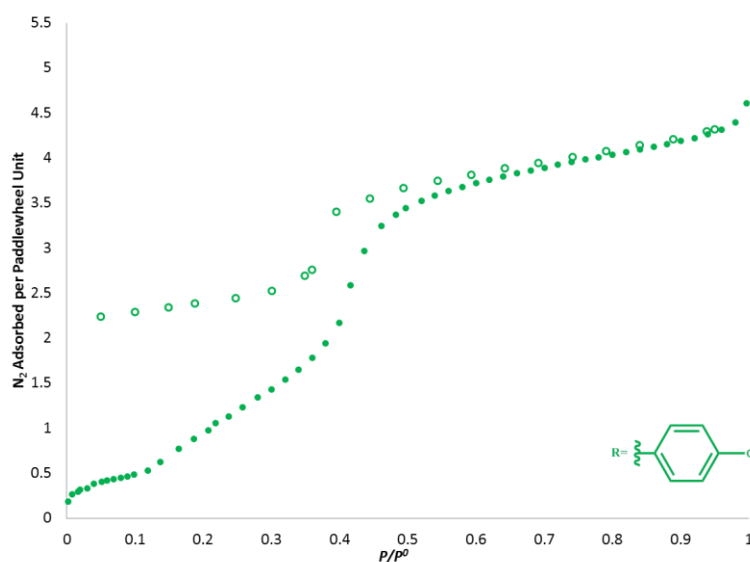


Figure 3.4.5-7. Volumetric N_2 isotherms for **3.2(Cl)** at 77 K (adsorption- solid circles, desorption-open circles).

The volumetric CO_2 analysisⁱ of **3.3(Cl)** resulted in a single-step isotherm, of type IV(b),⁴⁹ (**Figure 3.4.5-8**) with the step observed at p/p^0 of 0.1 and no hysteresis upon desorption (maximum uptake of three CO_2 molecules per formula unit). This type of isotherm suggests uniform cylindrical pores with tapered ends.⁴⁹ As previously observed for **3.2(Br)** a greater quantity of

ⁱ Performed on a different sample of **3.3(Cl)** than the N_2 adsorption.

N₂ (4.3 molecules per formula unit) than CO₂ (3 molecules per formula unit) was included. Adsorption of both gases is greater than observed for the pyrazine-containing analogue (**2.3(Cl)**, 2.75 CO₂ and 1.7 N₂ per formula unit).

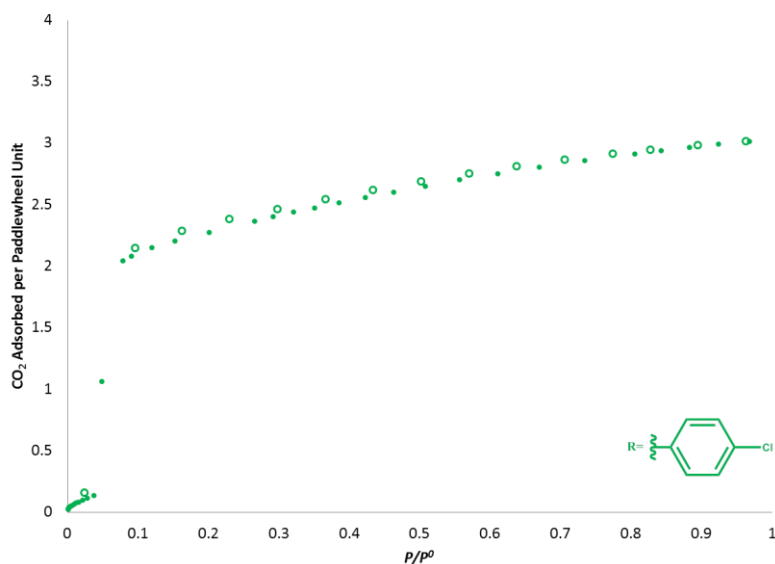


Figure 3.4.5-8. Volumetric CO₂ isotherms for **3.2(Cl)** at 195 K (adsorption- solid circles, desorption-open circles).

Finally, the volumetric N₂ adsorption study of **3.4(F)** (**Figure 3.4.5-9**) is analogous to that of the the pyrazine-containing analogue **2.4(F)**. The type IV(a)⁴⁹ isotherm indicates an initial adsorption of N₂ at very low pressure ($p/p^0 \approx 10^{-5}$) followed by a plateau and second step at p/p^0 of 0.4. This is accompanied by a hysteresis, during desorption, and a retention of *ca.* two N₂ molecules per formula unit. As with the N₂ adsorption study of **3.3(Cl)** this suggests cylindrical pores which are then obstructed during the desorption process.⁴⁹

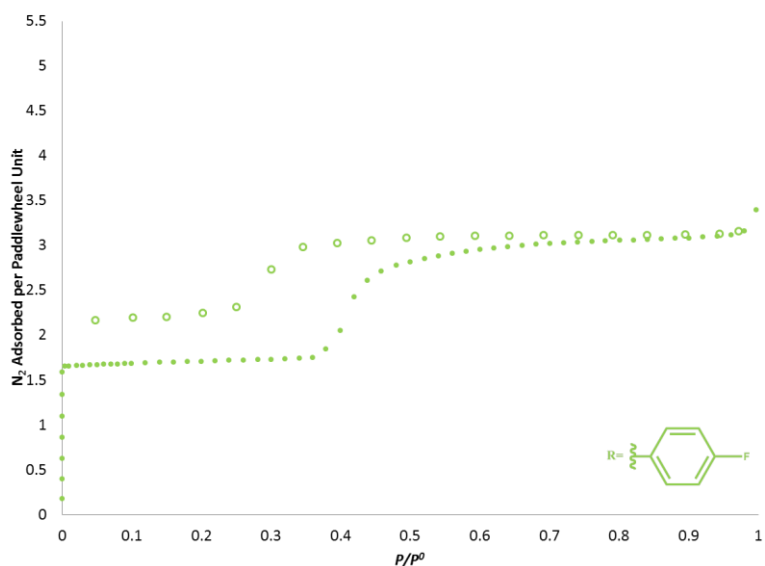


Figure 3.4.5-9. Volumetric N₂ isotherms for **3.4(F)** at 77 K (adsorption- solid circles, desorption-open circles).

The volumetric CO₂ adsorption studyⁱ of **3.4(F)** (Figure 3.4.5-10) shows a type I(b) isotherm⁴⁹ with no step. The large uptake at low p/p^0 suggests improved host-guest interaction within a narrow micro-pore. The isotherm displays no hysteresis suggesting that the pore blocking is only observed in the N₂ isotherm. The coordination polymer **3.4(F)** includes more CO₂ (3.65 molecules per formula unit) than N₂ (3.16 molecules per formula unit) contrary to that observed for **3.2(Br)** and **3.3(Cl)**. Maximum adsorption is greater for CO₂ but lower for N₂ when compared with the pyrazine-containing analogue **2.4(F)** (2.75 CO₂ and 3.75 N₂ molecules per formula unit).

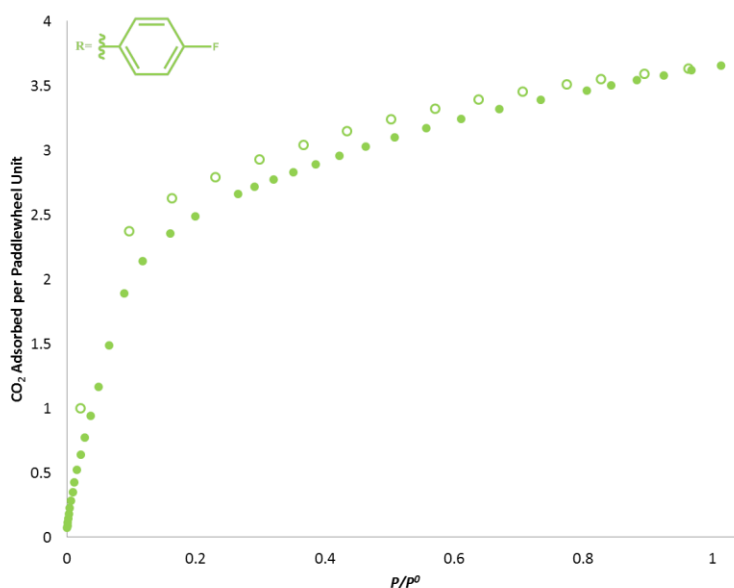


Figure 3.4.5-10. Volumetric CO₂ isotherms for **3.1(F)** at 195 K (adsorption- solid circles, desorption-open circles).

ⁱ Performed on a different sample to the N₂ adsorption study.

In conclusion the three interpenetrated coordination polymers **3.2(Br)**, **3.3(Cl)** and **3.4(F)** demonstrated uptake of both CO₂ and N₂ with two of the three (**3.2(Br)** and **3.3(Cl)**) showing a greater inclusion of N₂ than CO₂. The inclusion of CO₂ occurs at moderately low p/p^0 and a greater quantity is adsorbed in comparison to the pyrazine-containing analogues previously reported³⁵ and studied in Chapter 2. The presence of the NH₂ functionality has resulted in a shift (or removal) of the gate pressures observed in the parent pyrazine-containing materials. The presence of the NH₂ group also results in inclusion of N₂ in **3.2(Br)** which was not observed in the pyrazine-containing analogues.³⁵ The presence of the NH₂ group appears not obstruct the inclusion of CO₂ with all three NH₂pyz-containing coordination polymers (**3.2(Br)**, **3.3(Cl)** and **3.4(F)**), showing an increased uptake of CO₂ in comparison to the pyz-containing analogues (**2.2(Br)**, **2.3(Cl)** and **2.4(F)**). The coordination polymer **3.1(I)**, despite losing crystallinity upon filtration (and desolvation) does show inclusion of CO₂ suggesting the presence of pore spaces. It is, however, unclear whether the structure of this material is recovered in the presence of CO₂ or whether pore space is present in the predominantly amorphous state.

3.4.6 In situ Powder Diffraction and Single-Crystal Studies during CO₂ Adsorption/Desorption

3.4.6.1 Overview

In situ PXRD studies were carried out at a series increasing and decreasing pressures of CO₂ for compounds **3.2(Br)**, **3.3(Cl)** and **3.4(F)**. Samples were exposed to increasing and decreasing pressures of CO₂ allowing 25 min equilibration times between dosing and data acquisition. Single crystals of **3.3(Cl)** and **3.4(F)** were also exposed increasing and decreasing pressures of CO₂ in analogous *in situ* single-crystal diffraction studies. Details of the data processing and structure solutions are outlined in Section 3.3.7 (PXRD, Appendix 3.8.2) and Section 3.3.8 (single-crystal, Appendix 3.8.3). In this section, the changes in unit cell parameters are plotted as a function of relative pressure (p/p^0) are reported along with more detailed structural changes from the single-crystal diffraction studies.

Exposure to increasing CO₂ pressure resulted in a unit cell volume expansion for **3.2(Br)**, **3.3(Cl)** and **3.4(F)** (Figure 3.4.6-1), consistent with the CO₂ adsorption determined by volumetric analysis. Volume expansion for coordination polymer **3.2(Br)** ($\Delta V = 297.1(5) \text{ \AA}^3$, 17.4 %) occurs via a phase transformation and a full conversion to the expanded phase was not observed. Coordination polymer **3.3(Cl)** undergoes a similar phase transformation with a mixed-phase PXRD pattern observed at p/p^0 0.09, with only a small discrepancy between the total volume expansion for the single-crystal diffraction ($\Delta V = 234.3(8) \text{ \AA}^3$, 13.4 %, which expands as one phase) and PXRD ($\Delta V = 190.3(9) \text{ \AA}^3$, 11 %) studies. Coordination polymer **3.4(F)** exhibits gradual volume expansion with similar volume expansions determined for the single-crystal diffraction ($\Delta V = 143.8(5) \text{ \AA}^3$, 8.6 %) and PXRD ($\Delta V = 140.8(12) \text{ \AA}^3$, 8.4 %) studies. These phase transformations all retain the *I2/m* space group during exposure to CO₂.

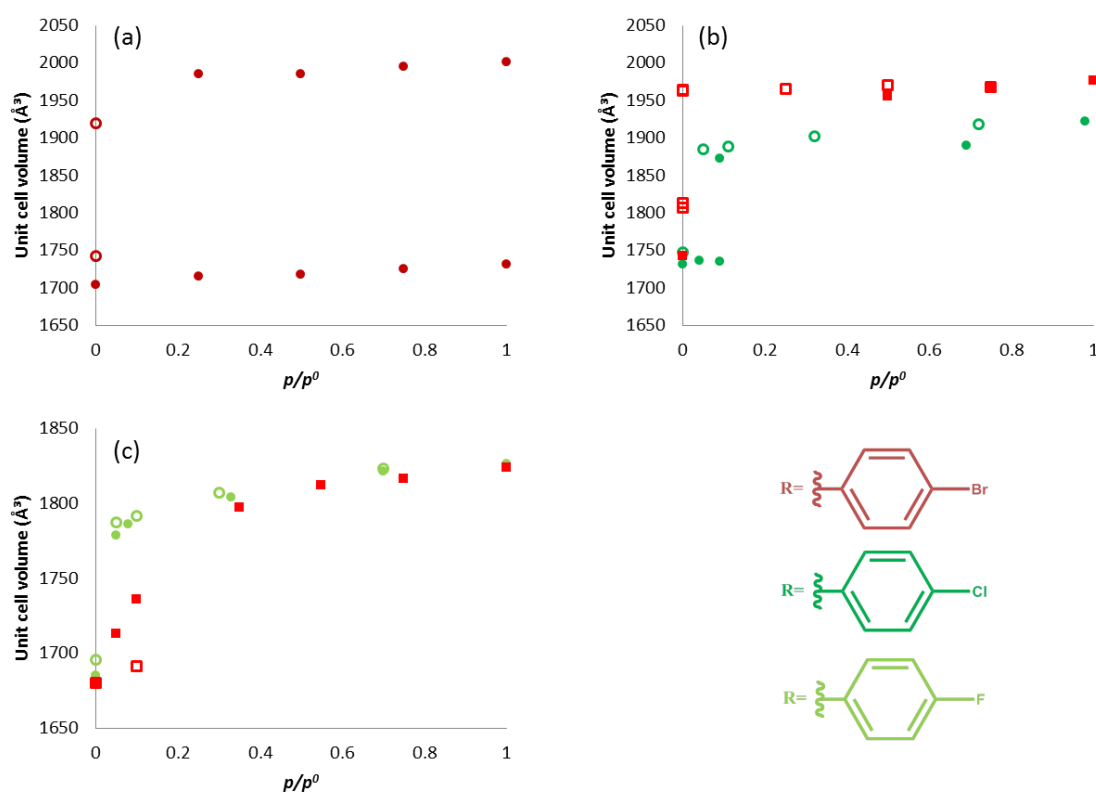


Figure 3.4.6-1. Change in unit cell volume as a function of relative CO_2 pressure (p/p^0) determined from powder diffraction (circles) and single-crystal diffraction (squares) studies for (a) **3.2(Br)**, (b) **3.3(Cl)** and (c) **3.4(F)**. Increasing pressure (filled shapes) and decreasing pressure (open shapes). Where two identical symbols are shown for a given relative pressure these refer to two phases.

3.4.6.2 Study of **3.2(Br)**

The *in situ* PXRD study for **3.2(Br)** initially showed the presence of peaks for an expanded phase at p/p^0 of 0.25 (**Figure 3.4.6-2**), with these peaks increasing in intensity as the CO_2 pressure was further increased. The presence of the expanded phase is consistent with the increasing uptake observed volumetrically at $p/p^0 < 0.1$. Despite the expanded phase being observed at low p/p^0 , the maximum conversion to this phase was of 55.7(9) % at p/p^0 1.0 (**Figure 3.4.6-2**).

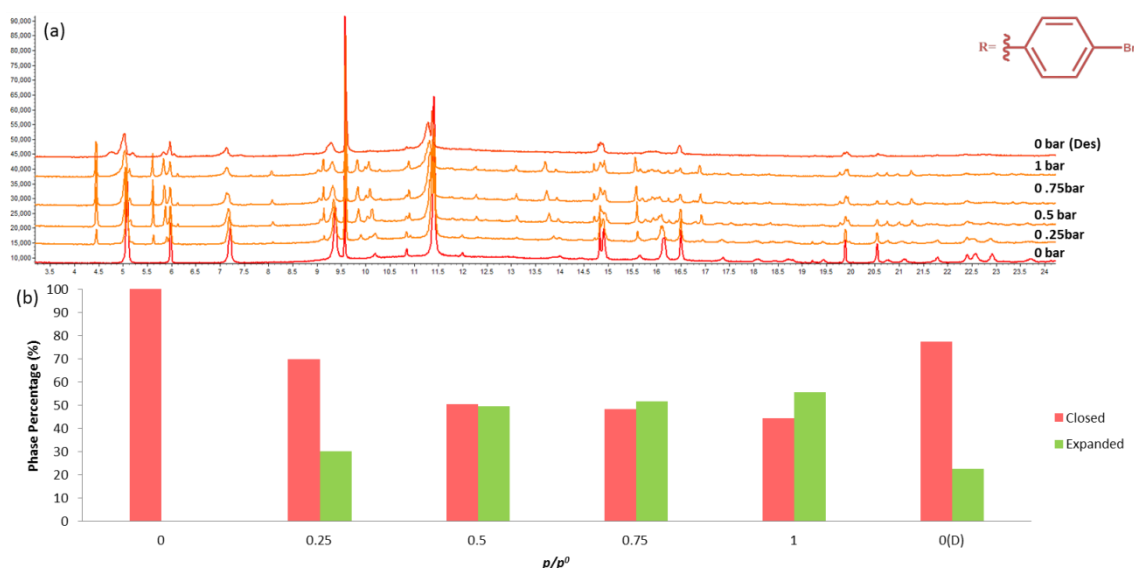


Figure 3.4.6-2. (a) Stacked PXRD patterns for **3.2(Br)** subjected to change in pressure of CO_2 . (b) Proportions of the closed (red) and expanded (green) phases at each pressure step determined by Rietveld refinement.³¹

The initial vacuum measurement of **3.2(Br)** revealed unit cell dimensions similar to the desolvated phase obtained by filtering under vacuum. Upon exposure to pressures of CO_2 an expanded phase was obtained. The expanded phase had similar unit cell dimensions to the solvated **3.2(Br)-DCM/MeOH** phase. The conversion between the closed phase and the expanded phase occurring by expansion of the c -axis ($\Delta c = 3.2553(26) \text{ \AA}$, 24.8 %) and a slight compression in the a -axis ($\Delta a = -0.6099(23) \text{ \AA}$, -4.6 %), but minimal change observed in the b axis ($\Delta b = -0.022(1) \text{ \AA}$, -0.2 %). The β angle also increases from $90.139(15)^\circ$ to $98.519(9)^\circ$. This behaviour is comparable to the pyrazine-containing analogues in Chapter 2 with the polymer chains moving apart and minimal compression or elongation of the polymer chains.

3.4.6.3 Studies of **3.3(Cl)**

Coordination polymer **3.3(Cl)** exhibited volume expansion upon increasing CO_2 pressure in both PXRD and single-crystal diffraction studies, presumed to be a result of CO_2 adsorption, with a marginally larger expansion being observed in the case of the single-crystal study. Large change in unit cell dimensions leading to a volume expansion occur at p/p^0 of 0.1, suggesting gated adsorption consistent with the volumetric adsorption data. The gate is evidenced by the mixed-phase powder pattern observed at p/p^0 of 0.09. Unfortunately, due to time constraints this gate pressure could not be probed in detail in the single-crystal study, but a similar change is observed between the initial vacuum measurement and the next pressure step at a p/p^0 of 0.5. Decreasing the CO_2 pressure highlights a slight discrepancy between the two studies. The PXRD study is consistent with the observed volumetric adsorption analysis with the volume returning to the original phase at a gate pressure p/p^0 0.05, *i.e.* small or negligible hysteresis. In the single-crystal study, on the other hand, the expanded phase is retained upon evacuation and only partially closes after evacuation (at room temperature) over a long duration (16.5 h). This suggests that the particle size affects the reversibility of this expansion. As previously observed for **3.2(Br)** and the pyrazine-containing materials discussed in Chapter 2 this volume expansion can be attributed to the changes in axes and angle (a -axis,

c -axis and β -angle) perpendicular to the direction of polymer propagation (the b -axis) (**Figure 3.4.6-3**).

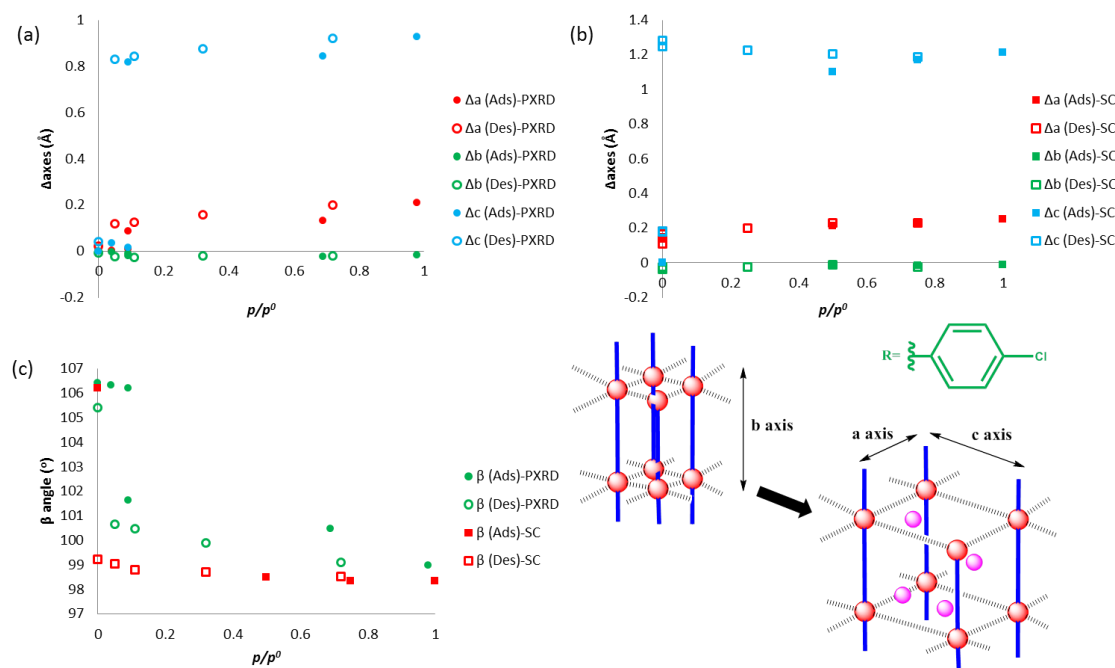


Figure 3.4.6-3. (a) Changes in unit cell axes vs p/p^0 (CO₂) (a) from PXRD study of **3.3(Cl)** and (b) from single-crystal diffraction study of **3.3(Cl)**. (c) Change in β -angle vs p/p^0 (CO₂) from single-crystal (squares) and powder (circles) diffraction studies. Increasing (filled shapes) and decreasing (empty shapes) pressure of CO₂.

The single-crystal diffraction study provides a more detailed picture of the structural changes that occur during the CO₂ adsorption. Similar changes are observed on guest inclusion to those of the pyrazine-containing coordination polymers described in Chapter 2. The volume expansion on CO₂ uptake is also accompanied with the straightening of the carboxylate ligand (i.e. rotation about the carboxylate O₂ vector) (**Figure 3.4.6-4**) with the straightened benzoate configuration being maintained upon desorption. Unfortunately storing the crystal under vacuum for a prolonged period (16.5 h) resulted in degradation of the sample such that although unit cell dimensions could be determined a full structure solution could not be obtained. It has therefore not been established that the benzoates rotate back to their original orientation, but considering the observations from Chapter 2, this is likely to be the case.

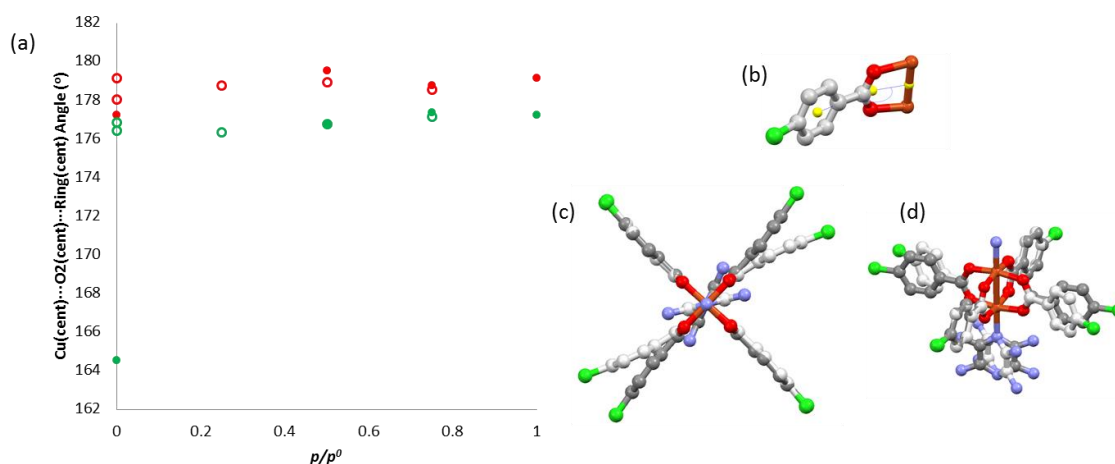


Figure 3.4.6-4. (a) Change in $\text{Cu}_{2(\text{cent})}\cdots\text{O}_{2(\text{cent})}\cdots\text{Ring}_{(\text{cent})}$ angle as a function of relative CO_2 pressure (p/p^0), from single-crystal structures of **3.3(Cl)** determined at increasing (filled circles) and decreasing (empty circles) pressures. (b) Definition of $\text{Cu}_{2(\text{cent})}\cdots\text{O}_{2(\text{cent})}\cdots\text{Ring}_{(\text{cent})}$ angle. (c and d) overlays of the structures determined for initial vacuum measurement (C, light grey) and 1 bar CO_2 (C, dark grey). Other colours consistent with **Figure 3.4.2-7**.

The interactions between polymer chains also exhibit similar changes to those of the pyrazine-containing analogues. There is a reduction in the $\text{C}-\text{Cl}\cdots\pi$ distance for the chlorines involved in the 1D halogen-bonding chain and expansion of the $\text{C}-\text{Cl}\cdots\pi$ distance larger the sum of van der Waals radii^{36,37} (**Figure 3.4.6-5**). Similarly the accompanying $\pi\cdots\pi$ interaction is compressed or elongated in a similar fashion (**Figure 3.4.6-5**). This demonstrates that the polymer chains maintain a 1D halogen-bonding network but move apart from one another in the remaining direction (**Figure 3.4.6-5**).

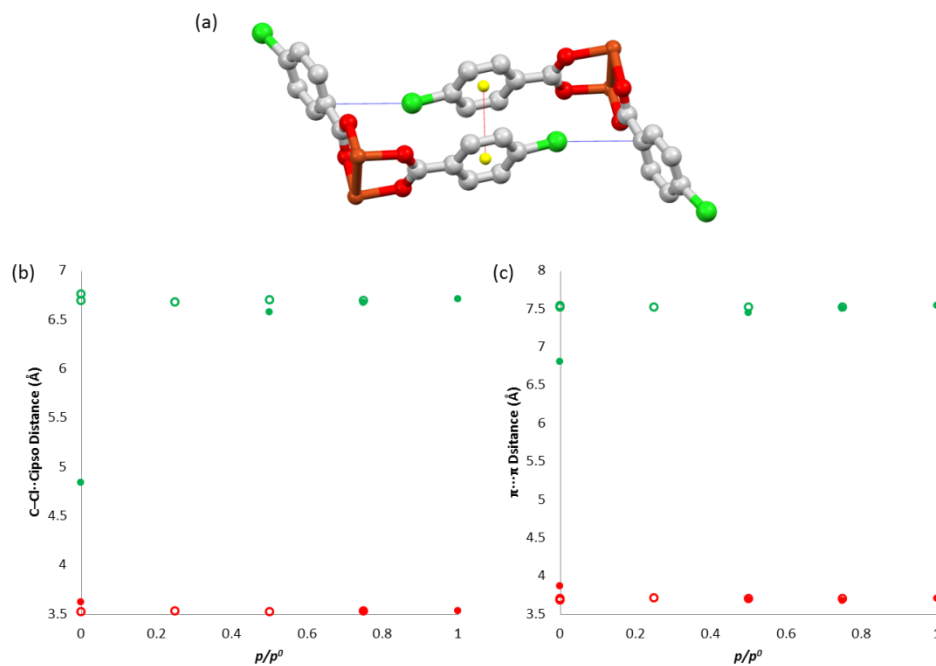


Figure 3.4.6-5. (a) Definition of $\text{C}-\text{Cl}\cdots\text{C}_{\text{ipso}}$ distance (blue dashed lines) and $\text{bz}_{(\text{cent})}\cdots\text{bz}_{(\text{cent})}$ distance (red dashed lines) (b) $\text{C}-\text{Cl}\cdots\text{C}_{\text{ipso}}$ distance vs p/p^0 (CO_2). (c) $\text{bz}_{(\text{cent})}\cdots\text{bz}_{(\text{cent})}$ distance vs p/p^0 (CO_2). Increasing (filled circles) and decreasing (empty circles) pressures of CO_2 . Colour scheme consistent with **Figure 3.4.2-7**, centroids; yellow spheres.

As speculated in Section 3.4.2, the inclusion of a guest (in this case CO₂) results in changes in the distances and angles between interpenetrated chains. Increase in CO₂ pressure results in the $\text{bz}_{(\text{cent})}\cdots\text{NH}_2\text{pyz}_{(\text{cent})}$ distance increasing while the $\text{C}-\text{Cl}\cdots\text{NH}_2\text{pyz}_{(\text{cent})}$ distance decreases (Figure 3.4.6-6) accompanied by the both angles ($\text{C}_{\text{ipso}}\cdots\text{bz}_{(\text{cent})}\cdots\text{NH}_2\text{pyz}_{(\text{cent})}$ and $\text{C}-\text{Cl}\cdots\text{NH}_2\text{pyz}_{(\text{cent})}$) increasing with the $\text{C}-\text{Cl}\cdots\text{NH}_2\text{pyz}_{(\text{cent})}$ angle approaching 90°. This motion is consistent with the sliding apart of polymer chains observed for the analogous coordination polymers discussed in Chapter 2.

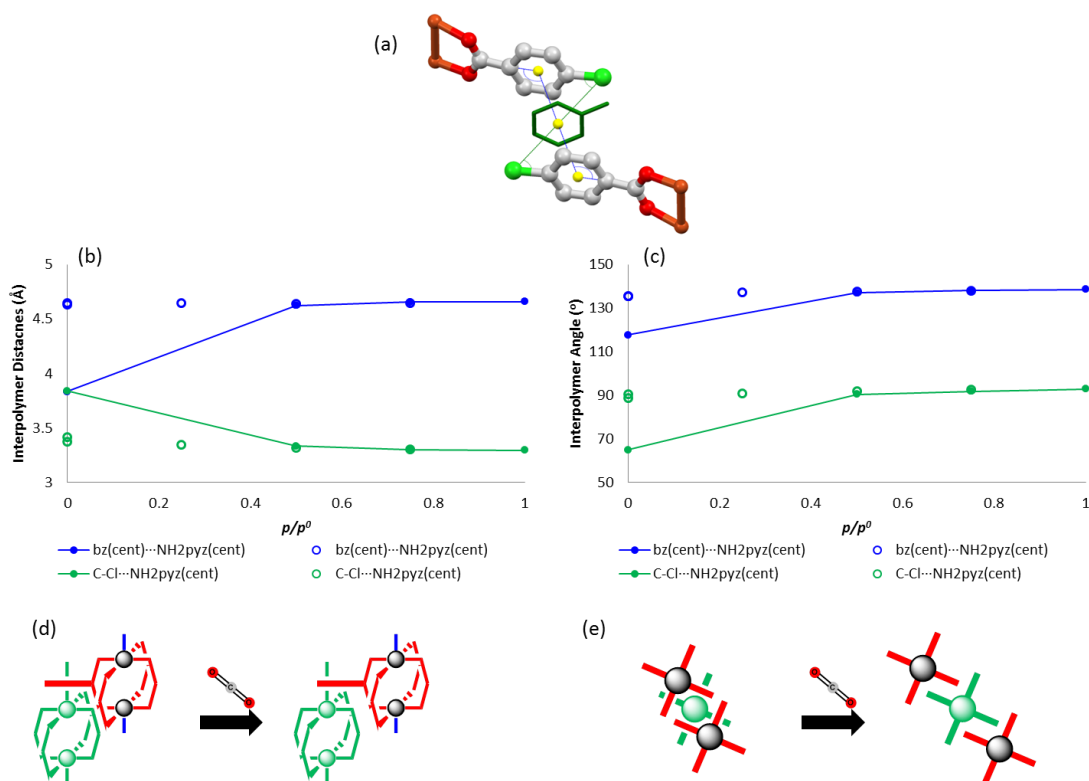


Figure 3.4.6-6. (a) Definitions of $\text{C}_{\text{ipso}}\cdots\text{bz}_{(\text{cent})}\cdots\text{NH}_2\text{pyz}$ angle (blue) and $\text{C}-\text{Cl}\cdots\text{NH}_2\text{pyz}_{(\text{cent})}$ angle (green). (b) $\text{bz}_{(\text{cent})}\cdots\text{NH}_2\text{pyz}_{(\text{cent})}$ distance (blue) and $\text{C}-\text{Cl}\cdots\text{NH}_2\text{pyz}_{(\text{cent})}$ distance (green) vs p/p^0 (CO₂) for **3.3(Cl)**. (c) $\text{C}_{\text{ipso}}\cdots\text{bz}_{(\text{cent})}\cdots\text{NH}_2\text{pyz}_{(\text{cent})}$ angle (blue) and $\text{C}-\text{Cl}\cdots\text{NH}_2\text{pyz}_{(\text{cent})}$ angle (green) vs p/p^0 (CO₂) for **3.3(Cl)**. Increasing (filled circles) and decreasing (empty circles) pressures of CO₂. (d) Schematic showing movement apart of interpenetrated polymer chains (red and green) on CO₂ and (e) alternative view.

3.4.6.4 Studies of 3.4(F)

The gradual volume expansion observed for **3.4(F)** (determined from both single-crystal diffraction and PXRD) is consistent with the volumetric CO₂ adsorption analysis presented in Section 3.4.5. The mode of expansion is consistent with those observed for **3.2(Br)**, **3.3(Cl)** and for the materials discussed in Chapter 2. This expansion occurs through increases in the α - and c -axes accompanied by a reduction in the β -angle and minimal change in the b -axis (Figure 3.4.6-7), characteristic of polymer chains moving apart due to CO₂ adsorption rather than being compressed due to external CO₂ pressure.

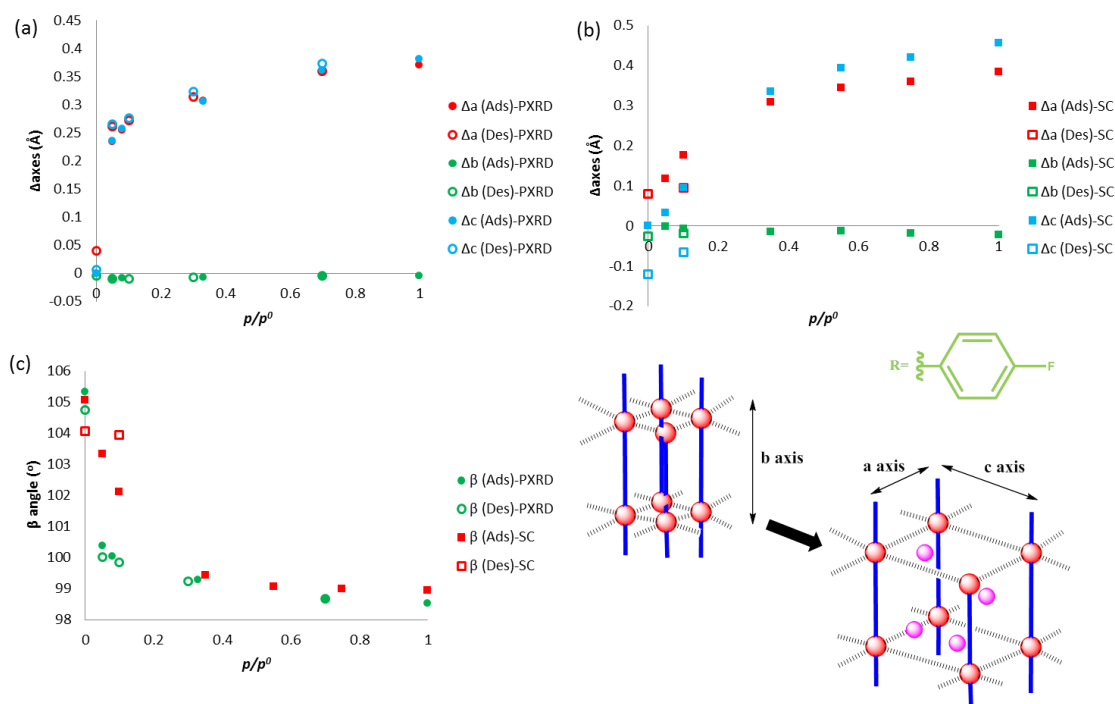


Figure 3.4.6-7. (a) Changes in unit cell axes vs p/p^0 (CO_2) (a) from PXRD study of **3.4(F)** and (b) from single-crystal diffraction study of **3.4(F)**. (c) Change in β -angle vs p/p^0 (CO_2) from single-crystal (squares) and powder (circles) diffraction studies. Increasing (filled shapes) and decreasing (empty shapes) pressure of CO_2 .

In both the PXRD and single-crystal diffraction studies of **3.4(F)**, reducing the pressure of CO_2 resulted in a gradual reduction in the unit cell volume, consistent with the absence of hysteresis observed in the volumetric analysis. Structure solution from the single-crystal data revealed the same structural trends observed for **3.3(Cl)** and for the pyrazine-containing analogues described in Chapter 2. This rotation of the benzoate ligands about the O_2 carboxylate vector leads to straightening of their orientation with increases in CO_2 pressure. This is reversed upon reducing CO_2 pressure (desorption) (**Figure 3.4.6-8**).

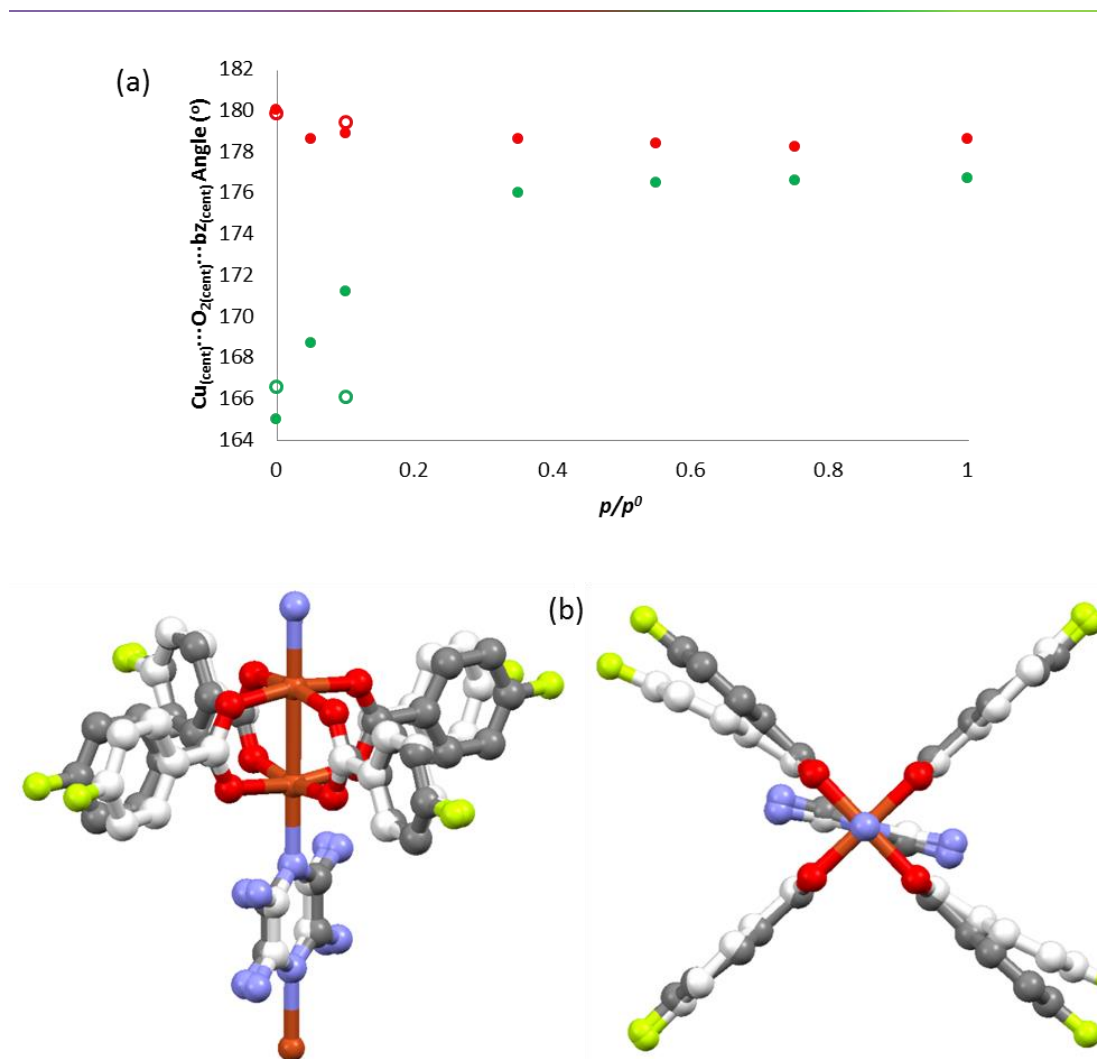


Figure 3.4.6-8. (a) Changes in $\text{Cu}_{2(\text{cent})}\cdots\text{O}_{2(\text{cent})}\cdots\text{bz}_{(\text{cent})}$ angle vs p/p^0 (CO_2). Increasing (filled circles) and decreasing (empty circles) pressures. (b) Overlays of the structures determined for initial vacuum measurement (C, light grey) and at 1 bar CO_2 (C, dark grey). Other colours consistent with **Figure 3.4.2-7**.

Again, analogous to that observed for **3.3(Cl)** and the materials in Chapter 2, the shorter $\text{C}-\text{F}\cdots\text{C}_{\text{ipso}}$ distance, accompanied by a $\pi\cdots\pi$ interaction, decreases and the longer $\text{C}-\text{F}\cdots\text{C}_{\text{ipso}}$ distance, where the $\pi\cdots\pi$ interaction is offset, increases (**Figure 3.4.6-9**). The neighbouring offset chains slide apart on CO_2 uptake (**Figure 3.4.6-10**). This results in an increase in the $\text{C}_{\text{ipso}}\cdots\text{bz}_{(\text{cent})}\cdots\text{NH}_2\text{pyz}_{(\text{cent})}$ distance and angle and a decrease in the $\text{C}-\text{F}\cdots\text{NH}_2\text{pyz}_{(\text{cent})}$ distance with the $\text{C}-\text{F}\cdots\text{NH}_2\text{pyz}_{(\text{cent})}$ angle approaching 90° (**Figure 3.4.6-10**).

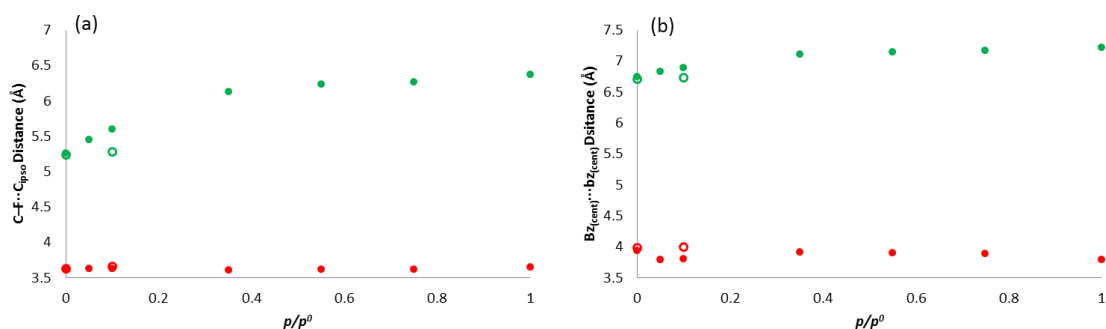


Figure 3.4.6-9. (a) $\text{C-F}\cdots\text{C}_{\text{ipso}}$ distance and (b) $\text{bz}_{(\text{cent})}\cdots\text{bz}_{(\text{cent})}$ distance vs p/p^0 (CO_2) for **3.4(F)**. Increasing (filled circles) and decreasing (empty circles) pressures CO_2 .

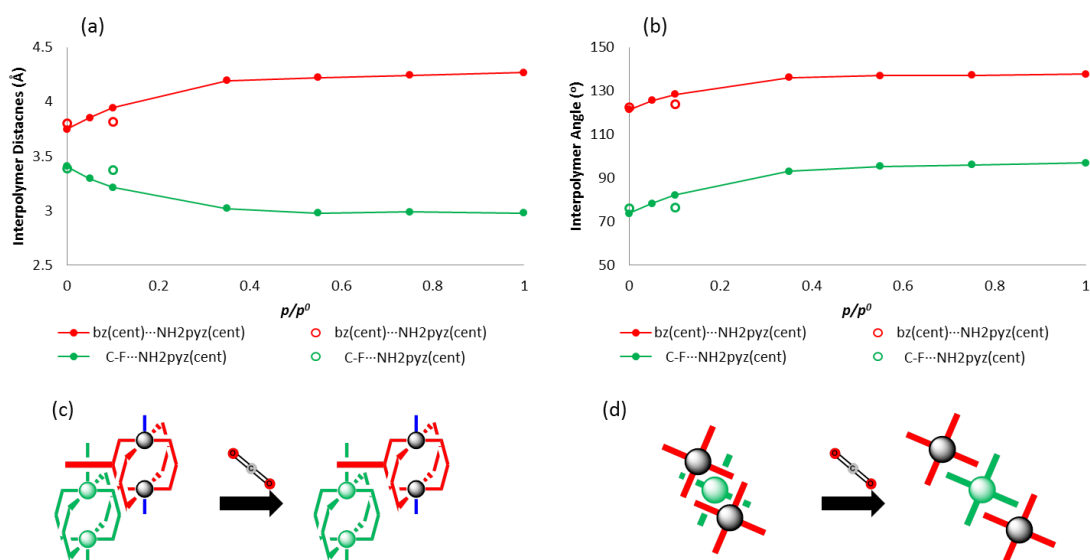


Figure 3.4.6-10. (a) $\text{bz}_{(\text{cent})}\cdots\text{NH}_2\text{pyz}_{(\text{cent})}$ distance (red) and $\text{C-F}\cdots\text{NH}_2\text{pyz}_{(\text{cent})}$ distance (green) vs p/p^0 (CO_2) for **3.4(F)**. (b) $\text{C}_{\text{ipso}}\cdots\text{bz}_{(\text{cent})}\cdots\text{NH}_2\text{pyz}_{(\text{cent})}$ angle (red) and $\text{C-F}\cdots\text{NH}_2\text{pyz}_{(\text{cent})}$ angle (green) vs p/p^0 (CO_2) for **3.4(F)**. Increasing (filled circles) and decreasing (empty circles) pressures of CO_2 . (c) Schematic showing movement apart of interpenetrated polymer chains (red and green) on CO_2 uptake and (d) alternative view.

3.4.6.5 Summary

In conclusion it has been successfully demonstrated that these polymers behave consistently to the volumetric studies and in a consistent fashion to the previously discussed pyrazine-containing analogues (**2.2(Br)**, **2.3(Cl)** and **2.4(F)**). The unit cell volume expansions (**3.2(Br)** 17.4 %, **3.3(Cl)** 13.4 and 11.0 % for single-crystal diffraction and PXRD studies, respectively and **3.4(F)** 8.6 % and 8.4 % for single-crystal diffraction and PXRD studies, respectively) are consistent for single-crystal diffraction and PXRD studies as well as comparable to the unit cell volume expansions for the pyrazine-containing analogues (**2.2(Br)** 13.9 %, **2.3(Cl)** 11.0 % and **2.4(F)** 2.5 % for the PXRD studies). The unit cell volumes expansion are also slightly larger than the expansions reported for $[\text{Cu}_2(\text{bz})_4(\text{pyz})]_n$ ($\Delta V = 6.38$ % at 293 K⁵⁰ and 7.29 %³ at 90 K). Increased pressure of CO_2 results in the polymer chains moving apart from one another with no compression or elongation of the coordination polymers. Minor structural changes of the polymer were also observed with increasing (and decreasing) CO_2 pressures with straightening of the benzoates ligands.

3.4.7 *In situ* Powder and Single-Crystal Diffraction Studies during N₂ Adsorption/Desorption

3.4.7.1 Overview

In situ single-crystal diffraction and PXRD studies were carried out at a series of increasing and decreasing pressures of N₂ for compounds **3.3(Cl)** and **3.4(F)**. Samples were exposed to successive increasing (and decreasing) pressures of N₂ allowing 30 min equilibration times between dosing and data acquisition. These studies could not be recorded at the same temperature as the volumetric adsorption analysis (77 K). Therefore data acquisition was undertaken at the lowest accessible temperature (90 K) and pressure steps were selected to cover the same relative pressure range ($0 \leq p/p^0 \leq 1$). Details of the data processing and structure solutions are outlined in Section 3.3.7 (PXRD, Appendix 3.8.2) and Section 3.3.8 (single-crystal, Appendix 3.8.3). In this section, the changes in unit cell parameters will be expressed as a function of relative pressure (p/p^0) are reported.

The PXRD studies determined that unit cell volume expansion occurs for **3.3(Cl)** and **3.4(F)** upon increased N₂ pressure (Figure 3.4.7-1). Coordination polymer **3.3(Cl)** displayed this expansion via a two-step phase transformation with diffraction peaks for an initial expanded phase ($\Delta V = 127.1(2) \text{ \AA}^3$, 7.4 %) growing in from p/p^0 of 0.1 followed by a second expanded phase ($\Delta V = 181.7(1) \text{ \AA}^3$, 10.6 %) initially observed at p/p^0 of 0.8. Coordination polymer **3.4(F)**, however, exhibited an overall 8.2 % expansion ($\Delta V = 136.8(1) \text{ \AA}^3$) indicated by a gradual shifting of peak positions. The single-crystal diffraction studies of both **3.3(Cl)** and **3.4(F)** demonstrated minimal volume change with increased N₂ pressure ($\Delta V = -0.8(2) \text{ \AA}^3$, -0.04% and $\Delta V = 9.0(2) \text{ \AA}^3$, -0.54 % for **3.3(Cl)** and **3.4(F)** respectively). This would suggest that the rate of diffusion of N₂ into these materials is affected by the particle size, a phenomenon that has been previously reported in MOFs and 2D soft porous crystals.^{51,52}

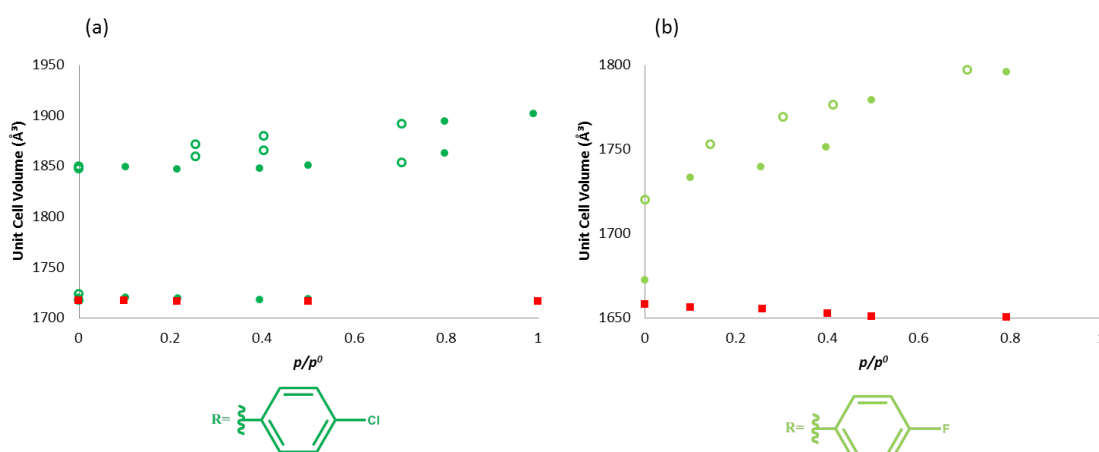


Figure 3.4.7-1. Unit cell volume vs p/p^0 (N₂) from single-crystal diffraction (red squares) and PXRD (green circles) studies of (a) **3.3(Cl)** and (b) **3.4(F)** subjected to increasing (filled shapes) and decreasing (empty shapes) pressures of N₂. Where two identical symbols are shown for a given pressure these refer to two phases.

3.4.7.2 Studies of 3.3(Cl)

The structural transformations of **3.3(Cl)** identified from the PXRD study occur at comparable relative pressures (p/p^0) to the steps observed in the volumetric N_2 adsorption analysis. The material undergoes two phase transformations with an initial partially expanded phase first being observed at p/p^0 of 0.1 ($p = 0.35$ bar) requiring patterns to be fitted as two-phase (closed and partially expanded). Upon increasing N_2 pressure, a new phase is observed, initially at a p/p^0 0.8 (2.79 bar), which becomes the single phase at p/p^0 1 (3.5 bar). On reduction of N_2 pressure, the material reforms the partially expanded phase which is retained upon return to vacuum. Conversion of the structure to the original closed form occurs for some of the materials after being exposed to vacuum (at room temperature) for long durations (12-17 h) (**Figure 3.4.7-2**). Inspection of the fits reveals a significant broadening of $h0l$ peaks (**Figure 3.4.7-2**) which was often not adequately described in the fit. This suggests that the $h0l$ planes have variable spacing, suggesting that the a - and c -axis lengths maybe better described as a continuum of values across the crystallites presents in the sample.

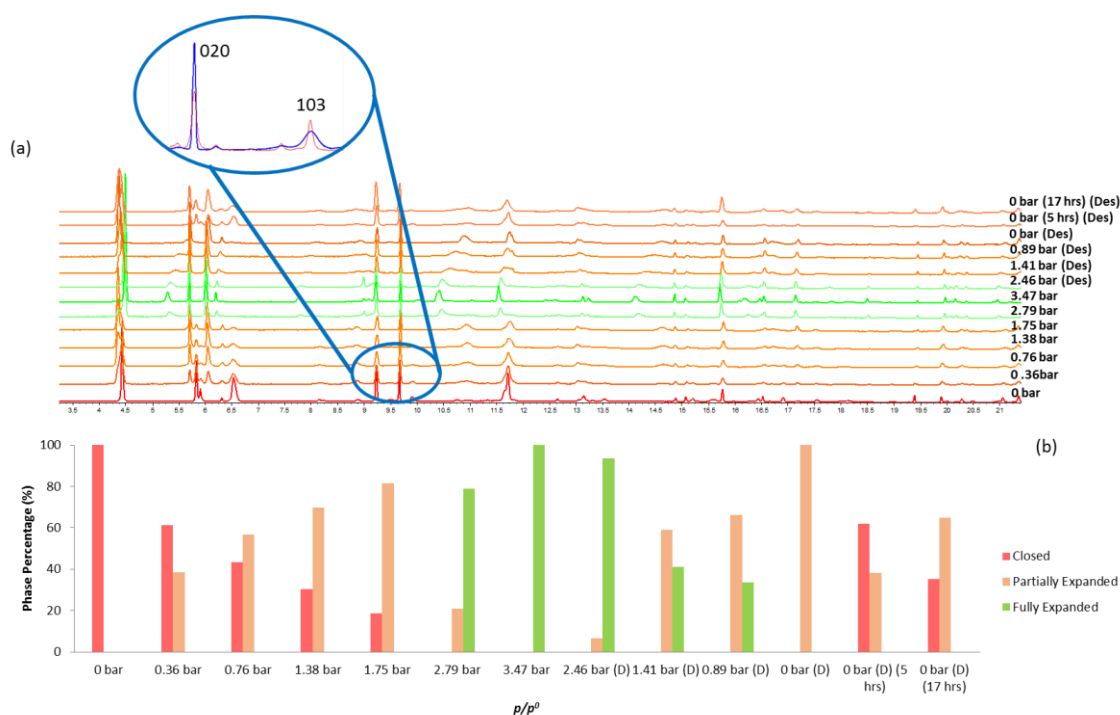


Figure 3.4.7-2. (a) Stacked PXRD patterns for **3.3(Cl)** subjected to increasing (and decreasing) pressures of N_2 , (inset: highlighting the observed broadening of $h0l$ peaks by comparison of the sharp 020 peak (on the left) with the broader 103 (on the right); experimental data in blue and fit in red). (b) Proportion of the closed (red), partially expanded (orange) and fully expanded (green) phases determined by Rietveld refinement.³¹

PXRD studies show that the volume expansion of **3.3(Cl)** when exposed to pressures of N_2 ($\Delta V = 181.7(1) \text{ \AA}^3$, 10.6 %) is similar to that in the CO_2 study of **3.3(Cl)** ($\Delta V = 190.3(9) \text{ \AA}^3$, 11 %). This expansion is due to increases in a - and c -axes ($\Delta a = 0.2405(6) \text{ \AA}$, 1.98 % and $\Delta c = 0.8565(9) \text{ \AA}$, 5.67 %) accompanied by a reduction in the β -angle (from $106.634(3)^\circ$ to $99.601(4)^\circ$) with minimal change in the b -axis ($\Delta b = -0.0296(5) \text{ \AA}$, -0.30 %)(**Figure 3.4.7-3**). This expansion

appears to happen in two stages with an initial large expansion in the c -axes (p/p^0) followed by a smaller expansion in the a -axis (p/p^0 0.8). The comparable overall expansion of the N_2 and CO_2 studies suggests comparable void space with the increased inclusion of N_2 , volumetrically, because of its smaller relative size. The size discrepancy may also be responsible for more N_2 being included than CO_2 in the volumetric analysis (Section 3.4.5).

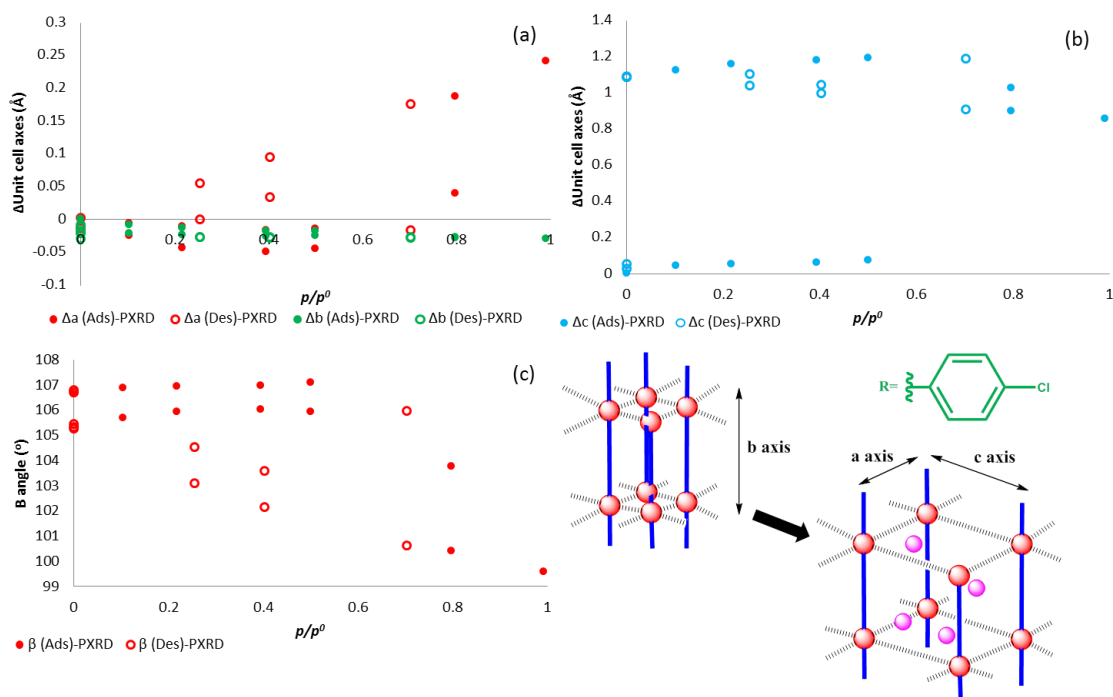


Figure 3.4.7-3. (a and b) Change in unit cell axes (a - and b -axes in (a) and c -axis in (b)) vs p/p^0 (N_2) for **3.3(Cl)**. (c) β angle plotted vs p/p^0 (N_2) for **3.3(Cl)**. Increasing (filled circles) and decreasing (empty circles) pressures of N_2 .

Rietveld refinements³¹ were performed using the fractional coordinates from the single-crystal study during CO_2 adsorption, in order to obtain proportions of each phase present as well as potentially identify possible N_2 locations (Section 3.4.8). The use of fractional coordinates from the CO_2 study requires the assumption that the polymer chains display the same straightening of the bridging benzoates as well as the same changes in inter-polymer distances.

3.4.7.3 Studies 3.4(F)

3.4(F) also showed comparable volume expansion ($\Delta V = 136.8(1) \text{ \AA}^3$, 8.2 %) to that observed in the CO_2 studies ($\Delta V = 140.8(12) \text{ \AA}^3$, 8.4 %). The volume expansion occurs in the same two-step process (**Figure 3.4.7-1**) seen in the volumetric adsorption analysis. This occurs through expansion of a single phase indicated by shifting of peak positions rather than growth of peaks for a new phase (**Figure 3.4.7-4**). Reducing the pressure of N_2 resulted in the material only partially closing upon returning to vacuum. The sample was therefore subjected to vacuum (at room temperature) for a prolonged period (12-17 h). The subsequent powder patterns, however, indicate an unexpected re-expansion. The expansion following extended evacuation may be due to insufficient equilibration time at 90 K before the sample was collected, but this assertion could not be tested due to synchrotron beam time availability related time

constraints. The study also exhibits *h0l* peak-broadening during expansion and contraction behaviour, as observed for **3.3(CI)**.

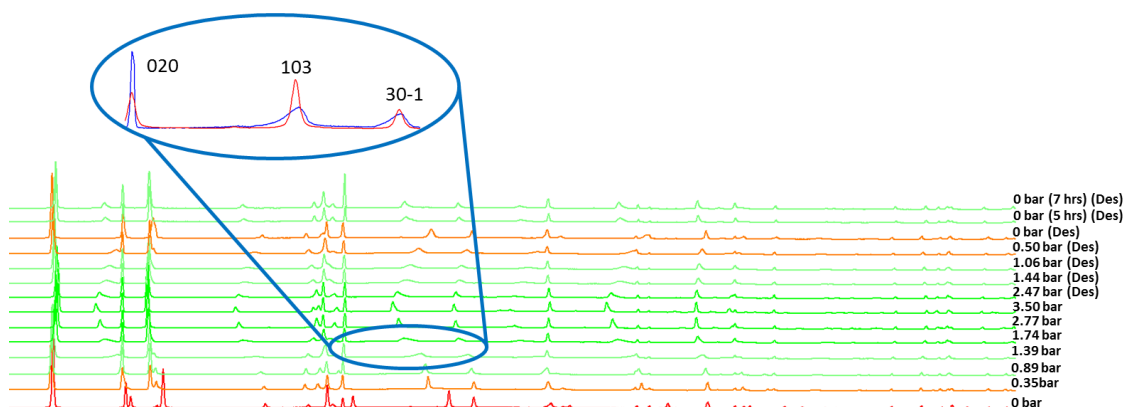


Figure 3.4.7-4. Stacked PXRD patterns of **3.4(F)** subjected to increasing (and decreasing) pressures of N_2 . Inset: Expansion highlighting the observed *h0l* peak broadening comparing the sharp 020 peak (on the left) with the broader 103 and 30-1 peak, experimental data in blue and fit in red.

As with the previous systems the unit cell volume expansion on gas adsorption occurs with (Figure 3.4.7-5) expansions in the a - and c -axes and minimal change in the b -axis. The change in unit cell axes against p/p^0 (Figure 3.4.7-5) reveals an initial expansion in c -axis followed by an expansion in the a -axis, as observed for **3.3(CI)**. The expansion in the a -axis appears to be accompanied by a slight compression (relaxation) in the c -axis, which could be due to increasing N_2 pressure resulting in a second structural rearrangement that allows access to a second guest site, consistent with the volumetric adsorption analysis. Alternatively the *h0l* peaks-broadening could be affecting the ability to fit consistent unit cell dimensions.

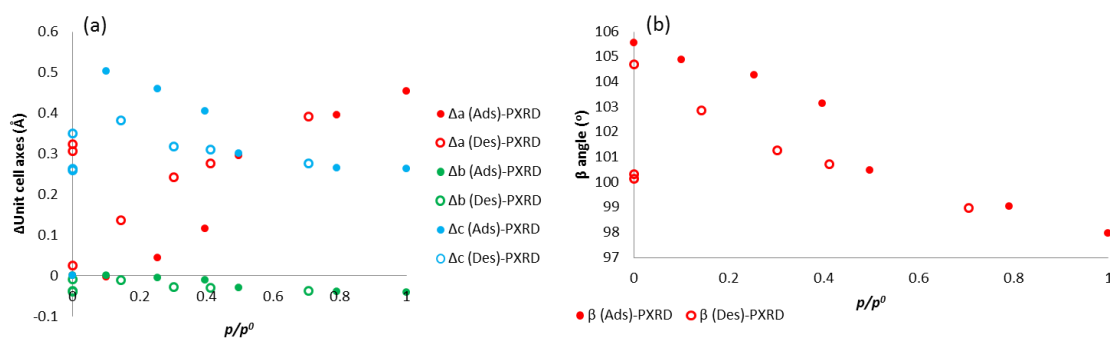


Figure 3.4.7-5. (a) Change in unit cell axes vs p/p^0 (N_2) for **3.4(F)**. (b) The change β angle vs p/p^0 (N_2) for **3.4(F)**. Increasing (filled circles) and decreasing (empty circles) pressures of N_2 .

As with the **3.3(CI)** N_2 study Rietveld refinements³¹ were carried using fractional coordinates from the *in situ* single-crystal study of **3.4(F)** during CO_2 adsorption. This required similar assumptions to be made about the straightening of the benzoate ligands and the validity of the atomic positions used. Evaluating the polymer positions results in similar observations to those of the previous CO_2 adsorption studies (**3.3(CI)** and **3.4(F)**) and the N_2 study of **3.3(CI)**, with rows of polymers being maintained (a -axis) in one dimension and moving apart in the second dimension (c -axis).

3.4.7.4 Summary

In conclusion N₂ uptake was observed in powdered samples of **3.3(CI)** and **3.4(F)** with the behaviour being consistent with the results of volumetric adsorption analysis. Both materials undergo two distinct phase transformations by either mixed phase transitions (**3.3(CI)**) or gradual shifting of diffraction peaks (**3.4(F)**). The maximum volume expansions observed ($\Delta V = 181.7(1) \text{ \AA}^3$, 10.6 % and $\Delta V = 136.8(1) \text{ \AA}^3$, 8.2 % for **3.3(CI)** and **3.4(F)**, respectively) were comparable to the CO₂ adsorption studies ($\Delta V = 190.3(9) \text{ \AA}^3$, 11 % and $\Delta V = 140.8(12) \text{ \AA}^3$, 8.4 % for **3.3(CI)** and **3.4(F)**, respectively) with this expansion being as a result of polymer chains moving apart with minimal compression or elongation of the polymer chains. The comparable volume expansion suggests that the solvent-accessible voids are also comparable with the discrepancies in the amount of gas included being due to the discrepancy in guest size (N₂ smaller than CO₂). Single-crystal diffraction experiments were performed on **3.3(CI)** and **3.4(F)** while increasing N₂ pressure, but these showed minimal unit cell volume change, suggesting particle size affects the N₂ uptake kinetics of these materials.

3.4.8 Crystallographic Determination of CO₂ and N₂ molecule location(s)

3.4.8.1 Single-crystal diffraction studies

Single crystals of **3.3(CI)** and **3.4(F)** that had been exposed to increasing (and decreasing pressures of CO₂ and N₂ (at 195 K and 90 K respectively) were analysed using PLATON SQUEEZE.^{13,14} The determined solvent-accessible void volume (**Figure 3.4.8-1**) was seen to increase with increasing CO₂ pressure but remained constant with increasing N₂ pressure. This void space (visualised in Mercury¹⁵) was shown to change, with increased CO₂ pressure, from discrete cavities to channels (**Figure 3.4.8-1**).

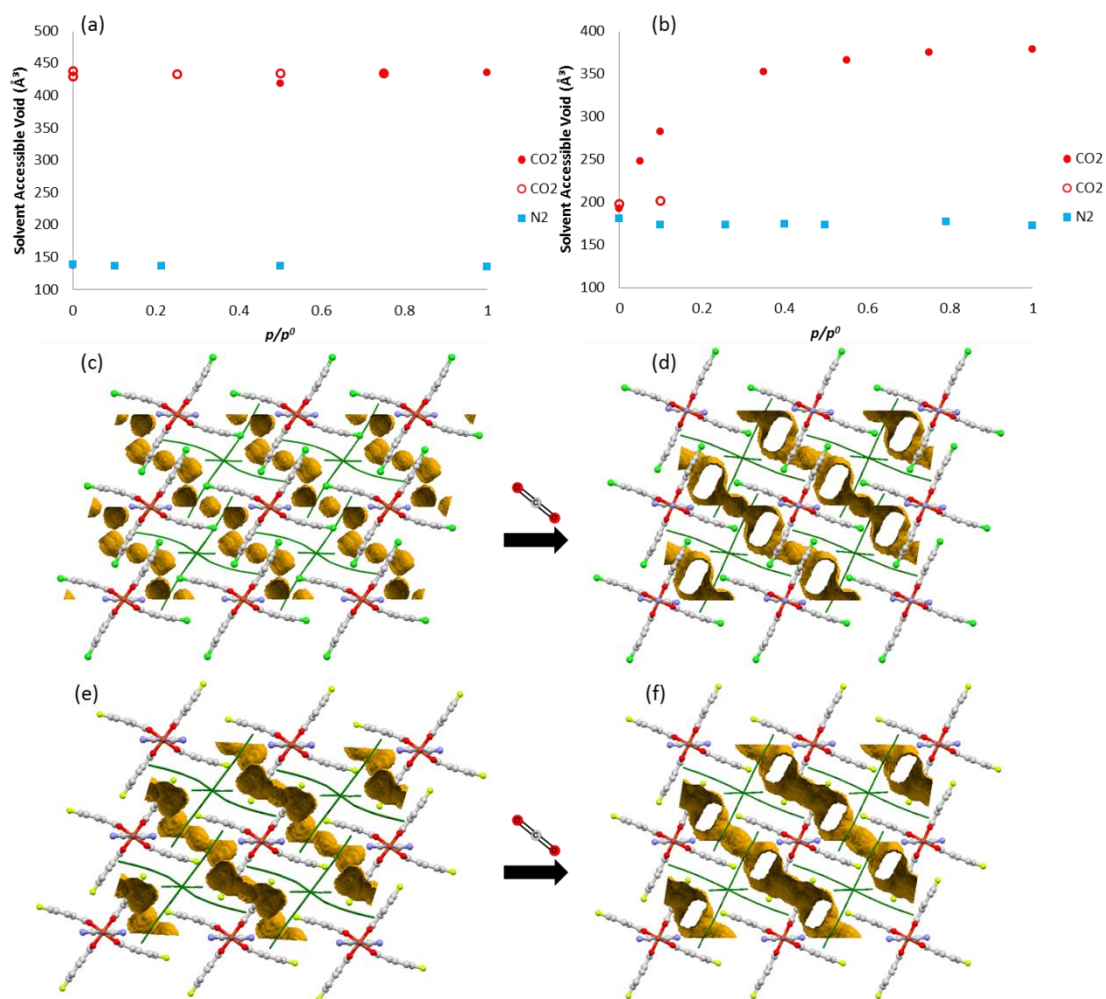


Figure 3.4.8-1. (a and b) Solvent-accessible void volume determined by PLATON CALC SQUEEZE^{13,14} against p/p^0 for single-crystals of (a) **3.3(Cl)** and (b) **3.4(F)** while being subjected to increasing (filled shapes) and decreasing (empty shapes) pressures of CO₂ at 195 K (red circles) or N₂ at 90 K (blue squares). (c, d, e and f) Void volumes, rendered in Mercury,¹⁵ of the initial vacuum measurements of (c) **3.3(Cl)** and (e) **3.4(F)** and the structures at 1 bar CO₂ pressure (p/p^0 1.0) for (d) **3.3(Cl)** and (f) **3.4(F)**. Images created in Mercury¹⁵ with 1.2 Å probe radius and 0.2 Å grid spacing. Colour scheme; C, grey; O, red, N, blue; Cl, green; F, yellow; interpenetration, green capped sticks; void space, yellow.

PLATON SQUEEZE^{13,14} was also used to determine the unassigned electron density in the structure model (Figure 3.4.8-2). As with the void space, this electron count increases with increasing CO₂ pressure for both **3.3(Cl)** and **3.4(F)** with minimal change in the corresponding electron count observed for the N₂ studies. Upon reducing CO₂ pressure on the single-crystal of **3.3(Cl)** this electron count is retained suggesting CO₂ retention, in contrast to the results of the volumetric adsorption/desorption analysis. This discrepancy is also reflected in the void space and unit cell volumes not changing upon reducing CO₂ pressure, which suggests particle size being a factor in the kinetics of desorption. The maximum electron count can be attributed to roughly 2.1 and 2.7 molecules of CO₂ per formula unit for **3.3(Cl)** and **3.4(F)**, respectively, this being one CO₂ molecule fewer than observed in the volumetric analysis (3.0 and 3.6 CO₂ molecules per formula unit for **3.3(Cl)** and **3.4(F)**, respectively).

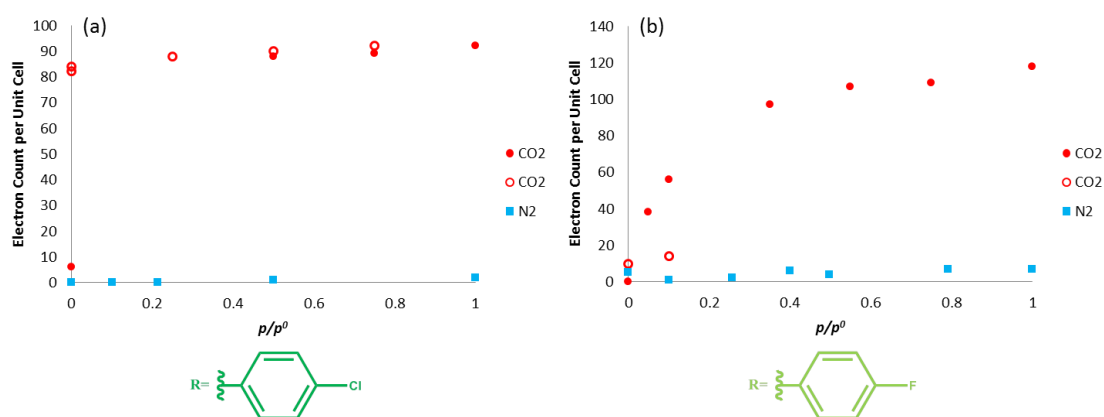


Figure 3.4.8-2. Electron count per unit cell determined by PLATON CALC SQUEEZE^{13,14} vs p/p^0 for single-crystals of (a) **3.3(Cl)** and (b) **3.4(F)** at increasing (filled shapes) and decreasing (empty shapes) pressures of CO₂ at 195 K (red circles) and N₂ at 90 K (blue squares).

Despite the PLATON SQUEEZE^{13,14} analysis suggesting each paddlewheel unit should be accompanied by at least two CO₂ molecules the residual electrons density peaks are relatively small with the largest, being $1.8 \text{ e}^{-\text{\AA}^{-3}}$ for both studies (**Figure 3.4.8-3**). This largest peak is situated either in the cleft of the paddlewheel unit or close to the aromatic ring of the benzoate linker (**Figure 3.4.8-3**) both location consistent with the observations of Takamizawa^{3,38-47,53,54} and the results from coordination polymers in Chapter 2. Despite these peaks being present there is too much disorder for the unassigned electron density to be modelled confidently as CO₂ molecules.

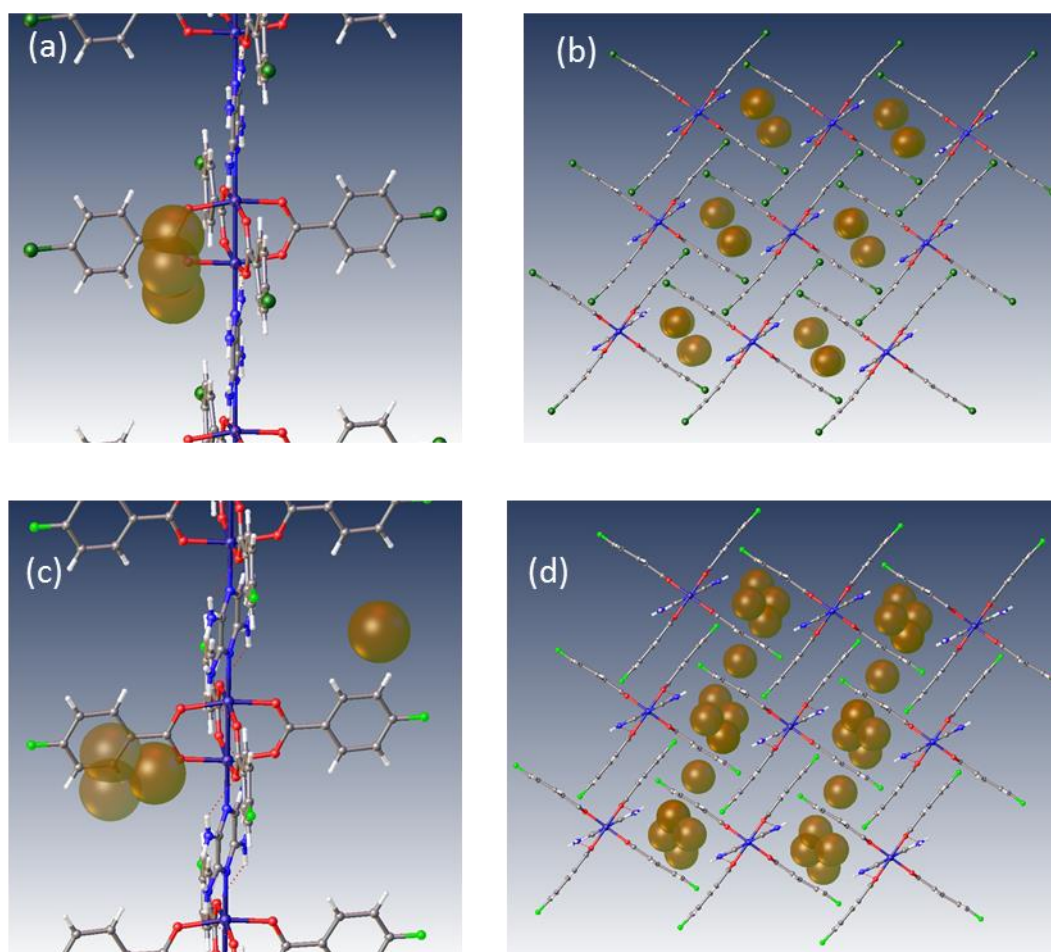


Figure 3.4.8-3. Residual electron density peaks for (a and b) **3.3(Cl)** and (c and d) **3.4(F)** at 195 K (p/p^0 1.0 of CO_2) showing the location in relation to the (a and c) paddlewheel SBU and (b and d) the structure viewed along the b -axis. Colour scheme Cu, dark blue; C, grey; H, white; O, red; N, blue; Cl, dark green; F, green; Query peaks, brown space filled in size.

3.4.8.2 Powder diffraction studies

Guest modelling was attempted for the *in situ* PXRD studies of samples of **3.2(Br)**, **3.3(Cl)** and **3.4(F)** subjected to increasing (and decreasing) pressures of CO_2 and N_2 . This modelling was attempted, as outlined in Section 3.3.7 (results in Appendix 3.8.2), with the use of rigid-body models for the guests allowing for both the position and occupancy of the guest to refine. The model for coordination polymer was not further refined.

The position of the modelled CO_2 molecules were modelled in the expanded phase of **3.2(Br)**. The position remained consistent throughout increasing CO_2 pressures steps (**Figure 3.4.8-5**) and is situated in the same cleft as that observed for coordination polymers studied in Chapter 2. The CO_2 molecule is in a position that would suggest a halogen-bonding interaction with the bromine functionality on the benzoate ligand (**Figure 3.4.8-5**), but the CO_2 is situated at an unusually short $\text{C}-\text{Br}\cdots\text{O}=\text{C}=\text{O}$ distance (2.71 Å, 81 % of the sum of the O and Br van der Waals radii^{36,37}), albeit with a plausible $\text{C}-\text{Br}\cdots\text{O}=\text{C}$ angle of 164.5°. The halogen-bond distance is slightly shorter than all reported $\text{C}-\text{Br}\cdots\text{O}=\text{C}$ distances in the CSD^{55,56} (**Figure 3.4.8-6**). This potential CO_2 site may be more reliably determined if a full conversion to the expanded phase

could be achieved for the PXRD study or if a single-crystal diffraction study could be undertaken. The maximum uptake of **3.2(Br)** that could be established from modelling residual electron density was 0.84 CO₂ per formula unit (**Table 3.4.8-1**), which is much lower than the 3.5 molecules per formula unit determined from the volumetric adsorption analysis, suggesting further CO₂ sites have yet to be identified and extensive guest disorder. Attempts to identify a second site were unsuccessful.

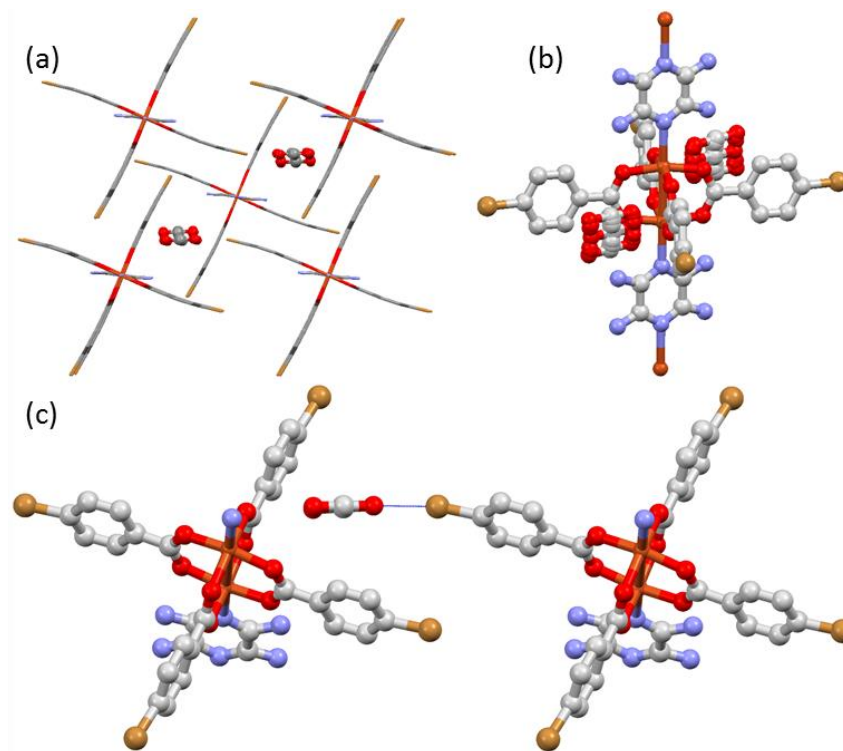


Figure 3.4.8-5. (a and b) Overlay of modelled CO₂ positions determined from in situ PXRD study of **3.2(Br)**. (c) Position of modelled CO₂ molecule in relation to the neighbouring polymer chain showing possible C–Br...O halogen bond.

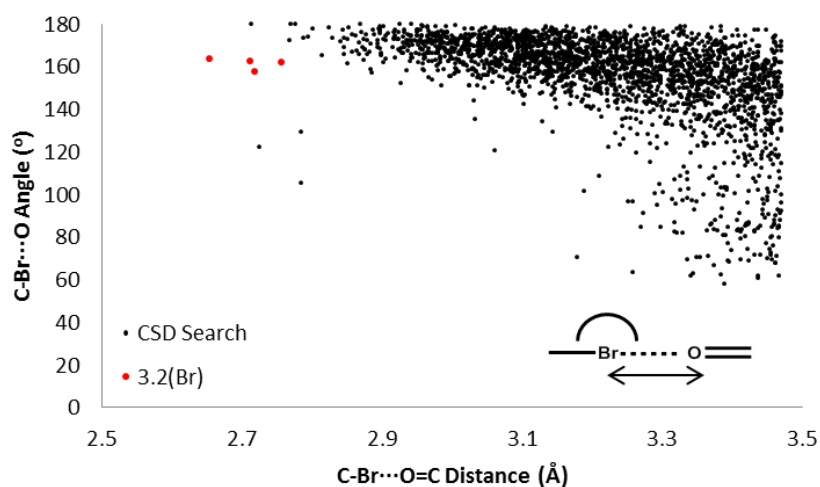


Figure 3.4.8-6. Plot of C–Br...O distance vs C–Br...O angle for all data in the CSD (black) and the four CO₂ positions (red) modelled in the four expanded phases in the in situ PXRD study for **3.2(Br)**.

Table 3.4.8-1. The modelled occupancy of CO₂ molecules in the in situ PXRD study of **3.2(Br)**

	Phase %	CO ₂ Molecules per Formula Unit in Expanded Phase	Total no. of CO ₂ Molecules per Formula Unit in Sample
3.2(Br)-195K-Vac	100		
3.2(Br)-195K-0.25bar CO₂	69.9(13) ^a		
	30.1(13) ^b	1.76(4)	0.53(4)
3.2(Br)-195K-0.5bar CO₂	50.4(8) ^a		
	49.6(8) ^b	1.44(2)	0.71(2)
3.2(Br)-195K-0.75bar CO₂	48.4(9) ^a		
	51.6(9) ^b	1.42(2)	0.73(2)
3.2(Br)-195K-1bar CO₂	44.3(9) ^a		
	55.7(9) ^b	1.50(2)	0.84(2)
3.2(Br)-195K-Vac (D)	77.4(19) ^a		
	22.6(19) ^b	2.00(7)	0.45(7)

^a Closed phase ^b Expanded phase

Similarly in the PXRD study of **3.3(Cl)** during CO₂ adsorption/desorption refinement of CO₂ molecule positions revealed a consistent location (**Figure 3.4.8-6**). The CO₂ was situated in the same cleft of the paddlewheel previously observed for **3.2(Br)** and the work in Chapter 2. However, the CO₂ molecules are orientated such that they form a chain running parallel to the coordination polymer with potential interactions between the amine and the aromatic rings. As with the previous study the occupancy of this CO₂ molecule increases with increasing CO₂ pressure (**Table 3.4.8-2**). This occupancy corresponds roughly to a maximum inclusion of one CO₂ per formula unit which again is a fairly large discrepancy with the observed maximum (three CO₂ per formula unit) in the volumetric adsorption analysis. This therefore suggests a similar unidentified secondary site with similar problems in locating a second site as observed in the previous study of **3.2(Br)**.

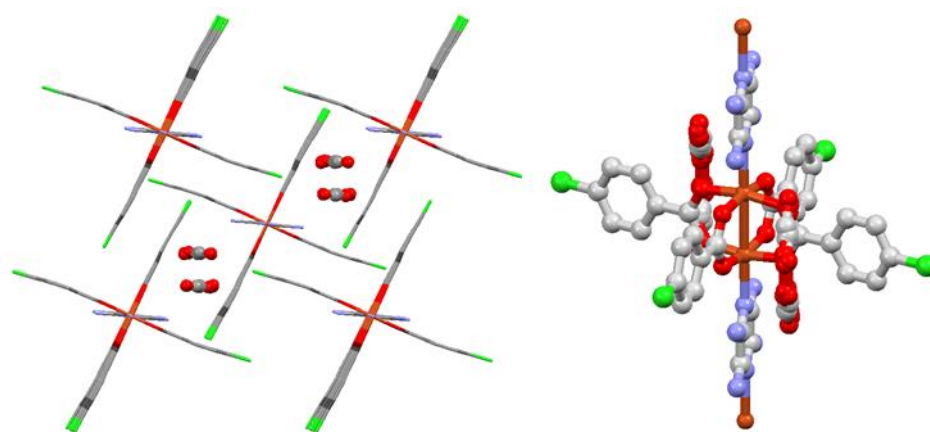


Figure 3.4.8-7. Overlay of modelled CO₂ positions determined from the in situ PXRD study of **3.3(Cl)**.

Table 3.4.8-2. The modelled occupancy of CO₂ molecules in the *in situ* PXRD study of **3.3(Cl)**

	Phase %	No. CO ₂ Molecules Per Formula Unit in Expanded Phase	Total no. of CO ₂ Molecules per Formula Unit in Sample
3.3(Cl)-195K-Vac	100 ^a		
3.3(Cl)-195K-0.04bar CO₂	100 ^a		
3.3(Cl)-195K-0.09bar CO₂	72.1(3) ^a		
	27.9(3) ^b	0.458(10)	0.128(10)
3.3(Cl)-195K-0.69bar CO₂	100 ^b	0.668(6)	0.668(6)
3.3(Cl)-195K-0.98bar CO₂	100 ^b	0.958(5)	0.958(5)
3.3(Cl)-195K-0.72bar CO₂ (D)	100 ^b	0.920(5)	0.920(5)
3.3(Cl)-195K-0.32bar CO₂ (D)	100 ^b	0.696(5)	0.696(5)
3.3(Cl)-195K-0.11bar CO₂ (D)	100 ^b	0.684(6)	0.684(6)
3.3(Cl)-195K-0.05bar CO₂ (D)	100 ^b	0.730(7)	0.730(7)
3.3(Cl)-195K-Vac(D)	100 ^b		

^aClosed phase ^bExpanded phase

In the study N₂ uptake of **3.3(Cl)**, similarly one N₂ site could be successfully modelled with its position being variable but always located in the cleft of the paddlewheel unit (**Figure 3.4.8-7**). The broadening for *h0l* reflection discussed in Section 3.4.7 has an impact on the quality of the Rietveld fits. However, the refined occupancies demonstrate a slight correlation between increasing N₂ pressure and the refined occupancy, but are inconsistent with mixed-phase fits that contain partially expanded and fully expanded phases typically displaying higher quantities of N₂ than the pure fully expanded phases. This coupled with the *h0l* peak-broadening would suggest that the refined values do not represent the true occupancy. It can therefore only be concluded that N₂ is situated in the same cleft as the CO₂ molecule but the exact position and occupancy is uncertain.

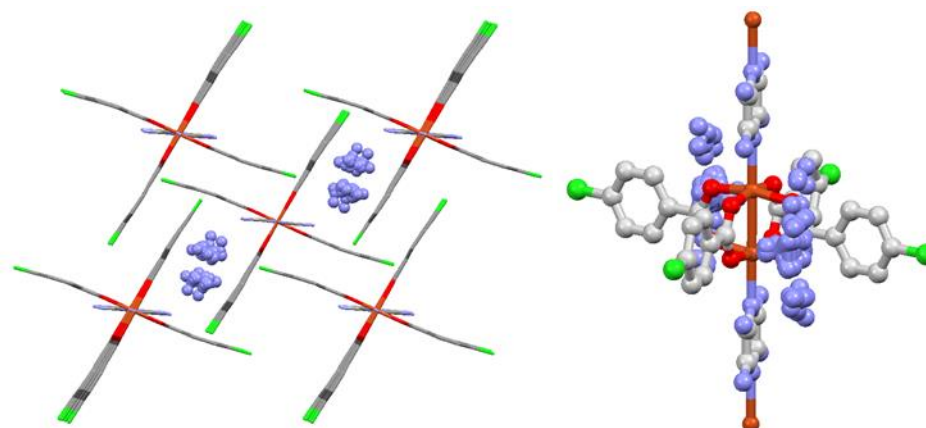


Figure 3.4.8-8. Overlay of modelled N₂ positions determined from the *in situ* PXRD study of **3.3(Cl)**.

Table 3.4.8-3. The modelled occupancy of N₂ molecules in the *in situ* PXRD study of **3.3(Cl)**

	Phase %	No. N ₂ Molecules Per Formula Unit in Expanded Phase	Total no. of N ₂ Molecules per Formula Unit in Sample
3.3(Cl)-90K-Vac	100 ^a		
3.3(Cl)-90K-0.36bar N₂	61.4(5) ^a 38.6(5) ^b	0.932(20)	0.360(20)
3.3(Cl)-90K-0.76bar N₂	43.3(5) ^a 56.7(5) ^b	0.792(13)	0.449(13)
3.3(Cl)-90K-1.38bar N₂	30.4(5) ^a 69.6(5) ^b	0.760(11)	0.529(11)
3.3(Cl)-90K-1.75bar N₂	18.5(6) ^a 81.5(6) ^b	0.736(10)	0.600(10)
3.3(Cl)-90K-2.79bar N₂	21.0(8) ^b 79.0(8) ^c	1.596(35) 0.660(16)	0.335(35) 0.521(16)
3.3(Cl)-90K-3.47bar N₂	100 ^c 6.6(6) ^b	0.626(9) 2.00(7)	0.626(9) 0.13(7)
3.3(Cl)-90K-2.46bar N₂ (D)	93.4(6) ^c 58.9(10) ^b	0.650(15) 0.750(24)	0.607(15) 0.442(24)
3.3(Cl)-90K-1.41bar N₂ (D)	41.1(10) ^c 66.3(10) ^b	1.064(16) 0.856(18)	0.437(16) 0.568(18)
3.3(Cl)-90K-0.89bar N₂ (D)	33.7(10) ^c 100 ^b	1.152(21) 0.648(10)	0.388(21) 0.648(10)
3.3(Cl)-90K-Vac (D)	100 ^b 38.2(5) ^b	0.648(10) 0.580(18)	0.648(10) 0.222(18)
3.3(Cl)-90K-Vac (D)- 5 hrs	61.8(5) ^a 64.8(6) ^b		
3.3(Cl)-90K-Vac (D)- 17hrs	35.2(6) ^a	0.500(17)	0.324(17)

^a Closed phase ^b Partially Expanded Phase ^c Fully Expanded Phase

Finally coordination polymer **3.4(F)**, which was tested for both CO₂ and N₂ adsorption, showed promising results with two potential sites being identified, one situated in the paddlewheel cleft as observed in the previous systems (**3.2(Br)** and **3.3(Cl)**) and a second site situated close to the one of the benzoate ligands. Comparison of these positions (**Figure 3.4.8-8**) demonstrated that the positions of the modelled guest was fairly variable and not as clearly defined as the previous examples (**3.2(Br)** and **3.3(Cl)**). The refined occupancies of these guests increase with increasing gas pressure, with the occupancy of the second site, in the case of the N₂ study, only being observed at the higher pressure, consistent with the observed gating in the volumetric adsorption analysis. However limitation due to the *h0l* peak-broadening will contribute to reducing the reliability of the guest modelling and to the discrepancy between the crystallographically modelled quantities of guest and those recorded volumetrically.

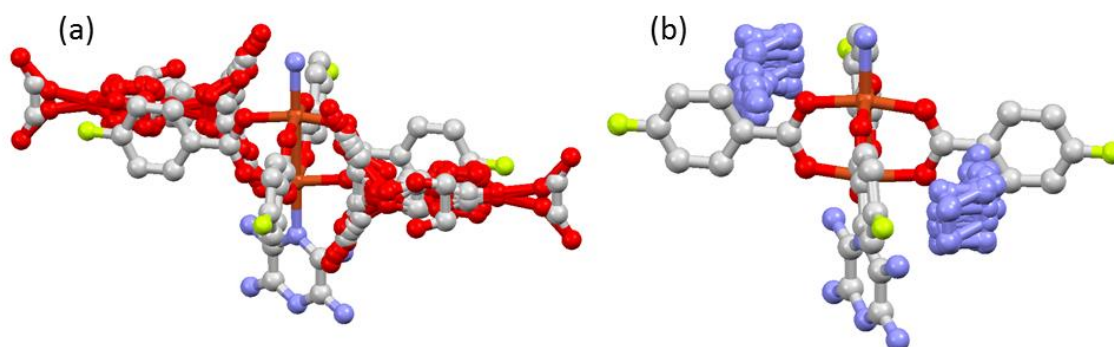


Figure 3.4.8-9. Overlay of modelled positions of (a) CO₂ and (b) N₂ of *in situ* PXRD studies of 3.4(F).

Table 3.4.8-4. The modelled occupancy of CO₂ molecules in the *in situ* PXRD study of 3.4(F)

	No. CO ₂ Molecules Per Formula Unit		Total no. of CO ₂ Molecules per Formula Unit in Sample
	Site 1	Site 2	
3.3(F)-195K-Vac			
3.3(F)-195K-0.05bar CO ₂	0.488(10)	0.174(9)	0.662(13)
3.3(F)-195K-0.08bar CO ₂	0.468(17)	0.248(16)	0.716(23)
3.3(F)-195K-0.33bar CO ₂	0.556(11)	0.450(11)	1.006(16)
3.3(F)-195K-0.7bar CO ₂	0.624(9)	0.526(9)	1.15(13)
3.3(F)-195K-1bar CO ₂	0.620(9)	0.620(10)	1.24(13)
3.4(F)-195K-0.7bar CO ₂ (D)	0.626(9)	0.546(9)	1.172(13)
3.4(F)-195K-0.3bar CO ₂ (D)	0.712(5)	0.342(5)	1.054(7)
3.4(F)-195K-0.1bar CO ₂ (D)	0.634(7)	0.364(11)	0.998(13)
3.4(F)-195K-0.05bar CO ₂ (D)	0.432(20)	0.182(20)	0.614(28)
3.4(F)-195K-Vac(D)			

Table 3.4.8-5. The modelled occupancy of N₂ molecules in the *in situ* PXRD study of 3.4(F)

	No. N ₂ Molecules Per Formula Unit		Total no. of N ₂ Molecules per Formula Unit in Sample
	Site 1	Site 2	
3.3(F)-90K-Vac			
3.3(F)-90K-0.35bar N ₂	0.800(6)		0.800(6)
3.3(F)-90K-0.89bar N ₂	0.856(6)		0.856(6)
3.3(F)-90K-1.39bar N ₂	0.620(10)		0.620(10)
3.3(F)-90K-1.74bar N ₂	0.480(10)	0.602(8)	1.082(13)
3.3(F)-90K-2.77bar N ₂	0.774(6)	0.542(5)	1.316(8)
3.3(F)-90K-3.50bar N ₂	0.832(7)	0.448(5)	1.280(9)
3.4(F)-90K-2.47bar N ₂ (D)	0.556(8)	0.472(7)	1.028(11)
3.4(F)-90K-1.44bar N ₂ (D)	0.438(10)	0.510(8)	0.948(13)
3.4(F)-90K-1.06bar N ₂ (D)	0.314(10)	0.432(9)	0.746(13)
3.4(F)-90K-0.5bar N ₂ (D)	0.486(9)		0.486(9)
3.3(Cl)-90K-Vac (D)	0.536(8)		0.536(8)
3.3(F)-90K-Vac (D)- 5 hours		0.538(8)	0.538(8)
3.3(F)-90K-Vac (D)- 17 hours	0.686(11)		0.686(11)

3.4.8.3 Summary

In conclusion, observations of the largest unassigned electron density peaks in the *in situ* single-crystal studies ultimately identified a potential guest site consistent with that observed in the previous work discussed in Chapter 2. However, these peaks were insufficiently large to confidently model as guest molecules. These observations did prompt attempts to fit guest molecules using the *in situ* PXRD studies, with varying levels of success. This modelling resulted in guests being modelled in sites consistent with those observed in Chapter 2. The total occupancy of the guest was smaller than that determined in the volumetric adsorption analysis, suggesting unidentified sites potential due to high levels of disorder and low occupancy of sites and/or inadequate modelling of the coordination polymer due to the dynamic nature of the materials.

3.5 Conclusions

In conclusion, this chapter has demonstrated that despite the initially promising pursuit of a 50% void sustained through a 2D halogen-bonding network, this void was ultimately shown to be unstable in the absence of the solvent guest for **3.1(I)**. This system did however demonstrate some porosity with the inclusion of CO₂ in its largely amorphous desolvated state. This chapter then went on to look at further, as yet unreported, systems with the formula [Cu₂(4-Xbz)₄(NH₂pyz)]_n (X = Br, Cl or F). It was shown that these systems, with bromo (**3.2(Br)**), chloro (**3.3(Cl)**) and fluoro (**3.4(F)**) functionality, had analogous packing to their pyrazine-containing analogues with **3.3(Cl)** and **3.4(F)** coordination polymers being produced in the absence of solvent and **3.2(Br)** being easily desolvated at room temperature.

These three systems (**3.2(Br)**, **3.3(Cl)** and **3.4(F)**) then tested for volumetric adsorption of CO₂ and N₂, demonstrating a higher uptake of N₂ (at 77 K) over CO₂ (at 195 K). Comparison between the analogous systems in Chapter 2 established that the presence of the amino functionality resulted in a reduction in the gate pressure in the case of the CO₂ and inclusion of N₂ for **3.2(Br)**, which was not observed for **2.2(Br)**.³⁵

Subsequent *in situ* PXRD studies where samples were exposed to increasing (and decreasing) pressures of CO₂ at 195 K (for **3.2(Br)**, **3.3(Cl)** and **3.4(F)**) and N₂ at 90 K (for **3.3(Cl)** and **3.4(F)**) showed comparable volume expansions, suggesting larger volumetric uptake of N₂ was as a result of N₂ being smaller in size than CO₂. The secondary gated uptakes observed in the N₂ volumetric adsorption analysis are most likely due to forcing access of the N₂ into a secondary guest site. It was observed that when single-crystals of **3.3(Cl)** and **3.4(F)** were exposed to increasing pressures of N₂ no phase change was observed, suggesting particle size affects the uptake kinetics of N₂. Guest modelling was possible for the PXRD studies showing sites in the paddlewheel cleft, consistent with that observed for the pyrazine-containing coordination polymers in Chapter 2.

3.6 Future Work

This work focused on testing this family of materials for gaseous guest inclusion of CO₂ and N₂ with the conclusion that both gases invoked the same overall expansion of the materials with the difference in molar uptake being a result of guest size. A logical next step would be to test these materials for the inclusion of other guests, to determine the mode of uptake as well as the volume expansion. This work could focus on testing the limitation of these materials and establishing the maximum possible expansion. Takamizawa has previously demonstrated that [M₂(bz)₄(pyz)]_n guest inclusion is not constrained to gaseous guests with the demonstration of vapour inclusion of a variety of solvent guest.^{41,43,47,57,58} This, therefore, suggests a large scope for further testing of this family of materials.

The *in situ* CO₂ study of **3.2(Br)** identified a potential CO₂ site which suggests a halogen-bonding interaction between the bromine and the CO₂ molecules. This observation although plausible and promising does come with a large amount of uncertainty due the quality of the data and the fits. Therefore investigation of this binding site would benefit from further *in situ* single-crystal diffraction studies and computational modelling.⁵⁹

This work has also demonstrated that functionality present on the bridging benzoate and the propagating pyrazine linker does have an effect on the gas uptake properties; therefore further exploration of this functionality could be pursued. The original report of the three pyrazine-containing analogues **2.1(I)**, **2.2(Br)** and **2.3(Cl)** studied in Chapter 2, also presents an analogous polymer [Cu₂(4-OMebz)₄(pyz)]_n (4-OMe = 4-methoxybenzoate), which demonstrates an interesting volumetric adsorption for CO₂ (**Figure 3.6.1**). This material exhibits gated uptake of CO₂ at *ca.* p/p^0 0.7 (195 K) with the desorption occurring via a two-step process.

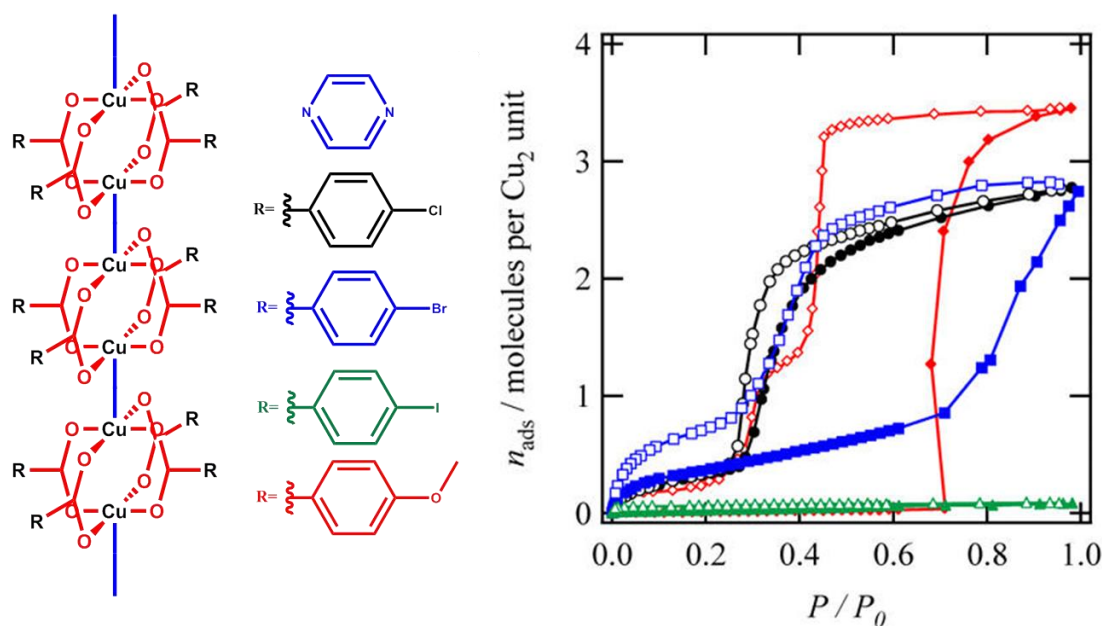


Figure 3.6.1. Volumetric CO₂ adsorption analysis of [Cu₂(4-Xbz)₄pyz]_n at 195 K (X = I (green), Br (blue), Cl (black) and OMe (red)) reported by Takahashi.³⁵ Isotherms replicated from reference 35 with permission.

Further work could be carried out on this system as well as analogues with extension of the alkoxy group on the benzoate ligands. This would involve characterising the two-step desorption as well as seeing how the volumetric isotherms were affected by extending the alkoxy chain. This work could then be further extended using the approach employed in this chapter by exploring the effect of functionalising the pyrazine linker (**Figure 3.6.2**).

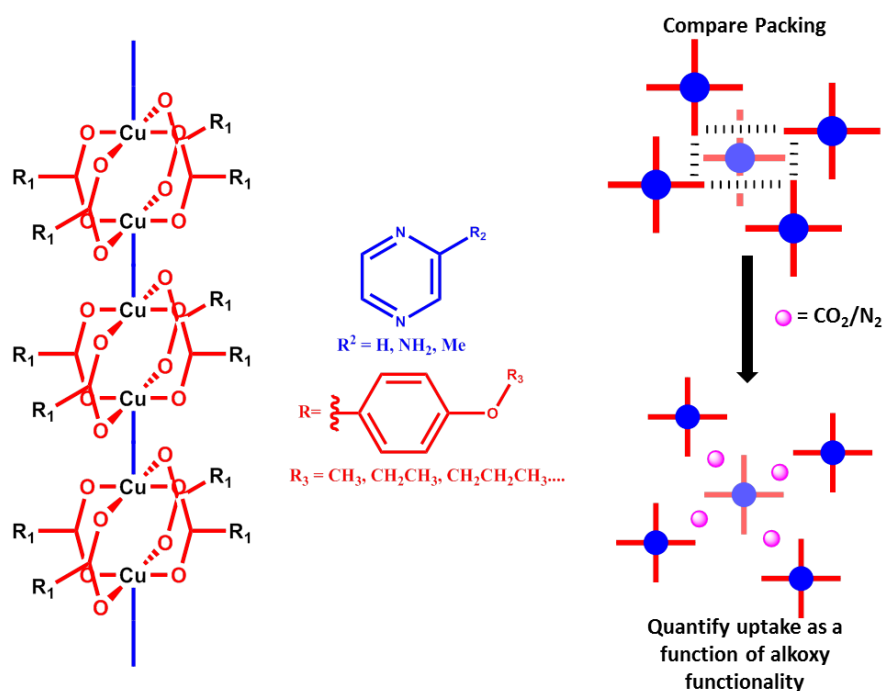


Figure 3.6.2. Proposed study looking at the effect of extension of the alkoxy group, relative to that of $[\text{Cu}_2(4\text{-OMebz})_4\text{pyz}]_n$, reported by Takahashi, on the CO_2 uptake at 195 K.³⁵

3.7 References

- 1 S. Takamizawa, E. Nakata and T. Akatsuka, *Angew. Chem. Int. Ed.*, 2006, **45**, 2216–2221.
- 2 S. Takamizawa, E. Nakata, T. Akatsuka, C. Kachi-terajima and R. Miyake, *J. Am. Chem. Soc.*, 2008, **130**, 17882–17892.
- 3 S. Takamizawa, E. I. Nataka, T. Akatsuka, R. Miyake, Y. Kakizaki, H. Takeuchi, G. Maruta and S. Takeda, *J. Am. Chem. Soc.*, 2010, **132**, 3783–3792.
- 4 S. Takamizawa, K. Kojima and T. Akatsuka, *Inorg. Chem.*, 2006, **45**, 4580–4582.
- 5 S. Takamizawa and M. Kohbara, *Dalton Trans.*, 2007, 3640–3645.
- 6 Y. Takasaki and S. Takamizawa, *J. Am. Chem. Soc.*, 2014, **136**, 6806–6809.
- 7 W. Kosaka, K. Yamagishi, H. Yoshida, R. Matsuda, S. Kitagawa, M. Takata and H. Miyasaka, *Chem. Commun.*, 2013, **49**, 1594–1596.
- 8 W. Kosaka, K. Yamagishi, A. Hori, H. Sato, R. Matsuda, S. Kitagawa, M. Takata and H.

- Miyasaka, *J. Am. Chem. Soc.*, 2013, **135**, 18469–18480.
- 9 W. Kosaka, K. Yamagishi, J. Zhang and H. Miyasaka, *J. Am. Chem. Soc.*, 2014, **136**, 12304–12313.
- 10 W. Kosaka, K. Yamagishi, R. Matsuda, S. Kitagawa, M. Takata and H. Miyasaka, *Chem. Lett.*, 2014, **43**, 890–892.
- 11 J. Zhang, W. Kosaka, H. Fukunaga, S. Kitagawa, M. Takata and H. Miyasaka, *Inorg. Chem.*, 2016, **55**, 12085–12092.
- 12 A. D. Burrows, M. F. Mahon, P. R. Raithby, A. J. Warren, S. J. Teat and J. E. Warren, *CrystEngComm*, 2012, **14**, 3658–3666.
- 13 A. L. Spek, *Acta Crystallogr. Sect. D: Biol. Crystallogr.*, 2009, **65**, 148–155.
- 14 A. L. Spek, *Acta Crystallogr. Sect. C: Struct. Chem.*, 2015, **71**, 9–18.
- 15 C. F. Macrae, I. J. Bruno, J. A. Chisholm, P. R. Edgington, P. McCabe, E. Pidcock, L. Rodriguez-Monge, R. Taylor, J. Van De Streek and P. A. Wood, *J. Appl. Crystallogr.*, 2008, **41**, 466–470.
- 16 D. R. Allan, S. P. Collins, G. Evans, D. Hall, K. McAuley, R. L. Owen, T. Sorensen, C. C. Tang, F. von Delft, A. Wagner and H. Wilhelm, *Eur. Phys. J. Plus*, 2015, **130**, 1–20.
- 17 B. Arstad, H. Fjellvåg, K. O. Kongshaug, O. Swang and R. Blom, *Adsorption*, 2008, **14**, 755–762.
- 18 Z. Zhang, Z.-Z. Yao, S. Xiang and B. Chen, *Energy Environ. Sci.*, 2014, **7**, 2868–2899.
- 19 E. J. Carrington, I. J. Vitórica-Yrezábal and L. Brammer, *Acta Crystallogr. Sect. B: Struct. Sci. Cryst. Eng. Mater.*, 2014, **70**, 404–422.
- 20 G. M. Sheldrick, *SADABS, Empirical Absorption Correction program, Univ. Göttingen*, 1995, based on the methods of Blessing.
- 21 L. Krause, R. Herbst-Irmer, G. M. Sheldrick and D. Stalke, *J. Appl. Crystallogr.*, 2015, **48**, 3–10.
- 22 R. H. Blessing, *Acta Crystallogr. Sect. A: Found. Adv.*, 1995, **A51**, 33–38.
- 23 G. M. Sheldrick, *Acta Crystallogr. Sect. C: Struct. Chem.*, 2015, **71**, 3–8.
- 24 O. V. Dolomanov, L. J. Bourhis, R. J. Gildea, J. A. K. Howard and H. Puschmann, *J. Appl. Crystallogr.*, 2009, **42**, 339–341.
- 25 G. S. Pawley, *J. Appl. Crystallogr.*, 1981, **14**, 357–361.
- 26 A. A. Coelho, *Topas Academic, Version 4.1, see <http://www.topas-academic.net>*.
- 27 A. A. Coelho, J. Evans, I. Evans, A. Kern and S. Parsons, *Powder Diffr.*, 2011, **26**, S22–S25.
- 28 N. Tartoni, S. P. Thompson, C. C. Tang, B. L. Willis, G. E. Derbyshire, A. G. Wright, S. C. Jaye, J. M. Homer, J. D. Pizzey and A. M. T. Bell, *J. Synchrotron Radiat.*, 2007, **15**, 43–49.

- 29 S. P. Thompson, J. E. Parker, J. Potter, T. P. Hill, A. Birt, T. M. Cobb, F. Yuan and C. C. Tang, *Rev. Sci. Instrum.*, 2009, **80**, (075107) 1–9.
- 30 S. P. Thompson, J. E. Parker, J. Marchal, J. Potter, A. Birt, F. Yuan, R. D. Fearn, A. R. Lennie, S. R. Street and C. C. Tang, *J. Synchrotron Radiat.*, 2011, **18**, 637–648.
- 31 H. M. Rietveld, *J. Appl. Crystallogr.*, 1969, **2**, 65–71.
- 32 H. Nowell, S. A. Barnett, K. E. Christensen, S. J. Teat and D. R. Allan, *J. Synchrotron Radiat.*, 2012, **19**, 435–441.
- 33 S. A. Barnett, H. Nowell, M. R. Warren, A. Wilcox and D. R. Allan, *Protein Pept. Lett.*, 2015, **23**, 211–216.
- 34 CrysAlisPRO, *Oxford Diffraction /Agilent Technologies UK Ltd*, Yarnton, England.
- 35 K. Takahashi, N. Hoshino, T. Takeda, S. Noro, T. Nakamura, S. Takeda and T. Akutagawa, *Inorg. Chem.*, 2015, **54**, 9423–9431.
- 36 A. Bondi, *J. Phys. Chem.*, 1964, **68**, 441–451.
- 37 S. Alvarez, *Dalton Trans.*, 2013, **42**, 8617–8636.
- 38 S. Takamizawa, E. Nakata and T. Saito, *Inorg. Chem. Commun.*, 2003, **6**, 1415–1418.
- 39 S. Takamizawa, E. Nakata, T. Saito, T. Akatsuka and K. Kojima, *CrystEngComm*, 2004, **6**, 197–199.
- 40 S. Takamizawa, E. Nakata and T. Saito, *Chem. Lett.*, 2004, **33**, 538–539.
- 41 S. Takamizawa, T. Saito, T. Akatsuka and E. Nakata, *Inorg. Chem.*, 2005, **44**, 1421–1424.
- 42 S. Takamizawa and E. Nakata, *CrystEngComm*, 2005, **7**, 476–479.
- 43 S. Takamizawa, C. Kachi-Terajima, M.-A. Kohbara, T. Akatsuka and T. Jin, *Chem. Asian J.*, 2007, **2**, 837–848.
- 44 C. Kachi-Terajima, T. Akatsuka, M. Kohbara and S. Takamizawa, *Chem. Asian J.*, 2007, **2**, 40–50.
- 45 T. Ueda, K. Kurokawa, T. Eguchi, C. Kachi-terajima and S. Takamizawa, *J. Phys. Chem.*, 2007, **2**, 1524–1534.
- 46 S. Takamizawa, E. Nakata and T. Akatsuka, *J. Am. Chem. Soc.*, 2008, **130**, 17882–17892.
- 47 S. Takamizawa and R. Miyake, *Chem. Commun.*, 2009, **0**, 4076–4078.
- 48 S. Kitagawa and K. Uemura, *Chem. Soc. Rev.*, 2005, **34**, 109–119.
- 49 M. Thommes, K. Kaneko, A. V. Neimark, J. P. Olivier, F. Rodriguez-Reinoso, J. Rouquerol and K. S. W. Sing, *Pure Appl. Chem.*, 2015, **87**, 1051–1069.
- 50 S. Takamizawa, Y. Takasaki and R. Miyake, *Chem. Commun.*, 2009, **2**, 6625–6627.
- 51 Y. Hijikata, S. Horike, D. Tanaka, J. Groll, M. Mizuno, J. Kim, M. Takata and S. Kitagawa, *Chem. Commun.*, 2011, **47**, 7632–7634.

- 52 C. Zhang, J. A. Gee, D. S. Sholl and R. P. Lively, *J. Phys. Chem. C*, 2014, **118**, 20727–20733.
- 53 S. Takamizawa, E. Nakata, T. Saito and T. Akatsuka, *Inorg. Chem.*, 2005, **44**, 1362–1366.
- 54 S. Takamizawa, E.-I. Nakata and R. Miyake, *Dalton Trans.*, 2009, **2**, 1752–1760.
- 55 A. G. Orpen, *Acta Crystallogr. Sect. B: Struct. Sci.*, 2002, **58**, 398–406.
- 56 C. R. Groom and F. H. Allen, *Angew. Chem. Int. Ed.*, 2014, **53**, 662–671.
- 57 S. Takamizawa and R. Miyake, *CrystEngComm*, 2010, **12**, 2728–2733.
- 58 S. Takamizawa, T. Akatsuka and R. Miyake, *CrystEngComm*, 2010, **12**, 82–84.
- 59 A. G. P. Maloney, P. A. Wood and S. Parsons, *CrystEngComm*, 2016, **18**, 3273–3281.

3.8 Appendices

Appendix 3.8.1: Single-Crystal Data

Table 3.3.2-1. Summary of the as synthesised single crystal data of the target $[\text{Cu}_2(4\text{-Xbz})_4(\text{NH}_2\text{pyz})]_n$ polymers produced in Chapter 3

	3.1(I)-BnOH/MeOH $[\text{Cu}_2(4\text{-Ibz})_4(\text{NH}_2\text{pyz})]_n\text{-Sol}$ $\text{C}_{32}\text{H}_{21}\text{Cu}_2\text{I}_4\text{N}_3\text{O}_8$	3.1(I)-DCM/MeOH $[\text{Cu}_2(4\text{-Ibz})_4(\text{NH}_2\text{pyz})]_n\text{-Sol}$ $\text{C}_{32}\text{H}_{21}\text{Cu}_2\text{I}_4\text{N}_3\text{O}_8$	3.2(Br)-BnOH/MeOH $[\text{Cu}_2(4\text{-Brbz})_4(\text{NH}_2\text{pyz})]_n\text{-Sol}$ $\text{C}_{32}\text{H}_{21}\text{Br}_4\text{Cu}_2\text{N}_3\text{O}_8$	
Crystal habit	Plate	Plate	Needle	
Crystal colour	Dull Bluish Green	Dull Bluish Green	Clear Bluish Green	
Crystal size (mm)	0.10×0.07×0.03	0.48×0.14×0.075	0.15×0.04×0.04	
Crystal system	Tetragonal	Tetragonal	Monoclinic	
Space group	$P4_1$	$P4/ncc$	$I2/m$	
a (Å)	12.7411(3)	25.2526(10)	12.3050(4)	
b (Å)	12.7411(3)	25.2526(10)	9.8208(3)	
c (Å)	38.9872(16)	19.2611(11)	16.8297(8)	
α (°)	90	90	90	
β (°)	90	90	100.1947(19)	
γ (°)	90	90	90	
V (Å ³)	6329.0(4)	12282.7(12)	2001.68(13)	
Density (g cm ⁻³)	1.270	1.309	1.696	
Temperature (K)	99.88	100	100.01	
μ (mm ⁻¹)	16.406	2.734	6.393	
Wavelength (Å)	1.542	0.711	1.542	
2 θ range (°)	6.938 to 128.238	2.28 to 55.092	8.246 to 122.62	
Reflns. collected	87802	192086	10214	
Independent reflns. [R_{int}]	10164 [0.1162]	7087 [0.1149]	1621 [0.0597]	
Reflns. used in refinement, n	10164	7087	1621	
LS parameters, p	394	227	132	
Restraints, r	411	183	15	
$R1$ (F^a) / >2.0 $\sigma(I)$	0.0911	0.1447	0.0405	
$wR2$ (F^2) ^a , all data	0.2269	0.3819	0.0973	
$S(F^2)$ ^a , all data	1.039	1.244	1.044	
	3.2(Br)-DCM/MeOH $[\text{Cu}_2(4\text{-Brbz})_4(\text{NH}_2\text{pyz})]_n\text{-4MeOH}$ $\text{C}_{36}\text{H}_{37}\text{Br}_4\text{Cu}_2\text{N}_3\text{O}_{12}$	3.3(Cl)-BnOH/MeOH $[\text{Cu}_2(4\text{-Clbz})_4(\text{NH}_2\text{pyz})]_n\text{-}\frac{1}{2}\text{BnOH}$ $\text{C}_{35.5}\text{H}_{25}\text{Cu}_2\text{Cl}_4\text{N}_3\text{O}_{8.5}$	3.3(Cl)-DCM/MeOH $[\text{Cu}_2(4\text{-Clbz})_4(\text{NH}_2\text{pyz})]_n$ $\text{C}_{32}\text{H}_{21}\text{Cu}_2\text{Cl}_4\text{N}_3\text{O}_8$	3.4(F) $[\text{Cu}_2(4\text{-Fbz})_4(\text{NH}_2\text{pyz})]_n$ $\text{C}_{32}\text{H}_{21}\text{Cu}_2\text{F}_4\text{N}_3\text{O}_8$
Crystal habit	Needle	Needle	Needle	Needle
Crystal colour	Clear Bluish Green	Clear Bluish Green	Clear Bluish Green	Clear Bluish Green
Crystal size (mm)	0.24×0.05×0.03	0.20×0.02×0.02	0.13×0.05×0.05	0.20×0.03×0.02
Crystal system	Monoclinic	Monoclinic	Monoclinic	Monoclinic
Space group	$I2/m$	$I2/m$	$I2/m$	$I2/m$
a (Å)	12.3484(7)	12.1711(16)	12.1211(4)	11.7460(4)
b (Å)	9.8072(6)	9.7585(11)	9.7915(3)	9.7284(3)
c (Å)	16.8871(15)	16.608(3)	15.0596(7)	15.0360(7)
α (°)	90	90	90	90
β (°)	98.715(4)	101.267(9)	106.673(2)	105.470(2)
γ (°)	90	90	90	90
V (Å ³)	2021.5(2)	1934.5(5)	1712.19(11)	1655.92(11)
Density (g cm ⁻³)	1.89	1.543	1.638	1.562
Temperature (K)	100.02	99.99	99.99	99.94
μ (mm ⁻¹)	6.487	4.364	4.876	2.267
Wavelength (Å)	1.54178	1.54178	1.54178	1.54178
2 θ range (°)	8.3 to 123.524	8.284 to 123.562	8.292 to 122.544	10.954 to 117.514
Reflns. collected	10392	8412	9238	6790
Independent reflns. [R_{int}]	1665 [0.0644]	1590 [0.1459]	1402 [0.0539]	1251 [R_{int}]=0.0686]
Reflns. used in refinement, n	1665	1590	1402	1251
LS parameters, p	152	152	131	131
Restraints, r	2	12	15	0
$R1$ (F^a) / >2.0 $\sigma(I)$	0.0600	0.0925	0.0348	0.0432
$wR2$ (F^2) ^a , all data	0.1662	0.2697	0.0853	0.1002
$S(F^2)$ ^a , all data	1.066	1.086	1.061	1.045

$$^a R1(F) = \frac{\sum(|F_o| - |F_c|)}{\sum|F_o|}; wR2(F^2) = \frac{[\sum w(F_o^2 - F_c^2)^2]}{[\sum wF_o^4]^{1/2}}; S(F^2) = \frac{[\sum w(F_o^2 - F_c^2)^2]}{(n + r - p)}^{1/2}$$

Table 3.3.5-1. Summary of the partial solution of the desolvated single crystal data of **3.2(Br)** polymer obtained by drying single crystals at room temperature

3.2(Br)-Desolvated	
[Cu₂(4-Brbz)₄(NH₂pyz)]_n	
C₃₂H₂₁Br₄Cu₂N₃O₈	
Crystal habit	Needle
Crystal colour	Clear Bluish Green
Crystal size (mm)	0.16 × 0.06 × 0.02
Crystal system	Monoclinic
Space group	<i>I</i> 2/ <i>m</i>
<i>a</i> (Å)	12.9994(5)
<i>b</i> (Å)	9.8571(4)
<i>c</i> (Å)	13.0755(9)
α (°)	90
β (°)	90.291(2)
γ (°)	90
<i>V</i> (Å ³)	1675.43(14)
Density (g cm ⁻³)	2.01
Temperature (K)	100
μ (mm ⁻¹)	7.637
Wavelength (Å)	1.54178
2θ range (°)	9.57 to 117.896
Reflns. collected	7096
Independent reflns. [<i>R</i> _{int}]	1295 [0.0700]
Reflns. used in refinement, <i>n</i>	1295
LS parameters, <i>p</i>	169
Restraints, <i>r</i>	225
<i>R</i> 1 (<i>F</i>) ^a / >2.0σ(<i>I</i>)	0.1229
<i>wR</i> 2 (<i>F</i> ²) ^a , all data	0.3841
<i>S</i> (<i>F</i> ²) ^a , all data	1.647

$$^a = R1(F) = \Sigma(|F_o| - |F_c|) / \Sigma|F_o| ; wR2(F^2) = [\Sigma w(F_o^2 - F_c^2)^2 / \Sigma w F_o^4]^{1/2} ; S(F^2) = [\Sigma w(F_o^2 - F_c^2)^2 / (n + r - p)]^{1/2}$$

Appendix 3.8.2: *In situ* PXRD Data

Table 3.3.7-1. Pawley fits of *in situ* PXRD data during CO₂ adsorption for **3.2(Br)** at 195 K, $\lambda = 0.82525(1)$

P (bar)	Space Group	Volume (Å ³)	a (Å)	b (Å)	c (Å)	α (°)	β (°)	γ (°)	R_{wp}	R_{wp}'	Parameters
0	<i>I2/m</i>	1704.73(8)	13.0999(4)	9.8872(2)	13.1618(5)	90	90.223(3)	90	0.1028	0.2617	985
0.25	<i>I2/m</i>	1710.5(1)	13.1215(5)	9.8836(2)	13.1896(5)	90	90.230(3)	90	0.0737	0.1784	1265
	<i>I2/m</i>	1971.5(5)	12.4792(14)	9.8592(15)	16.2293(24)	90	99.119(11)	90			
0.5	<i>I2/m</i>	1721.9(1)	13.1590(5)	9.8844(5)	13.2386(7)	90	90.185(4)	90	0.0597	0.1147	1267
	<i>I2/m</i>	1984.7(1)	12.4959(3)	9.8695(2)	16.2787(7)	90	98.674(3)	90			
0.75	<i>I2/m</i>	1735.7(2)	13.2015(5)	9.8821(5)	13.3043(8)	90	90.238(4)	90	0.0549	0.0832	1268
	<i>I2/m</i>	1993.7(1)	12.5093(3)	9.8673(2)	16.3343(5)	90	98.567(2)	90			
1	<i>I2/m</i>	1727.5(3)	13.1643(18)	9.8808(11)	13.2818(10)	90	90.566(8)	90	0.0559	0.1442	1270
	<i>I2/m</i>	2001.2(1)	12.5188(4)	9.8674(2)	16.3822(7)	90	98.540(4)	90			
0	<i>I2/m</i>	1712.4(2)	13.1324(11)	9.8537(8)	13.2348(11)	90	90.983(6)	90	0.0647	0.1428	1265
	<i>I2/m</i>	1913.0(3)	12.3193(10)	9.8422(6)	15.9428(15)	90	98.269(6)	90			

Table 3.3.7-2. Rietveld fits of *in situ* PXRD data during CO₂ adsorption for **3.2(Br)** at 195 K, $\lambda = 0.82525(1)$ Å

P (bar)	Space Group	Volume	a	b	c	α	β	γ	% of each phase present	CO ₂ Occupancy	R_{wp}	R_{wp}'	Parameters
0	<i>I2/m</i>	1704.4(4)	13.130(2)	9.889(1)	13.126(2)	90	90.14(2)	90	100	n/a	0.2120	0.6504	21
0.25	<i>I2/m</i>	1715.2(5)	13.154(2)	9.892(1)	13.182(2)	90	90.25(2)	90	69.9(13)	n/a	0.1829	0.5657	36
	<i>I2/m</i>	1985.4(10)	12.518(3)	9.891(3)	16.241(5)	90	99.13(3)	90	30.1(13)	0.88(4)			
0.5	<i>I2/m</i>	1718.0(5)	13.192(3)	9.878(1)	13.185(2)	90	90.16(2)	90	50.4(8)	n/a	0.1500	0.4931	36
	<i>I2/m</i>	1985.6(3)	12.501(1)	9.868(1)	16.280(2)	90	98.62(1)	90	49.6(8)	0.72(2)			
0.75	<i>I2/m</i>	1726.0(7)	13.223(4)	9.873(2)	13.221(3)	90	90.25(2)	90	48.4(9)	n/a	0.1473	0.5100	36
	<i>I2/m</i>	1994.6(3)	12.513(1)	9.868(1)	16.335(2)	90	98.53(1)	90	51.6(9)	0.71(2)			
1	<i>I2/m</i>	1731.8(9)	13.240(5)	9.870(3)	13.253(3)	90	90.38(3)	90	44.3(9)	n/a	0.135	0.5094	36
	<i>I2/m</i>	2001.5(3)	12.520(1)	9.867(1)	16.381(2)	90	98.52(1)	90	55.7(9)	0.75(2)			
0	<i>I2/m</i>	1743.1(14)	13.256(7)	9.874(4)	13.318(6)	90	90.67(5)	90	77.4(19)	n/a	0.1552	0.6617	36
	<i>I2/m</i>	1920.1(20)	12.408(6)	9.874(5)	15.84(1)	90	98.34(7)	90	22.6(19)	1.00(7)			

Table 3.3.7-3. Pawley fits of *in situ* PXRD data during CO₂ adsorption for **3.3(Cl)** at 195 K, $\lambda = 0.82520(1)$ Å

	P (bar)	Space Group	Volume (Å ³)	a (Å)	b (Å)	c (Å)	α (°)	β (°)	γ (°)	R_{wp}	R_{wp}'	Parameters
	0	<i>I2/m</i>	1732.4(1)	12.1606(3)	9.8200(3)	15.1194(7)	90	106.360(3)	90	0.1223	0.3060	603
	0.04	<i>I2/m</i>	1736.9(1)	12.1633(3)	9.8184(3)	15.1534(8)	90	106.306(4)	90	0.1210	0.3016	599
	0.09	<i>I2/m</i>	1738.10(9)	12.1732(3)	9.8161(2)	15.1429(6)	90	106.148(3)	90	0.0788	0.1708	1244
		<i>I2/m</i>	1876.78(11)	12.2539(4)	9.8029(4)	15.9414(5)	90	101.454(3)	90			
	0.69	<i>I2/m</i>	1890.96(8)	12.2919(2)	9.7997(2)	15.9631(5)	90	100.451(2)	90	0.1090	0.2861	657
3.3(Cl)- 195 K-CO₂	0.98	<i>I2/m</i>	1921.27(7)	12.3669(2)	9.8030(2)	16.0448(4)	90	98.992(2)	90	0.0910	0.2470	669
	0.72	<i>I2/m</i>	1918.76(7)	12.3601(2)	9.8024(2)	16.0393(4)	90	99.112(2)	90	0.0921	0.2485	669
	0.32	<i>I2/m</i>	1902.10(8)	12.3187(2)	9.8008(2)	15.9918(5)	90	99.881(2)	90	0.1045	0.2801	661
	0.11	<i>I2/m</i>	1889.90(8)	12.2880(3)	9.7963(2)	15.9645(5)	90	100.446(2)	90	0.1049	0.2846	657
	0.05	<i>I2/m</i>	1885.66(9)	12.2811(3)	9.7965(2)	15.9470(5)	90	100.633(3)	90	0.1118	0.3044	657
	0	<i>I2/m</i>	1749.6(2)	12.1862(6)	9.8155(5)	15.1668(11)	90	105.332(6)	90	0.1410	0.3691	609

Table 3.3.7-4. Rietveld fits of *in situ* PXRD data during CO₂ adsorption for **3.3(Cl)** at 195 K, $\lambda = 0.82520(1)$ Å

	P (bar)	Space Group	Volume (Å ³)	a (Å)	b (Å)	c (Å)	α (°)	β (°)	γ (°)	% of each phase present	CO ₂ Occupancy	R_{wp}	R_{wp}'	Parameters
	0	<i>I2/m</i>	1731.6(1)	12.1608(5)	9.8214(5)	15.1137(7)	90	106.403(3)	90	100	N/A	0.1342	0.4134	21
	0.04	<i>I2/m</i>	1736.3(1)	12.1645(5)	9.8185(5)	15.1478(7)	90	106.321(3)	90	100	N/A	0.1276	0.3982	21
	0.09	<i>I2/m</i>	1734.8(2)	12.1689(6)	9.8130(5)	15.1286(8)	90	106.208(4)	90	72.1(3)	N/A	0.1084	0.3585	32
		<i>I2/m</i>	1872.9(2)	12.2463(8)	9.8015(7)	15.9300(11)	90	101.620(6)	90	27.9(3)				
	0.69	<i>I2/m</i>	1890.3(1)	12.2919(3)	9.8001(3)	15.9581(6)	90	100.472(3)	90	100	0.334(6)	0.1275	0.4276	29
3.3(Cl)- 195 K- CO₂	0.98	<i>I2/m</i>	1921.9(9)	12.3702(3)	9.8048(3)	16.0422(5)	90	98.982(2)	90	100	0.479(5)	0.1161	0.3951	29
	0.72	<i>I2/m</i>	1918.6(1)	12.3615(4)	9.8029(3)	16.0353(6)	90	99.112(2)	90	100	0.460(5)	0.1171	0.4004	29
	0.32	<i>I2/m</i>	1902.3(1)	12.3204(3)	9.8020(3)	15.9896(6)	90	99.886(3)	90	100	0.348(5)	0.1241	0.4241	28
	0.11	<i>I2/m</i>	1889.2(1)	12.2882(5)	9.7966(5)	15.9587(7)	90	100.461(3)	90	100	0.342(6)	0.1254	0.4310	29
	0.05	<i>I2/m</i>	1885.2(1)	12.2810(5)	9.7972(4)	15.9437(7)	90	100.659(3)	90	100	0.365(7)	0.1261	0.4373	29
	0	<i>I2/m</i>	1747.5(3)	12.1848(12)	9.8162(11)	15.1553(17)	90	105.413(6)	90	100	0	0.1460	0.4830	21

Table 3.3.7-5. Pawley fits of *in situ* PXRD data during CO₂ adsorption for **3.4(F)** at 195 K, $\lambda = 0.82520(1)$ Å

	P (bar)	Space Group	Volume (Å ³)	<i>a</i> (Å)	<i>b</i> (Å)	<i>c</i> (Å)	α (°)	β (°)	γ (°)	<i>R</i> _{wp}	<i>R</i> _{wp'}	Parameters
3.4(F)- 195 K- CO₂	0	<i>I2/m</i>	1685.06(6)	11.8464(2)	9.7481(2)	15.1293(4)	90	105.318(2)	90	0.0457	0.2026	580
	0.05	<i>I2/m</i>	1780.08(7)	12.0829(2)	9.7406(2)	15.3741(4)	90	100.337(2)	90	0.0508	0.2321	621
	0.08	<i>I2/m</i>	1785.89(6)	12.1009(2)	9.7404(2)	15.3874(4)	90	100.041(1)	90	0.0494	0.1718	624
	0.33	<i>I2/m</i>	1803.43(5)	12.1531(2)	9.7416(2)	15.4354(3)	90	99.292(1)	90	0.0435	0.1673	628
	0.7	<i>I2/m</i>	1821.10(5)	12.2043(2)	9.7433(2)	15.4924(3)	90	98.678(1)	90	0.0412	0.1866	634
	1	<i>I2/m</i>	1825.88(5)	12.2163(2)	9.7433(2)	15.5118(3)	90	98.537(1)	90	0.0394	0.1768	634
	0.7	<i>I2/m</i>	1822.97(5)	12.2072(2)	9.7434(2)	15.5038(3)	90	98.665(1)	90	0.0400	0.1772	634
	0.3	<i>I2/m</i>	1806.15(6)	12.1593(2)	9.7405(2)	15.4508(3)	90	99.255(1)	90	0.0439	0.1723	628
	0.1	<i>I2/m</i>	1791.21(6)	12.1177(2)	9.7390(2)	15.4049(4)	90	99.847(2)	90	0.0463	0.1813	624
	0.05	<i>I2/m</i>	1788.00(6)	12.1090(2)	9.7392(2)	15.3963(3)	90	100.024(1)	90	0.0458	0.1343	626
	0	<i>I2/m</i>	1696.55(8)	11.8895(3)	9.7446(3)	15.1439(4)	90	104.773(2)	90	0.0418	0.1524	586

Table 3.3.7-6. Rietveld fits of *in situ* PXRD data during CO₂ adsorption for **3.4(F)** at 195 K, $\lambda = 0.82520(1)$ Å

	P (bar)	Space Group	Volume (Å ³)	<i>a</i> (Å)	<i>b</i> (Å)	<i>c</i> (Å)	α (°)	β (°)	γ (°)	CO ₂ Occupancy		<i>R</i> _{wp}	<i>R</i> _{wp'}	Parameters
										Site 1	Site 2			
3.4(F)- 195 K- CO₂	0	<i>I2/m</i>	1685.42(8)	11.8471(3)	9.7487(2)	15.1312(5)	90	105.325(2)	90	n/a	n/a	0.0636	0.2877	21
	0.05	<i>I2/m</i>	1778.92(16)	12.0821(6)	9.7405(5)	15.3670(9)	90	100.374(4)	90	0.244(10)	0.087(9)	0.0740	0.3952	35
	0.08	<i>I2/m</i>	1786.07(14)	12.1015(5)	9.7405(4)	15.3883(8)	90	100.047(3)	90	0.234(17)	0.124(16)	0.0729	0.3874	35
	0.33	<i>I2/m</i>	1803.86(10)	12.1542(4)	9.7415(3)	15.4375(6)	90	99.287(2)	90	0.278(11)	0.225(11)	0.0612	0.3314	35
	0.7	<i>I2/m</i>	1821.17(9)	12.2045(3)	9.7432(3)	15.4928(5)	90	98.679(2)	90	0.312(9)	0.263(9)	0.0570	0.3113	35
	1	<i>I2/m</i>	1826.23(9)	12.2173(3)	9.7438(3)	15.5126(5)	90	98.534(2)	90	0.310(9)	0.310(10)	0.0560	0.3110	35
	0.7	<i>I2/m</i>	1823.04(9)	12.2074(3)	9.7435(3)	15.5042(5)	90	98.666(2)	90	0.313(9)	0.273(9)	0.0565	0.3103	35
	0.3	<i>I2/m</i>	1806.89(10)	12.1612(4)	9.7408(3)	15.4541(6)	90	99.245(2)	90	0.356(5)	0.171(5)	0.0601	0.3252	35
	0.1	<i>I2/m</i>	1791.70(17)	12.1196(6)	9.7386(5)	15.4068(8)	90	99.837(3)	90	0.317(7)	0.182(11)	0.0730	0.3931	35
	0.05	<i>I2/m</i>	1787.62(20)	12.1081(7)	9.7381(6)	15.3962(10)	90	100.028(3)	90	0.216(20)	0.091(20)	0.0762	0.4102	35
	0	<i>I2/m</i>	1695.51(17)	11.8866(6)	9.7441(6)	15.1371(10)	90	104.744(4)	90	n/a	n/a	0.0620	0.3002	21

Table 3.3.5-7. Pawley fits of *in situ* PXRD data during N₂ adsorption for **3.3(Cl)** at 90 K. $\lambda = 0.82520(1)$ Å

P (bar)	Space Group	Volume (Å ³)	a (Å)	b (Å)	c (Å)	α (°)	β (°)	γ (°)	R_{wp}	R_{wp}'	Parameters
0	<i>I2/m</i>	1721.88(8)	12.1327(2)	9.8043(2)	15.1042(6)	90	106.592(3)	90	0.1146	0.3095	597
0.36	<i>I2/m</i>	1721.5(1)	12.1241(3)	9.7910(3)	15.1490(8)	90	106.810(4)	90	0.0743	0.1669	1233
	<i>I2/m</i>	1844.9(3)	12.0710(7)	9.7850(11)	16.2460(10)	90	105.960(5)	90			
0.76	<i>I2/m</i>	1716.7(1)	12.1116(4)	9.7801(3)	15.1400(7)	90	106.816(4)	90	0.0750	0.1503	1233
	<i>I2/m</i>	1840.0(2)	12.0636(6)	9.7658(6)	16.2433(9)	90	105.947(5)	90			
1.38	<i>I2/m</i>	1717.3(1)	12.1063(4)	9.7782(3)	15.1565(6)	90	106.837(4)	90	0.0743	0.1429	1233
	<i>I2/m</i>	1842.5(1)	12.0638(5)	9.7671(5)	16.2685(8)	90	106.014(4)	90			
1.75	<i>I2/m</i>	1716.7(1)	12.1059(3)	9.7760(3)	15.1580(6)	90	106.870(4)	90	0.0757	0.1664	1233
	<i>I2/m</i>	1844.6(1)	12.0633(5)	9.7696(5)	16.2803(7)	90	105.975(3)	90			
2.79	<i>I2/m</i>	1864.6(2)	12.1308(6)	9.8388(6)	16.1347(9)	90	104.466(4)	90	0.0952	0.2217	1296
	<i>I2/m</i>	1894.5(1)	12.3135(3)	9.7768(2)	16.0049(5)	90	100.498(3)	90			
3.47	<i>I2/m</i>	1901.84(7)	12.3684(3)	9.7738(2)	15.9563(4)	90	99.607(3)	90	0.1087	0.2838	660
	<i>I2/m</i>	1848.5(1)	12.1127(2)	9.7682(2)	16.2546(6)	90	106.025(2)	90			
2.46	<i>I2/m</i>	1887.0(1)	12.2956(5)	9.7693(5)	15.9801(6)	90	100.561(3)	90	0.0916	0.1848	1294
	<i>I2/m</i>	1869.0(2)	12.1430(6)	9.8167(7)	16.1530(11)	90	103.915(4)	90			
1.41	<i>I2/m</i>	1883.0(1)	12.2519(5)	9.7744(2)	16.0806(5)	90	102.092(3)	90	0.0756	0.0872	1293
	<i>I2/m</i>	1857.5(2)	12.1348(5)	9.7591(6)	16.1862(8)	90	104.299(4)	90			
0.89	<i>I2/m</i>	1889.8(1)	12.3034(4)	9.7768(2)	16.0712(5)	90	102.166(1)	90	0.0772	0.1262	1297
	<i>I2/m</i>	1848.0(1)	12.1073(3)	9.7731(3)	16.1895(7)	90	105.276(3)	90			
0 ^a	<i>I2/m</i>	1850.1(2)	12.1296(5)	9.7758(7)	16.1902(11)	90	105.488(6)	90	0.0702	0.1731	1228
	<i>I2/m</i>	1720.0(1)	12.1188(4)	9.7893(3)	15.1419(8)	90	106.770(4)	90			
0 ^c	<i>I2/m</i>	1845.7(2)	12.0964(8)	9.7781(6)	16.1803(10)	90	105.334(6)	90	0.0760	0.1888	1235
	<i>I2/m</i>	1724.0(1)	12.1290(3)	9.7894(3)	15.1506(8)	90	106.592(5)	90			

^a Initial vacuum measurement. ^b Sample evacuated for 5 h (at room temperature). ^c Sample evacuated for a further 12 h (total 17 h)

Table 3.3.5-8. Rietveld fits of *in situ* PXRD data during N₂ adsorption for **3.3(Cl)** at 90 K. $\lambda = 0.82520(1)$ Å

P (bar)	Space Group	Volume (Å ³)	a (Å)	b (Å)	c (Å)	α (°)	β (°)	γ (°)	% of each phase present	N ₂ Occupancy	R_{wp}	R_{wp}'	Parameters
0	<i>I2/m</i>	1720.3(1)	12.1288(4)	9.8036(3)	15.0994(6)	90	106.634(3)	90	100	n/a	0.1299	0.4226	21
0.36	<i>I2/m</i>	1720.3(2)	12.1219(9)	9.7941(7)	15.1423(13)	90	106.880(7)	90	61.4(5)	n/a	0.1165	0.3294	38
	<i>I2/m</i>	1849.2(4)	12.1030(14)	9.7822(11)	16.2238(20)	90	105.696(11)	90	38.6(5)	0.466(20)			
0.76	<i>I2/m</i>	1719.3(3)	12.1180(11)	9.7896(10)	15.1512(16)	90	106.953(9)	90	43.3(5)	n/a	0.1197	0.3391	38
	<i>I2/m</i>	1847.2(3)	12.0848(9)	9.7798(8)	16.2554(16)	90	105.952(8)	90	56.7(5)	0.396(13)			
1.38	<i>I2/m</i>	1718.3(4)	12.1122(15)	9.7854(13)	15.1593(19)	90	106.993(12)	90	30.4(5)	n/a	0.1228	0.3446	38
	<i>I2/m</i>	1847.4(2)	12.0785(8)	9.7765(7)	16.2784(14)	90	106.042(7)	90	69.6(5)	0.380(11)			
1.75	<i>I2/m</i>	1719.1(5)	12.1136(19)	9.7858(16)	15.1728(24)	90	107.098(16)	90	18.5(6)	n/a	0.1250	0.3521	38
	<i>I2/m</i>	1850.4(2)	12.0835(7)	9.7778(6)	16.2888(12)	90	105.951(6)	90	81.5(6)	0.368(10)			
2.79	<i>I2/m</i>	1863.0(5)	12.1676(16)	9.7759(14)	16.1255(27)	90	103.763(14)	90	21.0(8)	0.798(35)	0.1521	0.4419	45
	<i>I2/m</i>	1894.2(2)	12.3162(6)	9.7751(6)	15.9976(11)	90	100.429(6)	90	79.0(8)	0.330(16)			
3.47	<i>I2/m</i>	1902.0(1)	12.3693(5)	9.7740(4)	15.9559(7)	90	99.601(4)	90	100	0.313(9)	0.1441	0.3878	28
2.46	<i>I2/m</i>	1854.0(6)	12.1119(17)	9.7762(17)	16.2856(31)	90	105.966(16)	90	6.6(6)	1.00(7)	0.1559	0.4349	44
	<i>I2/m</i>	1891.9(2)	12.3042(6)	9.7748(5)	16.0047(11)	90	100.620(5)	90	93.4(6)	0.325(15)			
1.41	<i>I2/m</i>	1865.6(5)	12.1625(14)	9.7755(16)	16.1427(23)	90	103.587(14)	90	58.9(10)	0.375(24)	0.1459	0.4229	45
	<i>I2/m</i>	1879.7(2)	12.2232(7)	9.7747(6)	16.0927(13)	90	102.148(6)	90	41.1(10)	0.532(16)			
0.89	<i>I2/m</i>	1859.4(4)	12.1285(10)	9.7760(13)	16.2013(19)	90	104.540(10)	90	66.3(10)	0.428(18)	0.1461	0.4246	45
	<i>I2/m</i>	1871.8(3)	12.1836(8)	9.7758(8)	16.1364(15)	90	103.113(7)	90	33.7(10)	0.576(21)			

0 ^a	<i>I2/m</i>	1848.3(2)	12.1088(6)	9.7738(5)	16.1889(12)	90	105.268(6)	90	100	0.324(10)	0.1468	0.4256	28
0 ^b	<i>I2/m</i>	1847.4(4)	12.1079(13)	9.7814(10)	16.1837(21)	90	105.448(12)	90	38.2(5)	0.290(18)	0.1180	0.3527	38
	<i>I2/m</i>	1718.0(3)	12.1149(11)	9.7917(9)	15.1278(16)	90	106.789(8)	90	61.8(5)	n/a			
0 ^c	<i>I2/m</i>	1850.3(4)	12.1157(14)	9.7849(12)	16.1840(22)	90	105.335(12)	90	64.8(6)	0.250(17)	0.1404	0.3836	38
	<i>I2/m</i>	1723.9(4)	12.1299(16)	9.7942(12)	15.1505(21)	90	106.712(12)	90	35.2(6)	n/a			

^a Initial vacuum measurement. ^b Sample evacuated for 5 h (at room temperature). ^c Sample evacuated for a further 12 h (total 17 h)

Table 3.3.5-9. Pawley fits of *in situ* PXRD data during N₂ adsorption **3.4(F)** at 90 K. $\lambda = 0.82520(1)$ Å

	P (bar)	Space Group	Volume (Å ³)	<i>a</i> (Å)	<i>b</i> (Å)	<i>c</i> (Å)	α (°)	β (°)	γ (°)	<i>R</i> _{wp}	<i>R</i> _{wp'}	Parameters
3.4(F)- 90 K- N₂	0	<i>I2/m</i>	1672.37(4)	11.7960(1)	9.7490(1)	15.0953(2)	90	105.555(1)	90	0.0498	0.1390	574
	0.35	<i>I2/m</i>	1733.81(5)	11.7941(2)	9.7518(2)	15.5988(3)	90	104.892(1)	90	0.0566	0.1730	604
	0.89	<i>I2/m</i>	1739.68(5)	11.8407(2)	9.7457(1)	15.5544(3)	90	104.249(1)	90	0.0535	0.1442	604
	1.39	<i>I2/m</i>	1751.59(10)	11.9161(4)	9.7365(3)	15.4970(6)	90	103.044(3)	90	0.0792	0.2001	610
	1.74	<i>I2/m</i>	1778.93(10)	12.0916(4)	9.7192(3)	15.3933(6)	90	100.468(3)	90	0.0822	0.2376	621
	2.77	<i>I2/m</i>	1795.42(4)	12.1892(2)	9.7100(1)	15.3603(3)	90	99.042(1)	90	0.0582	0.1708	624
	3.5	<i>I2/m</i>	1809.22(5)	12.2488(2)	9.7083(1)	15.3629(3)	90	97.970(1)	90	0.0607	0.1752	627
	2.47	<i>I2/m</i>	1796.08(8)	12.1824(3)	9.7116(2)	15.3719(5)	90	99.034(2)	90	0.0802	0.2473	623
	1.44	<i>I2/m</i>	1776.51(10)	12.0739(3)	9.7203(3)	15.4061(6)	90	100.724(3)	90	0.0835	0.2473	621
	1.06	<i>I2/m</i>	1769.29(10)	12.0319(3)	9.7240(3)	15.4250(6)	90	101.369(3)	90	0.0839	0.2385	616
	0.5	<i>I2/m</i>	1753.69(9)	11.9325(3)	9.7378(2)	15.4823(5)	90	102.884(3)	90	0.0781	0.2051	610
	0 ^a	<i>I2/m</i>	1721.90(6)	11.8220(2)	9.7418(2)	15.4493(4)	90	104.587(1)	90	0.0554	0.1627	598
	0 ^b	<i>I2/m</i>	1776.60(6)	12.1077(2)	9.7100(2)	15.3568(4)	90	100.252(2)	90	0.0721	0.2102	621
	0 ^c	<i>I2/m</i>	1779.83(7)	12.1193(2)	9.7126(2)	15.3601(4)	90	100.133(2)	90	0.0797	0.2313	621

^a Initial vacuum measurement. ^b Sample evacuated for 5 h (at room temperature). ^c Sample evacuated for a further 12 h (total 17 h)

Table 3.3.5-10. Rietveld fits of *in situ* PXRD data during N₂ adsorption for **3.4(F)** at 90 K. $\lambda = 0.82520(1)$ Å

	P (bar)	Space Group	Volume (Å ³)	<i>a</i> (Å)	<i>b</i> (Å)	<i>c</i> (Å)	α (°)	β (°)	γ (°)	N ₂ Occupancy		<i>R</i> _{wp}	<i>R</i> _{wp'}	Parameters
										Site 1	Site 2			
3.4(F)- 90 K- N₂	0	<i>I2/m</i>	1672.37(6)	11.7957(2)	9.7489(2)	15.0964(4)	90	105.562(2)	90	n/a	n/a	0.0763	0.2188	21
	0.35	<i>I2/m</i>	1733.40(9)	11.7935(3)	9.7503(3)	15.5986(5)	90	104.897(2)	90	0.400(6)	n/a	0.0887	0.2765	28
	0.89	<i>I2/m</i>	1739.57(10)	11.8403(4)	9.7450(3)	15.5562(6)	90	104.268(3)	90	0.428(6)	n/a	0.0850	0.2616	28
	1.39	<i>I2/m</i>	1751.05(32)	11.9122(11)	9.7378(10)	15.5014(18)	90	103.139(7)	90	0.310(10)	n/a	0.1194	0.3861	28
	1.74	<i>I2/m</i>	1779.34(23)	12.0918(8)	9.7191(7)	15.3966(13)	90	100.464(6)	90	0.240(10)	0.301(8)	0.1243	0.4100	35
	2.77	<i>I2/m</i>	1795.77(7)	12.1903(3)	9.7102(2)	15.3611(4)	90	99.030(2)	90	0.387(6)	0.271(5)	0.0868	0.2711	35
	3.5	<i>I2/m</i>	1809.13(8)	12.2502(3)	9.7084(2)	15.3597(5)	90	97.964(2)	90	0.416(7)	0.224(5)	0.0930	0.3038	35
	2.47	<i>I2/m</i>	1797.29(14)	12.1879(5)	9.7111(4)	15.3736(8)	90	98.979(4)	90	0.278(8)	0.236(7)	0.1139	0.3685	35
	1.44	<i>I2/m</i>	1776.43(22)	12.0726(8)	9.7202(6)	15.4072(13)	90	100.726(6)	90	0.219(10)	0.255(8)	0.1211	0.3991	35
	1.06	<i>I2/m</i>	1769.42(21)	12.0384(7)	9.7224(6)	15.4153(12)	90	101.275(5)	90	0.157(10)	0.216(9)	0.1197	0.3910	35
	0.5	<i>I2/m</i>	1753.24(21)	11.9324(7)	9.7376(6)	15.4783(13)	90	102.876(5)	90	0.243(9)	n/a	0.1163	0.3724	28
	0 ^a	<i>I2/m</i>	1720.36(13)	11.8208(5)	9.7405(4)	15.4464(7)	90	104.691(4)	90	0.268(8)	n/a	0.0968	0.2968	28
	0 ^b	<i>I2/m</i>	1775.62(23)	12.1031(8)	9.7104(7)	15.3568(13)	90	100.319(6)	90	n/a	0.269(8)	0.1324	0.4549	28
	0 ^c	<i>I2/m</i>	1779.73(23)	12.1197(9)	9.7119(7)	15.3595(13)	90	100.127(5)	90	0.343(11)	n/a	0.1512	0.4717	28

^a Initial vacuum measurement. ^b Sample evacuated for 5 h (at room temperature). ^c Sample evacuated for a further 12 h (total 17 h)

Appendix 3.8.3: *In situ* Single-Crystal Data

Table 3.3.8-1. Summary of *in situ* single-crystal data during CO₂ adsorption (and desorption) for **3.3(Cl)** at 195 K

	3.3(Cl)-Vac [Cu ₂ (4-Clbz) ₄ (NH ₂ pyz)] _n C ₃₂ H ₂₁ Cl ₄ Cu ₂ N ₃ O ₈	3.3(Cl)-0.5bar CO₂ [Cu ₂ (4-Clbz) ₄ (NH ₂ pyz)] _n C ₃₂ H ₂₁ Cl ₄ Cu ₂ N ₃ O ₈	3.3(Cl)-0.75bar CO₂ [Cu ₂ (4-Clbz) ₄ (NH ₂ pyz)] _n C ₃₂ H ₂₁ Cl ₄ Cu ₂ N ₃ O ₈
Crystal habit	Plank	Plank	Plank
Crystal colour	Clear Bluish Green	Clear Bluish Green	Clear Bluish Green
Crystal size (mm)	0.07 × 0.03 × 0.03	0.07 × 0.03 × 0.03	0.07 × 0.03 × 0.03
Crystal system	Monoclinic	Monoclinic	Monoclinic
Space group	<i>I</i> 2/ <i>m</i>	<i>I</i> 2/ <i>m</i>	<i>I</i> 2/ <i>m</i>
<i>a</i> (Å)	12.190(2)	12.4035(16)	12.4229(15)
<i>b</i> (Å)	9.8337(11)	9.8140(10)	9.8197(9)
<i>c</i> (Å)	15.138(3)	16.241(4)	16.310(3)
α (°)	90	90	90
β (°)	106.19(2)	98.483(16)	98.341(15)
γ (°)	90	90	90
<i>V</i> (Å ³)	1742.7(6)	1955.3(6)	1968.6(5)
Density (g cm ⁻³)	1.609	1.434	1.425
Temperature (K)	195	195	195
μ (mm ⁻¹)	1.457	1.298	1.29
Wavelength (Å)	0.6889	0.6889	0.6889
2θ range (°)	4.848 to 54.678	4.328 to 54.676	4.31 to 54.676
Refins. collected	10530	11974	12172
Independent reflns. [<i>R</i> _{int}]	2256 [0.2008]	2536 [0.1355]	2560 [0.1237]
Refins. used in refinement, <i>n</i>	2256	2536	2560
LS parameters, <i>p</i>	131	131	131
Restraints, <i>r</i>	9	9	9
<i>R</i> 1 (<i>F</i>) ^a > 2.0σ(<i>I</i>)	0.1083	0.1145	0.1108
<i>wR</i> 2 (<i>F</i> ²) ^a , all data	0.3114	0.3786	0.3120
<i>S</i> (<i>F</i> ²) ^a , all data	1.0280	1.146	1.556
	3.3(Cl)-1.0bar CO₂ [Cu ₂ (4-Clbz) ₄ (NH ₂ pyz)] _n C ₃₂ H ₂₁ Cl ₄ Cu ₂ N ₃ O ₈	3.3(Cl)-0.75bar (D) CO₂ [Cu ₂ (4-Clbz) ₄ (NH ₂ pyz)] _n C ₃₂ H ₂₁ Cl ₄ Cu ₂ N ₃ O ₈	3.3(Cl)-0.5bar (D) CO₂ [Cu ₂ (4-Clbz) ₄ (NH ₂ pyz)] _n C ₃₂ H ₂₁ Cl ₄ Cu ₂ N ₃ O ₈
Crystal habit	Plank	Plank	Plank
Crystal colour	Clear Bluish Green	Clear Bluish Green	Clear Bluish Green
Crystal size (mm)	0.07 × 0.03 × 0.03	0.07 × 0.03 × 0.03	0.07 × 0.03 × 0.03
Crystal system	Monoclinic	Monoclinic	Monoclinic
Space group	<i>I</i> 2/ <i>m</i>	<i>I</i> 2/ <i>m</i>	<i>I</i> 2/ <i>m</i>
<i>a</i> (Å)	12.4398(16)	12.4207(14)	12.4184(15)
<i>b</i> (Å)	9.8231(9)	9.8109(7)	9.8222(9)
<i>c</i> (Å)	16.352(4)	16.327(3)	16.344(4)
α (°)	90	90	90
β (°)	98.335(16)	98.523(14)	98.688(16)
γ (°)	90	90	90
<i>V</i> (Å ³)	1977.0(5)	1967.6(4)	1970.7(5)
Density (g cm ⁻³)	1.418	1.425	1.423
Temperature (K)	195	195	195
μ (mm ⁻¹)	1.284	1.29	1.288
Wavelength (Å)	0.6889	0.6889	0.6889
2θ range (°)	4.302 to 54.678	4.318 to 54.672	4.324 to 54.672
Refins. collected	12203	12198	12210
Independent reflns. [<i>R</i> _{int}]	2566 [0.1190]	2556 [0.1262]	2561 [0.1303]
Refins. used in refinement, <i>n</i>	2566	2556	2561
LS parameters, <i>p</i>	131	131	131
Restraints, <i>r</i>	9	9	9
<i>R</i> 1 (<i>F</i>) ^a > 2.0σ(<i>I</i>)	0.11	0.1087	0.1135
<i>wR</i> 2 (<i>F</i> ²) ^a , all data	0.3647	0.3719	0.3854
<i>S</i> (<i>F</i> ²) ^a , all data	1.1420	1.135	1.135

$$^a = R1(F) = \frac{\sum(|F_o| - |F_c|)}{\sum|F_o|} ; wR2(F^2) = \frac{[\sum w(F_o^2 - F_c^2)^2 / \sum w F_o^4]^{1/2}}{\sum w F_o^2} ; S(F^2) = \frac{[\sum w(F_o^2 - F_c^2)^2 / (n + r - p)]^{1/2}}{\sum w F_o^2}$$

Table 3.3.8-1[cont]. Summary of *in situ* single-crystal data during CO₂ adsorption (and desorption) for **3.3(Cl)** at 195 K

	3.3(Cl)-0.25bar(D) CO₂ [Cu₂(4-Clbz)₄(NH₂pyz)]_n C ₃₂ H ₂₁ Cl ₄ Cu ₂ N ₃ O ₈	3.3(Cl)-Vac(D) CO₂ [Cu₂(4-Clbz)₄(NH₂pyz)]_n C ₃₂ H ₂₁ Cl ₄ Cu ₂ N ₃ O ₈	3.3(Cl)-Vac(D)-1hr CO₂ [Cu₂(4-Clbz)₄(NH₂pyz)]_n C ₃₂ H ₂₁ Cl ₄ Cu ₂ N ₃ O ₈
Crystal habit	Plank	Plank	Plank
Crystal colour	Clear Bluish Green	Clear Bluish Green	Clear Bluish Green
Crystal size (mm)	0.07 × 0.03 × 0.03	0.07 × 0.03 × 0.03	0.07 × 0.03 × 0.03
Crystal system	Monoclinic	Monoclinic	Monoclinic
Space group	<i>I</i> 2/ <i>m</i>	<i>I</i> 2/ <i>m</i>	<i>I</i> 2/ <i>m</i>
<i>a</i> (Å)	12.3884(18)	12.371(4)	12.356(5)
<i>b</i> (Å)	9.8077(10)	9.804(3)	9.810(4)
<i>c</i> (Å)	16.364(4)	16.387(9)	16.421(9)
α (°)	90	90	90
β (°)	98.800(18)	99.05(4)	99.22(5)
γ (°)	90	90	90
<i>V</i> (Å ³)	1964.9(6)	1962.7(13)	1964.6(16)
Density (g cm ⁻³)	1.426	1.429	1.427
Temperature (K)	195	195	195
μ (mm ⁻¹)	1.292	1.293	1.292
Wavelength (Å)	0.6889	0.6889	0.6889
2θ range (°)	4.332 to 54.676	4.344 to 54.676	4.352 to 54.672
Reflns. collected	12160	12107	12099
Independent reflns. [<i>R</i> _{int}]	2551 [0.1478]	2541 [0.1693]	2545 [0.2122]
Reflns. used in refinement, <i>n</i>	2551	2451	2545
LS parameters, <i>p</i>	135	131	131
Restraints, <i>r</i>	9	12	105
<i>R</i> 1 (<i>F</i>) ^a <i>I</i> > 2.0σ(<i>I</i>)	0.1259	0.1227	0.1384
<i>wR</i> 2 (<i>F</i> ²) ^a , all data	0.3996	0.4100	0.4441
<i>S</i> (<i>F</i> ²) ^a , all data	1.110	1.064	1.036

$$^a = R1(F) = \sum(|F_o| - |F_c|) / \sum|F_o| ; wR2(F^2) = [\sum w(F_o^2 - F_c^2)^2 / \sum w F_o^4]^{1/2} ; S(F^2) = [\sum w(F_o^2 - F_c^2)^2 / (n + r - p)]^{1/2}$$

Table 3.3.8-2. Summary of *in situ* single-crystal data during CO₂ adsorption (and desorption) for **3.4(F)** at 195 K

	3.4(F)-Vac [Cu₂(4-Fbz)₄(NH₂pyz)]_n C ₃₂ H ₂₁ F ₄ Cu ₂ N ₃ O ₈	3.4(F)-0.05bar CO₂ [Cu₂(4-Fbz)₄(NH₂pyz)]_n C ₃₂ H ₂₁ F ₄ Cu ₂ N ₃ O ₈	2.4(F)-0.1bar CO₂ [Cu₂(4-Fbz)₄(NH₂pyz)]_n C ₃₂ H ₂₁ F ₄ Cu ₂ N ₃ O ₈
Crystal habit	Needle	Needle	Needle
Crystal colour	Clear Bluish Green	Clear Bluish Green	Clear Bluish Green
Crystal size (mm)	0.17 × 0.017 × 0.017	0.17 × 0.017 × 0.017	0.17 × 0.017 × 0.017
Crystal system	Monoclinic	Monoclinic	Monoclinic
Space group	<i>I2/m</i>	<i>I2/m</i>	<i>I2/m</i>
<i>a</i> (Å)	11.8354(6)	11.9517(12)	12.0102(19)
<i>b</i> (Å)	9.7433(5)	9.7402(7)	9.7355(12)
<i>c</i> (Å)	15.0902(10)	15.122(2)	15.185(3)
α (°)	90	90	90
β (°)	105.069(6)	103.343(12)	102.125(18)
γ (°)	90	90	90
<i>V</i> (Å ³)	1680.29(17)	1712.8(3)	1736.0(5)
Density (g cm ⁻³)	1.539	1.51	1.49
Temperature (K)	195	195	195
μ (mm ⁻¹)	1.236	1.213	1.197
Wavelength (Å)	0.6889	0.6889	0.6889
2θ range (°)	3.796 to 53.216	3.81 to 53.45	3.824 to 53.54
Reflns. collected	10109	10212	10245
Independent reflns. [<i>R</i> _{int}]	2026 [0.0510]	2070 [0.0669]	2095 [0.0913]
Reflns. used in refinement, <i>n</i>	2026	2070	2095
LS parameters, <i>p</i>	131	131	131
Restraints, <i>r</i>	0	0	0
<i>R</i> 1 (<i>F</i>) ^a <i>I</i> > 2.0σ(<i>I</i>)	0.0381	0.0693	0.0805
<i>wR</i> 2 (<i>F</i> ²) ^a , all data	0.1043	0.2262	0.2787
<i>S</i> (<i>F</i> ²) ^a , all data	1.0420	1.037	0.996
	3.4(F)-0.35bar CO₂ [Cu₂(4-Fbz)₄(NH₂pyz)]_n C ₃₂ H ₂₁ F ₄ Cu ₂ N ₃ O ₈	3.4(F)-0.55bar CO₂ [Cu₂(4-Fbz)₄(NH₂pyz)]_n C ₃₂ H ₂₁ F ₄ Cu ₂ N ₃ O ₈	3.4(F)-0.75bar CO₂ [Cu₂(4-Fbz)₄(NH₂pyz)]_n C ₃₂ H ₂₁ F ₄ Cu ₂ N ₃ O ₈
Crystal habit	Needle	Needle	Needle
Crystal colour	Clear Bluish Green	Clear Bluish Green	Clear Bluish Green
Crystal size (mm)	0.17 × 0.017 × 0.017	0.17 × 0.017 × 0.017	0.17 × 0.017 × 0.017
Crystal system	Monoclinic	Monoclinic	Monoclinic
Space group	<i>I2/m</i>	<i>I2/m</i>	<i>I2/m</i>
<i>a</i> (Å)	12.1435(10)	12.1801(9)	12.1940(12)
<i>b</i> (Å)	9.7273(7)	9.7291(6)	9.7243(8)
<i>c</i> (Å)	15.4245(17)	15.4844(16)	15.510(2)
α (°)	90	90	90
β (°)	99.432(9)	99.072(8)	98.996(12)
γ (°)	90	90	90
<i>V</i> (Å ³)	1797.4(3)	1812.0(3)	1816.6(4)
Density (g cm ⁻³)	1.439	1.427	1.423
Temperature (K)	195	195	195
μ (mm ⁻¹)	1.156	1.147	1.144
Wavelength (Å)	0.6889	0.6889	0.6889
2θ range (°)	3.846 to 53.228	3.842 to 53.182	3.84 to 53.208
Reflns. collected	10676	10745	10673
Independent reflns. [<i>R</i> _{int}]	2174 [0.0846]	2193 [0.1021]	2196 [0.1011]
Reflns. used in refinement, <i>n</i>	2174	2193	2196
LS parameters, <i>p</i>	131	131	132
Restraints, <i>r</i>	0	0	0
<i>R</i> 1 (<i>F</i>) ^a <i>I</i> > 2.0σ(<i>I</i>)	0.1025	0.1086	0.1109
<i>wR</i> 2 (<i>F</i> ²) ^a , all data	0.3425	0.3467	0.3502
<i>S</i> (<i>F</i> ²) ^a , all data	1.1860	1.181	1.142

^a $-R1(F) = \sum(|F_o| - |F_c|) / \sum|F_o|$; $wR2(F^2) = [\sum w(F_o^2 - F_c^2)^2 / \sum wF_o^4]^{1/2}$; $S(F^2) = [\sum w(F_o^2 - F_c^2)^2 / (n + r - p)]^{1/2}$

Table 3.3.8-2[cont.]. Summary of *in situ* single-crystal data during CO₂ adsorption (and desorption) for **3.4(F)** at 195 K

	3.4(F)-1bar CO₂ [Cu₂(4-Fbz)₄(NH₂pyz)]_n C ₃₂ H ₂₁ F ₄ Cu ₂ N ₃ O ₈	3.4(F)-0.1bar CO₂ (D) [Cu₂(4-Fbz)₄(NH₂pyz)]_n C ₃₂ H ₂₁ F ₄ Cu ₂ N ₃ O ₈	3.4(F)-Vac (D) [Cu₂(4-Fbz)₄(NH₂pyz)]_n C ₃₂ H ₂₁ F ₄ Cu ₂ N ₃ O ₈
Crystal habit	Needle	Needle	Needle
Crystal colour	Clear Bluish Green	Clear Bluish Green	Clear Bluish Green
Crystal size (mm)	0.17 × 0.017 × 0.017	0.17 × 0.017 × 0.017	0.17 × 0.017 × 0.017
Crystal system	Monoclinic	Monoclinic	Monoclinic
Space group	<i>I</i> 2/ <i>m</i>	<i>I</i> 2/ <i>m</i>	<i>I</i> 2/ <i>m</i>
<i>a</i> (Å)	12.2197(14)	11.929(2)	11.9138(13)
<i>b</i> (Å)	9.7197(9)	9.7243(9)	9.7160(7)
<i>c</i> (Å)	15.546(3)	15.024(4)	14.968(2)
α (°)	90	90	90
β (°)	98.934(14)	103.94(2)	104.076(14)
γ (°)	90	90	90
<i>V</i> (Å ³)	1824.1(4)	1691.5(6)	1680.6(4)
Density (g cm ⁻³)	1.418	1.529	1.539
Temperature (K)	195	195	195
μ (mm ⁻¹)	1.139	1.228	1.236
Wavelength (Å)	0.6889	0.6889	0.6889
2θ range (°)	3.834 to 53.258	4.838 to 53.17	3.814 to 53.214
Reflns. collected	10746	2456	9923
Independent reflns. [<i>R</i> _{int}]	2204 [0.1048]	1692 [0.0430]	2027 [0.0812]
Reflns. used in refinement, <i>n</i>	2204	1692	2027
LS parameters, <i>p</i>	131	131	131
Restraints, <i>r</i>	0	0	0
<i>R</i> 1 (<i>F</i>) ^a / >2.0σ(<i>I</i>)	0.1124	0.0652	0.0645
<i>wR</i> 2 (<i>F</i>) ^a , all data	0.3504	0.2397	0.2072
<i>S</i> (<i>F</i>) ^a , all data	1.150	0.974	1.011

$$^a = R1(F) = \sum(|F_o| - |F_c|) / \sum|F_o| ; wR2(F^2) = [\sum w(F_o^2 - F_c^2)^2 / \sum w F_o^4]^{1/2} ; S(F^2) = [\sum w(F_o^2 - F_c^2)^2 / (n + r - p)]^{1/2}$$

Table 3.3.8-3. Summary of *in situ* single-crystal data during N₂ adsorption (and desorption) for **3.3(Cl)** at 90 K

	3.3(Cl)-Vac [Cu₂(4-Clbz)₄(NH₂pyz)]_n C ₃₂ H ₂₁ Cl ₄ Cu ₂ N ₃ O ₈	3.3(Cl)-0.35bar N₂ [Cu₂(4-Clbz)₄(NH₂pyz)]_n C ₃₂ H ₂₁ Cl ₄ Cu ₂ N ₃ O ₈	3.3(Cl)-0.75bar N₂ [Cu₂(4-Clbz)₄(NH₂pyz)]_n C ₃₂ H ₂₁ Cl ₄ Cu ₂ N ₃ O ₈
Crystal habit	Plank	Plank	Plank
Crystal colour	Clear Bluish Green	Clear Bluish Green	Clear Bluish Green
Crystal size (mm)	0.08 × 0.034 × 0.034	0.08 × 0.034 × 0.034	0.08 × 0.034 × 0.034
Crystal system	Monoclinic	Monoclinic	Monoclinic
Space group	<i>I</i> 2/ <i>m</i>	<i>I</i> 2/ <i>m</i>	<i>I</i> 2/ <i>m</i>
<i>a</i> (Å)	12.1267(5)	12.1332(5)	12.1378(5)
<i>b</i> (Å)	9.80445(13)	9.80429(13)	9.80315(13)
<i>c</i> (Å)	15.0663(6)	15.0495(7)	15.0332(7)
α (°)	90	90	90
β (°)	106.550(4)	106.433(5)	106.308(5)
γ (°)	90	90	90
<i>V</i> (Å ³)	1717.10(11)	1717.12(11)	1716.81(11)
Density (g cm ⁻³)	1.633	1.633	1.633
Temperature (K)	90	90	90
μ (mm ⁻¹)	1.478	1.478	1.479
Wavelength (Å)	0.6889	0.6889	0.6889
2θ range (°)	3.704 to 53.138	3.706 to 53.146	3.71 to 53.138
Refins. collected	10051	10004	10006
Independent reflns. [<i>R</i> _{int}]	1883 [0.0331]	1880 [0.0345]	1880 [0.0321]
Refins. used in refinement, <i>n</i>	1883	1880	1880
LS parameters, <i>p</i>	131	131	131
Restraints, <i>r</i>	0	0	0
<i>R</i> 1 (<i>F</i>) ^a >2.0σ(<i>I</i>)	0.0352	0.0348	0.0352
<i>wR</i> 2 (<i>F</i> ²) ^a , all data	0.1118	0.1093	0.1058
<i>S</i> (<i>F</i> ²) ^a , all data	1.130	1.1180	1.112
	3.3(Cl)-1.75bar N₂ [Cu₂(4-Clbz)₄(NH₂pyz)]_n C ₃₂ H ₂₁ Cl ₄ Cu ₂ N ₃ O ₈	3.3(Cl)-3.5bar N₂ [Cu₂(4-Clbz)₄(NH₂pyz)]_n C ₃₂ H ₂₁ Cl ₄ Cu ₂ N ₃ O ₈	
Crystal habit	Plank	Plank	
Crystal colour	Clear Bluish Green	Clear Bluish Green	
Crystal size (mm)	0.08 × 0.034 × 0.034	0.08 × 0.034 × 0.034	
Crystal system	Monoclinic	Monoclinic	
Space group	<i>I</i> 2/ <i>m</i>	<i>I</i> 2/ <i>m</i>	
<i>a</i> (Å)	12.1419(6)	12.1502(10)	
<i>b</i> (Å)	9.80289(14)	9.8024(2)	
<i>c</i> (Å)	15.0149(8)	14.9900(13)	
α (°)	90	90	
β (°)	106.176(5)	105.988(9)	
γ (°)	90	90	
<i>V</i> (Å ³)	1716.41(13)	1716.3(2)	
Density (g cm ⁻³)	1.634	1.634	
Temperature (K)	90	90	
μ (mm ⁻¹)	1.481	1.479	
Wavelength (Å)	0.6889	0.6889	
2θ range (°)	3.714 to 53.132	3.718 to 53.118	
Refins. collected	9987	9903	
Independent reflns. [<i>R</i> _{int}]	1882 [0.0345]	1879 [0.0503]	
Refins. used in refinement, <i>n</i>	1882	1879	
LS parameters, <i>p</i>	131	132	
Restraints, <i>r</i>	0	0	
<i>R</i> 1 (<i>F</i>) ^a >2.0σ(<i>I</i>)	0.0374	0.0516	
<i>wR</i> 2 (<i>F</i> ²) ^a , all data	0.1094	0.1522	
<i>S</i> (<i>F</i> ²) ^a , all data	1.076	1.050	

$$^a = R1(F) = \Sigma(|F_o| - |F_c|) / \Sigma|F_o| ; wR2(F^2) = [\Sigma w(F_o^2 - F_c^2)^2 / \Sigma w F_o^4]^{1/2} ; S(F^2) = [\Sigma w(F_o^2 - F_c^2)^2 / (n + r - p)]^{1/2}$$

Table 3.3.8-4. Summary of *in situ* single-crystal data during N₂ adsorption (and desorption) for **3.4(F)** at 90 K

	3.4(F)-Vac [Cu ₂ (4-Fbz) ₄ (NH ₂ pyz)] _n C ₃₂ H ₂₁ F ₄ Cu ₂ N ₃ O ₈	3.4(F)-0.35bar N₂ [Cu ₂ (4-Fbz) ₄ (NH ₂ pyz)] _n C ₃₂ H ₂₁ F ₄ Cu ₂ N ₃ O ₈	3.4(F)-0.9bar N₂ [Cu ₂ (4-Fbz) ₄ (NH ₂ pyz)] _n C ₃₂ H ₂₁ F ₄ Cu ₂ N ₃ O ₈
Crystal habit	Needle	Needle	Needle
Crystal colour	Clear Bluish Green	Clear Bluish Green	Clear Bluish Green
Crystal size (mm)	0.136 × 0.017 × 0.017	0.136 × 0.017 × 0.017	0.136 × 0.017 × 0.017
Crystal system	Monoclinic	Monoclinic	Monoclinic
Space group	<i>I</i> 2/ <i>m</i>	<i>I</i> 2/ <i>m</i>	<i>I</i> 2/ <i>m</i>
<i>a</i> (Å)	11.7509(5)	11.7514(5)	11.7541(5)
<i>b</i> (Å)	9.7381(3)	9.7353(3)	9.7319(3)
<i>c</i> (Å)	15.0239(8)	15.0074(8)	14.9964(9)
α (°)	90	90	90
β (°)	105.304(5)	105.264(5)	105.195(5)
γ (°)	90	90	90
<i>V</i> (Å ³)	1658.23(13)	1656.32(13)	1655.46(14)
Density (g cm ⁻³)	1.559	1.561	1.56
Temperature (K)	90	90	90
μ (mm ⁻¹)	1.255	1.254	1.255
Wavelength (Å)	0.6889	0.6889	0.6889
2θ range (°)	3.814 to 53.13	3.816 to 53.128	3.818 to 53.142
Reflns. collected	9958	9945	9916
Independent reflns. [<i>R</i> _{int}]	1988 [0.0699]	1986 [0.0608]	1985 [0.0636]
Reflns. used in refinement, <i>n</i>	1988	1986	1985
LS parameters, <i>p</i>	132	132	132
Restraints, <i>r</i>	0	0	0
<i>R</i> 1 (<i>F</i>) ^a > 2.0σ(<i>I</i>)	0.0453	0.0454	0.0472
<i>wR</i> 2 (<i>F</i> ²) ^a , all data	0.1179	0.128	0.1300
<i>S</i> (<i>F</i> ²) ^a , all data	1.053	1.0600	1.045

	3.4(F)-1.4bar N₂ [Cu ₂ (4-Fbz) ₄ (NH ₂ pyz)] _n C ₃₂ H ₂₁ F ₄ Cu ₂ N ₃ O ₈	3.4(F)-1.74bar N₂ [Cu ₂ (4-Fbz) ₄ (NH ₂ pyz)] _n C ₃₂ H ₂₁ F ₄ Cu ₂ N ₃ O ₈	3.4(F)-2.77bar N₂ [Cu ₂ (4-Fbz) ₄ (NH ₂ pyz)] _n C ₃₂ H ₂₁ F ₄ Cu ₂ N ₃ O ₈	3.4(F)-3.5bar N₂ [Cu ₂ (4-Fbz) ₄ (NH ₂ pyz)] _n C ₃₂ H ₂₁ F ₄ Cu ₂ N ₃ O ₈
Crystal habit	Needle	Needle	Needle	Needle
Crystal colour	Clear Bluish Green	Clear Bluish Green	Clear Bluish Green	Clear Bluish Green
Crystal size (mm)	0.136 × 0.017 × 0.017	0.136 × 0.017 × 0.017	0.136 × 0.017 × 0.017	0.136 × 0.017 × 0.017
Crystal system	Monoclinic	Monoclinic	Monoclinic	Monoclinic
Space group	<i>I</i> 2/ <i>m</i>	<i>I</i> 2/ <i>m</i>	<i>I</i> 2/ <i>m</i>	<i>I</i> 2/ <i>m</i>
<i>a</i> (Å)	11.7711(6)	11.7708(7)	11.7754(7)	11.7783(8)
<i>b</i> (Å)	9.7255(3)	9.7210(3)	9.7186(4)	9.7154(4)
<i>c</i> (Å)	14.9373(10)	14.9242(10)	14.9134(11)	14.8978(12)
α (°)	90	90	90	90
β (°)	104.891(6)	104.811(6)	104.743(7)	104.665(7)
γ (°)	90	90	90	90
<i>V</i> (Å ³)	1652.59(15)	1650.94(16)	1650.52(17)	1649.23(19)
Density (g cm ⁻³)	1.565	1.566	1.567	1.568
Temperature (K)	90	90	90	90
μ (mm ⁻¹)	1.257	1.258	1.259	1.26
Wavelength (Å)	0.6889	0.6889	0.6889	0.6889
2θ range (°)	3.826 to 53.134	3.83 to 53.14	3.832 to 53.136	3.834 to 53.14
Reflns. collected	9898	9910	9906	9870
Independent reflns. [<i>R</i> _{int}]	1982 [0.0653]	1981 [0.0677]	1981 [0.0725]	1979 [0.0744]
Reflns. used in refinement, <i>n</i>	1982	1981	1981	1979
LS parameters, <i>p</i>	132	132	132	132
Restraints, <i>r</i>	0	0	0	0
<i>R</i> 1 (<i>F</i>) ^a > 2.0σ(<i>I</i>)	0.0501	0.0525	0.0541	0.0560
<i>wR</i> 2 (<i>F</i> ²) ^a , all data	0.1414	0.1486	0.1475	0.1491
<i>S</i> (<i>F</i> ²) ^a , all data	1.046	1.030	1.040	1.052

$$^a = R1(F) = \sum(|F_o| - |F_c|) / \sum|F_o| ; wR2(F^2) = [\sum w(F_o^2 - F_c^2)^2 / \sum w F_o^4]^{1/2} ; S(F^2) = [\sum w(F_o^2 - F_c^2)^2 / (n + r - p)]^{1/2}$$

Appendix 3.8.4: TGA

Coordination polymer **3.1(I)-BnOH/MeOH** (Figure 3.8.4-1) observes an initial mass loss (100-200 °C), *ca.* 20 %, corresponding to the loss of *ca.* 2 methanols and 2 benzyl alcohols. This is followed by a 20 % loss in the range of 250 °C to 300 °C followed by further degradation to a final mass of *ca.* 11% of the original. This final mass is likely to be a copper oxide (10.67 % of the original mass). Unfortunately it is unclear what the secondary 20 % mass loss could correspond to, this is roughly twice the expected mass loss that would correspond to the loss of the connecting aminopyrazine ligand.

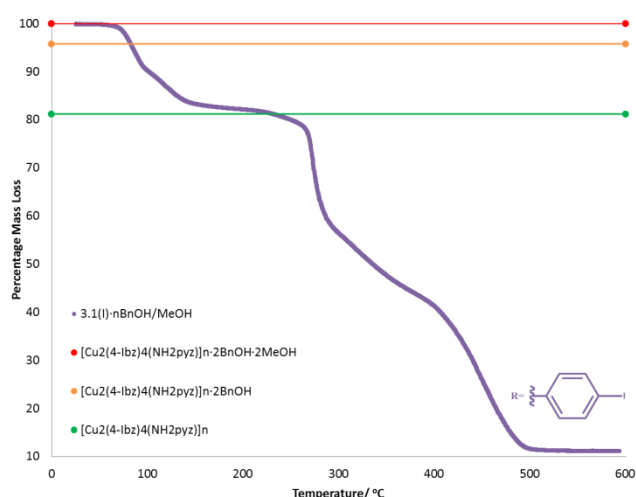


Figure 3.8.4-1. Thermogravimetric analysis of **3.1(I)-BnOH/MeOH**

The coordination polymer **3.1(I)** synthesised by method 2 (DCM/MeOH) (Figure 3.8.4-2) shows an initial loss of *ca.* 10 % between 25-150 °C corresponding to the loss of one DCM, this is then followed by further loss comparable to the degradation seen above. The sample remains stable up to 200 °C followed by a 20 % loss at 250-300 °C and finally degrading to 13 % of the original mass. The final mass being attributed to copper oxide (12.3 % of original). Similarly it is unclear what the secondary distinct mass corresponds to.

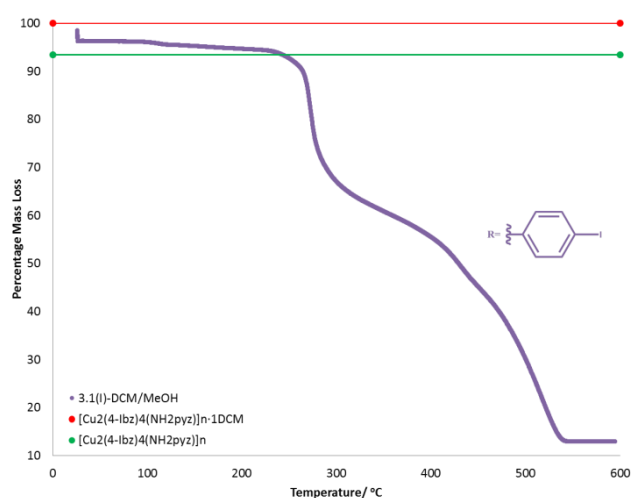


Figure 3.8.4-2. Thermogravimetric analysis of **3.1(I)-DCM/MeOH**

Both 4-bromobenzoate materials (**3.2(Br)-BnOH/MeOH** and **3.2(Br)-DCM/MeOH**) exhibit very similar mass losses with minimal initial mass loss followed by a large mass loss from 300 °C. The minimal initial mass loss observed from the benzyl alcohol potentially means one of two outcomes. Firstly the sample loses solvent during the filtration process, however the elemental analysis (prepared in the same way) suggest benzyl alcohol is still present. Alternatively this could suggest that solvent is retained up until the point the material degrades. The DCM layering synthesis exhibits an initial loss at moderate temperature, below 100 °C, which is attributed to a mixture of methanol and DCM. Both pieces of analysis then exhibit a large loss at *ca.* 300 °C followed by more gradual further degradation to 19 % and 24 % final percentage for **3.2(Br)-BnOH/MeOH** and **3.2(Br)-DCM/MeOH**, respectively. These final values however do not plateau suggesting further degradation at higher temperature will occur. As with the previous iodo systems the initial drastic degradation step does not correspond to the loss of a single component of the material being much larger than the aminopyrazine linker.

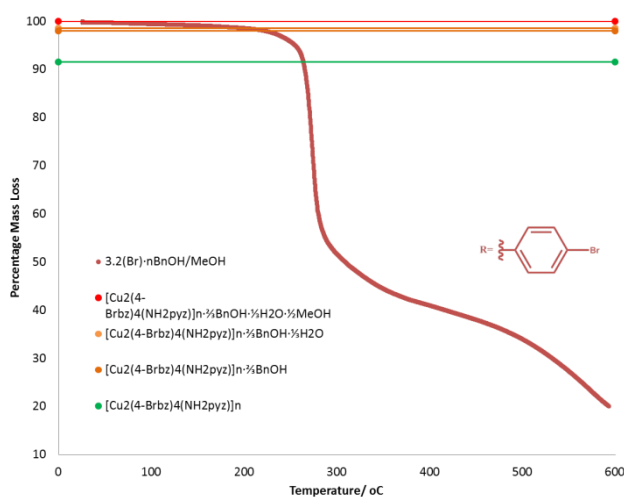


Figure 3.8.4-3. Thermogravimetric analysis of **3.2(Br)-BnOH/MeOH**

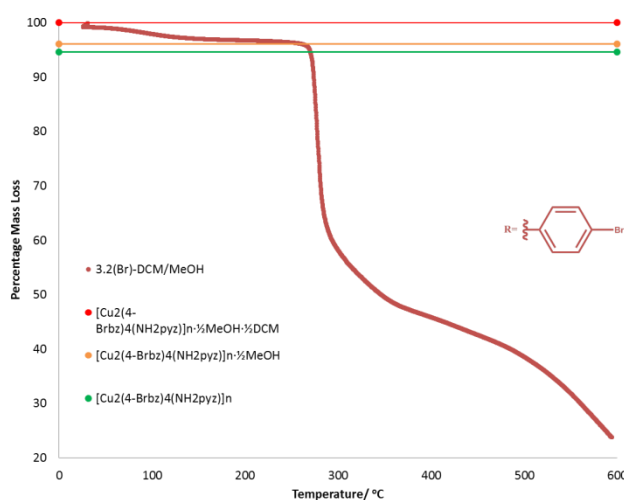


Figure 3.8.4-4. Thermogravimetric analysis of **3.2(Br)-DCM/MeOH**

The **3.3(Cl)-BnOH/MeOH** (synthesised by method 1) exhibits a mass loss more comparable to **3.1(I)-BnOH/MeOH** with an initial 15 % mass loss between 25-200 °C corresponding to the loss of 1 ½ methanol molecules and further loss of 1 benzyl alcohol molecule. This mass loss is comparable to the elemental analysis (**3.3(Cl)·1BnOH·½MeOH**) with the increased methanol content likely due to the amount of time the samples were stored out of solvent prior to analysis. This provides a stable intermediate for 100 °C followed by mass loss at 300 °C of *ca.* 30% followed by further degradation to a final percentage of 17% which corresponds to a mixture of copper oxide (14.3 % of original mass) and copper carbonate (22.1 % of original mass).

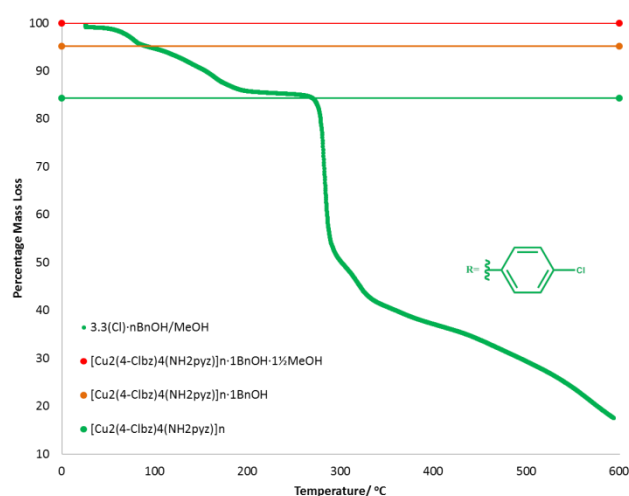


Figure 3.8.4-5. Thermogravimetric analysis of **3.3(Cl)-BnOH/MeOH**

In comparison **3.3(Cl)-DCM/MeOH** (method 2), which crystallised in a solvent-free form, shows no mass loss until degradation initially at 290 °C (with a 40 % loss) followed by a second step of 10 % and further degradation to a final 16 % of the original mass. The absence of solvent loss supports the solvent-free model determined by elemental analysis and single-crystal X-ray analysis. As with the previous systems the degradation at 290 °C does not correspond to the loss of distinct components of the structure. The final mass is less than the mass expected for copper oxide (18.8 % of original mass).

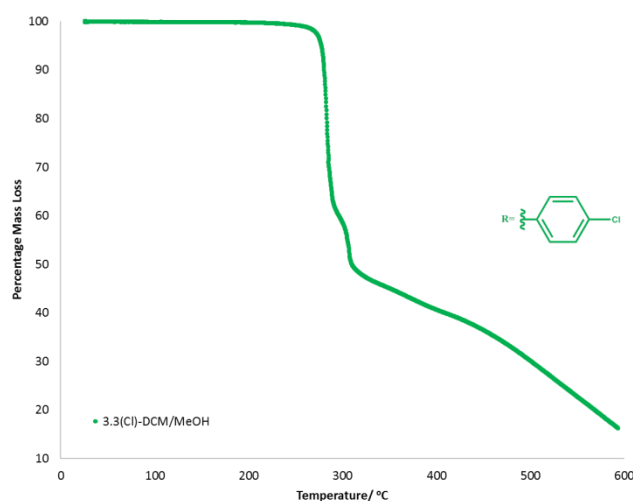


Figure 3.8.4-6. Thermogravimetric analysis of **3.3(Cl)-DCM/MeOH**

Finally the TGA of **3.4(F)** showed comparable behaviour to **3.3(Cl)-DCM/MeOH** with minimal initial loss, consistent with a solvent-free form determined crystallographically and from elemental analysis. The sample then begins to degrade at *ca.* 240 °C with an initial 40 % mass loss followed by two gradual 20 % mass losses in the ranges of 250-330 °C and 375-500 °C. The sample degrades fully with a final mass of 21.6 % of the original this corresponding to copper oxide (20.42 % of the original mass). It is unclear what the distinct mass losses correspond, with these mass losses not corresponding to the loss of a single component of the coordination polymer.

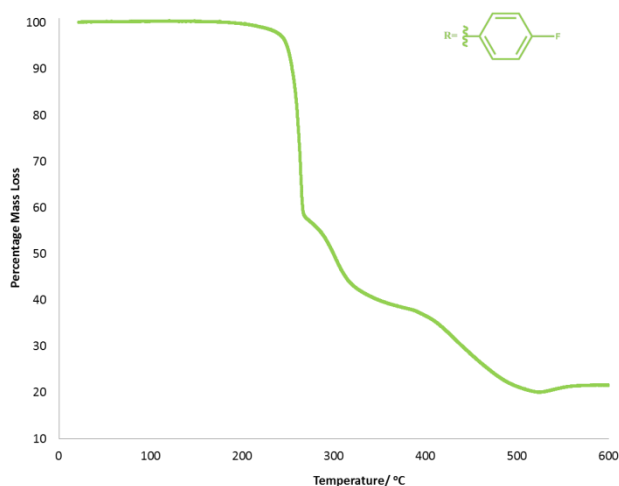


Figure 3.8.4-7. Thermogravimetric analysis of **3.4(F)**

The thermogravimetric analysis identified a clear benefit when considering which synthesis to pursue for testing these materials for gas uptake studies. Method 2 (DCM/MeOH layering) either producing solvent free materials (**3.3(Cl)** and **3.4(F)**) or phase where solvent could be removed at moderate temperatures (**3.1(I)** and **3.2(Br)**). The materials produced by method 1 (BnOH/MeOH layering) requiring higher temperatures closer to the point of polymer degradation.

Chapter 4:

***Gaseous Guest Inclusion
within a Family of Halogen-
Functionalised Stellated
Molecular Clusters***



4.1 Introduction

Conventionally porous materials are considered to have large rigidly defined pores sustained through multidimensional chemical bonding. However as demonstrated in the previous two chapters 1D coordination polymers ($[\text{Cu}_2(4\text{-Xbz})_4(\text{Ypyz})]_n$ ($X = \text{I, Br, Cl or F}$ and $Y = \text{H or NH}_2$) exhibit uptake of CO_2 and N_2 dependent on the functionality on the benzoate ligands and pyrazine linker. This family of coordination polymers (with the exception of $[\text{Cu}_2(4\text{-Ibz})_4(\text{NH}_2\text{pyz})]_n$) contained discrete cavities which transformed into channels with increased gas pressure. Porosity within systems that possess discrete cavities is not exclusive to coordination polymers, with numerous examples of molecular systems possessing discrete cavities demonstrating guest inclusion.

Porous molecular solids present an attractive alternative to MOFs and zeolites, potentially being easy to process. These materials, as discussed in Chapter 1, can be grouped into two categories (intrinsic or extrinsic porosity) dependent on the pores present, intrinsic pores being present within each molecule and extrinsic pores being the cavities between molecules. In the case of producing a system of extrinsic porosity one of the main driving forces is the promotion of inefficient packing. Inefficient packing can be achieved by designing awkwardly shaped molecules, typically using molecules with rigid bulky groups that protrude from a central point/surface.

The production of porous molecular crystals which sustain pores through inefficient packing has been heavily inspired by organic supramolecular chemistry. One particular example that has been studied for porosity is the class of macrocycles known as calixarenes (**Figure 4.1-1**). Calix[n]arenes (where n denotes the number of aromatic rings present) consist of phenol groups connected by CH_2 groups in a ring. This cycle results in a bowl shaped molecule which, in certain polymorphs, cannot pack efficiently resulting void spaces. The bowl shape also allows for functionality to be added to the upper rim of the calixarene (*para*- to the OH group) (**Figure 4.1-1**) to further promote inefficient packing. The majority of this work focused on the calix[4]arene macrocycle.^{1,2} Following the initial demonstration of porosity (for CH_4 and Freon) of the simple calix[4]arene³ (un-functionalised) further work was carried out on this system⁴⁻⁷ as well as calix[4]arenes with tertiary butyl and pentyl functionality on the upper rim.⁸⁻¹⁷ The majority of guest inclusion studies have focused on calix[4]arene with one example of a calix[8]arene used for organic vapour sensing.¹⁸

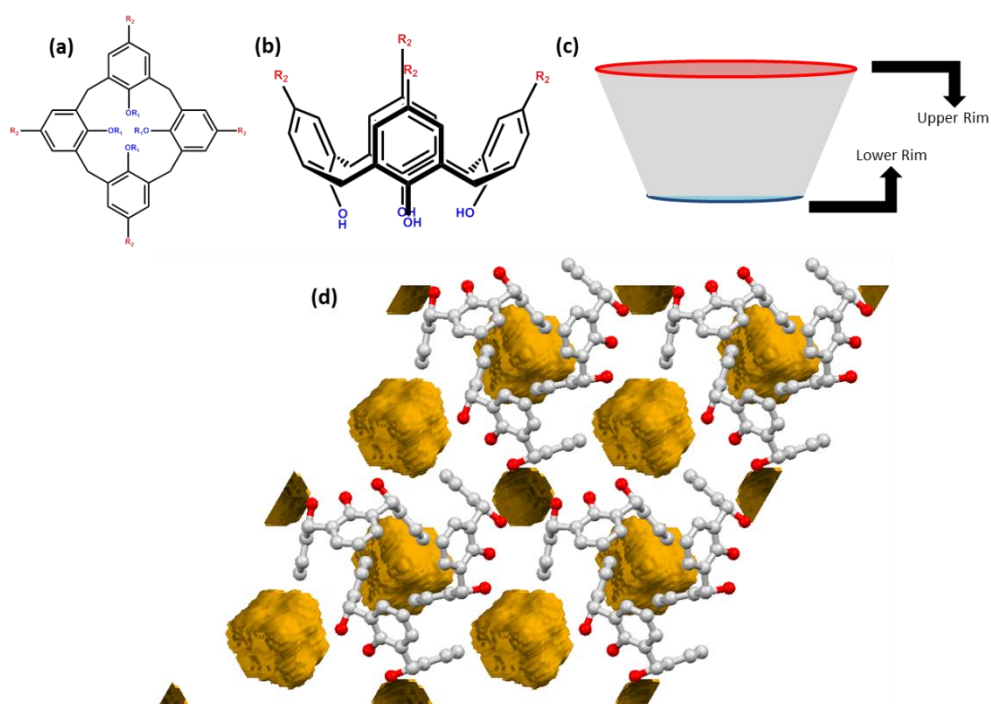


Figure 4.1-1. (a) The calix[4]arene, (b) the bowl conformation, (c) a simplified bowl shape highlighting the two surfaces (the upper and lower rims) that can be functionalised and (d) an example of the observed void space of calix[4]arene.³ Colour scheme C, grey; O, red; void space (1.2 Å probe radius, 0.2 Å grid spacing), yellow. Hydrogen atoms not shown.

The calix[4]arene was further exploited for inefficient packing through functionalisation of the lower rim either with the use of thiols¹⁹ or by forming alkoxy groups.^{20,21} Further development of this macrocycle looked at directing the assembly calix[4]arenes in the solid state by a combination of functionalisation of the upper and lower rims and the introduction of a co-former (pyridine) in an attempt to form systems with channels rather than discrete cavities (**Figure 4.1-2**).²²⁻²⁵ In more recent years an extension of studies on this versatile macrocycle has explored the use of calixarenes to form hydroxide bridged metal clusters and capsules²⁶⁻³³ with two examples being tested for gas sorption.^{32,33}

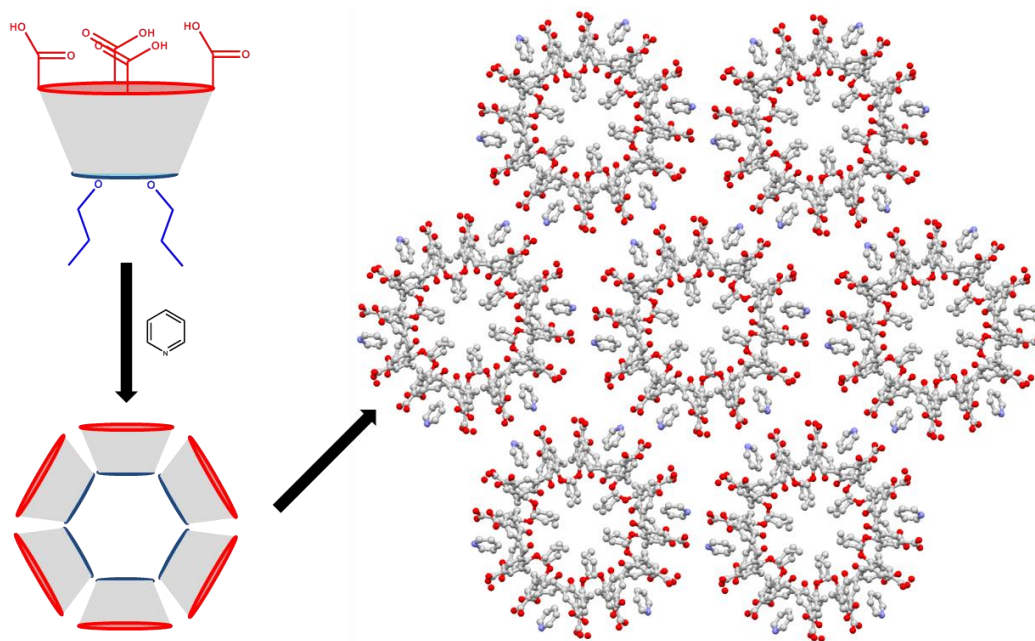


Figure 4.1-2. Upper and lower rim functionalisation of calix[4]arene to direct the assembly of calixarene nanotubes with pyridine as a co-former.²³ Colour scheme C, grey; O, red; N, blue.

Further inspiration from organic supramolecular chemistry demonstrated that porosity could be observed in a series of cucurbiturils,^{34–36} which demonstrated high selectivity for CO₂, as well as a series of other cyclic oligomers^{37–43}. In recent years the pursuit of porosity of molecular crystals has been progressed through mining the CSD⁴⁴ in an attempt to identify pre-existing, as yet untested, porous molecular crystals.^{45,46} This has resulted in the design of simple aromatics that can pack inefficiently to produce a porous material.^{47–49}

The field of extrinsic molecular porosity is heavily populated with organic supramolecular examples, with the larger of these systems arguably possessing intrinsic pores. However there are few examples of inorganic extrinsic porous molecular systems. Often cage or capsule type systems have been utilised to demonstrate intrinsic guest inclusion^{50–53} with examples of intrinsic porous systems showing high CO₂ selectivity.^{54,55} Considering that, as demonstrated by the studies on calixarenes, that porosity can be achieved through exploiting inefficient packing it is surprising that more examples of extrinsic molecular porosity for inorganic compounds have not been reported. As stated earlier, typically, inefficient packing can be achieved through the protrusions (or stellations) of rigid bulky groups from a central point or surface.

When considering stellation in the context of inorganic complexes it is conceivable that inefficient packing could be achieved by exploiting the coordination geometry of transition metals (**Figure 4.1-3**). Considering stellation further in the context of pre-existing porous materials there is a large proportion of metal-organic frameworks where the inorganic secondary building units (SBUs) consist of a central cluster of metals connected by a series of bridging linkers protruding from the centre (**Figure 4.1-3**).

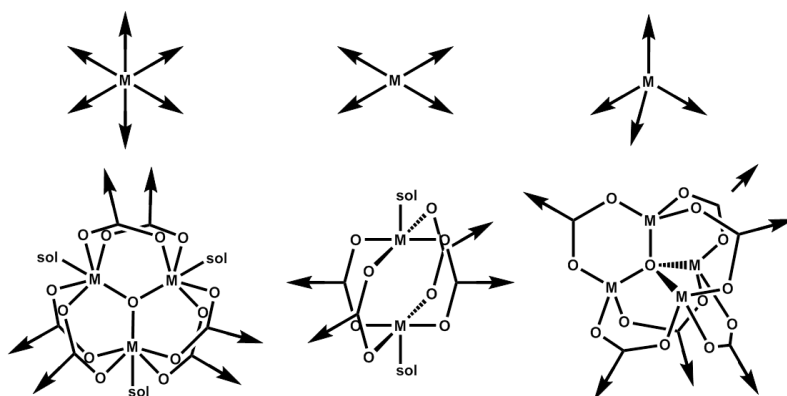


Figure 4.1-3. Common metal coordination geometries (top) and more complex clusters (bottom) featured as SBU within MOF research. M denotes a metal centre; O, oxygen; sol, coordinated solvent.

Some studies have demonstrated that simple inorganic complexes can exhibit spectroscopic changes in the presence/absence of solvent.^{56–58} For example work carried out by Raithby and co-workers⁵⁷ demonstrated that a platinum pincer complex (**Figure 4.1-4**) could be used as a sensor for volatile organic compounds (VOCs) due to the reversible vapochromic behaviour. These studies demonstrate that a seemingly close packed inorganic complex could possess guest inclusion.

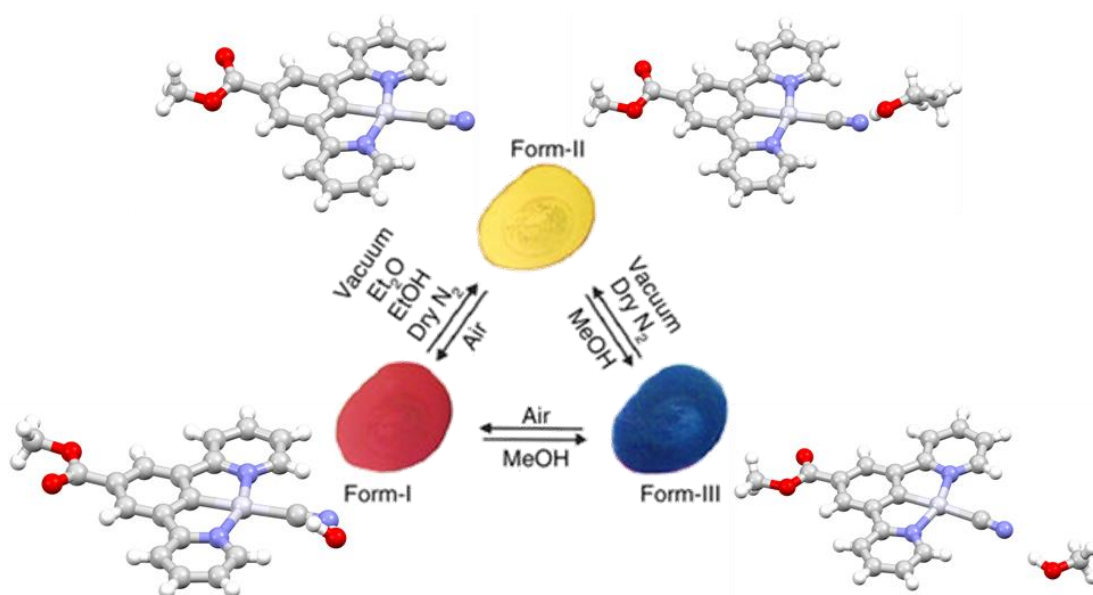


Figure 4.1-4. Vapochromic properties of the platinum pincer complex reported by Raithby et al.⁵⁷ Central schematic reproduced from reference 57 with permissions. Pt, silver; C, grey; O, red; N, blue; H, white.

Examples of gaseous guest inclusion within extrinsically porous inorganic clusters, reminiscent of the SBUs used in MOFs, was reported by Chun and co-workers.^{59,60} This work focused on the production of titanium-oxo molecular clusters with benzoate ligands (**Figure 4.1-5**). This work demonstrated that it is possible to produce an intrinsically porous cluster ($[\text{Ti}_8\text{O}_8(\text{bz})_{16}]$), with the use of benzoate (bz) ligands, which remained stable upon desolvation and showed a higher uptake of CO_2 than N_2 or CH_4 . This work also produced three additional titanium-oxo clusters when functionalised benzoate ligands were used ($[\text{Ti}_6\text{O}_6(\text{n-Xbz})_6(\text{O}^i\text{Pr})_6]$ (**A**) where n-X is 4- NH_2 ,

4-^tBu or 2-Ph, $[\text{Ti}_6\text{O}_6(\text{n-Xbz})_{10}(\text{O}^i\text{Pr})_2]$ (**B**) where n-X is 4-^tBu or 2-Ph and $[\text{Ti}_8\text{O}_{10}(4\text{-NH}_2\text{bz})_{12}]$ (**C**) (**Figure 4.1-5**). The hexanuclear cluster (**A**) was more densely packed than the other clusters (**B** and **C**) with all crystallising as solvates. Desolvation then demonstrated that the hexanuclear clusters (**A** and **B**) retained crystallinity with the octanuclear cluster (**C**) losing crystallinity. Despite this loss in crystallinity all clusters showed selectivity for CO_2 when the functionality was in the *para*- position (4- NH_2 and 4-^tBu) with the *ortho*-substituted clusters (2-Ph) showing reduced CO_2 inclusion. Independently from this work Kobayashi et al.⁶¹ demonstrated that a Ti_6O_8 cluster connected by pyrazine-2-carboxylates would lose crystallinity upon drying, but would regain crystallinity upon rehydration.

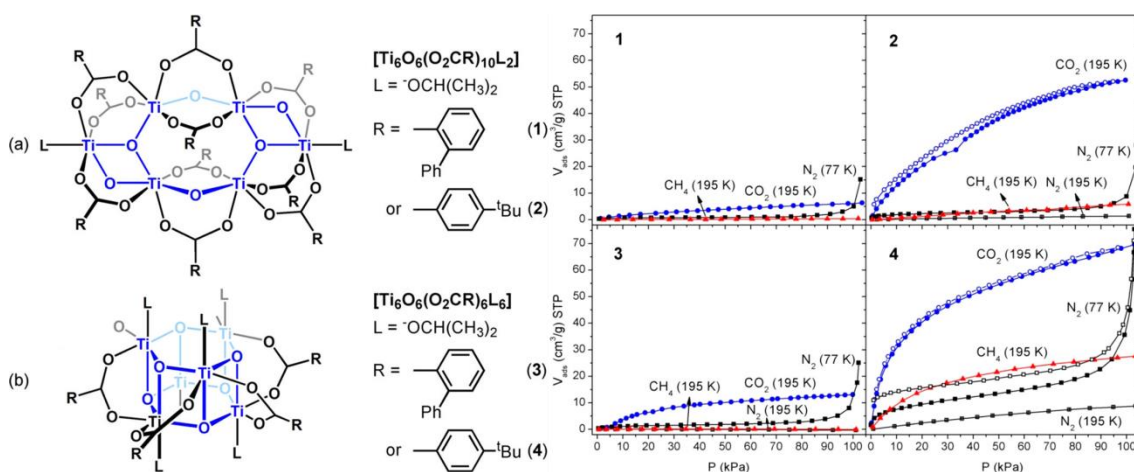


Figure 4.1-5. The titanium-oxo clusters $[\text{Ti}_6\text{O}_6(\text{n-Xbz})_6(\text{O}^i\text{Pr})_6]$ and $[\text{Ti}_6\text{O}_6(\text{n-Xbz})_{10}(\text{O}^i\text{Pr})_2]$, n-X = 4-^tBu or 2-Ph reported by Chun et al.⁶⁰ and the volumetric adsorption of CO_2 (blue, 195 K), N_2 (black, 77 K and 195 K) and CH_4 (red, 195 K). Figures reproduced from reference 60 with permission. Adsorption displayed with filled shapes and desorption with empty shapes.

A second example exploiting a more commonly used SBU is that of the work reported by Masaoka and co-worker.⁶² This work uses a paddlewheel motif comparable to the SBU used in the previous two chapters, but with rhodium instead of copper (**Figure 4.1-6**). As well as using a stellated SBU this work also uses a linker with neighbouring electron-rich/electron-poor aromatic rings (**Figure 4.1-7**). The combination of stellation and cooperative $\pi\cdots\pi$ stacking leads to 1D channels being observed (**Figure 4.1-7**). It was also demonstrated that the coordinated solvent had an effect on the packing and subsequent CO_2 uptake. This work is a nice example of applying common themes within crystal engineering to produce a porous molecular system.

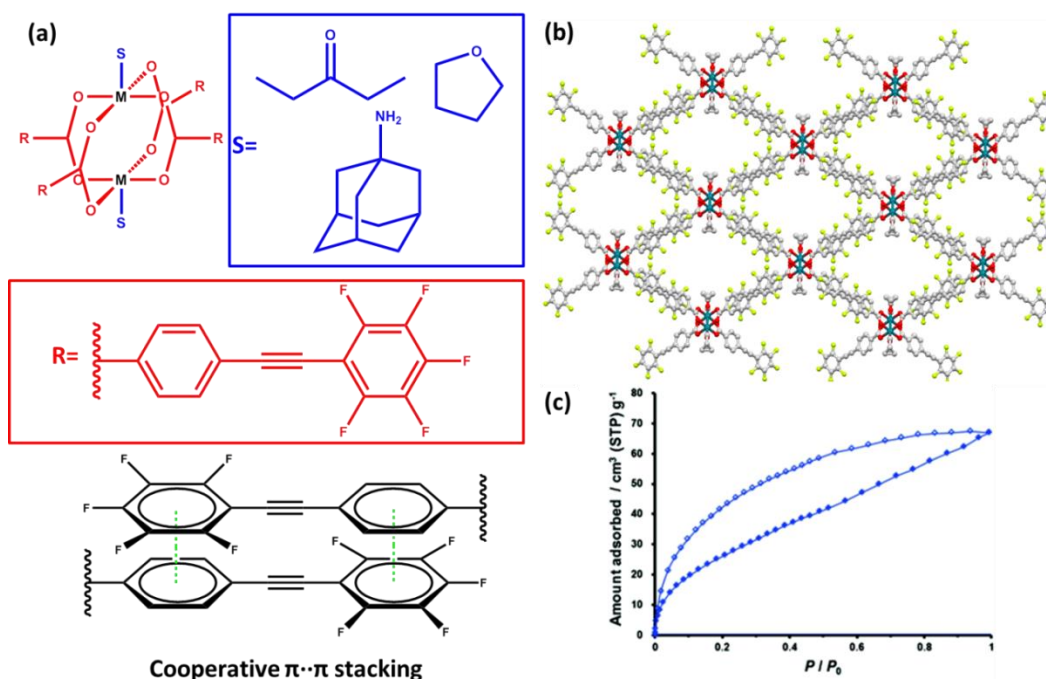


Figure 4.1-6. (a) The rhodium paddlewheel system reported by Masaoka *et al.*⁶², (b) an example of the packing of the THF system and (c) the volumetric adsorption (195 K, adsorption, filled circle; desorption, empty circle) of the THF coordinated system (reproduced from reference 62 with permission). Colour scheme Rh, emerald green; F, yellow; C, grey; O, red. Hydrogens not shown.

4.2 Aims

The work in this chapter looks to explore a series of extrinsically porous inorganic molecular materials. It is intended that this work will focus on inefficient packing of stellated clusters by taking inspiration from a commonly used SBU within MOF research. The SBU of interest, a trinuclear oxo-centred cluster (**Figure 4.2-1**), is a common feature in Cr- and Fe-based MOFs. For example, MIL-101⁶³ (Materials of Institute Lavoisier) consists of a trinuclear oxo-centred SBU (Cr or Fe) connected by 1,4-benzenedicarboxylate linkers. This system demonstrated high selectivity for CO₂^{63,64} and was subsequently studied for a variety of applications.^{65–68}

The main reason for selecting this SBU is that it consists of a central metal cluster and six protruding carboxylates. Also molecular trinuclear oxo-centred clusters have been successfully synthesised for over 100 years^{69–71} and therefore synthetic procedures are widely available.

This project will synthesise a family of chromium oxo-centred clusters [Cr₃O(4-Xbz)₆(MeOH)₃][NO₃] (X = I (**4.1(I)**), Br (**4.2(Br)**) and Cl (**4.3(Cl)**) (**Figure 4.2-1**). Following synthesis of the clusters, samples will initially be characterised by single-crystal X-ray diffraction to identify any common packing trends. The thermal stability of these systems will then be tested, followed by gaseous guest inclusion studies. This work is intended to demonstrate that porosity can be achieved using simple molecular cluster and the porosity can be affected by varying the *para*-substituent of the benzoate ligands.

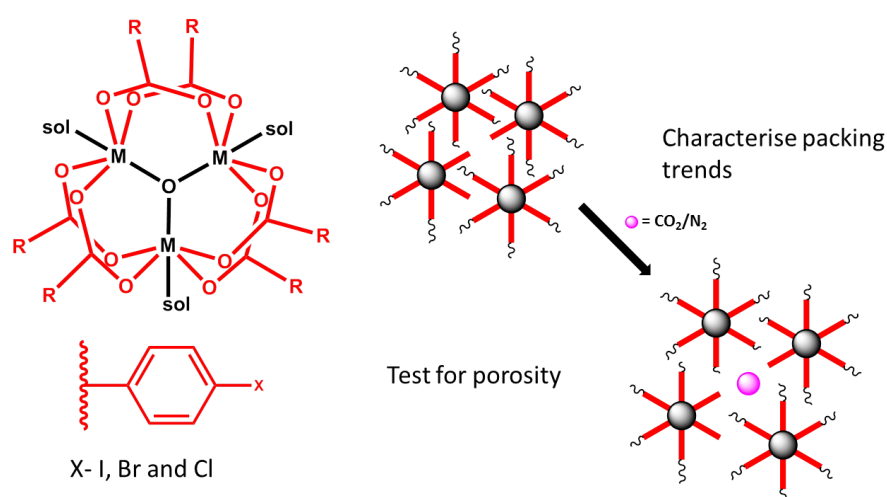


Figure 4.2-1. The trinuclear oxo-centred cluster of interest and the intended outcomes of this Chapter.

4.3 Experimental

4.3.1 Synthetic Procedure

All solvents (HPLC grade) and reagents were purchased from Sigma Aldrich, VWR or Alfa Aesar. Reagents and solvents were used as received without further purification.

A family of 4-halobenzoate trinuclear oxo-centred clusters, $[\text{Cr}_3\text{O}(4\text{-Xbz})_6(\text{MeOH})_3][\text{NO}_3]$ ($X = \text{I}, \text{Br}$ or Cl), were synthesised by adaptation of a procedure previously reported by Figuerola et al.⁷¹

Chromium(III) nitrate nonahydrate (0.2 mmol) and 4-halobenzoic acid (0.4 mmol) were placed into a 23 mL glass vial, to which 3 mL of methanol and 3 mL acetonitrile were added. The glass vial was then sealed with a Teflon-lined screw cap. The vials were swirled to aid dissolution of reagents and placed in the oven. The oven was heated to 65 °C at a rate of 1 °C/min. On reaching 65 °C the temperature was maintained for 12 h before cooling to 25 °C at a rate of 0.1 °C/min. Upon removal from the oven, clear green solutions were obtained with green crystals present for **4.1(I)**, **4.2(Br)** and **4.3(Cl)**. The yields could be improved by loosening the cap and allowing the solvent to slowly evaporate prompting further crystallisation of the product.

This procedure could also be scaled up using a 45 mL Teflon-lined steel autoclave and a ten-fold increase in reagents (2 mmol of chromium(III) nitrate nonahydrate and 4 mmol 4-halobenzoic acid) in a 15 mL: 15 mL methanol/acetonitrile mixture.

4.3.1.1 Synthesis of $[\text{Cr}_3\text{O}(4\text{-Ibz})_6(\text{MeOH})_3][\text{NO}_3]$ (**4.1(I)**)

Chromium(III) nitrate nonahydrate (87.4 mg, 0.218 mmol), 4-iodobenzoic acid (105.6 mg, 0.426 mmol). Yield (22.4 mg, 0.0124 mmol, 17.4 %). Elemental Calcd. for $[\text{Cr}_3\text{O}(4\text{-Ibz})_6(\text{MeOH})_3][\text{NO}_3]\cdot 5.75\text{H}_2\text{O}$: C 28.21, H 2.50, N 0.73, I 39.74 %. Found: C 28.18, H 2.13, N 0.81, I 39.67 %.

The solvothermal synthesis was scaled up in a 45 mL Teflon-lined steel autoclave. Chromium(III) nitrate nonahydrate (839.3 mg, 2.1 mmol), 4-iodobenzoic acid (797.2 mg, 3.2

mmol). Yield (356.0 mg, 0.196 mmol, 36.7 %). Elemental Calcd. for $[\text{Cr}_3\text{O}(\text{4-IBz})_6(\text{MeOH})_3][\text{NO}_3]\cdot 1.4\text{H}_2\text{O}$: C 29.41, H 2.12, N 0.76, I 41.43 %. Found: C 28.51, H 2.18, N 0.67, I 42.09 %.

4.3.1.2 Synthesis of $[\text{Cr}_3\text{O}(\text{4-Brbz})_6(\text{MeOH})_3][\text{NO}_3]$ (**4.2(Br)**)

Chromium(III) nitrate nonahydrate (105.9 mg, 0.265 mmol), 4-bromobenzoic acid (89.3 mg, 0.444 mmol). Yield (12.1 mg, 0.008 mmol, 10.7 %). Elemental Calcd. for $[\text{Cr}_3\text{O}(\text{4-BrBz})_6(\text{MeOH})_3][\text{NO}_3]\cdot 0.3\text{MeCN}\cdot 3.7\text{H}_2\text{O}$: C 34.04, H 2.77, N 1.13, Br 29.92 %. Found: C 33.93, H 2.78, N 1.31, Br 29.92 %.

The solvothermal synthesis was scaled up in a 45 mL Teflon-lined steel autoclave. Chromium(III) nitrate nonahydrate (812.7 mg, 2.0 mmol), 4-bromobenzoic acid (804.5 mg, 4.0 mmol). Yield (358.2 mg, 0.234 mmol, 35.09 %). Elemental Calcd. for $[\text{Cr}_3\text{O}(\text{4-BrBz})_6(\text{MeOH})_3][\text{NO}_3]\cdot 4.7\text{H}_2\text{O}$: C 33.47, H 2.83, N 0.87, Br 29.69 %. Found: C 33.10, H 2.32, N 0.89, Br 29.96 %.

4.3.1.3 Synthesis of $[\text{Cr}_3\text{O}(\text{4-Clbz})_6(\text{MeOH})_3][\text{NO}_3]$ (**4.3(Cl)**)

Chromium(III) nitrate nonahydrate (95.1 mg, 0.238 mmol), 4-chlorobenzoic acid (69.1 mg, 0.441 mmol). Yield (15.6 mg, 0.012 mmol, 5.29 %). Elemental Calcd. for $[\text{Cr}_3\text{O}(\text{4-ClBz})_6(\text{MeOH})_3][\text{NO}_3]\cdot 4.2\text{H}_2\text{O}$: C 40.36, H 3.34, N 1.05, Cl 15.88 %. Found: C 40.13, H 2.82, N 1.10, Cl 16.18 %.

The solvothermal synthesis was scaled up in a 45 mL Teflon-lined steel autoclave. Chromium(III) nitrate nonahydrate (796.0 mg, 2.0 mmol), 4-chlorobenzoic acid (577.1 mg, 3.7 mmol). Yield (158.3 mg, 0.125 mmol, 20.39 %). Elemental Calcd. for $[\text{Cr}_3\text{O}(\text{4-ClBz})_6(\text{MeOH})_3][\text{NO}_3]\cdot 2.3\text{MeOH}\cdot 2.6\text{H}_2\text{O}$: C 41.04, H 3.67, N 1.01, Cl 15.37 %. Found: C 41.07, H 2.93, N 1.01, Cl 14.91 %.

4.3.2 Single-Crystal X-Ray Diffraction

Single crystals of **4.1(I)**, **4.2(Br)** and **4.3(Cl)** suitable for structure determination were selected from samples extracted from the mother liquor, suspended in perfluoropolyether oil (FOMBLIN Y) and mounted onto a mylar tip. Data were collected on a Smart APEX-2 CCD diffractometer equipped with a graphite-monochromator Mo-K α sealed-tube source. Sample temperature was maintained using an Oxford Cryosystems Cryostream device. Data were corrected for absorption using empirical methods (SADABS) based on symmetry-equivalent reflections and measurements at different azimuthal angles.⁷²⁻⁷⁴ Structure solution was achieved by direct methods and the crystal structure was refined using full-matrix least-squares against weighted F^2 values using SHELXL⁷⁵ within Olex2.⁷⁶ Non-hydrogen and non-disordered atoms were refined anisotropically. Hydrogen atoms were placed in calculated positions, refined to idealized geometries (riding model) and assigned a fixed isotropic displacement parameter.

Structure determination of **4.1(I)**, **4.2(Br)** and **4.3(Cl)** revealed these systems crystallised as solvates (solvent contents determined crystallographically **4.1(I)** $\cdot 1\frac{1}{2}\text{MeOH}$, **4.2(Br)** $\cdot 1\text{MeOH}\cdot \frac{1}{2}\text{MeCN}$ and **4.3(Cl)** $\cdot 2\text{MeOH}\cdot \frac{3}{4}\text{MeCN}$). Disorder of two of the coordinated

methanol molecules was observed for **4.2(Br)** and **4.3(Cl)**. The two orientations were refined with occupancies of 50(2):50(2) for **4.2(Br)** and occupancies of 41(4):59(4) and 68(4):32(4) for **4.3(Cl)**. Details of the data collections are outlined in **Table 4.3.2-1** (Appendix 4.8.1).

4.3.3 Thermogravimetric Analysis (TGA)

Samples of **4.1(I)**, **4.2(Br)** and **4.3(Cl)** were filtered under vacuum and washed with methanol. The samples were then placed in a ceramic boat of a Perkin-Elmer Pyris1 Thermogravimetric Analyser. Following a 5 min dwell period the samples were heated from 25 °C to 600 °C at a rate of 5 °C per min.

Samples of **4.1(I)**, **4.2(Br)** and **4.3(Cl)** were also tested for isothermal thermogravimetric desolvation. Samples were placed in a ceramic boat on a Perkin Elmer Pyris1 Thermogravimetric Analyser. Samples were initially held at 25 °C for 5 min, before being heated to 30 °C at a rate of 5 °C/min. The temperature was maintained for 1 h before being increased to 65 °C at a rate of 5 °C/min. This temperature was maintained for 1 h. Finally the sample was heated to 100 °C at a rate of 5 °C/min and held at 100 °C for 2 h.

Samples of **4.1(I)**, **4.2(Br)** and **4.3(Cl)** studied by isothermal TGA were recovered and stored in glass vials for one week before being re-analysed to see whether water adsorption occurred upon storing the samples in air. These samples were loaded in a Perkin-Elmer Pyris 1 Thermogravimetric analysis and subjected to an initial dwell period of 5 min at 25 °C. Samples were then heated to 100 °C at a rate of 5 °C/min, this temperature was maintained for 2 h. Finally samples were then heated to 600 °C at a rate of 5 °C/min.

4.3.4 Single-Crystal Desolvation Studies

Single crystals of **4.1(I)·1½MeOH**, **4.2(Br)·1MeOH·½MeCN** and **4.3(Cl)·2MeOH·½MeCN** were removed from the mother liquor and placed on glass slides. The slides were stored at room temperature, allowing for the solvent to evaporate, for 30 min. The crystals were then covered with perfluoropolyether oil (FOMBLIN Y) to allow for crystal screening. A suitable crystal was selected and mounted onto a mylar tip. Data were collected on a Bruker D8 Venture Single Crystal Diffractometer equipped with a μ S Microfocus Cu-K α sealed-tube source and a Photon 100 CMOS (Complementary Metal Oxide Sensor) Detector with shutterless capability. Sample temperature was maintained using an Oxford Cryosystems Cryostream device. Data were corrected for absorption using empirical methods (SADABS) based on symmetry-equivalent reflections and measurements at different azimuthal angles.⁷²⁻⁷⁴ Structure solution was achieved by direct methods and the crystal structure was refined using full-matrix least-squares against weighted F^2 values using SHELXL⁷⁵ within Olex2.⁷⁶ Non-hydrogen and non-disordered atoms were refined anisotropically. Hydrogen atoms were placed in calculated positions, refined to idealized geometries (riding model) and assigned a fixed isotropic displacement parameter. Details of the data collection are outlined in **Table 4.3.2-1** (Appendix 4.8.1).

This method was appropriate to obtain desolvated forms of **4.1(I)** and **4.2(Br)**, but resulted in loss of single-crystal crystallinity for crystals of **4.3(Cl)**. This prompted two stability studies of **4.3(Cl)**. The first involved glueing a single crystal of **4.3(Cl)·xMeOH·yMeCN** on a glass fibre and

collecting small numbers of scans suitable for orientation matrix and unit cell determination on a Bruker D8 Venture Single Crystal Diffractometer at 100, 150, 200, 250 and 298 K to monitor the loss in crystallinity. The second was performed at Beamline I19 at Diamond Light Source.⁷⁷⁻⁷⁹ This study involved glueing a crystal onto a mylar tip and collecting full data sets at 250, 273 and 298 K. The temperature was maintained with the use of an Oxford Cryosystem Cryostream Plus 700 series low-temperature device for both studies.

The I19 data were processed with the CryAlisPro⁸⁰ programs, using a predetermined instrument model from a strongly diffracting reference crystal to enable more accurate determination of the orientation matrix used for integration of diffraction intensities. Data were corrected for absorption using empirical methods (SADABS) based on symmetry-equivalent reflections and measurements at different azimuthal angles.⁷²⁻⁷⁴ Structure solution was achieved by direct methods and the crystal structure was refined using full-matrix least-squares against weighted F^2 values using SHELXL⁷⁵ within Olex2.⁷⁶ Non-hydrogen and non-disordered atoms were refined anisotropically. Hydrogen atoms were placed in calculated positions, refined using idealized geometries (riding model) and assigned a fixed isotropic displacement parameter. Full structural characterisation was achieved for collection at 250 and 273 K, with a partial solution being obtained at 298 K. From the data collected at 298 K it was possible to model the cluster, but the location of the nitrate counter ion and the methyl groups of the coordinated methanol molecules could not be confidently modelled. A summary of the data processing is outlined in **Table 4.3.4-1** (Appendix 4.8.1).

4.3.5 Powder X-Ray Diffraction Analysis and Aging Studies

As-synthesised samples of **4.1(I)**, **4.2(Br)** and **4.3(Cl)** were filtered under vacuum and washed with methanol. Samples were then stored in an oven at 65 °C for 15 minutes before being ground into crystalline powders and loaded into 0.7 mm borosilicate capillaries. Data were collected using Bruker D8 Advance X-ray powder diffractometer equipped with a LynxEye Detector, a Cu-K α sealed-tube source and a focusing Göbel Mirror optic, and operating in capillary mode. Data were collected in the range $5^\circ \leq 2\theta \leq 60^\circ$ in steps of 0.015° while the capillary was rotated at 30 rpm. The capillaries were recovered and stored in air in sealed glass vials with powder patterns being recorded periodically over two months. The data were then analysed and Pawley refinements⁸¹ were carried out using the TOPAS program.^{82,83} Details of the fits are outlined in **Table 4.3.5-1** (Appendix 4.8.2).

4.3.6 Volumetric Nitrogen and Carbon Dioxide Adsorption Studies

Samples of **4.1(I)**, **4.2(Br)** and **4.3(Cl)** were analysed for adsorption of N₂ and CO₂ gases using a Micromeritics 2020 Plus volumetric gas analyser. N₂ isotherms were recorded at 77 K and CO₂ isotherms at 195 K. Prior to isotherms being recorded samples were initially stored in a vacuum oven at 80 °C for 16 h. Following this treatment samples were subjected to a degas condition on the Micromeritics instrument, which consisted of an evacuation in which the sample was heated to 60 °C (10 °C/min) and pressure was reduced to 4 μ mHg (at 5 mmHg/s). Following this evacuation phase a heating phase was applied in which the sample was held under vacuum at 100 °C for 1000 mins.

Following volumetric analysis samples were recovered and analysed using a Bruker D8 Advance X-ray powder diffractometer equipped with a LynxEye XE Detector, a Cu-K α sealed-tube source and a variable motorised slit. Samples were placed onto a low-background sample holder and data were collected while rotating the sample stage at 15 rpm. Data were collected at room temperature in the range $4^\circ \leq 2\theta \leq 60^\circ$ in steps of 0.02° . Pawley refinements⁸¹ were carried out using TOPAS.^{82,83} The results of the refinements are outlined in **Table 4.3.6-1** (Appendix 4.8.2).

Samples were recovered and stored in air in sealed sample vials at room temperature. The samples were stored out of direct sunlight for between 144-175 days (**Table 4.3.6-1**). After this time the samples were prepared for volumetric analysis of CO₂ and N₂ using the same strategy as outlined above. PXRD patterns were also collected following volumetric analysis. Data were collected in using the same procedure as outlined above and Pawley refinements⁸¹ were carried out using TOPAS.^{82,83} The results of the fits are outlined in **Table 4.3.6-1** (Appendix 4.8.2).

4.3.7 Gravimetric Carbon Dioxide Adsorption Studies

Samples of **4.1(I)**, **4.2(Br)** and **4.3(Cl)** were analysed for gravimetric adsorption of CO₂ using an Intelligent Gravimetric Analyser (IGA) model 003 supplied by Hiden Isochema Ltd. The balance and pressure control system of the instrument are fully thermostated to 0.1 K, and the microbalance has a weighing resolution of 0.2 μg . Prior to the measurements, the samples were outgassed using conditions specific to each run (as specified in the subsequent sections). During the measurements, the pressure was gradually increased over roughly 15 s, avoiding disruption to the microbalance. Pressure control used two pressure transducers, with ranges of 0-0.1 and 0-2 MPa, each with an accuracy of 0.02 % in the specified range. The pressure was maintained at the set point by active computer control. The mass uptake was measured as a function of time and the approach to equilibrium monitored in real time with a computer algorithm. The maximum time for equilibration of any one pressure point was 6 h. After equilibration was established, the pressure of gas was increased to the next set value. The sample temperature was monitored and maintained throughout the experiment using a thermo-stirrer. Samples were returned 2 years after analysis and the phase purity was checked by PXRD, using the same strategy outlined in Section 4.3.6. Data were fitted using Pawley refinement⁸¹ using TOPAS,^{82,83} details of these fits are outlined in **Table 4.3.7-1** (Appendix 4.8.2).

4.3.7.1 CO₂ Uptake of 4.1(I) at 298 K

The sample was outgassed at 298 K under high vacuum ($\leq 10^{-6}$ mbar) for a period of 12 h, resulting mass loss of 2.31 % before equilibration. The sample was dosed as outlined above to 19.5 bar CO₂ at 298 K.

4.3.7.2 CO₂ Uptake of 4.2(Br) at 298 K

The sample was outgassed at 298 K under high vacuum ($\leq 10^{-6}$ mbar) for a period of 12 h, resulting mass loss of 3.51 % before equilibration. The sample was dosed as outlined above to 19.5 bar CO₂ at 298 K.

4.3.7.3 CO₂ Uptake of 4.3(CI) at 298 K

The sample was outgassed at 298 K under high vacuum ($\leq 10^{-6}$ mbar) for a period of 12 h, resulting mass loss of 4.44 % before equilibration. The sample was dosed as outlined above to 19.5 bar CO₂ at 298 K.

4.3.8 *In situ* Powder X-Ray Diffraction during CO₂ Adsorption and Desorption

Samples of **4.1(I)** and **4.2(Br)** were studied by PXRD during CO₂ adsorption by utilising an *in situ* gas cell at beamline I11 at Diamond Light Source.^{84–86} Sample of **4.1(I)** was filtered and washed with methanol, samples were placed in an oven at 65 °C for 15 minute to ensure desolvation of the sample. Sample of **4.2(Br)** was filtered and washed with methanol and heated, while on the beamline, under vacuum to ensure desolvation. Samples were then ground and loaded into a 0.7 mm quartz capillary and sealed in a gas cell. Samples were then evacuated ($\approx 10^{-5}$ mbar) on the beamline before an initial powder pattern was recorded. Samples were then dosed to sequential increasing pressures of CO₂ allowing for a 30-min equilibration period prior to data collection. These experiments were recorded at 298 K using a PSD (position-sensitive detector).⁸⁶ Data were fitted by Pawley refinement⁸¹ using the TOPAS program.^{82,83} Details of refinement are outlined in **Table 4.3.8-1** and **Table 4.3.8-2** (Appendix 4.8.3).

Samples of **4.1(I)** and **4.3(CI)** were prepared in the same way as **4.1(I)** above. These samples were stored in sample vials out of direct sunlight for one month. Samples were then tested utilising the *in situ* gas cell at beamline I11 at Diamond Light Source.^{84–86} Samples were dosed with increasing pressures of CO₂ at room temperature. Data were collected using a PSD (position-sensitive detector).⁸⁶ Data were fitted using Pawley refinement⁸¹ using the TOPAS program.^{82,83} Details of refinement are outlined in **Table 4.3.8-3** and **Table 4.3.8-4** (Appendix 4.8.3).

4.3.9 *In situ* Single-crystal X-Ray Diffraction Studies during CO₂ Adsorption

Single crystals of **4.1(I)** and **4.2(Br)** were structurally characterised during CO₂ adsorption on beamline I19 at Diamond Light Source^{77–79} utilising the *in situ* gas cell instrumentation developed at the beamline. Single crystals were selected directly from the mother liquor and glued on to a long mylar microloop. Once the glue had dried these loops were then inserted into a capillary gas cell with glue being applied to the edge of the pin to ensure samples did not move during data collection. The single-crystal was initially aligned and screened under an atmospheric environment. Once an appropriate crystal was obtained the gas cell was evacuated ($\approx 10^{-5}$ mbar) on the beamline. Single-crystals were dosed with successive pressures of CO₂ allowing for 30-minute equilibration time between dosing and data collection. Both experiments were carried out at 298 K.

The data were processed using CryAlisPro⁸⁰ using a predetermined instrument model from a strongly diffracting reference crystal to enable a more accurate determination of the orientation matrix used for integration of diffraction intensities. Data were corrected for absorption using empirical methods (SADABS) based on symmetry-equivalent reflections and measurements at different azimuthal angles.^{72–74} Structure solution was achieved by direct methods and the crystal structure was refined using full-matrix least-squares against weighted F^2 values using SHELXL⁷⁵ within Olex2.⁷⁶ Non-hydrogen and non-disordered atoms were refined

anisotropically. Hydrogen atoms were placed in calculated positions, refined using idealized geometries (riding model) and assigned a fixed isotropic displacement parameter. A summary of the data processing is outlined in **Table 4.3.9-1** to **Table 4.3.9-3** (Appendix 4.8.4).

Data quality was initially poor and diminished in resolution with increased pressures of CO₂. Partial solutions of the trinuclear cluster could be obtained for the first three/four pressure steps for both **4.1(I)** and **4.2(Br)** with latter pressure steps allowing for the determination of only the unit cell dimensions. These partial solutions allowed for modelling of the cluster, but the nitrate counter ion and the methyl groups of the coordinated methanols could not be confidently modelled. The ring geometries were constrained either to be regular hexagons or with atom distance restraints being applied in the case of the rings that aligned on mirror planes. A restraint was also applied to the direction and size of anisotropic displacement parameters of bonded atoms.⁸⁷

4.4 Results and Discussion

4.4.1 Synthesis of 4.1(I), 4.2(Br) and 4.3(Cl)

Trinuclear-oxo clusters **4.1(I)**, **4.2(Br)** and **4.3(Cl)** were synthesised, initially using a small-scale synthesis. These reactions were low yielding, but did produce crystals of appropriate size and quality to characterise by single-crystal X-ray diffraction. The yields of these reactions could be improved by slow evaporation following the solvothermal synthesis. Following successful synthesis of these three systems the synthetic method was scaled up (by a factor of 10) with the use of Teflon-lined steel autoclaves. These scaled-up syntheses produced the desired cluster with improved yields, but crystalline powders were obtained.

The purity of the three clusters was confirmed by elemental analysis; the observed elemental compositions were in good agreement with that expected. The discrepancies between the expected and observed elemental analysis was attributed to the presence of solvent. This solvent content is inconsistent with the solvent determined crystallographically (discussed in Section 4.4.2), but the reason for this discrepancy will be discussed in later sections.

4.4.2 Crystal Packing

Single crystals of the three systems were characterised by single-crystal X-ray analysis, which identified all three systems (**4.1(I)**, **4.2(Br)** and **4.3(Cl)**) as crystallising in the monoclinic $P2_1/n$ space group. The three systems also crystallised as solvates. Cluster **4.3(Cl)** has been previously reported⁸⁸ as well as analogous clusters with 4-chlorobenzoate ligands being reported.^{89,90}

The syntheses produced analogous trinuclear-oxo centred clusters (**Figure 4.4.2-1**) consisting of a central μ_3 -oxide connected to three Cr(III) centres. The chromium atoms in turn have six 4-halobenzoates coordinated (bridging two Cr centres each) with a methanol coordinated opposite to the central μ_3 -oxide. The cluster's positive charge is then balanced by a non-coordinating nitrate counter ion. Disorder of methyl groups of the coordinated methanols was observed in the case of **4.2(Br)** and **4.3(Cl)** (**Figure 4.4.2-1**).

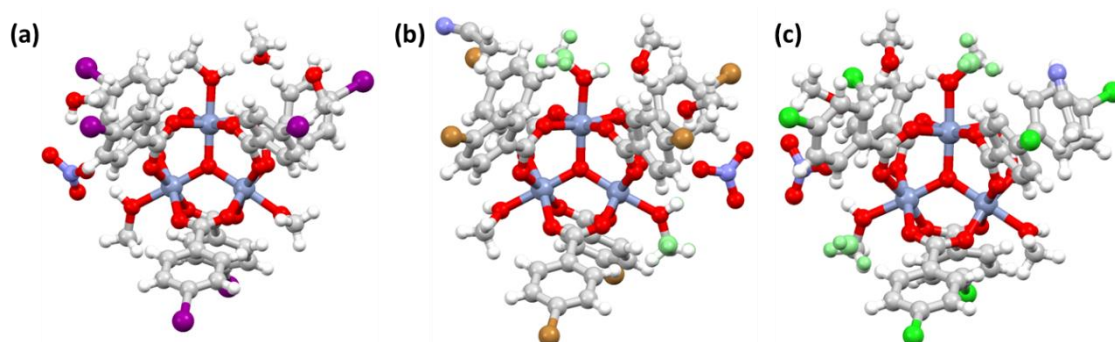


Figure 4.4.2-1. The trinuclear clusters (including non-coordinated solvent and anion) (a) **4.1(I)**, (b) **4.2(Br)** and (c) **4.3(Cl)**. Colour scheme Cr, bluish grey; O, red; C, grey; N, blue; I, purple; Br, brown; Cl, green; H, white; Disorder, mint green.

In the crystal structure of each of the three clusters (**4.1(I)**, **4.2(Br)** and **4.3(Cl)**) two of the halogens present interact with aromatic rings of neighbouring clusters, forming a 2D halogen-bonding network propagating along the *ac*-plane (**Figure 4.4.2-2**). The 2D halogen-bonding layers in turn pack in an offset anti-parallel fashion (**Figure 4.4.2-2**) with the interaction between halogens in adjacent layers not involved in the 2D propagating the halogen-bonding layers.

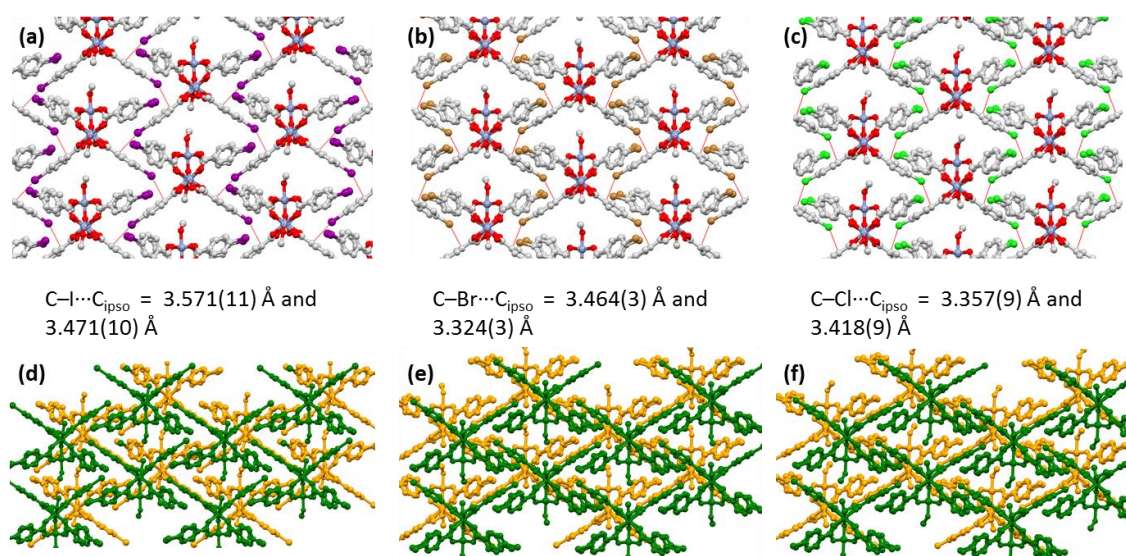


Figure 4.4.2-2. 2D halogen-bonding layers in (a) **4.1(I)**, (b) **4.2(Br)** and (c) **4.3(Cl)** and the antiparallel stacking of 2D halogen-bonding layer for (d) **4.1(I)**, (e) **4.2(Br)** and (f) **4.3(Cl)**. Colour scheme consistent with **Figure 4.4.2-1**; C–X...C_{ipso} interactions, red dashed lines; layers distinguished by yellow and green. Solvent molecules and counter-ions and hydrogen atoms omitted for clarity.

In the case of **4.1(I)** the iodines protruding from the halogen-bonding layers form C–I... π interactions (**Figure 4.4.2-3**) between layers, which is also accompanied by an interaction between the iodine and the nitrate counter-ion of neighbouring layers. In the case of clusters **4.2(Br)** and **4.3(Cl)** the halogens protruding from the layers form type II C–X...X–C halogen-bonding interactions⁹¹ (**Figure 4.4.2-3**) and are accompanied by a halogen-bond to the nitrate counter-ion, as in **4.1(I)**.

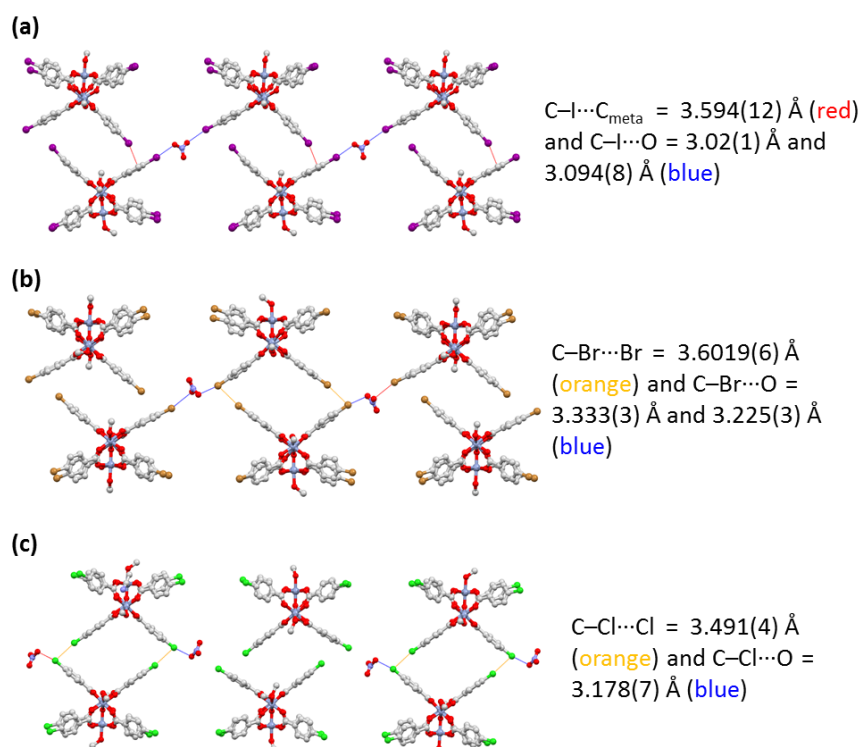


Figure 4.4.2-3. Interlayer interactions in (a) **4.1(I)**, (b) **4.2(Br)** and **4.3(Cl)**. Colour scheme consistent with **Figure 4.4.2-1**. Solvent molecules and hydrogen atoms omitted for clarity.

Once the cluster and counter-ion were successfully modelled additional unassigned electron density was present. This was attributed to solvent molecules resulting in $1 \frac{1}{2}$ methanol molecules for **4.1(I)** and 2 methanol and 1 acetonitrile molecules for **4.2(Br)** and 2 methanol and $\frac{3}{4}$ acetonitrile molecules for **4.3(Cl)** being modelled. These solvent quantities are inconsistent with the solvent determined from the elemental analysis; this could be as a result of volatile solvents being lost from the cavities upon filtration prior to elemental analysis. The solvent is situated in between the 2D halogen-bonding layers. The solvent, in turn, forms a series of hydrogen bonds between the coordinated methanols and the nitrate counter ion (**Figure 4.4.2-5**)

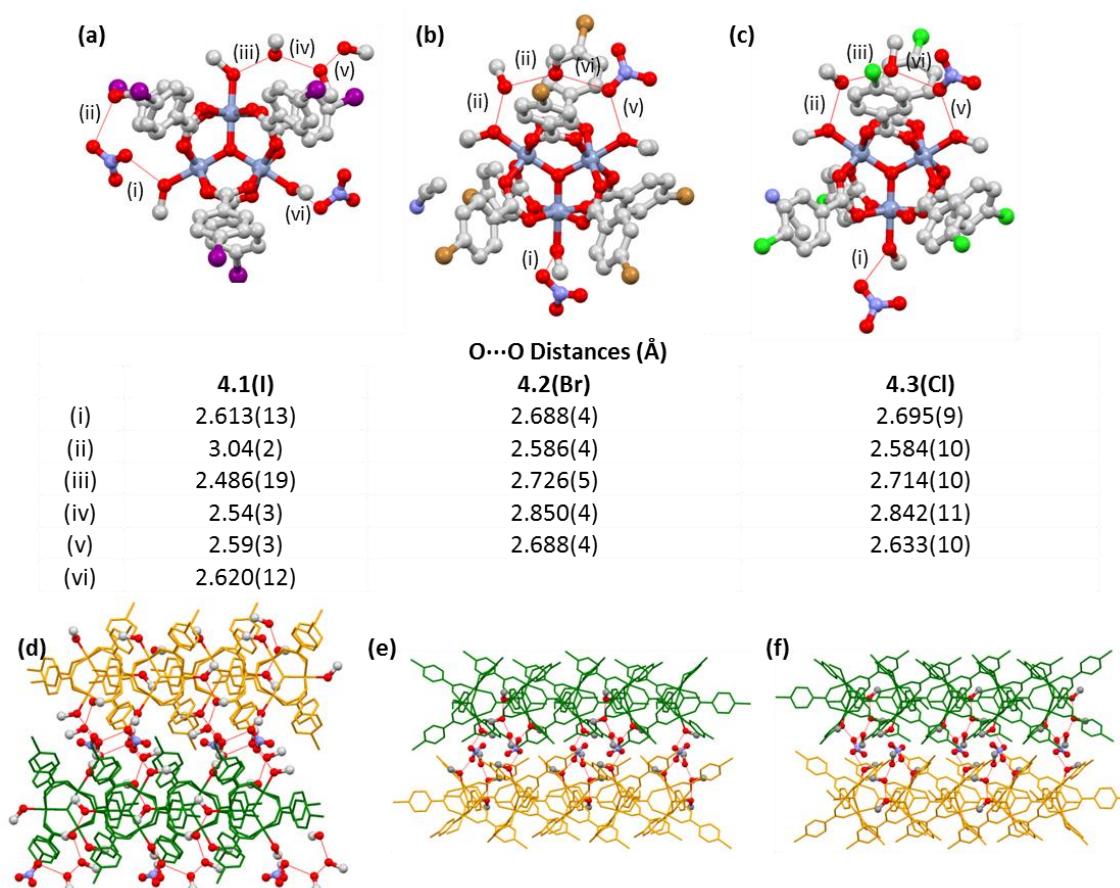


Figure 4.4.2-5. Solvent modelled in (a) **4.1(I)**, (b) **4.2(Br)** and **4.3(Cl)** and the position of the solvent molecules relative to the 2D halogen bonding layers (d, e and f for **4.1(I)**, **4.2(Br)** and **4.3(Cl)**, respectively). Colour scheme consistent with **Figure 4.4.2-2**.

The solvent-accessible volumes for the three clusters were determined using the PLATON program.^{92–94} To calculate the total solvent-accessible void, non-coordinated solvent molecules, counter-ions and minor components of disordered ligands were first removed from the model. This analysis revealed that the three isostructural clusters possessed comparable void volumes (283.8 Å³, 292.8 Å³ and 294.9 Å³ per formula unit equating to 17.8, 19.9 and 20.5 % of the unit cell volumes of **4.1(I)**, **4.2(Br)** and **4.3(Cl)**, respectively), with a minor increase in void volume along the series I→Br→Cl in halogen functionality. The voids in each structure form narrow channels running in the direction of the *a*-axis between the 2D halogen-bonded layers (**Figure 4.4.2-6**).

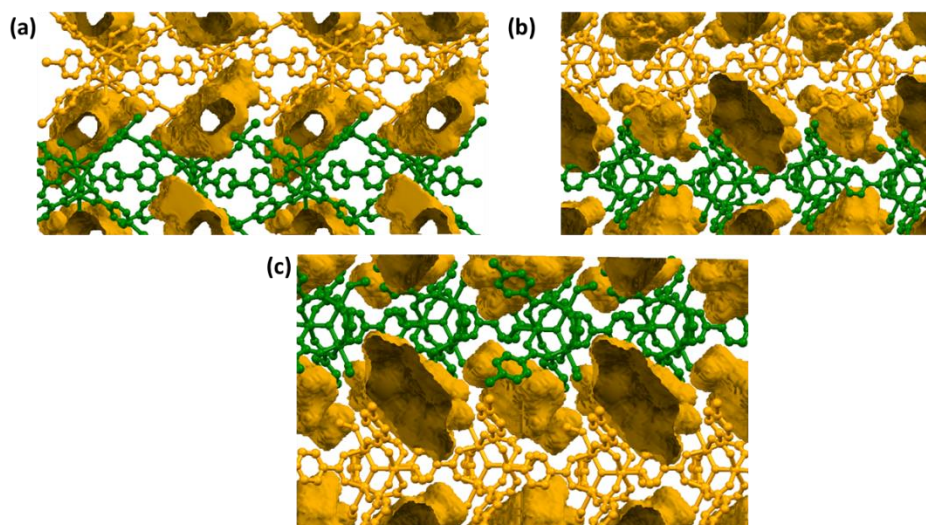


Figure 4.4.2-6. Solvent-accessible void volumes present in (a) **4.1(I)**, (b) **4.2(Br)** and (c) **4.3(Cl)** with void spaces visualised using Mercury⁹⁵ (1.2 probe radius and 0.2 grid spacing). Colour scheme consistent with **Figure 4.4.2-2**, void spaces as yellow surfaces.

In conclusion structural characterisation of the three clusters revealed a clear trend in the packing. The three clusters formed a regular packing motif, resulting in the formation of 2D halogen-bonding layers. The layers in turn pack in an anti-parallel fashion with further C–X \cdots π (**4.1(I)**) or C–X \cdots X (**4.2(Br)** and **4.3(Cl)**) halogen bonds occurring between layers. Solvent molecules were also successfully modelled between layers. These in turn formed hydrogen-bonding interactions between the coordinated methanols and the nitrate counter ion. The solvent-accessible void volumes were situated where the solvent had been modelled between halogen-bonded layers. It was also noted that the void space increased with decreasing halogen size.

4.4.3 Thermogravimetric analysis (TGA)

Samples of **4.1(I)**, **4.2(Br)** and **4.3(Cl)** were filtered under vacuum and washed with methanol before being analysed for mass loss while increasing temperature. A standard TGA strategy was used, initially, with samples being heated from 25 °C to 600 °C at 5 °C/min.

The standard TGA of **4.1(I)** (**Figure 4.4.3-1**) resulted in an gradual mass loss of 4.3 % from 25 °C to 170 °C, this was attributed to the loss of two methanol molecules and one water molecule per cluster, comparable to the solvent content observed crystallographically. A secondary mass loss was observed of 5 % between 200 and 250 °C, this being as a result of loss of the coordinated solvent. Following loss of the coordinated methanols the sample underwent a large mass loss, this being suspected to be due to decomposition of the cluster. Following this decomposition the final mass (25.5 %) had not reached a plateau, suggesting that full decomposition to chromium oxide (12 %) has not been observed.

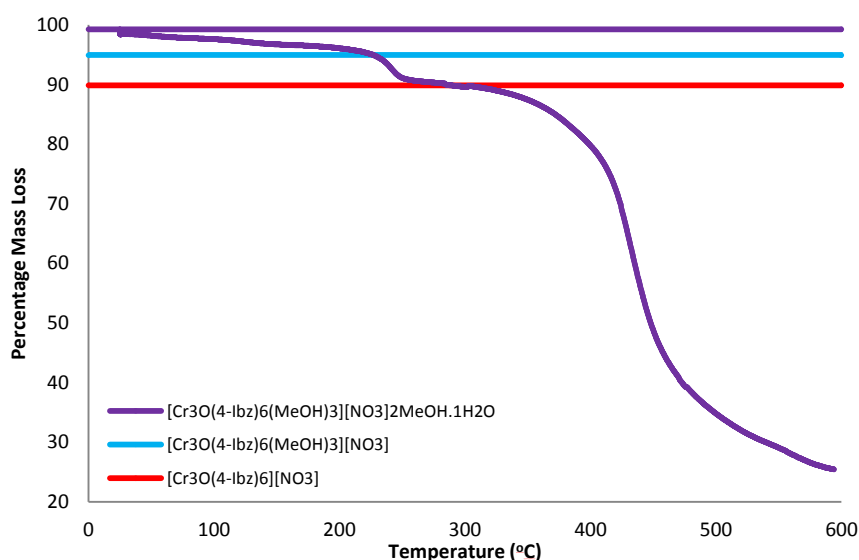


Figure 4.4.3-1. Standard TGA of 4.1(I)

The TGA of **4.2(Br)** and **4.3(Cl)** (Figure 4.4.3-2) showed comparable mass losses. In the temperature range 25-85 °C, an initial mass loss of 5.7 % and 6.8 % was observed for **4.2(Br)** and **4.3(Cl)**, respectively; this was attributed to the loss of three methanol molecules per cluster. This was then followed by a secondary mass loss of 2.4 % and 4.0 % in the range of 100-200 °C and 95-150 °C for **4.2(Br)** and **4.3(Cl)**, respectively; this is suspected to be the loss of one acetonitrile and one water. This solvent content is higher than the content determined crystallographically, which could be due to additional surface solvent. Both samples then displayed a third mass loss of 5.7 % and 6.8 % in the range 210-250 °C and 175-235 °C for **4.2(Br)** and **4.3(Cl)**, respectively. This mass loss was attributed to loss of coordinated methanol and occurs in a temperature range consistent with the corresponding loss observed for **4.1(I)**. Following the loss of the coordinated methanol the samples undergo a large mass loss from 300 and 280 °C for **4.2(Br)** and **4.3(Cl)**, respectively, believed to be as a result of further decomposition of the cluster. The final masses (28.5 and 28.7 % for **4.2(Br)** and **4.3(Cl)**, respectively) are yet to reach a plateau at 600 °C, suggesting that full decomposition to chromium oxide (13.5 % and 16.1 % for **4.2(Br)** and **4.3(Cl)**, respectively) has not been observed.

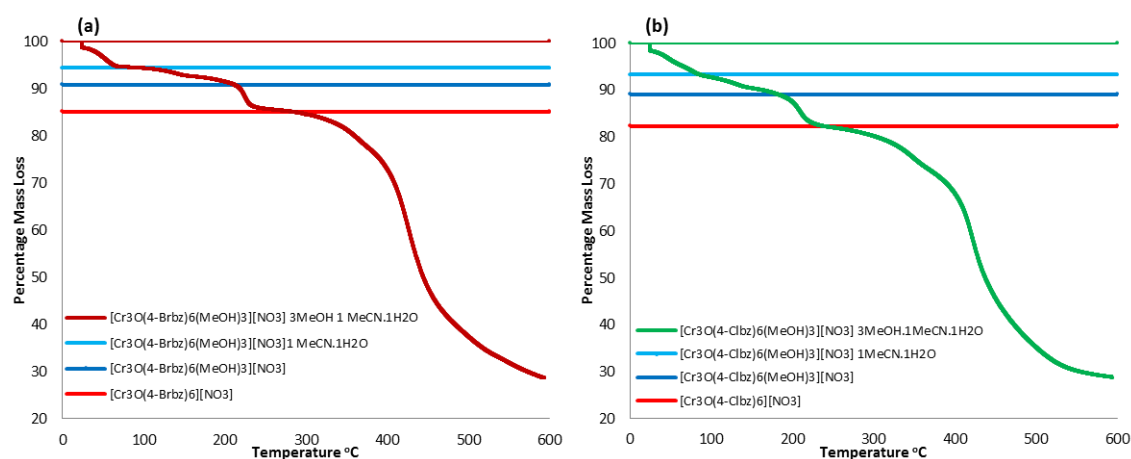


Figure 4.4.3-2. Standard TGAs of (a) 4.2(Br) and (b) 4.3(Cl)

In each case these standard TGAs revealed a mass loss, believed to be non-coordinated solvent, occurring from room temperature. This is a promising outcome because it would allow for activation of these materials at moderately low temperatures. To confirm that this is possible, isothermal TGAs were carried out on samples of the three clusters. This involved recording mass loss while the sample was held sequentially at 30 °C for 1 h, 65 °C for 1 h and 100 °C for 2 h. For each sample, mass loss was observed during the first 30 °C dwell period (Figure 4.4.3-3), suggesting that desolvation can be achieved by storing samples at room temperature. The final mass losses of 4.1(I) (7.3 %), 4.2(Br) (7.3 %) and 4.3(Cl) (9.0 %) lead to a plateau, suggesting loss of all non-coordinated solvent. These mass losses are comparable to those observed in the standard TGAs suggesting comparable solvent contents.

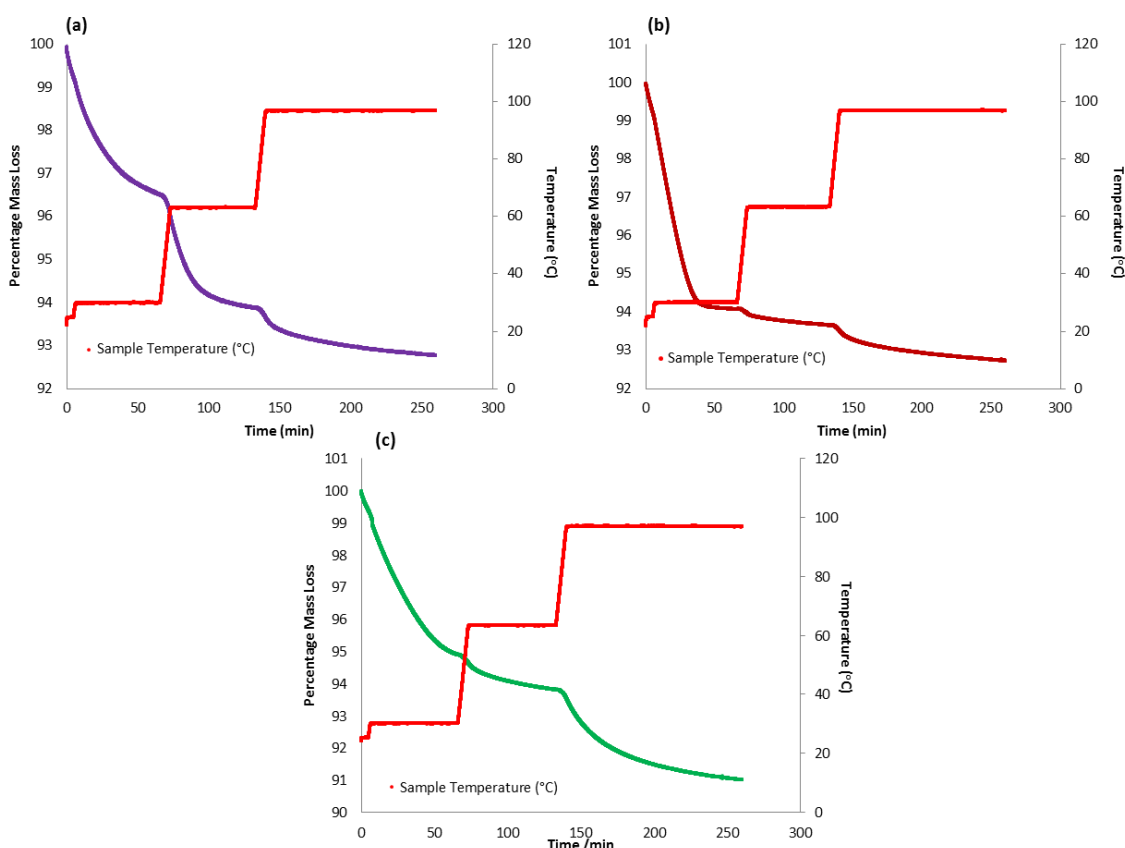


Figure 4.4.3-3 Isothermal TGAs of (a) **4.1(I)**, (b) **4.2(Br)** and (c) **4.3(Cl)**. Mass loss (left) and temperature (right) plotted of separate y axes vs time (min).

Following isothermal analysis the samples were recovered and stored for one week in an attempt to determine whether samples take up water when being stored in air. The samples were then re-analysed by TGA, initially heating the samples to 100 °C (5 °C/min) at which point the temperature was maintained for 2 h before being heated to 600 °C (5 °C/min). These aged samples all show mass loss during the initial heating period to 100 °C (**Figure 4.4.3-4**) with the mass reaching a plateau during the dwell period. The mass loss of **4.1(I)** (2.4 %), **4.2(Br)** (2.3 %) and **4.3(Cl)** (6.0 %) can be attributed, respectively, to the loss of 2.5, 2 and 4.5 water molecules per cluster. During the heating from 100-600 °C, the first mass loss is observed in the range of 150-280 °C and attributed to the loss of the coordinated methanol. This mass loss also occurs in a temperature range consistent with the mass losses observed in the standard TGAs. Finally further mass loss is observed up to 440 °C resulting in final mass percentage of 13.1 %, 15.2 % and 18.1 % for **4.1(I)**, **4.2(Br)** and **4.3(Cl)**, respectively. This final mass remains constant when heated from 440 °C to the final temperature (600 °C). This final mass is most likely to be chromium oxide (12.3 %, 14.6 % and 17.0 % of original mass for **4.1(I)**, **4.2(Br)** and **4.3(Cl)**, respectively), but the discrepancy could be due to the presence of a small quantity of chromium carbonate (22.9 %, 27.2 % and 31.7 % of original mass for **4.1(I)**, **4.2(Br)** and **4.3(Cl)**, respectively).

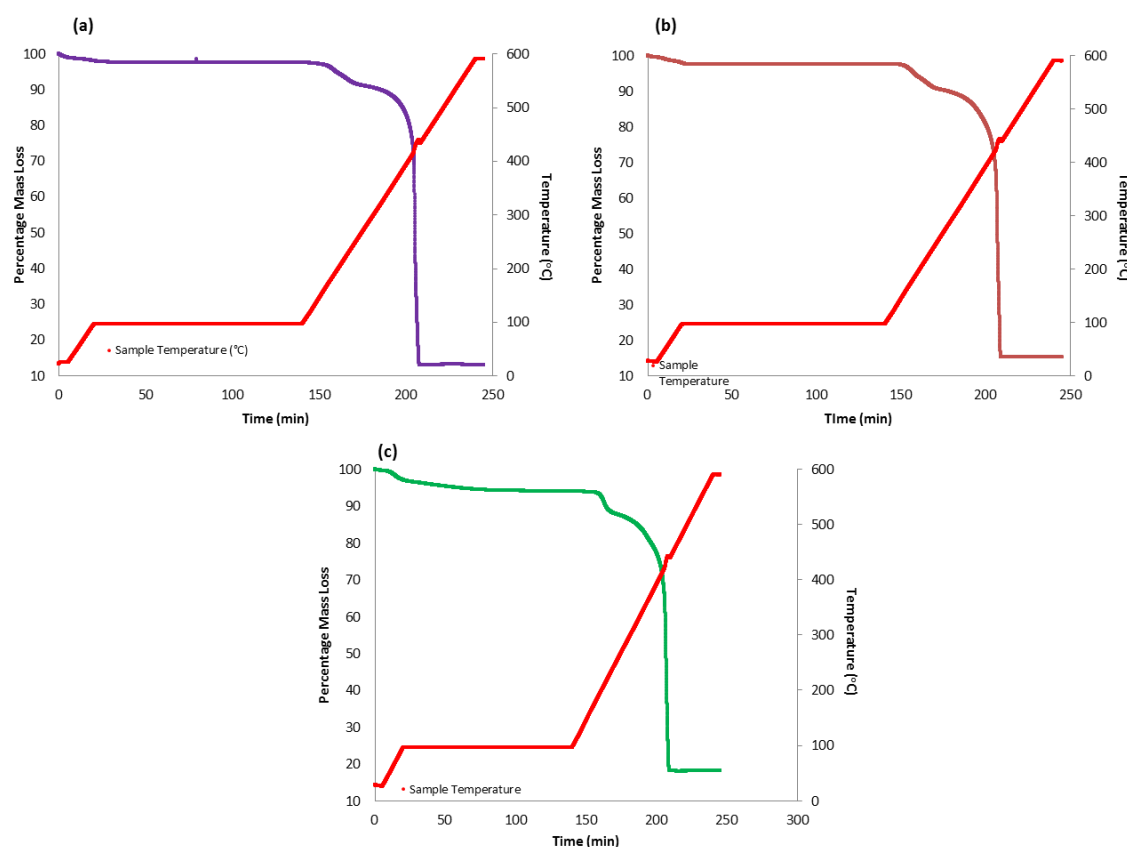


Figure 4.4.3-4. TGAs of (a) **4.1(I)**, (b) **4.2(Br)** and (c) **4.3(Cl)** after being stored for 1 week out of solvent. Mass loss (left) and temperature (right) plotted of separate y axes vs time (min).

4.4.4 Single-Crystal Desolvation Studies

The isothermal TGA demonstrated that mass loss occurred when samples of **4.1(I)**, **4.2(Br)** and **4.3(Cl)** were stored at 30 °C, therefore in order confirm this was due to loss of solvent present in the cavities a series of desolvation studies were performed, monitoring the crystals by single-crystal X-ray diffraction. The first of these desolvation tests involved removing single crystals of **4.1(I)**, **4.2(Br)** and **4.3(Cl)** from the mother liquor and placing them on a glass slide for 30 min to allow the solvent to evaporate. Following the solvent evaporation the crystals were then submerged in perfluoropolyether oil to allow for crystal screening. Samples suffered slight degradation in comparison to the solvated phase but, for **4.1(I)** and **4.2(Br)**, crystals of sufficient quality were selected. Structure solution revealed that this protocol produced solvent-free forms of **4.1(I)** and **4.2(Br)**.

Desolvation leads to a space group transformation from $P2_1/n$ to $P2_1/m$, resulting in a change in Z from 4 to 2 and an effective 12.1 % ($\Delta V/Z = 193.9(4) \text{ \AA}^3$) and 11.7 % ($\Delta V/Z = 178.0(4) \text{ \AA}^3$) reduction in the unit cell volume for **4.1(I)** and **4.2(Br)**, respectively. The phase transformation occurs with retention of the 2D halogen-bonding layers (Figure 4.4.4-1). In the case of **4.1(I)** the desolvation has minimal effect on the C–I $\cdots\pi$ interactions with negligible reduction in the C–I \cdots C_{ipso} distances ($\Delta(\text{C–I}\cdots\text{C}_{\text{ipso}}) = -0.02(2) \text{ \AA}$, -0.55 % and $-0.08(2) \text{ \AA}$, -2.26 %) in comparison to the solvated form. For cluster **4.2(Br)** the halogen-bonding network is retained, but with a compression of one of the C–Br \cdots C_{ipso} distances ($\Delta(\text{C–Br}\cdots\text{C}_{\text{ipso}}) = -0.31(1) \text{ \AA}$, -9.2 %) and an

elongation of the other C–Br...C_{ipso} distance (Δ C–Br...C_{ipso} = 0.08(2) Å, 2.2 %) in comparison to the solvated form.

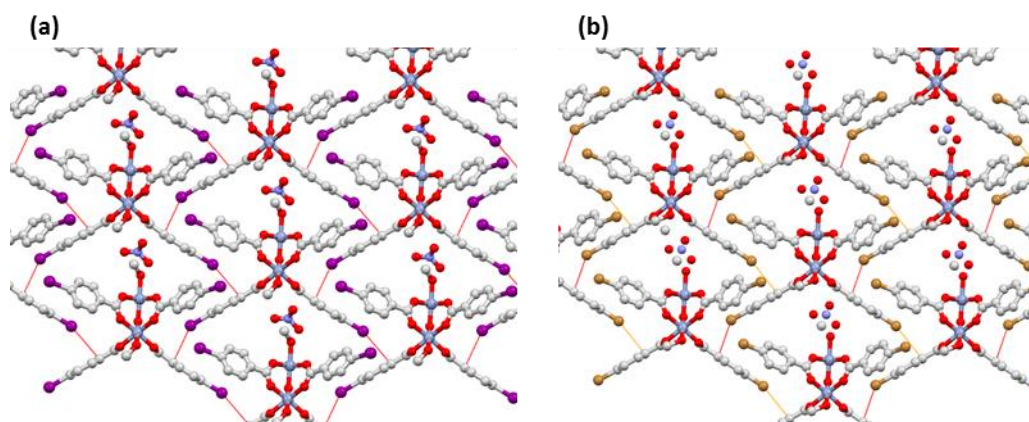


Figure 4.4.4-1. Retained 2D halogen-bonding layers of the solvent free forms of (a) **4.1(I)** and (b) **4.2(Br)**. The red dashed lines representing the C–Br...C_{ipso} distances that have been compressed and the orange dashed lines the C–Br...C_{ipso} distances that are elongated. Colour scheme consistent with **Figure 4.4.2-1**.

The 2D halogen-bonding layers pack anti-parallel to neighbouring layers, as previously observed in the solvated forms (Section 4.4.2). However, the absence of solvent situated between layers results in the layers shifting and compressing. This results in interlayer interaction featuring a secondary C–X... π interaction observed in the solvent-included phases shifting such that the C–X bond is orientated towards the C_{ipso} and the C_{carboxylate} rather than previously towards the C_{meta}. This is accompanied by a π ... π stacking between neighbouring clusters (**Figure 4.4.4-2**). In the solvated forms the layers were also connected by halogen-bonding interactions with the nitrate counter-ion. In the solvent free forms the movement of the nitrate counter ion leads to these interactions being replaced with a type I⁹¹ halogen-halogen interaction (**Figure 4.4.4-2**).

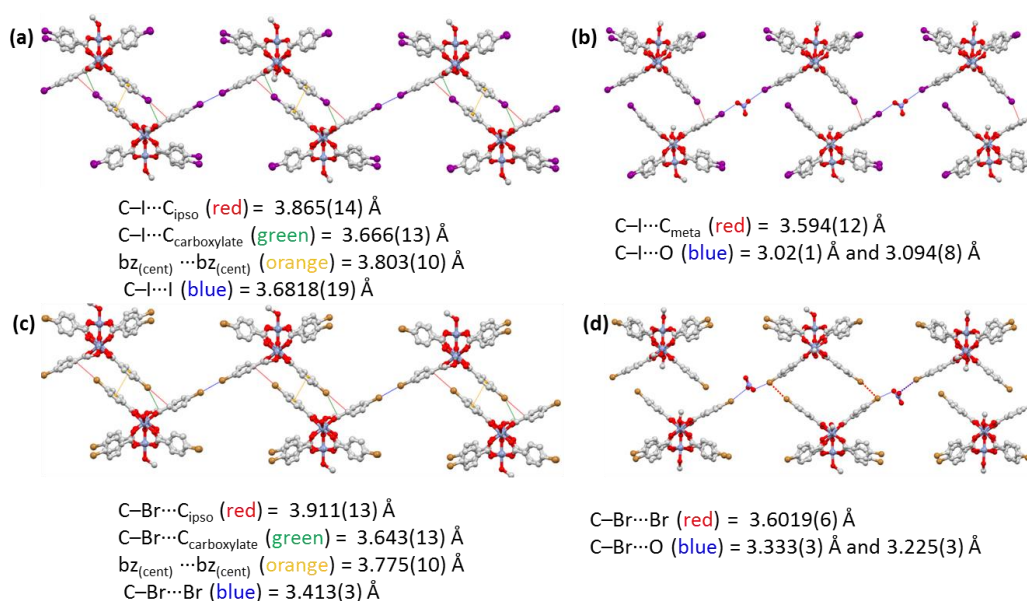


Figure 4.4.4-2. The interactions between the 2D halogen-bonding layers for (a and c) the solvent-free forms in comparison to the (b and d) the solvates of **4.1(I)** and **4.2(Br)**. Colour scheme consistent with **Figure 4.4.2-1**.

The absence of solvent, which formed hydrogen-bonding between layers, results in the nitrate moving closer to the coordinated methanols. This leads to a 1D hydrogen-bonding chain being observed between the oxygens of the nitrate and the methanols, with N–O⋯O distance of 2.60(4) Å and 2.58(3) Å for **4.1(I)** and 2.50(3) Å and 2.55(2) Å for **4.2(Br)** (Figure 4.4.4-3).

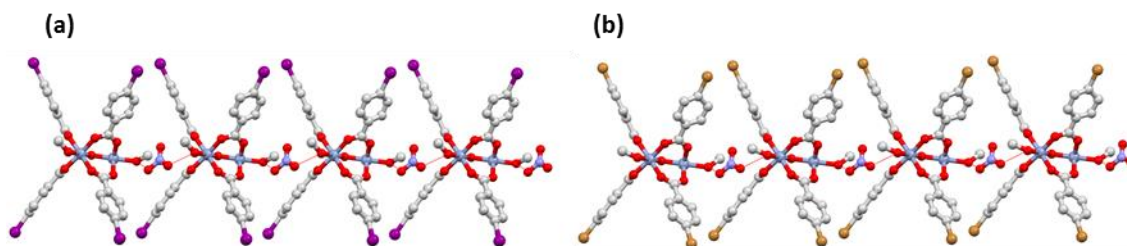


Figure 4.4.4-3. Hydrogen-bonding chain present in the solvent-free forms of (a) **4.1(I)** and (b) **4.2(Br)**. Colour scheme consistent with Figure 4.4.2-5.

The phase transformation observed upon leaving single crystals in air for 30 minutes and the reduction in cell volume suggested that desolvation had occurred, however in order to confirm this PLATON SQUEEZE⁹³ was applied to quantify the unassigned electron density. The unassigned electron density present in **4.1(I)** and **4.2(Br)** was calculated to be 8 and 0 electrons per unit cell respectively (4 and 0 per cluster). The absence of significant quantities of unassigned electrons therefore suggests the desolvation has been successful. PLATON⁹²⁻⁹⁴ was also used to quantify the total solvent-accessible void, after removing the nitrate counter-ion and the minor components of disordered ligands from the model. This analysis revealed a significant reduction in void volume (43.9 Å³ and 153.9 Å³ per formula unit equating to 3.3 % and 9.9 % of the unit cell volumes for **4.1(I)** and **4.2(Br)**, respectively) in comparison the solvent-included forms ((283.8 Å³ and 292.8 Å³ per formula unit, equating to 17.8 % and 19.9 % of the unit cell volumes of **4.1(I)** and **4.2(Br)**, respectively). In both cases the void volume (Figure 4.4.4-4) consists of discrete cavities between layers, with the void volumes in **4.2(Br)** also protruding into the halogen-bonding 2D layers.

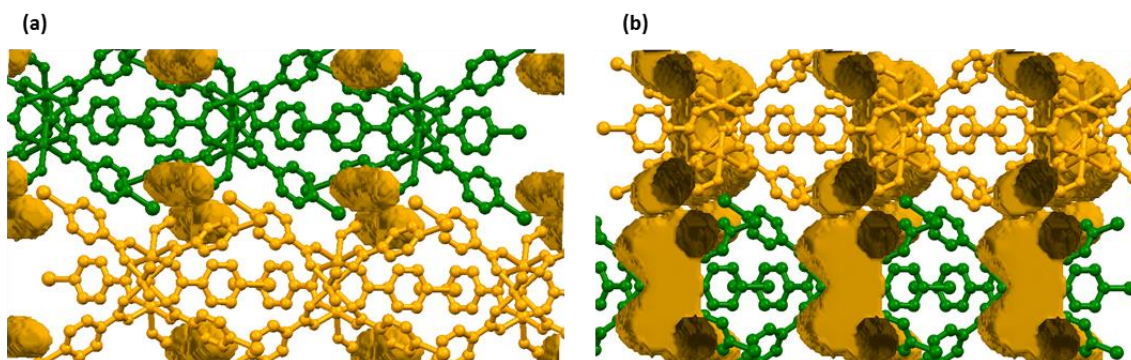


Figure 4.4.4-4. Solvent-accessible void space for (a) **4.1(I)** and (b) **4.2(Br)**. View from between 2D halogen-bonding layers (defined in green and yellow). Visualised using Mercury⁹⁵ using a 1.2 probe radius and 0.2 grid spacing. Colour scheme consistent with Figure 4.4.2-6.

The same desolvation approach was attempted to obtain a desolvated phase of **4.3(Cl)**, however this resulted in a significant reduction in the crystallinity of the crystals. Therefore an alternative approach was taken. For a solvated single crystal of **4.3(Cl)** a short series of scans was recorded sufficient to enable determination of an orientation matrix and unit cell parameters at successive temperatures of 100, 150, 200, 250 and 298 K. It can be clearly seen from the diffraction images that the diffraction remains consistent from 100-250 K (**Figure 4.4.4-5**), with the 298 K data visibly changing. The determined unit cell parameters for each scan set revealed a reduction in the number of observed reflections ($I > 10 \sigma(I)$) on increasing temperature from 100-250 K as well as an increase in the unit cell volume (**Table 4.4.4-1**). The number of reflections drops dramatically at 298 K to 73 (806 reflections being observed for analogous scans at 100 K). From the recorded reflections it was not possible to determine a suitable unit cell using the conventional unit cell determination algorithm in APEX3,⁹⁶ with CELL_NOW⁹⁷ being employed to determine a unit cell from 50 of the observed reflections, suggesting the crystal fractures upon solvent loss at 298 K. The unit cell at 298 K does resemble that of the desolvated phases of **4.1(I)** and **4.2(Br)** and, assuming the same transformation occurs, there is a 9.4 % volume reduction ($\Delta V/Z = -139(30) \text{ \AA}^3$) comparing the unit cell volume at 100 K and the unit cell volume at 298 K. The drastic loss in crystallinity results in a large uncertainty in this result, which meant that further information, could not be obtained.

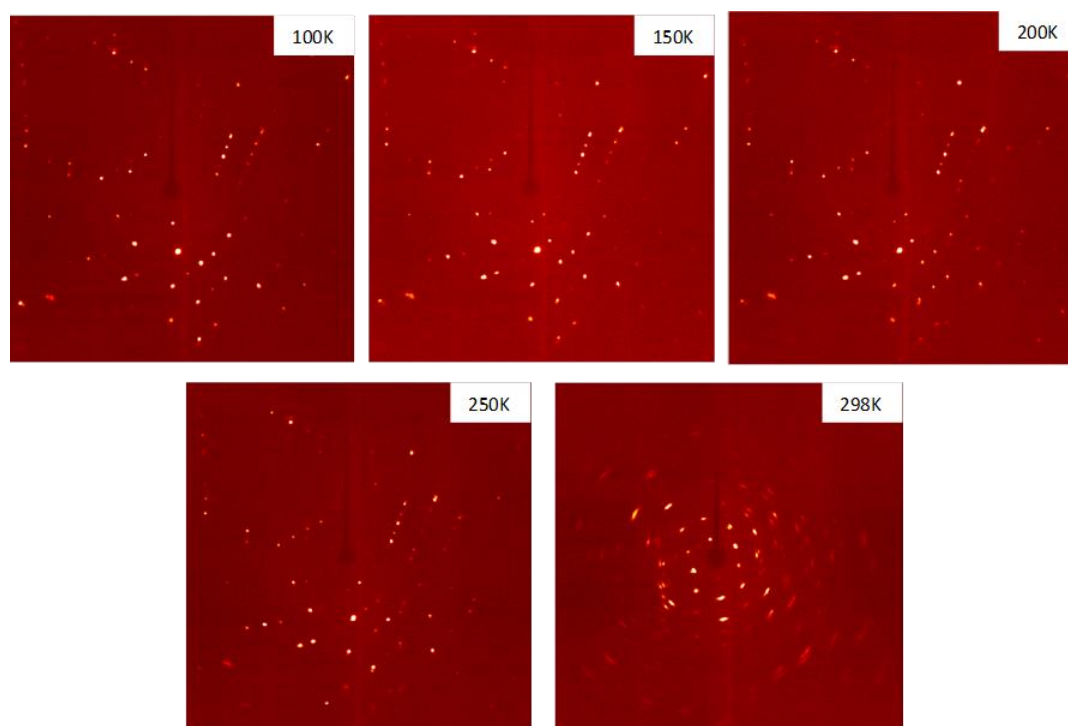


Figure 4.4.4-5. Single frame images (from the same orientation) of **4.3(Cl)** at variable temperature with the 298 K image showing clear degradation.

Table 4.4.4-1. Unit cell dimensions determined for **4.3(CI)** at variable temperature using a predetermined matrix scan strategy (4 runs of 20 frames, 0.5 °/frame and 10 s/frame).

T (K)	I/σ	Reflections	Crystal System	FOM	Volume (Å ³)	a (Å)	b (Å)	c (Å)	α (°)	β (°)	γ (°)
100	10	806	Monoclinic P	0.91	5914(2)	12.453(2)	24.306(5)	19.762(5)	90	98.63(2)	90
150	10	714	Monoclinic P	0.87	5965(3)	12.465(2)	24.392(5)	19.824(6)	90	98.29(2)	90
200	10	599	Monoclinic P	0.8	6035(3)	12.468(2)	24.485(5)	19.967(7)	90	98.11(2)	90
250	10	578	Monoclinic P	0.79	6103(3)	12.476(3)	24.582(5)	20.095(7)	90	98.00(3)	90
298	10	73	Monoclinic P ^a	0.26	2680(30)	11.00(6)	21.03(20)	12.51(4)	90	112.3(4)	90

^a Unit cell determined using CELL_NOW⁹⁷ where 50 reflections corresponded to that domain.

This stability study was, in part, replicated at the beamline I19 at Diamond Light Source,^{77–79} with full data sets being recorded at 250, 273 and 298 K. The unit cell volume expands between 250 K and 273 K, (**Table 4.4.4-2**) this being a thermal effect. The volume at 298 K then reduces in comparison with the lower temperatures, suggesting desolvation. The reduction in volume occurs with retention of the $P2_1/n$ space group unlike the transformation observed for **4.1(I)** and **4.2(Br)**. Full structure solutions were obtained for data recorded at 250 K and 273 K with evidence of solvent still being present, but for the 298 K data the cluster could be resolved but definitive positions of methyl groups of the coordinated methanol or the nitrate could not be modelled.

Table 4.4.4-2. Unit cell parameters determined for **4.3(CI)** at variable temperature. Data collected at beamline I19^{77–79}

T (K)	Space Group	Volume (Å ³)	a (Å)	b (Å)	c (Å)	α (°)	β (°)	γ (°)
250	$P2_1/n$	6185.7(3)	12.5320(3)	24.6796(7)	20.2103(7)	90	98.276(3)	90
273	$P2_1/n$	6221.2(3)	12.5498(4)	24.6819(7)	20.2972(7)	90	98.303(3)	90
298	$P2_1/n$	6136.0(9)	11.0773(9)	24.278(2)	22.8187(16)	90	90.860(7)	90

Comparison of the packing shows a consistent 2D halogen-bonding layer with the 298 K data exhibiting an elongation of one of the two C–Cl...C_{ipso} distances (**Figure 4.4.4-6**), consistent with the desolvation of **4.2(Br)**. The layers pack in the same antiparallel fashion previously observed (Section 4.4.2). The interactions between layers also feature the same interaction between the chlorine functional groups and the nitrate counter ion (**Figure 4.4.4-7**), as well as the same type II halogen-halogen interaction. Unfortunately the inability to model the nitrate anion at room temperature means its position is unclear, but the C–Cl...Cl distance increases suggesting a shifting apart of layers.

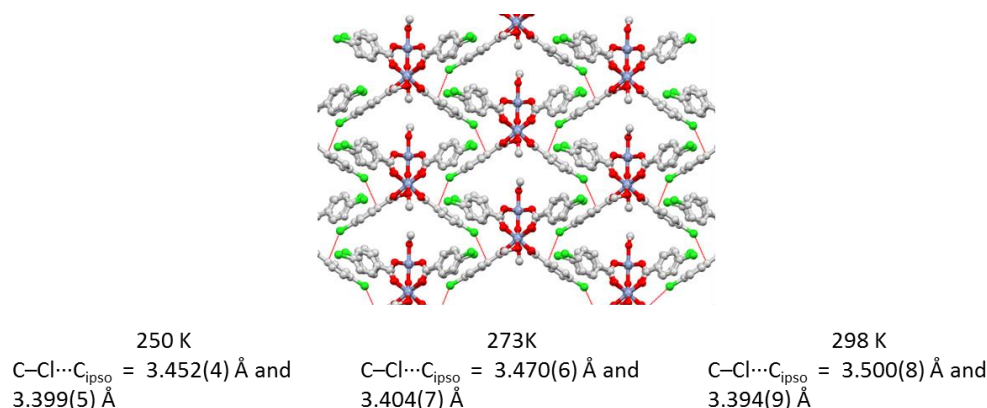


Figure 4.4.4-6. 2D halogen-bonded layers from crystal structures of **4.3(Cl)** at variable temperature (image shown from structure at 250 K).

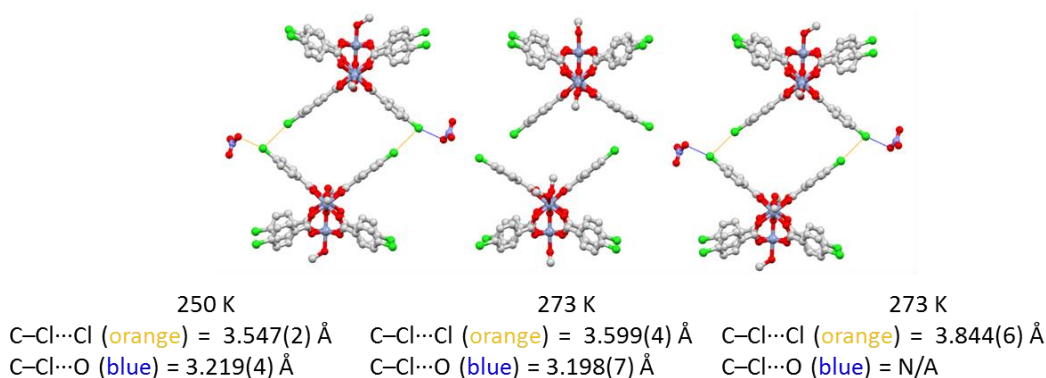


Figure 4.4.4-7. Interactions between 2D halogen-bonded layers of **4.3(Cl)** at variable temperature (image shown from structure at 250 K). Nitrate anion could not be modelled for 298 K data. Colour scheme consistent with **Figure 4.4.2-1**.

The inability to model the coordinated solvent molecules and counter-ion at 298 K would suggest that if non-coordinated solvent was still present it also would not be resolved. In an attempt to confirm or deny effective desolvation, PLATON SQUEEZE^{92,93} was used to quantify the unassigned electron count. This analysis identified 321 electrons (per unit cell) which has not been modelled. This electron count corresponds to 80.25 electrons per cluster, which is greater than the unaccounted for electrons of the counter-ion and the coordinated solvent combined. This suggests that this study has obtained a partially desolvated phase of **4.3(Cl)**. The inability to model the counter-ion and the methyl groups at 298 K meant that comparison of the solvent-accessible void volumes was carried out, using PLATON,^{92–94} on partial structure models, with the nitrate and methyl groups being removed, for the lower temperature structures. This analysis revealed a minor reduction in void volume (**Figure 4.4.4-8**), much smaller than the reductions observed for **4.1(I)** and **4.2(Br)**. The solvent-accessible void volumes are situated between halogen-bonded layers, forming channels consistent with the channel for the solvated forms (**Figure 4.4.4-8**).

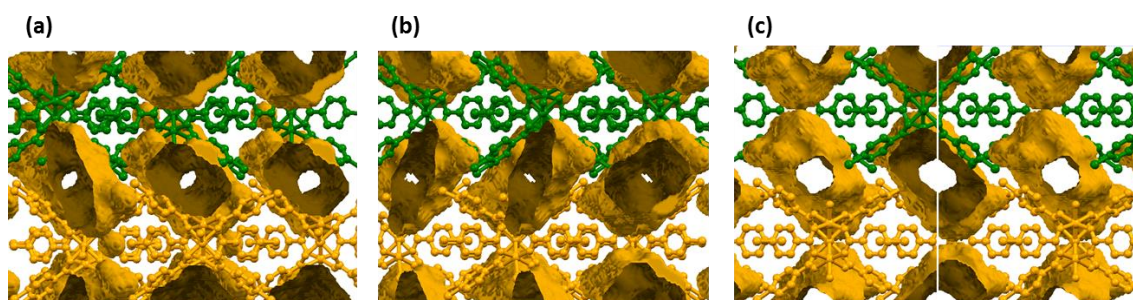


Figure 4.4.4-8. Solvent-accessible void volume for **4.3(Cl)** at (a) 250 K, (b) 273 K and (c) 298 K. Colour scheme consistent with **Figure 4.4.4-4**.

In conclusion, successful desolvation of **4.1(I)** and **4.2(Br)** was achieved by a single-crystal-to-single-crystal process at room temperature. This confirmed that desolvation could be achieved under mild condition consistent with the isothermal TGA results. The desolvation occurred by a phase transformation involving a change in space group from $P2_1/n$ to $P2_1/m$, with a reduction in the unit cell volume and a significant reduction in the solvent-accessible void volume. The desolvation retains the 2D layer with a slight elongation and compression of C–X \cdots C_{ipso} distances, and with the layers compressing in the absence of solvent. Cluster **4.3(Cl)** did not desolvate via a single-crystal-to-single-crystal process, with a loss of crystallinity observed at 298 K. A partially desolvated phase was obtained which showed a retention of 2D halogen-bonded layers and an expansion of the type II halogen-halogen interaction between layers. The PLATON SQUEEZE⁹³ analysis led to the conclusion that complete desolvation had not been achieved. For the structure solution at 298 K it was not possible to resolve the nitrate counterion or the methyl groups of the coordinated methanols, suggesting a significant amount of motion or disorder within the solvent cavity at room temperature.

4.4.5 Powder X-Ray Diffraction (PXRD) Aging Studies

Samples of **4.1(I)**, **4.2(Br)** and **4.3(Cl)** were tested by PXRD firstly to confirm successful desolvation and secondly to determine the stability of the materials when stored in air for long durations. These studies involved filtering the samples under vacuum, washing with methanol, placing them in an oven at 65 °C for 15 min to ensure desolvation, grinding them into a powder before being loaded into a capillary, and collecting a diffraction pattern. Following data collection, the capillaries were stored in sample vials in air at room temperature with data being collected after 6, 12, 31 and 65 days of ageing.

The initial patterns of **4.1(I)** and **4.2(Br)** confirmed desolvation had occurred, both being fitted to $P2_1/m$ phases analogous to those from the single-crystal desolvation studies. Following aging of the samples, both **4.1(I)** and **4.2(Br)** showed a slight reduction in unit cell volume in the first 12 days ($\Delta V = -16.0(6)$ and $-18.6(3)$ Å³, -0.54 and -0.66 % for **4.1(I)** and **4.2(Br)**, respectively) (**Figure 4.4.5-1**). After 1 month **4.2(Br)** maintains the same rate of closure ($\Delta V = -39.1(3)$ Å³, -1.38 %), whereas **4.1(I)** exhibited a larger reduction in the unit cell volume ($\Delta V = -146.9(6)$ Å³, -4.98 %,) (**Figure 4.4.5-1**). After 65 days **4.1(I)** shows minimal additional change ($\Delta V = -157.9(5)$ Å³, -5.35 %) and **4.2(Br)** was fitted to a mixed-phase model with the (new) phase with the smaller unit cell volume exhibiting a similar unit cell volume reduction to **4.1(I)** ($\Delta V = -136.0(3)$ Å³, -4.81 %).

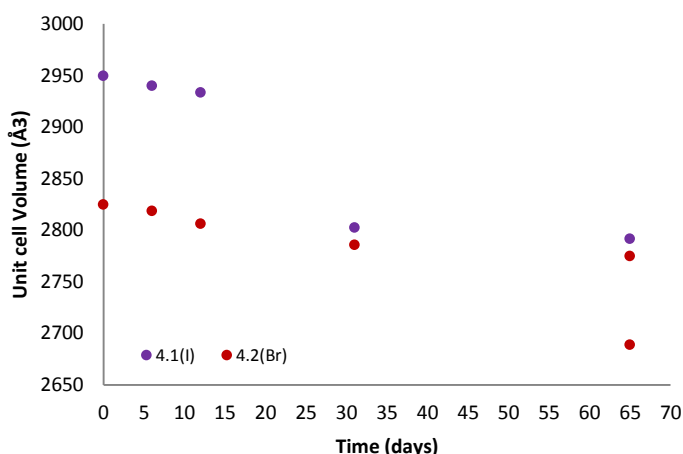


Figure 4.4.5-1. Unit cell volume vs time for samples of **4.1(I)** (purple) and **4.2(Br)** (maroon), where two points at the same time (and colour) represents the presence of two phases.

The initial pattern of **4.3(Cl)** could not be indexed or fitted to a single phase, with attempts to fit the pattern to a mixture of solvated and desolvated phases also proving unsuccessful. Despite this initial unknown phase the sample was retained and patterns were recorded at the same time intervals as **4.1(I)** and **4.2(Br)**. Following storage for 6 days the pattern had changed and could be indexed to a C2 phase, with a minor peak not included in the fit, (**Figure 4.4.5-2**) further ageing led to a pure C2 phase. Attempts were made to identify the packing of this system using Rietveld⁹⁸ refinements, but these were unsuccessful. Storing this sample saw the unit cell volume reduce overtime ($\Delta V = -83.5(6)$, -1.6% , after 65 days) (**Figure 4.4.5-2**).

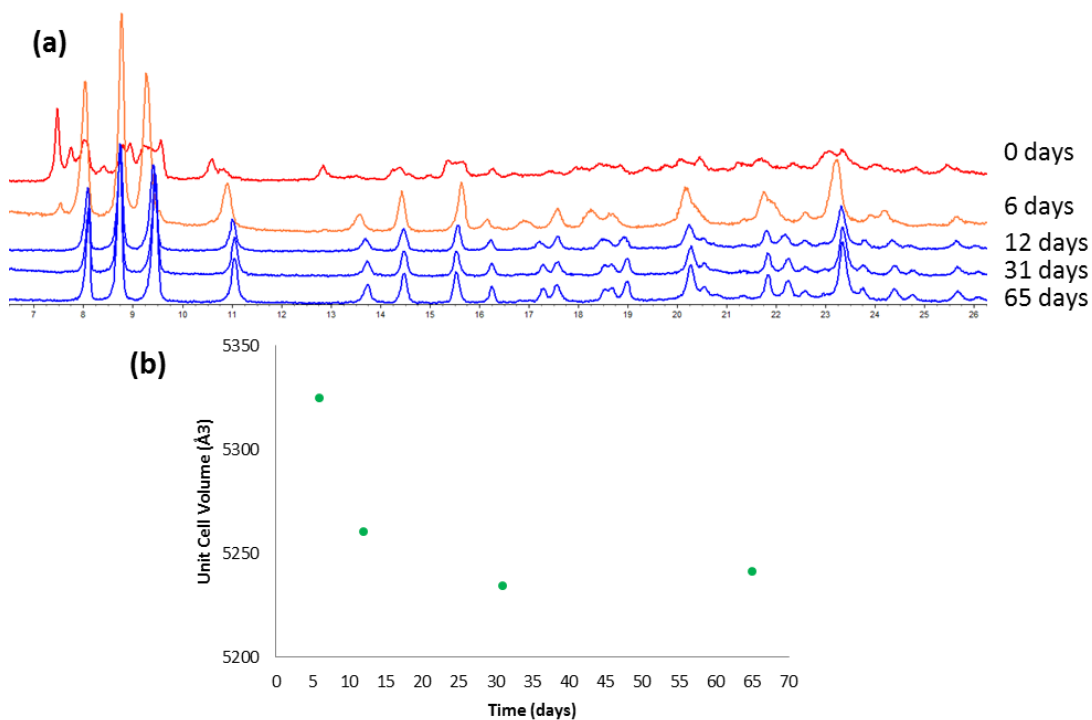


Figure 4.4.5-2. (a) Stacked PXRD patterns of **4.3(Cl)** stored in air for an extended duration and (b) unit cell volume vs time for **4.3(Cl)**.

In conclusion, storing samples of **4.1(I)** and **4.2(Br)** in air at room temperature results in a reduction in the unit cell volume. The reduction in unit cell volume mainly occurs during the first month of storing the sample. Cluster **4.3(Cl)** also shows volume reduction. This is much smaller than for **4.1(I)** and **4.2(Br)** and occurs after a phase transformation from an unknown mixed phase to a C2 phase. Unfortunately the packing present in this new phase could not be determined, so it is uncertain whether the 2D halogen-bonding layers are maintained.

4.4.6 Volumetric and Gravimetric N₂ and CO₂ Adsorption Studies for **4.1(I)**, **4.2(Br)** and **4.3(Cl)**

Samples of **4.1(I)**, **4.2(Br)** and **4.3(Cl)** were tested for volumetric gas adsorption (and desorption) of N₂ and CO₂ at 77 K and 195 K, respectively. This involved filtering crystals of the three clusters, grinding into powders, storing in a vacuum oven at 80 °C (for 16 h) and checking the phase purity using PXRD, before conducting volumetric adsorption analysis by using the degas and analysis procedure outlined in Section 4.3.6. Samples were recovered and powder patterns were recorded before being stored and the volumetric analysis being repeated after 144-175 days of being stored out of solvent.

The volumetric N₂ adsorption studies of the fresh samples (**Figure 4.4.6-1**) all displayed linear uptake with minimal hysteretic behaviour. The minimal uptake observed for **4.2(Br)** suggests a type III nonporous material.⁹⁹ The largest uptake (at p/p^0 0.9) was observed in **4.1(I)** (1.7 N₂ molecules per cluster) with a smaller uptake observed for **4.3(Cl)** (0.5 N₂ molecules per cluster) and the smallest for **4.2(Br)** (0.2 N₂ per molecules cluster). The PXRD patterns recorded following the adsorption studies revealed an expansion in the unit cell volume for **4.1(I)** ($\Delta V = 128.5(8) \text{ \AA}^3$, 4.39 %) and minimal volume changes for **4.2(Br)** and **4.3(Cl)** ($\Delta V = -0.6(3)$ and $-36.6(31) \text{ \AA}^3$, -0.02 and -0.69 %, respectively) in comparison to the patterns measured prior to adsorption measurements, but following heating in the post vacuum oven.

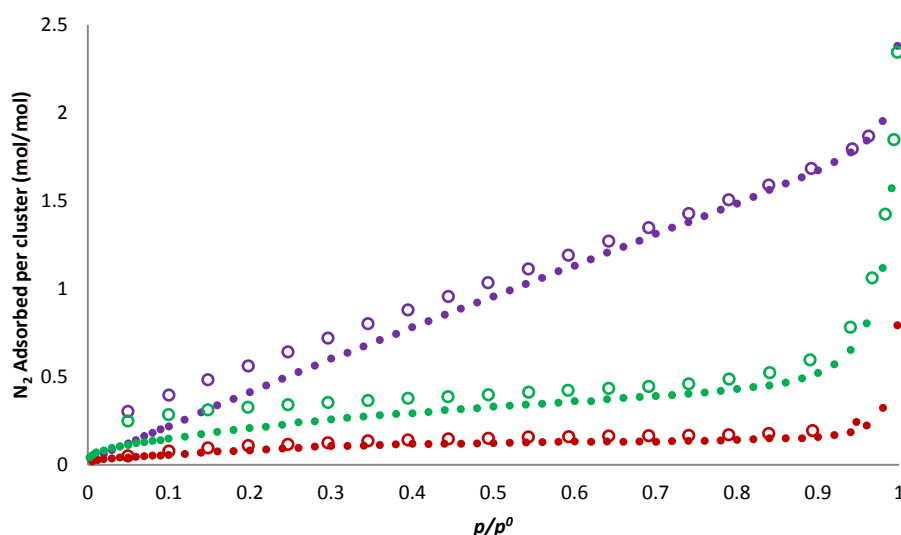


Figure 4.4.6-1. Volumetric N₂ isotherms for fresh samples of **4.1(I)** (purple), **4.2(Br)** (maroon) and **4.3(Cl)** at 77 K (adsorption- solid circles, desorption- open circles).

These samples were then retained and stored for between 144 to 175 days before repeating the volumetric adsorption isotherm measurements. Prior to gas sorption samples were again placed in a vacuum oven at 80 °C for 16 h and the phase-purity was then checked by PXRD. These patterns all displayed unit cell volume reductions in comparison to the sample after original heating in the vacuum oven. Cluster **4.1(I)** had undergone a phase transformation from space group $P2_1/m$ to $P-1$, with a volume reduction ($\Delta V = -138.3(4) \text{ \AA}^3$, -4.8%), comparable in magnitude to the volume reduction observed after 65 days in the PXRD ageing experiment (Section 4.4.5). Cluster **4.2(Br)**, which was aged for 175 days, retained a $P2_1/m$ phase and the unit cell volume reduction ($\Delta V = -649.8(4) \text{ \AA}^3$, -23.2%) was much greater than that observed for the aged powder sample after 65 days (Section 4.4.5). Cluster **4.3(Cl)** retained its $C2$ phase and displayed minor volume reduction ($\Delta V = -63.9(11) \text{ \AA}^3$, -1.20%). Subsequent volumetric N_2 adsorption analysis was consistent with previous measurements for **4.2(Br)** (0.2 N_2 molecules per cluster) and **4.3(Cl)** (0.9 N_2 molecules per cluster). The inclusion of N_2 was dramatically reduced, however, for **4.1(I)** (0.2 N_2 molecules per cluster), and was comparable to the uptake observed for **4.2(Br)** (Figure 4.4.6-2). Following volumetric adsorption analysis samples were recovered and PXRD patterns were recorded. For clusters **4.2(Br)** and **4.3(Cl)** minor unit cell volume reductions were observed in comparison to the samples prior to gas adsorption ($\Delta V = -45.2(6)$ and $-7.2(11) \text{ \AA}^3$, -2.1 and -0.14% for **4.2(Br)** and **4.3(Cl)**, respectively). Cluster **4.1(I)**, despite showing minimal N_2 inclusion, demonstrate significant degradation and peak broadening following the volumetric study.

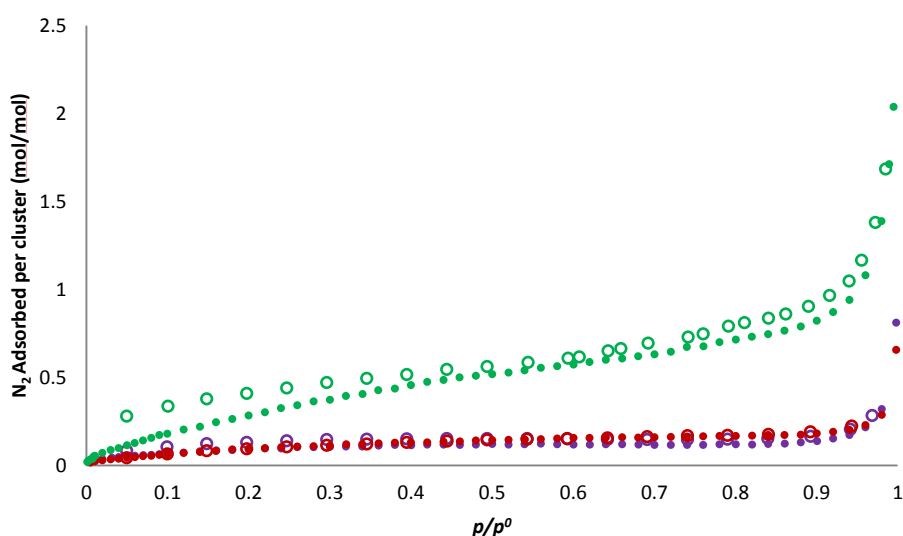


Figure 4.4.6-2. Volumetric N_2 isotherms for aged samples of **4.1(I)** (purple), **4.2(Br)** (maroon) and **4.3(Cl)** at 77 K (adsorption- solid circles, desorption- open circles).

Fresh samples of the three clusters were also tested for CO_2 adsorption (and desorption) at 195 K, following the same procedure outlined above for N_2 adsorption. All three materials display comparable adsorption with type IV(a) isotherms⁹⁹ with a small step (gradient change) in uptake at a p/p^0 of 0.55 and hysteretic behaviour upon desorption (Figure 4.4.6-3). The largest uptake is observed for **4.1(I)** (2.2 CO_2 molecules per cluster) with clusters **4.2(Br)** and **4.3(Cl)** showing similar maximum uptake (1.15 CO_2 molecules per cluster). Following

volumetric adsorption analysis samples were recovered and PXRD patterns were recorded, which demonstrated a minor unit cell volume change in all three cases ($\Delta V = -2.0(5)$, $-13.8(3)$ and $-23.8(8) \text{ \AA}^3$, -0.07 , -0.49 and -0.45% for **4.1(I)**, **4.2(Br)** and **4.3(Cl)**, respectively).

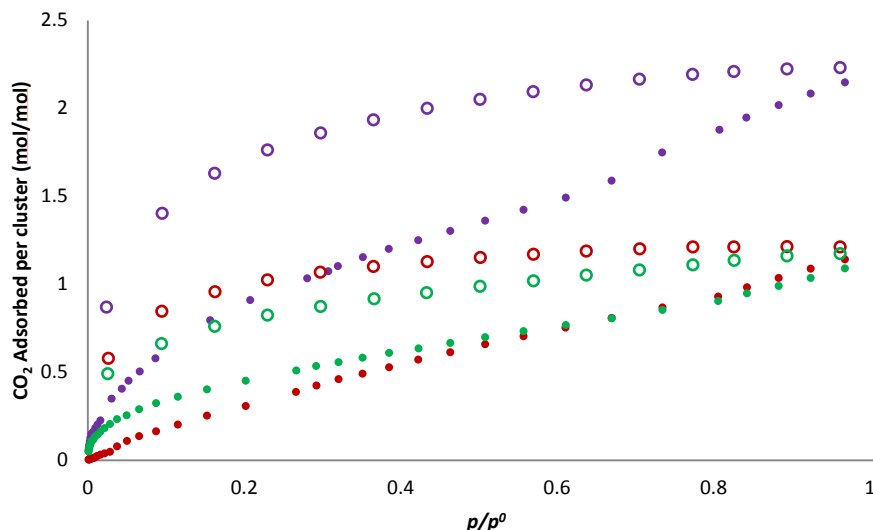


Figure 4.4.6-3. Volumetric CO_2 isotherms for fresh samples of **4.1(I)** (purple), **4.2(Br)** (maroon) and **4.3(Cl)** at 195 K (adsorption- solid circles, desorption- open circles).

The three samples were retained for between 144 to 171 days before volumetric CO_2 adsorption analysis was repeated, following the same procedure outlined before. Prior to volumetric analysis, PXRD patterns were recorded which indicated similar unit cell volume reductions ($\Delta V = -137.6(4)$, $-646.0(4)$ and $-61.9(9) \text{ \AA}^3$, -4.7 , -23.1 and -1.15% for **4.1(I)**, **4.2(Br)** and **4.3(Cl)**, respectively) and phase transformations (for **4.1(I)**) to those observed for the aged samples studied by N_2 adsorption. The volumetric analysis shows similar adsorption isotherms to the fresh samples, but the quantity of CO_2 included and trend was inconsistent (**Figure 4.4.6-4**). All three samples have a larger inclusion of CO_2 than previously observed, with similar uptakes for **4.1(I)** and **4.3(Cl)** and less CO_2 included in **4.2(Br)**. The increase in uptake of CO_2 for all three clusters seems counter-intuitive considering aging the samples results in a reduction in the unit cell volume, suggesting a more densely packed material. Samples were recovered following the second volumetric CO_2 adsorption analysis and PXRD patterns were recorded. Cluster **4.1(I)** showed analogous peak broadening and degradation to that observed in the N_2 adsorption study, **4.2(Br)** demonstrated a minor volume reduction ($\Delta V = -38.0(7) \text{ \AA}^3$, -1.76%) and **4.3(Cl)** demonstrated a minor volume expansion ($\Delta V = 29.7(13) \text{ \AA}^3$, 0.56%).

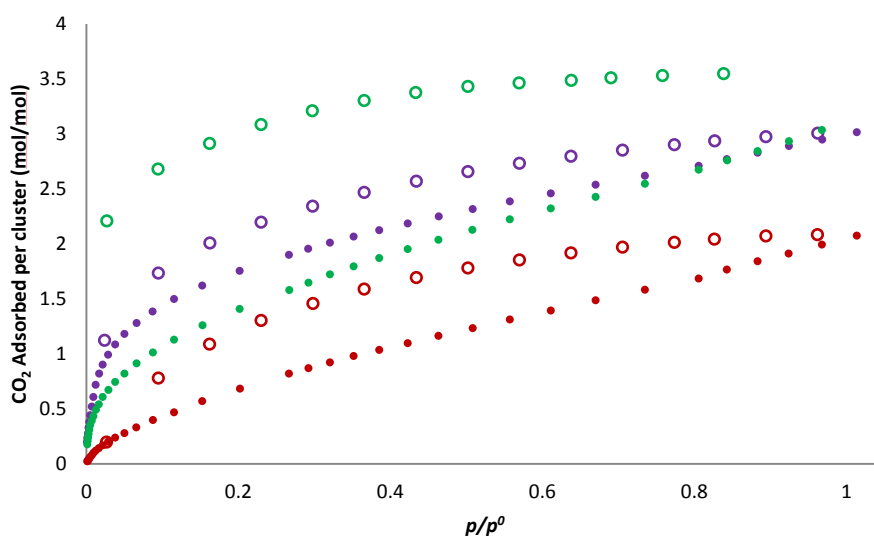


Figure 4.4.6-4. Volumetric CO₂ isotherms for aged samples of **4.1(I)** (purple), **4.2(Br)** (maroon) and **4.3(Cl)** at 195 K (adsorption- solid circles, desorption- open circles).

Samples of the three clusters were also analysed for gravimetric gas adsorption of CO₂, procedure outlined in Section 4.3.7, by collaborators at University of Strathclyde. Samples were exposed to increasing (and decreasing) pressures of CO₂ at room temperature. This analysis (**Figure 4.4.6-5**) showed similar uptake profiles to the volumetric adsorption studies, but a different trend in the relative uptakes. In the case of the gravimetric studies the largest uptake was observed in for **4.3(Cl)** (0.9 CO₂ molecules per cluster at p/p^0 0.35, 19.5 bar CO₂) with lower uptake for **4.2(Br)** (0.6 CO₂ molecules per cluster) and the lowest uptake for **4.1(I)** (0.4 CO₂ molecules per cluster). This trend matches neither the fresh or aged volumetric adsorption studies, suggesting that the uptake properties of these materials are affected by temperature. Unfortunately samples were not analysed for phase-purity by PXRD during or directly after gravimetric analysis so it is unclear what phase the samples were in when they were analysed for uptake. Considering that the samples were sent to collaborators in the absence of the mother liquor and the experiments were not conducted immediately, it is likely that the samples will have at least partially closed. The samples were recovered and returned 2 years later with powder patterns confirming closed-phase forms. The samples of **4.1(I)** and **4.3(Cl)** had unit cell parameters which were similar to the unit cell parameters of the aged volumetric adsorption samples. Cluster **4.2(Br)** had unit cell parameters comparable to those found after the desolvation ageing studies, but had a much greater unit cell volume than the sample analysed after volumetric CO₂ adsorption. The adsorption could also be affected by the temperature it was recorded at, but further work would be required to confirm this.

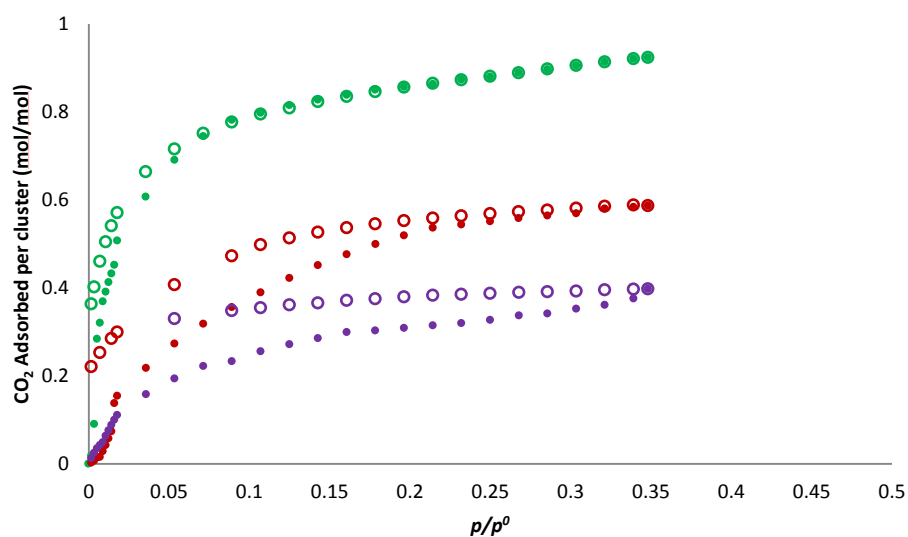


Figure 4.4.6-5. Gravimetric CO₂ isotherms for samples of **4.1(I)** (purple), **4.2(Br)** (maroon) and **4.3(Cl)** at 298 K (adsorption- solid circles, desorption- open circles).

In conclusion, the three clusters (**4.1(I)**, **4.2(Br)** and **4.3(Cl)**) were tested for gaseous guest inclusion of N₂ and CO₂. These experiments were carried out on both freshly prepared samples and samples that had been stored in air in order to quantify the effect of a reducing unit cell volume, observed in the aging studies, has on guest inclusion. The volumetric N₂ studies only demonstrated change for **4.1(I)** with a reduction in uptake (from 1.7 to 0.2 N₂ per cluster) with the other two clusters (**4.2(Br)** and **4.3(Cl)**) being unaffected by the reduction in unit cell volume. The CO₂ studies proved more complex with samples stored in air for between 144 to 175 days demonstrating a larger uptake than the freshly prepared samples. The trends of maximum uptake relative to halogen are also inconsistent with maximum uptake in the volumetric studies being the iodo functionalised cluster which has the lowest uptake in the gravimetric data. It is unclear what the reason for this discrepancy is.

4.4.7 *In situ* Powder X-Ray Diffraction and Single-Crystal Diffraction Studies During CO₂ Adsorption/Desorption

4.4.7.1 Overview

In order to quantify how CO₂ is included within these clusters a series of *in situ* diffraction experiments were carried on both powder and single-crystal samples using the gas-cell set-ups on the I11⁸⁶ and I19^{77,79} beamlines at Diamond Light Source.

4.4.7.2 Studies of 4.1(I)

Both single-crystal and powder samples of **4.1(I)** were tested for CO₂ inclusion at room temperature. The fresh powder sample (**Table 4.3.8-1**, Appendix 4.8.3), which was placed in an oven (65 °C) for 15 min prior to *in situ* study, had initial unit cell dimensions consistent with the fresh sample recorded prior to volumetric CO₂ adsorption. Upon exposure to CO₂ pressure the volume increased with increasing pressure (**Figure 4.4.7-1**) with a maximum expansion of 1.14 % ($\Delta V = 33.55(6) \text{ \AA}^3$) at 20 bar CO₂ (p/p^0 0.36). A second powder sample which was aged for *ca.*

1 month prior to the *in situ* study (Table 4.3.8-3, Appendix 4.8.3) was Pawley fitted⁸¹ with an initial unit cell volume *ca.* 10 Å³ smaller than the aged sample prior to volumetric CO₂ adsorption, but showed no expansion with increased CO₂ pressure (Figure 4.4.7-1). The *in situ* single crystal data recorded for 4.1(I) (Table 4.3.9-1, Appendix 4.8.4) also demonstrated unit cell volume expansion with a 3.00 % volume expansion ($\Delta V = 85(3) \text{ \AA}^3$) up to 20 bar (p/p^0 0.36) and further expansion at 40 bar ($\Delta V = 94(6) \text{ \AA}^3$, 3.31 %, p/p^0 0.7) (Figure 4.4.7-1). The initial unit cell volume, however, is *ca.* 100 Å³ smaller than the fresh powder sample and it is unclear whether this is due to sample preparation, water inclusion or vacuum having a greater effect on single-crystals than powdered samples. The PXRD study of the fresh sample showed that it returned to the original unit cell volume when the pressure was reduced back to vacuum ($\Delta(V_{vac(D)} - V_{vac}) = -5.85(8) \text{ \AA}^3$, -0.20 %).

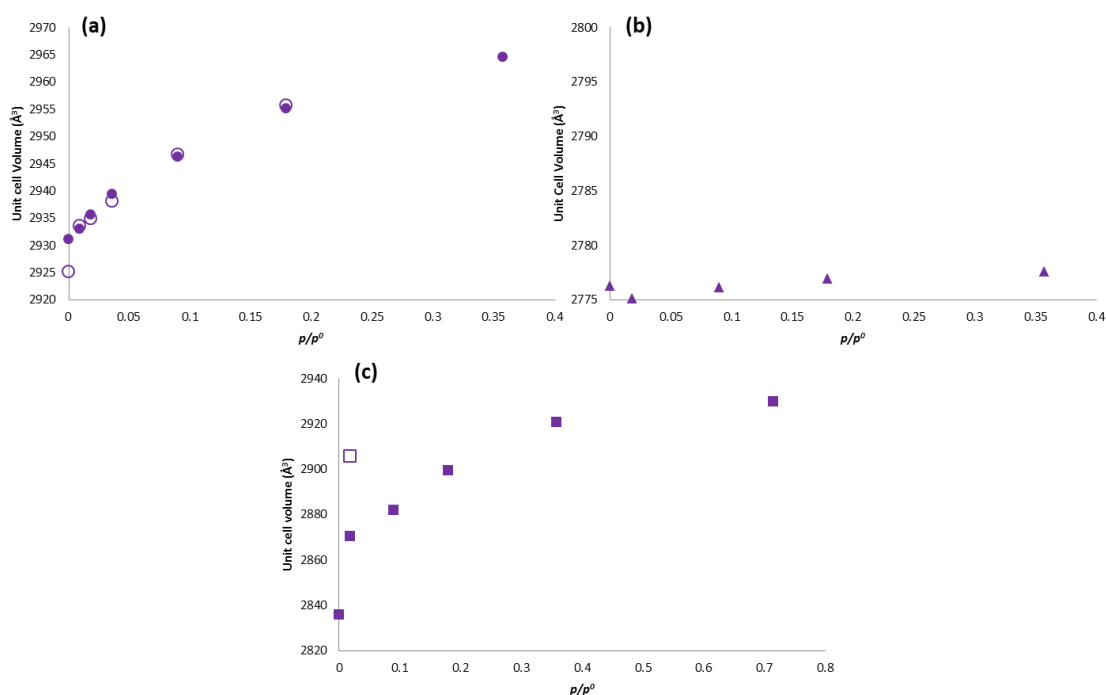


Figure 4.4.7-1. Unit cell volume vs p/p^0 for *in situ* PXRD (a = fresh sample; b = aged sample) and (c) single-crystal diffraction studies of 4.1(I) exposed to increasing (filled shapes) and decreasing (empty shapes) pressures of CO₂ at room temperature.

The unit cell volume expansion for both PXRD and single-crystal diffraction studies can be attributed to changes in the *a*- and *b*-axes (Figure 4.4.7-2) with minimal change in the *c*-axis. The PXRD study also exhibits minimal change in the β angle (from 110.1936(7) ° to 110.8365(5) °), whereas the single-crystal diffraction study exhibits an expansion in the β angle (107.21(2) ° vacuum to 110.52(7) ° at 20 bar). As discussed in Section 4.4.2 the 2D halogen-bonding layers propagate in the *a*- and *c*-axes. The expansion in unit cell dimensions therefore suggest moving apart of the 2D halogen-bonding layers (expansion in the *b*-axis) as well as either a shifting of the 2D halogen-layers in one dimension or a disruption of the halogen-bonding layers (expansion in the *a*-axis) (Figure 4.4.7-2).

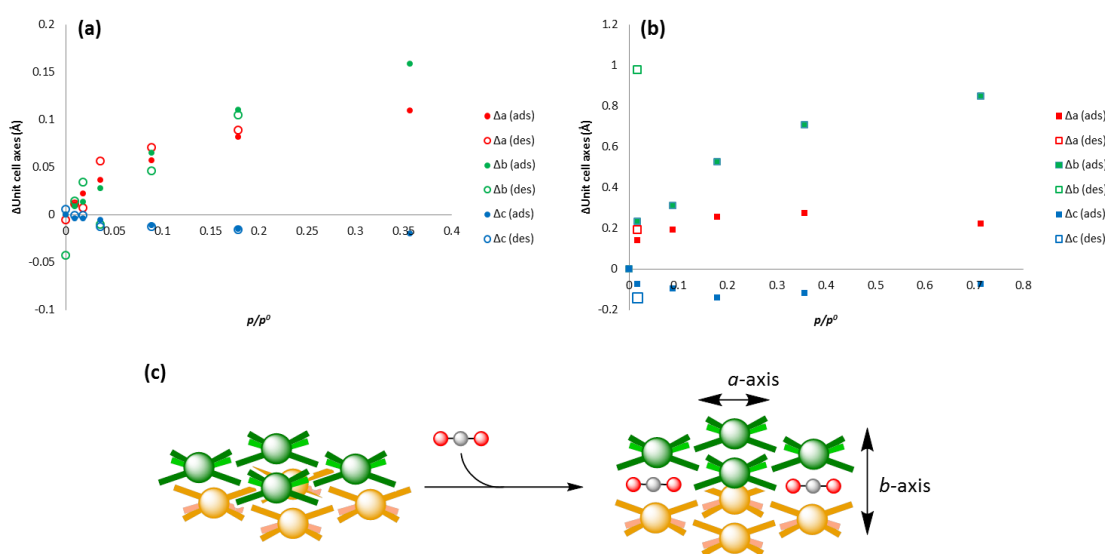


Figure 4.4.7-2. Change in unit cell axes vs p/p^0 for in situ (a) PXRD and (b) single-crystal diffraction studies of **4.1(I)** at 298 K. Increasing (filled shapes) and decreasing (empty shapes) pressures of CO_2 . (c) Schematic of the movement of clusters upon volume expansion.

4.4.7-3 Studies of 4.2(Br)

Both PXRD (Table 4.3.8-2, Appendix 4.8.3) and single-crystal diffraction (Table 4.3.9-2, Appendix 4.8.4) studies of fresh samples of **4.2(Br)** were performed. As with **4.1(I)**, increasing pressure of CO_2 resulted in a unit cell volume expansion (Figure 4.4.7-3). The initial vacuum measurement of the powder study was consistent with the unit cell dimensions of the fresh sample directly prior to volumetric CO_2 adsorption analysis. Heating the sample, under vacuum, in the capillary reduced the unit cell volume by *ca.* 10 \AA^3 . Exposure to increased pressure of CO_2 resulted in a unit cell expansion of 2.17 % at 20 bar (p/p^0 0.36) CO_2 ($\Delta V = 60.5(2) \text{ \AA}^3$) and further expansion at 40 bar (p/p^0 0.7) of CO_2 ($\Delta V = 68.7(2) \text{ \AA}^3$, 2.47 %). Unfortunately for the single-crystal study a vacuum measurement was not recorded, as the sample was screened under air, before being evacuated and dosed with 1 bar CO_2 prior to the next data set being recorded. Comparison of the atmosphere and 1 bar CO_2 unit cell volumes reveals a 1.49 % reduction ($\Delta V = -42(2) \text{ \AA}^3$), suggesting significant reduction as a result of evacuation. Increased pressures of CO_2 resulted the unit cell volume expansion, returning to comparable unit cell dimensions to the original atmospheric pressure unit cell dimensions at 10 bar (p/p^0 0.18) and further expanded at 20 bar (p/p^0 0.36) ($\Delta V = -96.6(32) \text{ \AA}^3$, -3.45 %, in comparison to the measurement at 1 bar CO_2).

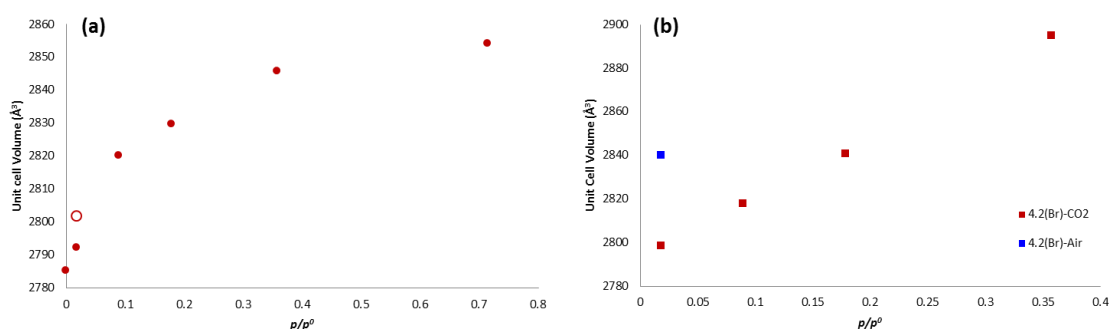


Figure 4.4.7-3. Unit cell volume vs p/p^0 for in situ (a) PXRD and (b) single crystal diffraction studies of **4.2(Br)** at 298 K. Increasing (filled shapes) and decreasing (empty shapes) pressures of CO_2 .

The unit cell volume expansion can be attributed expansions in the a - and b -axes with minimal change in the c -axis (**Figure 4.4.7-4**). Both powder and single crystal studies also exhibit a slight expansion in the β angle (from $111.043(2)^\circ$ to $113.065(2)^\circ$ and $109.79(3)^\circ$ to $111.31(7)^\circ$ for the PXRD and single-crystal diffraction studies, respectively). As discussed for **4.1(I)**, the change in the b -axis suggests a moving apart of the 2D halogen-bonding layers (**Figure 4.4.7-4**). The expansion in the a -axis also suggests shifting of the 2D halogen-bonding layers or an expansion in the layers in one direction.

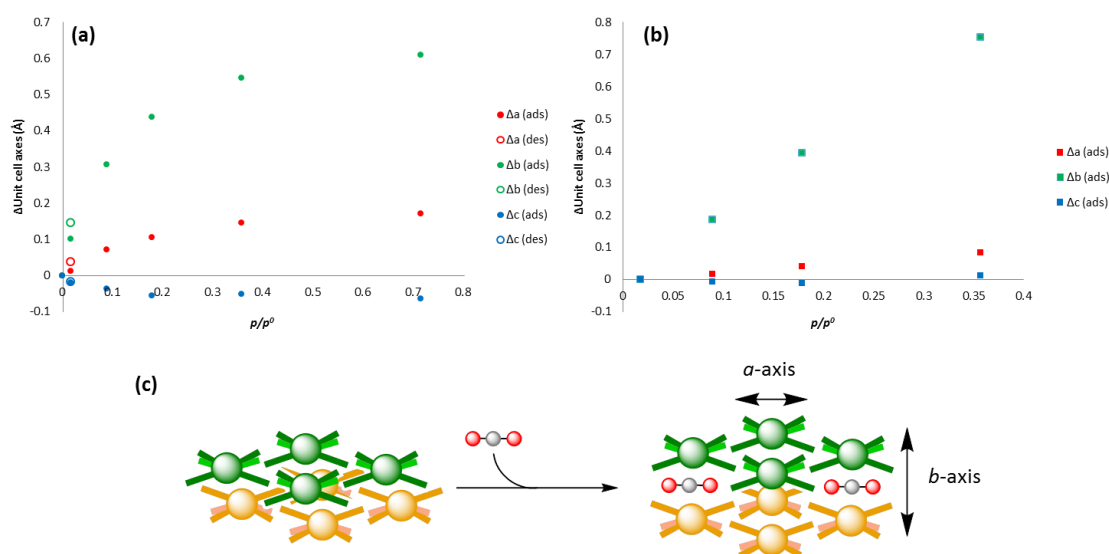


Figure 4.4.7-4. Change in unit cell axes vs p/p^0 for in situ (a) PXRD and (b) single diffraction studies of **4.2(Br)** at 298 K. Increasing (filled shapes) and decreasing (empty shapes) pressures of CO_2 . (c) Schematic of the movement of clusters upon volume expansion.

4.4.7-4 Study of **4.3(Cl)**

Desolvation attempts for single crystals of **4.3(Cl)** (Section 4.4.4) revealed that the sample loses single-crystal crystallinity at room temperature. This meant that recording an *in situ* single-crystal diffraction study was not possible. The *ex situ* PXRD desolvation and aging studies also revealed that samples which were activated by storing in the oven at 65°C 15 min consisted of an unknown mixture of phases. Therefore analysis of a fresh sample while under increasing pressures of CO_2 was not attempted. In light of these two observations focus was placed on recording data on an aged sample of **4.3(Cl)**. A sample was therefore filtered and washed with methanol, ground and stored in an oven at 65°C for 15 min before being stored in a sample vial *ca.* 1 month. The initial vacuum measurement (**Table 4.3.8-4**, Appendix 4.8.3) revealed an aged phase which had a unit cell volume *ca.* 20 \AA^3 smaller than the aged sample used for volumetric CO_2 adsorption analysis. The initial pressure steps (1 and 5 bar, p/p^0 0.02 and 0.08, respectively) showed minimal change relative to the vacuum measurement (**Figure 4.4.7-5**). Exposing the sample to 10 bar CO_2 (p/p^0 0.18) resulted in a 0.44 % unit cell volume expansion ($\Delta V = 22.9(7) \text{ \AA}^3$) with the unit cell volume expanding further when dosed to 20 bar CO_2 (p/p^0 0.36) ($\Delta V = 29.6(7) \text{ \AA}^3$, 0.56 %). This volume expansion can be attributed to expansions in the b - and c -axes ($\Delta b = 0.0325(8) \text{ \AA}$, 0.31 %, $\Delta c = 0.0303(21) \text{ \AA}$, 0.12 %) with

minimal change in the a -axis ($\Delta a = -0.0084(15)$ Å, -0.037%) and β angle (from $117.814(3)^\circ$ to $117.628(3)^\circ$). Attempts were made to use Rietveld refinement⁹⁸ to identify the packing of clusters in this $C2$ phase, these attempts were ultimately unsuccessful. Therefore, without detailed knowledge of the packing of this phase it is unclear how expansion in the b - and c -axes can be described in the context of the stellated clusters or whether the 2D halogen-bonding layers are retained in this unknown phase.

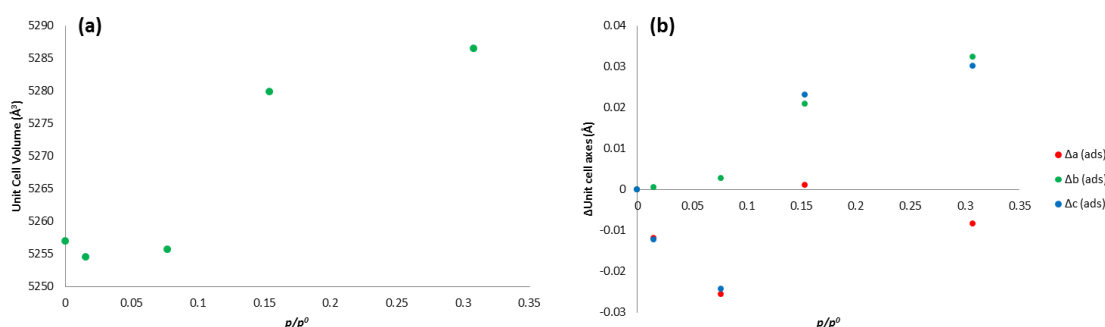


Figure 4.4.7-5. (a) Unit cell volume vs p/p^0 for **4.3(Cl)** at 298 K. (b) Change in unit cell axes vs p/p^0 for **4.3(Cl)** at 298 K.

4.4.7-5 Structural Characterisation

The single-crystal heating study of **4.3(Cl)** (Section 4.4.4) revealed that for the room temperature data collection the central trinuclear cluster could be modelled, but exact positions of the methyl groups of the coordinated methanol and the nitrate counter-ion could not be confidently identified. For the *in situ* single-crystal diffraction studies of **4.1(I)** and **4.2(Br)** it was also not possible to confidently model the counter-ion or the methyl groups of the coordinated methanols. As the pressure was increased the crystal quality diminished, meaning that structure solutions could only be obtained for the first three pressure points of each study. Diminishing crystal quality and structure solutions being obtained for the first three pressure point (for both **4.1(I)** and **4.2(Br)**) meant that changes detected in intermolecular interactions were minimal (Table 4.4.7-1). The same 2D halogen-bonded layers were observed, with layers connected by the same cooperative $C-X\cdots C_{\text{ipso}}$ and type I halogen-halogen interaction to those identified in the desolvated forms (Section 4.4.4).

Table 4.4.7-1. Intermolecular distances (Å) from *in situ* single-crystal diffraction studies of **4.1(I)** and **4.2(Br)**

4.1(I)					
Pressure (bar)	2D-Halogen-Bonding Layers		Inter-layer interactions		
	$C-X\cdots C_{\text{ipso}}$	$C-X\cdots C_{\text{ipso}}$	$C-X\cdots C_{\text{ipso}}$	$bz_{(\text{cent})}\cdots bz_{(\text{cent})}$	$C-X\cdots X$
0	3.39(3)	4.03(2)	4.06(2)	3.84(2)	3.98(1)
1	3.42(3)	3.95(2)	3.96(2)	3.81(2)	3.84(1)
5	3.39(3)	3.94(2)	3.88(2)	3.81(2)	3.75(1)
4.2(Br)					
1	3.41(3)	3.77(2)	3.83(2)	3.89(1)	3.64(1)
5	3.40(3)	3.69(1)	3.83(1)	3.94(1)	3.62(1)
10	3.43(5)	3.71(3)	3.90(3)	4.08(3)	3.64(2)

The solvent-accessible voids and the electron count of these models, determined by PLATON,^{93,100} revealed an increase in the solvent-accessible void with increasing pressure (**Figure 4.4.7-7**). This void space increase was accompanied by an increase in electron count (106 electrons to 146 electrons from vacuum to 5 bar) for **4.1(I)**, but a decrease in electron count for **4.2(Br)** (**Figure 4.4.7-7**). The solvent-accessible volume is consistent with those previously observed in the desolvated forms (Section 4.4.4), with discrete cavities between layers. However, with increased CO₂ pressure, rather than seeing the cavities transform into channels running between the halogen-bonding layers, the cavities appear to connect and pass through the halogen-bonding layers (**Figure 4.4.7-7**). This may explain the change observed in the *a*-axis with increase CO₂ pressure causing a shifting apart of halogen-bonding layers as well as the layers themselves expanding laterally to generate channels running through the halogen-bonding layers. Modelling of the methyl groups may result in these channels remaining as discrete cavities which could be accessed through the motions of the methyl groups.

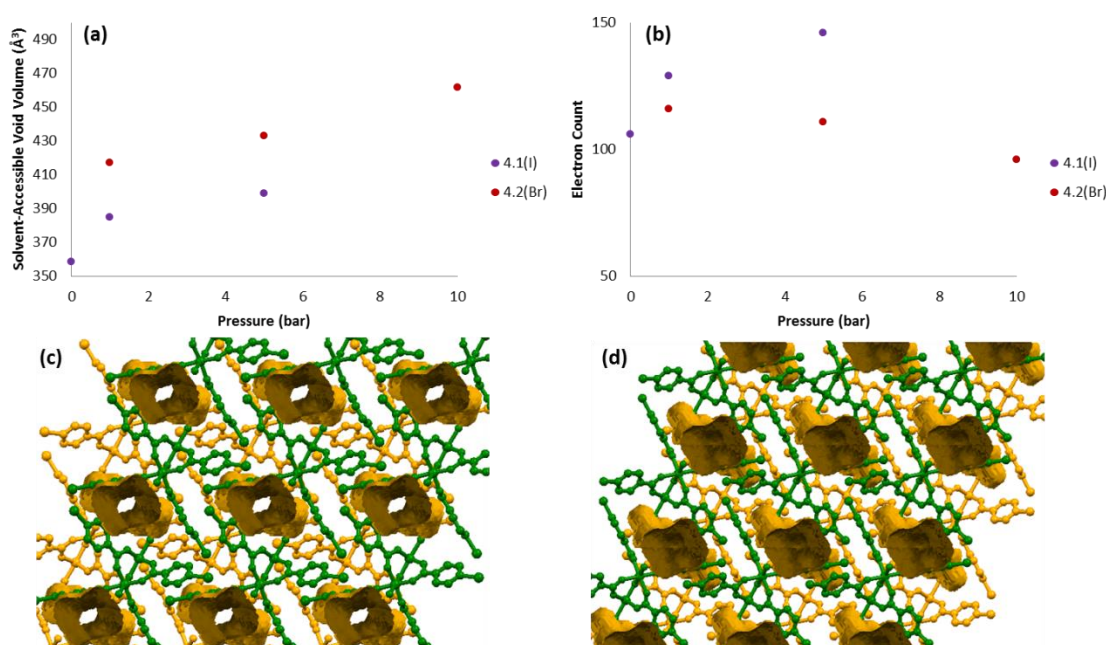


Figure 4.4.7-7. (a) Solvent-accessible void volume and (b) electron count vs pressure for *in situ* diffraction studies of **4.1(I)** and **4.2(Br)** determined using PLATON.^{92,93} Void spaces visualised in Mercury⁹⁵ showing the channels running through (c) **4.1(I)** and (d) **4.2(Br)** at 5 and 10 bar CO₂ pressure, respectively.

Attempts were made to obtain structural information from the *in situ* PXRD data, using Rietveld⁹⁸ fitting, was unsuccessful. Attempts were also made to obtain structural information of the aged samples also without success.

4.4.7-6 Conclusion

In conclusion, it was demonstrated that exposure to increased CO₂ pressures for **4.1(I)**, **4.2(Br)** and **4.3(Cl)** resulted in unit cell volume expansions. This expansion, in the case of **4.1(I)** and **4.2(Br)**, was attributed to a moving apart of the 2D halogen-bonded layers (expansion in the *b*-axis) as well as an expansion in the *a*-axis suggesting a lateral expansion within the layers in one direction. The change in the *a*-axis may also lead to an opening of channels running

through the halogen-bonding layer, suggested from the void space analysis. However, poor data quality and inability to fit the PXRD data by Rietveld methods meant that these changes could not be correlated with changes in intermolecular interactions. An aged sample of **4.1(I)** was also analysed while increased CO₂ pressure was applied; this showed no change in unit cell volume. Considering the unit cell volume decreases upon storage for long duration, suggesting a more dense material, it is unclear how gas would enter the material to account for the uptake observed in both the gravimetric and volumetric data. More detailed structural information is needed for this closed phase to establish how accessible the internal cavities may be.

4.5 Conclusion

This work has demonstrated that porous molecular crystals can be prepared by use of metal clusters analogous to the SBUs used within MOF materials. It was shown that a trinuclear oxo-centred cluster, [Cr₃O(4-Xbz)₆(MeOH)₃][NO₃] (X = I, Br and Cl), could be produced in moderate yields. The three clusters are isostructural, all crystallising as solvates with the solvent present being held in channels between layers of 2D halogen-bonded networks. The 2D halogen-bonding layers are formed by two of the peripheral halogens interacting with aromatic rings of neighbouring clusters. These layers are in turn connected by the four additional halogens (per cluster) protruding from the layers.

TGA measurements and single-crystal desolvation studies revealed that the solvent present could be removed under mild conditions (at room temperature) for **4.1(I)** and **4.2(Br)** with **4.3(Cl)** losing single-crystal crystallinity at room temperature. Desolvation of **4.1(I)** and **4.2(Br)** resulted in a loss of the solvent channels present in the solvent-included phases and the halogen-bonded layers being compressed. PXRD studies of samples of the three clusters revealed that storing the samples in air over a long duration (*ca.* 65 days) resulted in further reduction in unit cell volume as well as, for **4.1(I)** and **4.3(Cl)**, phase transformations to unknown phases. The reduction, for **4.1(I)** and **4.2(Br)**, mainly occurs in the *a*- and *b*-axes suggesting further compression of halogen-bonded layers as well as a lateral compression of the halogen-bonded layers in one dimension. However, detailed structural information could not be obtained for these studies, so the exact change in the packing that occurs remains unclear.

These materials were also tested for volumetric (to p/p^0 1.0 for N₂ and CO₂ at 77 K and 195 K, respectively) and gravimetric (to p/p^0 0.36 for CO₂ at 298 K) gas adsorption. The gravimetric study revealed a clear trend with **4.3(Cl)** including the largest quantity of CO₂ (0.9 CO₂ molecules per cluster) with **4.1(I)** including the smallest quantity of CO₂ (0.4 CO₂ molecules per cluster). The volumetric analysis on the other hand exhibited the largest inclusion (2.2 CO₂ molecules per cluster) for **4.1(I)** with **4.2(Br)** and **4.3(Cl)** showing smaller, but comparable, maximum uptakes (1.15 CO₂ molecules per cluster). It was uncertain whether the samples sent for gravimetric analysis had changed phase before being analysed, so aged samples of the three materials were analysed for volumetric uptake of CO₂. This analysis revealed all three materials included more CO₂ than the fresh samples, but the trend did not match the

gravimetric results, with **4.1(I)** and **4.3(Cl)** exhibiting comparable uptake and **4.2(Br)** including less CO₂. The volumetric N₂ adsorption revealed only a change in uptake for **4.1(I)** with the aged sample including less N₂ than the fresh sample.

Following these gas sorption studies *in situ* diffraction studies (both single-crystal and PXRD) were performed on samples while increasing pressure of CO₂ was applied. These studies revealed unit cell volume expansions when samples of **4.1(I)** (single-crystal and powder), **4.2(Br)** (single-crystal and powder) and **4.3(Cl)** (powder) were exposed to pressures of CO₂. In the case of **4.1(I)** and **4.2(Br)** this unit cell volume expansion was attributed to a moving apart of 2D halogen-bonded layers as well as a lateral expansion of the halogen-bonded layer in one direction, this potentially being due to an alignment of the clusters to form channels running through the halogen-bonded layers. For **4.3(Cl)** the unit cell expansion was due to expansion in the *b*- and *c*-axes, but without structural information for this unknown phase it is unclear how this relates to the locations and interactions of the clusters. An aged sample of **4.1(I)** was also tested for CO₂ inclusion, this revealed negligible unit cell changes upon increased CO₂ pressure. This would suggest the aged sample of **4.1(I)** has accessible channels with no structural changes required to include CO₂.

This work has therefore demonstrated that packing inefficiency of inorganic molecular clusters can be exploited to form porous molecular materials. However, the gas studies have demonstrated that, for these systems, the materials in the absence of solvent are not stable and undergo further change when stored in air. This instability has been demonstrated through a series of gas sorption studies which display different uptake properties. Therefore the true potential of these materials is unclear and further work is required to understand the packing of the aged samples and its effect on uptake potential.

4.6 Future Work

Despite this work proving that porosity can be achieved with the application of stellated inorganic clusters there is still more work required to understand the packing of materials that have been stored in air for a long duration. Further work could, however, focus on exploring other functional groups. Firstly synthesis of [Cr₃O(4-Fbz)₆(MeOH)₆][NO₃] (**4.4(F)**) could be attempted to see the effect of a smaller halogen would have on the packing of these systems. The absence of halogen-bond capabilities would probably result in the absence of the regular 2D halogen-bonded layers present in the three reported clusters (**4.1(I)**, **4.2(Br)** and **4.3(Cl)**). Alternatively other functionalised benzoates could be explored to see the effect on packing and subsequent gas storage capabilities. This work could also emulate the work by Chun et al.⁶⁰ to see whether the position of the substituent affects the gas storage capabilities.

Further development of these materials could follow the same approach employed by Dalgarno and coworkers²³ to the calixarene systems. Their work focused on upper- and lower-rim functionalisation of calix[4]arene and the use of co-formers to direct the packing. The trinuclear oxo-centred clusters also feature an upper and lower rim (**Figure 4.6-1**) which, in this case, was functionalised with halogens. This unit could therefore be used with a co-former to try and direct the assembly of these clusters. Alternatively attempts could be made to design

trinuclear clusters with different upper and lower rim functionality. This strategy could also be a method of constructing systems analogous to supramolecular organic frameworks.⁴⁰

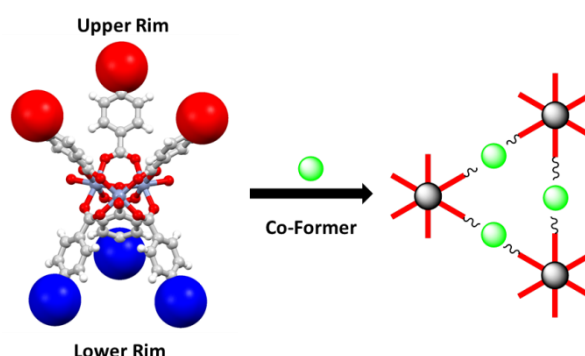


Figure 4.6-1. Upper and lower rim functionalisation and incorporation of a co-former to produce self-assembled networks.

This work focused on clusters taking inspiration from MOF SBUs, therefore other SBUs could be selected with a higher level of stellation to further exploit packing inefficiency. For example, the tetranuclear ($[\text{Zn}_4\text{O}(\text{L})_6]$) or hexanuclear ($[\text{Zr}_6\text{O}_4(\text{OH})_4(\text{L})_{12}]$) (**Figure 4.6-2**) are commonly used within MOF research, which could form interesting stellated analogues to the trinuclear clusters reported in this work. Alternatively, as stated earlier, the field of porous organic molecular crystals has, in part, been developed through mining of the CSD⁴⁴ and computation to find suitable candidates.^{45,46} The same approach could be employed to identify potential inorganic candidates, of course this would require the removal of all pre-existing MOF and coordination polymer from the database¹⁰¹ prior to searching for candidates.

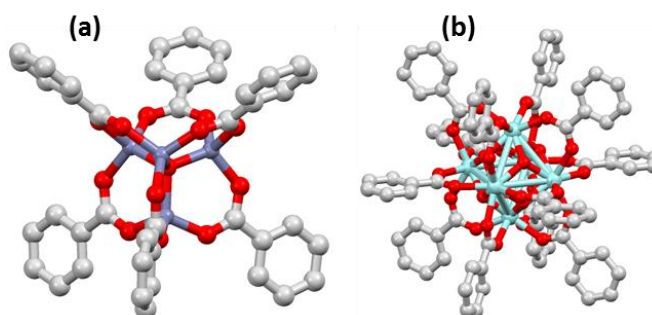


Figure 4.6-2. Examples of other commonly used SBUs, (a) tetranuclear cluster and (b) hexanuclear cluster, that could be exploited for inefficient packing.

4.7 References

- 1 J. A. Ripmeester, G. D. Enright, C. I. Ratcliffe, K. A. Udachin and I. L. Moudrakovski, *Chem. Commun.*, 2006, 4986–4996.
- 2 S. J. Dalgarno, P. K. Thallapally, L. J. Barbour and J. L. Atwood, *Chem. Soc. Rev.*, 2007, **36**, 236–245.

- 3 J. L. Atwood, L. J. Barbour and A. Jerga, *Science*, 2002, **296**, 2367–2369.
- 4 J. E. Adams, J. R. Cox, A. J. Christiano and C. A. Deakayne, *J. Phys. Chem. A*, 2008, **112**, 6829–6839.
- 5 N. S. Venkataramanan, R. Sahara, H. Mizuseki and Y. Kawazoe, *Comput. Mater. Sci.*, 2010, **49**, 1–5.
- 6 N. Hontama, Y. Inokuchi, T. Ebata, C. Dedonder-Lardeux, C. Jouvét and S. S. Xantheas, *J. Phys. Chem. A*, 2010, **114**, 2967–2972.
- 7 S. Kaneko, Y. Inokuchi, T. Ebata, E. Aprà and S. S. Xantheas, *J. Phys. Chem. A*, 2011, **115**, 10846–10853.
- 8 J. L. Atwood, L. J. Barbour, A. Jerga and B. L. Schottel, *Science*, 2002, **298**, 1000–1002.
- 9 G. D. Enright, K. A. Udachin, I. L. Moudrakovski and J. A. Ripmeester, *J. Am. Chem. Soc.*, 2003, **125**, 9896–9897.
- 10 P. K. Thallapally, T. B. Wirsig, L. J. Barbour and J. L. Atwood, *Chem. Commun.*, 2005, 4420–4422.
- 11 J. L. Atwood, L. J. Barbour, P. K. Thallapally and T. B. Wirsig, *Chem. Commun.*, 2005, 51–53.
- 12 P. K. Thallapally, L. Dobrzańska, T. R. Gingrich, T. B. Wirsig, L. J. Barbour and J. L. Atwood, *Angew. Chem. Int. Ed.*, 2006, **45**, 6506–6509.
- 13 J. L. Daschbach, P. K. Thallapally, J. L. Atwood, B. P. McGrail and L. X. Dang, *J. Chem. Phys.*, 2007, **127**, (104703) 1-4.
- 14 P. K. Thallapally, B. Peter McGrail, S. J. Dalgarno, H. T. Schaef, J. Tian and J. L. Atwood, *Nat. Mater.*, 2008, **7**, 146–150.
- 15 P. K. Thallapally, P. B. McGrail, S. J. Dalgarno and J. L. Atwood, *Cryst. Growth Des.*, 2008, **8**, 2090–2092.
- 16 D. H. Brouwer, I. L. Moudrakovski, K. A. Udachin, G. D. Enright and J. A. Ripmeester, *Cryst. Growth Des.*, 2008, **8**, 1878–1885.
- 17 K. A. Udachin, I. L. Moudrakovski, G. D. Enright, C. I. Ratcliffe and J. A. Ripmeester, *Phys. Chem. Chem. Phys.*, 2008, **10**, 4636–4643.
- 18 R. Çapan, Z. Özbek, H. Gökteş, S. Şen, F. G. Önce, M. E. Özel, G. A. Stanciu and F. Davis, *Sensors Actuators, B Chem.*, 2010, **148**, 358–365.
- 19 S. A. Herbert, A. Janiak, P. K. Thallapally, J. L. Atwood and L. J. Barbour, *Chem. Commun.*, 2014, **50**, 15509–15512.
- 20 G. V. Zyryanov, Y. Kang and D. M. Rudkevich, *J. Am. Chem. Soc.*, 2003, **125**, 2997–3007.
- 21 P. Murphy, S. J. Dalgarno and M. J. Paterson, *J. Phys. Chem. A*, 2017, **121**, 7986–7992.
- 22 S. J. Dalgarno, J. E. Warren, J. Antesberger, T. E. Glass, J. L. Atwood and E. Glass, *New J. Chem.*, 2007, **31**, 1891–1894.

- 23 S. Kennedy and S. J. Dalgarno, *Chem. Commun.*, 2009, 5275–5277.
- 24 S. Kennedy, I. E. Dodgson, C. M. Beavers, S. J. Teat and S. J. Dalgarno, *Cryst. Growth Des.*, 2012, **12**, 688–697.
- 25 S. Kennedy, P. Cholewa, R. D. McIntosh and S. J. Dalgarno, *CrystEngComm*, 2013, **15**, 1520–1523.
- 26 S. M. Taylor, S. Sanz, R. D. McIntosh, C. M. Beavers, S. J. Teat, E. K. Brechin and S. J. Dalgarno, *Chem. Eur. J.*, 2012, **18**, 16014–16022.
- 27 R. McLellan, K. M. Kennedy, M. Denis, R. D. McIntosh, E. K. Brechin and S. J. Dalgarno, *Polyhedron*, 2013, **64**, 388–392.
- 28 H. Kumari, P. Jin, S. J. Teat, C. L. Barnes, S. J. Dalgarno and J. L. Atwood, *Angew. Chem. Int. Ed.*, 2014, **53**, 13088–13092.
- 29 M. Coletta, R. McLellan, A. Waddington, S. Sanz, K. J. Gagnon, S. J. Teat, E. K. Brechin and S. J. Dalgarno, *Chem. Commun.*, 2016, **52**, 14246–14249.
- 30 P. Murphy, S. J. Dalgarno and M. J. Paterson, *J. Phys. Chem. A*, 2016, **120**, 824–839.
- 31 M. Coletta, R. McLellan, J. M. Cols, K. J. Gagnon, S. J. Teat, E. K. Brechin and S. J. Dalgarno, *Supramol. Chem.*, 2016, **28**, 557–566.
- 32 M. Coletta, R. McLellan, P. Murphy, B. T. Leube, S. Sanz, R. Clowes, K. J. Gagnon, S. J. Teat, A. I. Cooper, M. J. Paterson, E. K. Brechin and S. J. Dalgarno, *Chem. Eur. J.*, 2016, **22**, 8791–8795.
- 33 X. Zhu, S. Wang, H. Han, X. Hang, W. Xie and W. Liao, *Cryst. Growth Des.*, 2017, **18**, 225–229.
- 34 H. Kim, Y. Kim, M. Yoon, S. Linn, S. M. Park, G. Seo and K. Kim, *J. Am. Chem. Soc.*, 2010, **132**, 12200–12202.
- 35 J. Tian, S. Ma, P. K. Thallapally, D. Fowler, B. P. McGrail and J. L. Atwood, *Chem. Commun.*, 2011, **47**, 7626–7628.
- 36 J. Tian, J. Liu, J. Liu and P. K. Thallapally, *CrystEngComm*, 2013, **15**, 1528–1531.
- 37 J. Tian, P. K. Thallapally, S. J. Dalgarno, P. B. McGrail and J. L. Atwood, *Angew. Chem. Int. Ed.*, 2009, **48**, 5492–5495.
- 38 P.-S. Huang, C.-H. Kuo, C.-C. Hsieh and Y.-C. Horng, *Chem. Commun.*, 2012, **48**, 3227–3229.
- 39 R. S. Patil, D. Banerjee, C. M. Simon, J. L. Atwood and P. K. Thallapally, *Chem. Eur. J.*, 2016, **22**, 12618–12623.
- 40 R. S. Patil, C. Zhang, C. L. Barnes and J. L. Atwood, *Cryst. Growth Des.*, 2016, **17**, 7–10.
- 41 C. M. Kane, A. Banisafar, T. P. Dougherty, L. J. Barbour and K. T. Holman, *J. Am. Chem. Soc.*, 2016, **138**, 4377–4392.
- 42 M. B. Dewal, M. W. Lufaso, A. D. Hughes, S. A. Samuel, P. Pellechia and L. S. Shimizu,

- Chem. Mater.*, 2006, **18**, 4855–4864.
- 43 C. M. Kane, O. Ugono, L. J. Barbour and K. T. Holman, *Chem. Mater.*, 2015, **27**, 7337–7354.
- 44 C. R. Groom, I. J. Bruno, M. P. Lightfoot and S. C. Ward, *Acta Crystallogr. Sect. B: Struct. Sci. Cryst. Eng. Mater.*, 2016, **72**, 171–179.
- 45 N. B. McKeown, *J. Mater. Chem.*, 2010, **20**, 10588–10597.
- 46 J. D. Evans, D. M. Huang, M. Haranczyk, A. W. Thornton, C. J. Sumbly and C. J. Doonan, *CrystEngComm*, 2016, **18**, 4133–4141.
- 47 R. G. D. Taylor, C. G. Bezzu, M. Carta, K. J. Msayib, J. Walker, R. Short, B. M. Kariuki and N. B. McKeown, *Chem. Eur. J.*, 2016, **22**, 2466–2472.
- 48 Y. Sheng, Q. Chen, J. Yao, Y. Lu, H. Liu and S. Dai, *Angew. Chem. Int. Ed.*, 2016, **55**, 3378–3381.
- 49 A. Aguilar-Granda, S. Perez-Estrada, E. Sánchez-González, J. R. Álvarez, J. Rodríguez-Hernandez, M. Rodríguez, A. E. Roa, S. Hernandez-Ortega, I. A. Ibarra and B. Rodríguez-Molina, *J. Am. Chem. Soc.*, 2017, **139**, 7549–7557.
- 50 L. Dobrzańska, G. O. Lloyd, H. G. Raubenheimer and L. J. Barbour, *J. Am. Chem. Soc.*, 2006, **128**, 698–699.
- 51 T. Jacobs and L. J. Barbour, *CrystEngComm*, 2013, **15**, 1512–1514.
- 52 V. I. Nikolayenko, A. Heyns and L. J. Barbour, *Chem. Commun.*, 2017, **53**, 11306–11309.
- 53 V. I. Nikolayenko, L. J. Barbour, A. Arauzo, J. Campo, J. M. Rawson and D. A. Haynes, *Chem. Commun.*, 2017, **53**, 11310–11313.
- 54 J. S. Wright, A. J. Metherell, W. M. Cullen, J. R. Piper, R. Dawson and M. D. Ward, *Chem. Commun.*, 2017, **53**, 4398–4401.
- 55 I. J. Vitorica-Yrezábal, D. F. Sava, G. A. Timco, M. S. Brown, M. Savage, H. G. W. Godfrey, F. Moreau, M. Schröder, F. Siperstein, L. Brammer, S. Yang, M. P. Attfield, J. J. W. McDouall and R. E. P. Winpenny, *Angew. Chem. Int. Ed.*, 2017, **56**, 5527–5530.
- 56 H. Imoto, S. Tanaka, T. Kato, T. Yumura, S. Watase, K. Matsukawa and K. Naka, *Organometallics*, 2016, **35**, 3647–3650.
- 57 M. J. Bryant, J. M. Skelton, L. E. Hatcher, C. Stubbs, E. Madrid, A. R. Pallipurath, L. H. Thomas, C. H. Woodall, J. Christensen, S. Fuertes, T. P. Robinson, C. M. Beavers, S. J. Teat, M. R. Warren, F. Pradaux-Caggiano, A. Walsh, F. Marken, D. R. Carbery, S. C. Parker, N. B. McKeown, R. Malpass-Evans, M. Carta and P. R. Raithby, *Nat. Commun.*, 2017, **8**, (1800) 1–9.
- 58 C. N. Dzesse T, E. N. Nfor and S. A. Bourne, *Cryst. Growth Des.*, 2018, **18**, 416–423.
- 59 K. Hong and H. Chun, *Inorg. Chem.*, 2013, **52**, 9705–9707.
- 60 K. Hong, W. Bak and H. Chun, *Inorg. Chem.*, 2014, **53**, 7288–7293.

- 61 M. Kobayashi, T. Okuhara, H. Kato, S. Sato and M. Kakihana, *Chem. Lett.*, 2015, **44**, 1050–1052.
- 62 T. Itoh, M. Kondo, H. Sakamoto, K. Wakabayashi, M. Kanaike, K. Itami and S. Masaoka, *Dalton Trans.*, 2015, **44**, 15334–15342.
- 63 G. Férey, C. Mellot-Draznieks, C. Serre, F. Millange, J. Dutour, S. Surblé and I. Margiolaki, *Science*, 2005, **309**, 2040–2042.
- 64 K. Munusamy, G. Sethia, D. V. Patil, P. B. Somayajulu Rallapalli, R. S. Somani and H. C. Bajaj, *Chem. Eng. J.*, 2012, **195–196**, 359–368.
- 65 Z. Saedi, S. Tangestaninejad, M. Moghadam, V. Mirkhani and I. Mohammadpoor-Baltork, *Catal. Commun.*, 2012, **17**, 18–22.
- 66 N. V. Maksimchuk, O. V. Zalomaeva, I. Y. Skobelev, K. A. Kovalenko, V. P. Fedin and O. A. Kholdeeva, *Proc. R. Soc. A*, 2012, **468**, 2017–2034.
- 67 P. Horcajada, C. Serre, M. Vallet-Regí, M. Sebban, F. Taulelle and G. Férey, *Angew. Chem. Int. Ed.*, 2006, **45**, 5974–5978.
- 68 K. M. L. Taylor-Pashow, J. Della Rocca, Z. Xie, S. Tran and W. Lin, *J. Am. Chem. Soc.*, 2009, **131**, 14261–14263.
- 69 R. Weinland and P. Dinkelacker, *Ber. Deut. Chem. Ges.*, 1909, **42**, 2997–3018.
- 70 A. Earnshaw, B. N. Figgis and J. Lewis, *J. Chem. Soc. A*, 1966, 1656–1663.
- 71 A. Figuerola, V. Tangoulis, J. Ribas, H. Hartl, I. Bru, M. Maestro, C. Diaz, F. De Ciencias and U. Corun, *Inorg. Chem.*, 2007, **46**, 11017–11024.
- 72 G. M. Sheldrick, *SADABS, Empirical Absorption Correction program, Univ. Göttingen*, 1995, based on the methods of Blessing.
- 73 L. Krause, R. Herbst-Irmer, G. M. Sheldrick and D. Stalke, *J. Appl. Crystallogr.*, 2015, **48**, 3–10.
- 74 R. H. Blessing, *Acta Crystallogr. Sect. A: Found. Adv.*, 1995, **A51**, 33–38.
- 75 G. M. Sheldrick, *Acta Crystallogr. Sect. C: Struct. Chem.*, 2015, **71**, 3–8.
- 76 O. V. Dolomanov, L. J. Bourhis, R. J. Gildea, J. A. K. Howard and H. Puschmann, *J. Appl. Crystallogr.*, 2009, **42**, 339–341.
- 77 H. Nowell, S. A. Barnett, K. E. Christensen, S. J. Teat and D. R. Allan, *J. Synchrotron Radiat.*, 2012, **19**, 435–441.
- 78 S. A. Barnett, H. Nowell, M. R. Warren, A. Wilcox and D. R. Allan, *Protein Pept. Lett.*, 2015, **23**, 211–216.
- 79 D. R. Allan, S. P. Collins, G. Evans, D. Hall, K. McAuley, R. L. Owen, T. Sorensen, C. C. Tang, F. von Delft, A. Wagner and H. Wilhelm, *Eur. Phys. J. Plus*, 2015, **130**, 1–20.
- 80 CrysAlisPRO, *Oxford Diffraction /Agilent Technologies UK Ltd*, Yarnton, England.

- 81 G. S. Pawley, *J. Appl. Crystallogr.*, 1981, **14**, 357–361.
- 82 A. A. Coelho, *Topas Academic, Version 4.1*, see <http://www.topas-academic.net>.
- 83 A. A. Coelho, J. Evans, I. Evans, A. Kern and S. Parsons, *Powder Diffr.*, 2011, **26**, S22–S25.
- 84 N. Tartoni, S. P. Thompson, C. C. Tang, B. L. Willis, G. E. Derbyshire, A. G. Wright, S. C. Jaye, J. M. Homer, J. D. Pizzey and A. M. T. Bell, *J. Synchrotron Radiat.*, 2007, **15**, 43–49.
- 85 S. P. Thompson, J. E. Parker, J. Potter, T. P. Hill, A. Birt, T. M. Cobb, F. Yuan and C. C. Tang, *Rev. Sci. Instrum.*, 2009, **80**, (075107) 1–9.
- 86 S. P. Thompson, J. E. Parker, J. Marchal, J. Potter, A. Birt, F. Yuan, R. D. Fearn, A. R. Lennie, S. R. Street and C. C. Tang, *J. Synchrotron Radiat.*, 2011, **18**, 637–648.
- 87 A. Thorn, B. Dittrich and G. M. Sheldrick, *Acta Crystallogr. Sect. A: Found. Crystallogr.*, 2012, **68**, 448–451.
- 88 Z. F. Shi, J. M. Li, Y. Z. Yin, L. Zhang, N. Huang and R. Y. Feng, *Appl. Mech. Mater.*, 2013, **275–277**, 2010–2013.
- 89 Y. Bing and C. Zhi-da, *J. Coord. Chem.*, 2002, **55**, 241–249.
- 90 I. Khosravi, M. Mirzaei, A. Bauzá, A. Frontera and M. Eftekhar, *Polyhedron*, 2014, **81**, 349–355.
- 91 G. Cavallo, P. Metrangolo, R. Milani, T. Pilati, A. Priimagi, G. Resnati and G. Terraneo, *Chem. Rev.*, 2016, **116**, 2478–2601.
- 92 A. L. Spek, *Acta Crystallogr. Sect. D: Biol. Crystallogr.*, 2009, **65**, 148–155.
- 93 A. L. Spek, *Acta Crystallogr. Sect. C: Struct. Chem.*, 2015, **71**, 9–18.
- 94 H. Küppers, F. Liebau and A. L. Spek, *J. Appl. Crystallogr.*, 2006, **39**, 338–346.
- 95 C. F. Macrae, I. J. Bruno, J. A. Chisholm, P. R. Edgington, P. McCabe, E. Pidcock, L. Rodriguez-Monge, R. Taylor, J. Van De Streek and P. A. Wood, *J. Appl. Crystallogr.*, 2008, **41**, 466–470.
- 96 Apex3. Bruker AXS Inc., Madison, Wisconsin, USA.
- 97 G. M. Sheldrick, 2008, CELL_NOW, University of Göttingen, Germany.
- 98 H. M. Rietveld, *J. Appl. Crystallogr.*, 1969, **2**, 65–71.
- 99 M. Thommes, K. Kaneko, A. V. Neimark, J. P. Olivier, F. Rodriguez-Reinoso, J. Rouquerol and K. S. W. Sing, *Pure Appl. Chem.*, 2015, **87**, 1051–1069.
- 100 A. L. Spek, *J. Appl. Crystallogr.*, 2003, **36**, 7–13.
- 101 P. Z. Moghadam, A. Li, S. B. Wiggin, A. Tao, A. G. P. Maloney, P. A. Wood, S. C. Ward and D. Fairen-Jimenez, *Chem. Mater.*, 2017, **29**, 2618–2625.

4.8 Appendices

Appendix 4.8.1 Single-Crystal X-Ray Diffraction Data

Table 4.3.2-1. Summary of the single-crystal data of the target $[\text{Cr}_3\text{O}(4\text{-Xbz})_6(\text{MeOH})_3][\text{NO}_3]$ clusters in as-synthesised and solvent-free forms (Section 4.3.4) of **4.1(I)** and **4.2(Br)**

	4.1(I)-1.5MeOH [Cr ₃ O(4-lbz) ₆ (MeOH) ₃] [NO ₃] ₁ ·1½MeOH C _{46.5} H ₄₂ Cr ₃ I ₆ NO _{20.5}	4.2(Br)-2MeOH 0.5MeCN [Cr ₃ O(4-Brbz) ₆ (MeOH) ₃][NO ₃] ₂ ·2MeOH 1MeCN C ₄₉ H ₄₇ Br ₆ Cr ₃ N ₂ O ₂₁	4.3(Cl)-2MeOH.0.75MeCN [Cr ₃ O(4-Clbz) ₆ (MeOH) ₃] [NO ₃] ₂ ·2MeOH·¾MeCN C _{48.5} H _{43.57} Cl ₆ Cr ₃ N _{1.75} O ₂₁
Crystal habit	Plate	Block	Plate
Crystal colour	Dark Green	Dark Green	Dark Green
Crystal size (mm)	0.218 × 0.128 × 0.04	0.37 × 0.24 × 0.15	0.37 × 0.26 × 0.06
Crystal system	Monoclinic	Monoclinic	Monoclinic
Space group	<i>P</i> 2 ₁ / <i>n</i>	<i>P</i> 2 ₁ / <i>n</i>	<i>P</i> 2 ₁ / <i>n</i>
<i>a</i> (Å)	11.1132(3)	12.6365(3)	12.438(6)
<i>b</i> (Å)	23.9833(7)	24.1114(6)	24.370(15)
<i>c</i> (Å)	24.1335(6)	20.2024(5)	19.778(12)
α (°)	90	90	90
β (°)	94.551(2)	98.7450(10)	98.685(14)
γ (°)	90	90	90
<i>V</i> (Å ³)	6412.1(3)	6083.8(3)	5926(6)
Density (g cm ⁻³)	1.927	1.785	1.519
Temperature (K)	100	100	100
μ (mm ⁻¹)	3.454	4.54	0.885
Wavelength (Å)	0.71073	0.71073	0.71073
2θ range (°)	2.398 to 49.902	2.648 to 55.096	2.67 to 54.916
Refins. collected	99459	118532	52353
Independent refins. [<i>R</i> _{int}]	11219 [0.0643]	14012 [0.0527]	13351 [0.2195]
Refins. used in refinement, <i>n</i>	11219	14012	13351
LS parameters, <i>p</i>	738	739	728
Restraints, <i>r</i>	5	15	4
<i>R</i> 1 (<i>F</i> ^a) > 2.0 <i>s</i> (<i>I</i>)	0.0709	0.0398	0.0961
<i>wR</i> 2 (<i>F</i> ²) ^a , all data	0.2003	0.1062	0.3071
<i>S</i> (<i>F</i> ²) ^a , all data	1.0250	1.021	0.955
	4.1(I) [Cr ₃ O(4-lbz) ₆ (MeOH) ₃][NO ₃] C ₄₅ H ₃₅ Cr ₃ I ₆ NO ₁₉	4.2 (Br) [Cr ₃ O(4-Brbz) ₆ (MeOH) ₃][NO ₃] C ₄₅ H ₃₅ Br ₆ Cr ₃ NO ₁₉	
Crystal habit	Plate	Plate	
Crystal colour	Dark Green	Dark Green	
Crystal size (mm)	0.17 × 0.1 × 0.056	0.24 × 0.23 × 0.05	
Crystal system	Monoclinic	Monoclinic	
Space group	<i>P</i> 2 ₁ / <i>m</i>	<i>P</i> 2 ₁ / <i>m</i>	
<i>a</i> (Å)	10.8966(4)	10.8864(5)	
<i>b</i> (Å)	21.0566(9)	20.7086(9)	
<i>c</i> (Å)	13.0355(6)	12.6032(5)	
α (°)	90	90	
β (°)	109.564(3)	109.041(3)	
γ (°)	90	90	
<i>V</i> (Å ³)	2818.3(2)	2685.8(2)	
Density (g cm ⁻³)	2.134	1.891	
Temperature (K)	100	100	
μ (mm ⁻¹)	31.091	10.776	
Wavelength (Å)	1.54178	1.54178	
2θ range (°)	7.196 to 123.454	9.596 to 133.476	
Refins. collected	27063	25578	
Independent refins. [<i>R</i> _{int}]	4493 [0.0808]	4801 [0.1523]	
Refins. used in refinement, <i>n</i>	4493	4801	
LS parameters, <i>p</i>	374	380	
Restraints, <i>r</i>	351	7	
<i>R</i> 1 (<i>F</i> ^a) > 2.0 <i>s</i> (<i>I</i>)	0.0660	0.0950	
<i>wR</i> 2 (<i>F</i> ²) ^a , all data	0.1596	0.2285	
<i>S</i> (<i>F</i> ²) ^a , all data	1.181	1.123	

^a $\mathbf{R1}(F) = \Sigma(|F_o| - |F_c|) / \Sigma|F_o|$; $\mathbf{wR2}(F^2) = [\Sigma w(F_o^2 - F_c^2)^2 / \Sigma w F_o^4]^{1/2}$; $\mathbf{S}(F^2) = [\Sigma w(F_o^2 - F_c^2)^2 / (n + r - p)]^{1/2}$

Table 4.3.4-1. Summary of the variable temperature single-crystal diffraction data for **4.3(Cl)** recorded at 119.⁷⁷

	4.3(Cl)·1½MeOH·½MeCN [Cr ₃ O(4-Clbz) ₆ (MeOH) ₃] [NO ₃]:1½MeOH·½MeCN C _{47.5} H _{43.06} Cl ₆ Cr ₃ N _{1.5} O _{20.5}	4.3(Cl)·1½MeOH [Cr ₃ O(4-Clbz) ₆ (MeOH) ₃] [NO ₃]:1½MeOH C _{46.5} H _{41.16} Cl ₆ Cr ₃ NO _{20.5}	4.3(Cl)-nSol [Cr ₃ O(4-Clbz) ₆ (MeOH) ₃] [NO ₃]:nSol C ₄₅ H ₃₆ NO ₁₉ Cl ₆ Cr ₃
Crystal habit	Plate	Plate	Plate
Crystal colour	Dark Green	Dark Green	Dark Green
Crystal size (mm)	0.15 × 0.15 × 0.03	0.15 × 0.15 × 0.03	0.15 × 0.15 × 0.03
Crystal system	Monoclinic	Monoclinic	Monoclinic
Space group	<i>P</i> 2 ₁ / <i>n</i>	<i>P</i> 2 ₁ / <i>n</i>	<i>P</i> 2 ₁ / <i>n</i>
<i>a</i> (Å)	12.5320(3)	12.5498(4)	11.0773(9)
<i>b</i> (Å)	24.6796(7)	24.6819(7)	24.278(2)
<i>c</i> (Å)	20.2103(7)	20.2973(7)	22.8187(16)
α (°)	90	90	90
β (°)	98.276(3)	98.303(3)	90.860(7)
γ (°)	90	90	90
<i>V</i> (Å ³)	6185.7(3)	6221.2(3)	6136.0(9)
Density (g cm ⁻³)	1.43	1.399	1.368
Temperature (K)	250	273	298
μ (mm ⁻¹)	0.782	0.776	0.782
Wavelength (Å)	0.6889	0.6889	0.6889
2θ range (°)	3.2 to 53.144	3.198 to 53.142	3.252 to 53.14
Reflns. collected	45410	46025	46639
Independent reflns. [<i>R</i> _{int}]	13835 [0.0753]	13895 [0.1198]	13671 [0.0751]
Reflns. used in refinement, <i>n</i>	13835	13895	13671
LS parameters, <i>p</i>	722	673	604
Restraints, <i>r</i>	15	20	648
<i>R</i> 1 (<i>F</i>) ^a / >2.0σ(<i>I</i>)	0.0888	0.1454	0.1415
<i>wR</i> 2 (<i>F</i> ²) ^a , all data	0.2672	0.4107	0.4880
<i>S</i> (<i>F</i> ²) ^a , all data	1.045	1.483	1.345

$$^a R1(F) = \sum(|F_o| - |F_c|) / \sum|F_o| ; wR2(F^2) = [\sum w(F_o^2 - F_c^2)^2 / \sum wF_o^4]^{1/2} ; S(F^2) = [\sum w(F_o^2 - F_c^2)^2 / (n + r - p)]^{1/2}$$

Appendix 4.8.2 Powder X-Ray Diffraction Data

Table 4.3.5-1. Summary of Pawley refinements of **4.1(I)**, **4.2(Br)** and **4.3(Cl)** recorded periodically over a period of two months (sample ageing study)

Duration	Space Group	Volume (Å ³)	<i>a</i> (Å)	<i>b</i> (Å)	<i>c</i> (Å)	α (°)	β (°)	γ (°)	<i>R</i> _{wp}	<i>R</i> _{wp} '	Parameters
4.1(I)											
Fresh	<i>P</i> 2 ₁ / <i>m</i>	2949.4(5)	11.232(1)	21.556(2)	13.019(1)	90	110.662(6)	90	0.0610	0.2504	413
6 days	<i>P</i> 2 ₁ / <i>m</i>	2939.8(3)	11.2495(8)	21.4074(14)	13.0156(8)	90	110.300(5)	90	0.0428	0.1425	921
12 days	<i>P</i> 2 ₁ / <i>m</i>	2933.4(3)	11.2507(6)	21.3738(10)	12.9978(7)	90	110.195(4)	90	0.0368	0.0903	923
31 days	<i>P</i> 2 ₁ / <i>m</i>	2802.5(3)	10.9604(7)	20.3880(12)	13.0772(8)	90	106.461(5)	90	0.0499	0.2261	469
65 days	<i>P</i> 2 ₁ / <i>m</i>	2791.5(2)	10.9339(4)	20.3597(6)	13.0699(5)	90	106.372(2)	90	0.0309	0.1067	547

Chapter 4: Gaseous Guest Inclusion within a Family of Halogen-Functionalised Stellated Molecular Clusters

4.2(Br)											
Fresh	$P2_1/m$	2824.9(2)	11.2508(3)	21.5023(7)	12.6160(4)	90	112.247(2)	90	0.0434	0.0787	898
6 days	$P2_1/m$	2818.5(1)	11.2436(3)	21.4713(7)	12.6078(3)	90	112.178(2)	90	0.0444	0.0803	893
12 days	$P2_1/m$	2806.3(2)	11.2149(4)	21.3595(7)	12.6106(5)	90	111.722(3)	90	0.0488	0.0892	892
31 days	$P2_1/m$	2785.8(2)	11.1552(4)	21.2182(6)	12.6045(4)	90	110.969(2)	90	0.0457	0.0850	882
65 days ^a	$P2_1/m$	2774.9(1)	11.0672(3)	21.1409(6)	12.6310(3)	90	110.119(2)	90	0.0329	0.0537	1715
	$P2_1/m$	2688.9(2)	11.0122(6)	20.3359(10)	12.6243(5)	90	107.993(4)	90			
4.3(Cl)											
Fresh	UNKNOWN PHASE										
6 days	$C2$	5324.7(6)	22.6157(12)	10.7469(7)	24.6079(14)	90	117.091(4)	90	0.0571	0.1093	880
12 days	$C2$	5260.4(5)	22.7741(12)	10.5818(5)	24.6612(14)	90	117.732(4)	90	0.0594	0.1273	868
31 days	$C2$	5234.0(5)	22.8046(10)	10.5367(4)	24.6240(13)	90	117.796(4)	90	0.0570	0.1243	868
65 days	$C2$	5241.2(4)	22.8340(8)	10.5352(4)	24.6483(11)	90	117.879(4)	90	0.0563	0.1208	869

^a Pattern fitted as a mixture of two phases

Table 4.3.6-1. Summary of Pawley refinements of **4.1(I)**, **4.2(Br)** and **4.3(Cl)** samples before and after volumetric N_2 and CO_2 adsorption studies

Treatment	Space Group	Volume (\AA^3)	a (\AA)	b (\AA)	c (\AA)	α ($^\circ$)	β ($^\circ$)	γ ($^\circ$)	R_{wp}	R_{wp}'	Parameters
4.1(I)											
Post Vac Oven	$P2_1/m$	2924.3(3)	11.2370(6)	21.3031(12)	12.9899(9)	90	109.874(5)	90	0.1140	0.1945	921
Post CO_2	$P2_1/m$	2922.3(4)	11.2180(7)	21.2845(14)	13.0059(10)	90	109.773(6)	90	0.0883	0.1561	919
Post N_2	$P2_1/m$	3052.8(7)	10.9396(12)	22.9399(27)	13.0134(18)	90	110.807(11)	90	0.0593	0.1357	946
4.1(I) Aged											
CO_2 : Aged (145 days) and Post Vac Oven	$P-1$	2786.7(2)	10.5768(3)	20.7580(6)	13.2702(5)	92.836(3)	104.208(3)	97.941(2)	0.0887	0.1320	1654
CO_2 : Aged (145 days) and Post CO_2	DEGRADED										
N_2 : Aged (146 days) and Post Vac Oven	$P-1$	2786.0(3)	10.5873(6)	20.7560(13)	13.2599(8)	92.803(5)	104.350(4)	97.859(5)	0.0836	0.1828	1654
N_2 : Aged (146 days) and Post N_2	DEGRADED										
4.2(Br)											
Post Vac Oven	$P2_1/m$	2795.5(2)	11.1820(5)	21.2849(8)	12.6092(6)	90	111.332(3)	90	0.0715	0.1191	880
Post CO_2	$P2_1/m$	2781.7(2)	11.1301(5)	21.2501(9)	12.6121(7)	90	111.170(3)	90	0.0672	0.0966	879
Post N_2	$P2_1/m$	2827.1(2)	11.2055(4)	21.4003(8)	12.6976(6)	90	111.801(3)	90	0.0784	0.1095	899
4.2(Br) Aged											
CO_2 : Aged (171 days) and Post Vac Oven	$P2_1/m$	2149.5(3)	10.0829(9)	20.3522(15)	11.1526(8)	90	110.080(7)	90	0.1598	0.2218	682
CO_2 : Aged (171 days) and Post CO_2	$P2_1/m$	2111.5(6)	10.0478(17)	20.2942(33)	11.0637(18)	90	110.622(11)	90	0.0861	0.1904	686
N_2 : Aged (175 days) and Post Vac Oven	$P2_1/m$	2145.7(3)	10.0769(10)	20.3320(16)	11.1521(9)	90	110.104(8)	90	0.1743	0.2863	686
N_2 : Aged (175 days) and Post N_2	$P2_1/m$	2100.5(5)	10.0433(14)	20.2734(28)	11.0384(16)	90	110.840(9)	90	0.0815	0.1476	677
4.4(Cl)											
Post Vac Oven	$C2$	5339.9(6)	22.6869(16)	10.7317(6)	24.6437(13)	90	117.128(4)	90	0.0839	0.1144	882
Post CO_2	$C2$	5316.1(6)	22.6849(15)	10.6848(6)	24.6520(13)	90	117.166(5)	90	0.0770	0.0939	880
Post N_2	$C2$	5303.3(30)	22.796(7)	10.7304(36)	24.3733(74)	90	117.187(18)	90	0.1067	0.2919	888

4.3(Cl) Aged											
CO ₂ : Aged (144 days) and Post Vac Oven	C2	5278.0(7)	22.8238(19)	10.5812(8)	24.6933(19)	90	117.742(5)	90	0.1043	0.1039	879
CO ₂ : Aged (144 days) and Post CO ₂	C2	5307.7(11)	22.8485(26)	10.6115(12)	24.7403(30)	90	117.767(8)	90	0.0964	0.1931	883
N ₂ : Aged (144 days) and Post Vac Oven	C2	5276.0(9)	22.8887(22)	10.5549(9)	24.7107(22)	90	117.898(6)	90	0.0985	0.2164	876
N ₂ : Aged (144 days) and Post N ₂	C2	5268.8(7)	22.8718(15)	10.5534(7)	24.7134(18)	90	117.963(5)	90	0.0771	0.1716	874

Table 4.3.7-1. Summary of Pawley refinements of **4.1(I)**, **4.2(Br)** and **4.3(Cl)** samples after gravimetric adsorption studies (returned 2 years after gravimetric analysis).

	Space Group	Volume (Å ³)	<i>a</i> (Å)	<i>b</i> (Å)	<i>c</i> (Å)	α (°)	β (°)	γ (°)	<i>R</i> _{wp}	<i>R</i> _{wp'}	Parameters
4.1(I)	<i>P</i> -1	2774.9(2)	10.5463(5)	20.7186(11)	13.2686(7)	92.850(4)	104.084(4)	97.903(4)	0.0686	0.1420	1646
4.2(Br)	<i>P</i> 2 ₁ / <i>m</i>	2680.0(2)	10.9792(6)	20.2944(9)	12.6398(7)	90	107.904(4)	90	0.0884	0.1496	854
4.3(Cl)	<i>C</i> 2	5297.5(4)	22.8053(11)	10.6299(4)	24.6742(9)	90	117.668(4)	90	0.0837	0.1061	876

Appendix 4.8.3 *In situ* Powder X-Ray Diffraction Data

Table 4.3.8-1. Pawley fits of *in situ* PXRD data during CO₂ adsorption for **4.1(I)** at 298 K, λ = 0.82602(1) Å

	P (Bar)	Space Group	Volume (Å ³)	<i>a</i> (Å)	<i>b</i> (Å)	<i>c</i> (Å)	α (°)	β (°)	γ (°)	<i>R</i> _{wp}	<i>R</i> _{wp'}	Parameters
4.1(I)	0	<i>P</i> 2 ₁ / <i>m</i>	2931.13(5)	11.2135(1)	21.3859(2)	13.0231(1)	90	110.1936(7)	90	0.0432	0.1136	1903
	0.5	<i>P</i> 2 ₁ / <i>m</i>	2933.06(5)	11.2251(1)	21.3949(2)	13.0196(1)	90	110.2735(6)	90	0.0421	0.1101	1903
	1	<i>P</i> 2 ₁ / <i>m</i>	2935.77(5)	11.2362(1)	21.3997(2)	13.0192(1)	90	110.3153(6)	90	0.0418	0.1094	1903
	2	<i>P</i> 2 ₁ / <i>m</i>	2939.55(5)	11.2502(1)	21.4136(2)	13.0173(1)	90	110.3865(6)	90	0.0431	0.1210	1903
	5	<i>P</i> 2 ₁ / <i>m</i>	2946.33(5)	11.2710(1)	21.4514(2)	13.0121(1)	90	110.5240(7)	90	0.0441	0.1209	1924
	10	<i>P</i> 2 ₁ / <i>m</i>	2955.22(5)	11.2956(1)	21.4961(2)	13.0083(1)	90	110.6715(6)	90	0.0417	0.1141	1910
	20	<i>P</i> 2 ₁ / <i>m</i>	2964.68(4)	11.3230(1)	21.5449(2)	13.0031(1)	90	110.8365(5)	90	0.0373	0.1020	1919
	10	<i>P</i> 2 ₁ / <i>m</i>	2955.75(5)	11.3023(1)	21.4906(2)	13.0071(1)	90	110.6806(6)	90	0.0404	0.0992	1919
	5	<i>P</i> 2 ₁ / <i>m</i>	2946.73(6)	11.2846(1)	21.4321(3)	13.0103(2)	90	110.5296(8)	90	0.0440	0.1288	1921
	2	<i>P</i> 2 ₁ / <i>m</i>	2938.15(7)	11.2702(1)	21.3759(3)	13.0103(2)	90	110.3787(9)	90	0.0464	0.1432	1912
	1	<i>P</i> 2 ₁ / <i>m</i>	2935.01(4)	11.2208(1)	21.4205(2)	13.0228(1)	90	110.3356(5)	90	0.0386	0.0967	1905
	0.5	<i>P</i> 2 ₁ / <i>m</i>	2933.68(5)	11.2251(1)	21.4007(2)	13.0228(1)	90	110.3209(6)	90	0.0408	0.1087	1904
	0	<i>P</i> 2 ₁ / <i>m</i>	2925.28(6)	11.2077(1)	21.3431(3)	13.0286(2)	90	110.1757(8)	90	0.0472	0.1188	1902

Table 4.3.8-2. Pawley fits of *in situ* PXRD data during CO₂ adsorption for **4.2(Br)** at 298 K, λ = 0.82582(1) Å

	T (K)	P (Bar)	Space Group	Volume (Å ³)	<i>a</i> (Å)	<i>b</i> (Å)	<i>c</i> (Å)	α (°)	β (°)	γ (°)	<i>R</i> _{wp} ^a	<i>R</i> _{wp'}	Parameters
4.2(Br)	298	0	<i>P</i> 2 ₁ / <i>m</i>	2794.38(13)	11.2052(3)	21.1319(5)	12.6571(4)	90	111.190(2)	90	0.0087	0.1342	815
	343	0	<i>P</i> 2 ₁ / <i>m</i>	2798.17(12)	11.1999(3)	21.1569(5)	12.6643(3)	90	111.180(2)	90	0.0083	0.1222	817
	343	0	<i>P</i> 2 ₁ / <i>m</i>	2788.99(15)	11.1756(3)	21.1153(5)	12.6661(4)	90	111.074(2)	90	0.0091	0.1414	981
	298	0	<i>P</i> 2 ₁ / <i>m</i>	2785.45(14)	11.1689(3)	21.0997(5)	12.6643(4)	90	111.043(2)	90	0.0091	0.1308	813
	298	1	<i>P</i> 2 ₁ / <i>m</i>	2792.29(14)	11.1816(3)	21.2010(5)	12.6452(4)	90	111.332(2)	90	0.0085	0.1370	815
	298	5	<i>P</i> 2 ₁ / <i>m</i>	2820.33(10)	11.2415(2)	21.4063(4)	12.6279(2)	90	111.856(2)	90	0.0076	0.1103	820
	298	10	<i>P</i> 2 ₁ / <i>m</i>	2829.78(15)	11.2736(3)	21.5383(7)	12.6084(4)	90	112.436(2)	90	0.0096	0.1505	828
	298	20	<i>P</i> 2 ₁ / <i>m</i>	2845.92(11)	11.3139(2)	21.6451(4)	12.6120(3)	90	112.862(1)	90	0.0070	0.1090	830
	298	40	<i>P</i> 2 ₁ / <i>m</i>	2854.19(12)	11.3410(3)	21.7091(5)	12.6002(3)	90	113.065(2)	90	0.0087	0.1355	832
	298	1	<i>P</i> 2 ₁ / <i>m</i>	2801.96(11)	11.2075(3)	21.2453(4)	12.6471(3)	90	111.492(2)	90	0.0077	0.1225	819

^a *R*_{wp} values small due to the high background fluorescence as a consequence of recording data a sample containing bromine on the PSD.

Table 4.3.8-3. Pawley fits of *in situ* PXRD data during CO₂ adsorption for **4.1(I)** at 298 K, $\lambda = 0.82621(1)$ Å

	P (Bar)	Space Group	Volume (Å ³)	<i>a</i> (Å)	<i>b</i> (Å)	<i>c</i> (Å)	α (°)	β (°)	γ (°)	<i>R</i> _{wp}	<i>R</i> _{wp'}	Parameters
4.1(I)-Aged	0	<i>P</i> -1	2776.34(2)	10.55460(5)	20.6542(1)	13.32611(6)	93.0529(4)	104.1295(3)	98.2309(4)	0.0196	0.0435	4798
	1	<i>P</i> -1	2775.17(2)	10.55698(5)	20.6568(1)	13.32085(6)	93.0083(4)	104.1868(3)	98.2928(4)	0.0194	0.0431	4805
	5	<i>P</i> -1	2776.13(2)	10.56043(5)	20.6581(1)	13.32080(6)	93.0114(4)	104.1893(3)	98.3013(4)	0.0201	0.0431	4807
	10	<i>P</i> -1	2776.95(2)	10.56332(5)	20.6590(1)	13.32107(6)	93.0162(4)	104.1910(3)	98.3102(4)	0.0197	0.0457	4805
	20	<i>P</i> -1	2777.60(2)	10.56567(5)	20.6599(1)	13.32105(6)	93.0198(4)	104.1936(3)	98.3138(4)	0.0193	0.0460	4805

Table 4.3.8-4. Pawley fits of *in situ* PXRD data during CO₂ adsorption for **4.3(CI)** at 298 K, $\lambda = 0.82621(1)$ Å

	P (Bar)	Space Group	Volume (Å ³)	<i>a</i> (Å)	<i>b</i> (Å)	<i>c</i> (Å)	α (°)	β (°)	γ (°)	<i>R</i> _{wp}	<i>R</i> _{wp'}	Parameters
4.3(CI)-Aged	0	<i>C</i> 2	5257.0(5)	22.7106(11)	10.6399(6)	24.5973(13)	90	117.814(3)	90	0.0622	0.1851	1240
	1	<i>C</i> 2	5254.5(5)	22.6988(11)	10.6405(6)	24.5851(14)	90	117.760(3)	90	0.0615	0.1823	1245
	5	<i>C</i> 2	5255.7(5)	22.6851(10)	10.6428(6)	24.5730(13)	90	117.639(3)	90	0.0656	0.1667	1245
	10	<i>C</i> 2	5279.9(5)	22.7118(11)	10.6609(5)	24.6205(16)	90	117.663(3)	90	0.0749	0.1945	1247
	20	<i>C</i> 2	5286.6(5)	22.7022(10)	10.6724(6)	24.6276(16)	90	117.628(3)	90	0.0781	0.1864	1251

Appendix 4.8.4 *In situ* Single-Crystal X-Ray Diffraction Data

Table 4.3.9-1. Summary of *in situ* single-crystal data during CO₂ adsorption study for **4.1(I)** at 298 K.

	4.1(I)-Vac [Cr ₃ O(4- <i>lbz</i>) ₆ (MeOH) ₃][NO ₃] C ₄₅ H ₃₆ NO ₁₉ Cr ₃ I ₆	4.1(I)-1bar CO₂ [Cr ₃ O(4- <i>lbz</i>) ₆ (MeOH) ₃][NO ₃] C ₄₅ H ₃₆ NO ₁₉ Cr ₃ I ₆	4.1(I)-5bar CO₂ [Cr ₃ O(4- <i>lbz</i>) ₆ (MeOH) ₃][NO ₃] C ₄₅ H ₃₆ NO ₁₉ Cr ₃ I ₆
Crystal habit	Needle	Needle	Needle
Crystal colour	Dark Green	Dark Green	Dark Green
Crystal size (mm)	0.2 × 0.04 × 0.04	0.2 × 0.04 × 0.04	0.2 × 0.04 × 0.04
Crystal system	Monoclinic	Monoclinic	Monoclinic
Space group	<i>P</i> 2 ₁ / <i>m</i>	<i>P</i> 2 ₁ / <i>m</i>	<i>P</i> 2 ₁ / <i>m</i>
<i>a</i> (Å)	11.086(3)	11.226(2)	11.278(2)
<i>b</i> (Å)	20.522(4)	20.755(3)	20.832(3)
<i>c</i> (Å)	13.051(3)	12.978(2)	12.9539(19)
α (°)	90	90	90
β (°)	107.21(2)	108.32(2)	108.751(18)
γ (°)	90	90	90
<i>V</i> (Å ³)	2836.0(11)	2870.6(9)	2882.0(9)
Density (g cm ⁻³)	2.122	2.097	2.088
Temperature (K)	298	298	298
μ (mm ⁻¹)	3.611	3.568	3.554
Wavelength (Å)	0.6889	0.6889	0.6889
2 θ range (°)	3.706 to 41.416	3.704 to 41.278	3.696 to 41.238
Reflns. collected	12245	12729	12979
Independent reflns. [<i>R</i> _{int}]	3210 [0.0969]	3246 [0.0703]	3271 [0.0721]
Reflns. used in refinement, <i>n</i>	3210	3246	3271
LS parameters, <i>p</i>	295	295	295
Restraints, <i>r</i>	338	339	338
<i>R</i> 1 (<i>F</i>) ^a / >2.0 σ (<i>I</i>)	0.1693	0.1630	0.1960
<i>wR</i> 2 (<i>F</i> ²) ^a , all data	0.5074	0.5117	0.5538
<i>S</i> (<i>F</i> ²) ^a , all data	2.104	2.080	2.115

$$^a = R1(F) = \sum(|F_o| - |F_c|) / \sum F_o; wR2(F^2) = [\sum w(F_o^2 - F_c^2)^2 / \sum w F_o^4]^{1/2}; S(F^2) = [\sum w(F_o^2 - F_c^2)^2 / (n + r - p)]^{1/2}$$

Table 4.3.9-2. Unit cells from in situ single-crystal data during CO₂ adsorption study for 4.1(I) at 298 K.

P (Bar)	Space Group	Volume (Å ³)	<i>a</i> (Å)	<i>b</i> (Å)	<i>c</i> (Å)	α (°)	β (°)	γ (°)
0 ^a	<i>P2₁/m</i>	2836.0(11)	11.086(3)	20.522(4)	13.051(3)	90	107.21(2)	90
1 ^a	<i>P2₁/m</i>	2870.6(9)	11.226(2)	20.755(3)	12.978(2)	90	108.32(2)	90
5 ^a	<i>P2₁/m</i>	2882.0(9)	11.278(2)	20.832(3)	12.9539(19)	90	108.751(18)	90
10 ^b	<i>P2₁/m</i>	2899.7(16)	11.342(4)	21.050(5)	12.909(3)	90	109.81(4)	90
20 ^b	<i>P2₁/m</i>	2921(3)	11.359(8)	21.230(9)	12.933(7)	90	110.52(7)	90
40 ^b	<i>P2₁/m</i>	2930(6)	11.309(13)	21.373(16)	12.978(15)	90	110.92(13)	90
1 ^b	<i>P2₁/m</i>	2906(13)	11.28(3)	21.50(2)	12.91(4)	90	111.9(3)	90

^aPartially structure solution could be modelled (Table 4.3.9-1). ^b structure solution could not be modelled due to diminishing crystal quality.

Table 4.3.9-3. Summary of *in situ* single-crystal data during CO₂ adsorption study for **4.2(Br)** at 298 K.

	4.2 (Br)-Air [Cr ₃ O(4-Brbz) ₆ (MeOH) ₃][NO ₃] C ₄₅ H ₃₆ NO ₁₉ Cr ₃ Br ₆	4.2 (Br)-1bar CO₂ [Cr ₃ O(4-Brbz) ₆ (MeOH) ₃][NO ₃] C ₄₅ H ₃₆ NO ₁₉ Cr ₃ Br ₆	4.2 (Br)-5bar CO₂ [Cr ₃ O(4-Brbz) ₆ (MeOH) ₃][NO ₃] C ₄₅ H ₃₆ NO ₁₉ Cr ₃ Br ₆
Crystal habit	Plate	Plate	Plate
Crystal colour	Dark Green	Dark Green	Dark Green
Crystal size (mm)	0.05 × 0.034 × 0.017	0.05 × 0.034 × 0.017	0.05 × 0.034 × 0.017
Crystal system	Monoclinic	Monoclinic	Monoclinic
Space group	<i>P</i> 2 ₁ / <i>m</i>	<i>P</i> 2 ₁ / <i>m</i>	<i>P</i> 2 ₁ / <i>m</i>
<i>a</i> (Å)	11.283(4)	11.309(3)	11.325(3)
<i>b</i> (Å)	21.324(7)	20.813(5)	20.999(4)
<i>c</i> (Å)	12.630(4)	12.636(3)	12.630(3)
α (°)	90	90	90
β (°)	110.84(4)	109.79(3)	110.25(3)
γ (°)	90	90	90
<i>V</i> (Å ³)	2840.0(19)	2798.4(12)	2818.0(11)
Density (g cm ⁻³)	1.789	1.6851	1.803
Temperature (K)	298	298	298
μ (mm ⁻¹)	4.456	4.511	4.49
Wavelength (Å)	0.6889	0.6889	0.6889
2θ range (°)	3.702 to 41.46	3.32 to 41.34	3.332 to 41.292
Reflns. collected	12146	10419	11714
Independent reflns. [<i>R</i> _{int}]	3252 [0.1531]	3099 [0.0793]	3208 [0.0630]
Reflns. used in refinement, <i>n</i>	3252	3099	3208
LS parameters, <i>p</i>	295	295	295
Restraints, <i>r</i>	334	12	338
<i>R</i> 1 (<i>F</i>) ^a > 2.0σ(<i>I</i>)	0.2358	0.2002	0.2005
<i>wR</i> 2 (<i>F</i> ²) ^b , all data	0.6104	0.5780	0.5470
<i>S</i> (<i>F</i> ²) ^c , all data	2.316	2.3130	1.930
	4.2 (Br)-10bar CO₂ [Cr ₃ O(4-Brbz) ₆ (MeOH) ₃][NO ₃] C ₄₅ H ₃₆ NO ₁₉ Cr ₃ Br ₆	4.2 (Br)-20bar CO₂ [Cr ₃ O(4-Brbz) ₆ (MeOH) ₃][NO ₃] UNRESOLVED	
Crystal habit	Plate	Plate	
Crystal colour	Dark Green	Dark Green	
Crystal size (mm)	0.05 × 0.034 × 0.017	0.05 × 0.034 × 0.017	
Crystal system	Monoclinic	Monoclinic	
Space group	<i>P</i> 2 ₁ / <i>m</i>	<i>P</i> 2 ₁ / <i>m</i>	
<i>a</i> (Å)	11.350(3)	11.392(7)	
<i>b</i> (Å)	21.206(6)	21.566(10)	
<i>c</i> (Å)	12.625(4)	12.648(8)	
α (°)	90	90	
β (°)	110.79(3)	111.31(7)	
γ (°)	90	90	
<i>V</i> (Å ³)	2840.9(15)	2895(3)	
Density (g cm ⁻³)	1.789		
Temperature (K)	298	298	
μ (mm ⁻¹)	4.454		
Wavelength (Å)	0.6889	0.6889	
2θ range (°)	3.344 to 33.548		
Reflns. collected	6756		
Independent reflns. [<i>R</i> _{int}]	1801 [0.1056]		
Reflns. used in refinement, <i>n</i>	1801		
LS parameters, <i>p</i>	295		
Restraints, <i>r</i>	344		
<i>R</i> 1 (<i>F</i>) ^a > 2.0σ(<i>I</i>)	0.2792		
<i>wR</i> 2 (<i>F</i> ²) ^b , all data	0.6295		
<i>S</i> (<i>F</i> ²) ^c , all data	2.623		

^a $R1(F) = \frac{\sum(|F_o| - |F_c|)}{\sum|F_o|}$; $wR2(F^2) = \frac{[\sum w(F_o^2 - F_c^2)^2]}{[\sum w F_o^4]^{1/2}}$; $S(F^2) = \frac{[\sum w(F_o^2 - F_c^2)^2]}{(n + r - p)]^{1/2}}$

Chapter 5:

Solvent-Induced Structural Transformations within a Porous Molecular Solid

5.1 Introduction

Prior to the turn of the 21st century the general consensus was that in order for a material to be porous it has to contain an infinite rigidly defined pore channel.¹ This led to Kitagawa defining the generations of porous materials with 1st generation materials only containing pores in the presence of the crystallisation solvent and 2nd generation materials consisting of rigidly defined pores.^{2,3} Further development in the field highlighted a 3rd generation, that of materials with dynamic pores which change size and shape in presence/absence of guests.⁴⁻⁹ In the past two decades it has also been demonstrated that porosity is not exclusive to polymeric framework materials (Zeolites, Metal-Organic Frameworks and Covalent-Organic Frameworks) but can be observed in molecular materials.^{1,10} As discussed in chapter 1 molecules that exhibit porosity can be grouped into two types of pore. Materials with intrinsic pores (supramolecular cages, crowns etc)¹¹⁻¹³ and materials with extrinsic pores.¹⁴⁻²¹

The field of molecular extrinsic porosity utilises two key techniques, the first being the design of a molecular system that will exhibit inefficient packing and the second being to utilise favourable interactions to propagate and sustain a void space. This field has also benefitted from mining the Cambridge Structure Database (CSD) for prospective porous materials.^{18,22} Initial examples within this field mainly exploited the inefficient packing of molecular systems.^{14,15,23,24} For example $[M(en)_3]Cl_3$ ($M = Co(III), Cr(III), Rh(III)$ and $Ir(III)$ and $en =$ ethylenediamine) when crystallised as a racemic mixture (**Figure 5.1-1**), results in columns of $[M(en)_3]Cl_3$ which pack with channels present (**Figure 5.1-1**). Although it was long speculated that these materials were porous^{25,26} it was not until 2003 that desolvation demonstrated no structural change²⁴ with later work by Takamizawa and co-workers demonstrating that this system could include a range of different guests following desolvation.^{14,15}

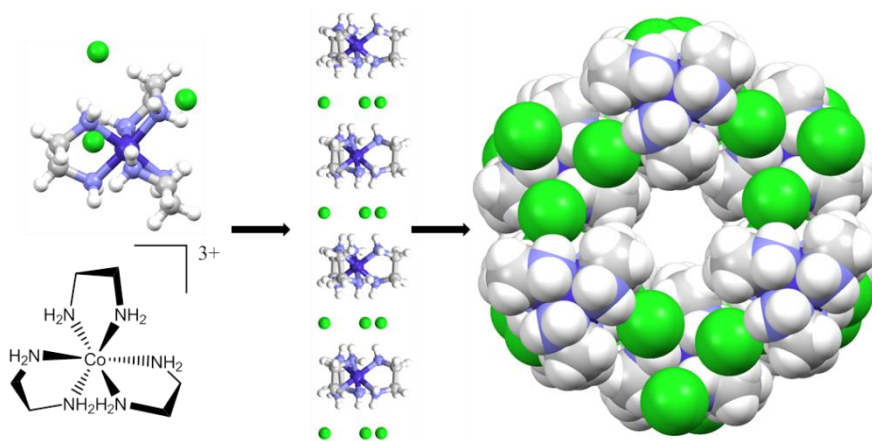


Figure 5.1-1. The packing of columns of $[Co(en)_3] \cdot 3Cl$ and how these columns arrange to form 1D channels in the crystalline state.¹⁵

In more recent years groups have looked at coupling the inefficient packing of molecules with functional groups that will sustain and propagate a porous network.^{16,17,21,27-38} Some of these materials have been referred to as Hydrogen-Bonded Organic Frameworks (HOFs), echoing the acronyms of the well-established coordination polymer field. In many cases these porous molecular materials utilise the core concepts of crystal engineering either intentionally or by

accident. For example, a nice example from Miljanić is a tripyrazole initially intended as a ligand for a MOF (**Figure 5.1-2**).^{16,17} However, the combination of the hydrogen-bonding of the pyrazoles and the electron-rich/electron-poor aromatic rings, leading to complementary $\pi\cdots\pi$ stacking, resulted in a hexagonal channels sustained by intermolecular interactions (**Figure 5.1-2**). The hexagonal network was, in turn, maintained in the absence of the solvent guest and showed high affinity for several chlorofluorocarbons (CFCs).

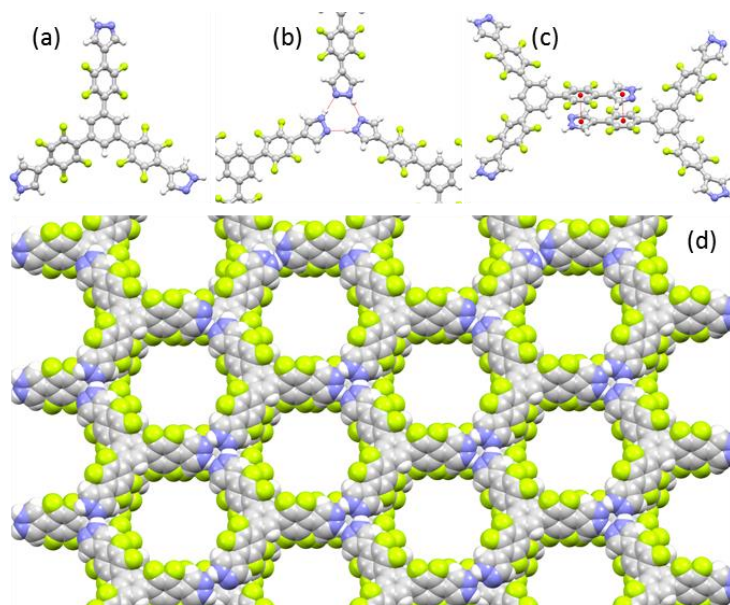


Figure 5.1-2. (a) The tripyrazole system synthesised by Miljanić and coworkers,¹⁶ (b) the hydrogen-bonded trimers, (c) the $\pi\cdots\pi$ stacking and (d) the stable channels produced.

As mentioned earlier development within this field has, in part, progressed through the mining of the CSD³⁹ to identify prospective porous materials.^{18,22} One family of molecules that was identified as being of interest was tris-(4-halophenoxy)-triazine (where the halogen is either a iodine, bromine or chlorine).^{40–52} These compounds were of interest (especially the bromo derivative) due to the three distinct phases that had been reported (**Figure 5.1-3**). The first (the closed phase) consists of offset neighbouring molecules with the halogens involved in a C–X $\cdots\pi$ interactions, and forms a densely packed guest-free phase. The second (the cavity phase) consists of staggered molecules forming a halogen trimer interaction, which results in guest molecules being contained within discrete cavities. The final (the channel phase) and arguably the most interesting of the three forms consists of eclipsed molecules connected by halogen-bonded trimers leading to 1D channels present. Initial work on tris-(4-halophenoxy)-triazines focused on using slow evaporation co-crystallisation to observe which guest-including phases could be formed.^{40,42,44,45} A later study by Saha and coworkers⁵¹ concluded that the cavity phase was more thermal stable than the channel phase.

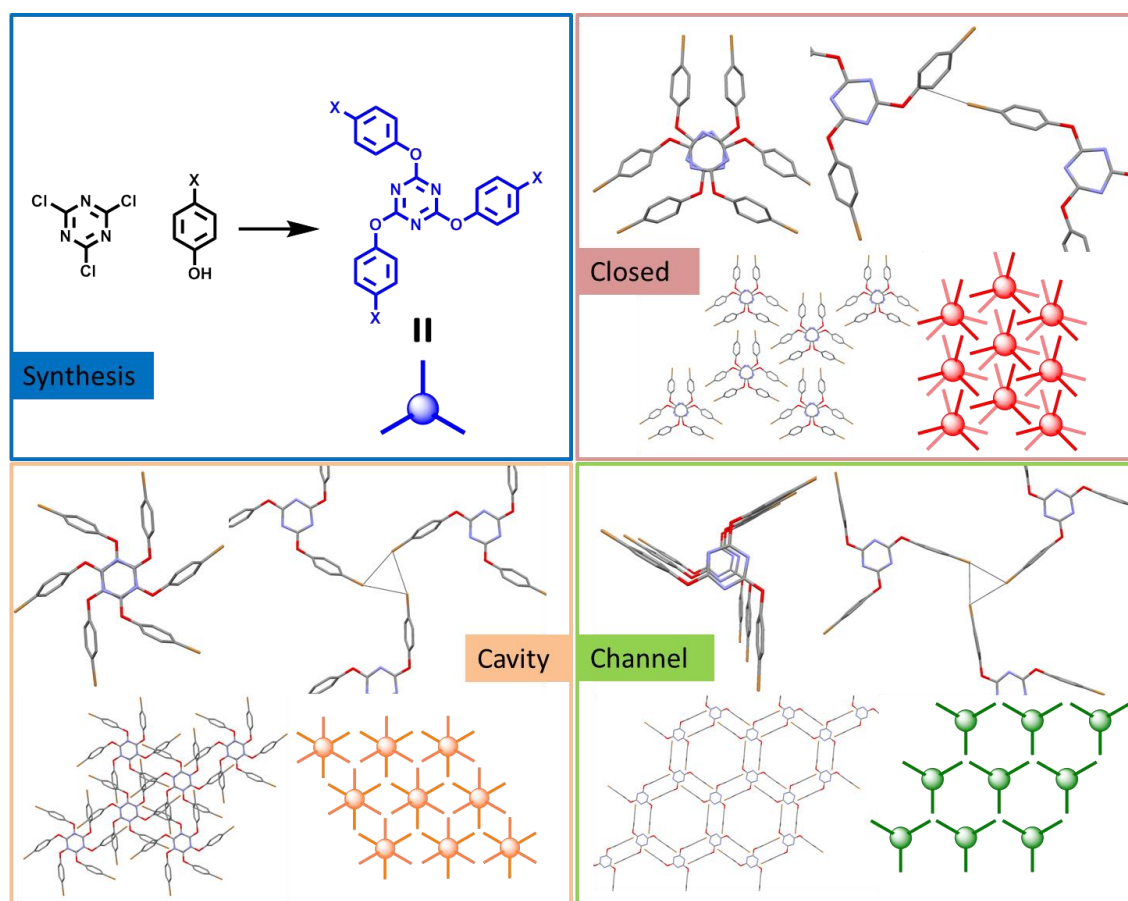


Figure 5.1-3. Synthesis of (tris-(4-halophenoxy)triazine and the three published phases of tris-(4-bromophenoxy)triazine (the closed phase, the cavity phase and the channel phase).

An extension of this work looked at fluorination as a method of improving the thermal stability of these materials.^{53–55} This proved to be successful, but the positions of the fluorine were crucial in maintaining the desired conformation of molecule (**Figure 5.1-4**). A number of guest-included phases of these fluorinated systems have been reported.

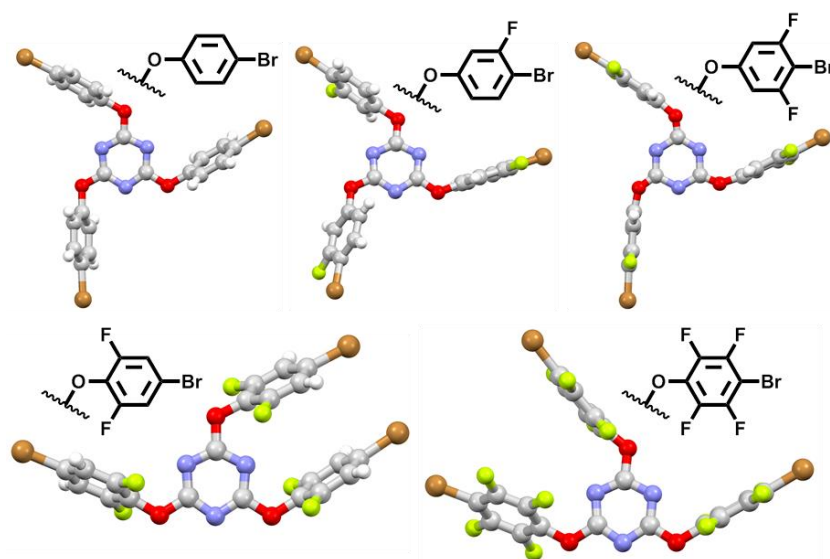


Figure 5.1-4. Conformational change of phenoxy groups upon fluorination of tris-(4-bromophenoxy)triazine as reported by Reichenbacher et al.^{53–55}

5.2 Aims

Despite a range of guest-included phases being reported for the original tris(4-halophenoxy)triazine materials, the majority of the work focused on large polysubstituted aromatics as guest molecules. The aim of the work in this chapter is to focus on tris(4-bromophenoxy)triazine (**5(Br)**) and test this system for the inclusion of a range of (small) solvent molecules. Firstly, a wide range of solvents will be screened through mechanochemical liquid-assisted grinding (LAG) to survey solvents which form the desired guest-included phases. Following this screening a smaller set of samples will be focused on, employing thermogravimetric analysis (TGA) and *in situ* diffraction techniques to determine whether the guest-included phases are stable in the absence of solvent. The experimental plan is summarised in **Figure 5.2-1**.

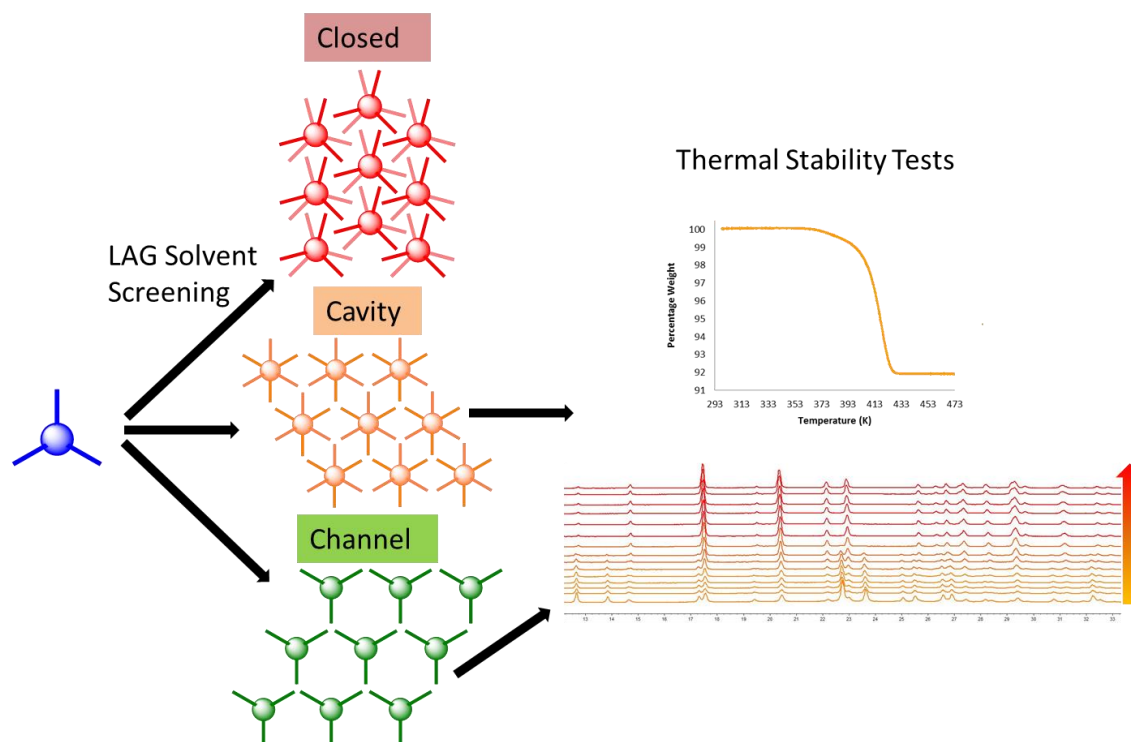


Figure 5.2-1. Summary of the planned studies of **5(Br)**

5.3 Experimental

5.3.1 Synthetic Procedure

All solvents and reagents were purchased from Sigma Aldrich, VWR or Alfa Aesar. Solvents and reagents were used as received without further purification. **5(Br)** was synthesised according to a literature procedure.⁵⁶

4-bromophenol (3.81 g, 22 mmol) and potassium hydroxide (1.22 g, 21.75 mmol) were dissolved in 50 mL acetone cooled to 0 °C. The reaction mixture was stirred at 0 °C for 30

minutes at which point cyanuric chloride (1.00 g, 5.44 mmol) was added. The reaction mixture was stirred at 0 °C for 1 h at which point the ice bath was removed and the white emulsion was stirred at room temperature for 48 h. After stirring for this long duration the reaction mixture was poured over ice, filtered and washed with methanol. A white solid was obtained (2.8113 g, 87.26 %). The synthesis produced a pure product. $^1\text{H NMR}$ (400 MHz, CDCl_3): δ 7.01 (d, 6H, $^{\text{Ar}}\text{CH}$, $J=7.01\text{Hz}$), δ 7.50 (d, 6H, $^{\text{Ar}}\text{CH}$ $J= 7.49\text{Hz}$). $^{13}\text{C NMR}$ (400 MHz, CDCl_3): δ 119.69, 123.32, 132.78, 150.57, 173.59. **MS (ES+)**: m/z 595.8 (MH⁺). Elemental Calcd: C 42.46, H 2.04, N 7.07, Br 40.35 %. Found: C 41.99, H 2.24, N 6.94, Br 39.61 %.

5.3.2 Mechanochemical Liquid-Assisted Grinding (LAG)

Following the successful synthesis of **5(Br)**, a series of solvents were screened by LAG. Samples (*ca.* 100 mg) of **5(Br)** were placed in a steel vessel to which a ball bearing and 100 μL of solvent was added. The vessel was then sealed and attached to a Retsch MM200 Ball Mill. Samples were then ground at a frequency of 25 Hz for 30 min. Following milling, samples were then recovered and analysed by powder X-ray diffraction, the procedure for which is outlined in Section 5.3.3.

Ground samples that exhibited a cavity or channel phases following LAG were stored in sealed sample vials at room temperature. PXRD patterns were recorded periodically over a period of 42 days. Details of the fitting of patterns are outlined in Section 5.3.3.

5.3.3 Powder X-Ray Diffraction of LAG samples

Following LAG experiments samples were analysed by PXRD on a Bruker D8 Advance X-ray powder diffractometer equipped with a LynxEye XE Detector, a Cu-K α sealed-tube source and a variable motorised slit. Samples were placed onto a low-background sample holder and data were collected while rotating the sample at 15 rpm. Data were collected at room temperature between $4^\circ \leq 2\theta \leq 60^\circ$ in steps of 0.02° . The data were then analysed and Pawley fitting⁵⁷ was carried out using the TOPAS program with input files being prepared using jEdit.^{58,59} Details of these fits are outlined in **Table 5.3.3-1** (Appendix 5.8.1). LAG experiments that produced a guest-included phase were retained, stored in glass vials and data recorded periodically over a period of 42 days. Data were recorded and analysed in the same way, details of these fits are outlined in **Table 5.3.3-2** (Appendix 5.8.1).

5.3.4 Crystallisation of **5(Br)** Solvates

Single crystals of solvates (toluene, *p*-xylene, *o*-xylene, *m*-xylene) were obtained by solvothermal methods. This involved sealing *ca.* 200 mg of **5(Br)** with 8 mL of solvent in a 24 mL glass vial with a Teflon lined screw cap. These vials were then placed in an oven at 25 °C and heated to 80 °C at a rate of 1 °C per min. Upon reaching the target temperature the samples were then held at this temperature for 12 h and then cooled to 25 °C at a rate of 0.1 °C per min. Single crystals were tested for thermal stability by variable temperature single-crystal X-ray diffraction, variable temperature powder X-ray diffraction and thermogravimetric analysis.

Single crystals of **5(Br)·CHCl₃** and **5(Br)·DCM** (DCM = dichloromethane) were obtained by solvothermal methods. This involved sealing *ca.* 100 mg of **5(Br)** with 4 mL of solvent (chloroform or DCM) in a 24 mL glass vial with a Teflon lined screw cap. These vials were then placed in an oven at 25 °C at heated to 40 °C at a rate of 1 °C per min. Upon reaching the target temperature the samples were held at this temperature for 12 h and then cooled to 25 °C at a rate of 0.1 °C per min. The DCM crystallisation resulted in a colourless solution; this was cooled to 10 °C for 1 h to allow for crystal growth. Single crystals were tested for thermal stability by variable temperature single-crystal X-ray diffraction, variable temperature powder X-ray diffraction and thermogravimetric analysis. Crystals of **5(Br)·CHCl₃** could also be obtained by slow evaporation of a solution of **5(Br)** in CHCl₃ at room temperature, with crystal formation being observed after 3 days.

5.3.5 Thermogravimetric Analysis

Single crystals of **5(Br)·toluene**, **5(Br)·p-xylene**, **5(Br)·o-xylene**, **5(Br)·m-xylene**, **5(Br)·CHCl₃** and **5(Br)·DCM** obtained by solvothermal crystallisation, were filtered under vacuum and washed with the crystallisation solvent. Samples were then placed in a ceramic boat of a Perkin-Elmer Pyris1 Thermogravimetric Analyser. Following a 5 min dwell period at 25 °C samples were then heated under N₂ to 200 °C at a rate of 2°C per min with the mass loss being recorded.

5.3.6 In situ Powder X-Ray Diffraction Studies during Variable Temperature

Single crystals of the six solvates were filtered under vacuum and washed with the solvent used in the crystallisation. Single crystals were then ground and packed in to a 0.7 mm borosilicate capillary. The capillary was then centred on a D8 Advance X-ray powder diffractometer equipped with a Cu-K_α sealed-tube source and a focusing Göbel Mirror operating in capillary mode. The diffractometer was also equipped with an Oxford Cryosystems Cryostream Plus 700 series, allowing for variable temperature analysis to be carried out. Data were collected at a series of temperatures, after increasing temperature (at 360 K/hour) and a 15-min dwell period at the temperature prior a 15-min collection scan in the range 5 ° ≤ 2θ ≤ 60 ° (step size of 0.02 °, sample rotation 30 rpm).

Data were fitted initially by Pawley refinement⁵⁷ using the TOPAS program.^{58,59} Data were then fitted by Rietveld refinement⁶⁰ using TOPAS.^{58,59} Atom positions of **5(Br)** were obtained from single crystal data. Solvent molecules (apart from **5(Br)·CHCl₃**) were fitted using a rigid body, allowing for refinement of position and occupancy of the solvent. Refinement details are outlined in **Table 5.3.6-1-12** (Appendix 5.8.2).

5.3.7 In situ Single-Crystal Diffraction Studies during Variable Temperature

Single crystals of the six obtained solvates were analysed pre- and post-heating on either a Bruker D8 Diffractometer equipped with a IμS Microfocus Cu-K_α sealed-tube source and a Photon 100 CMOS (Complementary Metal Oxide Sensor) Detector with shutterless capability or a Smart Apex-2 CCX Diffractometer equipped with the graphite monochromator Mo-K_α sealed-tube source. Each diffractometer was equipped with an Oxford Cryosystems Cryostream device. A single-crystal of each solvate were selected directly from the mother liquor and glued onto a glass fibre with epoxy resin ensuring crystals were not encapsulated in glue. A full intensity data set was recorded initially at 100 K before the crystal was heated (360 K/hour) to a temperature corresponding to (solvent) mass loss observed in the TGA. The

crystal was left to dwell at the desired temperature for 20 min before being cooled back down to 100 K and a second full intensity data set was recorded. In the case of **5(Br)·m-xylene** two heated temperatures were examined (353 K and 413 K) in an attempt to monitor the two-stage mass loss observed in the TGA. In the case of **5(Br)·DCM**, **5(Br)·o-xylene** and **5(Br)·m-xylene** the heating of single crystals resulted in complete degradation of the single crystal meaning that characterisation of the desolvated phase was not possible.

Data were corrected for absorption using empirical methods (SADABS) based on symmetry-equivalent reflections and measurements at different azimuthal angles.^{61–63} Structure solution was achieved by direct methods and the crystal structure was refined using full-matrix least-squares against weighted F^2 values using SHELXL⁶⁴ within Olex2.⁶⁵ Non-hydrogen and non-disordered atoms were refined anisotropically. Hydrogen atoms were placed in calculated positions, refined to idealized geometries (riding model) and assigned a fixed isotropic displacement parameter. Details of the data collection are outlined in **Tables 5.3.7-1** and **Table 5.3.7-2** (Appendix 5.8.3).

Disorder of the aromatic rings was observed in the toluene and *p*-xylene solvates. The two ring orientations were refined with occupancies of 46(4):54(4) and 45(4):55(4) (for the initial and post 333 K structures of **5(Br)·toluene**, respectively) and occupancies of 48(3):52(3) and 58.9(17):41.1(17) (for the initial and post-333 K structures of **5(Br)·p-xylene**).

The solvent cavity contained diffuse electron density which could not be modelled confidently as solvent molecules (apart from in the case of **5(Br)·CHCl₃**). Therefore PLATON SQUEEZE^{66,67} was employed to estimate the unassigned electron density and remove its contribution to the diffraction intensities.

5.4 Results and Discussion

5.4.1 Synthesis

The synthesis of **5(Br)** occurs under mild conditions in good yield with ¹H NMR spectra being consistent with the previous report⁵¹ and powder pattern of the as-synthesised material matching the previously reported closed phase. Occasionally excess starting material was observed in the NMR spectrum of the crude product. This can be removed by recrystallization from chloroform, which forms the previously unreported chloroform solvate (*vide infra*), and returns to the closed (solvent-free) phase upon drying.

5.4.2 Mechanochemical Solvent Screening

In order to screen a large series of prospective solvents for formation of solvates, **5(Br)·solvent**, LAG was employed. This involved grinding *ca.* 100 mg of **5(Br)** with 100 μ L of solvent for 30 min at 30 Hz. These mechanochemical experiments proved to be a useful screening tool in identifying solvents of interest. The LAG experiments demonstrated a clear trend between the solvent and the ability to form particular inclusion phases. As observed in previously reported work,⁵¹ the channel and cavity phases were formed when larger aromatic or halogenated solvents (toluene, xylenes and DCM) were used. Smaller sized solvents (alcohols, acetonitrile acetone etc.) were ineffective at producing a solvent-included phase.

The use of 100 μL of solvent yielded a pure phase in all cases except the LAG experiment with *m*-xylene. Grinding with *m*-xylene resulted in a channel phase as the major product, but in the PXRD pattern, each peak had a shoulder which, when stored at room temperature for 11 days, resulted in two defined peaks (**Figure 5.4.2-1**). These patterns could be fitted to two channel phases with only a small difference in their unit cell parameters (Appendix 5.8.1). It is unclear what the cause of this observation is, but it may be due to channels being able to swell or contract dependent on the quantity of solvent present. This would require further variable-solvent-volume LAG experiments to see whether solvent quantity is a factor.

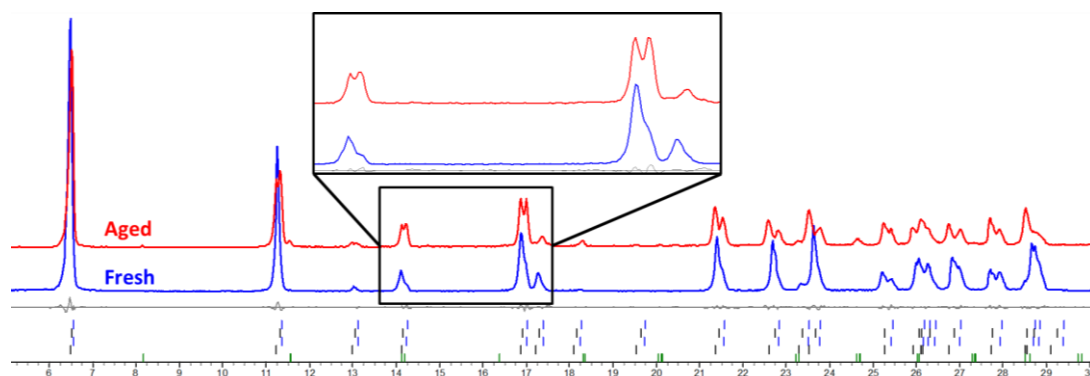


Figure 5.4.2-1. Powder pattern of **5(Br)-*m*-xylene** showing the pattern of the as-synthesised material (blue) and of an aged (stored in air for 11 days) sample (red). Inset: The initial pattern has shoulders on peaks which then become separate peaks in the aged sample.

The application of a LAG process also provided the opportunity to identify previously unreported inclusion phases. This was demonstrated in the LAG experiment with chloroform. Grinding **5(Br)** with chloroform resulted in a phase with the same $P6_3/m$ symmetry as the channel structure, but with shorter *a*- and *b*-axes and a longer *c*-axis. Previous reports indicated that slow evaporation of chloroform produced the channel phase, although the volatility of the solvent meant that this phase was not fully characterised.^{40,42}

The samples that formed an inclusion phase were then kept and stored at *ca.* 20 °C with PXRD patterns being recorded periodically to monitor how stable the inclusion phases were when stored at room temperature. The toluene and *p*-xylene samples, which were initially the channel phase, changed to the closed phase within 11 and 13 days, respectively. The phase transformation from channel to closed is believed to be as a result of solvent loss, leading to the channels closing. The chloroform-containing phase also exhibits a similar open-to-closed transformation, fully closing after 23 days.

The *o*-xylene and *m*-xylene solvates, which formed the channel phase, appear to partially close when stored at room temperature. The partial closing occurs through a phase transformation from the channel phase to the cavity phase (after 4 and 11 days for *o*- and *m*-xylene, respectively). After storage in air at room temperature for 13 days the *m*-xylene solvate shows evidence of formation of the closed phase, whereas the *o*-xylene solvate remains as the pure cavity phase after 23 days. Further ageing (a maximum of 35 and 42 days for *o*- and *m*-xylene, respectively) results in the *m*-xylene solvate becoming mainly the closed phase, but the *o*-xylene solvate remains in the cavity phase. It seems that storing the solvated materials at room temperature for an extended period yields a secondary included phase. Previous work on

5(Br)⁵¹ had determined that slow evaporation from solutions of **5(Br)** in a variety of solvents (DCM, tetrahydrofuran and hexamethylbenzene) yielded both channel- and cavity-phase single crystals. The LAG experiments suggest that, for *o*-xylene and *m*-xylene, the channel phase is a kinetic product and the cavity phase is the thermodynamic product. The cavity phase can still be observed after leaving the LAG-synthesised material in air at room temperature for a month, supporting the previous conclusion that the cavity phase is more stable than the channel phase.⁵¹

The LAG experiment in DCM yielded a pure cavity phase initially, which became a mixture of all three phases (cavity, channel and closed) after just four days. This either suggests that the channel phase is the thermodynamic (solvated) product or that the inaccessibility of the cavities requires the material to convert to the channel phase in order to desolvate. Further ageing (a maximum of 35 days) saw the cavity phase disappearing and closed phase becoming the major phase, suggesting that solvent loss occurs via the channel phase as an intermediate.

In conclusion the grinding experiments were a useful screening technique allowing for quick identification of solvents of interest. These experiments also identified an as yet unpublished chloroform including phase. Ageing studies revealed discrepancies in the stability, at room temperature, of the different solvates. The toluene, *p*-xylene and chloroform phase forming the closed phase after two weeks. The *o*-xylene, *m*-xylene and DCM phase on the other hand changed phase to the alternate inclusion phase, prior to fully desolvating. This supports the observation that DCM solvates consist of the both channel and cavity phase upon slow evaporation of solvent,⁵¹ however this is the first demonstration that these transformations can occur in the solid state.

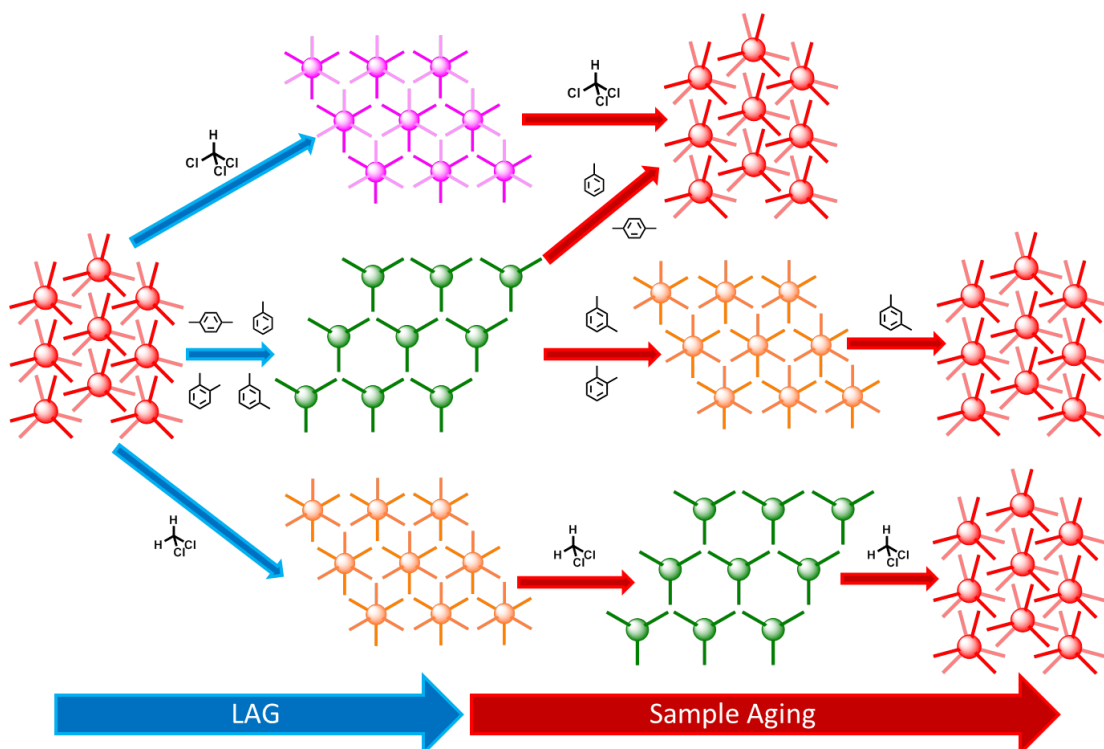


Figure 5.4.2-2. Summary of the observed transitions under different solvent environments upon LAG and upon subsequent storage of the LAG-synthesised samples in air at room temperature (ageing). Solvent molecules shown with each arrow indicate the solvents involved in each transition. Blue arrows indicate solvent addition and red arrows indicate solvent loss.

5.4.3 Structural Characterisation and Thermal Stability Tests of **5(Br)·CHCl₃**

As stated in Section 5.4.2 the LAG experiment with chloroform resulted in a previously unreported phase. This prompted growing of single crystals of this phase either by slow evaporation or solvothermal techniques (Section 5.3.4). Single-crystal diffraction enabled structure determination, revealing some similarities to the previously reported channel and cavity phases. This inclusion phase crystallises in the same space group, $P6_3/m$, as the channel phase, but the orientation of neighbouring **5(Br)** molecules is staggered similar to the cavity phase with CHCl_3 solvents situated in smaller channels (**Figure 5.4.3-1**).

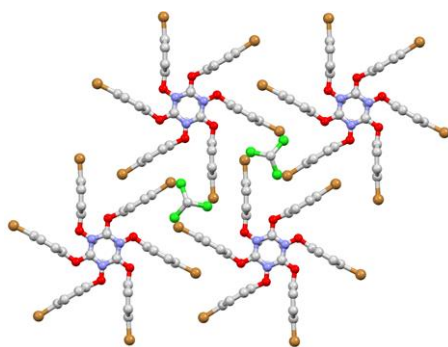


Figure 5.4.3-1. Packing observed in **5(Br)·CHCl₃**. C, grey; N, blue; O, red; Br, brown; Cl, green.

In the channel and cavity phases the bromine atoms are involved in a $\text{Br}\cdots\text{Br}\cdots\text{Br}$ halogen-bonding trimer (**Figure 5.4.3-2**). In the chloroform solvate (**5(Br)·CHCl₃**) this trimer is replaced by a $\text{Br}\cdots\pi$ halogen-bonded trimer with $\text{C}-\text{Br}\cdots\text{C}_{\text{para}}$ distance of 3.509(4) Å and angle of 157.0(2)° (**Figure 5.4.3-2**). A potential reason for the difference in the halogen-bonding could be due to a new halogen-bonding interaction between the aromatic rings and the chlorine of the chloroform ($\text{C}-\text{Cl}\cdots\text{C}_{\text{ipso}}$ 3.344(4) Å, 161.4(4)°) (**Figure 5.4.3-2**).

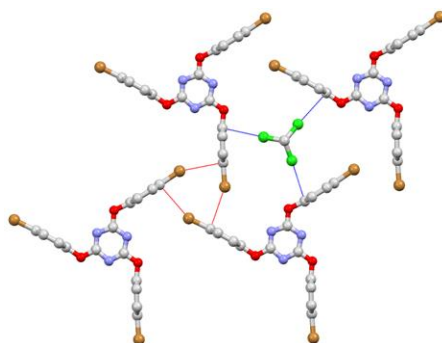


Figure 5.4.3-2. Single layer of **5(Br)·CHCl₃** showing the halogen-bonding interactions. Colour scheme consistent with **Figure 5.4.3-1**; $\text{C}-\text{Br}\cdots\text{C}_{\text{para}}$ interaction, red dashed lines; $\text{C}-\text{Cl}\cdots\text{C}_{\text{ipso}}$ interaction, blue dashed lines

The chloroform molecule was successfully modelled, the three chlorine atoms being situated on a mirror plane resulting in two half-occupancy positions of the disordered carbon and hydrogen atoms, establishing a 1:1 **5(Br):CHCl₃** stoichiometry. The chloroform solvent is situated in a previously unobserved cavity. In the previously published cavity phases,^{46,50,51} solvent molecules were observed in cavities between neighbouring staggered **5(Br)** molecules (**Figure 5.4.3-3**), often with the solvent being disordered, in some cases preventing direct

modelling and requiring the application of PLATON SQUEEZE.^{66,67} In the case of **5(Br)·CHCl₃** the chloroform molecule is also situated in a cavity with bromine atoms situated above and below, unlike the cavities between triazine rings in other solvates previously reported^{46,50,51} (**Figure 5.4.3-3**).

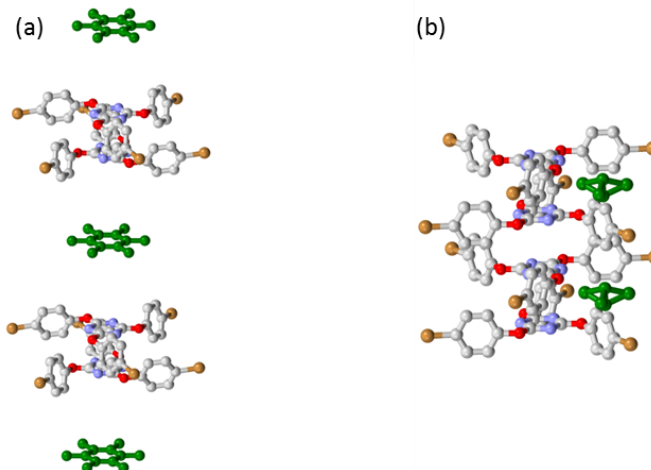


Figure 5.4.3-3. Solvent locations of the previously reported (a) **5(Br)·hexamethylbenzene**⁵¹ in comparison with (b) **5(Br)·CHCl₃** relative to pairs of staggered **5(Br)** molecules. Colour scheme consistent with **Figure 5.4.3-1**; solvent, green.

Following structural characterisation at 100 K the single crystal of **5(Br)·CHCl₃** was heated to 298 K (360 K/hour) and a full data set was recorded. The room-temperature data collection displayed the same **5(Br)·CHCl₃** phase as the 100 K measurement, prompting the single crystal to be heated to 333 K (360 K/hour). Following heating to 333 K the sample was returned to 298 K at which point sufficient frames to determine the unit cell dimensions were recorded. This revealed a phase transformation to the *R3c* closed phase, prompting a full data collection at 100 K. Despite the sample suffering slight degradation from heating, a crystal structure could be determined. The initial structure solution modelled, with constraints, the closed phase although this solution left a large quantity of unmodelled electron density (**Figure 5.4.3-4**). The residual electron density suggested positional disorder of the entire **5(Br)** molecule. It was possible, with restraints, to construct a two-component disorder model (**Figure 5.4.3-4**), but unfortunately the poor data quality prevented satisfactory convergence of the least-squares refinement with the displacement parameters for a few atoms refining to non-positive definite values.

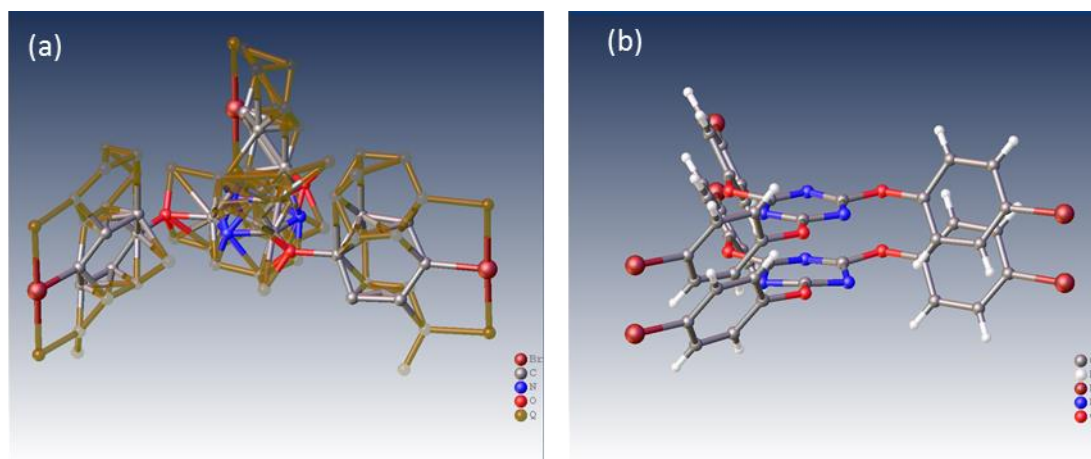


Figure 5.4.3-4. (a) Structure model with residual electron density peaks from the initial structure solution for $5(\text{Br})\cdot\text{CHCl}_3$ and (b) structure model showing complete positional disorder of the $5(\text{Br})$ molecules. Colour scheme C, grey; O, red; N, blue; Br, maroon; H, white.

A sample of $5(\text{Br})\cdot\text{CHCl}_3$ was also analysed by TGA. The TGA showed a single mass loss starting at 333 K with a plateau at 353 K. This mass loss of 16.5 % is attributed to 1 CHCl_3 molecule per molecule of $5(\text{Br})$. This mass loss is consistent with the single-crystal-to-single-crystal phase transformation observed when a crystal of $5(\text{Br})\cdot\text{CHCl}_3$ was heated to 333 K.

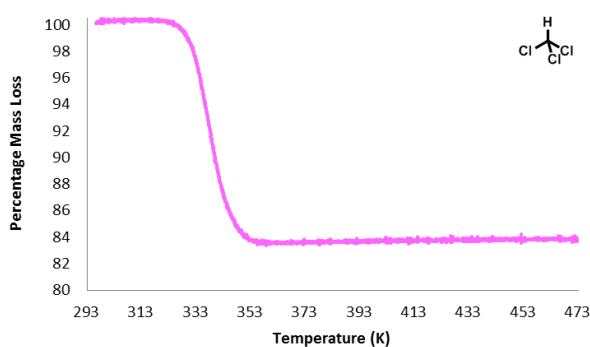


Figure 5.4.3-5. Thermogravimetric analysis of $5(\text{Br})\cdot\text{CHCl}_3$.

Following the TGA analysis a powder sample of $5(\text{Br})\cdot\text{CHCl}_3$ was investigated *in situ* using variable temperature PXRD. The sample was exposed to increasing temperature with data collected at each temperature step. Visual inspection of the PXRD patterns reveals peaks diminishing and increasing in intensity (**Figure 5.4.3-6**).

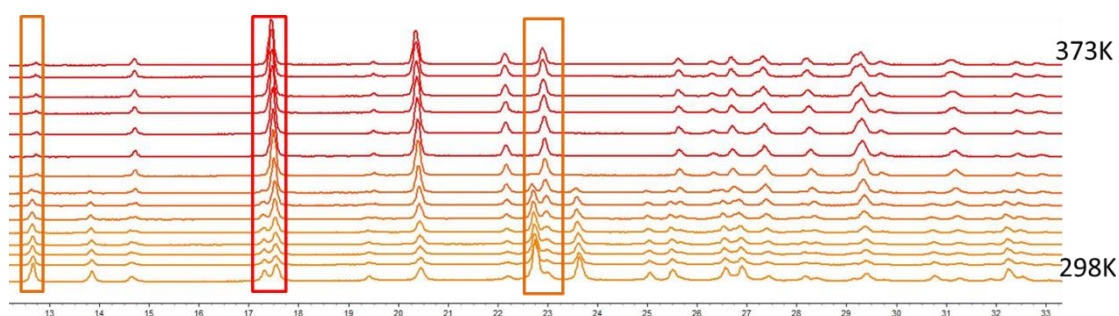


Figure 5.4.3-6. Stacked PXRD patterns from the *in situ* heating study of $5(\text{Br})\cdot\text{CHCl}_3$

The powder patterns when fitted initially by Pawley⁵⁷ and then Rietveld⁶⁰ techniques in TOPAS,^{58,59} with atom coordinates from single-crystal structures used to provide the structure model for the latter. The initial 298 K pattern showed presence of both the newly determined **5(Br)·CHCl₃** phase (69.1(4) %) and the guest-free (closed) phase (30.9(4) %). The presence of the latter is believed to be as a result of partial desolvation during sample preparation. As the temperature was increased, the **5(Br)·CHCl₃** phase diminished (**Figure 5.4.3-7**) until a phase-pure guest-free phase was observed at 347 K. The complete conversion was at a slightly higher temperature than the conversion observed through a single-crystal-to-single-crystal process (333 K), but considering the phase conversion is observed from room temperature upwards it is conceivable that full conversion would be observed for a sample stored at a lower temperature for a longer duration, as observed in the ageing studies of the LAG-synthesised sample.

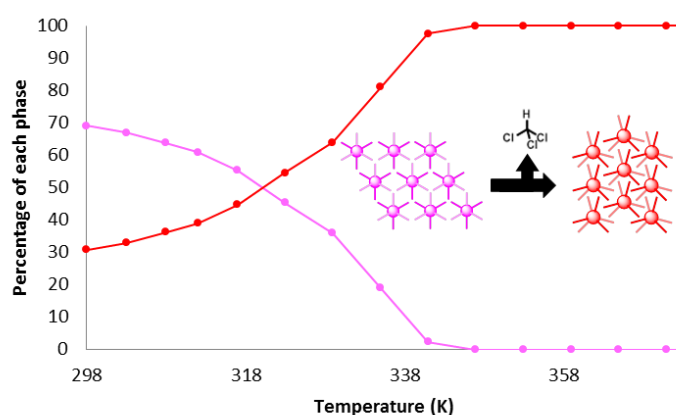


Figure 5.4.3-7. Percentage of the **5(Br)·CHCl₃** phase (pink) and the closed **5(Br)** phase (red) upon heating of a powder sample, as determined by Rietveld refinement.⁶⁰

5.4.4 Thermal Stability Tests of **5(Br)·toluene** and **5(Br)·p-xylene**

The LAG synthesis experiments with toluene and *p*-xylene resulted in similar observations, so these materials will be discussed together.

Firstly, the stability of samples of **5(Br)·toluene** and **5(Br)·p-xylene** was tested by TGA. This showed mass loss from the initial 5 min dwell period at 298 K and continuous mass loss being observed on heating, before a plateau at 353 K at 87.2 % and 91.2 % mass for **5(Br)·toluene** and **5(Br)·p-xylene**, respectively. These masses loss correspond to roughly 1 toluene and ½ *p*-xylene molecule per **5(Br)** molecule.

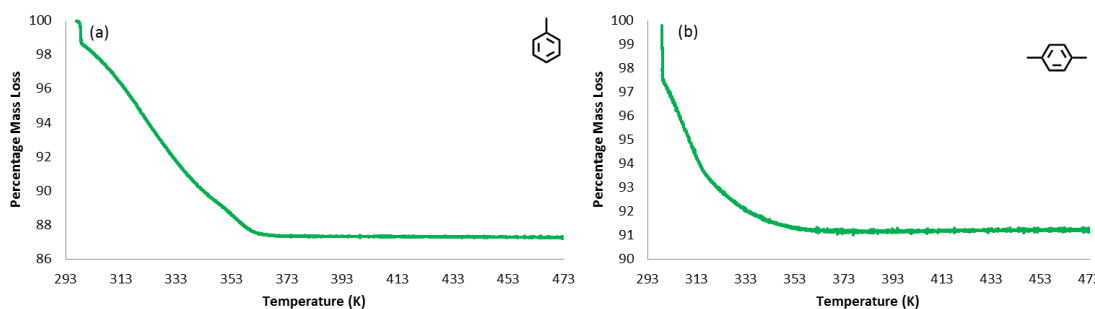


Figure 5.4.4-1. Thermogravimetric analysis of (a) **5(Br)·toluene** and (b) **5(Br)·p-xylene**

Single-crystal and powder samples of **5(Br)·toluene** and **5(Br)·p-xylene** were also investigated *in situ* at variable temperature in an attempt to monitor the stability of both powder and single-crystal samples. The powder heating studies of both **5(Br)·toluene** and **5(Br)·p-xylene** initially started with mixed-phase patterns indicating the channel and closed phases (**Figure 5.4.4-2**). The presence of both phases believed is to be as a result of solvent loss at room temperature, consistent with the loss observed in the TGA. Upon heating both, **5(Br)·toluene** and **5(Br)·p-xylene** result in the channel phase diminishing and the closed phase increasing at moderately low temperatures, with the both materials becoming phase-pure closed phase at 347 and 341 K for **5(Br)·toluene** and **5(Br)·p-xylene**, respectively (**Figure 5.4.4-2**).

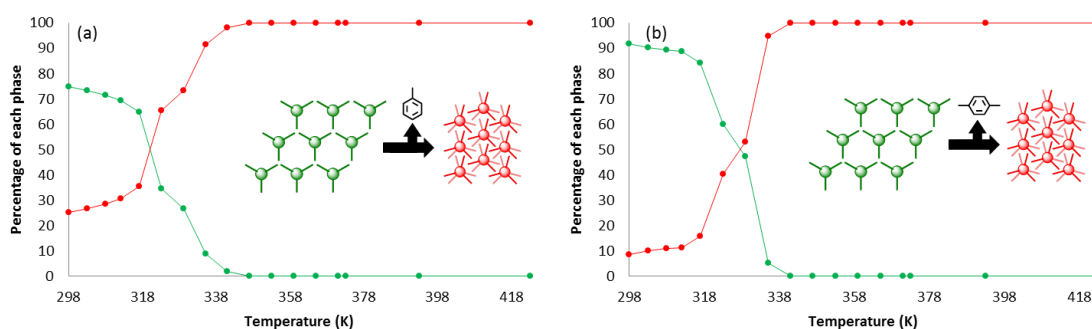


Figure 5.4.4-2. Percentage of the open phase (green) and the closed phase (red) upon heating of powder samples of (a) **5(Br)·toluene** and (b) **5(Br)·p-xylene**, as determined by Rietveld refinement.⁶⁰

Initial single-crystal *in situ* heating studies involved heating a single-crystal to a specific temperature, holding the temperature for 15 mins and then returning to 298 K and determining unit cell dimensions to ascertain the point at which the crystal degraded. It was observed that **5(Br)·toluene** maintained the channel phase until 358 K with heating to 378 K leading to the sample becoming polycrystalline. The **5(Br)·p-xylene** was stable up to 378 K, but similar polycrystallinity was observed at 398 K. This demonstrates that single crystals of the channel phase of both **5(Br)·toluene** and **5(Br)·p-xylene** remain stable to higher temperatures than the powder studies (347 and 341 K). This prompted a second heating study on these systems in which a full collection was recorded (at 100 K) followed by heating each crystal to 333 K, dwelling at this temperature for 20 min, cooling back to 100 K and collecting a full data set. In both cases single-crystals of **5(Br)·toluene** and **5(Br)·p-xylene** retained the channel phase. Comparison of the residual electron density (using PLATON SQUEEZE^{66,67}) revealed comparable quantities electron density present in the channels before and after heating (**Table 5.4.4-1**), despite the crystals being heated to a temperature corresponding to the mass losses observed in the TGAs. This would suggest that there is a particle-size effect in relation to guest retention.

Table 5.4.4-1. Table of the determined void space and electron counts of **5(Br)·toluene** and **5(Br)·*p*-xylene** as determined by PLATON SQUEEZE^{66,67}

Solvent	Treatment	Solvent Accessible void (Å ³)	Electron Count per unit cell
Toluene	Initial	411	134
	Post 333 K	411	133
<i>p</i> -xylene	Initial	422	135
	Post 333 K	463	223

5.4.5 Thermal Stability Tests of **5(Br)·*o*-xylene** and **5(Br)·DCM**

Solvothermal crystallisation of **5(Br)·*o*-xylene** and **5(Br)·DCM** resulted in pure cavity phases being obtained. This observation is consistent with the LAG synthesis of **5(Br)·DCM**, but is inconsistent with respect to the LAG synthesis of **5(Br)·*o*-xylene**. This would suggest that the thermodynamic product in excess solvent and with a long heating period (12 h) is the cavity phase for these two solvents.

Thermogravimetric analysis of these two cavity phases saw a maintained mass at low temperature with a single mass loss being observed in both cases (**Figure 5.4.5-1**). The mass loss is observed at initially at 333 K and 370 K (for **5(Br)·DCM** and **5(Br)·*o*-xylene**, respectively) with a plateau in mass at 353 K and 433 K, and final masses of 87.7 % and 91.9 % for **5(Br)·DCM** and **5(Br)·*o*-xylene**, respectively. The final masses loss corresponds to ca. 1 DCM or ½ *o*-xylene molecule per molecule of **5(Br)**. These TGAs are consistent with the previous work⁵¹ on this inclusion material, with the cavity phase exhibiting a higher thermal stability than the channel phases (**5(Br)·toluene** and **5(Br)·*p*-xylene**).

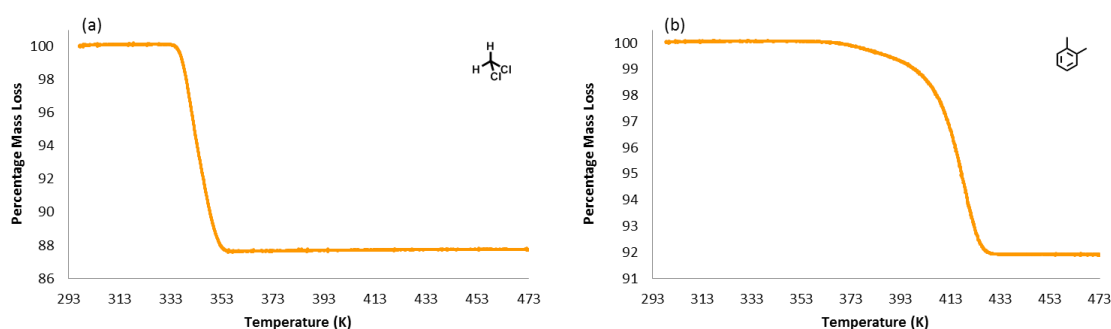


Figure 5.4.5-1. Thermogravimetric analysis of (a) **5(Br)·DCM** and (b) **5(Br)·*o*-xylene**

Variable temperature single-crystal and powder diffraction studies were carried out on these materials. The powder studies confirmed the stability of these two cavity phases with the samples remaining phase-pure up to 308 K and 365 K for **5(Br)·DCM** and **5(Br)·*o*-xylene** respectively. Further heating revealed a transformation to the closed phase, with the DCM-containing material being phase-pure closed phase at 341 K and the *o*-xylene-containing material remaining a mixture of cavity and closed phases at the end of the study (423 K) (**Figure 5.4.5-2**).

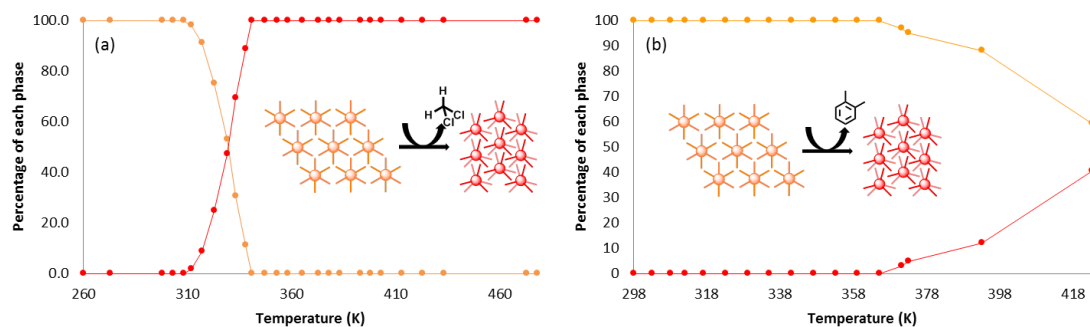


Figure 5.4.5-2. Percentage of the cavity phase (orange) and the closed phase (red) upon heating of powder samples of (a) **5(Br)·DCM** and (b) **5(Br)·o-xylene**, as determined by Rietveld refinement.⁶⁰

Single-crystal heating studies were attempted on these two inclusion phases. These studies involved recording data, initially, at 100K before the crystals were heated to temperatures consistent with the mass losses observed in the TGA analysis (353 K and 413 K for **5(Br)·DCM** and **5(Br)·o-xylene**, respectively). Heating the single crystals to these temperatures resulted in degradation of the sample, with insufficient reflections being recorded to determine the unit cell. The degradation suggests that the cavity-to-closed phase transformation does not occur via a single-crystal-to-single-crystal process in contrast to that observed for **5(Br)·CHCl₃**.

5.4.6 Thermal Stability tests of **5(Br)·m-xylene**

Solvothermal crystallisation of **5(Br)** in *m*-xylene also yielded crystals, which were in turn analysed by TGA and *in situ* variable temperature diffraction techniques. The TGA analysis (**Figure 5.4.6-1**) revealed in two distinct mass losses, the first 1.5 % mass loss is observed from the start (298 K) to 353 K, the second loss of 7.5 % starts at 373 K with a plateau at 413 K, resulting in a final mass of 91.0 % of the original. These two mass loss steps equate to roughly 0.55 of an *m*-xylene molecule per molecule of **5(Br)**. This two-stage loss suggests two solvent environments one being more strongly held than the other.

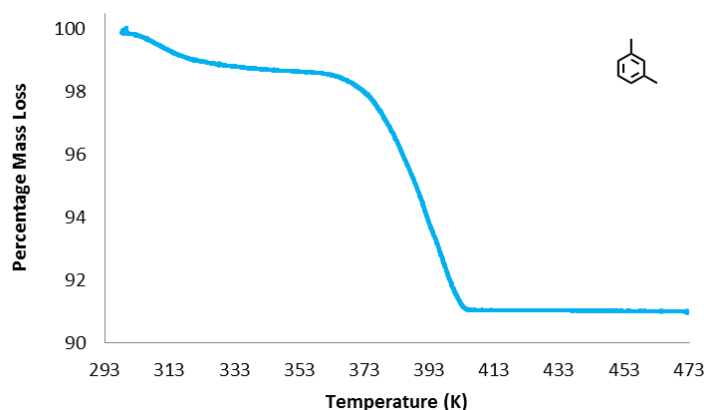


Figure 5.4.6-1. Thermogravimetric analysis of **5(Br)·m-xylene**

A sample of the **5(Br)·m-xylene** crystals was then tested for stability by variable temperature PXRD (Appendix 5.8.2). The initial powder pattern corresponded to a mixture of the channel and cavity phases. This explains the two-stage mass loss observed in the TGA with the channel phase losing solvent at lower temperatures than the cavity phase as observed in Section 5.4.3

and Section 5.4.4. When this powder was subjected to increasing temperatures it was observed that peaks for the channel phase decreased in intensity but rather than seeing evidence of formation of the closed phase (as observed in Section 5.4.3) peaks for the cavity phase increased in intensity. The channel phase had completely disappeared by 373 K, at which point peaks indicating the formation of the closed phase are observed (**Figure 5.4.6-2**).

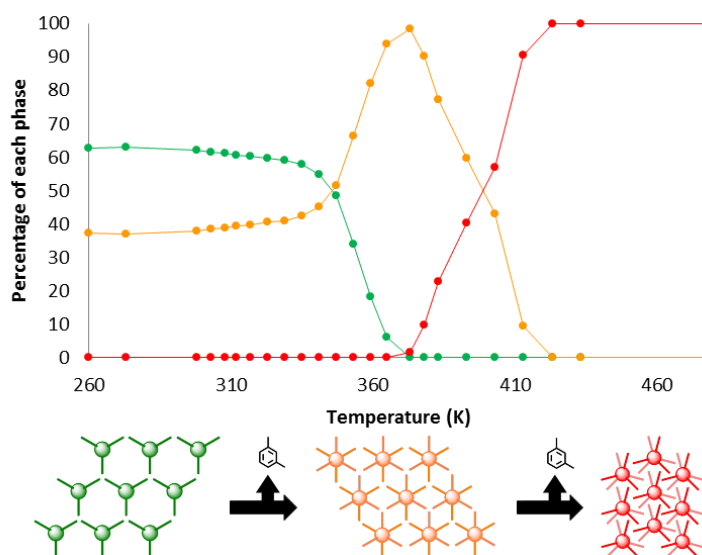


Figure 5.4.6-2. Percentage of the channel phase (green), the cavity phase (orange) and the closed phase (red) upon heating of powder sample **5(Br)·m-xylene**, as determined by Rietveld refinement.⁶⁰

This two stage phase transformation is consistent with the observation of the room-temperature ageing studies. Aging the LAG-synthesised material resulted in formation of a pure channel phase material, which upon ageing underwent a transition into a mixture of all three phases, before becoming mainly the closed phase after 1 month of storage at room temperature.

A single-crystal heating study was also attempted for **5(Br)·m-xylene** with two heating steps being recorded (353 K and 413 K) in an attempt to observe the two-stage phase transformation. Following heating to 353 K a significant reduction in diffraction intensity and resolution was observed. It was, however, possible to determine unit cell parameters, which corresponded to the channel phase. Further heating to 413 K resulted in complete degradation of the sample and therefore unit cell parameters could not be determined.

5.5 Conclusions

This chapter focused on the previously reported organic inclusion compound tris-(4-bromophenoxy)triazine (**5(Br)**). This compound had already been reported to possess three distinct phases. This work demonstrated that these phases could be accessed with the application of liquid-assisted grinding (LAG). These LAG experiments proved a useful solvent screening tool as well as identifying a fourth, previously unreported, solvent-included phase (**5(Br)·CHCl₃**). This previously unreported phase features chloroform solvent in cavities between bromine functional group, with a C–Br··· π trimer being observed instead of the C–Br···Br trimers present in the previously reported inclusion phases.

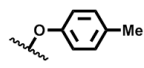

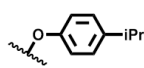

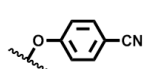
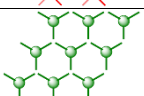
These LAG experiments identified six solvents that yielded inclusion phases. These solvated samples were then stored at room temperature in air with their PXRD patterns being recorded periodically. These ageing studies revealed that three solvents (CHCl_3 , toluene and *p*-xylene) were readily lost over a two week period, with a transition from the solvent-included phase to the closed phase being observed. Material containing the other two xylenes (*m*-xylene and *o*-xylene) underwent a transition from the channel phase to the cavity phase, with the *o*-xylene-containing material remaining stable at this point and the *m*-xylene-containing material desolvating further to generate the closed phase. The DCM-containing material appeared to transform from the cavity phase to the channel phase, followed by converting to the closed phase.

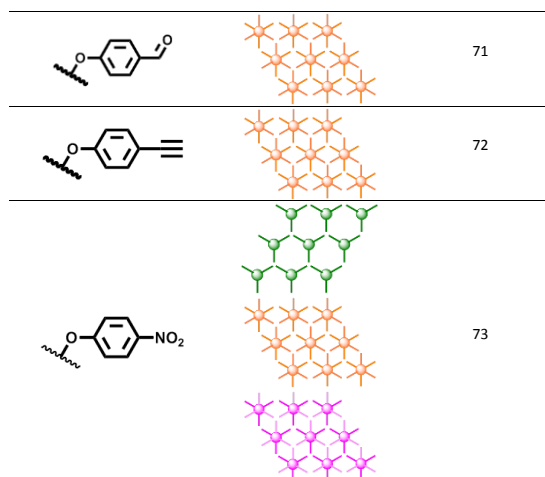
Following these ageing experiments the thermal stability of fresh material obtained solvothermally was tested by TGA and *in situ* variable temperature diffraction techniques. These experiments revealed that the phases with 1D channels (toluene and *p*-xylene) had poor thermal stability, with solvent loss occurring at low temperature (from 298 K), resulting in a phase transformation from the channel phase to the closed phase. The solvates formed as the cavity phase (DCM and *o*-xylene) were more thermally stable, with solvent loss resulting in a phase transition from cavity phase to closed phase from 312 K and 371 K for DCM and *o*-xylene, respectively. Crystals grown from *m*-xylene by solvothermal methods resulted in a mixture of channel and cavity phases. When this mixture was heated it revealed a two-step phase transformation from the channel phase to the cavity phase and finally to the closed phase upon further heating. All materials were tested for single-crystal desolvation with a successful transformation being obtained for **5(Br)·CHCl₃**, but heating of single crystals of the other solvates resulting in loss of single-crystal crystallinity.

5.6 Future Work

This work has demonstrated that mechanochemistry can be successfully employed in screening solvents to form solvated forms of **5(Br)**. This work could therefore be extended further by screening more solvents or solvent mixtures. These LAG experiments could also be extended to analogous molecules with different *para* functionality. As mentioned in the introduction, examples of inclusion phases of the chloro^{40,41,43,44} and iodo^{46,50,52} functionalised tris(4-halophenoxy)triazine have been reported, but there are analogous phases observed with a range of functional groups (Table 5.6-1).

Table 5.6-1. Summary of the observed phases of para-functionalised tris-(phenoxy)-triazines

Functional Group	Phase	Reference
		68,69
		52
		70



Therefore an extension of this work could involve producing a series of tris-(phenoxy)triazines with a range of *para* substituents. The LAG synthesis experiments could be used as a solvent screening tool, followed by thermal stability tests. This work could also look at fluorination as a method of improving thermal stability to extend the work of Reichenbacher et al.^{53–55}

Alternatively, this work has demonstrated that solvent-included phases could be produced solvothermally and mechanochemically, with heating studies showing that conversion back to the original closed phase can occur. This currently categorises **5(Br)** as a 1st generation porous material,² although whether these materials display 3rd generation porous properties is not yet disproven. In light of this, preliminary vapour-phase inclusion experiments were carried out (**Figure 5.6-1**). This involved loading a capillary with the as-synthesised powder and storing it in an environment that contained a small quantity of solvent. These studies resulted in phase transformations being observed in the case of CHCl_3 and *m*-xylene solvent vapour after 48 hours and 13 days, respectively. This observation suggests the characteristics of a 3rd generation porous material, although this requires confirmation by gravimetric adsorption studies as well as performing *in situ* vapour inclusion studies, for example by following the methods previously reported by Friščić⁷⁴ and Nassimbeni.⁶⁹ Such studies would be especially interesting to observe whether these conversions occur through any intermediate phases, for example in the case of *m*-xylene does this occur via the cavity phase.

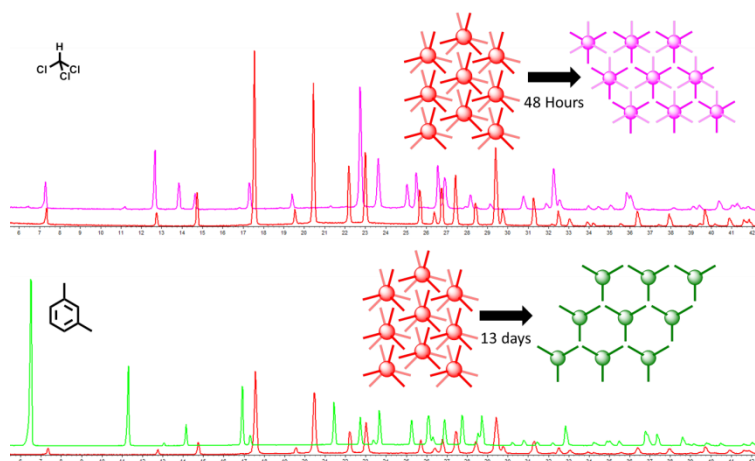


Figure 5.6-1. Preliminary demonstration of vapour induced phase transformations from the as-synthesised closed phase to the solvent including phase **5(Br)·CHCl₃** and **5(Br)·*m*-xylene**.

5.7 References

- 1 J. Tian, P. K. Thallapally and B. P. McGrail, *CrystEngComm*, 2012, **14**, 1909–1919.
- 2 S. Kitagawa and K. Uemura, *Chem. Soc. Rev.*, 2005, **34**, 109–119.
- 3 K. Uemura, R. Matsuda and S. Kitagawa, *J. Solid State Chem.*, 2005, **178**, 2420–2429.
- 4 E. J. Carrington, C. A. McAnally, A. J. Fletcher, S. P. Thompson, M. R. Warren and L. Brammer, *Nat. Chem.*, 2017, **9**, 882–889.
- 5 A. J. Fletcher, K. M. Thomas and M. J. Rosseinsky, *J. Solid State Chem.*, 2005, **178**, 2491–2510.
- 6 G. Férey and C. Serre, *Chem. Soc. Rev.*, 2009, **38**, 1380–1399.
- 7 C. Serre, C. Mellot-Draznieks, S. Surblé, N. Audebrand, Y. Filinchuk and G. Férey, *Science*, 2007, **315**, 1828–1831.
- 8 J.-P. Zhang, P.-Q. Liao, H.-L. Zhou, R.-B. Lin and X.-M. Chen, *Chem. Soc. Rev.*, 2014, **43**, 5789–5814.
- 9 D. N. Dybtsev, H. Chun and K. Kim, *Angew. Chem. Int. Ed.*, 2004, **43**, 5033–5036.
- 10 J. Lü and R. Cao, *Angew. Chem. Int. Ed.*, 2016, **55**, 9474–9480.
- 11 K. H. Zangana, E. M. Pineda, I. J. Vitórica-Yrezábal, E. J. L. McInnes and R. E. P. Winpenny, *Dalton Trans.*, 2014, **43**, 13242–13249.
- 12 J. S. Wright, A. J. Metherell, W. M. Cullen, J. R. Piper, R. Dawson and M. D. Ward, *Chem. Commun.*, 2017, **53**, 4398–4401.
- 13 T. Tozawa, J. T. a Jones, S. I. Swamy, S. Jiang, D. J. Adams, S. Shakespeare, R. Clowes, D. Bradshaw, T. Hasell, S. Y. Chong, C. C. Tang, S. P. Thompson, J. Parker, A. Trewin, J. Bacsá, A. M. Z. Slawin, A. Steiner and A. I. Cooper, *Nat. Mater.*, 2009, **8**, 973–978.
- 14 S. Takamizawa, M. Kohbara, T. Akatsuka and R. Miyake, *New J. Chem.*, 2008, **32**, 1782–1787.
- 15 S. Takamizawa, T. Akatsuka and T. Ueda, *Angew. Chem. Int. Ed.*, 2008, **47**, 1689–1692.
- 16 T.-H. Chen, I. Popov, W. Kaveevivitchai, Y.-C. Chuang, Y.-S. Chen, O. Daugulis, A. J. Jacobson and O. Š. Miljanic, *Nat. Commun.*, 2014, **5**, (5131) 1-7.
- 17 M. I. Hashim, C. W. Hsu, H. T. M. Le and O. Š. Miljanic, *Synlett*, 2016, **27**, 1907–1918.
- 18 N. B. McKeown, *J. Mater. Chem.*, 2010, **20**, 10588–10597.
- 19 R. G. D. Taylor, C. G. Bezzu, M. Carta, K. J. Msayib, J. Walker, R. Short, B. M. Kariuki and N. B. McKeown, *Chem. Eur. J.*, 2016, **22**, 2466–2472.
- 20 M. Mastalerz, *Chem. Eur. J.*, 2012, **18**, 10082–10091.
- 21 M. Mastalerz and I. M. Oppel, *Angew. Chem. Int. Ed.*, 2012, **51**, 5252–5255.

- 22 J. D. Evans, D. M. Huang, M. Haranczyk, A. W. Thornton, C. J. Sumbly and C. J. Doonan, *CrystEngComm*, 2016, **18**, 4133–4141.
- 23 K. J. Msayib, D. Book, P. M. Budd, N. Chaukura, K. D. M. M. Harris, M. Helliwell, S. Tedds, A. Walton, J. E. Warren, M. Xu and N. B. McKeown, *Angew. Chem. Int. Ed.*, 2009, **48**, 3273–3277.
- 24 T. Ueda, G. M. Bernard, R. McDonald and R. E. Wasylshen, *Solid State Nucl. Magn. Reson.*, 2003, **24**, 163–183.
- 25 H. Chihara and K. Nakatsu, *Bull. Chem. Soc. Jpn*, 1959, **32**, 903–908.
- 26 K. Nakatsu, Y. Saito, H. Kuroya, S. Crystal, M. Tris-ethylenediamine-complexes, C. Yoshihiko, R. January and B. K. Nakatsu, *Bull. Chem. Soc. Jpn*, 1956, **29**, 428–434.
- 27 S. Nandi, D. Chakraborty and R. Vaidhyanathan, *Chem. Commun.*, 2016, **52**, 7249–7252.
- 28 H. Wang, B. Li, H. Wu, T. L. Hu, Z. Yao, W. Zhou, S. Xiang and B. Chen, *J. Am. Chem. Soc.*, 2015, **137**, 9963–9970.
- 29 F. Hu, C. Liu, M. Wu, J. Pang, F. Jiang, D. Yuan and M. Hong, *Angew. Chem. Int. Ed.*, 2017, **56**, 2101–2104.
- 30 I. Hisaki, E. N. Q. Affendy and N. Tohnai, *CrystEngComm*, 2017, **19**, 4892–4898.
- 31 H. Wang, H. Wu, J. Kan, G. Chang, Z. Yao, B. Li, W. Zhou, S. Xiang, J. C.-G. Zhao and B. Chen, *J. Mater. Chem. A*, 2017, **5**, 8292–8296.
- 32 Y.-L. Wu, N. E. Horwitz, K.-S. Chen, D. A. Gomez-Gualdron, N. S. Luu, L. Ma, T. C. Wang, M. C. Hersam, J. T. Hupp, O. K. Farha, R. Q. Snurr and M. R. Wasielewski, *Nat. Chem.*, 2017, **9**, 466–472.
- 33 I. Hisaki, N. Ikenaka, N. Tohnai and M. Miyata, *Chem. Commun.*, 2016, **52**, 300–303.
- 34 W. Xiao, C. Hu and M. D. Ward, *J. Am. Chem. Soc.*, 2014, **136**, 14200–14206.
- 35 Y. Liu, W. Xiao, J. J. Yi, C. Hu, S. J. Park and M. D. Ward, *J. Am. Chem. Soc.*, 2015, **137**, 3386–3392.
- 36 Z. Zhang, M. I. Hashim and O. Š. Miljanic, *Chem. Commun.*, 2017, **53**, 10022–10025.
- 37 T. Itoh, M. Kondo, H. Sakamoto, K. Wakabayashi, M. Kanaike, K. Itami and S. Masaoka, *Dalton Trans.*, 2015, **44**, 15334–15342.
- 38 K. Raatikainen and K. Rissanen, *Chem. Sci.*, 2012, **3**, 1235–1239.
- 39 C. R. Groom, I. J. Bruno, M. P. Lightfoot and S. C. Ward, *Acta Crystallogr. Sect. B: Struct. Sci. Cryst. Eng. Mater.*, 2016, **72**, 171–179.
- 40 A. Anthony, G. R. Desiraju, R. K. R. Jetti, S. S. Kuduva, N. N. L. Maghavi, A. Nangia, R. Thaimattam and V. R. Thalladi, *Cryst. Eng.*, 1998, **1**, 1–18.
- 41 V. R. Thalladi, S. Brasselet, H. C. Weiss, D. Bläser, A. K. Katz, H. L. Carrell, R. Boese, J. Zyss, A. Nangia and G. R. Desiraju, *J. Am. Chem. Soc.*, 1998, **120**, 2563–2577.
- 42 R. K. R. Jetti, F. Xue, T. C. W. Mak and A. Nangia, *Cryst. Eng.*, 1999, **2**, 215–224.

- 43 C. K. Broder, J. A. K. Howard, D. A. Keen, C. C. Wilson, F. H. Allen, R. K. R. Jetti, A. Nangia and G. R. Desiraju, *Acta Crystallogr. Sect. B: Struct. Sci.*, 2000, **B56**, 1080–1084.
- 44 R. K. R. Jetti, A. Nangia, F. Xue and T. C. W. Mak, *Chem. Commun.*, 2001, **627**, 919–920.
- 45 H. I. Süss, M. Lutz and J. Hulliger, *CrystEngComm*, 2002, **4**, 610–612.
- 46 B. K. Saha, R. K. R. Jetti, L. S. Reddy, S. Aitipamula and A. Nangia, *Cryst. Growth Des.*, 2005, **5**, 887–899.
- 47 H. I. Süss and J. Hulliger, *Microporous Mesoporous Mater.*, 2005, **78**, 23–27.
- 48 B. Naydenov, C. Spudat, W. Harneit, H. I. Süss, J. Hulliger, J. Nuss and M. Jansen, *Chem. Phys. Lett.*, 2006, **424**, 327–332.
- 49 G. Couderc, M. Bonin, G. Labat, R. Berger and J. Hulliger, *J. Incl. Phenom. Macrocycl. Chem.*, 2008, **61**, 377–379.
- 50 M. Bonin, G. Labat, G. Couderc, T. a Luthi, K. Reichenbacher, J. Hulliger and H. B. Burgi, *J. Chem. Crystallogr.*, 2012, **42**, 645–650.
- 51 V. G. Saraswatula, M. A. Bhat, S. Bhattacharya and B. K. Saha, *J. Chem. Sci.*, 2014, **126**, 1265–1273.
- 52 P. Bombicz, N. B. Báthori and A. Kálmán, *Struct. Chem.*, 2015, **26**, 1611–1619.
- 53 K. Reichenbacher, H. I. Süss, H. Stoeckli-Evans, S. Bracco, P. Sozzani, E. Weber and J. Hulliger, *New J. Chem.*, 2004, **28**, 393–397.
- 54 K. Reichenbacher, A. Neels, H. Stoeckli-Evans, P. Balasubramaniyan, K. Müller, Y. Matsuo, E. Nakamura, E. Weber and J. Hulliger, *Cryst. Growth Des.*, 2007, **7**, 1399–1405.
- 55 K. Reichenbacher, G. Couderc, A. Neels, K. Krämer, E. Weber and J. Hulliger, *J. Incl. Phenom. Macrocycl. Chem.*, 2008, **61**, 127–130.
- 56 B. K. Saha, S. Aitipamula, R. Banerjee, A. Nangia, R. K. R. Jetti, R. Boese, C. K. Lam and T. C. W. Mak, *Mol. Cryst. Liq. Cryst.*, 2005, **440**, 295–316.
- 57 G. S. Pawley, *J. Appl. Crystallogr.*, 1981, **14**, 357–361.
- 58 A. A. Coelho, *Topas Academic, Version 4.1*, see <http://www.topas-academic.net>.
- 59 A. A. Coelho, J. Evans, I. Evans, A. Kern and S. Parsons, *Powder Diffr.*, 2011, **26**, S22–S25.
- 60 H. M. Rietveld, *J. Appl. Crystallogr.*, 1969, **2**, 65–71.
- 61 G. M. Sheldrick, *SADABS, Empirical Absorption Correction program*, Univ. Göttingen, 1995, based on the methods of Blessing.
- 62 L. Krause, R. Herbst-Irmer, G. M. Sheldrick and D. Stalke, *J. Appl. Crystallogr.*, 2015, **48**, 3–10.
- 63 R. H. Blessing, *Acta Crystallogr. Sect. A: Found. Adv.*, 1995, **A51**, 33–38.
- 64 G. M. Sheldrick, *Acta Crystallogr. Sect. C: Struct. Chem.*, 2015, **71**, 3–8.
- 65 O. V. Dolomanov, L. J. Bourhis, R. J. Gildea, J. A. K. Howard and H. Puschmann, *J. Appl.*

- Crystallogr.*, 2009, **42**, 339–341.
- 66 A. L. Spek, *Acta Crystallogr. Sect. D: Biol. Crystallogr.*, 2009, **65**, 148–155.
- 67 A. L. Spek, *Acta Crystallogr. Sect. C: Struct. Chem.*, 2015, **71**, 9–18.
- 68 V. R. Thalladi, R. Boese, S. Brasselet, I. Ledoux, J. Zyss, R. K. R. Jetti and G. R. Desiraju, *Chem. Commun.*, 1999, 1639–1640.
- 69 L. Fébián, P. Bombicz, M. Czugler, A. Kálmán, E. Weber and M. Hecker, *Supramol. Chem.*, 2006, **11**, 151–167.
- 70 H. I. Süß, A. Neels and J. Hulliger, *CrystEngComm*, 2005, **7**, 370–373.
- 71 D. C. Tahmassebi and T. Sasaki, *J. Org. Chem.*, 1998, **63**, 728–731.
- 72 B. K. Saha and A. Nangia, *Cryst. Growth Des.*, 2007, **7**, 393–401.
- 73 R. K. R. Jetti, P. K. Thallapally, A. Nangia, C. Lam and C. W. Thomas, *Chem. Commun.*, 2002, **2**, 952–953.
- 74 I. Huskić, J.-C. Christopherson, K. Užarević and T. Friščić, *Chem. Commun.*, 2016, **52**, 5120–5123.
- 75 N. M. Sykes, H. Su, E. Weber, S. A. Bourne and L. R. Nassimbeni, *CrystEngComm*, 2017, **19**, 5892–5896.

5.8 Appendices

Appendix 5.8.1 Mechanochemistry and Aging PXRD Data

Table 5.3.2-1. Pawley Phase fits of mechanochemical LAG experiments of **5(Br)^a**

Solvent	Quantity (μL)	Space Group	Volume (Å ³)	<i>a</i> (Å)	<i>b</i> (Å)	<i>c</i> (Å)	α (°)	β (°)	γ (°)	<i>R</i> _{wp}	<i>R</i> _{wp'}	Parameters
toluene	100	<i>P</i> 6 ₃ / <i>m</i>	1517.57(8)	15.7641(3)	15.7641(3)	7.0515(2)	90	90	120	0.0919	0.1498	192
<i>p</i> -xylene	100	<i>P</i> 6 ₃ / <i>m</i>	1525.39(11)	15.7760(4)	15.7760(4)	7.0771(4)	90	90	120	0.1562	0.2373	192
<i>o</i> -xylene	100	<i>P</i> 6 ₃ / <i>m</i>	1460.03(10)	15.5208(4)	15.5208(4)	6.9984(4)	90	90	120	0.1252	0.1902	192
<i>m</i> -xylene	100	<i>P</i> 6 ₃ / <i>m</i>	1466.14(9)	15.5608(4)	15.5608(4)	6.9917(3)	90	90	120	0.0719	0.1043	369
		<i>P</i> 6 ₃ / <i>m</i>	1491.72(7)	15.6352(3)	15.6352(3)	7.0461(2)	90	90	120			
chloroform	100	<i>P</i> 6 ₃ / <i>m</i>	1272.04(5)	13.9673(2)	13.9673(2)	7.5291(2)	90	90	120	0.1000	0.1579	163
DCM	100	<i>R</i> -3	3826.87(13)	15.2456(2)	15.2456(2)	19.0120(3)	90	90	120	0.0776	0.1243	259
methanol	100	<i>R</i> 3 <i>c</i>	3305.96(23)	24.0540(7)	24.0540(7)	6.5977(3)	90	90	120	0.0900	0.1419	130
ethanol	100	<i>R</i> 3 <i>c</i>	3289.13(17)	24.0228(5)	24.0228(5)	6.5812(2)	90	90	120	0.0993	0.1698	129
acetonitrile	100	<i>R</i> 3 <i>c</i>	3295.99(19)	24.0309(4)	24.0309(4)	6.5904(3)	90	90	120	0.0876	0.1495	129
benzyl alcohol	100	<i>R</i> 3 <i>c</i>	3286.52(23)	24.0198(7)	24.0198(7)	6.5776(3)	90	90	120	0.1238	0.2572	129
acetone	100	<i>R</i> 3 <i>c</i>	3297.54(14)	24.0339(4)	24.0339(4)	6.5919(2)	90	90	120	0.0848	0.1321	129
water	100	<i>R</i> 3 <i>c</i>	3297.44(20)	24.0412(5)	24.0412(5)	6.5877(3)	90	90	120	0.1173	0.2002	129

^a colour coding denoting the channel phase (green), the cavity phase (orange), the closed phase (red) and a as yet unpublished phase (pink).

Table 5.3.2-2. Pawley Phase fits of aged mechanochemical LAG experiments of **5(Br)^a**

Solvent	Days Aged	Space Group	Volume (Å ³)	<i>a</i> (Å)	<i>b</i> (Å)	<i>c</i> (Å)	α (°)	β (°)	γ (°)	<i>R</i> _{wp}	<i>R</i> _{wp'}	Parameters
Toluene	11 days	R3c	3297.32(12)	24.0327(3)	24.0327(3)	6.5921(2)	90	90	120	0.0841	0.1279	130
<i>p</i> -xylene	11 days	P6 ₃ /m	1509.53(21)	15.7281(4)	15.7281(4)	7.0463(9)	90	90	120	0.0715	0.1091	311
		R3c	3293.89(11)	24.0247(3)	24.0247(3)	6.5897(1)	90	90	120			
	13 days	R3c	3295.23(13)	24.0293(4)	24.0293(4)	6.5898(2)	90	90	120	0.0810	0.1239	130
<i>o</i> -xylene	4 days	P6 ₃ /m	1459.85(6)	15.5195(3)	15.5195(3)	6.9988(2)	90	90	120	0.0716	0.0958	442
		R-3	3779.29(27)	15.2202(4)	15.2202(4)	18.8383(8)	90	90	120			
	7 days	P6 ₃ /m	1459.56(10)	15.5182(5)	15.5182(5)	6.9985(3)	90	90	120	0.0707	0.0990	442
		R-3	3778.11(17)	15.2191(3)	15.2191(3)	18.8352(5)	90	90	120			
	23 days	R-3	3775.08(15)	15.2148(3)	15.2148(3)	18.8306(4)	90	90	120	0.0700	0.1054	261
	35 days	R-3	3776.91(20)	15.2180(3)	15.2180(3)	18.8319(6)	90	90	120	0.0849	0.1357	261
<i>m</i> -xylene	11 days	P6 ₃ /m	1470.94(10)	15.5733(5)	15.5733(5)	7.0033(3)	90	90	120			
		P6 ₃ /m	1509.45(7)	15.7272(3)	15.7272(3)	7.0467(2)	90	90	120	0.0667	0.0987	615
		R-3	3791.46(49)	15.2697(9)	15.2697(9)	18.7764(12)	90	90	120			
	13 days	P6 ₃ /m	1513.90(6)	15.7463(3)	15.7463(3)	7.0503(2)	90	90	120			
		P6 ₃ /m	1472.67(15)	15.5823(6)	15.5823(6)	7.0034(4)	90	90	120	0.0605	0.0924	743
		R-3	3825.20(42)	15.2988(6)	15.2988(6)	18.8716(14)	90	90	120			
	30 days	R3c	3298.54(31)	24.0353(9)	24.0353(9)	6.5932(4)	90	90	120			
		P6 ₃ /m	1515.63(22)	15.7323(5)	15.7323(5)	7.0710(9)	90	90	120	0.0645	0.1003	561
		R-3	3803.38(59)	15.2883(9)	15.2883(9)	18.7897(20)	90	90	120			
	42 day	R3c	3296.63(13)	24.0319(4)	24.0319(4)	6.5912(1)	90	90	120			
		R-3	3808.69(70)	15.2884(9)	15.2884(9)	18.8158(27)	90	90	120	0.0821	0.1334	380
		R3c	3303.34(20)	24.0513(6)	24.0513(6)	6.5940(2)	90	90	120			
chloroform	4 days	P6 ₃ /m	1271.03(5)	13.9642(2)	13.9642(2)	7.5265(2)	90	90	120	0.0734	0.1164	282
		R3c	3295.29(25)	24.0258(7)	24.0258(7)	6.5918(3)	90	90	120			
	7 days	P6 ₃ /m	1272.49(25)	13.9692(12)	13.9692(12)	7.5298(8)	90	90	120	0.0777	0.1205	282
		R3c	3302.29(35)	24.0424(10)	24.0424(10)	6.5967(4)	90	90	120			
	23 days	R3c	3299.97(23)	24.0378(7)	24.0378(7)	6.5946(3)	90	90	120	0.0792	0.1268	130
DCM	4 days	P6 ₃ /m	1501.76(27)	15.7394(12)	15.7394(12)	7.0000(7)	90	90	120			
		R-3	3294.71(55)	24.0186(16)	24.0186(16)	6.5946(6)	90	90	120	0.0646	0.0981	566
		R3c	3821.09(10)	15.2370(2)	15.2370(2)	19.0047(3)	90	90	120			
	7 days	P6 ₃ /m	1500.63(27)	15.7367(12)	15.7367(12)	6.9970(8)	90	90	120			
		R-3	3819.98(16)	15.2358(3)	15.2358(3)	19.0020(4)	90	90	120	0.0632	0.1007	564
		R3c	3294.42(24)	24.0207(7)	24.0207(7)	6.5929(3)	90	90	120			
	23 days	P6 ₃ /m	1502.32(35)	15.7442(15)	15.7442(15)	6.9983(10)	90	90	120	0.0644	0.1037	311
		R3c	3297.44(20)	24.0306(6)	24.0306(6)	6.5936(2)	90	90	120			
	35 Days	P6 ₃ /m	1500.96(55)	15.7422(23)	15.7422(23)	6.9937(15)	90	90	120	0.0696	0.1132	311
		R3c	3298.11(22)	24.0339(6)	24.0339(6)	6.5931(3)	90	90	120			

Channel Unpublished Cavity Closed

^acolour coding denoting the channel phase (green), the cavity phase (orange), the closed phase (red) and a as yet unpublished phase (pink).

Appendix 5.8.2 Variable Temperature PXRD Data

Table 5.3.6-1. Pawley fits of *in situ* PXRD study of **5(Br)-Toluene** during variable temperature measurements. ^a

T (K)	Space Group	Volume (Å ³)	<i>a</i> (Å)	<i>b</i> (Å)	<i>c</i> (Å)	α (°)	β (°)	γ (°)	<i>R</i> _{wp}	<i>R</i> _{wp'}	Parameters
298	P6 ₃ /m	1505.70(3)	15.7051(2)	15.7051(2)	7.04895(8)	90	90	120	0.0547	0.0915	309
	R3c	3287.54(18)	24.0149(5)	24.0149(5)	6.5823(2)	90	90	120			
303	P6 ₃ /m	1507.24(3)	15.7077(2)	15.7077(2)	7.05383(8)	90	90	120	0.0561	0.0946	309
	R3c	3290.58(18)	24.0188(5)	24.0188(5)	6.5863(2)	90	90	120			
308	P6 ₃ /m	1508.45(3)	15.7091(2)	15.7091(2)	7.05831(8)	90	90	120	0.0548	0.0929	309
	R3c	3293.25(16)	24.0223(5)	24.0223(5)	6.5897(2)	90	90	120			
312	P6 ₃ /m	1508.34(3)	15.7087(2)	15.7087(2)	7.05815(9)	90	90	120	0.0543	0.0924	309
	R3c	3293.46(16)	24.0229(5)	24.0229(5)	6.5898(2)	90	90	120			
317	P6 ₃ /m	1510.83(4)	15.7122(2)	15.7122(2)	7.06665(9)	90	90	120	0.0537	0.0929	309
	R3c	3298.85(14)	24.0296(4)	24.0296(4)	6.5969(2)	90	90	120			
323	P6 ₃ /m	1512.70(5)	15.7150(2)	15.7150(2)	7.0729(1)	90	90	120	0.0501	0.0909	309

	<i>R3c</i>	3302.20(9)	24.0340(3)	24.0340(3)	6.6012(1)	90	90	120			
329	<i>P6₃/m</i>	1512.47(7)	15.7140(3)	15.7140(3)	7.0726(2)	90	90	120	0.0515	0.0936	309
	<i>R3c</i>	3301.99(9)	24.0332(3)	24.0332(3)	6.6012(1)	90	90	120			
335	<i>P6₃/m</i>	1514.54(18)	15.7134(8)	15.7134(8)	7.0829(5)	90	90	120	0.0515	0.0939	309
	<i>R3c</i>	3308.27(8)	24.0407(3)	24.0407(3)	6.6096(1)	90	90	120			
341	<i>P6₃/m</i>	1516.1(15)	15.7081(48)	15.7081(48)	7.0948(57)	90	90	120	0.0487	0.0870	309
	<i>R3c</i>	3311.69(8)	24.0452(2)	24.0452(2)	6.6140(9)	90	90	120			
347	<i>R3c</i>	3315.25(8)	24.0508(3)	24.0508(3)	6.6180(1)	90	90	120	0.0520	0.0938	130
353	<i>R3c</i>	3318.66(9)	24.0556(3)	24.0556(3)	6.6221(1)	90	90	120	0.0508	0.0922	130
359	<i>R3c</i>	3322.57(9)	24.0614(3)	24.0614(3)	6.6268(1)	90	90	120	0.0508	0.0928	130
365	<i>R3c</i>	3325.78(9)	24.0655(3)	24.0655(3)	6.6309(1)	90	90	120	0.0512	0.0942	130
371	<i>R3c</i>	3329.57(9)	24.0711(3)	24.0711(3)	6.6354(1)	90	90	120	0.0504	0.0929	130
373	<i>R3c</i>	3330.37(9)	24.0719(3)	24.0719(3)	6.6365(1)	90	90	120	0.0507	0.0938	130
393	<i>R3c</i>	3341.23(10)	24.0864(3)	24.0864(3)	6.6502(1)	90	90	120	0.0516	0.0970	130
423	<i>R3c</i>	3358.24(12)	24.1074(4)	24.1074(4)	6.6724(1)	90	90	120	0.0544	0.1050	130
298	<i>R3c</i>	3288.83(7)	24.0091(2)	24.0091(2)	6.5881(8)	90	90	120	0.0428	0.0741	130

Channel Closed

^acolour coding denoting the channel phase (green) and the closed phase (red)

Table 5.3.6-2. Rietveld fits of *in situ* PXRD study of **5(Br)-Toluene** during variable temperature measurements.^a

T (K)	Space Group	Volume (Å ³)	<i>a</i> (Å)	<i>b</i> (Å)	<i>c</i> (Å)	α (°)	β (°)	γ (°)	Percentage of each phase	<i>R</i> _{wp}	<i>R</i> _{wp} '	Parameters	Toluene ^b
298	<i>P6₃/m</i>	1505.77(5)	15.7055(2)	15.7055(2)	7.0490(1)	90	90	120	74.7(3)	0.0772	0.1297	34	1.596(2)
	<i>R3c</i>	3287.38(26)	24.0148(8)	24.0148(8)	6.5821(3)	90	90	120	25.3(3)				
303	<i>P6₃/m</i>	1507.29(5)	15.7080(2)	15.7080(2)	7.0539(1)	90	90	120	73.4(3)	0.0777	0.1316	34	1.602(2)
	<i>R3c</i>	3290.46(26)	24.0190(8)	24.0190(8)	6.5860(3)	90	90	120	26.6(3)				
308	<i>P6₃/m</i>	1508.55(5)	15.7095(2)	15.7095(2)	7.0584(1)	90	90	120	71.4(3)	0.0764	0.1302	34	1.602(2)
	<i>R3c</i>	3293.16(24)	24.0226(7)	24.0226(7)	6.5893(3)	90	90	120	28.6(3)				
312	<i>P6₃/m</i>	1508.38(5)	15.7089(2)	15.7089(2)	7.0581(1)	90	90	120	69.4(3)	0.0767	0.1311	34	1.596(2)
	<i>R3c</i>	3293.23(23)	24.0228(7)	24.0228(7)	6.5894(3)	90	90	120	30.6(3)				
317	<i>P6₃/m</i>	1510.81(5)	15.7122(2)	15.7122(2)	7.0665(1)	90	90	120	64.7(3)	0.0766	0.1330	34	1.578(2)
	<i>R3c</i>	3298.56(21)	24.0294(6)	24.0294(6)	6.5964(2)	90	90	120	35.3(3)				
323	<i>P6₃/m</i>	1512.46(8)	15.7141(4)	15.7141(4)	7.0725(2)	90	90	120	34.6(3)	0.0762	0.1386	34	1.536(3)
	<i>R3c</i>	3301.59(14)	24.0328(4)	24.0328(4)	6.6006(2)	90	90	120	65.4(3)				
329	<i>P6₃/m</i>	1512.24(10)	15.7131(4)	15.7131(4)	7.0724(3)	90	90	120	26.7(3)	0.0771	0.1409	34	1.530(4)
	<i>R3c</i>	3301.42(13)	24.0320(4)	24.0320(4)	6.6007(2)	90	90	120	73.3(3)				
335	<i>P6₃/m</i>	1513.96(30)	15.7111(13)	15.7111(13)	7.0822(8)	90	90	120	8.7(4)	0.0829	0.1520	34	1.548(13)
	<i>R3c</i>	3307.46(14)	24.0390(4)	24.0390(4)	6.6090(2)	90	90	120	91.3(4)				
341	<i>P6₃/m</i>	1517.3(24)	15.7073(79)	15.7073(79)	7.1015(85)	90	90	120	2.0(4)	0.0844	0.1517	33	1.96(5)
	<i>R3c</i>	3310.89(14)	24.0434(4)	24.0434(4)	6.6134(2)	90	90	120	98.0(4)				
347	<i>R3c</i>	3314.62(14)	24.0494(4)	24.0494(4)	6.6175(2)	90	90	120	100.0(0)	0.0851	0.1538	19	
353	<i>R3c</i>	3317.85(15)	24.0538(5)	24.0538(5)	6.6215(2)	90	90	120	100.0(0)	0.0863	0.1570	19	
359	<i>R3c</i>	3321.88(16)	24.0598(5)	24.0598(5)	6.6263(2)	90	90	120	100.0(0)	0.0880	0.1612	19	
365	<i>R3c</i>	3325.47(16)	24.0648(5)	24.0648(5)	6.6307(2)	90	90	120	100.0(0)	0.0879	0.1622	19	
371	<i>R3c</i>	3329.26(17)	24.0704(5)	24.0704(5)	6.6352(2)	90	90	120	100.0(0)	0.0890	0.1646	19	
373	<i>R3c</i>	3330.02(17)	24.0711(5)	24.0711(5)	6.6363(2)	90	90	120	100.0(0)	0.0889	0.1651	19	
393	<i>R3c</i>	3340.88(19)	24.0856(6)	24.0856(6)	6.6499(2)	90	90	120	100.0(0)	0.0922	0.1740	19	
423	<i>R3c</i>	3357.68(22)	24.1062(7)	24.1062(7)	6.6719(2)	90	90	120	100.0(0)	0.0958	0.1853	19	
298	<i>R3c</i>	3287.90(11)	24.0072(3)	24.0072(3)	6.5873(1)	90	90	120	100.0(0)	0.0695	0.1209	19	

Channel Closed

^acolour coding denoting the channel phase (green) and the closed phase (red). ^bno. of toluene molecules per formula unit

Table 5.3.6-3. Pawley fits of *in situ* PXRD study of **5(Br)-*p*-xylene** during variable temperature measurements.^a

T (K)	Space Group	Volume (Å ³)	<i>a</i> (Å)	<i>b</i> (Å)	<i>c</i> (Å)	α (°)	β (°)	γ (°)	<i>R</i> _{wp}	<i>R</i> _{wp'}	Parameters
293	<i>P6₃/m</i>	1515.30(6)	15.7454(3)	15.7454(3)	7.0577(2)	90	90	120	0.0979	0.1595	309
	<i>R3c</i>	3290.02(58)	24.0225(18)	24.0225(18)	6.5831(6)	90	90	120			
303	<i>P6₃/m</i>	1517.05(3)	15.7485(1)	15.7485(1)	7.06298(7)	90	90	120	0.0503	0.0806	309
	<i>R3c</i>	3290.34(33)	24.0155(10)	24.0155(10)	6.5876(4)	90	90	120			
308	<i>P6₃/m</i>	1518.76(3)	15.7515(1)	15.7515(1)	7.0684(7)	90	90	120	0.0499	0.0802	309
	<i>R3c</i>	3293.49(30)	24.0214(9)	24.0214(9)	6.5907(3)	90	90	120			
312	<i>P6₃/m</i>	1518.69(3)	15.7512(1)	15.7512(1)	7.06829(7)	90	90	120	0.0504	0.0810	309
	<i>R3c</i>	3293.66(29)	24.0218(9)	24.0218(9)	6.5908(3)	90	90	120			
317	<i>P6₃/m</i>	1521.49(3)	15.7551(1)	15.7551(1)	7.07775(7)	90	90	120	0.0493	0.0807	309
	<i>R3c</i>	3298.71(20)	24.0275(6)	24.0275(6)	6.5978(2)	90	90	120			
323	<i>P6₃/m</i>	1522.88(3)	15.7560(2)	15.7560(2)	7.08345(8)	90	90	120	0.0458	0.0790	309
	<i>R3c</i>	3302.27(10)	24.0328(3)	24.0328(3)	6.6020(1)	90	90	120			
329	<i>P6₃/m</i>	1522.80(4)	15.7558(2)	15.7558(2)	7.0833(1)	90	90	120	0.0462	0.0815	309
	<i>R3c</i>	3302.24(8)	24.0326(3)	24.0326(3)	6.6020(1)	90	90	120			
335	<i>P6₃/m</i>	1524.85(24)	15.7540(10)	15.7540(10)	7.0944(7)	90	90	120	0.0442	0.0805	309
	<i>R3c</i>	3309.86(7)	24.0425(2)	24.0425(2)	6.61180(8)	90	90	120			
341	<i>R3c</i>	3313.56(7)	24.0475(2)	24.0475(2)	6.61642(8)	90	90	120	0.0471	0.0852	130
347	<i>R3c</i>	3316.91(7)	24.0517(2)	24.0517(2)	6.62080(8)	90	90	120	0.0466	0.0842	130
353	<i>R3c</i>	3320.62(7)	24.0567(2)	24.0567(2)	6.62545(9)	90	90	120	0.0475	0.0856	130
359	<i>R3c</i>	3323.85(8)	24.0621(2)	24.0621(2)	6.62893(9)	90	90	120	0.0478	0.0866	130
365	<i>R3c</i>	3327.50(8)	24.0681(2)	24.0681(2)	6.63290(9)	90	90	120	0.0482	0.0875	130
371	<i>R3c</i>	3331.13(8)	24.0737(2)	24.0737(2)	6.6370(1)	90	90	120	0.0488	0.0892	130
373	<i>R3c</i>	3332.10(9)	24.0754(3)	24.0754(3)	6.6381(1)	90	90	120	0.0510	0.0934	130
393	<i>R3c</i>	3343.12(11)	24.0915(3)	24.0915(3)	6.6511(1)	90	90	120	0.0545	0.1017	130
423	<i>R3c</i>	3360.71(12)	24.1120(4)	24.1120(4)	6.6747(1)	90	90	120	0.0574	0.1098	130
298	<i>R3c</i>	3289.44(7)	24.0072(2)	24.0072(2)	6.59033(9)	90	90	120	0.0454	0.0781	130

Channel Closed

^acolour coding denoting the channel phase (green) and the closed phase (red)**Table 5.3.6-4.** Rietveld fits of *in situ* PXRD study of **5(Br)-*p*-xylene** during variable temperature measurements.^a

T (K)	Space Group	Volume (Å ³)	<i>a</i> (Å)	<i>b</i> (Å)	<i>c</i> (Å)	α (°)	β (°)	γ (°)	Percentage of each phase	<i>R</i> _{wp}	<i>R</i> _{wp'}	Parameters <i>p</i> -xylene ^b	
293	<i>P6₃/m</i>	1515.17(7)	15.7449(3)	15.7449(3)	7.0575(2)	90	90	120	91.6(5)	0.1169	0.1606	34	1.206(2)
	<i>R3c</i>	3289.2(10)	24.0197(30)	24.0197(30)	6.5830(10)	90	90	120	8.4(5)				
303	<i>P6₃/m</i>	1517.05(4)	15.7486(2)	15.7486(2)	7.0630(1)	90	90	120	90.1(3)	0.0688	0.1017	34	1.272(1)
	<i>R3c</i>	3290.29(46)	24.0150(14)	24.0150(14)	6.5877(5)	90	90	120	9.9(3)				
308	<i>P6₃/m</i>	1518.77(4)	15.7515(2)	15.7515(2)	7.0683(1)	90	90	120	89.2(3)	0.0698	0.1032	34	1.278(1)
	<i>R3c</i>	3293.35(43)	24.0204(13)	24.0204(13)	6.5909(5)	90	90	120	10.8(3)				
312	<i>P6₃/m</i>	1518.71(4)	15.7513(2)	15.7513(2)	7.0683(1)	90	90	120	88.7(3)	0.0710	0.1048	34	1.272(1)
	<i>R3c</i>	3293.55(43)	24.0214(13)	24.0214(13)	6.5908(5)	90	90	120	11.3(3)				
317	<i>P6₃/m</i>	1521.53(4)	15.7553(2)	15.7553(2)	7.0778(1)	90	90	120	84.2(3)	0.0696	0.1049	34	1.266(1)
	<i>R3c</i>	3298.72(29)	24.0274(9)	24.0274(9)	6.5978(3)	90	90	120	15.8(3)				
323	<i>P6₃/m</i>	1522.90(5)	15.7562(2)	15.7562(2)	7.0834(1)	90	90	120	59.8(3)	0.0670	0.1092	34	1.260(2)
	<i>R3c</i>	3302.16(15)	24.0325(5)	24.0325(5)	6.6019(2)	90	90	120	40.2(3)				
329	<i>P6₃/m</i>	1522.82(6)	15.7559(3)	15.7559(3)	7.0833(2)	90	90	120	47.1(3)	0.0692	0.1158	34	1.284(2)
	<i>R3c</i>	3302.12(13)	24.0323(4)	24.0323(4)	6.6019(2)	90	90	120	52.9(3)				
335	<i>P6₃/m</i>	1523.93(48)	15.7503(19)	15.7503(19)	7.0934(15)	90	90	120	5.3(5)	0.0794	0.1391	34	1.146(16)
	<i>R3c</i>	3308.78(12)	24.0403(4)	24.0403(4)	6.6109(1)	90	90	120	94.7(5)				
341	<i>R3c</i>	3312.63(13)	24.0455(4)	24.0455(4)	6.6157(2)	90	90	120	100.0(0)	0.0852	0.1502	19	
347	<i>R3c</i>	3316.00(14)	24.0496(4)	24.0496(4)	6.6201(2)	90	90	120	100.0(0)	0.0862	0.1523	19	
353	<i>R3c</i>	3319.91(14)	24.0552(4)	24.0552(4)	6.6249(2)	90	90	120	100.0(0)	0.0883	0.1550	19	
359	<i>R3c</i>	3323.13(15)	24.0606(5)	24.0606(5)	6.6283(2)	90	90	120	100.0(0)	0.0901	0.1577	19	

365	R3c	3327.02(16)	24.0671(5)	24.0671(5)	6.6325(2)	90	90	120	100.0(0)	0.0919	0.1587	19
371	R3c	3330.33(17)	24.0720(5)	24.0720(5)	6.6364(2)	90	90	120	100.0(0)	0.0913	0.1608	19
373	R3c	3331.47(17)	24.0741(5)	24.0741(5)	6.6375(2)	90	90	120	100.0(0)	0.0929	0.1643	19
393	R3c	3342.29(21)	24.0897(6)	24.0897(6)	6.6505(2)	90	90	120	100.0(0)	0.0980	0.1768	19
423	R3c	3360.07(24)	24.1106(8)	24.1106(8)	6.6743(3)	90	90	120	100.0(0)	0.1029	0.1933	19
298	R3c	3287.58(13)	24.0037(4)	24.0037(4)	6.5886(1)	90	90	120	100.0(0)	0.0757	0.1225	19

Channel Closed

^acolour coding denoting the channel phase (green) and the closed phase (red). ^b*p*-xylene molecules per formula unit.**Table 5.3.6-5.** Pawley fits of *in situ* PXRD study of **5(Br)-*o*-xylene** during variable temperature measurements.^a

T (K)	Space Group	Volume (Å ³)	<i>a</i> (Å)	<i>b</i> (Å)	<i>c</i> (Å)	α (°)	β (°)	γ (°)	<i>R</i> _{wp}	<i>R</i> _{wp'}	Parameters
298	R-3	3757.38(8)	15.1924(1)	15.1924(1)	18.7975(2)	90	90	120	0.0644	0.1075	261
303	R-3	3761.39(8)	15.1946(1)	15.1946(1)	18.8122(2)	90	90	120	0.0649	0.1089	261
308	R-3	3765.85(9)	15.1973(1)	15.1973(1)	18.8278(2)	90	90	120	0.0651	0.1097	261
312	R-3	3766.19(8)	15.1972(1)	15.1972(1)	18.8298(2)	90	90	120	0.0642	0.1079	261
317	R-3	3773.84(8)	15.2016(1)	15.2016(1)	18.8572(2)	90	90	120	0.0636	0.1079	261
323	R-3	3779.14(8)	15.2043(1)	15.2043(1)	18.8769(2)	90	90	120	0.0618	0.1054	261
329	R-3	3778.95(8)	15.2040(1)	15.2040(1)	18.8767(2)	90	90	120	0.0634	0.1076	261
335	R-3	3789.88(8)	15.2099(1)	15.2099(1)	18.9165(2)	90	90	120	0.0599	0.1028	261
341	R-3	3794.97(8)	15.2124(1)	15.2124(1)	18.9358(2)	90	90	120	0.0598	0.1030	261
347	R-3	3800.94(8)	15.2158(1)	15.2158(1)	18.9571(2)	90	90	120	0.0601	0.1044	261
353	R-3	3805.75(9)	15.2180(1)	15.2180(1)	18.9756(2)	90	90	120	0.0616	0.1071	261
359	R-3	3811.39(8)	15.2209(1)	15.2209(1)	18.9965(2)	90	90	120	0.0596	0.1047	261
365	R-3	3816.77(9)	15.2237(2)	15.2237(2)	19.0163(3)	90	90	120	0.0623	0.1108	261
371	R-3	3821.43(8)	15.2257(1)	15.2257(1)	19.0345(2)	90	90	120	0.0561	0.0971	380
	R3c	3343.84(10)	24.1023(31)	24.1023(31)	6.6466(11)	90	90	120			
	R-3	3823.13(9)	15.2268(1)	15.2268(1)	19.0402(2)	90	90	120	0.0572	0.1017	380
373	R3c	3341.82(85)	24.0911(26)	24.0911(26)	6.6487(9)	90	90	120			
	R-3	3837.82(9)	15.2336(2)	15.2336(2)	19.0962(3)	90	90	120	0.0566	0.1054	380
393	R3c	3351.08(41)	24.0979(12)	24.0979(12)	6.6634(5)	90	90	120			
	R-3	3860.52(14)	15.2438(2)	15.2438(2)	19.1836(4)	90	90	120	0.0583	0.1163	385
423	R3c	3368.21(18)	24.1182(5)	24.1182(5)	6.6862(2)	90	90	120			
	R-3	3762.32(12)	15.1931(2)	15.1931(2)	18.8207(3)	90	90	120	0.0501	0.0905	380
298	R3c	3291.66(15)	24.0042(4)	24.0042(4)	6.5964(2)	90	90	120			

Cavity Closed

^acolour coding denoting the channel phase (green) and the closed phase (red)**Table 5.3.6-6.** Rietveld fits of *in situ* PXRD study of **5(Br)-*o*-xylene** during variable temperature measurements.^a

T (K)	Space Group	Volume (Å ³)	<i>a</i> (Å)	<i>b</i> (Å)	<i>c</i> (Å)	α (°)	β (°)	γ (°)	Percentage of each phase	<i>R</i> _{wp}	<i>R</i> _{wp'}	Parameters	<i>o</i> -xylene ^b
298	R-3	3757.11(12)	15.1921(2)	15.1921(2)	18.7970(3)	90	90	120	100.0(0)	0.0883	0.1474	26	0.535(2)
303	R-3	3761.14(12)	15.1943(2)	15.1943(2)	18.8117(3)	90	90	120	100.0(0)	0.0890	0.1494	26	0.527(2)
308	R-3	3765.44(12)	15.1968(2)	15.1968(2)	18.8271(3)	90	90	120	100.0(0)	0.0894	0.1508	26	0.542(2)
312	R-3	3765.84(12)	15.1967(2)	15.1967(2)	18.8291(3)	90	90	120	100.0(0)	0.0894	0.1503	26	0.535(2)
317	R-3	3773.56(12)	15.2012(2)	15.2012(2)	18.8567(3)	90	90	120	100.0(0)	0.0872	0.1480	26	0.533(2)
323	R-3	3778.77(12)	15.2039(2)	15.2039(2)	18.8761(3)	90	90	120	100.0(0)	0.0874	0.1491	26	0.533(2)
329	R-3	3778.73(12)	15.2038(2)	15.2038(2)	18.8762(3)	90	90	120	100.0(0)	0.0896	0.1524	26	0.545(2)
335	R-3	3789.60(12)	15.2096(2)	15.2096(2)	18.9159(3)	90	90	120	100.0(0)	0.0871	0.1493	26	0.534(2)
341	R-3	3794.80(12)	15.2122(2)	15.2122(2)	18.9354(3)	90	90	120	100.0(0)	0.0877	0.1511	26	0.533(2)
347	R-3	3800.58(12)	15.2154(2)	15.2154(2)	18.9564(3)	90	90	120	100.0(0)	0.0872	0.1514	26	0.525(2)
353	R-3	3805.53(12)	15.2178(2)	15.2178(2)	18.9751(3)	90	90	120	100.0(0)	0.0875	0.1527	26	0.521(2)
359	R-3	3811.15(13)	15.2206(2)	15.2206(2)	18.9960(3)	90	90	120	100.0(0)	0.0873	0.1537	26	0.5241(2)
365	R-3	3816.28(13)	15.2230(2)	15.2230(2)	19.0155(4)	90	90	120	100.0(0)	0.0903	0.1608	26	0.523(2)
	R-3	3820.97(14)	15.2251(2)	15.2251(2)	19.0336(4)	90	90	120	96.9(6)	0.0870	0.1563	34	0.523(2)
371	R3c	3341.2(29)	24.0894(92)	24.0894(92)	6.6485(28)	90	90	120	3.1(6)				
373	R-3	3822.47(14)	15.2260(2)	15.2260(2)	19.0390(4)	90	90	120	95.0(5)	0.0875	0.1585	34	0.522(2)

	R3c	3340.58(17)	24.0851(53)	24.0851(53)	6.6496(17)	90	90	120	5.0(5)				
393	R-3	3837.28(15)	15.2330(3)	15.2330(3)	19.0951(4)	90	90	120	88.0(5)	0.0874	0.1642	34	0.533(2)
	R3c	3350.29(70)	24.0955(22)	24.0955(22)	6.6632(7)	90	90	120	12.0(5)				
423	R-3	3860.59(22)	15.2439(4)	15.2439(4)	19.1836(6)	90	90	120	59.3(4)	0.0872	0.1764	34	0.525(3)
	R3c	3368.16(29)	24.1175(9)	24.1175(9)	6.6865(3)	90	90	120	40.7(4)				
298	R-3	3760.914(19)	15.1913(3)	15.1913(3)	18.8180(5)	90	90	120	49.3(3)	0.0756	0.1373	34	0.545(3)
	R3c	3290.21(24)	24.0021(7)	24.0021(7)	6.5947(3)	90	90	120	50.7(3)				
		Cavity	Closed										

^acolour coding denoting the cavity phase (orange) and the closed phase (red). ^b*o*-xylene molecules per formula unit.

Table 5.3.6-7. Pawley fits of *in situ* PXRD study of **5(Br)-*m*-xylene** during variable temperature measurements.^a

T (K)	Space Group	Volume (Å ³)	<i>a</i> (Å)	<i>b</i> (Å)	<i>c</i> (Å)	α (°)	β (°)	γ (°)	R_{wp}	R_{wp}'	Parameters
260	<i>P6₃/m</i>	1467.02(4)	15.5874(2)	15.5874(2)	6.9720(1)	90	90	120	0.0596	0.0979	440
	R-3	3753.70(20)	15.2276(3)	15.2276(3)	18.6924(6)	90	90	120			
273	<i>P6₃/m</i>	1468.92(4)	15.5860(2)	15.5860(2)	6.9823(1)	90	90	120	0.0552	0.0909	440
	R-3	3767.10(19)	15.2536(2)	15.2536(2)	18.6954(8)	90	90	120			
298	<i>P6₃/m</i>	1490.88(4)	15.6334(2)	15.6334(2)	7.0437(1)	90	90	120	0.0532	0.0900	440
	R-3	3784.96(16)	15.2689(3)	15.2689(3)	18.7464(5)	90	90	120			
303	<i>P6₃/m</i>	1492.43(4)	15.6350(2)	15.6350(2)	7.0496(1)	90	90	120	0.0539	0.0917	440
	R-3	3790.26(14)	15.2726(2)	15.2726(2)	18.7633(5)	90	90	120			
308	<i>P6₃/m</i>	1493.35(4)	15.6344(2)	15.6344(2)	7.0545(1)	90	90	120	0.0546	0.0928	440
	R-3	3793.18(15)	15.2731(2)	15.2731(2)	18.7766(4)	90	90	120			
312	<i>P6₃/m</i>	1494.25(4)	15.6345(2)	15.6345(2)	7.0587(1)	90	90	120	0.0544	0.0930	440
	R-3	3797.03(14)	15.2755(2)	15.2755(2)	18.7898(4)	90	90	120			
317	<i>P6₃/m</i>	1495.98(4)	15.6369(2)	15.6369(2)	7.0647(1)	90	90	120	0.0532	0.0913	440
	R-3	3801.62(13)	15.2786(2)	15.2786(2)	18.8049(4)	90	90	120			
323	<i>P6₃/m</i>	1498.15(4)	15.6397(2)	15.6397(2)	7.0724(1)	90	90	120	0.0541	0.0933	440
	R-3	3806.38(13)	15.2810(2)	15.2810(2)	18.8226(4)	90	90	120			
329	<i>P6₃/m</i>	1499.66(4)	15.6403(2)	15.6403(2)	7.0790(1)	90	90	120	0.0544	0.0943	440
	R-3	3811.15(13)	15.2832(2)	15.2832(2)	18.8406(4)	90	90	120			
335	<i>P6₃/m</i>	1501.63(4)	15.6426(2)	15.6426(2)	7.0862(1)	90	90	120	0.0544	0.0950	440
	R-3	3816.88(13)	15.2864(2)	15.2864(2)	18.8612(3)	90	90	120			
341	<i>P6₃/m</i>	1503.76(4)	15.6458(2)	15.6458(2)	7.0934(1)	90	90	120	0.0542	0.0953	440
	R-3	3822.22(12)	15.2891(2)	15.2891(2)	18.8808(3)	90	90	120			
5(Br)- <i>m</i> -xylene	<i>P6₃/m</i>	1506.62(4)	15.6512(2)	15.6512(2)	7.1019(1)	90	90	120	0.0534	0.0944	440
	R-3	3827.27(11)	15.2912(2)	15.2912(2)	18.9005(3)	90	90	120			
347	<i>P6₃/m</i>	1508.62(6)	15.6537(3)	15.6537(3)	7.1091(1)	90	90	120	0.0531	0.0953	447
	R-3	3833.28(10)	15.2947(2)	15.2947(2)	18.9216(3)	90	90	120			
353	<i>P6₃/m</i>	1510.04(9)	15.6540(4)	15.6540(4)	7.1155(3)	90	90	120	0.0525	0.0954	447
	R-3	3838.54(10)	15.2967(2)	15.2967(2)	18.9427(3)	90	90	120			
359	<i>P6₃/m</i>	1510.79(34)	15.6509(14)	15.6509(14)	7.1219(10)	90	90	120	0.0530	0.0942	447
	R-3	3843.64(10)	15.2987(2)	15.2987(2)	18.9629(3)	90	90	120			
365	R3c	3366.3(10)	24.3455(33)	24.3455(33)	6.5581(9)	90	90	120	0.0568	0.1041	384
373	R-3	3850.56(10)	15.3025(2)	15.3025(2)	18.9876(3)	90	90	120			
	R3c	3337.81(40)	24.0732(12)	24.0732(12)	6.6506(5)	90	90	120	0.0535	0.1006	391
378	R-3	3854.10(11)	15.3040(2)	15.3040(2)	19.0011(3)	90	90	120			
	R3c	3340.43(22)	24.0775(6)	24.0775(6)	6.6535(3)	90	90	120	0.0534	0.1037	391
383	R-3	3857.45(12)	15.3055(2)	15.3055(2)	19.0141(3)	90	90	120			
	R3c	3346.76(15)	24.0853(4)	24.0853(4)	6.6618(2)	90	90	120	0.0528	0.1062	391
393	R-3	3865.16(15)	15.3087(3)	15.3087(3)	19.0441(4)	90	90	120			
	R3c	3353.15(13)	24.0941(4)	24.0941(4)	6.6697(2)	90	90	120	0.0516	0.1066	391
403	R-3	3872.27(17)	15.3115(3)	15.3115(3)	19.0722(4)	90	90	120			
	R3c	3357.84(12)	24.0994(4)	24.0994(4)	6.6760(1)	90	90	120	0.0543	0.1113	391
413	R-3	3879.11(63)	15.3140(11)	15.3140(11)	19.0995(15)	90	90	120			
	R3c	3363.87(13)	24.1071(4)	24.1071(4)	6.6837(2)	90	90	120	0.0563	0.1156	131
423	R-3	3870.16(13)	24.1151(4)	24.1151(4)	6.6918(2)	90	90	120	0.0562	0.1162	131
433	R3c	3370.16(13)	24.1151(4)	24.1151(4)	6.6918(2)	90	90	120	0.0569	0.1224	131
478	R3c	3399.52(15)	24.1528(4)	24.1528(4)	6.7291(2)	90	90	120	0.0557	0.1021	130
298	R3c	3285.46(9)	24.0044(3)	24.0044(3)	6.5839(1)	90	90	120			
		Channel	Cavity	Closed							

^acolour coding denoting the channel phase (green), cavity phase (orange) and the closed phase (red)

Table 5.3.6-8. Rietveld fits of *in situ* PXRD study of **5(Br)·m-xylene** during variable temperature measurements.^a

T (K)	Space Group	Volume (Å ³)	<i>a</i> (Å)	<i>b</i> (Å)	<i>c</i> (Å)	α (°)	β (°)	γ (°)	Percentage of each phase	R_{wp}	R_{wp}'	Parameters	<i>m</i> -xylene ^b
260	<i>P6₃/m</i>	1467.03(5)	15.5875(2)	15.5875(2)	6.9719(1)	90	90	120	62.7(3)	0.0780	0.1288	41	1.334(2)
	<i>R-3</i>	3756.48(22)	15.2548(4)	15.2548(4)	18.6395(7)	90	90	120	37.3(3)				0.484(2)
273	<i>P6₃/m</i>	1468.91(5)	15.5862(2)	15.5862(2)	6.9821(1)	90	90	120	63.1(3)	0.0756	0.1256	41	1.329(2)
	<i>R-3</i>	3766.69(31)	15.2610(5)	15.2610(5)	18.6751(10)	90	90	120	36.9(3)				0.493(2)
298	<i>P6₃/m</i>	1490.91(5)	15.6336(2)	15.6336(2)	7.0437(1)	90	90	120	62.1(3)	0.0680	0.1157	41	1.297(1)
	<i>R-3</i>	3785.70(20)	15.2700(3)	15.2700(3)	18.7473(6)	90	90	120	37.9(3)				0.493(2)
303	<i>P6₃/m</i>	1492.41(5)	15.6350(2)	15.6350(2)	7.0496(1)	90	90	120	61.5(3)	0.0692	0.1182	41	1.292(1)
	<i>R-3</i>	3790.06(19)	15.2726(3)	15.2726(3)	18.7625(6)	90	90	120	38.5(3)				0.495(2)
308	<i>P6₃/m</i>	1493.32(5)	15.6343(2)	15.6343(2)	7.0545(1)	90	90	120	61.1(3)	0.0686	0.1174	41	1.289(1)
	<i>R-3</i>	3793.53(19)	15.2741(3)	15.2741(3)	18.7759(6)	90	90	120	38.9(3)				0.498(2)
312	<i>P6₃/m</i>	1494.23(5)	15.6345(2)	15.6345(2)	7.0586(1)	90	90	120	60.7(3)	0.0697	0.1198	41	1.283(1)
	<i>R-3</i>	3797.23(18)	15.2763(3)	15.2763(3)	18.7889(5)	90	90	120	39.3(3)				0.493(2)
317	<i>P6₃/m</i>	1495.93(5)	15.6366(2)	15.6366(2)	7.0647(1)	90	90	120	60.4(3)	0.0691	0.1191	41	1.294(1)
	<i>R-3</i>	3801.47(17)	15.2786(3)	15.2786(3)	18.8042(5)	90	90	120	39.6(3)				0.497(2)
323	<i>P6₃/m</i>	1498.13(5)	15.6395(2)	15.6395(2)	7.0725(1)	90	90	120	59.5(3)	0.0686	0.1187	41	1.264(1)
	<i>R-3</i>	3806.26(17)	15.2809(3)	15.2809(3)	18.8222(5)	90	90	120	40.5(3)				0.500(3)
329	<i>P6₃/m</i>	1499.65(5)	15.6402(2)	15.6402(2)	7.0790(1)	90	90	120	59.0(3)	0.0687	0.1195	41	1.276(1)
	<i>R-3</i>	3811.20(17)	15.2832(3)	15.2832(3)	18.8409(5)	90	90	120	41.0(3)				0.499(2)
335	<i>P6₃/m</i>	1501.66(5)	15.6427(2)	15.6427(2)	7.0863(1)	90	90	120	57.7(3)	0.0677	0.1187	41	1.276(2)
	<i>R-3</i>	3816.70(16)	15.2860(3)	15.2860(3)	18.8613(4)	90	90	120	42.3(3)				0.500(2)
341	<i>P6₃/m</i>	1503.81(5)	15.6458(2)	15.6458(2)	7.0936(1)	90	90	120	54.8(3)	0.0676	0.1195	41	1.272(2)
	<i>R-3</i>	3822.10(16)	15.2889(3)	15.2889(3)	18.8809(4)	90	90	120	45.2(3)				0.500(2)
347	<i>P6₃/m</i>	1506.64(6)	15.6512(3)	15.6512(3)	7.1020(2)	90	90	120	48.6(3)	0.0678	0.1208	41	1.273(2)
	<i>R-3</i>	3827.13(15)	15.2910(3)	15.2910(3)	18.9005(4)	90	90	120	51.4(3)				0.500(2)
353	<i>P6₃/m</i>	1508.55(8)	15.6536(3)	15.6536(3)	7.1089(2)	90	90	120	33.8(3)	0.0672	0.1211	41	1.282(2)
	<i>R-3</i>	3832.89(13)	15.2940(2)	15.2940(2)	18.9214(4)	90	90	120	66.2(3)				0.500(2)
359	<i>P6₃/m</i>	1510.01(13)	15.6540(5)	15.6540(5)	7.1154(4)	90	90	120	18.1(3)	0.0698	0.1270	41	1.285(4)
	<i>R-3</i>	3838.21(13)	15.2961(2)	15.2961(2)	18.9425(3)	90	90	120	81.9(3)				0.500(2)
365	<i>P6₃/m</i>	1511.49(56)	15.6548(20)	15.6548(20)	7.1216(19)	90	90	120	6.2(6)	0.0761	0.1378	41	1.530(2)
	<i>R-3</i>	3843.61(14)	15.2986(2)	15.2986(2)	18.9630(4)	90	90	120	93.8(6)				0.500(1)
373	<i>R3c</i>	3336.8(51)	24.079(16)	24.079(16)	6.6454(47)	90	90	120	1.7(6)	0.0762	0.1402	34	0.500(2)
	<i>R-3</i>	3850.39(14)	15.3021(2)	15.3021(2)	18.9876(4)	90	90	120	98.3(6)				
378	<i>R3c</i>	3337.89(59)	24.0747(18)	24.0747(18)	6.6500(6)	90	90	120	9.7(4)	0.0731	0.1386	34	0.500(2)
	<i>R-3</i>	3853.85(15)	15.3037(3)	15.3037(3)	19.0009(4)	90	90	120	90.3(4)				
383	<i>R3c</i>	3340.22(32)	24.0771(10)	24.0771(10)	6.6533(3)	90	90	120	22.7(4)	0.0736	0.1445	34	0.500(2)
	<i>R-3</i>	3857.10(17)	15.3050(3)	15.3050(3)	19.0137(4)	90	90	120	77.3(4)				
393	<i>R3c</i>	3346.91(24)	24.0857(7)	24.0857(7)	6.6619(2)	90	90	120	40.3(4)	0.0746	0.1519	34	0.500(2)
	<i>R-3</i>	3865.32(21)	15.3089(4)	15.3089(4)	19.0443(5)	90	90	120	59.7(4)				
403	<i>R3c</i>	3353.45(22)	24.0945(7)	24.0945(7)	6.6700(2)	90	90	120	56.9(4)	0.0786	0.1644	34	0.500(3)
	<i>R-3</i>	3872.67(26)	15.3120(5)	15.3120(5)	19.0727(6)	90	90	120	43.1(4)				
413	<i>R3c</i>	3357.24(24)	24.0978(7)	24.0978(7)	6.6757(2)	90	90	120	90.6(6)	0.0970	0.2011	34	0.42(1)
	<i>R-3</i>	3878.0(13)	15.3128(21)	15.3128(21)	19.0972(31)	90	90	120	9.4(6)				
423	<i>R3c</i>	3363.74(25)	24.1067(8)	24.1067(8)	6.6837(3)	90	90	120	100.0(0)	0.0987	0.2042	19	
433	<i>R3c</i>	3370.23(26)	24.1151(8)	24.1151(8)	6.6919(3)	90	90	120	100.0(0)	0.0995	0.2074	19	
478	<i>R3c</i>	3399.75(30)	24.1530(9)	24.1530(9)	6.7294(3)	90	90	120	100.0(0)	0.1024	0.2216	19	
298	<i>R3c</i>	3284.13(14)	24.0017(4)	24.0017(4)	6.5828(2)	90	90	120	100.0(0)	0.0808	0.1491	19	

^acolour coding denoting the channel phase (green), cavity phase (orange) and the closed phase (red). ^b*m*-xylene molecules per formula unit.

Table 5.3.6-9. Pawley fits of *in situ* PXRD study of **5(Br)-CHCl₃** during variable temperature measurements.^a

T (K)	Space Group	Volume (Å ³)	a (Å)	b (Å)	c (Å)	α (°)	β (°)	γ (°)	R _{wp}	R _{wp'}	Parameters
298	P6 ₃ /m	1268.98(6)	13.9570(3)	13.9570(3)	7.5221(2)	90	90	120	0.0572	0.1110	280
	R3c	3288.40(39)	24.0076(12)	24.0076(12)	6.5881(4)	90	90	120			
303	P6 ₃ /m	1270.82(6)	13.9634(3)	13.9634(3)	7.5262(2)	90	90	120	0.0577	0.1113	281
	R3c	3292.59(37)	24.0172(11)	24.0172(11)	6.5912(4)	90	90	120			
308	P6 ₃ /m	1272.07(6)	13.9679(3)	13.9679(3)	7.5286(2)	90	90	120	0.0575	0.1109	281
	R3c	3294.17(32)	24.0185(10)	24.0185(10)	6.5936(4)	90	90	120			
312	P6 ₃ /m	1272.17(6)	13.9681(3)	13.9681(3)	7.5291(2)	90	90	120	0.0571	0.1104	281
	R3c	3294.15(27)	24.0188(8)	24.0188(8)	6.5934(3)	90	90	120			
317	P6 ₃ /m	1274.81(6)	13.9776(3)	13.9776(3)	7.5344(2)	90	90	120	0.0560	0.1085	281
	R3c	3298.59(23)	24.0249(7)	24.0249(7)	6.5990(3)	90	90	120			
323	P6 ₃ /m	1276.76(6)	13.9842(3)	13.9842(3)	7.5388(2)	90	90	120	0.0575	0.1118	282
	R3c	3302.43(20)	24.0323(6)	24.0323(6)	6.6026(2)	90	90	120			
329	P6 ₃ /m	1276.40(6)	13.9828(3)	13.9828(3)	7.5382(2)	90	90	120	0.0557	0.1083	282
	R3c	3301.02(16)	24.0287(5)	24.0287(5)	6.6017(2)	90	90	120			
335	P6 ₃ /m	1280.43(9)	13.9974(4)	13.9974(4)	7.5462(3)	90	90	120	0.0546	0.1065	282
	R3c	3308.85(14)	24.0400(4)	24.0400(4)	6.6112(2)	90	90	120			
341	P6 ₃ /m	1229.4(62)	13.619(25)	13.619(25)	7.653(26)	90	90	120	0.0473	0.0745	282
	R3c	3312.71(11)	24.0457(3)	24.0457(3)	6.6157(1)	90	90	120			
347	R3c	3316.70(13)	24.0520(4)	24.0520(4)	6.6202(2)	90	90	120	0.0553	0.1066	130
353	R3c	3320.03(13)	24.0574(4)	24.0574(4)	6.6239(2)	90	90	120	0.0557	0.1078	130
359	R3c	3324.04(14)	24.0626(4)	24.0626(4)	6.6290(2)	90	90	120	0.0557	0.1082	130
365	R3c	3327.78(14)	24.0677(4)	24.0677(4)	6.6337(2)	90	90	120	0.0548	0.1068	130
371	R3c	3331.10(14)	24.0711(4)	24.0711(4)	6.6384(2)	90	90	120	0.0569	0.1116	130
373	R3c	3332.19(14)	24.0724(4)	24.0724(4)	6.6399(2)	90	90	120	0.0562	0.1104	131
298	R3c	3290.54(11)	24.0034(3)	24.0034(3)	6.5947(1)	90	90	120	0.0492	0.0903	131

Unpublished Closed

^a colour coding denoting the unpublished phase (pink) and the closed phase (red)**Table 5.3.6-10.** Rietveld fits of *in situ* PXRD study of **5(Br)-CHCl₃** during variable temperature measurements.^a

T (K)	Space Group	Volume (Å ³)	a (Å)	b (Å)	c (Å)	α (°)	β (°)	γ (°)	Percentage of each phase	R _{wp}	R _{wp'}	Parameters
298	P6 ₃ /m	1268.74(8)	13.9563(4)	13.9563(4)	7.5214(2)	90	90	120	69.1(4)	0.0707	0.1375	27
	R3c	3288.98(54)	24.0149(17)	24.0149(17)	6.5852(6)	90	90	120	30.9(4)			
303	P6 ₃ /m	1270.41(8)	13.9622(4)	13.9622(4)	7.5250(2)	90	90	120	67.0(4)	0.0714	0.1388	27
	R3c	3292.16(49)	24.0198(15)	24.0198(15)	6.5889(5)	90	90	120	33.0(4)			
308	P6 ₃ /m	1271.69(8)	13.9667(4)	13.9667(4)	7.5277(2)	90	90	120	63.8(4)	0.0718	0.1387	27
	R3c	3293.96(42)	24.0211(13)	24.0211(13)	6.5918(5)	90	90	120	36.2(4)			
312	P6 ₃ /m	1271.78(8)	13.9668(4)	13.9668(4)	7.5281(2)	90	90	120	61.0(4)	0.0711	0.1376	27
	R3c	3293.68(37)	24.0208(11)	24.0208(11)	6.5914(4)	90	90	120	39.0(4)			
317	P6 ₃ /m	1274.54(7)	13.9765(4)	13.9765(4)	7.5340(2)	90	90	120	55.3(4)	0.0695	0.1349	27
	R3c	3298.21(30)	24.0263(9)	24.0263(9)	6.5974(3)	90	90	120	44.7(4)			
323	P6 ₃ /m	1276.34(8)	13.9826(4)	13.9826(4)	7.5381(2)	90	90	120	45.4(4)	0.0711	0.1385	27
	R3c	3301.32(25)	24.0309(8)	24.0309(8)	6.6011(3)	90	90	120	54.6(4)			
329	P6 ₃ /m	1276.19(8)	13.9819(4)	13.9819(4)	7.5379(2)	90	90	120	36.0(3)	0.0707	0.1376	27
	R3c	3300.51(22)	24.0286(7)	24.0286(7)	6.6007(2)	90	90	120	64.0(3)			
335	P6 ₃ /m	1280.10(13)	13.9960(6)	13.9960(6)	7.5458(4)	90	90	120	19.0(4)	0.0744	0.1451	27
	R3c	3307.82(20)	24.0383(6)	24.0383(6)	6.6100(2)	90	90	120	81.0(4)			
341	P6 ₃ /m	1283.14(13)	14.0054(62)	14.0054(62)	7.5535(42)	90	90	120	2.4(4)	0.0786	0.1506	27
	R3c	3310.27(19)	24.0400(6)	24.0400(6)	6.6140(2)	90	90	120	97.6(4)			
347	R3c	3315.96(20)	24.0508(6)	24.0508(6)	6.6194(2)	90	90	120	100.0(0)	0.0807	0.1558	19
353	R3c	3319.23(21)	24.0557(6)	24.0557(6)	6.6232(2)	90	90	120	100.0(0)	0.0829	0.1611	19
359	R3c	3323.39(21)	24.0613(7)	24.0613(7)	6.6284(2)	90	90	120	100.0(0)	0.0835	0.1629	19
365	R3c	3327.15(22)	24.0666(7)	24.0666(7)	6.6330(2)	90	90	120	100.0(0)	0.0836	0.1638	19
371	R3c	3330.98(22)	24.0710(7)	24.0710(7)	6.6382(2)	90	90	120	100.0(0)	0.0850	0.1675	19
373	R3c	3331.98(22)	24.0721(7)	24.0721(7)	6.6397(2)	90	90	120	100.0(0)	0.0854	0.1688	19
298	R3c	3289.33(16)	24.0009(5)	24.0009(5)	6.5936(2)	90	90	120	100.0(0)	0.0705	0.1308	19

Unpublished Closed

^a colour coding denoting the unpublished phase (pink) and the closed phase (red)

Table 5.3.6-11. Pawley fits of *in situ* PXRD study of **5(Br)-DCM** during variable temperature measurements.^a

T (K)	Space Group	Volume (Å ³)	<i>a</i> (Å)	<i>b</i> (Å)	<i>c</i> (Å)	α (°)	β (°)	γ (°)	<i>R</i> _{wp}	<i>R</i> _{wp'}	Parameters
260	R-3	3779.9(1)	15.2013(2)	15.2013(2)	18.8881(3)	90	90	120	0.0736	0.1382	261
273	R-3	3790.1(1)	15.2097(2)	15.2097(2)	18.9180(3)	90	90	120	0.0731	0.1395	261
298	R-3	3810.7(1)	15.2253(2)	15.2253(2)	18.9821(3)	90	90	120	0.0755	0.1470	261
303	R-3	3815.4(1)	15.2288(2)	15.2288(2)	18.9966(3)	90	90	120	0.0728	0.1433	261
308	R-3	3820.1(1)	15.2325(2)	15.2325(2)	19.0109(3)	90	90	120	0.0744	0.1477	261
312	R-3	3824.1(1)	15.2356(2)	15.2356(2)	19.0229(3)	90	90	120	0.0697	0.1399	376
	R3c	3292.3(9)	23.9870(22)	23.9870(22)	6.6071(13)	90	90	120			
317	R-3	3827.9(1)	15.2378(2)	15.2378(2)	19.0366(3)	90	90	120	0.0685	0.1346	379
	R3c	3298.6(10)	24.0189(30)	24.0189(30)	6.6026(13)	90	90	120			
323	R-3	3833.7(1)	15.2418(2)	15.2418(2)	19.0552(4)	90	90	120	0.0659	0.1347	380
	R3c	3300.3(5)	24.0220(14)	24.0220(14)	6.6039(6)	90	90	120			
329	R-3	3839.5(2)	15.2456(3)	15.2456(3)	19.0747(5)	90	90	120	0.0659	0.1347	380
	R3c	3302.6(3)	24.0250(8)	24.0250(8)	6.6068(3)	90	90	120			
333	R-3	3843.6(2)	15.2482(4)	15.2482(4)	19.0884(7)	90	90	120	0.0638	0.1283	380
	R3c	3304.5(2)	24.0283(6)	24.0283(6)	6.6089(3)	90	90	120			
338	R-3	3848.0(5)	15.2503(7)	15.2503(7)	19.1051(15)	90	90	120	0.0662	0.1274	385
	R3c	3307.4(2)	24.0330(6)	24.0330(6)	6.6122(2)	90	90	120			
341	R3c	3309.8(2)	24.0369(6)	24.0369(6)	6.6148(2)	90	90	120	0.0705	0.1316	130
347	R3c	3313.4(2)	24.0426(6)	24.0426(6)	6.6189(2)	90	90	120	0.0701	0.1315	130
353	R3c	3316.8(2)	24.0473(6)	24.0473(6)	6.6231(2)	90	90	120	0.0702	0.1321	130
358	R3c	3320.1(2)	24.0527(6)	24.0527(6)	6.6268(2)	90	90	120	0.0673	0.1272	130
365	R3c	3324.2(2)	24.0577(6)	24.0577(6)	6.6321(2)	90	90	120	0.0668	0.1271	130
373	R3c	3328.7(2)	24.0637(6)	24.0637(6)	6.6378(2)	90	90	120	0.0689	0.1323	130
378	R3c	3331.5(2)	24.0678(6)	24.0678(6)	6.6410(2)	90	90	120	0.0692	0.1334	130
383	R3c	3334.8(2)	24.0722(6)	24.0722(6)	6.6452(2)	90	90	120	0.0679	0.1309	130
393	R3c	3340.1(2)	24.0784(6)	24.0784(6)	6.6523(2)	90	90	120	0.0672	0.1309	130
398	R3c	3343.1(2)	24.0819(6)	24.0819(6)	6.6563(2)	90	90	120	0.0662	0.1294	130
403	R3c	3345.9(2)	24.0853(6)	24.0853(6)	6.6600(2)	90	90	120	0.0688	0.1350	130
413	R3c	3351.5(2)	24.0923(6)	24.0923(6)	6.6672(2)	90	90	120	0.0660	0.1301	130
423	R3c	3357.4(2)	24.1001(6)	24.1001(6)	6.6747(2)	90	90	120	0.0673	0.1343	130
433	R3c	3363.2(2)	24.1072(6)	24.1072(6)	6.6824(2)	90	90	120	0.0690	0.1382	130
473	R3c	3386.3(2)	24.1358(7)	24.1358(7)	6.7122(2)	90	90	120	0.0664	0.1371	130
478	R3c	3388.7(2)	24.1379(7)	24.1379(7)	6.7159(3)	90	90	120	0.0684	0.1421	130
298	R3c	3287.5(2)	23.9915(5)	23.9915(5)	6.5951(2)	90	90	120	0.0703	0.1263	130

Cavity Closed

^a colour coding denoting the cavity phase (orange) and the closed phase (red)

Table 5.3.6-12. Rietveld fits of *in situ* PXRD study of **5(Br)-DCM** during variable temperature measurements.^a

T (K)	Space Group	Volume (Å ³)	a (Å)	b (Å)	c (Å)	α (°)	β (°)	γ (°)	Percentage of each phase	R _{wp}	R _{wp} '	Parameters	DCM ^b
260	R-3	3780.4(2)	15.2022(3)	15.2022(3)	18.8886(5)	90	90	120	100.0(0)	0.1262	0.2378	26	0.957(3)
273	R-3	3790.1(2)	15.2100(3)	15.2100(3)	18.9176(5)	90	90	120	100.0(0)	0.1230	0.2354	26	0.927(3)
298	R-3	3811.1(2)	15.2259(3)	15.2259(3)	18.9824(5)	90	90	120	100.0(0)	0.1093	0.2128	26	0.495(1)
303	R-3	3815.5(2)	15.2290(3)	15.2290(3)	18.9968(5)	90	90	120	100.0(0)	0.1181	0.2333	26	0.933(3)
308	R-3	3820.1(2)	15.2325(3)	15.2325(3)	19.0109(5)	90	90	120	100.0(0)	0.1174	0.2339	26	0.924(3)
312	R-3	3823.8(2)	15.2351(3)	15.2351(3)	19.0227(5)	90	90	120	98.0(8)	0.1171	0.2368	34	0.906(3)
	R3c	3285(11)	23.959(36)	23.959(36)	6.608(10)	90	90	120	2.0(8)				
317	R-3	3827.8(2)	15.2376(4)	15.2376(4)	19.0365(6)	90	90	120	91.1(9)	0.1153	0.2367	34	0.912(3)
	R3c	3294(3)	24.008(10)	24.008(10)	6.601(3)	90	90	120	8.9(9)				
323	R-3	3833.5(2)	15.2415(4)	15.2415(4)	19.0550(6)	90	90	120	75.2(7)	0.1070	0.2221	34	0.912(4)
	R3c	3298.6(9)	24.019(3)	24.019(3)	6.6025(10)	90	90	120	24.8(7)				
329	R-3	3839.0(3)	15.2449(5)	15.2449(5)	19.0739(7)	90	90	120	52.9(6)	0.1014	0.2098	34	0.921(4)
	R3c	3301.4(5)	24.0225(14)	24.0225(14)	6.6058(5)	90	90	120	47.1(6)				
333	R-3	3842.5(4)	15.2469(6)	15.2469(6)	19.0862(9)	90	90	120	30.7(5)	0.0918	0.1859	34	0.900(5)
	R3c	3302.8(3)	24.0244(10)	24.0244(10)	6.6076(4)	90	90	120	69.3(5)				
338	R-3	3846.4(8)	15.2481(13)	15.2481(13)	19.103(2)	90	90	120	11.3(6)	0.0912	0.1781	34	0.879(12)
	R3c	3305.6(3)	24.0294(9)	24.0294(9)	6.6105(3)	90	90	120	88.7(6)				
341	R3c	3307.7(3)	24.0330(8)	24.0330(8)	6.6126(2)	90	90	120	100.0(0)	0.0930	0.1744	19	
347	R3c	3311.1(3)	24.0383(9)	24.0383(9)	6.6167(3)	90	90	120	100.0(0)	0.0933	0.1756	19	
353	R3c	3314.3(3)	24.0425(9)	24.0425(9)	6.6207(3)	90	90	120	100.0(0)	0.0944	0.1784	19	
358	R3c	3317.9(3)	24.0483(9)	24.0483(9)	6.6247(3)	90	90	120	100.0(0)	0.0933	0.1772	19	
365	R3c	3322.5(3)	24.0544(9)	24.0544(9)	6.6304(3)	90	90	120	100.0(0)	0.0934	0.1788	19	
373	R3c	3327.0(3)	24.0602(9)	24.0602(9)	6.6363(3)	90	90	120	100.0(0)	0.0950	0.1834	19	
378	R3c	3329.8(3)	24.0644(10)	24.0644(10)	6.6396(3)	90	90	120	100.0(0)	0.0974	0.1886	19	
383	R3c	3333.5(3)	24.0697(9)	24.0697(9)	6.6441(3)	90	90	120	100.0(0)	0.0967	0.1876	19	
393	R3c	3339.3(3)	24.0767(10)	24.0767(10)	6.6516(3)	90	90	120	100.0(0)	0.0964	0.1888	19	
398	R3c	3342.0(3)	24.0795(10)	24.0795(10)	6.6555(3)	90	90	120	100.0(0)	0.0969	0.1907	19	
403	R3c	3344.7(3)	24.0827(10)	24.0827(10)	6.6591(3)	90	90	120	100.0(0)	0.0983	0.1941	19	
413	R3c	3351.2(3)	24.0917(10)	24.0917(10)	6.6670(3)	90	90	120	100.0(0)	0.0968	0.1920	19	
423	R3c	3357.3(3)	24.0999(10)	24.0999(10)	6.6746(3)	90	90	120	100.0(0)	0.0994	0.1994	19	
433	R3c	3362.7(3)	24.1059(11)	24.1059(11)	6.6820(3)	90	90	120	100.0(0)	0.1006	0.2026	19	
473	R3c	3386.4(4)	24.1360(12)	24.1360(12)	6.7124(4)	90	90	120	100.0(0)	0.1024	0.2129	19	
478	R3c	3388.7(4)	24.1377(12)	24.1377(12)	6.7160(4)	90	90	120	100.0(0)	0.1049	0.2190	19	
298	R3c	3285.6(2)	23.9881(7)	23.9881(7)	6.5932(3)	90	90	120	100.0(0)	0.0876	0.1580	19	

Cavity Closed

^acolour coding denoting the cavity phase (orange) and the closed phase (red). ^bDCM molecules per formula unit.

Appendix 5.8.3 Variable Temperature Single-Crystal Data

Table 5.3.7-1. Summary of the *in situ* variable temperature single-crystal data of **5(Br)·CHCl₃**

	5(Br)·CHCl₃ tris-(4-bromophenoxy)-triazine chloroform solvate C ₂₂ H ₁₃ Br ₃ Cl ₃ N ₃ O ₃	5(Br)·CHCl₃ tris-(4-bromophenoxy)-triazine chloroform solvate C ₂₂ H ₁₃ Br ₃ Cl ₃ N ₃ O ₃	5(Br)-post 333 K tris-(4-bromophenoxy)-triazine C ₂₁ H ₁₂ Br ₃ N ₃ O ₃
Crystal habit	Needle	Needle	Needle
Crystal colour	Colourless	Colourless	Colourless
Crystal size (mm)	0.08 × 0.08 × 0.05	0.08 × 0.08 × 0.05	0.08 × 0.08 × 0.05
Crystal system	Hexagonal	Hexagonal	Trigonal
Space group	<i>P6₃/m</i>	<i>P6₃/m</i>	<i>R3c</i>
<i>a</i> (Å)	13.7848(5)	13.960(2)	23.871(6)
<i>b</i> (Å)	13.7848(5)	13.960 (2)	23.871(6)
<i>c</i> (Å)	7.3953(3)	7.527 (1)	6.449(2)
α (°)	90	90	90
β (°)	90	90	90
γ (°)	120	120	120
<i>V</i> (Å ³)	1217.0(1)	1270.4(3)	3182(2)
Density (g cm ⁻³)	1.947	1.865	1.860
Temperature (K)	100	298	100
<i>m</i> (mm ⁻¹)	5.333	5.109	5.733
Wavelength (Å)	0.71073	0.71073	0.71073
2 θ range (°)	5.91 to 54.942	3.368 to 54.976	3.412 to 41.71
Reflns. collected	5261	5484	3278
Independent reflns. [<i>R</i> _{int}]	1003 [0.0644]	1049 [0.0989]	739 [0.0963]
Reflns. used in refinement, <i>n</i>	1003	1049	739
LS parameters, <i>p</i>	64	64	290
Restraints, <i>r</i>	0	0	170
<i>R</i> 1 (<i>F</i>) ^a <i>I</i> > 2.0 σ (<i>I</i>)	0.0367	0.0490	0.0655
<i>wR</i> 2 (<i>F</i> ²) ^a , all data	0.0823	0.1089	0.1569
<i>S</i> (<i>F</i> ²) ^a , all data	1.062	1.000	1.116

$$^a = R1(F) = \Sigma(|F_o| - |F_c|) / \Sigma|F_o| ; wR2(F^2) = [\Sigma w(F_o^2 - F_c^2)^2 / \Sigma w F_o^4]^{1/2} ; S(F^2) = [\Sigma w(F_o^2 - F_c^2)^2 / (n + r - p)]^{1/2}$$

Table 5.3.7-2. Summary of the *in situ* variable temperature single-crystal data of **5(Br)·toluene** and **5(Br)·p-xylene**

	5(Br)·toluene	5(Br)·toluene	5(Br)·p-xylene	5(Br)·p-xylene
	tris-(4-bromophenoxy)- triazine toluene solvate	tris-(4-bromophenoxy)- triazine toluene solvate	tris-(4-bromophenoxy)- triazine p-xylene solvate	tris-(4-bromophenoxy)- triazine p-xylene solvate
	$C_{21}H_{12}Br_3N_3O_3$	$C_{21}H_{12}Br_3N_3O_3$	$C_{21}H_{12}Br_3N_3O_3$	$C_{21}H_{12}Br_3N_3O_3$
Crystal habit	Rhombohedral	Rhombohedral	Rhombohedral	Rhombohedral
Crystal colour	Colourless	Colourless	Colourless	Colourless
Crystal size (mm)	0.26 × 0.12 × 0.12	0.26 × 0.12 × 0.12	0.33 × 0.06 × 0.06	0.33 × 0.06 × 0.06
Crystal system	Hexagonal	Hexagonal	Hexagonal	Hexagonal
Space group	$P6_3/m$	$P6_3/m$	$P6_3/m$	$P6_3/m$
<i>a</i> (Å)	15.4995(5)	15.4975(5)	15.635(6)	15.657(1)
<i>b</i> (Å)	15.4995(5)	15.4975(5)	15.635(6)	15.657(1)
<i>c</i> (Å)	6.8263(2)	6.8271(2)	6.797(3)	6.9208(5)
α (°)	90	90	90	90
β (°)	90	90	90	90
γ (°)	120	120	120	120
<i>V</i> (Å ³)	1420.2(1)	1420.0(1)	1439(1)	1469.3(2)
Density (g cm ⁻³)	1.389	1.389	1.371	1.343
Temperature (K)	100	100	100	100
<i>m</i> (mm ⁻¹)	5.454	5.454	5.382	5.271
Wavelength (Å)	1.54178	1.54178	1.54178	1.54178
2 θ range (°)	6.584 to 132.94	6.586 to 132.958	6.528 to 104.534	6.518 to 104.336
Reflns. collected	5961	5998	1225	3255
Independent reflns. [<i>R</i> _{int}]	912 [0.0474]	912 [0.0411]	584 [0.0585]	607 [0.0479]
Reflns. used in refinement, <i>n</i>	912	912	584	607
LS parameters, <i>p</i>	74	74	54	54
Restraints, <i>r</i>	0	0	0	0
<i>R</i> 1 (<i>F</i>) ^a / >2.0 σ (<i>I</i>)	0.0645	0.0648	0.0935	0.0265
<i>wR</i> 2 (<i>F</i> ²) ^a , all data	0.1436	0.1429	0.2183	0.598
<i>S</i> (<i>F</i> ²) ^a , all data	1.276	1.306	1.117	1.089

$$^a R1(F) = \sum(|F_o| - |F_c|) / \sum|F_o| ; wR2(F^2) = [\sum w(F_o^2 - F_c^2)^2 / \sum w F_o^4]^{1/2} ; S(F^2) = [\sum w(F_o^2 - F_c^2)^2 / (n + r - p)]^{1/2}$$

Chapter 6:

Overall Conclusions



6.1 Overall Conclusions

The first two research chapters within this thesis directly followed on from the work of Takamizawa¹ and Takahashi² with the production of a series of 1D copper paddlewheel coordination polymers $[\text{Cu}_2(4\text{-Xbz})_4(\text{Ypyz})]_n$ (bz = benzoate, pyz = pyrazine, X = I, Br, Cl or F and Y = H or NH₂). In chapter 2 it was demonstrated that the pyrazine coordination polymers displayed halogen dependent gaseous guest inclusion, with the gate pressure of the materials being dependent on the halogen-bonding interactions. This work also involved extensive *in situ* powder and single-crystal diffraction studies with crystalline materials being exposed to increasing (and decreasing) pressures of CO₂. These *in situ* studies demonstrated that uptake of CO₂ occurred through a shifting apart of polymer chains with minimal compression or elongation of the polymer chains; this also led to a disruption of the inter-polymer halogen-bonding interactions. Guest inclusion also resulted in a straightening of the bridging benzoates with the $\text{Cu}_{\text{cent}} \cdots \text{O}_{2\text{cent}} \cdots \text{ring}_{\text{cent}}$ angles tending to 180°. Guest modelling also revealed guest sites consistent with those observed crystallographically by Takamizawa.¹ Chapter 3 followed on from this work, and the themes present in the work by Takamizawa,¹ with the use of a functionalised pyrazine linker (aminopyrazine). The presence of the amino group resulted in a lack of interpenetration for the iodo system (**3.1(I)**) and interpenetration for the three other halogens (**3.2(Br)**, **3.3(Cl)** and **3.4(F)**) isostructural to the pyrazine analogues (**2.2(Br)**, **2.3(Cl)** and **2.4(F)**). The aminopyrazine linker did however result in solvate materials being formed, which led to the exploration of alternate synthetic routes and desolvation studies to obtain solvent free materials. The aminopyrazine linker also resulted in a shifting of the gate pressure to lower relative pressures in comparison to the pyrazine analogues, as well as uptake of N₂ in the bromo system (**3.2(Br)**) which did not occur in the pyrazine analogue (**2.2(Br)**). The iodo system (**3.1(I)**) although demonstrating a loss of crystallinity upon solvent removal did display inclusion of CO₂ by volumetric gas adsorption, suggesting some form of 3rd generation porosity.³ Following these volumetric studies a series of *in situ* powder and single-crystal diffraction studies were performed on crystalline materials with increasing and decreasing pressures of gas (CO₂ and N₂) being applied to the isostructural systems to chapter 2 (**3.2(Br)**, **3.3(Cl)** and **3.4(F)**). These diffraction studies demonstrated a similar dynamic motion to the pyrazine analogues with polymer chains moving apart with minimal polymer chain compression or elongation. Guest modelling within these systems also demonstrated that the presence of the amino functionality had minimal effect on the guest site, with gases being observed in the same cleft as the pyrazine analogues. This work, as a whole, was a good demonstration of how functionalisation can be successfully employed to tailor the porous properties of a family of 1D coordination polymers.

The second half of this work focused designing porosity within molecular crystals. This work focused on the exploitation of two key packing traits. Firstly the promotion of inefficient packing through stellation with the use of rigid groups protruding from a central point or surface. Secondly halogen functional groups were used to promote inefficient packing through favourable intermolecular interactions. In chapter 4 a series of stellated clusters ($[\text{Cr}_3\text{O}(4\text{-Xbz})_6(\text{MeOH})_3][\text{NO}_3]$, X = I, Br and Cl) were explored for the inclusion of CO₂. It was observed that all three systems formed the same 2D halogen-bonding network, with solvent present

between the halogen-bonded layers. Following desolvation studies it was concluded that in the case of stronger halogen-bonded networks (**4.1(I)** and **4.2(Br)**) solvent could be removed at room temperature without loss of single-crystal crystallinity. Despite solvent loss being achieved at room temperature it was also observed that a further phase transformation occurred when powder samples were stored out of solvent over prolonged periods. This phase transformation did, in turn, have an effect on the quantity of CO₂ included in all three materials. Crystalline samples of the three materials were then exposed to increasing and decreasing pressure of CO₂ in an attempt to understand how uptake of CO₂ occurred. These studies demonstrated that uptake occurred through a moving apart of 2D halogen-bonded layers as well as a lateral expansion of the halogen-bonded layer in one direction. The final chapter focused on the inclusion compound tris-(4-bromophenoxy)-triazine (**5(Br)**) which had been previously reported in three distinct phases.⁴ This work looked to demonstrate the phase transformations that occur between the two guest including phases and the guest excluding phase. It was initially demonstrated that liquid assisted grinding (LAG) could be successfully employed to screen a large variety of solvents. These mechanochemical LAG experiments not only identified the solvents that produced the two desired guest-including phases, but also identified a previously unreported guest-including phase (**5(Br)-CHCl₃**). Following solvent screening it was then demonstrated that the channel phase, with channels running through the crystalline material, lost solvent at lower temperatures than the cavity phase, which held solvent in discrete cavities, with the use of variable temperature *in situ* powder diffraction studies and thermogravimetric analysis. The *in situ* diffraction studies demonstrated that solvent loss occurred with a phase transformation from the channel or cavity phases to the closed phase. Interestingly solvothermal synthesis with *m*-xylene produced both channels and cavities which, upon heating, led to an initial loss of the channel phase and a phase pure cavity phase with further heating leading to the formation of the closed phase. It was also demonstrated that the previously unreported chloroform-including phase (**5(Br)-CHCl₃**) underwent a single-crystal-to-single-crystal phase transformation to the closed phase, whereas as all other inclusion phases lost single crystal crystallinity.

Overall this work has demonstrated that halogen functionality can be used to successfully tailor the gas sorption properties of a family of materials (chapters 2 and 3) and the same functionality can be employed to promote inefficient packing through favourable halogen-bonding interactions

6.2 References

- 1 S. Takamizawa, E. I. Nataka, T. Akatsuka, R. Miyake, Y. Kakizaki, H. Takeuchi, G. Maruta and S. Takeda, *J. Am. Chem. Soc.*, 2010, **132**, 3783–3792.
- 2 K. Takahashi, N. Hoshino, T. Takeda, S. Noro, T. Nakamura, S. Takeda and T. Akutagawa, *Inorg. Chem.*, 2015, **54**, 9423–9431.
- 3 S. Kitagawa and K. Uemura, *Chem. Soc. Rev.*, 2005, **34**, 109–119.
- 4 V. G. Saraswatula, M. A. Bhat, S. Bhattacharya and B. K. Saha, *J. Chem. Sci.*, 2014, **126**, 1265–1273.

